PHASE-AVERAGED STEREO-PIV FLOW FIELD AND FORCE/MOMENT/MOTION MEASUREMENTS FOR SURFACE COMBATANT IN PMM MANEUVERS

by

Hyunse Yoon

A thesis submitted in partial fulfillment
of the requirements for the Doctor of
Philosophy degree in Mechanical Engineering
in the Graduate College of
The University of Iowa

December 2009

Thesis Supervisor: Professor Frederick Stern
Associate Research Engineer Joseph Longo

Graduate College
The University of Iowa
Iowa City, Iowa

CERTIFICATE OF APPROVAL

_____

PH.D. THESIS

_____

This is to certify that the Ph.D. thesis of

Hyunse Yoon

has been approved by the Examining Committee
for the thesis requirement for the Doctor of Philosophy
degree in Mechanical Engineering at the December 2009 graduation.

Thesis Committee: _____
Frederick Stern, Thesis Supervisor

_____
Joseph Longo, Thesis Co-Supervisor

_____
H. S. Udaykumar

_____
Albert Ratner

_____
Larry Weber

To Woon

An egg that struggles inside out of the shell becomes a bird; an egg that is helped out of the shell becomes someone's morning breakfast.

An elder brother of my father, the great mentor

ACKNOWLEDGMENTS

This research was sponsored by the Office of Naval Research under Grant N00014-01-1-0073 under the administration of Dr. Pat Purtell whose support is greatly appreciated. The author also appreciates Dr. Kihan Kim at the Office of Naval Research for his kind encouragement.

The author is very grateful for the opportunity and guidance provided by Dr. Fred Stern. It is an honor for the author to have had the chance to study under super vision of Dr. Fred Stern.

The author is extremely thankful for the opportunity to work closely with Dr. Joe Longo. The assistance and mentoring provided by Dr. Joe Longo in performing this research is invaluable.

Invaluable assistance was provided by the IIHR mechanical and electronic shops in support of this research. The author would like to give special thanks to the University of Iowa mechanical and civil engineering undergraduate students who helped the data acquisition phase of this study.

The author wishes to thank Mr. Seokcheon Go of Hyundai Heavy Industry, who was a visiting scholar to IIHR in 2006, for his invaluable expertise and wisdom in ship model testing and for his mentoring.

The most important thanks are to my wife Woon and my children Taejune and Taelim for their patience to put up with this humble period of their lives, far away from home country and waiting for me to finish. Lastly, great thanks are to my parents and parents-in-law from the bottom of my heart for their support and their heartbreaking time missing offspring for years.

ABSTRACT

Towing-tank experiments are performed for a surface combatant as it undergoes static and dynamic planar motion mechanism maneuvers in calm water. The data includes global forces/moment/motions and phase-averaged local flow-fields, and uncertainty assessment. The geometry is DTMB model 5512, which is a 1/46.6 scale geosym of DTMB model 5415, with L = 3.048 m. The experiments are performed in a 3.048 × 3.048 × 100 m towing tank. The measurement system features a planar motion mechanism, a towed stereoscopic particle image velocimetry, a Krypton contactless motion tracker, and a 6-component loadcell. The forces/moment and UA are conducted in collaboration with two international facilities (FORCE and INSEAN), including overlapping tests using the same model geometry but with different scales. Quality of the data is assessed by monitoring the statistical convergence. Uncertainty is assessed following the ASME Standards (1998 and 2005). Hydrodynamic derivatives are determined from the forces/moment data by using the Abkowitz (1966) model, with two different '*Multiple-Run* (MR)' and '*Single-Run* (SR)' methods. Hydrodynamic derivatives are compared between the facilities data and as well between different mount conditions. The results indicate that the MR method is more rigorous than the SR that gives considerably larger errors in reconstructing the forces/moment, particularly when the PMM motion is small; the scale effect is small for sway derivatives whereas considerable for yaw derivatives; the linear derivatives values are less sensitive with the mount conditions, whereas the non-linear derivatives are considerably different between the mount conditions (fixed vs. free) with correlated with the heave, pitch, and roll motions. Phase-averaged flowfield results indicate maneuvering-induced vortices and their interactions with the turbulent boundary layer. The test program is undertaken to create a validation dataset for unsteady Reynolds-averaged Navier Stokes maneuvering simulations.

TABLE OF CONTENTS

LIST OF TABLES

Table

LIST OF FIGURES

Figure

CHAPTER 1 INTRODUCTION

Predictions of ship-maneuvering performance have been one of the most challenging topics in ship hydrodynamics research because of its highly complex unsteady and non-linear nature. Due to the lack of analytical methods for ship maneuverability, maneuvering predictions have traditionally relied on either empirical methods using database or experimental model tests. The empirical database methods usually use mathematical model and maneuvering coefficients based on either empiricism or mixed semi-theoretical and semi-empirical methods. The methods include such as the cross flow drag model (Hooft, 1994), database regression methods (such as, Wagner Smitt, 1971, Norrbin, 1971, Inoue et al. 1981, Clarke et al., 1983, and Oltmann, 1992), the Kijima method (Kijima et al., 2003), and more recently the combined slender body and the cross flow drag theories (Martinussen et al., 2008, and Toxopeus et al., 2008). The empirical database methods are relatively simple and quick to use, however, typically these methods are only effective when main dimensions of the ship of interest are in the database and the accuracy of predictions is often limited by the sensitivity of the parameters used in the regressions. Experimental model test method includes free and captive model tests. Free model test (e.g., Martinussen and Linnerrud, 1987) is using a scaled model that is self-propelled and –steered. For the test, the model performs definitive maneuvers such as spiral, zigzag, or turning maneuvers. Free model test is usually conceived as the closest to reality (except for scale effect) as no mathematic model or assumption is made. However, usually free model test yields only the final results/information, thus the test results may be less insightful to the individual maneuvering factors. Recent studies to extract more information from the free model test results, so-called the system identification method, show progresses by using either mathematical models (Oltmann, 2000, Depascale et al., 2002, Viviani et al., 2003, Aryszuk, 2003, and Yoon et al., 2003) or a Neural Network logic (Hess and Faller, 2000, Moreira and Soares, 2003, and Hess et al., 2008). On the

other hand, captive model test may comprise of oblique towing test, rotating arm test (or circular motion mechanism, CMT), and planar motion mechanism (PMM) test (Gertler, 1966, Strøm-Tejsen, J. and Chislett, M.S., 1966). Captive model test is based on mathematical modeling of the ship motion equations, from which hydrodynamic derivatives (or maneuvering coefficients) of the mathematic model are determined experimentally.

Recently, computational fluid dynamics (CFD) based methods have shown promise for computing complex hydrodynamic forces for steady and unsteady maneuvers. Significant progress has been made toward this goal by applying Reynolds-averaged Navier-Stokes (RANS)-based CFD codes to static maneuvers (Tahara et al., 2002, Simonsen and Stern, 2003a, b and c, Cura Hochbaum and Vogt, 2003, Toxopeus, 2006, Simonsen et al., 2006, Simonsen and Stern, 2006, Carrica et al., 2006, Xing et al., 2007, Bhushan et al., 2007), to dynamic maneuvers (Kim and Rhee, 2002, Burg and Marcum, 2003, Di Mascio and Broglia, 2003, Di Mascio et al., 2004, Broglia et al., 2006, Cura-Hochbaum, 2006, Dimascio et al., 2007, Wilson et al., 2007, Sakamoto et al., 2009), and to trajectories (Pankajakshan et al., 2002, Jensen et al. 2004) or more direct six-degree-of-freedom (6DOF) maneuvering predictions (Carrica and Stern, 2008), with generally good agreements with experimental data. The CFD simulations provide more insight to the entire flow structure around the hull, and the simulation results can be used to compute the forces and moment acting on the hull and to determine hydrodynamic derivatives. Although RANS methods are considered promising, they are still challenged by difficulties associated with time-accurate schemes, 6DOF ship motions, the implementations of complex hull appendages and propulsors, and environmental effects such as wind, waves, and shallow water. Furthermore, to be accepted as a credible simulation tool by end-users such as industry or navy, and ultimately to be used for simulation-based design (SBD), they are required to be verified and validated (V&V, Stern et al., 2001) for practical ship geometries and conditions. V&V and benchmarking of unsteady RANS for ship hydrodynamics, however, as well remains a challenge due in part to lack of available

experimental fluid dynamics (EFD) validation data, especially for ship motions and maneuvering.

To meet the demands on EFD validation data, procurement of detailed global and local flow benchmark EFD data for fluid physics, model development, and validation of RANS ship hydrodynamics CFD codes has been an ongoing effort since 1970's. Recent efforts have focused on modern tanker (KVLCC1 and KVLCC2), container (KCS), and surface combatant (DTMB 5415) hull forms, as per the Gothenburg 2000 Workshop (Larsson et al., 2003) and Tokyo 2005 Workshop (Hino et al., 2005). Kim et al. (2001) and Lee et al. (2003) provided steady-flow data for KVLCC2 and KCS. For DTMB 5415, data procurement has been part of an international collaboration between IIHR[1], INSEAN[2], and DTMB[3], more than 10 years. Initially steady-flow data were procured, including rigorous uncertainty analysis (Longo et al., 2005), identification of facility biases (Stern et al., 2000, and Stern et al., 2005), mean flow map (Olivieri et al, 2001), steady nominal wake PIV (Gui et al, 2001a), and propeller-hull interaction (Ratcliffe et al., 2001). Subsequently, unsteady-flow data was procured, including wave breaking (Olivieri et al., 2004), forward-speed diffraction forces, moment, and wave pattern (Gui et al., 2001b and 2002) and phase-averaged PIV nominal wake (Longo et al., 2007) and pitch and heave tests (Irvine et al., 2008) in regular head waves. More recent effort has been made at the SMMAN 2008 Workshop (Stern et al., 2008). The purpose of the workshop was to benchmark the prediction capabilities of different ship maneuvering simulation methods including the systems- and CFD based methods through comparisons with results. For SIMMAN 2008, the same tanker (KVLCC), container ship (KCS), and

---

[1] IIHR-Hydroscience and Engineering, University of Iowa, Iowa City, IA.

[2] Instituto Nazionale per Studi ed Esperienze di Architettura Navale, Rome, Italy.

[3] Naval Surface Warfare Center/Carderock Division (formerly David Taylor Model Basin), Bethesda, MD.

surface combatant (DTMB 5415) hull forms are used as for the earlier Gothenburg 2000 and Tokyo 2005 Workshops, however, the focus has been on benchmarking the maneuvering prediction capability. The international collaboration for captive and free model EFD validation data involves 11 International Towing Tank Conference (ITTC) institutions and ten countries from Europe, Asia, and America. The benchmark EFD data included PMM and free model tests for KVLCC, PMM/CMT and free model tests for KCS, and free mode test with an appended model and PMM test with bare model for DTMB 5415. Particularly, the PMM test for DTMB bare model (the present work) was in collaboration between IIHR, FORCE[4], and INSEAN including uncertainty analysis. The SIMMAN 2008 Workshop results demonstrated the potential of RANS simulations to provide data fully equivalent to PMM/CMT model test data and a possibility of direct 6DOF maneuvering simulations. However, the workshop has also concluded that more EFD benchmark data is needed including uncertainty analysis for more quantitative verification and validation.

PIV studies for ship velocity fields have been conducted for various specialized purposes, may or may not be directly intended as benchmark data for RANS simulations (mainly as per reviewed by Longo et al., 2004). Dong et al. (1997) measured the bow flow of a 3.05 m ship model in a towing tank, from which the authors investigated the cross plane vector fields and considerable vorticity entrained into the toe of the bow wave. Roth et al. (1999) studied the mean and turbulent bow flow of a 7.01 m ship model including convergence test. Paik et al. (2004) conducted PIV analysis of flow around a container ship model with a rotating propeller. PIV studies have also been made for submarine applications. Fu et al. (2002) studied dominant cross-flow separation induced by a 5.18 m submarine model in a turn. Atsavapranee et al. (2004) presented stereo PIV

[4] Force Technology (formerly Danish Maritime Institute, DMI), Lyngby, Denmark.

measurements performed on a submarine towed with steady drift angle. Many of PIV studies as well have been performed for propeller wake flow. Di Felice and De Gregorio (2000) investigated the turbulent wake of a 5.41 m ship model equipped with two, four-bladed propellers in a circulating water channel, at a range of phase angles. Calcagno et al. (2002) used stereoscopic PIV in a circulating water tunnel to investigate the phase-averaged turbulent propeller wake flow of a 6.096 m ship model equipped with a 0.222 m diameter, 5-bladed propeller. Controni et al. (2000) and Di Felice et al. (2000) investigated the phase-averaged wake flow of two, four-bladed propellers in a cavitation tunnel. Judge et al. (2001) measured tip leakage vortices from a 0.8506 m diameter, three-bladed, ducted rotor with PIV. Lee et al. (2004) measured three-component velocity field of propeller wake using stereo PIV.

The present study is to provide benchmark EFD data and UA for DTMB model 5512, a geosym (L = 3.048 m) of DTMB model 5415 for the US Navy DDG51. The EFD data includes time histories of global forces and moment and motion measurements and phase-averaged SPIV local flow velocity and turbulent Reynolds stress field measurements together with their UA. The measurement system features a custom design comprised of a PMM for captive model testing with an integrated stereoscopic particle image velocimetry (SPIV) for procuring instantaneous and phase-averaged flow maps. The PMM consists of a PMM sway/yaw motion mechanism unit, an integrated SPIV system with an automated traverse, roll/pitch/heave free/fixed mounts, and a six-component load cell, and a Krypton contactless motion tracker. The approach is complementary CFD, EFD, and uncertainty assessment. CFD is used to guide EFD, EFD is used for validation and model development, and lastly CFD is validated and fills in sparse data for complete documentation and diagnostics of the flow. Forces and moment and motions are measured for several towing speeds and mounting conditions for static drift and dynamic maneuvering tests. Several drift angles, frequencies, amplitudes, and yaw rates are investigated. The forces and moment measurements and UA are conducted in collabora-

tion with FORCE, INSEAN, and the 24th-25th ITTC Maneuvering Committee, including overlapping tests using the same model geometry for validation of procedures and identification of facility biases and scale effects. Results will be presented for both static and dynamic PMM, in the latter case including pure sway, pure yaw, and yaw and drift tests. The current project builds on previous work including forward-speed diffraction problem (Gui et al. 2001a; Gui et al. 2002; Longo et al. 2005), pitch and heave motions (Irvine et al., 2008), and investigations of roll motions with and without bilge keels (Bishop et al. 2004; Felli et al. 2004; Irvine et al. 2004) and is part of a collaborative effort between IIHR, DTMB, and INSEAN which has been ongoing as part of an international project for 6DOF ship hydrodynamics research. The overall focus is on benchmark CFD validation data for surface combatant DTMB model 5415 (Stern et al., 2000).

CHAPTER 2 BACKGROUND THEORY

2.1 Overview of Maneuvering Simulations

The Maneuvering Committee (MC) of the 24th International Towing Tank Conference (ITTC) reviewed state-of-the-art progress in maneuvering predictions, and categorized typical maneuvering prediction methods into three groups: No Simulation, System Based Simulation, and CFD Based Simulation methods.

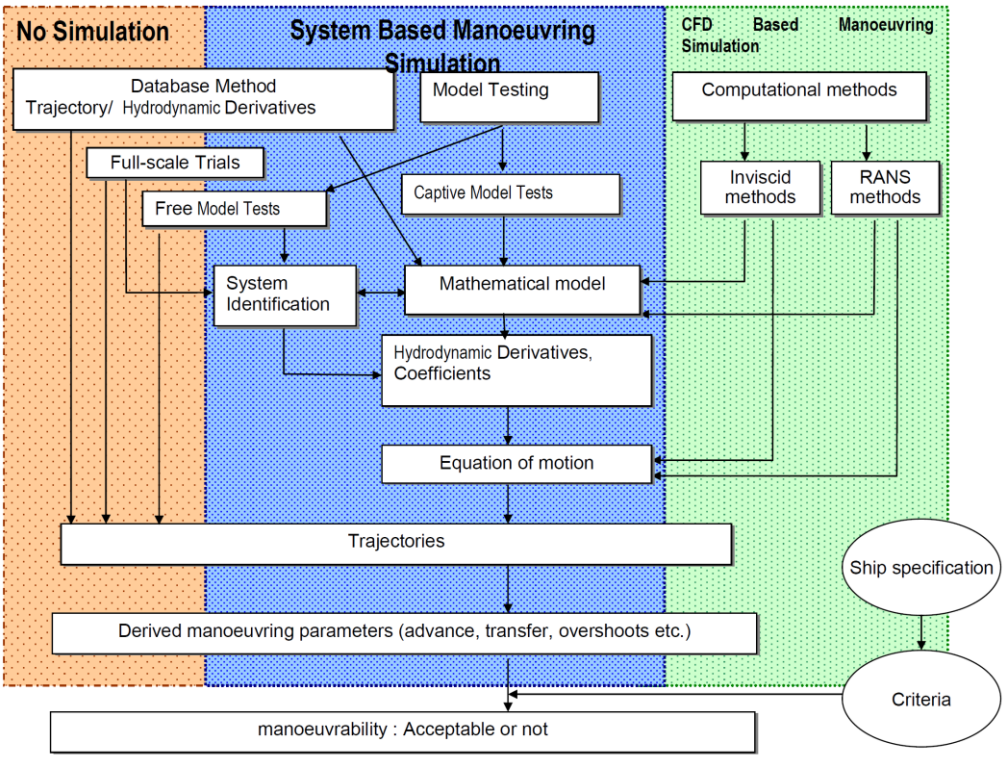

Figure 2-1 Overview of Maneuvering prediction methods (Proceedings of 25th ITTC, Vol. I, pp. 145).

The No Simulation method needs no mathematical model and thus no hydrodynamic derivative or maneuvering coefficient. Maneuvering parameters such as ship advance, transfer, overshoot, and etc. are directly measured from the full-scale trial or mod-

el-scale free-model test by measuring the ship trajectories or by using a database of existing full- and/or model-scale data.

The System Based Simulation method, by contrast, simulates the ship trajectories by solving the motion equations using appropriate mathematical modeling along with hydrodynamic derivatives (or maneuvering coefficients). This method includes 1) database, 2) model testing, and 3) system identification methods. First, the database method establishes an empirical formula or regression equations from databases of full- and/or model-scale test results to obtain hydrodynamic derivatives (Oltmann 1992, Wagner-Smitt 1971, Norrbin 1971, Inoue et al. 1981, Clarke et al. 1983, Kijima et al. 1990 and 1993). The database can be also combined with theoretical models such as the Japanese Mathematical Model Group (MMG) model (Kijima et al. 1993) or the cross-flow drag model (Hooft, 1994). These methods are simple and quick to use, but the prediction accuracy and/or reliability can be limited when the ship dimensions are outside the database. Next, the model test method includes free- and captive-model tests. For free model tests (Martinussen et al. 1987), a self-propelled scale model ship is remotely controlled performing definitive maneuvers such as turning circle, zig-zag, and reverse spiral to evaluate turning performance and course keeping stability. This method is direct and effective since the maneuvering parameters are directly obtained without simulation, but with issues about viscous scale effects (Burcher 1975). On the other hand, the captive model tests are based on mathematical modeling of motion equations. For the tests, a model-scale ship is forced to move in prescribed motions over a range of parameters such as drift angle, sway/yaw motion amplitude and frequency, rudder angle, etc. to obtain the relevant hydrodynamic derivatives. Details of the captive model tests are provided in the following Section 2.3. Lastly, the system identification method (Artyszuk 2003, Hess and Faller 2000, Moreira and Soares 2003, Oltmann 2003, Viviani et al. 2003, Depascale et al. 2002, Yoon et al. 2003) obtains hydrodynamic derivatives from full-scale sea trial or free-model test results using measured ship motion and rudder angle as input parameters.

CFD Based Simulation method also simulates the ship trajectory to predict the maneuvering parameters similarly as the System Based Simulation method but by using numerical schemes to evaluated the hydrodynamic derivatives of the mathematic models used or to solve the motion equations directly.

2.2 Mathematic Modeling and Hydrodynamic Derivatives

The generalized motion equations for a rigid vessel in a ship-fixed, non-inertial frame of reference xyz that is moving relative to an Earth-fixed, inertial reference frame $x_E y_E z_E$ (Fig. 2-2) can be derived as (Fossen 1994):

$$m[\dot{u} - rv + wq - x_G(q^2 + r^2) + y_G(pq - \dot{r}) + z_G(pr + \dot{q})] = X \quad (2.1a)$$

$$m[\dot{v} - wp + ur - y_G(r^2 + p^2) + z_G(qr - \dot{p}) + x_G(qp + \dot{r})] = Y \quad (2.1b)$$

$$m[\dot{w} - uq + vp - z_G(p^2 + q^2) + x_G(rp - \dot{q}) + y_G(rq + \dot{p})] = Z \quad (2.1c)$$

$$I_x\dot{p} + (I_z - I_y)qr + m[y_G(\dot{w} - uq + vp) - z_G(\dot{v} - wp + ur)] = K \quad (2.1d)$$

$$I_y\dot{q} + (I_x - I_z)rp + m[z_G(\dot{u} - vr + wq) - x_G(\dot{w} - uq + vp)] = M \quad (2.1e)$$

$$I_z\dot{r} + (I_y - I_x)pq + m[x_G(\dot{v} - wp + ur) - y_G(\dot{u} - vr + wq)] = N \quad (2.1f)$$

The origin of the ship-fixed reference frame is located at the mid-ship position. The x, y, and z axes correspond to the longitudinal, lateral, and vertical direction of the vessel, respectively, so that the products of moment of inertia such as I_{xy}, I_{xz}, or I_{yz} vanish from the motion equations. In the equations, X, Y, Z are the external forces acting on the vessel in surge, x, sway, y, and heave, z directions, respectively. K, M, N are the external angular moments in roll, ϕ, pitch, θ, and yaw, ψ, directions, respectively. m is the mass of the vessel and I_x, I_y, I_z are the moments of inertia of the vessel with respect to each axis. x_G, y_G, z_G are the location of the center of gravity of the vessel. u, v, w are surge, sway, and heave velocities, $\dot{x}$, $\dot{y}$, $\dot{z}$, respectively, and $\dot{u}$, $\dot{v}$, $\dot{r}$ are surge, sway, and heave

accelerations, $\ddot{x}$, $\ddot{y}$, $\ddot{z}$, respectively. p, q, r are roll, pitch, yaw rates, $\dot{\phi}$, $\dot{\theta}$, $\dot{\psi}$, respectively, and $\dot{p}$, $\dot{q}$, $\dot{r}$ are roll, pitch, yaw accelerations, $\ddot{\phi}$, $\ddot{\theta}$, $\ddot{\psi}$, respectively.

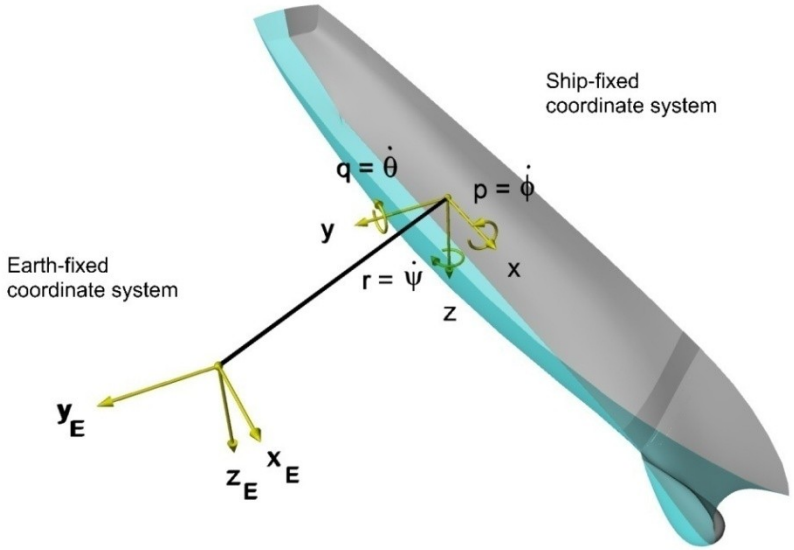

Figure 2-2 Earth- and ship-fixed coordinate systems.

For maneuvering applications of the equations (2.1) for surface ships moving on unbounded, calm, and deep water, it is typically assumed that the heave, roll, and pitch motions can be neglected such that $w = p = q = \dot{w} = \dot{p} = \dot{q} = 0$ and that the vessel geometry has the xz-plane symmetry, i.e. $y_G = 0$. Then, the equations reduce to the following equations:

$$m(\dot{u} - rv - x_G r^2) = X \tag{2.2a}$$

$$m(\dot{v} + ur - x_G \dot{r}) = Y \tag{2.2b}$$

$$I_z \dot{r} + m x_G (\dot{v} + ur) = N \tag{2.2c}$$

for surge, sway, and yaw, respectively. In general the external forces and moment X, Y, N at the right hand sides of the equations (2.2) include hydrodynamic forces due to the

surrounding fluid, control surface forces such as rudder forces, and propulsion forces such as propeller forces, which need to be described in proper mathematical forms for the motion equations to be solved. One of the common mathematic modeling of those forces is by assuming that the forces are functions of ship motion parameters u, v, r, $\dot{u}$, $\dot{v}$, $\dot{r}$ and rudder deflection angle δ (Abkowitz, 1964) based on the 'quasi-steady state' assumption which states that the value of the forces at any instant depends on the motion parameters defining the instantaneous motion of the vessel.

$$\left.\begin{matrix} X \\ Y \\ N \end{matrix}\right\} = f(u, v, r, \dot{u}, \dot{v}, \dot{r}, \delta) \tag{2.3}$$

Abkowitz (1964) also proposed to use a 3rd-order Taylor Series expansion of the equation (2.3) with following additional assumptions:

a) Forces and moments have appropriate port and starboard symmetry except for a constant force and moment caused by the propeller, and
b) There are no second- or higher-order acceleration terms, and that cross-coupling between acceleration and velocity parameters is negligible,

as per re-stated by Strom-Tejsen and Chislett (1966). Then, for small disturbances of the ship motions from a reference state, i.e. steady straight advancing with a constant speed U, the equation (2.3) are written as following (Strom-Tejsen and Chislett 1966):

$$\begin{aligned} X = {} & X_* + X_{\dot{u}}\dot{u} + X_u\Delta u + X_{uu}\Delta u^2 + X_{uuu}\Delta u^3 + \\ & X_{vv}v^2 + X_{rr}r^2 + X_{\delta\delta}\delta^2 + X_{vvu}v^2\Delta u + X_{rru}r^2\Delta u + X_{\delta\delta u}\delta^2\Delta u + \\ & X_{vr}vr + X_{v\delta}v\delta + X_{r\delta}r\delta + X_{vru}vr\Delta u + X_{v\delta u}v\delta\Delta u + X_{r\delta u}r\delta\Delta u \end{aligned} \tag{2.4a}$$

$$\begin{aligned} Y = {} & Y_* + Y_u\Delta u + Y_{uu}\Delta u^2 + Y_{uuu}\Delta u^3 + \\ & Y_{\dot{v}}\dot{v} + Y_v v + Y_{vvv}v^3 + Y_{vrr}vr^2 + Y_{v\delta\delta}v\delta^2 + Y_{vu}v\Delta u + Y_{vuu}v\Delta u^2 + \\ & Y_{\dot{r}}\dot{r} + Y_r r + Y_{rrr}r^3 + Y_{rvv}rv^2 + Y_{r\delta\delta}r\delta^2 + Y_{ru}r\Delta u + Y_{ruu}r\Delta u^2 + \end{aligned}$$

$$Y_\delta \delta + Y_{\delta\delta\delta}\,\delta^3 + Y_{\delta vv}\,\delta v^2 + Y_{\delta rr}\,\delta r^2 + Y_{\delta u}\,\delta\Delta u + Y_{\delta uu}\,\delta\Delta u^2 +$$

$$Y_{\delta\delta\delta u}\,\delta^3\Delta u + \; Y_{vr\delta}\,vr\delta \tag{2.4b}$$

$$N = N_* + N_u\Delta u + N_{uu}\,\Delta u^2 + N_{uuu}\,\Delta u^3 +$$

$$N_{\dot v}\dot v + N_v v + N_{vvv}v^3 + N_{vrr}\,vr^2 + N_{v\delta\delta}\,v\delta^2 + N_{vu}\,v\Delta u + N_{vuu}\,v\Delta u^2 +$$

$$N_{\dot r}\dot r + N_r r + N_{rrr}\,r^3 + N_{rvv}\,rv^2 + N_{r\delta\delta}\,r\delta^2 + N_{ru}\,r\Delta u + N_{ruu}\,r\Delta u^2 +$$

$$N_\delta \delta + N_{\delta\delta\delta}\,\delta^3 + N_{\delta vv}\,\delta v^2 + N_{\delta rr}\,\delta r^2 + N_{\delta u}\,\delta\Delta u + N_{\delta uu}\,\delta\Delta u^2 +$$

$$N_{\delta\delta\delta u}\,\delta^3\Delta u + \; N_{vr\delta}\,vr\delta \tag{2.4c}$$

where $\Delta u \equiv u - U$ is the disturbance in surge velocity. The terms X_*, Y_*, N_* are the reference steady state values of X, Y, N, respectively. Typically, X_* is zero for ships advancing straight with a constant speed as the ship total resistance R_T is balanced by the propeller thrust T, however, Y_* and N_* may have non-zero values when the ship has a single propeller or multiple propellers rotating in the same direction. The coefficients of Taylor Series terms at the right hand sides of (2.4) with subscripts of motion parameters, such as $X_{\dot u} \equiv \partial X/\partial\dot u$ or $X_{vv} \equiv \frac{1}{2}\partial^2 X/\partial v^2$, are the reduced expressions of the Taylor Series expansion following the simplified derivative notation of SNAME (Nomenclature, 1952), so-called 'hydrodynamic derivatives' or 'maneuvering coefficients', evaluated at the reference steady state. Note that, although the Taylor Series were assumed as 3rd-order expansions, Strom-Tejsen and Chislett (1966) also used fourth-order as well for the rudder force terms such as $Y_{\delta\delta\delta u}\,\delta^3\Delta u$ and $N_{\delta\delta\delta u}\,\delta^3\Delta u$ to obtain sufficient flexibility in expressing the influence of surge velocity on the rudder action. Note also that the surge velocity expansion terms for Y and N such as $Y_u\Delta u$, $Y_{uu}\,\Delta u^2$, $Y_{uuu}\,\Delta u^3$ and $N_u\Delta u$, $N_{uu}\,\Delta u^2$, $N_{uuu}\,\Delta u^3$ in (2.4) replaced the terms $Y_{*u}\Delta u$, $Y_{*uu}\,\Delta u^2$ and $N_{*u}\Delta u$, $N_{*uu}\,\Delta u^2$, respectively, in Strom-Tejsen and Chislett (1966) as the former expressions are considered to be more consistent with the mathematical definitions of Taylor Series expansion in that the reference state values Y_* or N_* are not expanded.

2.3 PMM Tests

General descriptions and procedures of PMM tests including the static drift, pure sway, pure yaw, and yaw and drift tests and determination of hydrodynamic derivatives are provided. The procedures for rudder related tests such as static rudder, static drift and rudder, and yaw and rudder tests are not provided herein as the present research objective is focused on the PMM applications for a bare hull form, i.e. without rudders, propellers, and appendages except for bilge keels.

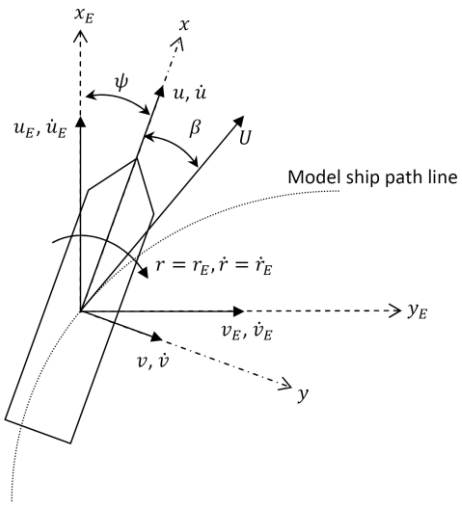

Figure 2-3 General PMM test coordinate system and motion parameters.

2.3.1 Definitions of Motions

Two coordinate systems are shown in Fig. 2-3: the Earth-fixed $x_E y_E$-coordinate system (dashed arrows) and the ship-fixed xy-coordinate system (dash-dot arrows). The Earth-fixed coordinates are fixed at the towing tank with x_E and y_E coordinates aligned with the longitudinal and lateral directions of towing tank, respectively. The ship-fixed coordinates are moving with the model with x and y coordinates aligned with the longitudinal and lateral directions of the model, respectively. For convenience, in the figure the Earth-fixed coordinate system is shown overlaid on the ship-fixed coordinate system

at a certain instant. Vectors u_E and v_E are the velocities and $\dot{u}_E$ are $\dot{v}_E$ are the accelerations of the model in the x_E and y_E directions of the Earth-fixed coordinate system, respectively; and u and v are the velocities and $\dot{u}$ and $\dot{v}$ are the accelerations of model in the x and y directions of the ship-fixed coordinate system, respectively. The advance speed U is the resultant of u_E and v_E or the resultant of u and v such that

$$U = \sqrt{u_E^2 + v_E^2} = \sqrt{u^2 + v^2} \tag{2.5}$$

always tangent to the model path line (dotted line) that is the trajectory of the mid-ship point. Drift angle, β, is defined as the model orientation with respect to U, i.e., the actual direction of model with respect to its heading, which can be written as

$$\beta = -\arctan(v/u) \tag{2.6}$$

Heading (or yaw angle) ψ is defined as the model orientation with respect to a reference direction, x_E. Note that yaw rate $\dot{\psi}$ and acceleration $\ddot{\psi}$ are identical in both the Earth-fixed and the ship-fixed coordinate systems, i.e. $r_E = r = \dot{\psi}$ and $\dot{r}_E = \dot{r} = \ddot{\psi}$. Lastly, the vector transformations between the Earth- and ship-fixed coordinate systems are given as following:

$$u = u_E \cos\psi + v_E \sin\psi \tag{2.7a}$$

$$v = -u_E \sin\psi + v_E \cos\psi \tag{2.7b}$$

$$r = r_E \tag{2.7c}$$

$$\dot{u} = \dot{u}_E \cos\psi + \dot{v}_E \sin\psi + r_E(-u_E \sin\psi + v_E \cos\psi) \tag{2.7d}$$

$$\dot{v} = -\dot{u}_E \sin\psi + \dot{v}_E \cos\psi - r_E(u_E \cos\psi + v_E \sin\psi) \tag{2.7e}$$

$$\dot{r} = \dot{r}_E \tag{2.7f}$$

2.3.2 PMM Motions

PMM motions are the forced model trajectories comprised of three basic motions x_E, y_E, and ψ described in the $x_E y_E$-coordinate system:

$$x_E = U_C t \tag{2.8}$$

$$y_E = -y_{max} \sin \omega t \tag{2.9}$$

$$\psi = -\arctan(\varepsilon \cos \omega t) + \beta \tag{2.10}$$

where U_C is the towing speed, y_{max} is the sway amplitude, and ε is the maximum tangent of model trajectory defined as

$$\varepsilon = \left(\frac{dy_E}{dx_E}\right)_{max} = \left(\frac{dy_E/dt}{dx_E/dt}\right)_{max} = \frac{y_{max}\,\omega}{U_C} \tag{2.11}$$

The x_E in (2.8) corresponds to straight advancing motion with speed U_C along the towing tank longitudinal direction. The y_E in (2.9) is a sinusoidal lateral motion with an amplitude y_{max} and frequency ω. The ψ in (2.10) is a combination of a sinusoidal yaw motion and any drift angle β. For static drift test, y_{max} = ε = ω = 0 in (2.9) and (2.10) and β is a fixed value in time, which corresponds to an oblique towing motion as shown in Fig. 2-4 (a) and (e). For pure sway test, y_{max} and ω are non-zero values in (2.9) thus a sinusoidal lateral motion but the model heading is kept in straight, i.e ψ = 0 in (2.10), as illustrated in Fig. 2-4 (b), which makes a continuously changing drift angle $\beta = \arctan(\varepsilon \cos \omega t)$ from (2.10) as shown in Fig. 2-4 (f). For pure yaw test, y_{max} and ω are non-zero in (2.9) and (2.10) similarly as pure sway test but β = 0 in (2.10), then the model is always tangent to its path-line as shown Fig. 2-4 (c) and (g). For yaw and drift test, y_{max} and ω are the same as for pure yaw test but β is set to a non-zero constant value in (2.10), which makes an asymmetric yaw motion as shown in Fig. 2-4 (d) and (h). For all tests, U_C in (2.8) is constant in time. From those model trajectories, the model velocities and accele-

rations in the Earth-fixed coordinates, i.e. $u_E = \dot{x}_E$, $v_E = \dot{y}_E$, $r_E = \dot{\psi}_E$, $\dot{u}_E = \ddot{x}_E$, $\dot{v}_E = \ddot{y}_E$, and $\dot{r}_E = \ddot{\psi}_E$, and in the ship-fixed coordinates u, v, r, $\dot{u}$, $\dot{v}$, and $\dot{r}$ as per the relationships (2.7) are summarized in Tables 2-1 and 2-2, respectively.

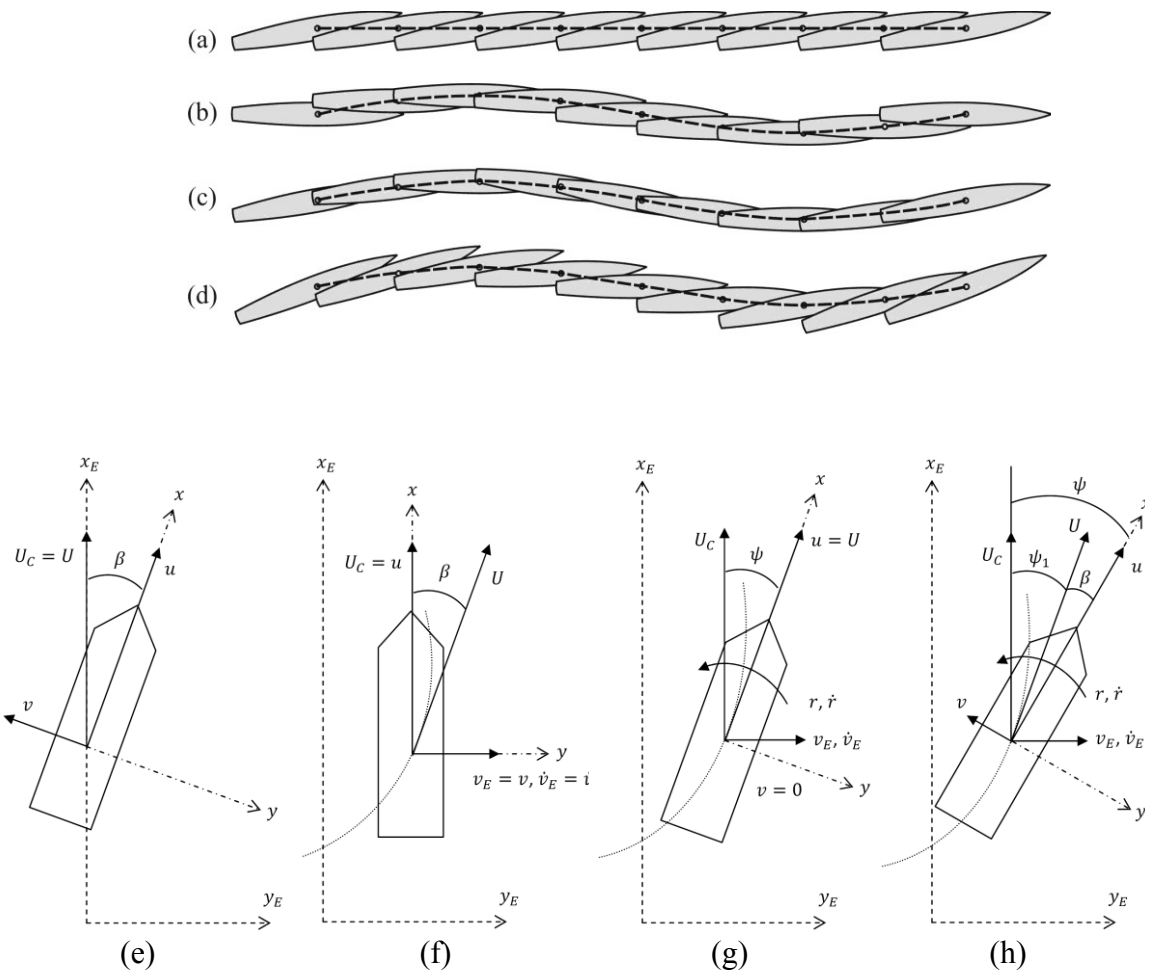

Figure 2-4 Illustrations of typical PMM motions for (a) static drift, (b) pure sway, (c) pure yaw, and (d) yaw and drift tests, and definitions of PMM motion parameters in the PMM coordinate systems for (e) static drift, (f) pure sway, (g) pure yaw, and (h) yaw and drift tests.

Table 2-1 PMM Motions in the Earth-fixed Coordinates.

Motion	Static drift	Pure sway	Pure yaw	Yaw and drift
u_E	U_C	U_C	U_C	U_C
$\dot{u}_E$	0	0	0	0
v_E	0	$-y_{max}\,\omega\cos\omega t$	$-y_{max}\,\omega\cos\omega t$	$-y_{max}\,\omega\cos\omega t$
$\dot{v}_E$	0	$y_{max}\,\omega^2\sin\omega t$	$y_{max}\,\omega^2\sin\omega t$	$y_{max}\,\omega^2\sin\omega t$
r_E	0	0	$\varepsilon\omega\sin\omega t\dfrac{1}{1+\varepsilon^2\cos^2\omega t}$	$\varepsilon\omega\sin\omega t\dfrac{1}{1+\varepsilon^2\cos^2\omega t}$
$\dot{r}_E$	0	0	$\varepsilon\omega^2\cos\omega t\dfrac{1+\varepsilon^2(1+\sin^2\omega t)}{(1+\varepsilon^2\cos^2\omega t)^2}$	$\varepsilon\omega^2\cos\omega t\dfrac{1+\varepsilon^2(1+\sin^2\omega t)}{(1+\varepsilon^2\cos^2\omega t)^2}$

Table 2-2 PMM Motions in the Ship-fixed Coordinates.

Motion	Static drift	Pure sway	Pure yaw	Yaw and drift
u	$U_C\cos\beta$	U_C	$U_C\sqrt{1+\varepsilon^2\cos^2\omega t}=u_1$	$u_1\cos\beta$
$\dot{u}$	0	0	$-U_C\omega\cdot\dfrac{\varepsilon^2\sin 2\omega t}{2\sqrt{1+\varepsilon^2\cos^2\omega t}}=\dot{u}_1$	$\dot{u}_1\cos\beta$
v	$-U_C\sin\beta$	$-y_{max}\,\omega\cos\omega t$	0	$-u_1\sin\beta$
$\dot{v}$	0	$y_{max}\,\omega^2\sin\omega t$	0	$-\dot{v}_1\sin\beta$
r	0	0	$\varepsilon\omega\sin\omega t\cdot\dfrac{1}{1+\varepsilon^2\cos^2\omega t}=r_1$	r_1
$\dot{r}$	0	0	$\varepsilon\omega^2\cos\omega t\cdot\dfrac{1+\varepsilon^2(1+\sin^2\omega t)}{(1+\varepsilon^2\cos^2\omega t)^2}=\dot{r}_1$	$\dot{r}_1$

The PMM motions, however, may violate the steady advance speed U condition for the Taylor-series expansions of hydrodynamic forces and moment shown in (2.4). If the surge $u_E = \dot{x}_E$ and sway $v_E = \dot{y}_E$ velocities from (2.8) and (2.9), respectively, are used in (2.5), then U becomes time-dependent (except for static drift case where $U = U_C$) and suggests PMM motions should be small such that

$$U = U_C\sqrt{1+\varepsilon^2\cos^2\omega t} = U_C + O(\varepsilon^2) \approx U_C \quad \text{for } \varepsilon \ll 1 \tag{2.12}$$

Then, the PMM motions summarized in Table 2-1 can be simplified as follows.

Static drift:

$$v = -U_C \sin\beta \tag{2.13}$$

Pure sway:

$$y = -y_{max} \sin\omega t \tag{2.14a}$$

$$v = -v_{max} \cos\omega t; \qquad v_{max} = y_{max}\,\omega \tag{2.14b}$$

$$\dot{v} = \dot{v}_{max} \sin\omega t; \qquad \dot{v}_{max} = y_{max}\,\omega^2 \tag{2.14c}$$

Then, drift angle β is from (6) as

$$\beta(t) = \beta_{max} \cos\omega t; \qquad \beta_{max} = \frac{y_{max}\,\omega}{U_C} \tag{2.15}$$

Pure yaw:

$$\psi = -\psi_{max} \cos\omega t; \qquad \psi_{max} = \frac{y_{max}\,\omega}{U_C} \tag{2.16a}$$

$$r = r_{max} \sin\omega t; \qquad r_{max} = \psi_{max}\,\omega \tag{2.16b}$$

$$\dot{r} = \dot{r}_{max} \cos\omega t; \qquad \dot{r}_{max} = \psi_{max}\,\omega^2 \tag{2.16c}$$

Yaw and drift:

$$\psi = -\psi_{max} \cos\omega t + \beta; \qquad \psi_{max} = \frac{y_{max}\,\omega}{U_C} \tag{2.17a}$$

$$v = -U_C \sin\beta \tag{2.17b}$$

where r and $\dot{r}$ for yaw and drift test are same as (2.16b) and (2.16c) for pure yaw test. For such small motions, i.e. $\varepsilon \ll 1$, and additionally for small β for static drift and yaw and drift tests, surge velocity $u \approx U_C$ and thus $\Delta u = u - U = 0$ for all tests.

2.3.3 Simplified Mathematic Models for PMM

For a bare model without propellers or rudders, the Abkowitz's mathematic models for hydrodynamic forces and moment shown in (2.4) can be reduced by dropping the terms related to rudder angle δ as:

$$X = X_* + X_{vv}v^2 + X_{rr}r^2 + X_{vr}vr + X_u\Delta u + X_{uu}\Delta u^2 + X_{uuu}\Delta u^3 + X_{vvu}v^2\Delta u + X_{rru}r^2\Delta u + X_{vru}vr\Delta u \quad (2.18a)$$

$$Y = Y_{\dot{v}}\dot{v} + Y_v v + Y_{vvv}v^3 + Y_{\dot{r}}\dot{r} + Y_r r + Y_{rrr}r^3 + Y_{vrr}vr^2 + Y_{rvv}rv^2 + Y_{vu}v\Delta u + Y_{vuu}v\Delta u^2 + Y_{ru}r\Delta u + Y_{ruu}r\Delta u^2 \quad (2.18b)$$

$$N = N_{\dot{v}}\dot{v} + N_v v + N_{vvv}v^3 + N_{\dot{r}}\dot{r} + N_r r + N_{rrr}r^3 + N_{vrr}vr^2 + N_{rvv}rv^2 + N_{vu}v\Delta u + N_{vuu}v\Delta u^2 + N_{ru}r\Delta u + N_{ruu}r\Delta u^2 \quad (2.18c)$$

The math-models (18) are further simplified by using the simplified motions (2.13) – (2.17) to leave terms for the variables of interest and to determine the hydrodynamic derivatives.

Static drift:

$$X = X_* + X_{vv}v^2 \quad (2.19a)$$

$$Y = Y_v v + Y_{vvv}v^3 \quad (2.19b)$$

$$N = N_v v + N_{vvv}v^3 \quad (2.19c)$$

Pure sway:

$$X = X_* + X_{vv}v^2 \quad (2.20a)$$

$$Y = Y_{\dot{v}}\dot{v} + Y_v v + Y_{vvv}v^3 \quad (2.20b)$$

$$N = N_{\dot{v}}\dot{v} + N_v v + N_{vvv}v^3 \quad (2.20c)$$

or in harmonic forms by substituting (2.14b) and (2.14c) into (2.20),

$$X = X_0 + X_{C2}\cos 2\omega t \tag{2.21a}$$

$$Y = Y_{S1}\sin \omega t + Y_{C1}\cos \omega t + Y_{C3}\cos 3\omega t \tag{2.21b}$$

$$N = N_{S1}\sin \omega t + N_{C1}\cos \omega t + N_{C3}\cos 3\omega t \tag{2.21c}$$

Pure yaw:

$$X = X_* + X_{rr}r^2 \tag{2.22a}$$

$$Y = Y_{\dot{r}}\dot{r} + Y_r r + Y_{rrr}r^3 \tag{2.22b}$$

$$N = N_{\dot{r}}\dot{r} + N_r r + N_{rrr}v^3 \tag{2.22c}$$

or in harmonic forms by substituting (2.16b) and (2.16c) into (2.22),

$$X = X_0 + X_{C2}\cos 2\omega t \tag{2.23a}$$

$$Y = Y_{C1}\cos \omega t + Y_{S1}\sin \omega t + Y_{S3}\sin 3\omega t \tag{2.23b}$$

$$N = N_{C1}\cos \omega t + N_{S1}\sin \omega t + N_{S3}\sin 3\omega t \tag{2.23c}$$

Yaw and drift:

$$X = X_* + X_{vv}v^2 + X_{rr}r^2 + X_{vr}vr \tag{2.24a}$$

$$Y = Y_v v + Y_{vvv}v^3 + Y_{\dot{r}}\dot{r} + Y_r r + Y_{rrr}r^3 + Y_{vrr}vr^2 + Y_{rvv}rv^2 \tag{2.24b}$$

$$N = N_v v + N_{vvv}v^3 + N_{\dot{r}}\dot{r} + N_r r + N_{rrr}v^3 + N_{vrr}vr^2 + N_{rvv}rv^2 \tag{2.24c}$$

or in harmonic forms by substituting (2.16b), (2.16c), and (2.17b) into (2.24),

$$X = X_0 + X_{S1}\sin \omega t + X_{C2}\cos 2\omega t \tag{2.25a}$$

$$Y = Y_0 + Y_{C1}\cos \omega t + Y_{S1}\sin \omega t + Y_{C2}\cos 2\omega t + Y_{S3}\cos 3\omega t \tag{2.25b}$$

$$N = N_0 + N_{C1}\cos \omega t + N_{S1}\sin \omega t + N_{C2}\cos 2\omega t + N_{S3}\cos 3\omega t \tag{2.25c}$$

The expressions for the harmonics X_0, X_{Sn}, X_{Cn}, Y_0, Y_{Sn}, Y_{Cn}, N_0, N_{Sn}, and N_{Cn} for n = 1, 2, or 3 in (2.21), (2.23), and (2.25) are summarized in Table 2-3.

Table 2-3. Mathematic Models in Harmonics Forms.

Pure sway models:

$$X = X_0 + X_{C2}\cos 2\omega t$$

$$Y = Y_{C1}\cos\omega t + Y_{S1}\sin\omega t + Y_{C3}\cos 3\omega t$$

$$N = N_{C1}\cos\omega t + N_{S1}\sin\omega t + N_{C3}\cos 3\omega t$$

X model	Y model	N model
$X_0 = X_* + \frac{1}{2}X_{vv}v_{max}^2$	$Y_{C1} = -\left(Y_v v_{max} + \frac{3}{4}Y_{vvv}v_{max}^3\right)$	$N_{C1} = -\left(N_v v_{max} + \frac{3}{4}N_{vvv}v_{max}^3\right)$
$X_{C2} = \frac{1}{2}X_{vv}v_{max}^2$	$Y_{S1} = Y_{\dot{v}}\dot{v}_{max}$	$N_{S1} = N_{\dot{v}}\dot{v}_{max}$
	$Y_{C3} = -\frac{1}{4}Y_{vvv}v_{max}^3$	$N_{C3} = -\frac{1}{4}N_{vvv}v_{max}^3$

Pure yaw models:

$$X = X_0 + X_{C2}\cos 2\omega t$$

$$Y = Y_{S1}\sin\omega t + Y_{C1}\cos\omega t + Y_{S3}\sin 3\omega t$$

$$N = N_{S1}\sin\omega t + N_{C1}\cos\omega t + N_{S3}\sin 3\omega t$$

X model	Y model	N model
$X_0 = X_* + \frac{1}{2}X_{rr}r_{max}^2$	$Y_{S1} = Y_r r_{max} + \frac{3}{4}Y_{rrr}r_{max}^3$	$N_{S1} = N_r r_{max} + \frac{3}{4}N_{rrr}r_{max}^3$
$X_{C2} = -\frac{1}{2}X_{rr}r_{max}^2$	$Y_{C1} = Y_{\dot{r}}\dot{r}_{max}$	$N_{C1} = N_{\dot{r}}\dot{r}_{max}$
	$Y_{S3} = -\frac{1}{4}Y_{rrr}r_{max}^3$	$N_{S3} = -\frac{1}{4}N_{rrr}r_{max}^3$

Yaw and drift models:

$$X = X_0 + X_{S1}\sin\omega t + X_{C2}\cos 2\omega t$$

$$Y = Y_0 + Y_{S1}\sin\omega t + Y_{C1}\cos\omega t + Y_{C2}\cos 2\omega t + Y_{S3}\sin 3\omega t$$

$$N = N_0 + N_{S1}\sin\omega t + N_{C1}\cos\omega t + N_{C2}\cos 2\omega t + N_{S3}\sin 3\omega t$$

X model	Y model	N model
$X_0 = X_* + X_{vv}v^2 + \frac{1}{2}X_{rr}r_{max}^2$	$Y_0 = Y_v v + Y_{vvv}v^3 + \frac{1}{2}Y_{vrr}vr_{max}^2$	$N_0 = N_v v + N_{vvv}v^3 + \frac{1}{2}N_{vrr}vr_{max}^2$
$X_{S1} = X_{vr}vr_{max}$	$Y_{S1} = Y_r r_{max} + \frac{3}{4}Y_{rrr}r_{max}^3 + Y_{rvv}r_{max}v^2$	$N_{S1} = N_r r_{max} + \frac{3}{4}N_{rrr}r_{max}^3 + N_{rvv}r_{max}v^2$
$X_{C2} = -\frac{1}{2}X_{rr}r_{max}^2$	$Y_{C1} = Y_{\dot{r}}\dot{r}_{max}$	$N_{C1} = N_{\dot{r}}\dot{r}_{max}$
	$Y_{C2} = -\frac{1}{2}Y_{vrr}vr_{max}^2$	$N_{C2} = -\frac{1}{2}N_{vrr}vr_{max}^2$
	$Y_{S3} = -\frac{1}{4}Y_{rrr}r_{max}^3$	$N_{S3} = -\frac{1}{4}N_{rrr}r_{max}^3$

2.3.4 Non-dimensionalization

Non-dimensionlization follows the *Prime-system* of SNAME (Nomenclature, 1952) for which L, L/U, and $½\rho L^2 T$ are used as the characteristic scales for length, time, and mass, respectively, where L is the ship length, U is the ship advance speed, ρ is the water density, and T is the draft of the ship. Some of the non-dimensional variables are shown below:

$$y = \frac{y}{L}; \qquad y_{max}^{'} = \frac{y_{max}}{L} \tag{2.26a}$$

$$\omega^{'} = \frac{\omega L}{U} \approx \frac{\omega L}{U_C} \tag{2.26b}$$

$$\Delta u^{'} = u^{'} - 1 = \frac{u}{U} - 1 \tag{2.26c}$$

$$\dot{u}^{'} = \frac{\dot{u} L}{U^2} \tag{2.26d}$$

$$v^{'} = \frac{v}{U}; \qquad v_{max}^{'} = \frac{v_{max}}{U} \approx \left(\frac{y_{max}}{L}\right)\left(\frac{\omega L}{U_C}\right) \tag{2.26e}$$

$$\dot{v}^{'} = \frac{\dot{v} L}{U^2}; \qquad \dot{v}_{max}^{'} = \frac{\dot{v}_{max}\, L}{U^2} \approx \left(\frac{y_{max}}{L}\right)\left(\frac{\omega L}{U_C}\right)^2 \tag{2.26f}$$

$$r^{'} = \frac{rL}{U}; \qquad r_{max}^{'} = \frac{r_{max}\, L}{U} \approx \psi_{max}\left(\frac{\omega L}{U_C}\right) \tag{2.26g}$$

$$\dot{r}^{'} = \frac{\dot{r} L^2}{U^2}; \qquad \dot{r}_{max}^{'} = \frac{\dot{r}_{max}\, L^2}{U^2} \approx \psi_{max}\left(\frac{\omega L}{U_C}\right)^2 \tag{2.26h}$$

$$X^{'} = \frac{X}{1/2\rho U^2 LT} \tag{2.26i}$$

$$Y^{'} = \frac{Y}{1/2\rho U^2 LT} \tag{2.26j}$$

$$N^{'} = \frac{N}{1/2\rho U^2 L^2 T} \tag{2.26k}$$

Note that in the remainder of the thesis the prime symbol is omitted for simplicity.

2.3.5 Determination of hydrodynamic derivatives

Hydrodynamic derivatives (simply 'derivatives') in the mathematic models (2.18) are determined from the static drift, pure sway, pure yaw, and yaw and drift data. Sway-velocity derivatives X_*, X_{vv}, Y_v, Y_{vvv}, N_v, and N_{vvv} are determined from the static drift data and sway-acceleration derivatives $Y_{\dot{v}}$ and $N_{\dot{v}}$ are from the pure sway data. Sway-velocity derivatives can be determined as well from the pure sway data, however, derivatives determined from the static drift data are preferred in general as the derivatives from dynamic-test data are known as often frequency-dependent (van Leeuwen 1964). As the dynamic-motion frequency ω becomes large, the 'quasi-steady' or the 'slow-motion' assumptions for the math-models can fail and the hydrodynamic forces and moment during the PMM tests become dependent not only on the instantaneous motions but partly also on the previous motions (Bishop et al. 1970, 1972, 1973), known as the 'memory effect'. The yaw-rate derivatives X_{rr}, Y_r, Y_{rrr}, N_r, and N_{rrr} and the yaw-acceleration derivatives $Y_{\dot{r}}$ and $N_{\dot{r}}$ are determined from the pure yaw test. The cross-coupled derivatives between sway and yaw such as X_{vr}, Y_{vrr}, Y_{rvv}, N_{vrr}, and N_{rvv} are determined from the yaw and drift test that is a combination of pure yaw and static drift tests. The surge-coupled derivatives such as X_u, X_{uu}, X_{uuu}, X_{vvu}, Y_{vu}, Y_{vuu}, N_{vu}, and N_{vuu} are determined by repeating the static drift (or pure sway) test and X_{rru}, Y_{ru}, Y_{ruu}, N_{ru}, N_{ruu} are by repeating the pure yaw test over a range of towing speed, respectively. The sway-yaw-surge-coupled derivative X_{vru} can be determined by repeating the yaw and drift test, but typically of negligible value.

The derivatives are evaluated by curve-fitting the data for static drift test and by using either the 'Multiple-run (MR)' or 'Single-run (SR)' methods for dynamic tests as per introduced below:

2.3.5.1 Static drift test

Data are measured over a range of drift angle β and curve-fitted to polynomial functions as per the mathematic model (2.19):

$$y = A + Bx^2;\ y = X;\ x = v \tag{2.27a}$$

$$y = Ax + Bx^3;\ y = Y, N;\ x = v \tag{2.27b}$$

Then,

$$X_*, Y_v, N_v = A \tag{2.28a}$$

$$X_{vv}, Y_{vvv}, N_{vvv} = B \tag{2.28b}$$

respectively.

2.3.5.2 Dynamic tests

Derivatives can be determined from the math-models (2.20), (2.22), and (2.24) with expressed in harmonics form, summarized in Table 2-3. Then, the derivatives[5] are evaluated either by curve-fitting the harmonics data into those equations, named as the '*Multiple-Run*' method; or by solving the harmonics equations for the derivatives, named as the '*Single-Run*' method. The harmonics data are determined experimentally by measuring the X, Y, and N as time-histories from PMM tests as

$$X, Y, N = f(t) \tag{2.29}$$

and using a Fourier-integral equation as:

[5] Derivatives can be also determined by using a regression method, although not used herein. By using the math-models (2.19) as the regression equations, the PMM test data can be curve-fitted using such as a Least-square-error method to evaluate the derivatives.

$$X_0, Y_0, N_0 = \frac{1}{T}\int_0^T f(t)dt \tag{2.30a}$$

$$X_{Cn}, Y_{Cn}, N_{Cn} = \frac{2}{T}\int_0^T f(t)\cos n\omega t\, dt \tag{2.30b}$$

$$X_{Sn}, Y_{Sn}, N_{Sn} = \frac{2}{T}\int_0^T f(t)\sin n\omega t\, dt \tag{2.30c}$$

where $T = 2\pi/\omega$.

'Multiple-run' (MR) method: Derivatives are determined by using data from a series of PMM tests. For this, PMM tests are repeated over a range of input motions parameters such as v_{max} , r_{max} , or β, and then a set of harmonics data, evaluated from each test as per (2.30), is fitted into polynomial functions as

$$\left.\begin{matrix} X_0, Y_0, N_0 \\ X_{Sn}, Y_{Sn}, N_{Sn} \\ X_{Cn}, Y_{Cn}, N_{Cn} \end{matrix}\right\} = y(x);\ \ x = v_{max}\ ,\ \dot{v}_{max}\ ,\ r_{max}\ ,\ \dot{r}_{max}\ ,\ \text{or}\ v \tag{2.31}$$

Polynomial functions $y(x)$ in (2.31) for each harmonic are summarized in Table 2-4 where the resulting hydrodynamic derivatives are expressed with the polynomial coefficients. From Table 2-4, the non-linear derivatives such as X_{vv}, Y_{vvv}, N_{vvv}, X_{rr}, Y_{rrr}, N_{rrr}, Y_{vrr}, and N_{vrr} can be determined either from the 0th- or 1st-order (low-order) harmonics such as X_0, Y_0, Y_{C1}, Y_{S1}, N_0, N_{S1}, and N_{S1} or from the 2nd- or 3rd-order (high-order) harmonics such as X_{C2}, Y_{C2}, Y_{C3}, Y_{S3}, N_{C2}, N_{C3}, or N_{S3}, which are designated as the 'MR_L' and the 'MR_H' methods, respectively.

'Single-run' (SR) method: Hydrodynamic derivatives are determined by using data from a single realization (carriage-run) of dynamic PMM test (or from a mean-data by repeating the tests at the same condition). First, FS harmonics of the data are evaluated as per (2.30), and then the equations of harmonics amplitudes in Table 2-3 are solved for hydrodynamic derivatives such that

$$\left.\begin{matrix} X_*, X_{vv}, X_{rr}, X_{vr}; \\ Y_v, Y_{vvv}, Y_{\dot{v}}, Y_r, Y_{rrr}, Y_{\dot{r}}, Y_{vrr}, Y_{rvv}; \\ N_v, N_{vvv}, N_{\dot{v}}, N_r, N_{rrr}, N_{\dot{r}}, N_{vrr}, N_{rvv} \end{matrix}\right\} = f\begin{pmatrix} X_0, X_{Sn}, \text{or } X_{Cn}; \\ Y_0, Y_{Sn}, \text{or } Y_{Cn}; \\ N_0, N_{Sn}, \text{or } N_{Cn} \end{pmatrix} \quad (2.32)$$

respectively, where n = 1, 2, or 3. The solutions are summarized in Table 2-5, where two derivatives, Y_{vrr} and N_{vrr}, can be determined either from the 0th-order (low-order) harmonics Y_0 and N_0 or from the 2nd-order (high-order) harmonics Y_{C2} and N_{C2}, which are designated as the 'SR_L' and the 'SR_H' methods, respectively.

Table 2-4. '*Multiple-Run*' Method.

Test	Variable	Polynomial equation	y	x	Derivatives
Pure sway	X	$y = A + Bx^2$	X_0	v_{max}	$X_* = A;\ X_{vv} = 2B$
		$y = Cx^2$	X_{C2}	v_{max}	$X_{vv} = 2C$
	Y, N	$y = Ax + Bx^3$	Y_{C1}, N_{C1}	v_{max}	$Y_v, N_v = A;\ Y_{vvv}, N_{vvv} = \frac{4}{3}B$
		$y = Cx$	Y_{S1}, N_{S1}	$\dot{v}_{max}$	$Y_{\dot{v}}, N_{\dot{v}} = C$
`		$y = Dx^3$	Y_{C3}, N_{C3}	v_{max}	$Y_{vvv}, N_{vvv} = -4D$
Pure yaw	X	$y = A + Bx^2$	X_0	r_{max}	$X_* = A;\ X_{rr} = 2B$
		$y = Cx^2$	X_{C2}	r_{max}	$X_{rr} = -2C$
	Y, N	$y = Ax + Bx^3$	Y_{S1}, N_{S1}	r_{max}	$Y_r, N_r = A;\ Y_{rrr}, N_{rrr} = \frac{4}{3}B$
		$y = Cx$	Y_{C1}, N_{C1}	$\dot{r}_{max}$	$Y_{\dot{r}}, N_{\dot{r}} = C$
		$y = Dx^3$	Y_{S3}, N_{S3}	r_{max}	$Y_{rrr}, N_{rrr} = 4D$
Yaw and drift	X	$y = Ax$	X_{C1}	v	$X_{vr} = \frac{1}{r_{max}}A$
	Y, N	$y = Ax + Bx^3$	Y_0, N_0	v	$Y_{vrr} = \frac{2}{r_{max}^2}(A - Y_v);\ N_{vrr} = \frac{2}{r_{max}^2}(A - N_v)$
		$y = C + Dx^2$	Y_{S1}, N_{S1}	v	$Y_{rvv}, N_{rvv} = \frac{1}{r_{max}}D$
		$y = Ex$	Y_{C2}, N_{C2}	v	$Y_{vrr}, N_{vrr} = -\frac{2}{r_{max}^2}E$

Table 2-5. '*Single-Run*' Method.

Pure sway	Pure yaw	Yaw and drift
$X_* = X_0 - X_{C2}$	$X_* = X_0 + X_{C2}$	
$Y_v = -\frac{1}{v_{max}}(Y_{C1} - 3Y_{C3})$	$Y_r = \frac{1}{r_{max}}(Y_{S1} + 3Y_{S3})$	
$N_v = -\frac{1}{v_{max}}(N_{C1} - 3N_{C3})$	$N_r = \frac{1}{r_{max}}(N_{S1} + 3N_{S3})$	
$X_{vv} = \frac{2}{v_{max}^2}X_{C2}$	$X_{rr} = -\frac{2}{r_{max}^2}X_{C2}$	$X_{vr} = \frac{1}{vr_{max}}X_{S1}$
$Y_{vvv} = -\frac{4}{v_{max}^3}Y_{C3}$	$Y_{rrr} = -\frac{4}{r_{max}^3}Y_{S3}$	$Y_{vrr} = \frac{2}{vr_{max}^2}(Y_0 - Y_v v - Y_{vvv}v^3)$ or $-\frac{2}{vr_{max}^2}Y_{C2}$
$N_{rrr} = -\frac{4}{v_{max}^3}N_{C3}$	$N_{rrr} = -\frac{4}{r_{max}^3}N_{S3}$	$N_{vrr} = \frac{2}{vr_{max}^2}(N_0 - N_v v - N_{vvv}v^3)$ or $-\frac{2}{vr_{max}^2}N_{C2}$
$Y_{\dot{v}} = \frac{1}{\dot{v}_{max}}Y_{S1}$	$Y_{\dot{r}} = \frac{1}{\dot{r}_{max}}Y_{C1}$	$Y_{rvv} = \frac{1}{r_{max}\,v^2}\left(Y_{S1} - Y_r r_{max} - \frac{3}{4}Y_{rrr}r_{max}^3\right)$
$N_{\dot{v}} = \frac{1}{\dot{v}_{max}}N_{S1}$	$Y_{\dot{r}} = \frac{1}{\dot{r}_{max}}N_{C1}$	$N_{rvv} = \frac{1}{r_{max}\,v^2}\left(N_{S1} - N_r r_{max} - \frac{3}{4}N_{rrr}r_{max}^3\right)$

2.3.5.3 Speed variation test

Surge-derivatives such as X_u, X_{uu}, and X_{uuu} in (2.18) are determined by repeating the static drift test at the $\beta = 0$ for a range of U (i.e. U_C). The static drift X at $\beta = 0$, the steady reference state value X_*, corresponds to the resistance of the model at the speed U as no propeller is working. If the model towing speed is changed, say $U + \Delta u$, the X_* value will change as the model resistance increase (or decrease) such that

$$X_*(U + \Delta u) = X_*(U) + \Delta X \tag{2.33}$$

The changes in resistance ΔX in (2.33) can be written using a Taylor series expansion as

$$\Delta X = f(u) = \frac{\partial X}{\partial u}\Delta u + \frac{1}{2}\frac{\partial^2 X}{\partial u^2}\Delta u^2 + \frac{1}{6}\frac{\partial^3 X}{\partial u^3}\Delta u^3 + \cdots \tag{2.34}$$

where the differentiations of X are evaluated at $\Delta u = 0$ or $u = U$, which are identical with the definitions of surge hydrodynamic derivatives. When the test is repeated over a range of U, the measured X values can be expressed as a polynomial function of $\Delta u = u - U$ as

$$f(u) = a_0 + a_1\Delta u + a_2\Delta u^2 + a_3\Delta u^3 + \cdots \tag{2.35}$$

and hydrodynamic derivatives X_u, X_{uu}, X_{uuu} are determined as following:

$$X_u = \frac{\partial f}{\partial u} = a_1 \tag{2.36a}$$

$$X_{uu} = \frac{1}{2}\frac{\partial^2 f}{\partial u^2} = a_2 \tag{2.36b}$$

$$X_{uuu} = \frac{1}{6}\frac{\partial^3 f}{\partial u^3} = a_3 \tag{2.36c}$$

Derivatives such as X_{vv}, Y_v, N_v, and X_{rr}, Y_r, N_r, and X_{vr} evaluated at U may also change with Δu and can be expressed as appropriate polynomial functions $f(u)$ similarly as

(2.35) by repeating the static drift tests, pure yaw test, and yaw and drift test, respectively. Subsequently, the surge-coupled hydrodynamic derivatives such as X_{vvu}, X_{rru}, X_{vru}, Y_{vu}, Y_{vuu}, N_{vu}, N_{vuu} are determined as following:

$$\left.\begin{matrix} X_{vvu}, X_{rru}, X_{vru} \\ Y_{vu}, Y_{ru} \\ N_{vu}, N_{ru} \end{matrix}\right\} = \frac{\partial f}{\partial u} = a_1 \tag{2.37a}$$

$$\left.\begin{matrix} Y_{vuu}, Y_{ruu} \\ N_{vuu}, N_{ruu} \end{matrix}\right\} = \frac{1}{2}\frac{\partial^2 f}{\partial u^2} = a_2 \tag{2.37b}$$

CHAPTER 3 TEST DESIGN

3.1 Facility and coordinate systems

3.1.1 Towing Tank

Tests are conducted at the IIHR towing tank shown in Fig. 3-1. The tank is 100 m long, 3.048 m wide and 3.048 m deep, and equipped with a drive carriage, PMM carriage, Krypton camera module, automated wave dampener system, and wave-dampening beach. The drive carriage is instrumented with several data-acquisition computers, speed circuit, and signal conditioning for analog voltage measurements of such as forces and moments, ship motions, and carriage speed. The drive carriage pulls the PMM carriage that is used as a point of attachment for model 5512. The Krypton camera module, an infrared-camera-based motion tracking system, tracks the dynamic motions of the model. Wave dampeners and the wave-dampening beach enable twelve-minute intervals between carriage runs that is determined sufficient based on visual inspection of the free surface.

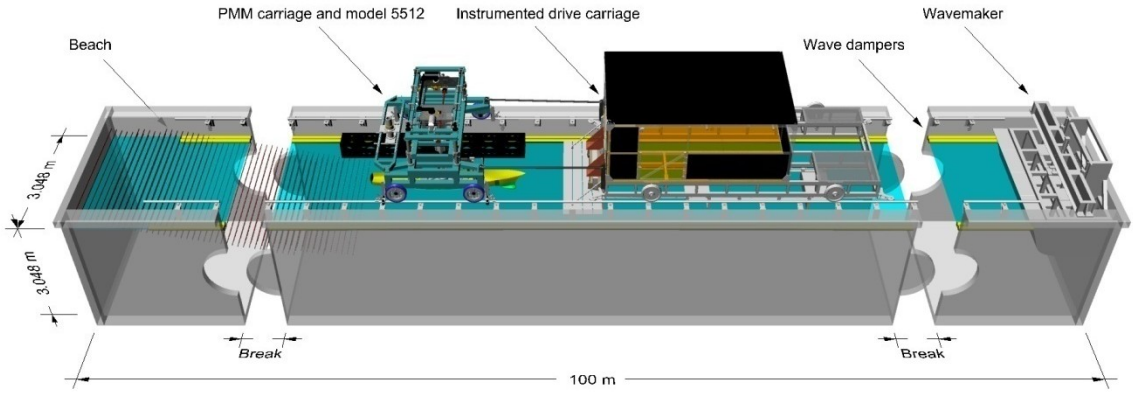

Figure 3-1 IIHR towing tank facility and maneuvering experimental setup.

3.1.2 PMM

Design and construction of the PMM is a collaborative effort by Sanshin Seisaku-sho Ltd. and Mori Engineering Ltd. for the mechanical and electrical systems, respectively. A four-wheel carriage supports the main PMM mechanical system that is towed behind the IIHR drive carriage. The mechanical system is a scotch-yoke type which converts rotational motion of an 11 kW AC servo motor to linear sway motion of a sway box and angular yaw motion of a yaw platter beneath the sway box (Fig. 3-2). The scotch yoke is driven through a control rack, PC, and software up to 0.25 Hz with maximum sway and yaw amplitudes of ±500 mm and ±30°, respectively. Two types of strongback, long (4 m) and short (1.5 m), are attached to the yaw platter for fixed- and free-mount conditions (See Section 3.2), respectively. Each strongback is pre-settable at drift angle β between ±30°. Factory calibrated linear and rotational potentiometers are installed on the PMM carriage to monitor and report the sway and yaw positions of the sway box and yaw platter, respectively. Static calibrations of the linear potentiometers are conducted periodically to check their output.

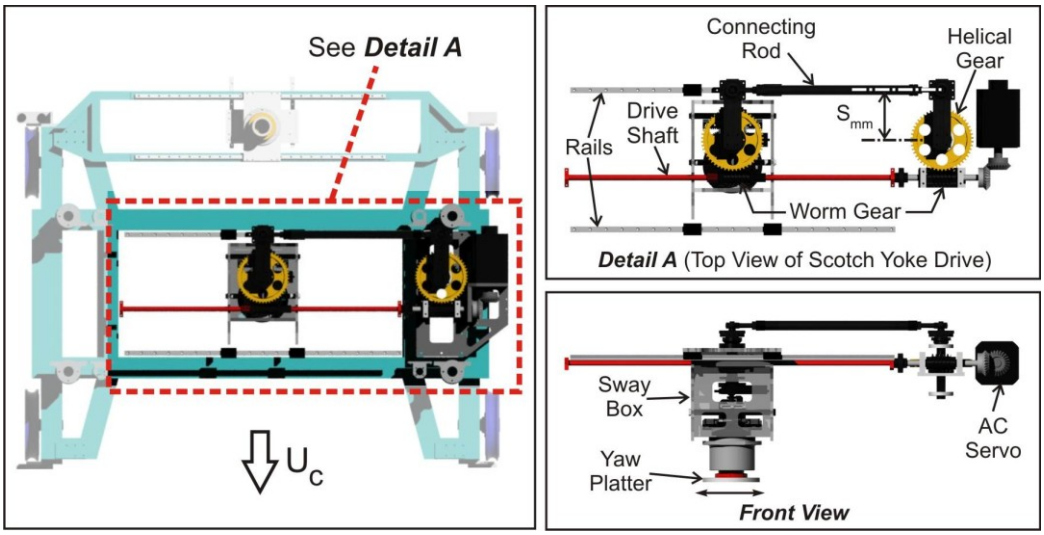

Figure 3-2 Top view of PMM carriage (top left), close up of the scotch yoke drive (top right), and towing tank PMM test coordinate systems (bottom).

3.1.3 Coordinate systems

The Earth-fixed (or the Towing-tank-fixed) x_E-y_E coordinate system (See Fig. 3-3) can be fixed at any arbitrary position in the towing tank, with its longitudinal axis x_E aligned with the towing tank centerline and pointed to the towing direction.

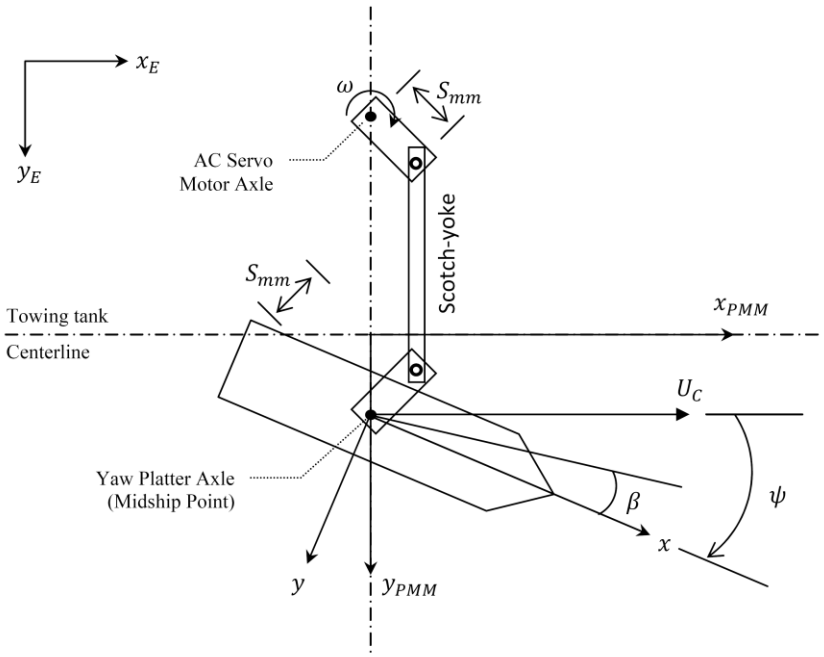

Figure 3-3 Coordinate systems for PMM test (Not scaled).

PMM-fixed x_{PMM}-y_{PMM} coordinate system (See Fig. 3-3) is fixed at the PMM carriage, traveling at a constant speed U_C, with its lateral axis y_{PMM} placed normal to the towing tank centerline. PMM motions for the Sanshin PMM carriage basically can be described in the PMM-fixed coordinate system by five quantities. These include 1) the carriage speed U_C, 2) sway crank amplitude S_{mm}, 3) yaw motion amplitude $\psi_{\max}$, 4) drift angle β, and 5) the number of PMM rotations per minute N. The following relations are used to setup static and dynamic tests according to the test conditions:

$$y_{PMM} = -2S_{mm} \sin \omega t \tag{3.1a}$$

$$v_{PMM} = -2S_{mm}\, \omega \cos \omega t \tag{3.1b}$$

$$\dot{v}_{PMM} = 2S_{mm}\, \omega^2 \sin \omega t \tag{3.1c}$$

$$\psi = -\psi_{max} \cos \omega t + \beta \tag{3.1d}$$

$$r_{PMM} = \psi_{max}\, \omega \sin \omega t \tag{3.1e}$$

$$\dot{r}_{PMM} = \psi_{max}\, \omega^2 \cos \omega t \tag{3.1f}$$

where, $\omega = 2\pi \mathrm{N}/60$.

Ship-fixed x-y coordinate system is fixed at the midship point of the model with its *x* and *y* coordinates aligned with the model longitudinal and lateral directions, respectively, and pointing to upstream and to the starboard side, respectively (See Fig. 3-3). The ship motion parameters such as model velocities and accelerations (at the midship point) in the ship-fixed coordinate system can be written using (2.7) as following:

$$u = U_C \cos \psi + v_{PMM} \sin \psi \tag{3.2a}$$

$$\dot{u} = \dot{v}_{PMM} \sin \psi + r(v_{PMM} \cos \psi - U_C \sin \psi) \tag{3.2b}$$

$$v = v_{PMM} \cos \psi - U_C \sin \psi \tag{3.2c}$$

$$\dot{v} = \dot{v}_{PMM} \cos \psi - r(U_C \cos \psi + v_{PMM} \sin \psi) \tag{3.2d}$$

$$r = r_{PMM} \tag{3.2e}$$

$$\dot{r} = \dot{r}_{PMM} \tag{3.2f}$$

Note that the carriage acceleration is assumed to be zero, i.e. $\dot{U}_C = \dot{u}_E = 0$. The motion parameters in (3.2) are shown as dimensional while those can be non-dimensionalized using the *Prime-System* shown in (2.26) when necessary.

For the PIV applications of the PMM, the PMM-fixed x_{PMM}-y_{PMM} coordinate system that is advancing forward with U_C is considered as stationary, instead an incoming

free stream velocity U_C is assumed, as depicted in Fig. 3-4. In the figure, the PMM-fixed x_{PMM} and y_{PMM} coordinates are re-designated as X and Y, respectively, and the direction of X coordinate is reverted from Fig. 3-3, pointing to downstream . Then, the PMM motion equations (3.1a) and (3.1d) are re-described as

$$Y = -Y_0 \sin \omega t \tag{3.3a}$$

$$\psi = -\psi_0 \cos \omega t \tag{3.3b}$$

respectively, where Y_0 and ψ_0 are renamed from $2S_{mm}$ and ψ_{max} in (3.1a) and (3.1d), respectively, and for (3.3b) the drift angle β in (3.1d) is set to zero. Accordingly, the sway velocity and the yaw rate, with designated as V_P and r, respectively, are written as

$$V_P = -Y_0 \omega \cos \omega t \tag{3.4a}$$

$$r = \psi_0 \omega \sin \omega t \tag{3.4b}$$

by re-describing the equations (3.1b) and (3.1e), respectively.

In Fig. 3-4, the ship-fixed x-y coordinate system is fixed at the forward perpendicular (FP) position and the direction of the x coordinate is reverted from that in Fig. 2-3, pointing to the stern side of the model. Then, as the model is undergoing a reciprocal lateral sway motion Y and an angular yaw motion ψ with pivoted at the midship point (x_0,y_0), as per the equations (3.3a) and (3.3b), respectively, the free stream velocity U_C can be described in the ship-fixed coordinate system. For a field point P(x,y) shown in Fig. 8, the free stream velocity components in x and y directions of the ship-fixed coordinate system, with designated as u_P and v_P, respectively, are written as

$$u_P = U_C \cos \psi + V_P \sin \psi - r \cdot dy \tag{3.5a}$$

$$v_P = -U_C \sin \psi + V_P \cos \psi + r \cdot dx \tag{3.5b}$$

where

$$dx = x - x_0 \tag{3.6a}$$

$$dy = y - y_0 \tag{3.6b}$$

and $(x_0, y_0) = (0.5L, 0)$, where L is the model length, is the mid-ship location or the yaw motion pivot point in the ship-fixed coordinate system.

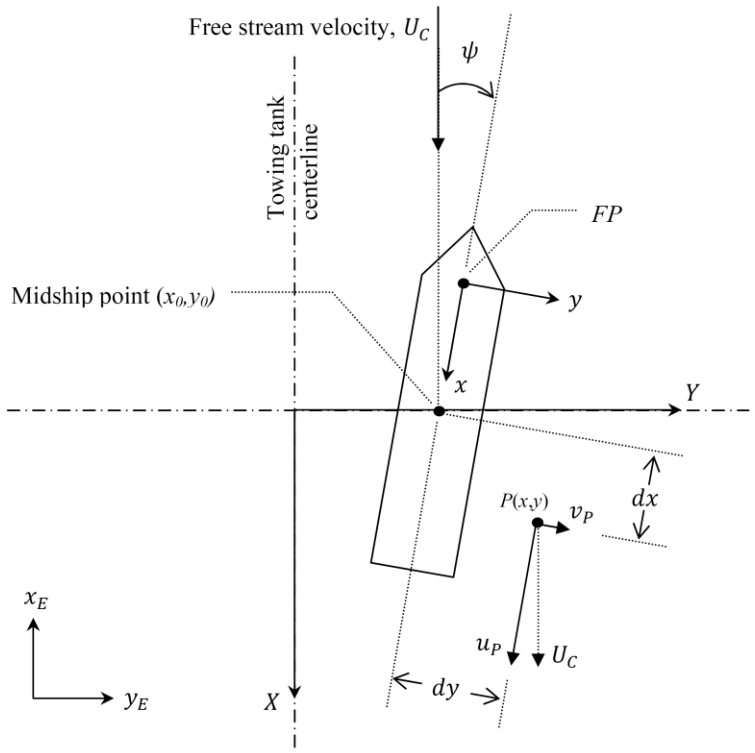

Figure 3-4 Coordinate systems for PIV test (Not scaled).

3.2 Model

The model geometry is DTMB model 5512 (Fig. 3-5), a 1:46.6 scale, L_{PP} = 3.048 m, fiber-reinforced Plexiglas hull with block coefficient, C_B = 0.506. DTMB model 5512 is a geosim of DTMB model 5415, which is a 1:24.8 scale, L_{PP} = 5.72 m model of the U.S. Navy's pre-contract design for a surface combatant (DDG-51) ca. 1980 with a sonar dome bow and transom stern. The model was manufactured at the Naval Surface Warfare Center (NSWC) of USA Navy. The model is un-appended except for port and starboard bilge keels, i.e., not equipped with shafts, struts, propulsors, or rudders. To initiate transition to turbulent flow, a row of cylindrical studs of 1.6 mm height and 3.2 mm diameter are fixed with 9.5 mm spacing at x = 0.45 (x = 0 at the mid-ship, forward positive). The stud dimensions and placement on the model are in accordance with the recommendations by the 23rd ITTC (ITTC, 2002).

Figure 3-5 Photographs of DTMB model 5512. The top view highlights the bilge keels.

Table 3-1 Full- and model-scale particulars.

		Ship	IIHR		FORCE	INSEAN
			Fix mount	Free mount		
Scale	-	1 : 1	1 : 46.588		1:35.48	1:24.83
L (L_{PP})	m	142.00	3.048		4.0023	5.7200
L_{WL}	m	142.18	3.052		4.0083	5.7273
B_{WL}	m	19.10	0.410		0.5382	0.7690
T (T_m)	m	6.16	0.136		0.1736	0.2480
∇	m^3	8472	0.086		0.1897	0.5540
Δ	Ton	8684	0.086		0.1897	0.5540
C_b	-	0.506	0.506		0.506	0.506
m	Kg		83.35	82.55	235.9	N/A
x_G	m		-0.0157			N/A
y_G	m		0.0000			N/A
z_G	m		N/A	0.084	N/A	N/A
I_x	$Kg{\cdot}m^2$		N/A	1.98	N/A	N/A
I_y	$Kg{\cdot}m^2$		N/A	53.88	225.3	1151.4
I_z	$Kg{\cdot}m^2$		44.35	49.99	235.9	N/A

Model- and full-scale geometric parameters for 5512 are summarized in Table 3-1. The length between perpendiculars L_{PP}, length at the design waterline L_{WL}, beam at the design waterline B_{WL}, mean draft T_m, volume ∇, displacement Δ, block coefficient C_B, and the longitudinal and transverse center of gravity (COG) x_G and y_G are provided by NSWC. Total mass m of the model is a sum of element mass parts including the bare model (shell), several ballast weights, and several fixing parts for model mounting. The vertical COG z_G is determined using the added ballast method as per M. Irvine et al. (2008). The moments of inertia in roll and pitch I_x and I_y are determined using the pendulum method as well per M. Irvine et al. (2008) by measuring the roll and pitch gyradius, respectively. The yaw moment of inertia I_z is determined by using a forced-yaw method[6]. Lastly, the FORCE and INSEAN model scale particulars are as well included in Table 3-1.

[6] Model is placed in air and forced to oscillate sinusoidally in yaw with known amplitude ψ and frequency ω to measure the yaw moment M_z. Then, the yaw moment of inertia I_z can be determined from the relation $M_z = I_z \cdot \dot{r}$, where $\dot{r} = \psi\omega^2$ and I_z, for a set of combinations of ψ and ω using such as a least-square-error method.

3.3 Mount and Mount Conditions

Model is installed to PMM using two types of mount, fix- or free-mount shown in Fig. 3-6 (a) and (b), respectively. The fix-mount constrains the model in all motions, whereas the free-mount allows the model to move freely in selective motions such as heave, pitch, and roll. The free-mount consists of the short strongback and a combination of three balances, the fore, midship, and aft balances that are identical in shape. Each balance is a crank-assembly with counter weights (colored in yellow in the figure) for a neutral angular moment of each crank part. The balances allow the model to move freely in heave and pitch while the mid balance (placed in normal direction with respect to the other balances) prevents the relative surge motion of the model while towed. At the end of each balance, two types of joints using roller or spherical bearings are used for model connection; the former prevents and the latter allows the roll motion, respectively, while transmitting the heave and pitch motions of the model.

Tests are carried out four mount conditions: 1) fixed at evenkeel (FX_0); 2) fixed sunk and trim ($FX_{\sigma\tau}$); 3) free to heave and pitch ($FR_{z\theta}$); and 4) free to heave, pitch and roll ($FR_{z\theta\phi}$). The FX_0 and $FX_{\sigma\tau}$ mount conditions are the model installations using the fix-mount (fixed-model setup, Fig. 3-6c). For the installations, the model is first assembled rigidly with the fix-mount and then ballasted to the static waterline position for the FX_0 condition and to the dynamic sinkage ($\sigma = 0.192 \times 10^{-2} L$) and trim ($\tau = -0.136°$, bow down) corresponding to $Fr = 0.280$ for the $FX_{\sigma\tau}$ condition, respectively. The $FR_{z\theta}$ and $FR_{z\theta\phi}$ mount conditions are using the free-mount (free-model setup, Fig. 3-6d). Model is first ballasted to the static waterline and then connected to the free-mount using the roller joint for the $FR_{z\theta}$ condition and using the spherical joint for the $FR_{z\theta\phi}$ condition, respectively. A summary of the mount conditions are presented in Table 3-2.

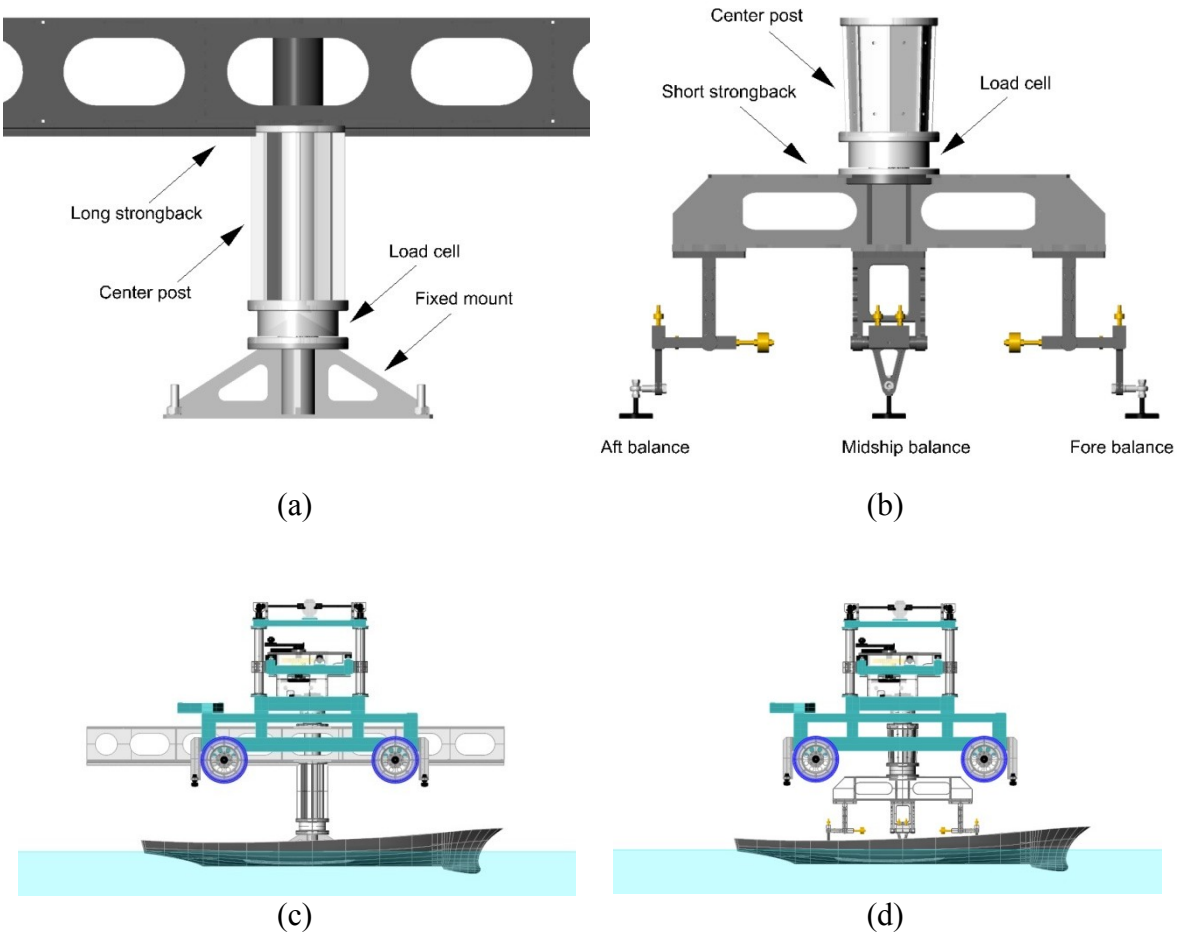

Figure 3-6 Sideviews show: (a) fixed- and (b) free-mounts, and (c) fixed- and (d) free-model setups.

Table 3-2 Mount Conditions.

Motion	Mount conditions			
	FX_0	$FX_{\sigma\tau}$	$FR_{z\theta}$	$FR_{z\theta\phi}$
Surge (x)	Forced	Forced	Forced	Forced
Sway (y)	Forced	Forced	Forced	Forced
Yaw (ψ)	Forced	Forced	Forced	Forced
Heave (z)	Fixed at 0.0	Fixed at $1.9209\times10^{-3}L$	Free	Free
Pitch (θ)	Fixed at 0.0	Fixed at -0.136°	Free	Free
Roll (ϕ)	Fixed at 0.0	Fixed at 0.0	Fixed at 0.0	Free

3.4 Test Conditions

Test conditions are summarized in Table 3-3. Static drift tests are conducted at three towing speeds corresponding to Fr = 0.138, 0.280, and 0.410, which are the low, medium, and high Fr condition, respectively. For low and medium Fr conditions, drift angle β values are varied between ±20°, whereas between ±12° for the high Fr condition limited by the capacity of load-cell. The largest drift angle values correspond to sway velocities v = 0.342 and 0.208, respectively. The angles are distributed symmetrically with respect to the $\beta = 0°$ line, i.e. the model towing direction, but distributed unevenly with clustered around β = ±10°. Pure sway tests are carried out at medium Fr only and at three maximum drift angles β_{max} = 2°, 4°, 10° which correspond to the maximum sway velocity values v_{max} = 0.035, 0.070, 0.174, respectively. Pure yaw tests are carried out for all three Fr cases, at six maximum yaw rates $r_{\max}$ = 0.05, 0.15, 0.30, 0.45, 0.60, and 0.75 for low and medium Fr cases and at first four maximum yaw rates for high Fr case, respectively, again limited by load-cell capacity. Yaw and drift tests are carried out for medium Fr case only and at three drift angles β = 9°, 10°, and 11° with the maximum yaw rate fixed at $r_{\max}$ = 0.3.

Sway motion amplitude $2S_{mm}$, yaw motion amplitude $\psi_{\max}$, and drift angle β used in (3.1) are determined to yield the motion parameters such as sway $v_{\max}$, $\dot{v}_{\max}$ and $r_{\max}$, $\dot{r}_{\max}$ with considerations of minimizing interferences between the PMM motions and the tank walls. PMM motion frequency N values are determined to avoid possible hydrodynamic effects such as tank resonance and memory effects associated with the dynamic tests. Typically, PMM motion frequencies are restricted in terms of three non-dimensional frequencies: $\omega_1 = \omega L/U_C$, $\omega_2 = \omega\sqrt{L/g}$, and $\omega_3 = \omega U_C/g$, where ω is the PMM motion frequency and g is the local value of gravity. ω_1 is related to non-stationary lift and memory effects (Nomoto 1975, Wagner Smitt & Chislett 1974, Milanov 1984, van Leeuwen 1969), ω_2 is related to tank resonance, and ω_3 is related to un-

realistic combinations of pulsation and translation (Brard 1948, Wehausen & Laitone 1960, van Leeuwen 1964). The ITTC Recommended Procedures and Guidelines 7.5-02-06-02.2 'Captive Model Test Procedures' recommends $\omega_1 = 1 \sim 4$, $\omega_2 = 0.15 \sim 0.2$, and $\omega_3 \ll 0.25$, however, the PMM motion frequencies in the present tests are $\omega_1 = 1.14 \sim 3.13$, $\omega_2 = 0.27 \sim 0.88$, and $\omega_3 = 0.04 \sim 0.34$ due to the facility limitations regarding dimensions and capabilities.

Tests are repeated 12 times at selected conditions (marked as bold characters) for the purpose of uncertainty analysis (UA) presented in Chapter 5. UA cases include β = ±10° for static drift test, β_{max} = 10° for pure sway test, r_{max} = 0.3 for pure yaw test, and β = 10° for yaw and drift test. For FX_0 and $FR_{z\theta}$ conditions, all the test cases listed in Table 3-3 are carried out. For $FX_{\sigma\tau}$ condition, test cases include static drift test at all *Fr* conditions and pure sway and pure yaw tests at the medium *Fr* conditions. For $FR_{z\theta\phi}$ condition, static drift test at all *Fr* and dynamic tests only at the UA cases.

PIV measurements are for pure sway and pure yaw tests. Both of the pure sway and pure yaw tests are carried out at the $FR_{\sigma\tau}$ mount condition and at Fr = 0.280. Test cases are highlighted in Table 3-3.

Table 3-3 PMM Test conditions.

Test	Fr	U_C	β	$\frac{y_{max}}{L}$	$\frac{v_{\max}}{U_C}$	$\frac{\dot{v}_{\max} L}{U_C^2}$	$\beta_{\max}$	$\psi_{\max}$	$\frac{r_{\max} L}{U_C}$	$\frac{\dot{r}_{\max} L}{U_C^2}$	$\frac{\omega L}{U_C}$	Mount condition
		(m/s)	(°)	(-)	(-)	(-)	(°)	(°)	(-)	(-)	(-)	
Static drift	0.138	0.754	-20, -16, -12, -11, **-10**‡, -9, -6, -2, 0, 2, 6, 9, **10**†, 11, 12, 16, 20	0	0	0	-	0	0	0	0	**FX_0, $FR_{z\theta}$, $FR_{z\theta\phi}$**
	0.280	1.531	-20, -16, -12, -11, **-10**‡, -9, -6, -2, 0, 2, 6, 9, **10**†, 11, 12, 16, 20	0	0	0	-	0	0	0	0	**FX_0, $FX_{\sigma\tau}$, $FR_{z\theta}$, $FR_{z\theta\phi}$**
	0.410	2.241	-12, -11, **-10**‡, -9, -6, -2, 0, 2, 6, 9, **10**†, 11, 12	0	0	0	-	0	0	0	0	**FX_0, $FR_{z\theta}$, $FR_{z\theta\phi}$**
Pure sway	0.280	1.531	0	0.021	0.035	0.058	2	0	0	0	1.672	FX_0, $FX_{\sigma\tau}$, $FR_{z\theta}$
			0	0.042	0.070	0.117	4	0	0	0	1.672	FX_0, $FX_{\sigma\tau}$, $FR_{z\theta}$
			0	**0.104**	**0.174**	**0.291**	**10**	**0**	**0**	**0**	**1.672**	**FX_0, $FX_{\sigma\tau}$, $FR_{z\theta}$, $FR_{z\theta\phi}$**
Pure yaw	0.138	0.754	0	0.013	0	0	-	1.5	0.05	0.10	0.956	FX_0, $FR_{z\theta}$
			0	0.040	0	0	-	4.4	0.15	0.29	0.956	FX_0, $FR_{z\theta}$
			0	**0.080**	**0**	**0**	**-**	**8.8**	**0.30**	**0.58**	**0.956**	**FX_0, $FR_{z\theta}$, $FR_{z\theta\phi}$**
			0	0.120	0	0	-	13.1	0.45	0.87	0.956	FX_0, $FR_{z\theta}$
			0	0.104	0	0	-	14.2	0.60	1.49	1.194	FX_0, $FR_{z\theta}$
			0	0.128	0	0	-	17.2	0.75	1.82	1.194	FX_0, $FR_{z\theta}$
	0.280	1.531	0	0.018	0	0	-	1.7	0.05	0.08	1.672	FX_0, $FX_{\sigma\tau}$, $FR_{z\theta}$
			0	0.054	0	0	-	5.1	0.15	0.25	1.672	FX_0, $FX_{\sigma\tau}$, $FR_{z\theta}$
			0	**0.107**	**0**	**0**	**-**	**10.2**	**0.30**	**0.50**	**1.672**	**FX_0, $FX_{\sigma\tau}$, $FR_{z\theta}$, $FR_{z\theta\phi}$**
			0	0.099	0	0	-	12.0	0.45	0.98	2.150	$FX_{\sigma\tau}$, $FR_{z\theta}$
			0	0.046	0	0	-	8.2	0.45	1.41	3.127	FX_0
			0	0.130	0	0	-	15.6	0.60	1.29	2.150	$FX_{\sigma\tau}$, $FR_{z\theta}$
			0	0.061	0	0	-	10.9	0.60	1.88	3.127	FX_0
			0	0.124	0	0	-	17.2	0.75	1.93	2.502	$FX_{\sigma\tau}$, $FR_{z\theta}$
			0	0.077	0	0	-	13.5	0.75	2.35	3.127	FX_0
	0.410	2.241	0	0.038	0	0	-	2.5	0.05	0.06	1.672	FX_0, $FR_{z\theta}$
			0	0.115	0	0	-	7.5	0.15	0.17	1.672	FX_0, $FR_{z\theta}$
			0	**0.072**	**0**	**0**	**-**	**8.4**	**0.30**	**0.61**	**2.986**	**FX_0, $FR_{z\theta}$, $FR_{z\theta\phi}$**
			0	0.108	0	0	-	12.5	0.45	0.92	2.986	FX_0, $FR_{z\theta}$
Yaw and drift	0.280	1.531	9	0.107	0	0	-	10.2	0.30	0.50	1.672	FX_0, $FR_{z\theta}$
			10	**0.107**	**0**	**0**	**-**	**10.2**	**0.30**	**0.50**	**1.672**	**FX_0, $FR_{z\theta}$, $FR_{z\theta\phi}$**
			11	0.107	0	0	-	10.2	0.30	0.50	1.672	FX_0, $FR_{z\theta}$

Bold: UA cases with 12 repeat tests; † UA cases for FX_0 and $FX_{\sigma\tau}$ conditions; ‡ UA cases for $FR_{z\theta}$ and $FR_{z\theta\phi}$ conditions.
Highlighted: PIV conditions.

3.5 Data Acquisition and Reduction Methodology

3.5.1 Forces and Moment and Motions

The present interest is in data acquisition of carriage speed U_C, forces and moments (F_x, F_y, F_z, M_x, M_y, M_z), and ship model motions (x_{PMM}, y_{PMM}, z_{mm}, ϕ, θ, ψ) for static and dynamic PMM tests. All variables are acquired as time histories through each carriage run. Static test variables (F_x, F_y, M_z, z_{mm}, θ, ϕ) are time-averaged whereas dynamic test variables (F_x, F_y, M_z, y_{PMM}, z_{mm}, ϕ, θ, ψ) are treated with harmonic analysis in the data reduction phases of the study which is explained in further detail below. y_{PMM}, z_{mm}, ϕ, θ, and ψ are measured only for free-model condition tests. Although not used in the data-reduction equations, x_{PMM}, F_z, M_x, M_y are also measured to monitor operation of the mount and loadcell. The measurement details for U_C are presented in Longo and Stern, (2005). First, the data reduction equations for static and dynamic PMM tests are presented followed by the data-reduction methodology.

The data reduction equations (DRE's) for hydrodynamic forces and moment are:

$$X = \frac{F_x + m\left(\dot{u} - vr - x_G r^2 - y_G \dot{r}\right)}{\frac{1}{2}\rho (u^2+v^2) LT} \tag{3.7a}$$

$$Y = \frac{F_y + m\left(\dot{v} + ur - y_G r^2 + x_G \dot{r}\right)}{\frac{1}{2}\rho (u^2+v^2) LT} \tag{3.7b}$$

$$N = \frac{M_z + I_z \dot{r} + m\left(x_G(\dot{v}+ur) - y_G(\dot{u}-vr)\right)}{\frac{1}{2}\rho (u^2+v^2) L^2 T} \tag{3.7c}$$

where y_G is assumed as non-zero from equations (2.1) for the purpose of uncertainty analysis in Section 5.1. Although the equations (3.7) are technically applicable DRE's for all tests herein, they can be simplified considerably by dropping the inertia terms for the case of static drift tests, which is done below in equations (3.8).

$$X = \frac{F_x}{\frac{1}{2}\rho U_C^2 LT} \tag{3.8a}$$

$$Y = \frac{F_y}{\frac{1}{2}\rho U_C^2 LT} \tag{3.8b}$$

$$N = \frac{M_z}{\frac{1}{2}\rho U_C^2 L^2 T} \tag{3.8c}$$

The PMM motion parameters u, v, r, $\dot{u}$, $\dot{v}$, and $\dot{r}$ in (3.7) are derived from the measured sway displacement y_{PMM} and yaw angle ψ data by using the coordinate transformations between the ship-fixed and PMM-fixed reference frames shown in (3.2). For this, first, time histories of the y_{PMM} and ψ data are FS reconstructed by using (3.11) for $\chi = y_{PMM}$ and ψ, respectively, and then v_{PMM}, $\dot{v}_{PMM}$ and r_{PMM}, $\dot{r}_{PMM}$ are obtained through successive differentiations of the χ's with respect to time t, respectively. The motions data, heave z, pitch θ, and roll ϕ are not reduced except for the nondimensionalization of z with the ship length L,

$$z = \frac{z_{mm}}{L} \tag{3.9}$$

where the z_{mm} is dimensional heave data as measured in mm unit.

For dynamic tests, time-histories of the data can be expressed in harmonic forms using a 6th-order Fourier-series (FS) equation as following:

$$\chi(t) = \chi_0 + \sum_{n=1}^{6}(\chi_{Sn} \sin n\omega t + \chi_{Cn} \cos n\omega t) \tag{3.10a}$$

where,

$$\chi_0 = \frac{1}{M}\sum_{i=1}^{M} \chi_i \tag{3.10b}$$

$$\chi_{Sn} = \frac{2}{M}\sum_{i=1}^{M} \chi_i \sin(n\omega t_i) \tag{3.10c}$$

$$\chi_{Cn} = \frac{2}{M}\sum_{i=1}^{M} \chi_i \cos(n\omega t_i) \tag{3.10d}$$

Here, χ is either X, Y, N, z, θ, or ϕ, subscript n is the order of the FS, M is the total number of data for FS, χ_i is the data sample at time t_i, ω is the PMM frequency, and χ_{Cn}

and χ_{Sn} are the n^{th}-order cosine and sine harmonic amplitudes, respectively. Alternatively, (3.10) can also be expressed as

$$\chi(t) = \chi_0 + \sum_{n=1}^{6} \chi_n \cos\left(n\omega t + \varphi_{\chi n}\right) \tag{3.11a}$$

where

$$\chi_n = \sqrt{\chi_{Sn}^2 + \chi_{Cn}^2} \tag{3.11b}$$

$$\varphi_{\chi n} = -\arctan\left(\frac{\chi_{Sn}}{\chi_{Cn}}\right) \tag{3.11c}$$

where, χ_n and φ_n are the n^{th}-order harmonic amplitude and phase, respectively, and χ_0, χ_{Sn}, and χ_{Cn} are as per (3.10).

3.5.2 Phase-Averaged Flow field

Data acquisition includes carriage speed U_C, PMM sway displacement Y and yaw angle ψ, and the flow velocity components U_i where i = 1, 2, 3 for U, V, W, respectively. All variables are acquired at a number N of phase γ positions per each PMM cycle of frequency f_{PMM}, and a total number L of data acquisitions during a carriage run where typically two and three quarters of PMM cycles are made. The nominal value of the phase position is given as $\gamma = (n-1) \cdot \Delta\gamma$ for n = 1, …, N, where the phase interval $\Delta\gamma = 2\pi/N$. If N = 32 phase positions per one PMM cycle, for example, a total L = 88 data per one carriage run and a $\Delta\gamma$ = 11.25° of phase interval. The data acquisition procedure is repeated for a total number K of carriage runs, accumulating data for the phase-averaging purpose.

The data acquisition time-point $t_{k,l}$ of the l^{th} data from the k^{th} carriage run is written as,

$$t_{k,l} = t_{0_k} + (l-1) \cdot \Delta t \tag{3.12}$$

for k = 1, …, K and l = 1, …, L, where t_{0_k} is the time when the first data sample of the k^{th} carriage run is acquired and $\Delta t = (f_{PMM})^{-1}/N$ is the time interval between adjacent data samples. Subsequently, the U_C, Y, ψ, and U_i data acquired at time $t_{k,l}$ are designated as $U_{C_{k,l}}$, $Y_{k,l}$, $\psi_{k,l}$, and $U_{i_{k,l}}$, respectively. The acquisition of $U_{C_{k,l}}$, $Y_{k,l}$, and $\psi_{k,l}$ data is the time-mean of twenty-five samplings of U_C, Y, and ψ signal, respectively, for a short time period, a 100 μs, and the acquisition of $U_{i_{k,l}}$ is result from cross-correlation of the Stereo PIV image pairs take at time $t_{k,l}$.

The phase position γ (not the nominal value but the actual value) at each data acquisition time $t_{k,l}$, designated as $\gamma_{k,l}$, may be found using the $Y_{k,l}$ and $\psi_{k,l}$ data from the equations (3a) and (3b) in Section 3.1.2, along with the relationship $\gamma = \omega t$, such that[7]

$$\gamma_{k,l} = \arctan\left(\frac{Y_{k,l}/Y_{0_k}}{\psi_{k,l}/\psi_{0_k}}\right) \tag{3.13}$$

where, Y_{0_k} and ψ_{0_k} are the sway and yaw motions amplitudes of the k^{th} carriage run, respectively, evaluated using Fourier Series expressions of the $Y_{k,l}$ and $\psi_{k,l}$ data such that

$$Y_{0_k} = -\frac{2}{L_{FS}}\sum_{l=1}^{L_{FS}}\{Y_{k,l}\cdot\sin(\omega t_{k,l})\} \tag{3.14}$$

$$\psi_{0_k} = -\frac{2}{L_{FS}}\sum_{l=1}^{L_{FS}}\{\psi_{k,l}\cdot\cos(\omega t_{k,l})\} \tag{3.15}$$

where, $L_{FS} = n_{cycle}\cdot N$ and n_{cycle} is the (integer) number of PMM cycles from the k^{th} carriage run.

The PIV measured velocity data $U_{i_{k,l}}$ are normalized with the carriage speed $U_{C_{k,l}}$ measured at the same time instant, $t_{k,l}$, as

---

[7] For pure sway tests, where the yaw amplitude ψ_0 = 0 in equation (3.3b); the phase is $\gamma_{k,l} = \arcsin(-Y_{k,l}/Y_{0_k})$.

$$U_{i}^{*}{}_{k,l} = U_{i}{}_{k,l} / U_{C}{}_{k,l} \tag{3.16}$$

Note that, hereafter, the '*' symbol in (3.16) is omitted for simplicity as only the normalized velocity is of interest herein, otherwise mentioned. Then, the $U_{i}{}_{k,l}$ data are sorted into N phase-groups by approximating the corresponding $\gamma_{k,l}$ value to the nearest nominal phase value, collecting a total number of M data for each phase-group. Subsequently, the $U_{i}{}_{k,l}$ data are re-indexed as $U_{i}{}_{m,n}$ for $n = 1, \ldots, N$ and $m = 1, \ldots, M$, indicating the m^{th} data of the n^{th} phase-group.

For a given n^{th} phase-group, the phase-averaged velocity component $\langle U_i \rangle$ can be computed from $U_{i}{}_{m,n}$ data such that

$$\langle U_i \rangle = \left(\sum_{m=1}^{M} U_{i}{}_{m,n} \right) / M \tag{3.17}$$

respectively for $i = 1, 2, 3$. Then, the turbulent velocity u_i for $U_{i}{}_{n,m}$ data is defined as the deviation from the phase-averaged velocity $\langle U_i \rangle$ such as

$$u_{i}{}_{n,m} = U_{i}{}_{n,m} - \langle U_i \rangle \tag{3.18}$$

Next, the phase-averaged turbulent Reynolds stress at the n^{th} phase is defined as the (co)variance between the turbulent velocity components and evaluated as

$$\langle u_i u_j \rangle = \left(\sum_{m=1}^{M} u_{i}{}_{n,m} \cdot u_{j}{}_{n,m} \right) / M \tag{3.19}$$

respectively for $i, j = 1, 2$, or 3. Note that, the '⟨ ⟩' symbol used for phase-averaged velocity U_i in (3.17) and Reynolds stress $u_i u_j$ in (3.19) is omitted hereafter for simplicity.

Turbulent kinetic energy k and axial vorticity ω_x are evaluated from the phase-averaged Reynolds stress $u_i u_j$ and velocity U_i fields, respectively. The turbulent kinetic energy is defined as one half of the sum of the phase-averaged Reynolds stress components $u_i u_i$ such that

$$k = \frac{1}{2}(uu + vv + ww) \tag{3.20}$$

The axial vorticity is the spatial differentiations of the phase-averaged cross-plane velocity components such that

$$\omega_x = \frac{\partial W}{\partial y} - \frac{\partial V}{\partial z} \tag{3.21}$$

where y and z are both non-dimensional with the model length L. Note that the vorticity components in the transverse and vertical directions are not evaluated, as no longitudinal gradient information is available from the stereo PIV data.

On the other hand, the U_C, Y, and ψ data are as well used to determine the free stream velocity components u_P and v_P (See Section 3.1.2) for the UA purposes in Section 5.2. For this, sway velocity V_P and yaw rate r are calculated from the Y and ψ data, respectively, from which u_P and v_P at a field point (x,y) are evaluated along with the U_C and ψ data as per the following equations

$$u_P = U_C \cos\psi + V_P \sin\psi - r \cdot dy \tag{3.5a}$$

$$v_P = -U_C \sin\psi + V_P \cos\psi + r \cdot dx \tag{3.5b}$$

respectively, derived in Section 3.1.2.

First, the mean carriage speed U_C is calculated from the $U_{C\,k,l}$ data as

$$U_C = \left[\sum_{k=1}^{K}\left\{\left(\sum_{l=1}^{L} U_{C\,k,l}\right)/L\right\}\right]/K \tag{3.22}$$

where the inner averaging (for index l) corresponds to the mean carriage speed of each k^{th} carriage run, and the outer averaging (for index k) corresponds to the mean of the all K carriage runs.

Next, the V_P and r values at each PMM phase position γ are evaluated as per the equations (3.3a) and (3.3b) in Section 3.1.2, respectively, and by using the relation $\gamma = \omega t$ as

$$V_P = -Y_0 \omega \cos\gamma \tag{3.23}$$

$$r = \psi_0 \omega \sin\gamma \tag{3.24}$$

where, $\omega = 2\pi f_{PMM}$ is the cyclic PMM frequency, and Y_0 and ψ_0 are the mean values of Y_{0_k} in (3.14) and ψ_{0_k} in (3.15), respectively, such that

$$Y_0 = \left(\sum_{k=1}^{K} Y_{0_k}\right)/K \tag{3.25}$$

$$\psi_0 = \left(\sum_{k=1}^{K} \psi_{0_k}\right)/K \tag{3.26}$$

The phase position γ in (3.23) and (3.24) can be calculated similarly as (3.13) such that

$$\gamma = \arctan\left(\frac{Y/Y_0}{\psi/\psi_0}\right) \tag{3.27}$$

where Y_0 and ψ_0 are from (3.25) and (3.26), respectively. Lastly, the mean heading angle ψ is as well by phase-sorting and re-indexing the $\psi_{k,l}$ data as $\psi_{m,n}$ and by averaging as

$$Y = \left(\sum_{m=1}^{M} Y_{m,n}\right)/M \tag{3.28}$$

$$\psi = \left(\sum_{m=1}^{M} \psi_{m,n}\right)/M \tag{3.29}$$

for each n^{th} phase-group.

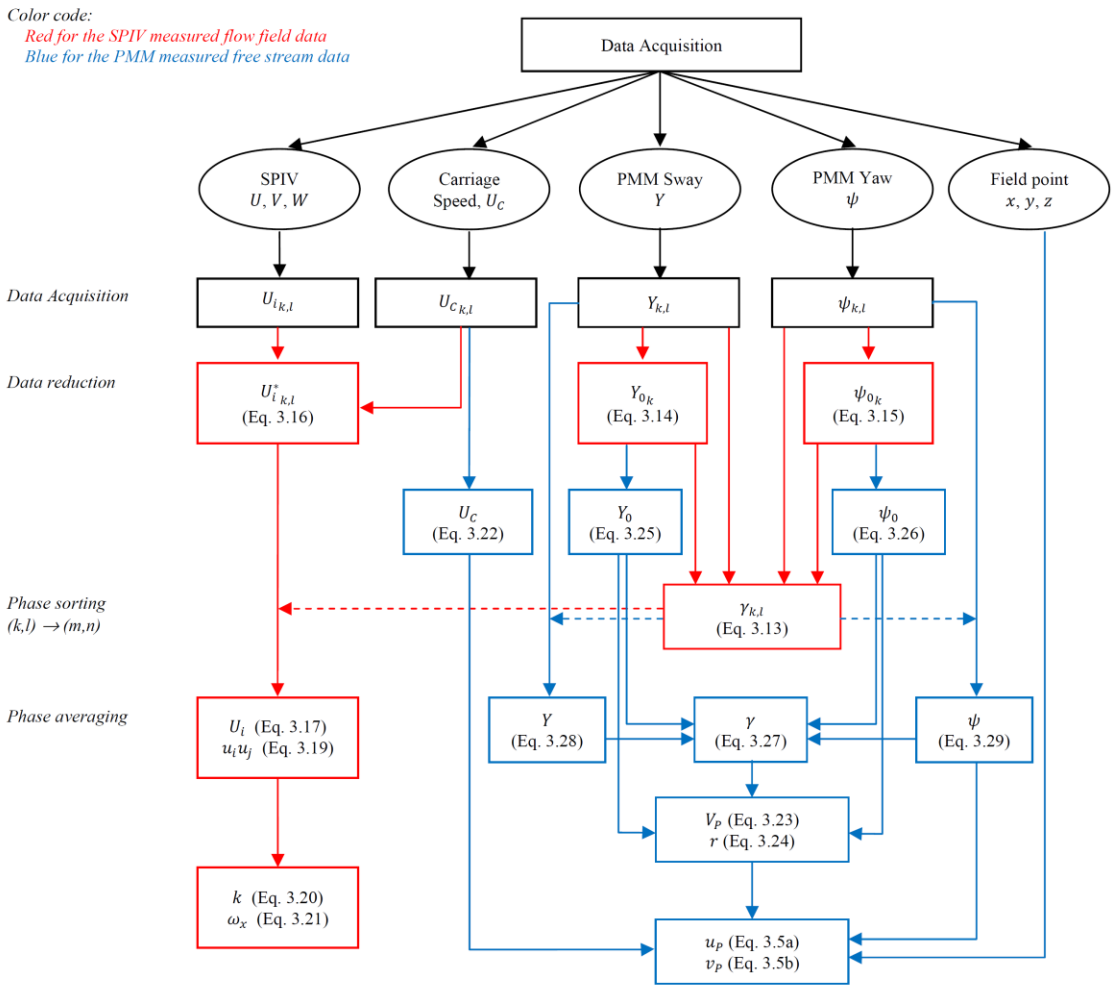

Figure 3-7 Data flow chart for data acquisition and reduction.

3.6 Measurement Systems and Calibration Procedures

3.6.1 Carriage Speed

Carriage speed is measured with an IIHR-designed and built speed circuit. The operating principle is integer pulse counting at a wheel-mounted encoder. The hardware consists of an 8000-count optical encoder, carriage wheel, sprocket pair and chain, analog-digital (AD) converter, and PC. Linear resolution of the encoder, sprocket pair and

chain, and wheel assembly is 0.15 mm/pulse. The speed circuit is periodically bench-calibrated to determine and adjust the frequency input/voltage output transfer function.

3.6.2 6-componet loadcell

Three forces and three moments are measured with an Izumi six-component strain-gage type loadcell, six Izumi amplifiers, 16-channel AD converter and PC. Maximum force and moment ranges are 500 N for F_x, F_y, F_z and 50 N-m, 50 N-m, 200 N-m for M_x, M_y, M_z, respectively. During the tests, the loadcell is calibrated internally at the amplifiers periodically. After the tests, the loadcell is statically calibrated on a test stand using standard weights.

Figure 3-8 Izumi six-component load cell (left) and Izumi amplifiers (right).

3.6.3 Motion Tracker

Ship model motions are measured using a Krypton Electronic Engineering Rodym DMM motion tracker. The Rodym DMM is a camera-based measurement system that triangulates the position of a target in 3D space for contactless measurement and evaluation of 6DOF motions. The hardware consists of a camera module comprising three fixed CCD cameras, target with 1-256 light-emitting diodes (LED's), camera control unit,

hand-held probe with six LED's, and PC. Krypton software is used for system calibration, and data acquisition and reduction.

Figure 3-9 Krypton Electronic Engineering Rodym DMM motion tracker.

The camera module measurement volume is determined by the overlapping field of views of the three CCD cameras. The measurement volume is 17 m^3, pyramidal-shaped with a ±30° viewing angle, and divided into three accuracy zones: (1) 1.5-3.0 m distance from camera module, zone #1; (2) 3.0-5.0 m distance from camera module, zone #2; and (3) 5.0-6.0 m distance from camera module, zone #3. Performance assessment results for the Rodym DMM using standard coordinate metrology procedures (ISO 10360-II, VDI 2617) are published by Krypton in a camera verification report as ±0.1 mm, ±0.2 mm, ±0.3 mm in zones #1, #2, #3, respectively.

A target with one or more affixed LED's is calibrated with the camera module and hand-held probe. 6DOF ascii data is reported at various data rates (dependent on the number of target LED's) from the camera controller on six analog channels. A seventh analog channel is used to report visibility of the target during the tests to ensure an unobstructed view between the camera module and target as the ship model moves through its trajectory.

3.6.4 Stereo PIV

The stereo PIV is a LaVision Inc. custom-designed and built measurement system (Fig. 3-10). It consists of a 120 mJ Nd:Yag laser, submerged lightsheet generator, two 1600x1200 pixel cross-correlation cameras fitted with 50 mm f/1.8 lenses, and computer and software for data acquisition and reduction of PIV recordings. The lenses are equipped with motors for automatic remote focusing and aperture adjustments. The camera bodies are equipped with motors for automatic remote Scheimpflug angle adjustments.

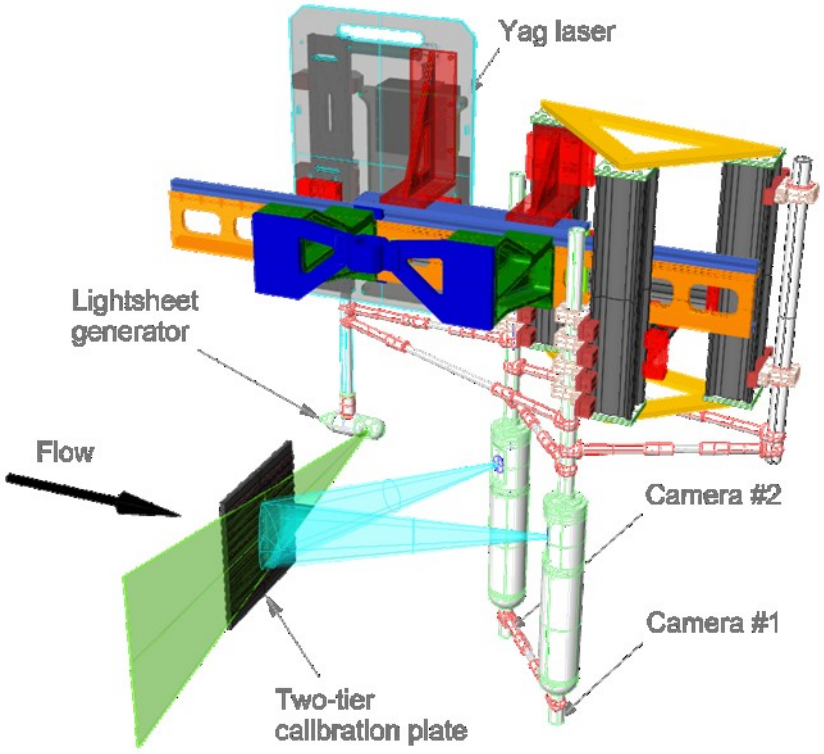

Figure 3-10 LaVision Stereo PIV System.

Both cameras are arranged asymmetrically in submerged enclosures downstream of the lightsheet to minimize wave and flowfield effects of the enclosures at the measurement area. The laser, lightsheet generator, and camera enclosures are assembled on a lightweight matrix of aluminum extrusions for adjustability and rigidity. The SPIV system is calibrated in situ by submerging and fixing a two-tier LaVision calibration plate in the plane of the lightsheet where both camera field of views overlap. Single images from each camera are used to create a mapping function of the plate markers which is used later to reconstruct 3D velocity vectors from particle image pairs. The original calibration is refined iteratively with a self-calibration procedure to account for translational or rotational misalignment of the calibration plate in the lightsheet plane.

3.7 Data Acquisition Procedures

3.7.1 Forces and Moments

3.7.1.1 Data Acquisition Setup

The forces and moment experimental setup is as shown in Fig. 3-6 (c) and (d). For the fixed-model condition cases (Fig. 3-6c), the yaw platter supports a 4-m strongback, rigid post, load cell, fixed mount, and ship model and restrains all translations and rotations of the model. Sinkage and trim is set at the fixed mount for $FX_{\sigma\tau}$ condition cases at Fr = 0.28. For the free-model condition cases (Fig. 3-6d), the yaw platter supports the loadcell, 1.5-m strongback, three balances that enable pitch, heave, and roll (fixed or free) motions and restrains surge, sway, yaw motions. Roll motion is enabled or disabled with spherical or one-degree-of-freedom connection bearings, respectively, at the fore and aft balances. In both fixed and free cases, model 5512 is mounted on the tank centerline at its design waterline (except for fixed tests with sinkage and trim) and either towed from z = 0.01m (fixed) or z = 0.0m (free). Force and moment data cables are run to six onboard amplifiers. For measuring sway position, a linear potentiometer is

fixed to the PMM carriage frame and linked to the sway box with wire loop, two pulley wheels, and bracket. For measuring yaw position, a rotational potentiometer is fixed inside the sway box and linked to the yaw platter with a wire loop. Data lines connect both potentiometers to amplifiers aboard the drive carriage.

The Krypton camera module is mounted backward-facing from the rear of the drive carriage for an unobstructed view of the LED target. The target is mounted near the bow and over the models centerline such that the LED's face the camera module. The targets position places it within zone #1 of the measurement volume. Axial (Δx_{LCG} = -593 mm) and vertical (Δz_{LCG} = 213 mm) measurements from the target center to the LCG are made to enable the Krypton software to shift local measurements at the targets origin to the LCG of model 5512. This shift is setup in software and occurs synchronously as data is acquired. 6DOF ascii motion data is reported from the camera controller at 40 Hz. Analog data lines from the loadcell, motion tracker, PMM potentiometers, and carriage speed circuit are run to the drive carriage to an onboard 16-channel AD card and PC.

3.7.1.2 Data Acquisition Procedures

First, at-rest reference voltages are measured for all instruments. Then, the PMM is activated and ten seconds elapse to allow enough time for the motion to reach a steady rate. Next, the carriage is started and accelerates through 10 m to a constant speed. Data acquisition commences after traveling another 10 m which allows the unsteady free surface to develop and reach a state where it is not in transition. Data acquisition occurs at 100 Hz / channel for 30, 20, 10 seconds, respectively, for cases where Fr = 0.138, 0.28, 0.41, respectively. For static drift tests, the PMM remains inactive during the carriage run, however, all other procedures above are followed.

3.7.2 Phase-Averaged Flowfield

3.7.2.1 Data Acquisition Setup

The phase-averaged flowfield experimental setup is shown in Fig. 3-11. Model 5512 is ballasted to its dynamic sinkage and trim for $Fr = 0.28$ and mounted on the tank centerline in the fixed condition. The PMM scotch yoke is adjusted for a 327.2 mm sway amplitude and a maximum heading angle of 10.2°. PMM potentiometers are incorporated in the sway carriage and yaw linkage to track the model maneuvers. Potentiometer cabling is run to onboard amplifiers. The SPIV system is assembled on an automated two-axis (y, z) traverse which slides on the 4 m strongback underneath the PMM carriage in the x-coordinate. The laser and lightsheet optics are arranged to deliver a vertical lightsheet in the (y, z) crossplane.

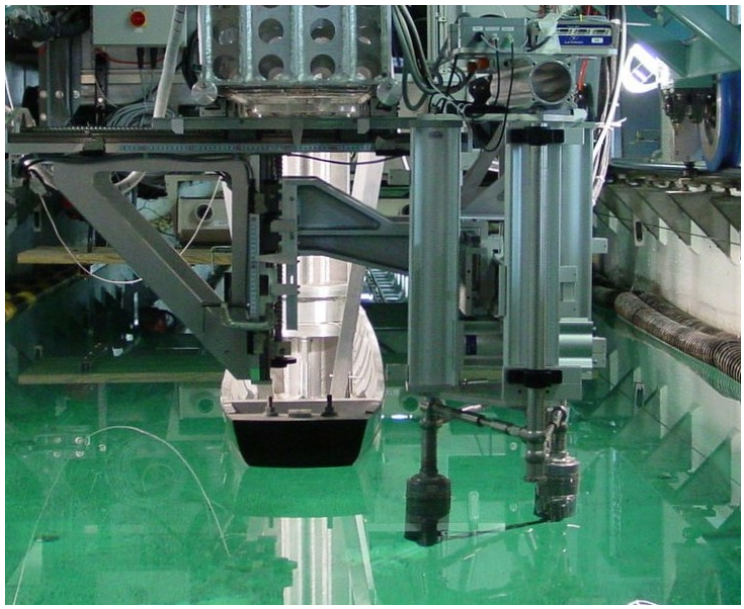

Figure 3-11 Experimental setup for the SPIV flow measurement tests.

Standoff distance between the lightsheet generator and the measurement area center is 553.91 mm (Fig 3-12). The cameras are arranged with equal standoff distances between the enclosures and the measurement area (643.96 mm), 33° of separation between cameras, and a 22° angle between camera #1 and the tank axis to provide clearance with the model and avoid an extremely shallow angle between camera #2 and the cross plane. A minimum separation angle of 30° between cameras is maintained to ensure good measurement quality.

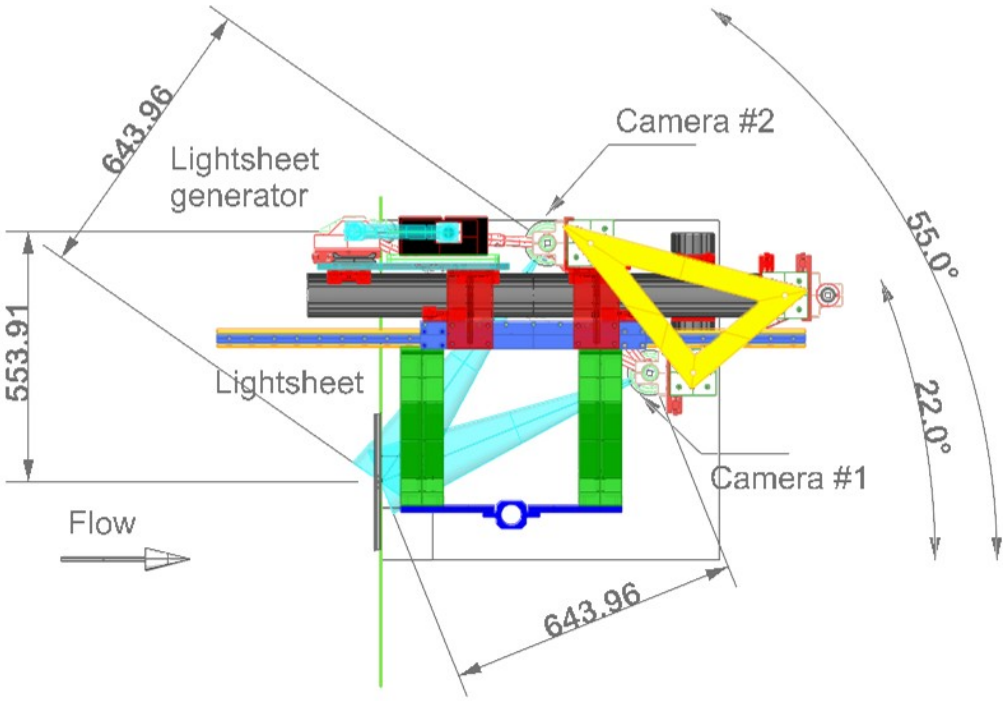

Figure 3-12 Overhead view of the Stereo PIV System.

Power, video, and trigger cables are routed through the strongback to the PIV computer onboard the drive carriage. The laser power supplies ride aboard the PMM carriage. A single umbilical for coolant and electronics cables links the power supplies and the laser head. Laser trigger lines also run through the strongback to the drive carriage

PIV computer. The SPIV computer is equipped with frame grabbers, a programmable timing unit, a TTL/IO board, and an 8-channel AD board capable of synchronously acquiring analog voltages and PIV recordings. An IIHR-designed and -built PIV synchronizer is used to provide equally-spaced trigger pulses to the SPIV computer in order to acquire PIV recordings at presettable, repeatable phase angles in the pure yaw maneuver. This is achieved as the synchronizer monitors the analog output from the PMM sway potentiometer. When a predetermined voltage corresponding to 45° on the rising side of the sway curve is reached, the synchronizer emits a burst of 32 TTL's, each having a 200 μsec pulse width and a time between triggers of 233 ms. Since the pure yaw motion frequency is $f = 0.134$ Hz, this enables a SPIV recording every 11.25° equally spaced through one PMM period. The process is then repeated on subsequent PMM cycles.

3.7.2.2 Data Acquisition Procedures

First, the PMM is activated and ten seconds elapse to allow enough time for the motion to reach a steady rate. A digital oscilloscope monitors the sway carriage analog voltage output and the synchronizer triggers. When they are synched-up, the carriage is started and accelerates through 10 m to a constant speed. Data acquisition commences after traveling another 10 m which allows the unsteady free surface and flowfield to develop and reach a state where they are not in transition. Data acquisition occurs at 4.288 Hz for 19 sec enabling 80-90 SPIV recordings or about 2.5 recordings per each of the 32 phases in the PMM cycle.

At least 100 carriage runs are performed for a given measurement area position to obtain enough recordings at each phase to achieve convergence of the data. Convergence is monitored as the data is acquired and data acquisition is typically stopped when the residual in the velocities drops by two orders of magnitude (Section 4.2). Data acquisition is completed at several overlapping zones at each x-station in order to piece together

a complete picture of the region of interest. Four or five zones are used at each *x*-station to cover the region of interest.

3.8 Data Reduction Procedures

3.8.1 Forces and Moment

Data is processed in batches with a FORTRAN program on a Windows PC. Groups of zero-point and carriage run raw data files are read. Analog voltages are scaled to engineering units with the calibration coefficients and the zero-point correction is computed. For the static drift tests, average values of force and moment are computed from the time histories. For the dynamic tests, the prime frequency of the motion is computed with a fast-Fourier transform (FFT), followed by computation of a 6^{th}-order FS expansion of the forces and moment. Additionally, the mount-mass effect is computed and subtracted from the dynamic data. For the free-model condition cases, the 6DOF motion of the ship model is analyzed as per the forces and moment harmonic analysis. It is important to note that that v_{PMM}, $\dot{v}_{PMM}$, r_{PMM}, $\dot{r}_{PMM}$ are not computed with equations (3.1), respectively, but are derived by differentiating potentiometer-measured values of y_{PMM} and ψ. All periodic data is expressed and output through one PMM cycle. Finally, the hydrodynamic derivatives are computed as per presented in Section 2 as the last data reduction step.

3.8.2 Phase-Averaged Flowfield

SPIV recordings are processed with LaVision DaVis v7.1 software in batch processes. First, the raw images are rotated and mirrored. Then the correlations are completed with one pass using 64 x 64 pixel interrogation windows followed by two passes using 32 x 32 pixel interrogation windows. Fifty percent overlap is used in the horizontal and vertical directions on all correlation passes. A high-accuracy Whitaker reconstruction of the vectors is used in the final pass. Vectors are range filtered using

median values of 0.65, -0.065, 0.065 for (U, V, W), respectively, and bands of ±0.65. A median filter follows, removing vectors if their magnitude is greater than two times the rms value of their neighboring vectors. Spurious vectors are not replaced with interpolated values, and blank spots in the measurement area are not filled. The vector fields and analog voltages (Sanshin sway and yaw and Krypton sway and yaw) are exported and organized according to zone number and carriage run. Then, a FORTRAN program is used to complete the phase-averaging part of the data reduction. Vectors from each carriage run are non-dimensionalized with the measured carriage speeds. Then, the vector fields are sorted into their respective phase groups by analyzing the sway and yaw analog voltage levels associated with each SPIV recording. When the phase-sorting is complete, the phase averaged velocities and Reynolds stresses are computed. The solution for the complete region of interest is stitched together from the multiple zones at the x-station. An averaging technique will be used in the overlapping regions of the multiple zones.

CHAPTER 4 STATISTICAL CONVERGENCE

4.1 Forces and Moment and Motions Data

Single records of forces and moment and motions data for static and dynamic PMM tests are analyzed and statistical convergence of data are estimated. Herein single record implies a set of data acquired during individual carriage runs. Analysis begins with classifications of data into either deterministic or random data where further into either periodic or transient for the former category and into either stationary or non-stationary for the latter category. The term 'deterministic' implies that data can be described explicitly by a mathematical relationship, on the other hand, the term 'random' means that data cannot be described by explicit mathematical relationship, instead, by means of probability statements and/or statistical averages (Bendat 1966, pp. 2). A practical decision whether or not data are deterministic or random, as per Bendat, is usually based on the ability to reproduce the data by controlled experiments. Accordingly, herein for PMM applications, only the time mean values of static drift test data and the harmonics of dynamic tests data are classified as deterministic, while all the other components of data including transient are considered as random. Once deterministic part of data is decided, the stationarity of the random part of data is of interest since only stationary data are guaranteed to converge. Stationarity of data is tested by using nonparametric (distribution-free) statistical procedures such as the 'run test' and 'trend test'. Next, statistical convergence of the time mean values of static drift test data is estimated based on the convergence of confidence interval of the mean values. Typically, data samples containing narrow-banded sinusoid components or transient components may not be distributed normally, thus confidence interval is estimated using the Tchebycheff inequality for unknown distributions rather than the Student-t for normal distributions. Statistical convergence, however, may not be applicable for dynamic tests data since usually two or three periods of data are available due to limited length of IIHR towing tank facility.

4.1.1 Time History of data

Typical examples of time history and Fast Fourier Transform (FFT) of data are shown in Fig. 4-1 for static drift test. Data includes carriage speed (U_C), drift angle (β), forces (F_x, F_y), moment (M_z), and motions (z_{mm}, θ, ϕ). Of those variables, U_C, β, and ϕ are the controlled (input) parameters set at the desired values 1.531 m/s, -10°, and 0°, respectively, whereas F_x, F_y, M_z, z_{mm}, and θ are the results (output) of the test. Data are sampled at a rate of 100Hz (i.e. $\Delta t = 0.01$ sec) for a time-period of $T = 20$ sec corresponding to $U_C \cdot T/L \approx 10$ where $L = 3.148$ m is the model length. Data acquisition commences after carriage acceleration and U_C nearly constant, which takes about 3 ~ 4 L. For FFT, total $N = 1{,}024$ data are selected from the time history of each variable, between t = 5 ~ 15 sec, which gives a frequency step $\Delta f = 1/N \cdot \Delta t \approx 0.1$ Hz in the FFT. Time histories are shown for one case out of 12 repeat tests at the same conditions, whereas the FFT results are shown for all the 12 cases emphasizing the repeatability of measurement. FFT data as well include two different β cases (0° and -20°) for possible hydrodynamic effects on the results, which may or may not increase with β, particularly in the frequency domain.

For U_C shown in Fig. 4-1 (a), time history exhibits random fluctuations of which root-mean-square (rms) value is 0.008 m/s (about 0.5% of the mean $U_C = 1.514$ m/s). Dominant frequency of the random fluctuation is between 1 ~ 2.5 Hz from the FFT that as well reveals the underlying long-period oscillations of data with frequencies between 0.1 ~ 0.6 Hz, otherwise seemingly white noise. Drift angle β shown in Fig. 4-1 (b) also exhibits long-period oscillations with an amplitude 0.06° (about 0.6% of the mean $\beta = -10.1°$) and dominant frequency between 0.1 – 0.3 Hz from the FFT otherwise white noise. Roll angle ϕ shown in Fig. 4-1 (c) is almost random fluctuation with an rms value 0.02° (about 36% of the mean $\phi = -0.05°$) and dominant frequencies 1.2 and 2 Hz maybe coherent with those for U_C. Possible sources for long period oscillations of U_C can be carriage speed control-loop feedback or non-perfectly straight rail alignments, and the sources for random fluctuations of U_C can be mechanical vibrations due to the irregular

surfaces of the carriage wheels and/or rails. Which may cause the long period oscillations and/or high frequency fluctuations in β and ϕ, too. Deviations of the mean values of those variables from the initial set-up values, -10° and 0°, respectively, can be attributed in part to the model mount flexibility and in part to model asymmetry. Note that although not shown, mean ϕ value grows with β, -0.004° and -0.07° at β = 0° and -20°, respectively.

Responses in forces and moment and motions to the aforementioned input parameters, U_C, β, and ϕ, are shown in Fig. 4-1 (d) – (h) for F_x, F_y, M_z, z_{mm}, and θ. From time histories, F_x, F_y, and M_z are random fluctuations with rms values 3.4 N, 3.3 N, and 3.4 Nm (32%, 12%, and 8% of the mean values -10.7 N, -28.1 N, and -43.4 Nm), respectively. From FFT, those random fluctuations are narrow banded, in general between 2 – 10 Hz with sharp peaks typically near at 3, 4, 5, and 10 Hz due mainly to mechanical vibrations as will be identified latter. On the other hand, heave and pitch motions z_{mm} and θ time histories shown in Fig. 4-1 (g) and (h) are random fluctuations superposed on apparently transient oscillations. The random fluctuations are with rms values 0.5 mm and 0.01° (5% of mean z_{mm} = 8.9 mm and 9% of mean θ = -0.153°) respectively. The transient oscillations are typically damped oscillations that can be written in a mathematic form as $Ae^{-at}\cos(2\pi f_{tr}t)$. The oscillation amplitude A is 1.13 mm and 0.09° (13% of mean z_{mm} and 59% of mean θ) respectively, however, subject to random depending on the time point where data sampling commences. The damping coefficient a = 0.08 sec^{-1} and the oscillation frequency f_{tr} = 0.255 Hz are the same for both z_{mm} and θ. Although not shown, in general A increases with β whereas a and f_{tr} are nearly constant. Those transient oscillations are due to start-up transient such that f_{tr} is far from z_{mm} and θ natural frequency $f_3 = f_5$ = 1.2 Hz estimated from hydrostatic restoring forces (Irvine et al. 2008). The heave natural frequency f_3 is clearly seen from the FFT for z_{mm} shown in Fig. 4-1 (g) while the pitch natural frequency f_5 is less distinctive from the FFT for θ shown in Fig. 4-1 (h). Note that it is not clear if the similar or same peak frequencies of U_C, i.e. near 0.2

Hz and 1.2 Hz form Fig. 4-1 (a), are coincidence or there may exist interactions between towing speed and model motions.

Dynamic test time history and FFT are shown in Fig. 4-2 similarly as for static drift test. Shown at the left column are the time histories of pure sway test data for one case out of 12 repeat tests at β_{max} = 10° condition. Carriage speed U_C, sway trajectory y, and heading angle ψ shown in (a) – (c) are the controlled (input) parameters for pure sway test. The overall trend of U_C (set at 1.531 m/s) is similar as for static drift test discussed previously. Sway trajectory $y = A \sin(2\pi f_{\mathrm{PMM}} t)$ is a forced sinusoidal oscillation with A = 0.317 m (about 0.1 L) and f_{PMM} = 0.134 Hz. Heading angle ψ is set at zero but exhibits an oscillation with amplitude 0.06° and almost out of phase with y. Although not shown, roll angle ϕ is also set at zero and shows an oscillation with amplitude 0.1° and out of phase with y. Forces and moment F_x, F_y, and M_z in (d) – (f) are random fluctuations with rms values 4.0 N, 4.7 N, and 2.3 Nm (54%, 4%, and 3% of the dynamic range 7.4 N, 114.4 N, and 92.7 Nm) respectively, over-riding the harmonic oscillations with f_{PMM} as the fundamental frequency. Heave z_{mm} and pitch θ motions in (g) and (h) are mixtures of harmonic oscillation, transient oscillation, and random fluctuations. Harmonic oscillations are with f_{PMM} as the fundamental frequency. Transient oscillations may be similar as for static drift test, however, it is difficult to identify them from the signal as the transient oscillation frequency f_{tr} = 0.255 Hz is close to the dominant harmonic (the 2nd order harmonic) frequency $2f_{PMM}$ = 0.268 Hz for both variables. Random fluctuations are with rms values 0.4 mm and 0.015° (7% of mean z_{mm} = 5.6 mm and 10% of mean θ = -0.164°) respectively. For dynamic test data, the harmonic oscillation component of each variable data is classified as deterministic and other components including transient oscillations and random fluctuations as random data, designated with a '*' symbol such that

$$x^* = x(t) - x_{\mathrm{FS}}(t) \tag{4.1}$$

where x can be any dynamic test variable (except for U_C) and x_{FS} is the harmonic component of x evaluated using a Fourier Series (FS) expansion of x with f_{PMM} as the fundamental frequency. Note that U_C is independent of f_{PMM} and not expanded with FS. Note also for z_{mm} and θ that x_{FS} can include the transient oscillation component of the variable data when $f_{tr} \approx n \cdot f_{PMM}$ for any integer number of n. At the right column of Fig. 4-2, shown are the FFT results of x^* for all types of dynamic test including pure sway, pure yaw, and yaw and drift tests, which are the UA cases of each test with 12 repeat tests. In general the FFT results for each type of dynamic tests are similar each other, and as well similar with those for static drift test shown in Fig. 4-1. For U_C in (a), same discussions can be make as for static drift test. For y and ψ in (b) and (c), two peak frequencies in the FFT are observed near at $3f_{PMM}$ and $5f_{PMM}$ but with very small amplitudes, usually much less than 0.1% of the range of the variables. For F_x, F_y, and M_z in (d) – (f), peak frequencies are usually near 3, 4, 5, 7, and 10 Hz similarly as static drift data. FFT's for z_{mm} and θ shown in (g) and (h) are almost same as those for static drift except for relatively smaller amplitudes at the frequency range between 0.1 – 0.3 Hz as $f_{tr} \approx 2f_{PMM}$ for all cases.

A separate set of tests were carried out identifying the sources of peak frequencies of the forces and moment data. Test was done first without the model and only the load-cell was installed to the PMM carriage that is connect to the driving carriage. Tests included total 11 cases arranged into five groups (A, B, C, D, and E) as summarized in Table 4-1. Model was not installed for Groups A, B, C, and D whereas installed for Group E but in air to avoid any possible hydrodynamic effects. Tests were stationary in surge direction for Groups A, B, and C with $U_C = 0$ whereas in towing motion for Groups D and E with $U_C = 1.531$ m/s (with two repeat tests for Group E). The PMM motor was turned on for all test groups rotating with one of the three cyclic frequencies $f_e = 0.01$, 0.96, or 0.134 Hz to excite the load-cell. Group A emphasizes the natural frequencies of the PMM system including the load-cell by minimizing any possible external noise sources but f_e. Groups B and C are intended to include the effects of mechanical vibra-

tions from the Scotch Yoke system for PMM. Groups D and E are to include mechanical vibrations of the PMM system from such as non-perfectly regular surfaces of the rails and/or wheels of carriages. The FFT results of the test are shown in Fig. 4-3, for which the harmonics of the excitation frequency f_e up to the 6^{th} order were filtered out from the signals using the equation (4.1). From Fig. 4-3 (a) – (f), the responses are at very specific frequencies near 5 and 7 Hz. From Fig. 4-3 (g) – (l), as the carriages are running, many of peak frequencies appear roughly between 2 – 10 Hz with sharp peaks near at 3, 4, 5, 7, and 10 Hz. Consequently, test results suggest that the sources of the 5 and 7Hz are the natural frequencies of the load-cell, the PMM carriage, or combined, and the sources of the 3, 4, and 10 Hz are from the mechanical vibration. However, more study is needed to determine whether a portion may be due to hydrodynamic sources such as flow turbulence, flow separation instabilities, and/or, vortex breakdown.

4.1.2 Stationarity Test

The time history data are tested for stationarity by using the two non-parametric statistical procedures known as 'Run test' and 'Trend test' (Bendat 1966, pp. 219 - 223). Four important assumptions made for the stationarity tests are: 1) If the data of interest are stationary, then the statistical properties computed for each sequence of short time intervals will not vary significantly from on time interval to the next; 2) Verification of weak stationarity (time invariance of the mean value and autocorrelation function) will be acceptable; 3) The sample record of the data to be investigated is very long compared to the random fluctuations of the data time history; 4) If the mean square value (or variance) of the data of interest is stationary, then the autocorrelation function for the data is also stationary. Some important features of the non-parametric (or distribution-free) procedures which do not assume a specific distribution for the random data are: 1) The frequency bandwidth of the data is not required; 2) The exact averaging time used to measure the mean and mean square values is not required; 3) It is not necessary for the data to

be completely random. Two non-parametric procedures 'Run test' and 'Trend test' are briefly summarized from Bendat (1966, pp. 156 – 159) as follows.

Run test: Consider a sequence of N observations of a random variable x where each observation is classified into one of two mutually exclusive categories, which may be identified simply by plus (+) or minus (-). The simplest example would be a sequence measured values x_i, i = 1, 2, 3, …, N, with a mean value $\bar{x}$, where each observation is $x_i \geq \bar{x}$ (+) or $x_i < \bar{x}$ (–). A run is defined as a sequence of identical observations that are followed or preceded by a different observation or no observation at all. For example; ++ (1), – (2), ++ (3), – (4), +++ (5), – (6), + (7), – – (8), + (9), – – (10), + (11), – – – (12). In this example there are r = 12 runs in the sequence of N = 20 observations. The number of runs which occur in a sequence of observations gives an indication as to whether or not results are independent random observations of the same random variable. Specifically, if a sequence of N observations are independent observations of the same random variable, that is, the probability of a (+) or (-) result does not change from one observation to the next, then the sampling distribution for the number of runs in the sequence is a random variable r with a mean value and variance as follows.

$$\mu_r = \frac{N}{2} + 1 \qquad (4.2)$$

$$\sigma_r^2 = \frac{N(N-2)}{4(N-1)} \qquad (4.3)$$

Trend test: Consider a sequence of N observations of a random variable x, where the observations are denoted by x_i, i = 1, 2, 3, …, N. Now, count the number of times that $x_i > x_j$ for i < j. Each such inequality is called a reverse arrangement. The total number of reverse arrangements is denoted by A. A general definition for A is as follows. From the set of observations $x_1, x_2, \ldots, x_N$, define

$$h_{ij} = \begin{cases} 1 & if\ xi > xj \\ 0 & otherwise \end{cases} \qquad (4.4)$$

Then

$$A = \sum_{i=1}^{N-1} A_i \qquad (4.5)$$

where

$$A_i = \sum_{j=i+1}^{N} h_{ij} \qquad (4.6)$$

If the sequence of N observations are independent observations of the same random variable, then the number of reverse arrangements is a random variable A with a mean and variance as follows.

$$\mu_A = \frac{N(N-1)}{4} \qquad (4.7)$$

$$\sigma_A^2 = \frac{N(2N+5)(N-1)}{72} \qquad (4.8)$$

In general, the trend test is more powerful than the run test for detecting monotonic trends in a sequence of observations, however, not powerful for detecting fluctuating trends.

For stationarity tests the time histories of static drift test and pure sway test data shown in Figs. 4-1 and 4-2 are divided into $N = 20$ equal time intervals with an interval size of 100 data per each interval (corresponding to 1 sec), where the data in each interval may be considered independent. Note for pure sway data (and for all dynamic tests data) that stationarity tests are applied only for the random component of data x^* defined in equation (4.1). Once proved the stationarity of its random part, then the dynamic data is referred herein as stationary. Next, a mean value ($\bar{x}_1, \bar{x}_2, \bar{x}_3, \ldots, \bar{x}_N$) and mean square value ($\overline{x_1^2}, \overline{x_2^2}, \overline{x_3^2}, \ldots, \overline{x_N^2}$) for each interval are computed and aligned in time sequence as shown in Fig. 4-4. It is hypothesized that the sequence of $\bar{x}$ and the sequence of $\overline{x^2}$ are each independent sample values of a random variable with a true mean value and mean square value, respectively. If this hypothesis is true, the variations in the sequence of sampled values will be random and display no trends. Hence, the number of runs in the sequence will be as expected for a sequence of independent random observations of the random variable. Moreover, the number of reverse arrangements in the sequence will be as expected for a sequence of independent random observations of the same variable. If the number of runs or reverse arrangements is significantly different from the expected number, the hypothesis of stationarity would be rejected.

Run and Trend tests results are presented in Table 4-2 for static drift and pure sway tests data, respectively. Both tests were performed at the 5% level of significance. Then, the acceptance region[8] is $6 \le r \le 15$ for the run test and $64 \le A \le 125$ for the trend

[8] The acceptance region can be read from a statistics tables (e.g. Bendat 1966, pp. 170 – 171) or calculated as follows.

test, respectively, for $N = 20$. From Table 4-2, r and A values of the mean square $\overline{x^2}$ for all variables are within the acceptance regions of run test and trend test, indicating there is no evidence of an underlying trend. However, r and A values of the mean $\bar{x}$ value for some variables are outside the acceptance regions, indicating possible non-stationarity of those variables. For static drift data, only β fails the run test ($r = 5$ for $\bar{x}$) whereas U_C, ϕ, and F_y fail the trend test ($A = 145$, 127, and 133 for $\bar{x}$, respectively). For pure sway data, F_x, F_y, and z_{mm} fail the run test ($r = 16$, 5, and 4 for $\bar{x}$, respectively) whereas U_C, y, and z_{mm} fail the trend test ($A = 136$, 126, and 129 for $\bar{x}$, respectively). When the tests are performed for collections of data from the 12 repeat tests, however, the average r and A values show that U_C, β, and ϕ fail the tests and the other variables F_x, F_y, M_z, z_{mm}, and θ are all stationary in an average sense. Nonetheless, the average r and A values for β ($r = 5$) and ϕ ($A = 130$, 126) are not significantly different from the acceptance regions such that can be considered as accepted if lower the level of significance of test to 1% of which acceptance region is $5 \le r \le 16$ for the run test and $59 \le A \le 130$ for the trend test, respectively. U_C fails both the run test ($r = 5$) and the trend test ($A = 143$, 140) revealing a strong evidence of an underlying trend. The underlying trend in U_C can be easily seen from Fig. 10 (a) where a step-wise decrease in the interval mean value of U_C is observed near at the 12th interval and as well from Figs. 4-1 (a) and 4-2 (a) where apparent decrease of U_C in the time histories neat at $t = 12$ sec. This decrease of U_C is considered as due to the lack in electric power for driving two carriages, the main driving carriage and the PMM carriage, at the same time. However, the amount of change of U_C is fairly

---

$(\mu_{r,A} + z_{1-\alpha/2} \cdot \sigma_{r,A}) \le r, A \le (\mu_{r,A} + z_{\alpha/2} \cdot \sigma_{r,A})$

where $\alpha = 0.05$ and $z_{\alpha/2} = -z_{1-\alpha/2} = 1.96$ for 5% level of significance and μ_r, σ_r, μ_A, σ_A are given in equations (4.2), (4.3), (4.7), (4.8), respectively. Note that the limit value of the acceptance region should be rounded down to an integer number.

small (usually 0.6 ~ 0.7% of mean U_C) such that the stationarity of other variables is not affected significantly or at least not noticeable.

4.1.3 Statistical Convergence

Convergence of a random data being measured as time history can be defined such that the result of data, e.g. the mean value, does not change as acquiring more and more data. The Law of Large Numbers (e.g., Feller, 1968) guarantees that for any random data, x, the sample mean converges to an expected value (the true mean of x) when an infinite number of data is available. However, the number of data collectable from practical situations is in general limited to a finite number N, hence the extent of difference between the true mean μ_x and the sample mean $\bar{x}$ of the N data is of interest. Herein, the difference is estimated using a statistical concept of confidence interval for $\bar{x}$ with a certain probability. When the limit of interval, d, is smaller than a predetermined (or desired) value as increasing the sample size N, then the variable x is said to be 'statistically converged' and d is defined as the 'statistical convergence error' in $\bar{x}$.

Confidence interval of $\bar{x}$ is usually estimated by assuming a normal distribution of the random variable x and subsequently by assuming the Student-t distribution of $\bar{x}$, which is the underlying basic concept of typical uncertainty analysis procedures estimating the precision limit. The normal distribution assumption is justified by virtue of the central limit theorem for the precision limit of which random variable is the mean of each x time histories from a collection (ensemble) of repeated tests at the same conditions. In general, however, a normal distribution assumption is not justified for a single record of time history data that may contain narrow band sinusoid components and/or transient components as discussed previously for time histories of the PMM test data. In such a case a more generous and robust inequality, the Tchebycheff inequality, may be used estimating the confidence interval for any variable x without knowing the exact distribu-

tion. The Tchebycheff inequality can be written in probability statement as follows (Bendat 1966, pp. 62).

$$\text{Prob}\left[|\bar{x} - \mu_x| \leq c \cdot \frac{\sigma_x}{\sqrt{N}}\right] \geq 1 - \frac{1}{c^2} \tag{4.9}$$

where μ_x and σ_x is the true mean and standard deviation of x, respectively, $\bar{x}$ is the sample mean and N is the sample size of the x time history, and c can be any positive real number. The meaning of Tchebycheff inequality is that the probability for the true mean to fall within an interval $(\bar{x} - d, \bar{x} + d)$ where $d = c \cdot \sigma_x/\sqrt{N}$ is larger than $p = 1 - 1/c^2$ regardless of underlying distribution of x. In other words, the absolute difference between the true mean and the sample mean would be smaller than d with a confidence of $100p$ percent, for example, 95% for $c = 4.5$. A difficulty in applications of the inequality (9), however, arise from the fact that the true standard deviation σ_x value is unknown for the most of practical cases. Thus, herein the sample standard deviation s_x is used as a best estimator of σ_x for practical application purposes such that an approximate confidence interval $\hat{d}$ and the statistical convergence error $E_{sc}(\%)$ are defined as follows.

$$\hat{d} \equiv c \cdot \frac{s_x}{\sqrt{N}} \tag{4.10}$$

$$E_{sc}(\%) \equiv \frac{\hat{d}}{\bar{x}} = \frac{c}{\sqrt{N}} \cdot \frac{s_x}{\bar{x}} \times 100 \tag{4.11}$$

where N is the sample size, $\bar{x}$ and s_x are the sample mean and standard deviation, respectively, and $c = 4.5$ for a 95% confidence. Note that $\hat{d}$ is equivalent to the confidence interval for a normal distribution when $N > 10$ and $c = t = 2.0$ in (10), which has the same 95% confidence level.

Knowing the normality of data is important to estimate the convergence as it allows one to use the Student t instead of the c in (11) along with the justification for the use of sample standard deviation. Normality of data is tested using the chi-square good-

ness-of-fit test (Bendat 1966, pp. 146). For the test, data are grouped into K class intervals determined by using the 'minimum optimum number of class' for a sample size of N (Williams, C.A., Jr., 1950), which gives

$$\mathrm{X}^2 = \sum_{i=1}^{K} \frac{(f_i - F_i)^2}{F_i} \tag{4.12}$$

where f_i and F_i are the observed frequency and the expected frequency in the ith class interval, respectively. The acceptance region for a hypothesis that the data of interest is normal is

$$\mathrm{X}^2 \leq \chi^2_{n;\alpha} \tag{4.13}$$

where $\chi^2_{n;\alpha}$ is the χ^2 value for a degree of freedom $n = K - 3$ and for an α level of significance of the test. If the sample value of X^2 is greater than $\chi^2_{n;\alpha}$, the normality hypothesis is rejected.

In Fig. 4-5, shown are the sample distributions of the static drift U_C, β, ϕ, F_x, F_y, M_z, z_{mm}, and θ data collected from 12 repeat tests (designated with symbols 1 ~ 9, A, B, and C in the figure) with compared to theoretical standard normal distribution. The $\overline{\mathrm{X}^2}$ values shown in the figure are the average X^2 values tested for each of the 12 repeat cases. An interval size $K = 39$ is used for the sample size $N = 2{,}000$ and the chi-square tests are done at the 5% level of significance ($\alpha = 0.05$), which gives $\chi^2_{36;0.05} = 51.0$. Test result is fail for all variables as X^2 values are larger than $\chi^2_{36;0.05}$, whereas relatively not significantly for F_x, F_y ,and M_z ($\overline{\mathrm{X}^2} = 60.5$, 72.1, and 119.8, respectively) showing their probability density functions (pdf's) close to a normal distribution in Fig. 4-5 (d) – (f). The $\overline{\mathrm{X}^2}$ values for z_{mm}, ϕ, and θ (121.5, 139.0, and 145.5,) are relatively moderately and those for U_C, and β (471.8 and 1737.3) are significantly larger than $\chi^2_{36;0.05}$, respectively, showing moderate and significant discrepancies of pdf from a normal distribution as

shown in Fig. 4-5 (g), (c), (h), respectively and in Fig. 4-5 (a) and (b), respectively, respectively.

Running mean $\bar{x}(N)$ and standard deviation $s_x(N)$ values are shown in Fig. 4-6 (left column) for static drift test data $x = U_C$, β, ϕ, F_x, F_y, M_z, z_{mm}, and θ of which time histories are shown in Fig. 4-1. The $\bar{x}(N)$ and $s_x(N)$ are the sample mean and sample standard deviation values for a subset of data with a sample size N increasing from 1 to 2,000 (in time-wise from $t = 0.01$ to 20.0 sec) by continuously adding more and more data to the sample. In Fig. 4-6, the $\bar{x}(N)$ and $s_x(N)$ are normalized with their final values, i.e. values at $N = 2{,}000$, designated as $\bar{x}^*(N)$ and $s_x^*(N)$, respectively, emphasizing the convergence of those values. In general, both $\bar{x}^*(N)$ and $s_x^*(N)$ at first oscillate and then converge to their final values, a unity, as N increasing. The statistical convergence error $E_{sc}(\%)$ values of those variables are as well shown in Fig. 4-6 (right column), evaluated as per equation (4-11) using the $\bar{x}(N)$ and $s_x(N)$ values at each N. Shown in the figure are the $E_{sc}(\%)$ values using two c values, $c = 2.0$ and $c = 4.5$, providing a 75% and a 95% confidence in $\hat{d}$, respectively, from the Tchebycheff inequality. Summarized in Table 4-3 are the confidence interval $(\bar{x}^*(N) - \hat{d}^*, \bar{x}^*(N) + \hat{d}^*)$ values at $N = 1{,}000$, where $\hat{d}^*$ is the normalized $\hat{d}$ value similarly as for $\bar{x}^*(N)$, and the $E_{sc}(\%)$ values at $N = 2{,}000$, which are the average values of 12 repeat tests. Discussions for the results follow.

From the left column of Fig. 4-6, the convergence of $\bar{x}^*(N)$ can be categorized into three types according to the trend of $s_x^*(N)$ with N after the initial oscillation phase; almost const (Type I), decreasing (Type II), or increasing (Type III) with N, respectively. Variables F_x, F_y, and M_z shown in Fig. 4-6 (d), (e), and (f) correspond to Type I, of which sample distributions were close to a normal distribution as discussed previously. Confidence interval of those variables evaluated at $N = 1{,}000$ (shown as dashed lines, green for $c = 2.0$ and red for $c = 4.5$) well include the future $\bar{x}^*(N)$ values up to $N = 2{,}000$ even with $c = 2.0$. Variables z_{mm} and θ shown in Fig. 4-6 (g) and (h) correspond to Type II, which are the variables contain transient components in their data time histories. Con-

fidence interval of those variables evaluated at N = 1,000 for the c = 4.5 case contains the future $\bar{x}^*(N)$ but not for the c = 2.0 case. Variables U_C, β, and ϕ shown in Fig. 4-6 (a), (b), and (c) correspond to Type III, which are the variables of which dominant frequencies in data time history are low near at 0.1 ~ 0.2 Hz. Confidence interval of those variables evaluated at N = 1,000 does not contain future $\bar{x}^*(N)$ even for the c = 4.5 case. For the Type I or II data, the sample standard deviation s_x is either constant or decreasing as the sample size N is increasing. The true standard deviation σ_x is expected to be similar with or smaller than the sample standard deviation, which may justify the use of s_x in equation (4-10) instead of σ_x. For a pure sine wave, for example, of which $\sigma_x = 1/\sqrt{2}$ is known, the ratio $s_x/\sigma_x \approx 1.04$ after about one cycle and $s_x/\sigma_x < 1.01$ after about four cycles. For the Type III data, however, the use of s_x instead of σ_x is not justified, possibly the data sampling time might not be long enough to include more than four cycles of the long period (low frequency) oscillation of data.

From the right column of Fig. 4-6, the statistical convergence error E_{sc}(%) typically decrease with N either fast or gradually. The rate of decrease of E_{sc}(%) with N seem to be with regardless of the type of convergence discussed above, rather related to the ratio $s_x/\bar{x}$ value summarized Table 4-3. For U_C and β shown in Fig. 4-6 (a) and (b), the ratio $s_x/\bar{x}$ = 0.006 and 0.003, respectively, is so small that E_{sc}(%) becomes immediately smaller than 0.2% and 0.1%, respectively. For F_y, M_z, and z_{mm} shown in Fig. 4-6 (e), (f), and (g), the ratio $s_x/\bar{x}$ = 0.11, 0.08, and 0.07, respectively, is moderate small and *Esc*(%) value becomes smaller than 1% after $N \approx 400$ ($U_C \cdot t/L \approx 2$) for c = 2.0 and after $N \approx 1{,}400$ ($U_C \cdot t/L \approx 7$) for c = 4.5 except for F_y for the latter case. For ϕ, F_x, and θ shown in Fig. 4-6 (c), (d), and (h), the ratio $s_x/\bar{x}$ = 0.36, 0.30, and 0.25, respectively, is relatively larger than other variables and E_{sc}(%) value is larger than 1% even at N = 2,000 for both c = 2.0 and c = 4.5 cases.

Consequently, three factors play important roles for statistical convergence of data, which are the normality, the trend of sample standard deviation, and the ratio of stan-

dard deviation to the mean value of the data, respectively. When data are normal or nearly normal (such as F_x, F_y, or M_z), the statistical convergence error E_{sc}(%) can be evaluated using the confidence interval d evaluated with the Student t = 2.0 for a 95% confidence level, similarly as for typical uncertainty analysis procedures estimating the precision limit, which is equivalent to using $\hat{d}$ in equation (4-10) with c = 2.0. However, when data are not normal the used of Student t may underestimate the convergence error more than two times at the same level of confidence (e.g. for 95%, c/t = 4.5/2.0 = 2.25), and the distribution-free Tchebycheff inequality should be used estimating the confidence interval. More specifically, when data are not normal but the sample standard deviation s_x is almost constant or decreasing with N (such as z_{mm} or θ) the use of s_x in the Tchebycheff inequality is justified and the E_{sc}(%) can be estimated using the confidence interval $\hat{d}$ in equation (4-10) with c = 4.5 for a 95% confidence level. When data are not normal and the s_x is increasing with N (such as U_C, β, or ϕ), however, the used of s_x in the Tchebycheff inequality is not justified and the E_{sc}(%) may not be estimated properly. Lastly, the statistical convergence of data is also dependent on the ratio $s_x/\bar{x}$; data converge fast when the ratio $s_x/\bar{x}$ is small (such as U_C or β), gradually for moderate $s_x/\bar{x}$ values (such as F_y, M_z, or z_{mm}), and rather slowly for larger $s_x/\bar{x}$ values (such as ϕ, F_x, or θ), respectively.

Table 4-1 Noise Test Conditions.

Group	Model	U_C (m/s)	$2S_{mm}$ (mm)	ψ_{max} (°)	f_e (Hz)
A	Not Installed	0	0	0	0.010, 0.096, 0.134
B	Not Installed	0	317	0	0.010, 0.096, 0.134
C	Not Installed	0	318	14.2	0.010, 0.096, 0.134
D	Not Installed	1.531	317	0	0.134
E	Installed (in air)	1.531	327	10.2	0.134

Table 4-2 Tests for Stationarity.

	Run Test, r †$(6 \le r \le 15$ for $N = 20)$				Trend Test, A †$(64 \le A \le 125$ for $N = 20)$			
	Static drift		Pure sway		Static drift		Pure sway	
Var.	$\bar{x}$	$\overline{x^2}$	$\bar{x}$	$\overline{x^2}$	$\bar{x}$	$\overline{x^2}$	$\bar{x}$	$\overline{x^2}$
U_C	6 (5)	11 (10)	6 (5)	12 (12)	145 (143)	104 (104)	136 (140)	116 (104)
β or y	5 (5)	12(11)	9 (9)	6 (8)	82(82)	71(89)	126 (105)	101 (95)
ϕ	7 (6)	9 (10)	9 (7)	6 (9)	127 (130)	78 (96)	121 (126)	68 (90)
F_x	12 (12)	10 (10)	16 (13)	10 (11)	108 (103)	100 (100)	92 (102)	76 (92)
F_y	8 (8)	12 (9)	5 (7)	6 (9)	133 (114)	76 (87)	67 (76)	82 (89)
M_z	6 (8)	10 (9)	11 (9)	13 (10)	121 (113)	106 (103)	90 (92)	103 (96)
z_{mm}	10 (10)	12 (12)	4 (7)	11 (10)	95 (106)	86 (103)	129 (116)	71 (83)
θ	11 (11)	14 (11)	10 (10)	9 (9)	102 (101)	108 (122)	100 (103)	77 (71)

† Acceptance region at the 5% level of significance
( ): Average value for 12 repeat tests;
Red: Outside the acceptance region.

Table 4-3 Statistical Convergence of Data (Averages for 12 repeat tests).

Var. x	Normality $\overline{X^2}$	†Confidence interval $\hat{d}$ at $N = 1{,}000$				E_{sc}(%) at $N = 2{,}000$		
		$c = 2.0$		$c = 4.5$		$s_x/\bar{x}$	$c = 2.0$	$c = 4.5$
		$\bar{x}^* - \hat{d}^*$	$\bar{x}^* + \hat{d}^*$	$\bar{x}^* - \hat{d}^*$	$\bar{x}^* + \hat{d}^*$			
U_C	471.8	1.002	1.003	1.002	1.003	0.006	0.03	0.06
β	1737.3	1.001	1.001	1.001	1.002	0.003	0.01	0.03
ϕ	139.0	0.924	0.966	0.898	0.992	0.36	1.6	3.6
F_x	60.5	0.977	1.015	0.953	1.039	0.30	1.3	3.0
F_y	72.1	0.990	1.004	0.982	1.012	0.11	0.5	1.1
M_z	119.8	0.993	1.002	0.987	1.008	0.08	0.3	0.8
z_{mm}	121.5	1.000	1.010	0.994	1.016	0.07	0.3	0.8
θ	145.5	0.959	0.997	0.936	1.020	0.25	1.1	2.5

†The cases for which the confidence interval contains the final value $\bar{x}^* = 1.0$ are colored in green, otherwise in red.

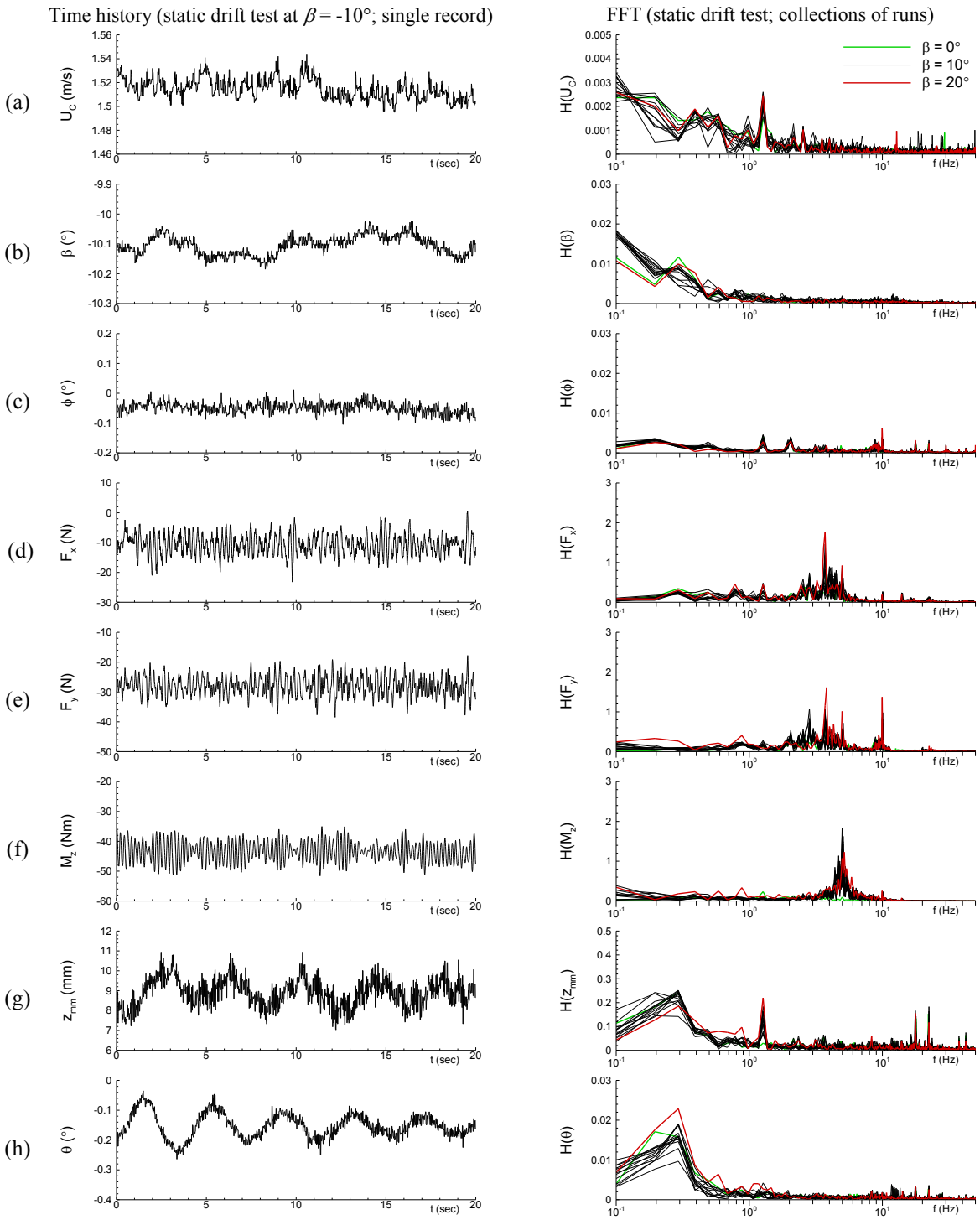

Figure 4-1 Time history (left) and FFT(right) of static drift test data: (a) U_C, (b) β, (c) ϕ, (d) F_x, (e) F_y, (f) M_z, (g) z_{mm}, and (h) θ. Tests are for $FR_{z\theta}$ mount condition and at $Fr = 0.280$.

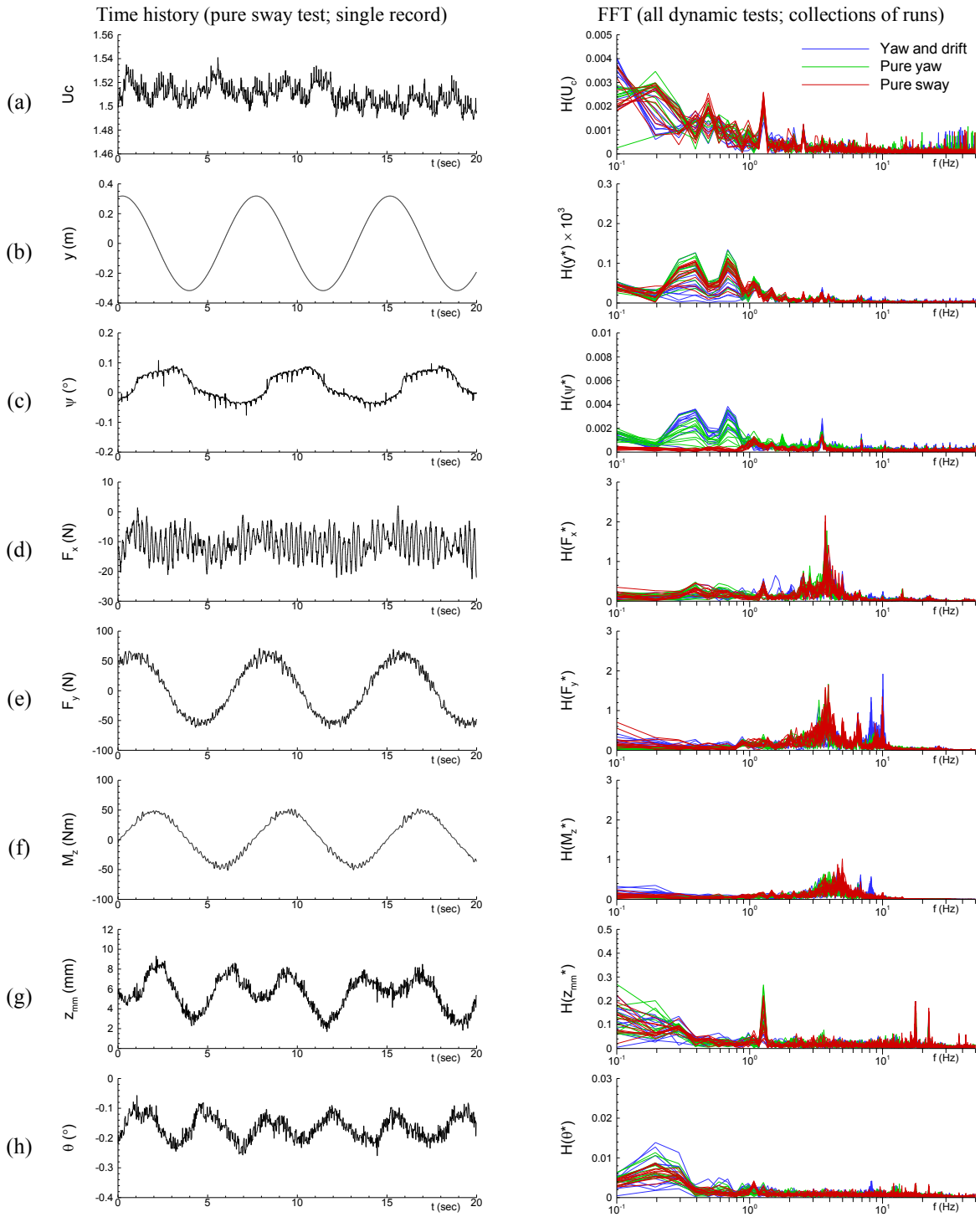

Figure 4-2 Time history (left) and FFT (right) of dynamic tests data: (a) U_C, (b) y, (c) ψ, (d) F_x, (e) F_y, (f) M_z, (g) z_{mm}, and (h) θ. Tests are for $FR_{z\theta}$ mount condition and at $Fr = 0.280$.

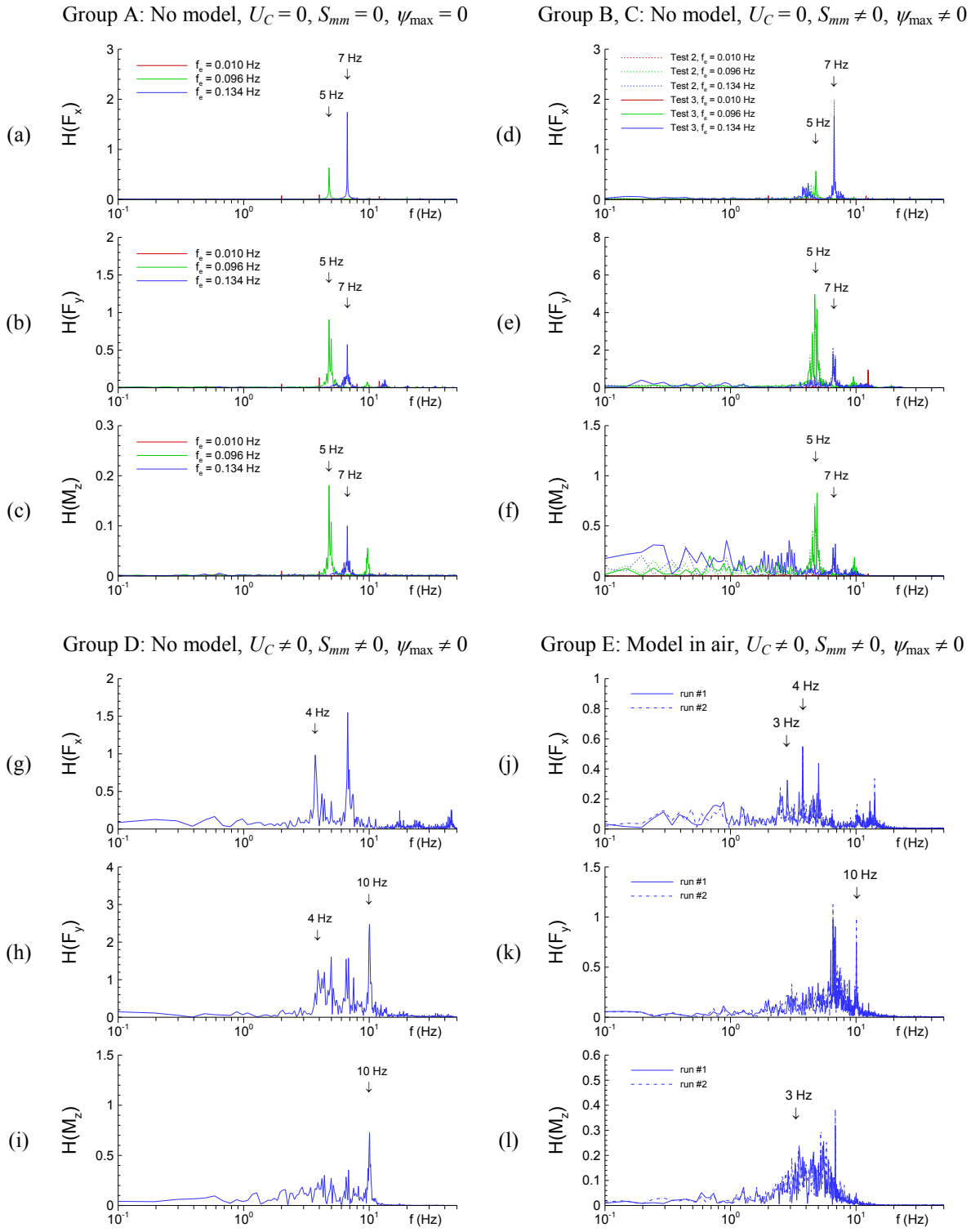

Figure 4-3 PMM noise test results: FFT for F_x, F_y, and M_z. Groups A, B, and C show noise sources for 5 and 7 Hz (natural frequencies of the load-cell) and Groups D and E for 3, 4, and 10 Hz (mechanical vibrations due to carriage speed), respectively.

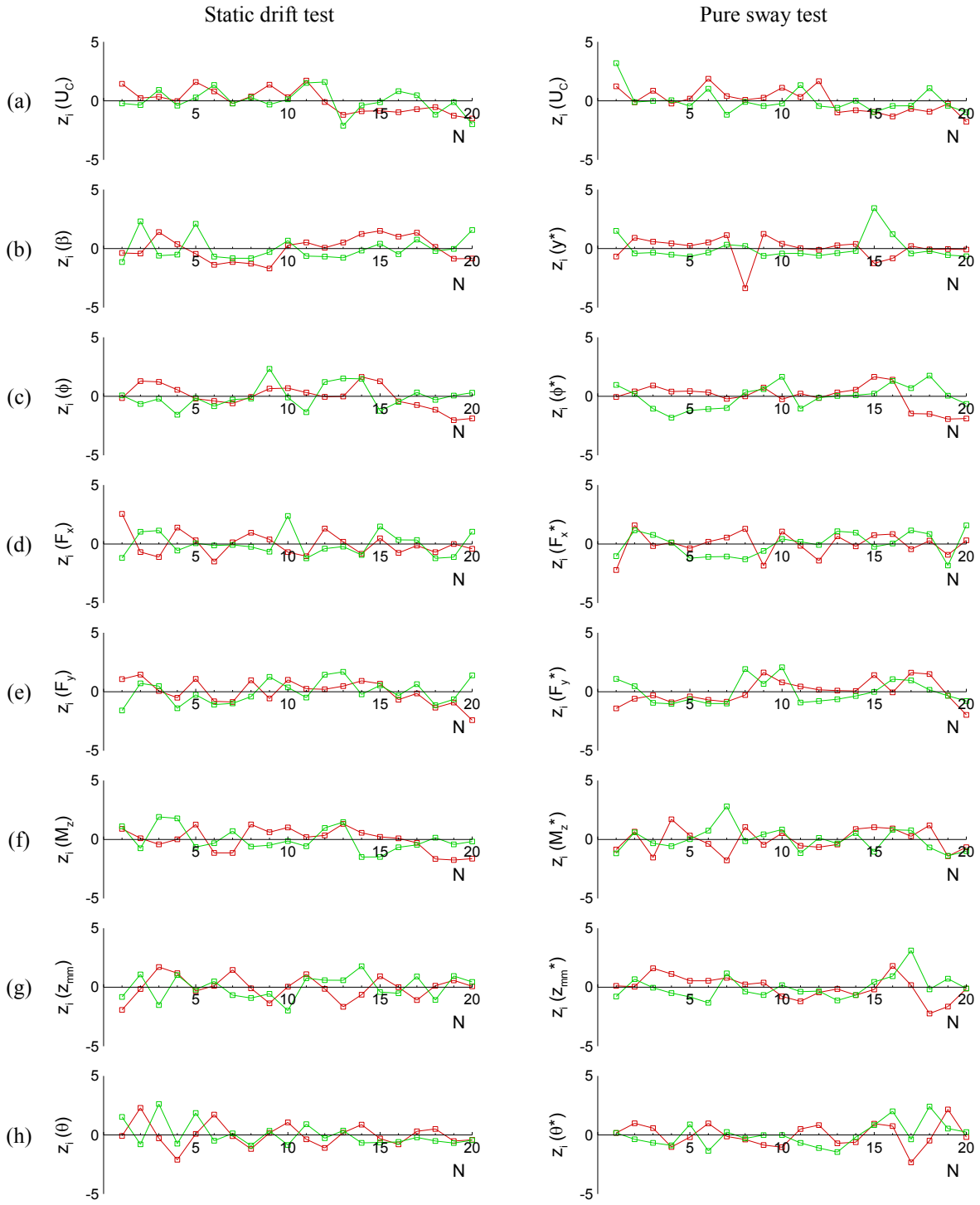

Figure 4-4 Tests for stationarity: Normalized interval mean ($\bar{x}_i$) and mean square ($\overline{x_i^2}$) values for (a) U_C, (b) β or y, (c) ϕ, (d) F_x, (e) F_y, (f) M_z, (g) z_{mm}, and (h) θ. Red: $\bar{x}_i$; green: x_i^2, which are normalized such that $z(y_i) = (y_i - m)/s$ where $y_i = \bar{x}_i$ or x_i^2 and m and s are the mean and standard deviation of y_i for $N = 20$, respectively.

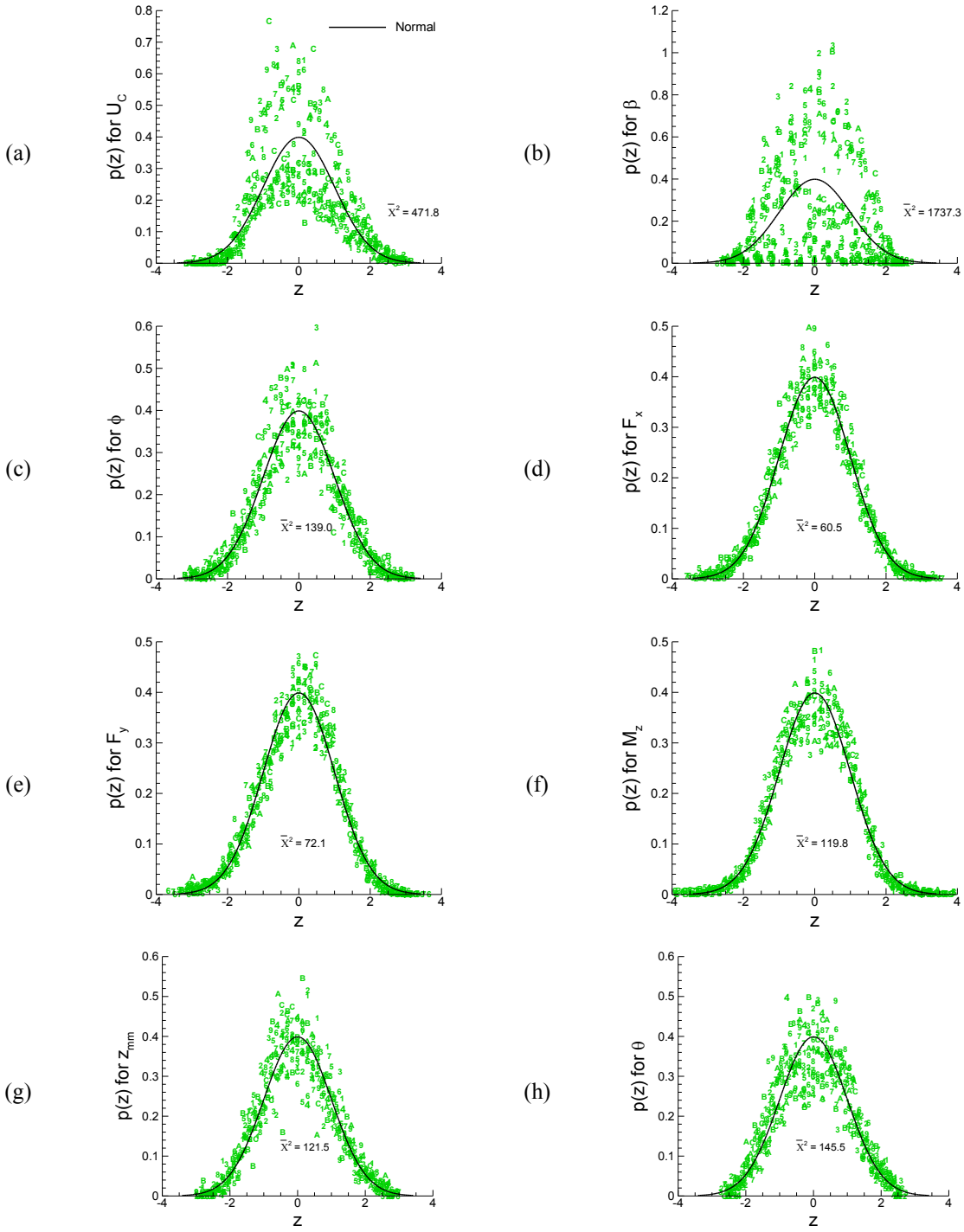

Figure 4-5 Probability density functions of the static drift test data for (a) U_C, (b) β, (c) ϕ, (d) F_x, (e) F_y, (f) M_z, (g) z_{mm}, and (h) θ, respectively. $\overline{X^2}$ is the average X^2 value of for 12 repeat tests. The acceptance region for a normality is $X^2 \leq \chi^2_{n:\alpha} = 51.0$ for $n = 36$ and $\alpha = 0.05$.

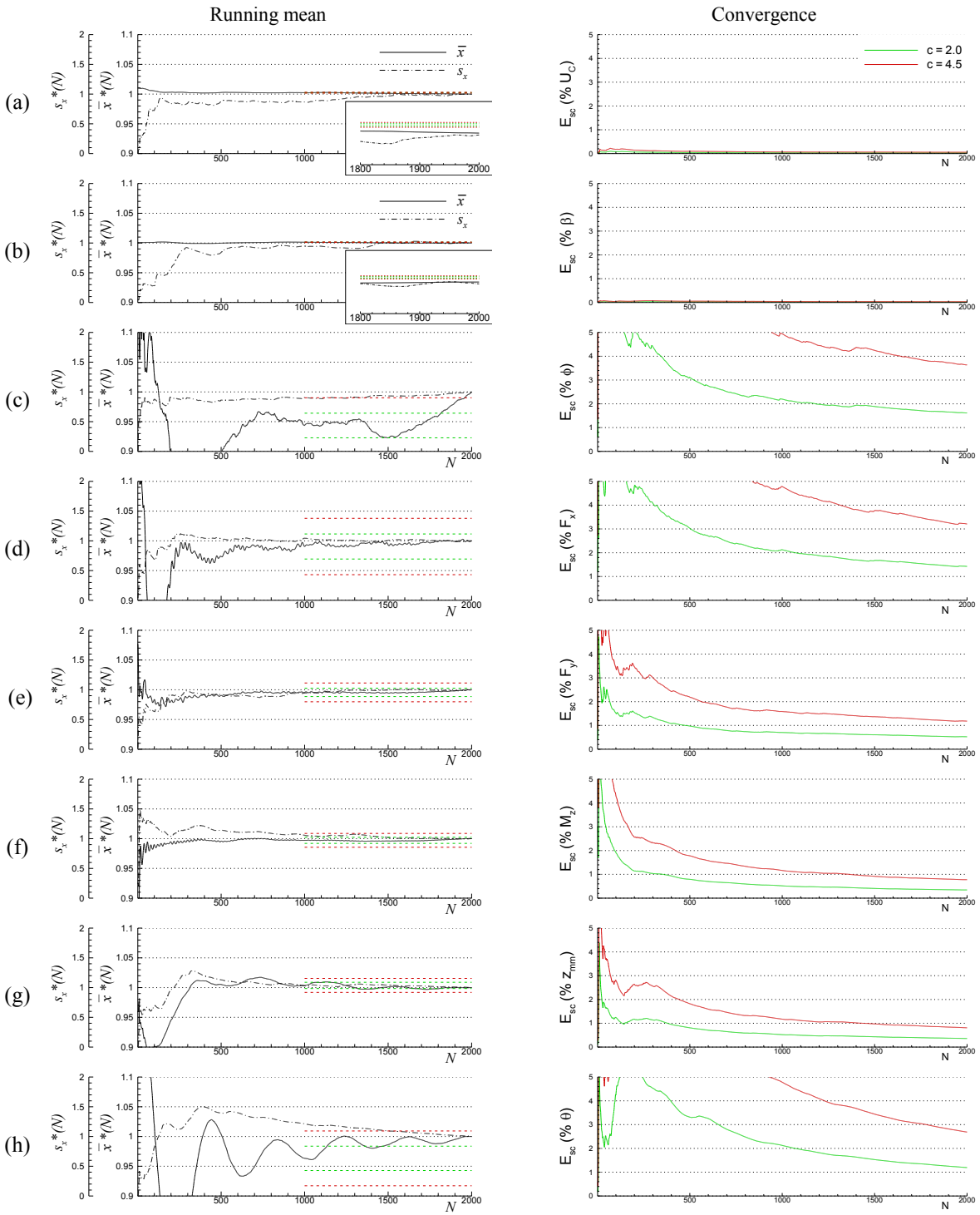

Figure 4-6 Normalized running mean $\bar{x}^*(N)$ and running standard deviation $s_x^*(N)$ (left column) and statistical convergence error E_{sc}(%) (right column) of (a) U_C, (b) β, (c) F_x, (d) F_y, (e) M_z, (f) z_{mm}, (g) θ, and (h) ϕ (Static drift test).

4.2 Phase-Averaged Flow Field Data

Statistical convergence of phase-averaged velocities (U, V, W) and Reynolds stresses (uu, vv, ww) are estimated based on the convergence of confidence interval of the variables. Let x be instantaneous velocities from N independent measurements, x at a given phase may be a stationary random variable of which statistical properties such as mean and variance values do not vary with time as the sample size N becomes large. Of interest herein is determining N where the mean and variance of the variable (i.e. the phased-averaged velocity and Reynolds stress, respectively) converge within a certain statistical confidence level, or vice versa estimating a confidence interval of the variable for a given N. For present study the confidence level are set at 95%.

The mean and variance of a sample of N independent observations from a random variable x are calculated as

$$\bar{x} = \frac{1}{N}\sum_{i=1}^{N} x_i \tag{4.14}$$

$$s^2 = \frac{1}{N-1}\sum_{i=1}^{N}(x_i - \bar{x})^2 \tag{4.15}$$

respectively. Assume x is normally distributed with a mean value of μ_x and a variance of σ_x^2. Then, the confidence interval can be established for the mean values μ_x based upon sample values $\bar{x}$ and s as follows (Bendat 1966).

$$\left[\left(\bar{x} - \frac{s \cdot t_n}{\sqrt{N}}\right) \leq \mu_x < \left(\bar{x} + \frac{s \cdot t_n}{\sqrt{N}}\right)\right] \tag{4.16}$$

where t_n is the 95% point of the Student t distribution with $n = N - 1$ degree of freedom. Which states "the true mean value μ_x falls within the noted interval with a confidence of 95%." In other words, the difference between the true and the sample mean would be

$$-\frac{st_n}{\sqrt{N}} \leq (\mu_x - \bar{x}) < \frac{st_n}{\sqrt{N}} \tag{4.17}$$

with a confidence of 95% for the sample size N. Then, the interval limit $d = st_n/\sqrt{N}$ can be used for defining the statistical convergence error for $\bar{x}$ such that

$$E \equiv \frac{d}{x_{ref}} = \frac{t_n}{\sqrt{N}} \cdot \left(\frac{s}{x_{ref}}\right) \tag{4.18}$$

indicating that the mean value of x (phase-averaged velocity) with N samples (PIV images) can has an error E of x_{ref} with a 95% confidence. Where, x_{ref} can be any reference value for x such as the phase-averaged velocities U, V, W, or the carriage towing speed U_C. From (4.18), the convergence error E is inversely proportional to the square root of sample size N and proportional to the standard deviation s of x, i.e., the turbulence intensity of the flow. If one expects a certain level of E for a mean velocity with known turbulent intensity, i.e. s/x_{ref}, then, the number of PIV images, i.e. N, can be estimated using the equation (4.18) as

$$N = \frac{4}{E^2} \cdot \left(\frac{s}{x_{ref}}\right)^2 \tag{4.19}$$

by approximating $t_n \approx 2$ for $N >> 10$.

The variance σ_x^2 for a normally distributed random variable x follows a χ^2 distribution, in contrast to the mean value μ_x following the Student t distribution as discussed above. Then, the confidence interval for the variance σ_x^2 based upon a sample variance s^2 from a sample of size N is (Bendat 1966)

$$\left[\frac{n\,s^2}{\chi^2_{n;0.025}} \leq \sigma_x^2 < \frac{n\,s^2}{\chi^2_{n;0.975}}\right] \tag{4.20}$$

where $\chi^2_{n;0.025}$ and $\chi^2_{n;0.975}$ are the 2.5% and 97.5% points, respectively, of the χ^2 distribution with $n = N - 1$ degree of freedom. Subsequently, the difference between the true variance σ_x^2 and the sample variance s^2 falls within an interval

$$-d_L \leq \sigma_x^2 - s^2 < d_U \tag{4.21}$$

with a 95% confidence, where the upper limit d_U and the lower limit d_L are

$$d_U = \frac{n\, s^2}{\chi^2_{n;0.975}} - s^2 \tag{4.22}$$

$$d_L = s^2 - \frac{n\, s^2}{\chi^2_{n;0.025}} \tag{4.23}$$

Note that as the χ^2 distribution is non-symmetric for $n > 2$, the upper and lower limits of the interval has difference values and the statistical convergence error E_U and E_L, respectively, is defined separately as follow.

$$E_U \equiv \frac{d_U}{s^2_{ref}} = \left(\frac{n}{\chi^2_{n;0.975}} - 1\right) \cdot \frac{s^2}{s^2_{ref}} \tag{4.24}$$

$$E_L \equiv \frac{d_L}{s^2_{ref}} = \left(1 - \frac{n}{\chi^2_{0.025}}\right) \cdot \frac{s^2}{s^2_{ref}} \tag{4.25}$$

where, s^2_{ref} can by any reference variance value for the random variable x such as the phase-averaged Reynolds stresses uu, vv, ww, or the turbulent kinetic energy k.

Typical examples of E, E_U, and E_L values versus the sample size N are shown in Fig. 4-7 as charts for several practical cases of the s/x_{ref} and s^2/s^2_{ref} values. The error values for an example flow field shown in Fig. 4-8 will be estimated by using the charts and the number of samples N necessary for a desired error levels. The example flow field shown in Fig. 4-8 (a) and (b) are the mean axial velocity U and the turbulent kinetic energy $k = \frac{1}{2}(uu + vv + ww)$ at the nominal wake region (x/L = 0.935) of the DTMB 5512 model in steady straight towing condition at Fr = 0.280. The mean velocity U and

the turbulent velocity fluctuations u, v, w are normalized with the model towing speed U_C = 1.531 m/s, respectively. The total number of PIV images used for the mean is N_{total} = 2,250 collected from a set of 30 carriage runs (75 images per each run). The effective number of data at the point A in Fig. 4-8 is N = 1,720 by excluding the null vectors due to insufficient PIV particle density at the point and by rejecting spurious vectors from the PIV image correlations process. Typically N is close to N_{total} at the outer flow regions and less than N_{total} inside the boundary layer or at spots where the turbulent intensity is high. At Point A, measured are the root-mean-square u = 0.09 (i.e. s of U) and the axial component of Reynolds stress uu = 0.0075 (i.e. s^2 of U), thus s/x_{ref} = 0.09 and s^2/s_{ref}^2 = 1.1 when $x_{ref} = U_C$ and s_{ref}^2 = 0.007 (the range of k), respectively, are used. From the charts in Fig. 4-7, then, the expected E for U is about 0.4% of U_C and E_U for uu is about 8% of k at $N \approx$ 1,700, respectively. For the latter case, if E_U less than 1% is desired, $N > 10^5$ is necessary. Note from Fig. 4-7 (b) that E_U is always larger than E_L and both have similar values as N increase, thus E_U can be considered as the representing E for statistical convergence of the Reynolds stresses.

The actual N = 1,720 samples of U, V, and W data measured at the point A of the previous example flow field are shown in Fig. 4-9, along with the statistics of the data and their convergence errors. The sample U_i, V_i, N_i data shown in Fig. 4-9 (a) are apparently stationary and random of which mean and variance values are $\bar{x}$ = 0.543, -0.023, 0.059, respectively, and s^2 = 0.0075, 0.0035, 0.0024, respectively. When data are normalized as $z = (x - \bar{x})/s$, all variables exhibit a standard normal distribution, shown in Fig. 4-9 (b), as assumed. The probability density functions $p(x)$ in the figure for U, V, and W are obtained by pooling the data sample into K = 35 equally spaced intervals and counting the frequency of data at each interval classes divided by N. The minimum optimum number K of class intervals was used as suggested for Chi-Square Goodness-of-Fit test (Williams 1950). Time histories of the mean values $\bar{x}$ and variance s^2 of the data using the equations (4-14) and (4-15) are shown in Fig. 4-9 (c) and (d), designated as $\bar{x}_N$

and s_N^2, respectively, as increasing the number of data sample N from 2 to 1,720. For each N, the variance s_N^2 is re-calculated using a new $\bar{x}_N$ value accounting for the newly added data sample x_N into the previous mean $\bar{x}_{N-1}$, for which the following recursive expressions are useful when N is large.

$$\bar{x}_N = \frac{1}{N}\left((N-1)\bar{x}_{N-1} + x_N\right) \tag{4.26}$$

$$s_N^2 = \left(\frac{N-2}{N-1}\right)s_{N-1}^2 + \left(\frac{N}{N-1}\right)(\bar{x}_{N-1}^2 - \bar{x}_N^2) + \left(\frac{1}{N-1}\right)(x_N^2 - \bar{x}_{N-1}^2) \tag{4.27}$$

for $N \geq 2$. As shown in Fig. 4-9 (c) and (d), the $\bar{x}_N$ converges fast for all variables typically for $N < 100$ whereas the s_N^2 first fluctuates large for $N < 500$ and converges slowly as N increases, demonstrating the stationary of the variables as assumed. Shown in Fig. 4-9 (e) are the E for U, V, W as per (4-18) and in Fig. 4-9 (f) are the E_U for uu, vv, ww as per (4-24), respectively. In the equations, the values of t_n and $\chi^2_{n;0.975}$ at each $n = N - 1$ can be found from typical textbooks on Statistics (e.g. Bendat 1966, pp. 162 and 163). The s and s^2 in the equations are evaluated by using the $\sqrt{s_N^2}$ and s_N^2 as per (4-27) at each N, respectively. Used as x_{ref} and s_{ref}^2 are the same U_C and k used at the previous paragraph. From Fig. 4-9 (e) and (f), the E and E_U exhibit similar curve shapes as those shown in Fig. 4-7 (a) and (b) at the corresponding s/x_{ref} (0.09, 0.06, 0.05 for U, V, W, respectively) and s^2/s_{ref}^2 (1.1, 0.5, 0.4 for uu, vv, ww, respectively), respectively. From Fig. 4-9 (e) and (f), at N = 1720, E = 0.4% for U and E_U = 8% for uu are the same as the chart readings from Fig. 4-7 (a) and (b), respectively, proving the validity of the method. The E's for V and W are smaller than for U, about 0.3%, respectively, and the E_U's for vv and ww are also smaller than for uu, 4% and 3%, respectively, as well agree with the chart readings.

The application of the method to phase-averaged PMM PIV measurement is shown in Fig. 19. Shown in the figure are the phased-averaged (a) mean axial velocity U and (b) turbulent kinetic energy k of the same model for the previous example case but in

a forced dynamic pure yaw motion. The measurement location is at the same x/L = 0.935 as for previous example flow case, whereas shifted in lateral direction more to the starboard side of the model. Selected for a presentation case out of the 32 phase groups of the PMM PIV measurements is the 180° case where the flow structure is largest at the port side thus slower convergences (larger convergence error) of the mean flow variable values are expected. Total 100 carriage runs were made to sample N_{total} = 250 PIV images collected from 2.5 PMM cycles per each run. As shown in Fig. 4-10, the flow field becomes more complex than the steady towing case shown in Fig. 4-8 due to the forced oscillatory PMM motions of the model, accordingly stronger turbulence of the flow with about two times larger range of turbulent kinetic energy, $[k]$ = 0.014. To see more global trend of the convergence, the flow field points are grouped into three categories: Group A ($0 < k/[k] \leq 0.1$), Group B ($0.1 < k/[k] \leq 0.5$), and Group C ($0.5 < k/[k] \leq 1.0$), representing the regions where fast, moderate, and slow convergence is expected, respectively. In Table 4-4, presented are the ranges and average values of the effective number of PIV images N, turbulence intensity $\sqrt{k}$ (approximately corresponds to the average of u, v, and w), the normalized turbulent kinetic energy $k/[k]$, and the convergence errors E and E_U for the Groups A, B, and C, respectively. The average effective PIV image numbers N = 235, 210, and 177 respectively for each group corresponds to 94%, 84%, 71% of N_{total}, respectively, due to the same reasons as explained previously for the steady flow case. The $\sqrt{k}$ and $k/[k]$ correspond to the statistical convergence parameters s/x_{ref} and s^2/s_{ref}^2, respectively, which can be used for the chart (Fig. 4-7) readings along with N estimating the convergence errors. The ranges and average values of E and E_U presented in the table are for all phase-averaged mean velocities U, V, W and Reynolds stresses uu, vv, ww, respectively. In spite of relatively smaller sample number, N ~ 200 (for the steady towing case N ~ 2,000), E for the mean velocities is usually smaller than 1% of U_C, at best about 2% for Group C, and E_U for the mean Reynolds stresses is also satisfactory less than 10% of $[k]$ in average. However, E_U can be significantly large

up to 36% at the region where $k/[k] \approx 1.0$ (upper left corner of Fig. 4-10) and the number of PIV images required to reduce E_U to 10% is $N \sim 1{,}000$ from Fig. 4-7, which requires more than 400 times of carriage runs.

From the above two example flow cases, it is shown that the statistical convergence of PIV measured mean velocities and Reynolds stresses can be estimated using the confidence intervals of the mean and variance values by assuming those variables are stationary and random following the normal distribution. From the first example flow, steady straight towing condition, where a large number of data ($N \sim 2{,}000$) is available, revealed that the instantaneous velocity data are stationary random variables following a normal distribution as assumed and accordingly their mean values follow Student t distribution and variance values χ^2 distribution. From the second example flow, forced oscillatory PMM motions, even with relatively small number of data ($N \sim 200$), statistical convergence errors E and E_U values are fairly small, usually less than 1% of U_C and 10% of $[k]$, for the phase-averaged velocities and Reynolds stresses, respectively. Those statistical convergence errors indicate that the true mean and variance values may differ from the sample mean and variance values by the amount of E and E_U, respectively, with a 95% confidence. However, the term 'true mean' should be distinguished from the term 'true value' as the former value may biased from the latter value, if exists, due to systematic errors which can be identified by calibrating the PIV system to a known standard. In the uncertainty analysis (UA) contexture, then, the convergence error can be considered as the precision limit at the '1st-order replication-level' (Coleman and Steel 1999 and Moffat 1982, 1985, and 1988) as all the PIV system remain the same as sample after sample is tested. Thus the 'true value' relative to the measurement values can be estimated at the '*N*th-order replication-level' including the random errors together with the systematic errors, which will be further discussed at the Section 4 'Uncertainty Analysis'. Lastly, estimating the '1st-order replication-level' precision limits of the mean Reynolds stresses, it should be noted that the typical UA procedures (assuming Student t distribu-

tion of data) can underestimate the precision limit significantly as the Reynolds stress data actually follow the χ^2 distribution which converges much slower than the Student t distribution.

Table 4-4 Statistical convergence of Phase-averaged velocity and Reynolds stress.

Group	A	B	C
N	62 ~ 251 (235)	106 ~ 243 (210)	107 ~ 232 (177)
$\sqrt{k}$	0.02 ~ 0.04 (0.03)	0.04 ~ 0.08 (0.06)	0.08 ~ 0.12 (0.09)
$k/[k]$	0.02 ~ 0.1 (0.06)	0.1 ~ 0.5 (0.25)	0.5 ~ 1.0 (0.62)
E (% U_C)	0.1 ~ 0.8 (0.3)	0.2 ~ 1.4 (0.6)	0.5 ~ 2.4 (1.1)
E_U (% $[k]$)	0.1 ~ 3.5 (0.9)	0.5 ~ 15.0 (3.8)	2.3 ~ 35.9 (10.4)

( ) : average value; $[k]$ is the range of k.

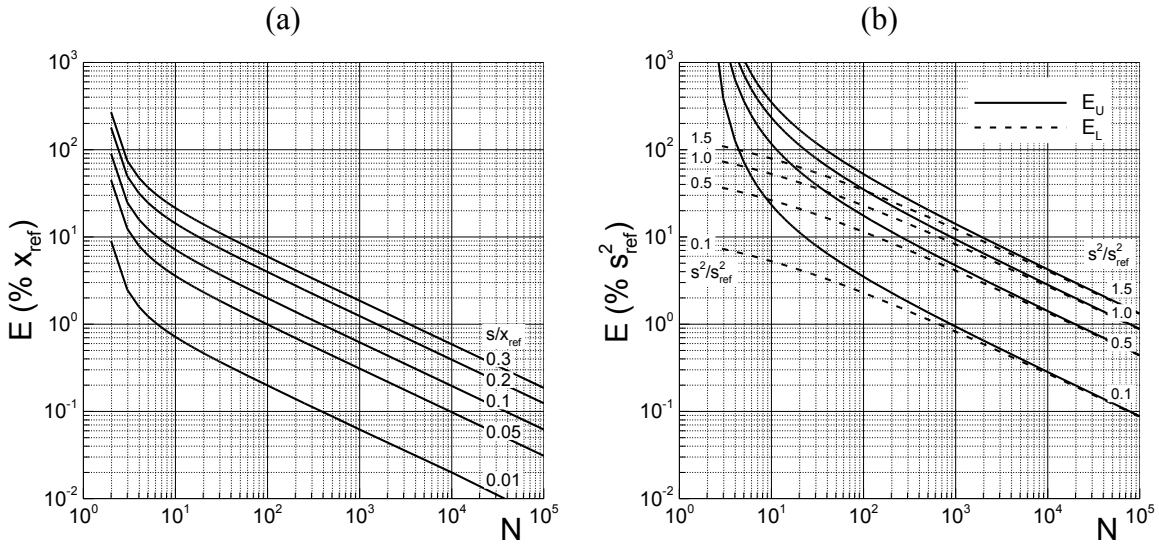

Figure 4-7 Statistical convergence errors of (a) the mean $\bar{x}$ and (b) variance s^2 for stationary random variable x.

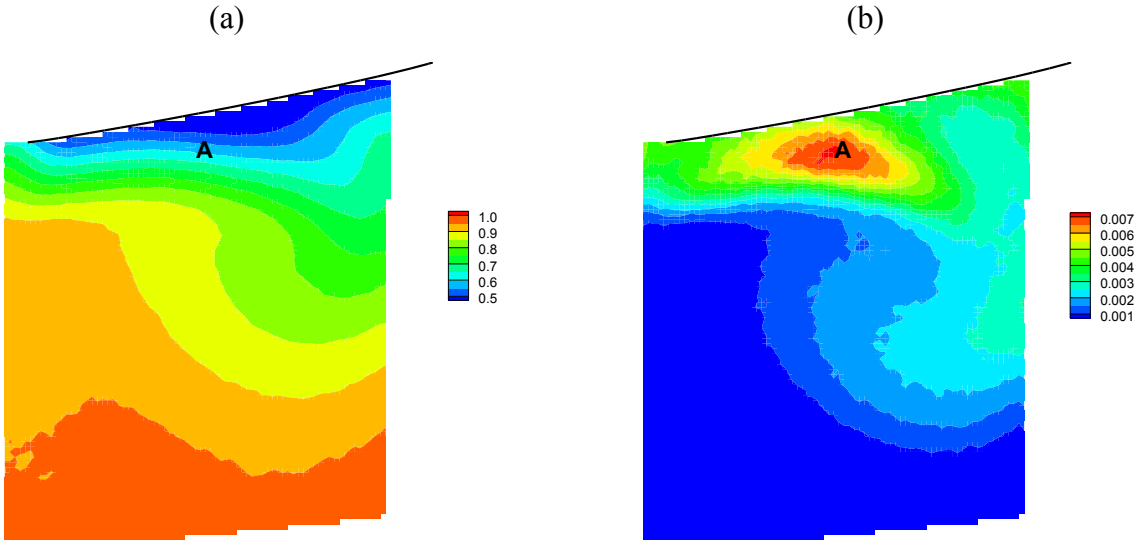

Figure 4-8 Example PIV flow field data: Contours of (a) mean axial velocity U and (b) mean turbulent kinetic energy k of DTMB 5512 model in steady straight towing at Fr = 0.280 condition. Measurement location is at x/L = 0.935, near the center plane of the model (port side). The total number of PIV images used for averaging N_{total} = 2,250 and the effective number N = 1,720 at Point A.

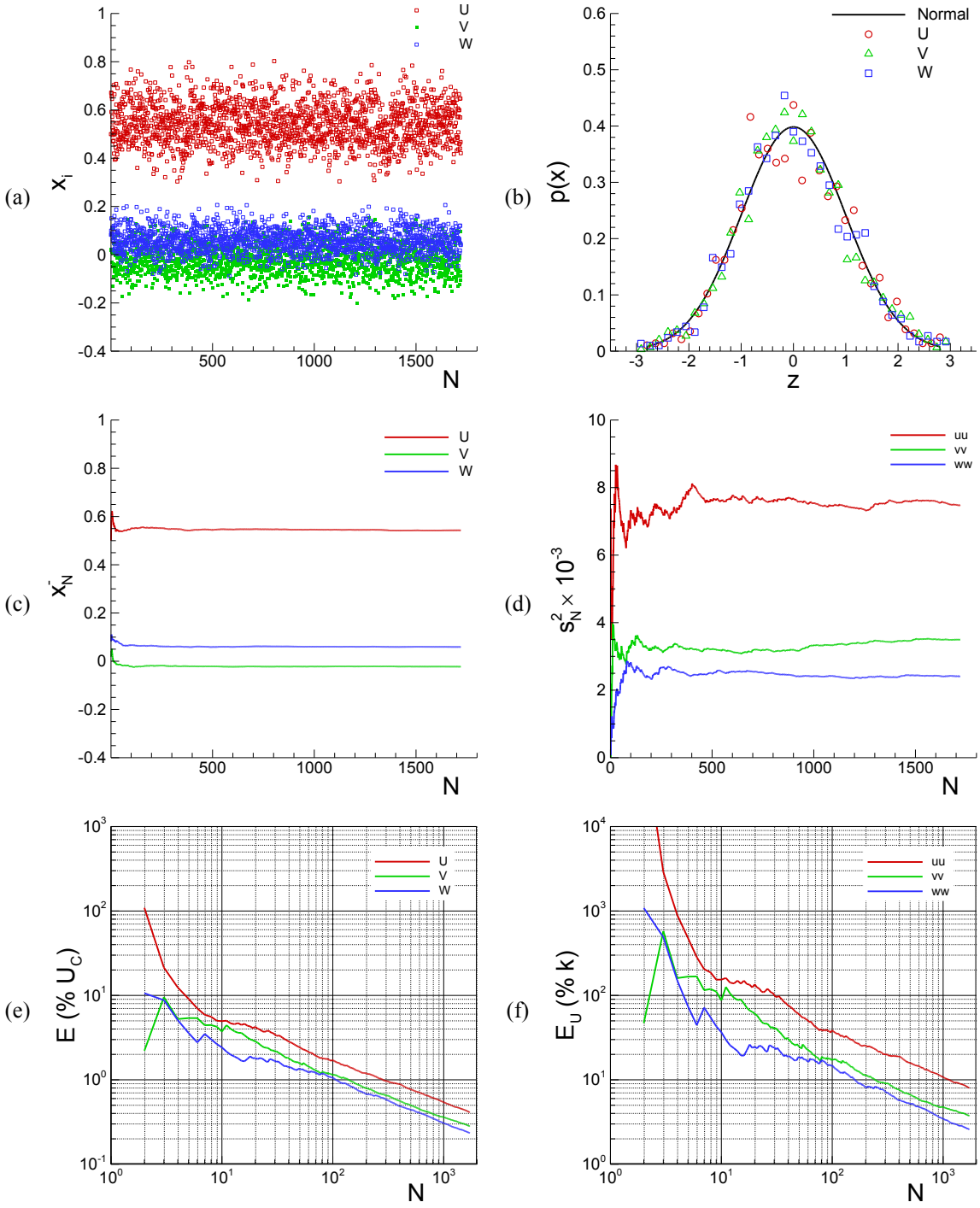

Figure 4-9 Flow data and statistics for Point A of the example flow: (a) instantaneous velocities U_i, V_i, W_i, (b) standard normal probability density function $p(x)$, (c) running mean $\bar{x}_N$, (d) running variance s_N^2, (e) E for U, V, W, and (f) E_U for uu, vv, ww, respectively.

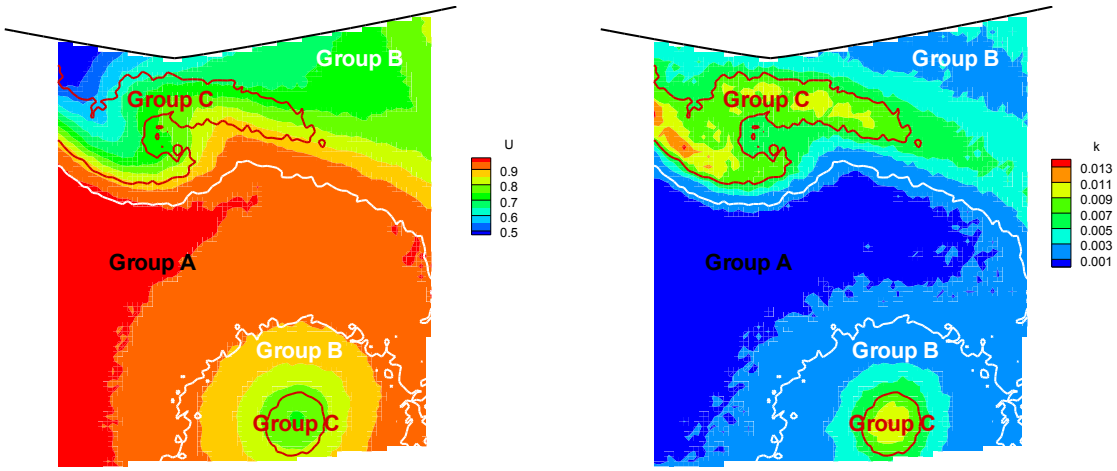

Figure 4-10 Example PMM PIV flow field data: Contours of phase-averaged (left) axial velocity U and (right) turbulent kinetic energy k of DTMB 5512 model in pure yaw motion ($\gamma = 180°$) at $Fr = 0.280$. Measurement location is at $x/L = 0.935$, near the keel of the model. The total number of PIV images $N_{total} = 254$.

CHAPTER 5 UNCERTAINTY ANALYSIS

5.1 UA for Forces and Moment and Motions

The purpose is to develop an uncertainty analysis (UA) procedure for planar motion mechanism (PMM) tests measurements including forces and moment and motions. The approach follows errors/uncertainties definitions, systematic/random categorizations, and large sample size/normal distribution 95% level of confidence assumptions, as provided by the AIAA (1999), ANSI/ASME (1998), and AGARD (1994) standard and guidelines. The present UA procedure is for a model scale towing tank PMM test for an un-appended model ship except bilge keels (i.e. without shafts, struts, propellers, and rudders) which is mounted free to heave and pitch, but fixed in roll. Bias and precision limits and total uncertainties for multiple runs are estimated for the non-dimensional forces and moment and motions in model scale for four types of PMM tests (static drift, pure yaw, pure sway, and yaw and drift). Other PMM tests, such as static rudder, static drift and rudder, static drift and heel, dynamic yaw and rudder, dynamic yaw and drift and rudder, are not considered. This procedure does not provide UA for hydrodynamic derivatives derived from the forces and moment data or their effect on the full scale maneuvering simulations.

Limitations of present UA procedures are listed as follows: The effect of data conditioning such as filtering or fairing, for example, Fourier Series (FS) reconstructions for the measured forces /moment and motions is not counted in this UA procedure. This procedure assumes that the measured forces/moment is the sum of those from all forces/moment gauges used for the case of multiple gauge system, and that the inertia forces/moment from parts for model installation are subtracted from the total measured forces and moments if the parts are suspended from the loadcells. This procedure also assumes that the model ship is free to heave and pitch, and fixed in roll. The effect of deviations from the upright position such as roll or heel angle is not considered in this

procedure. Finally, carriage speed is assumed to be constant, so the effect of acceleration caused by fluctuating carriage speed during runs is not considered.

Present UA procedure is developed in an international collaboration between the IIHR-Hydroscience & Engineering (IIHR, USA), Force Technology (FORCE, Denmark), Instituto Nazionale per Studi ed Esperienze di Architettura Navale (INSEAN, Italy), and the 24th – 25th International Towing Tank Conference (ITTC) Maneuvering Committee (MC). The collaboration includes overlapping tests using the same model geometry for comparisons of the results and for identifications of possible facility biases and scale effects. The basis of the UA procedure was first developed by FORCE (Simonsen 2004), followed by an application to INSEAN (Benedetti et al. 2006), and extended herein by including the definitions of the asymmetry bias and the facility bias as presented at the following sections.

The procedure has been accepted by the 25th ITTC (2008) as an ITTC Recommended Procedure and Guidelines (7.5-02-06.04 Uncertainty Analysis: Forces and moment; Example for Planar Motion Mechanism Test). For which the proposed procedure was reviewed by the Specialist Committee on Uncertainty Analysis (SCUA) of the 25th ITTC. The review included comments on ten (10) topics: 1) Jitter Method, 2) Assumptions, 3) Model Length, 4) Drift Angle, 5) Mass Uncertainty, 6) Force, 7) Calibration and Acquisition, 8) Water Density and Temperature, 9) Precision limit, and 10) Carriage speed. The comments focus on the traceability of error estimations to the known uncertainty such as NIST (National Institute of Standards and Technology) standards and as well on suggestions of alternative approaches that seem to follow more closely the ISO GUM (1995) and/or the US Guide (1997). In general, the comments can be grouped into three categories: (A) comments which lead to constructive improvements in the proposed procedure; (B) comments regarding insufficient descriptions in the proposed procedure; and (C) conceptual differences between AIAA/ASME and ISO/US Guide UA approaches. Topics 1), 3), 5), and 6) are considered as type (A) which are helpful for improving

the proposed procedure. Topics 2), 4) and 8) are considered as type (B) for which descriptions in the proposed procedure are insufficient and need to be revised based on the comments. Lastly, topics 7), 9), and 10) are considered as type (C) which may arise from differences between AIAA/ASME and ISO/US Guide UA approaches. Accordingly, herein the UA procedure was corrected for and/or added supplementary descriptions as per most of the editorial and technical comments, except for type (C) comments for which the proposed procedures based on the AIAA/ASME were retained. In general, differences between the AIAA/ASME and ISO/US Guide UA are usually conceptual and the final UA results do not differ significantly (Coleman and Steel, 1999). Nonetheless, as a new version of UA standard, the ASME PTC 19.1-2005 (2005) was released by the ASME, where more of harmonization between the two approaches was made, the type (C) comments can also be achieved for the next revision of the present PMM UA procedures by following the new ASME standards.

The organization is as follows: Definitions and estimation procedures for bias and precision limits and total uncertainty are provided in sections 5.1.1, 5.1.2, and 5.1.3, respectively, and UA results are discussed in section 5.1.4. A conceptual, data asymmetry bias is defined and evaluated in sections 5.1.5. Next, the UA results from three facilities data are compared in Section 5.1.6. Another conceptual, facility bias is defined and evaluated in Section 5.1.7.

5.1.1 Bias limits

For the forces and moment data, X, Y, and N, the DRE's (3.7) and (3.8) for the dynamic tests and static drift test, respectively, can be rewritten in functional forms as

$$\mathrm{r}(x) = \mathrm{r}(L, T, x_G, y_G, m, I_z, \rho, u, v, r, \dot{u}, \dot{v}, \dot{r}, F) \tag{5.1}$$

and

$$\mathrm{r}(x) = \mathrm{r}(L, T, \rho, U_C, F) \tag{5.2}$$

respectively, where the result r can be X, Y, or N, and the symbol F represents the forces and moment F_x, F_y, or M_z, respectively. For the motion data, the DRE (3.9) for z is re-written in a functional form as

$$z(x) = z(z_{mm}, L) \tag{5.3}$$

However, DRE's are not used for θ and ϕ data. From the DRE's (5.1) and (5.2), the error propagation equations can be written as

$$B_r^2 = \theta_L^2 B_L^2 + \theta_T^2 B_T^2 + \theta_{x_G}^2 B_{x_G}^2 + \theta_{y_G}^2 B_{y_G}^2 + \theta_m^2 B_m^2 + \theta_{I_z}^2 B_{I_z}^2 + \theta_\rho^2 B_\rho^2 + \theta_u^2 B_u^2 + \theta_v^2 B_v^2 + \theta_r^2 B_r^2 + \theta_{\dot{u}}^2 B_{\dot{u}}^2 + \theta_{\dot{v}}^2 B_{\dot{v}}^2 + \theta_{\dot{r}}^2 B_{\dot{r}}^2 + \theta_F^2 B_F^2 \tag{5.4}$$

and

$$B_r^2 = \theta_L^2 B_L^2 + \theta_T^2 B_T^2 + \theta_\rho^2 B_\rho^2 + \theta_{U_C}^2 B_{U_C}^2 + \theta_F^2 B_F^2 \tag{5.5}$$

for dynamic tests and static drift test, respectively. Of the element biases in (5.4), the bias limits for motion parameters, B_u, B_v, B_r, $B_{\dot{u}}$, $B_{\dot{v}}$, and $B_{\dot{r}}$, are through their own error propagation equations from the DRE's (5.2) as:

$$B_u^2 = \theta_{U_C}^2 B_{U_C}^2 + \theta_\psi^2 B_\psi^2 + \theta_{v_{PMM}}^2 B_{v_{PMM}}^2 \tag{5.6a}$$

$$B_v^2 = \theta_{U_C}^2 B_{U_C}^2 + \theta_\psi^2 B_\psi^2 + \theta_{v_{PMM}}^2 B_{v_{PMM}}^2 \tag{5.6b}$$

$$B_r^2 = B_{r_{PMM}}^2 \tag{5.6c}$$

$$B_{\dot{u}}^2 = \theta_{U_C}^2 B_{U_C}^2 + \theta_\psi^2 B_\psi^2 + \theta_r^2 B_r^2 + \theta_{v_{PMM}}^2 B_{v_{PMM}}^2 + \theta_{\dot{v}_{PMM}}^2 B_{\dot{v}_{PMM}}^2 \tag{5.6d}$$

$$B_{\dot{v}}^2 = \theta_{U_C}^2 B_{U_C}^2 + \theta_\psi^2 B_\psi^2 + \theta_r^2 B_r^2 + \theta_{v_{PMM}}^2 B_{v_{PMM}}^2 + \theta_{\dot{v}_{PMM}}^2 B_{\dot{v}_{PMM}}^2 \tag{5.6e}$$

$$B_{\dot{r}}^2 = B_{\dot{r}_{PMM}}^2 \tag{5.6f}$$

Further element biases, $B_{v_{PMM}}$, $B_{\dot{v}_{PMM}}$, B_{ψ}, $B_{r_{PMM}}$, $B_{\dot{r}_{PMM}}$ in (5.6) are again through their own DRE's in (3.1) as:

$$B_{v_{PMM}}^2 = \theta_{\mathrm{N}}^2 B_{\mathrm{N}}^2 + \theta_{S_{mm}}^2 B_{S_{mm}}^2 + \theta_t^2 B_t^2 \tag{5.7a}$$

$$B_{\dot{v}_{PMM}}^2 = \theta_{\mathrm{N}}^2 B_{\mathrm{N}}^2 + \theta_{S_{mm}}^2 B_{S_{mm}}^2 + \theta_t^2 B_t^2 \tag{5.7b}$$

$$B_{\psi}^2 = \theta_{\psi_{max}}^2 B_{\psi_{max}}^2 + \theta_{\mathrm{N}}^2 B_{\mathrm{N}}^2 + \theta_t^2 B_t^2 + \theta_{\beta}^2 B_{\beta}^2 \tag{5.7c}$$

$$B_{r_{PMM}}^2 = \theta_{\psi_{max}}^2 B_{\psi_{max}}^2 + \theta_{\mathrm{N}}^2 B_{\mathrm{N}}^2 + \theta_t^2 B_t^2 \tag{5.7d}$$

$$B_{\dot{r}_{PMM}}^2 = \theta_{\psi_{max}}^2 B_{\psi_{max}}^2 + \theta_{\mathrm{N}}^2 B_{\mathrm{N}}^2 + \theta_t^2 B_t^2 \tag{5.7e}$$

Thus, the biases of the motion parameters are from five elemental biases, $B_{S_{mm}}$, B_{N}, B_t, B_{β}, and $B_{\psi_{max}}$, through (5.7) and then (5.6) with B_{U_C}. Next for the motion data, the error propagation equations are written as

$$B_z^2 = \theta_{z_{mm}}^2 B_{z_{mm}}^2 + \theta_L^2 B_L^2 \tag{5.8a}$$

$$B_{\theta} = B_{\theta} \tag{5.8b}$$

$$B_{\phi} = B_{\phi} \tag{5.8c}$$

The sensitivity coefficients, θ's, in (5.4) – (5.8) are evaluated analytically by differentiating the DRE's with respect to each variable of interest, x, such that

$$\theta_x = \frac{\partial \mathrm{r}}{\partial x} \tag{5.9}$$

where r is the DRE variable. For a reference, the θ's for (5.4) and (5.5) are summarized in Tables 5-1 and 5-2 for dynamic and static tests, respectively. Note that the sensitivity coefficients can also be evaluated numerically by using, for example, a 'Jitter method' (Moffat 1982 and Coleman and Steele 1999). The estimations of the fifteen element bias limits, B_L, B_T, B_{x_G}, B_{y_G}, B_m, B_{I_z}, B_{ρ}, B_{U_C}, B_u, B_v, B_r, $B_{\dot{u}}$, $B_{\dot{v}}$, $B_{\dot{r}}$, and B_F, are as per Si-

mon et al. (2004), and the estimations of biases for the motion data, $B_{z_{mm}}$, B_θ, and B_ϕ are also presented.

Global variables (L, T, x_G, y_G, m, I_z, ρ): B_L is from the model manufacturing accuracy ±1 mm in all coordinates. Model 5512 was manufactured at NSWC (Naval Surface Warfare Center) of US Navy and underwent a laser-scan for the exterior surface geometry. Result confirmed the manufacturing accuracy. B_T is the RSS of two uncorrelated element biases, $B_{T,1}$ and $B_{T,2}$. $B_{T,1}$ is from the precisions of the draft-markers on the model surface, estimated at 0.1 mm, and $B_{T,2}$ is from the model ballasting accuracy with respect to the draft markers, 1 mm, from a tape measurement. B_{x_G} is the RSS of two uncorrelated element biases, $B_{x_G,1}$ and $B_{x_G,2}$. $B_{x_G,1}$ is the deviation of actual model center of gravity (COG) from its designed position, 5 mm, from empirical estimations based on model manufacturing. $B_{x_G,2}$ is the model installation error, estimated at 2 mm based on the installation accuracies. B_{y_G} is the RSS of two elemental biases, $B_{y_G,1}$ = 2 mm and $B_{y_G,2}$ = 1 mm, similarly as per B_{x_G}. B_m is the RSS of individual mass component measurement error B_{m_i} such that $B_m^2 = \sum_i B_{m_i}^2$. The element mass components (See Section 3.2) are measured with two types of commercial strain-gauge type scales. These are a Virtual Measurement & Control Inc. VW-321-S-30 Bench Scale and a Masterline MLG-500 Hanging Crane Scale, with 30 Kg and 227 Kg of maximum capacities, respectively, and with 0.023 Kg and 0.045 Kg reading accuracies, respectively. B_{I_z} is from the separate measurements of I_z. B_ρ is from the ITTC 1963 density-temperature formula for fresh water, $\rho(\mathrm{T}) = 999.784 + 0.0638\mathrm{T} - 0.00865\mathrm{T}^2 + 0.0000631\mathrm{T}^3$. The error propagation equation for ρ can be written as $B_\rho^2 = (\partial\rho/\partial\mathrm{T})^2 B_\mathrm{T}^2$ where B_T is the errors in water temperature T reading. Water temperature is measured with a resistive-type probe and signal conditioner, at a water-depth corresponding to model mid-draft. The temperature sensor and probe is an Omega Engineering Inc. DP465 model, specified with the probe accuracy as B_T = ±0.2°C. The uncertainties in the density formula were assumed as negligible.

Carriage speed: B_{U_C} is evaluated end-to-end by calibrating U_C with respect to the reference speed, $U_{\text{ref}} = \Delta L/\Delta t$. The reference speed is achieved by measuring the travel-time Δt for a known distance ΔL. Then, B_{U_C} is defined as

$$B_{U_C}^2 = B_{U_C,\text{ref}}^2 + B_{U_C,\text{fit}}^2 \tag{5.10}$$

where the $B_{U_C,\text{ref}}$ is from the accuracy of U_{ref} and the $B_{U_C,\text{fit}}$ is from scatter in the U_C calibration data set in relation to a linear least-squares regression curve fit. $B_{U_C,\text{ref}}$ is by applying the error propagation equation to U_{ref} such that

$$B_{U_C,\text{ref}}^2 = \theta_{\Delta L}^2 B_{\Delta L}^2 + \theta_{\Delta t}^2 B_{\Delta t}^2 \tag{5.11}$$

where $\theta_{\Delta L} = \partial U_{\text{ref}}/\partial \Delta L$ and $\theta_{\Delta t} = \partial U_{\text{ref}}/\partial \Delta t$, and $B_{\Delta L}$ = 0.005 m from the errors in tape measure of ΔL and $B_{\Delta t}$ = 0.0001 sec from the U_C sampling time interval 0.001 sec. $B_{U_C,\text{fit}}$ is evaluated as $2 \times SEE$ where the standard estimate of error (SEE) is from Coleman and Steele (1999) as,

$$B_{U_C,\text{fit}} = 2 \cdot SEE = 2 \cdot \sum_{i=1}^{\text{M}} \sqrt{\frac{\left(Y_i - Y_i^{'}\right)^2}{\text{M}-2}} \tag{5.12}$$

where Y_i is the measured U_C during the calibration, $Y_i^{'}$ is from the regression equation, and M is the number of data in the calibration. Calibration was done for three U_{ref}'s, 0.754, 1.531, and 2.241 m/s, with three repeat tests. Results revealed that $B_{U_C,\text{fit}}$ (0.010 m/s) is predominant over $B_{U_C,\text{ref}}$ (0.0014 m/s).

Motion parameters: B_u, B_v, B_r, $B_{\dot{u}}$, $B_{\dot{v}}$, $B_{\dot{r}}$ are from elemental biases, $B_{S_{mm}}$, B_{N}, B_t, B_β, $B_{\psi_{max}}$ and B_{U_C} through the error propagation equations (5.7) and (5.6). B_{U_C} is as per above. $B_{S_{mm}}$ is from the sway crank amplitude setting uncertainty, 0.5 mm. B_{N} is the uncertainty in PMM motion frequency, 0.0006 rpm, and B_t is the uncertainty in data-

sampling timescale, 0.001 sec, both determined empirically. B_β is the RSS of two uncorrelated elemental errors such that

$$B_\beta^2 = B_{\beta,\text{align}}^2 + B_{\beta,\text{drift}}^2 \tag{5.13}$$

where $B_{\beta,\text{align}}$ is from the errors in the initial model-installation with respect to straight towing direction and $B_{\beta,\text{drift}}$ is from the errors in setting the model at designated drift angles. The model alignment procedure consists of two steps, first the alignment of the strong-back with respect to towing direction and then alignment of the model ship with respect to the strong-back centerline. For the first step, the strong-back is aligned to the carriage towing direction guided by a laser-beam with its source fixed at the towing tank ceiling. For this, first the laser-beam is adjusted to point to the forward-end-center-point (C_{fwd}) of strong-back, and the carriage is driven forward until the laser-beam hits the rear-end of strong-back. Then, the distance between the rear-end-center-point (C_{rear}) of strong-back and the laser-beam, d, is measured, and then the orientation of strong-back is adjusted to compensate approximately a half d. The procedure is repeated until d becomes fairly smaller than the laser-beam diameter. For the second step, two plumb-bob strings are hanging from the C_{fwd} and C_{rear}, and the model center-line is aligned with the plumb-bob strings within a tolerance, ϵ. By assuming the two procedures are uncorrelated,

$$B_{\beta,align}^2 = \left(\arctan\frac{d}{D}\right)^2 + \left(\arctan\frac{\epsilon}{D}\right)^2 \tag{5.14}$$

where D is the distance between C_{fwd} and C_{rear}, i.e. the strong-back length. $B_{\beta,\text{align}}$ was evaluated as 0.03° for d = 2 mm corresponding to the laser-beam diameter, ϵ = 1mm, and D = 4 m. Next, $B_{\beta,\text{drift}}$ is attained end-to-end by calibrating the β readings with respect to reference angles. The reference drift angle β_{ref} is achieved by measuring the travel-distance, C, of a fixed-point at the model while it is rotated from straight-heading to a

designated β angle position, and measuring the distance, R, between the point and the rotation pivot (See Fig. 5-1), such that $\beta_{\text{ref}} = \arccos(1 - C^2/2R^2)$.
Subsequently, $B_{\beta,\text{drift}}$ is defined as the RSS of $B_{\beta,\text{drift,ref}}$ and $B_{\beta,\text{drift,fit}}$ similarly as B_{U_C} in (5.10),

$$B^2_{\beta,\text{drift}} = B^2_{\beta,\text{drift,ref}} + B^2_{\beta,\text{drift,fit}} \tag{5.15}$$

$B_{\beta,\text{drift,ref}}$ is the uncertainty in β_{ref} defined as $B^2_{\beta,\text{drift,ref}} = \theta_C^2 B_C^2 + \theta_R^2 B_R^2$, where $\theta_C = \partial\beta_{\text{ref}}/\partial C$ and $\theta_R = \partial\beta_{\text{ref}}/\partial R$ and B_C and B_R are the biases in C and R measurements. $B_{\beta,\text{drift,fit}} = 2 \cdot SEE$, similarly as per (5.12) for $Y = \beta$ and $Y' = \beta_{\text{ref}}$. From a calibration for twelve β_{ref} values (M = 12) between ±12°, $B_{\beta,\text{drift}}$ was evaluated as 0.22° as per (5.15) and with $B_C = B_R = 1$ mm. Lastly, $B_{\psi_{\max}}$ is the same as $B_{\beta,\text{drift}}$.

Forces and moment: B_F is from uncertainties in 1) force/moment gauges calibration, 2) model motions from the pre-described PMM motions, and 3) data-sampling timescales. The uncertainties 1) is common for dynamic and static test data and is composed of two element biases $B_{F,\text{ref}}$ and $B_{F,\text{fit}}$. The uncertainties 2) differ for dynamic and static test; $B_{F,u}$, $B_{F,\dot{u}}$, $B_{F,v}$, $B_{F,\dot{v}}$, $B_{F,r}$, and $B_{F,\dot{r}}$ for the former and $B_{F,\beta}$ and $B_{F,\text{align}}$ for the latter. The uncertainty 3) is only for dynamic test data, $B_{F,t}$. Accordingly, B_F is the RSS of those element biases as

$$B_F^2 = B^2_{F,\text{ref}} + B^2_{F,\text{fit}} + B^2_{F,u} + B^2_{F,\dot{u}} + B^2_{F,v} + B^2_{F,\dot{v}} + B^2_{F,r} + B^2_{F,\dot{r}} + B^2_{F,t} \tag{5.16}$$

for dynamic tests and

$$B_F^2 = B^2_{F,\text{ref}} + B^2_{F,\text{fit}} + B^2_{F,\text{align}} + B^2_{F,\beta} \tag{5.17}$$

for static drift test, respectively.

$B_{F,\text{ref}}$ is the uncertainty in the reference force or moment, F_{ref}, for gauges calibrations, i.e., the accuracy of calibration standard weights W. In that, $F_{\text{ref}} = W$ for force-

gauge calibrations, and $F_{\text{ref}} = W \times L$ for moment-gauge calibrations, respectively, where L is the moment-arm. When calibrations are repeated for several W's, then $B_{F,\text{ref}}$ is the RSS of the individual standard weight uncertainty B_{W_i} such that

$$B_{F,\text{ref}}^2 = \sum_i B_{W_i}^2 \tag{5.18}$$

for $F = F_x$ and $F = F_y$, and

$$B_{F,\text{ref}}^2 = \sum_i \left(\theta_{W_i}^2 B_{W_i}^2 + \theta_L^2 B_L^2\right) \tag{5.19}$$

for $F = M_z$, where W_i is the individual standard weight, $\theta_{W_i} = \partial F_{\text{ref}} / \partial W_i$ and $\theta_L = \partial F_{\text{ref}} / \partial L$ as per (5.9) for $\chi = F_{\text{ref}}$, and B_{W_i} and B_L are the errors in the standard weight and the moment arm dimension, respectively. Calibration was done with ASTM Class 4 standard weights with a 0.002% tolerance, from which $B_{F,\text{ref}}$ was rated at 0.002% of the full-scale for F_x and F_y gauges (50 N), and 0.014% for M_z gauge (200 Nm).

$B_{F,\text{fit}}$ is from the scatter in the calibration data set in relation to a linear least-squares regression curve fit, i.e., the volt-to-force conversion error of the force/moment gauges. In general, $B_{F,\text{fit}}$ exhibits dependency on the magnitude of F applied, rather than a fixed-amount such as $2 \cdot SEE$, and is fitted to a linear function of F as

$$B_{F,\text{fit}} = a|F| + b \tag{5.20}$$

For this, the differences between the measured and applied forces, i.e., $\Delta F = \left|F - F_{\text{ref}}\right|$, during the calibration are linear-curve-fitted as $\Delta F_{95\%} = a|F_{\text{ref}}| + b$ to evaluate the coefficients a and b in (5.20). The $\Delta F_{95\%}$ is defined as

$$\Delta F_{95\%} = \overline{\Delta F} + P_{\overline{\Delta F}} \tag{5.21}$$

where $\overline{\Delta F}$ is the mean ΔF from the M repeat measurements for each W_i and $P_{\overline{\Delta F}}$ is the precision limit of the ΔF measurements as per (5.26) for $\text{r} = \Delta F$ shown in the following

Section 5.1.2. Statistically, for M ≥ 10, the true ΔF falls within $\pm\Delta F_{95\%}$ in 95 out of 100 cases. Calibrations were repeated twelve times for each W_i (M = 12), and $B_{F,\text{fit}}$ was rated at 0.3%, 0.4%, and 0.3% of full-scales of the F_x, F_y, and M_z gauges, respectively. For the calibration, the g value of 9.8031 m/s^2 based on the local latitude of Iowa City, Iowa, USA (Halliday & Resnick 1981) was used and the local buoyancy was assumed as negligible.

$B_{F,\text{align}}$ and $B_{F,\beta}$ for static drift test data are the biases of F from $B_{\beta,\text{align}}$ in (5.14) and $B_{\beta,\text{drift}}$ in (5.15), respectively, defined as

$$B_{F,\text{align}}^2 = \theta_\beta^2 B_{\beta,\text{align}}^2 \tag{5.22}$$

$$B_{F,\beta}^2 = \theta_\beta^2 B_{\beta,\text{drift}}^2 \tag{5.23}$$

where the sensitivities $\theta_\beta = \partial F/\partial\beta$ was evaluated by curve-fitting the static drift F data as polynomial functions of β.

$B_{F,u}$, $B_{F,v}$, $B_{F,r}$, $B_{F,\dot{u}}$, $B_{F,\dot{v}}$, and $B_{F,\dot{r}}$ are the errors in F due to the uncertainties in the motion parameters, B_u, B_v, B_r, $B_{\dot{u}}$, $B_{\dot{v}}$, and $B_{\dot{r}}$, respectively, and are defined as

$$B_{F,x}^2 = \theta_x^2 B_x^2 \tag{5.24}$$

for $x = u, v, r, \dot{u}, \dot{v}, \dot{r}, t$, respectively, where $\theta_x = \partial F/\partial x$ and B_x's are the same as (5.6). Without the DRE for F, derivatives $\partial F/\partial x$'s are approximated by modeling the measured forces and moment F time-histories as polynomial functions of motion parameters, $\tilde{F}$, such that $\partial F/\partial x \approx \partial\tilde{F}/\partial x$. The model functions $\tilde{F}$ for each dynamic test are summarized in Table 5-3, where the coefficients, A's, B's, and C's of $\tilde{F}$ are determined by applying a least-squares-error method for multiple variables. For the implementation, a singular-value-decomposition (SVD) method was used solving the least-square matrix, and several coefficients such as A_r, A_{rr}, $A_{\dot{u}}$, B_r, $B_{\dot{u}}$, $B_{\dot{r}}$, C_r, $C_{\dot{u}}$, and $C_{\dot{r}}$ for the pure sway $\tilde{F}$ are set to zero to avoid singular matrices.

$B_{F,t}$ is the error due to uncertainties of the data sampling time scale B_t, written as

$$B_{F,t}^2 = \theta_t^2 B_t^2 \tag{5.25}$$

where $\theta_t = \partial F/\partial t$ was evaluated by differentiating numerically the time-histories of F, and B_t is the uncertainties in the data-sampling timescale.

Motion data: Of the four element biases in (8) for the motion data, B_L is the same as presented above and $B_{z_{mm}}$, B_θ, and B_ϕ are from the measurement errors of the Krypton motion tracker. As per the Krypton camera verification report, a value of ±0.1 mm is used for $B_{z_{mm}}$ since the target is in zone #1 of the camera module field of view (See Section 3.7.2). Biases for pitch and roll data B_θ and B_ϕ, respectively, are 0.04° for both from the previous UA results (Irvine et al. 2008).

5.1.2 Precision limits

The precision limits are determined from 12 repeat tests. The datasets are spaced in time at least 12 minutes between tests to minimize flow disturbances from previous runs, while spanning over a time period, usually one day, that is large relative to time scales of the factors that influence variability of the measurements. The same model ship, PMM motion generator, loadcell, and motion tracker are used for repeat tests due to limitations of time and experiment resources. The model is not dismounted and re-installed during the repeat tests. However, the PMM motion control parameters, such as drift angle, sway crank amplitude, or maximum heading angle settings are changed between tests. The precision limits are computed with the standard multiple-test equation

$$P_{\bar{\mathrm{r}}} = \frac{tS_{\bar{\mathrm{r}}}}{\sqrt{\mathrm{M}}} \tag{5.26}$$

for r = X, Y, N, z, θ, and ϕ, where t = 2 is the coverage factor for 95% confidence level and M = 12 is the number of repeat tests. $S_{\bar{\mathrm{r}}}$ is the standard deviation defined as

$$S_{\bar{\mathrm{r}}} = \left[\sum_{k=1}^{\mathrm{M}} \frac{(\mathrm{r}_k - \bar{\mathrm{r}})}{\mathrm{M}-1}\right]^{\frac{1}{2}} \tag{5.27}$$

and

$$\bar{\mathrm{r}} = \frac{1}{M}\sum_{k=1}^{\mathrm{M}} \mathrm{r}_k \tag{5.28}$$

where, r_k is X, Y, N, z, θ, or ϕ of the k^{th} run.

5.1.3 Total Uncertainty limits

The total uncertainty for the average result is the RSS of B_{r} and P_{r}.

$$U_{\mathrm{r}}^2 = B_{\mathrm{r}}^2 + P_{\mathrm{r}}^2 \tag{5.29}$$

A conceptual asymmetry bias B_{asym} is defined if data asymmetry with respect to the xz-plane is larger than U_{r} estimations, as following:

$$U_{T_1}^2 = U_{\mathrm{r}}^2 + B_{asym}^2 \tag{5.30}$$

Another conceptual facility bias B_{FB} is defined if the difference of each facility data from the facility mean is larger than U_{T_1}, as following:

$$U_{T_2}^2 = U_{T_1}^2 + B_{FB}^2 \tag{5.31}$$

Definitions, estimation procedures, and estimation results of the B_{asym} and B_{FB} are provided in sections 5.1.5 and 5.1.7, respectively.

5.1.4 UA Results and Discussions

UA results for the elemental biases $B_{L_{PP}}$, B_{T_m}, B_{x_G}, B_{y_G}, B_m, B_{I_z}, B_ρ, B_{U_C}, B_u, B_v, B_r, $B_{\dot{u}}$, $B_{\dot{v}}$, $B_{\dot{r}}$, and B_F in (5.4) and (5.5) are presented first with identifications of the primary error sources, and then, the total bias B_{r} and precision P_{r} limits and their contri-

butions to total uncertainty U_r are presented. For the dynamic test data, the period-mean values of uncertainty limits, $\langle B \rangle$, $\langle P \rangle$, and $\langle U \rangle$, are defined as

$$\langle B, P, U \rangle = \frac{1}{T}\int_0^T (B, P, U)dt \tag{5.32}$$

where T is the PMM motion period. Note for static drift and pure yaw data that, presented herein are the average values for three Fr cases otherwise mentioned, and also for static drift data that, the $\langle B \rangle$, $\langle P \rangle$, and $\langle U \rangle$ values are the same as B, P, and U values, respectively. Typically, the uncertainty limits B, P, and U are presented in $\%D$ values, where D is defined in different ways according to the characteristics of the variable and/or according to specific type of the test. For anti-symmetry variables (v, $\dot{v}$, r, $\dot{r}$, v_{PMM}, $\dot{v}_{PMM}$, ψ, r_{PMM}, $\dot{r}_{PMM}$, F_y, M_z, Y, N, and ϕ), D is defined as the dynamic range of the variable, and for symmetry variables (u, F_x, X, z, and θ), D is the period-mean value of the variable with defined similarly as (5.32).

Global variables and carriage speed: $B_{L_{PP}}$, B_{T_m}, B_{x_G}, B_{y_G}, B_m, B_{I_z}, B_ρ, and B_{U_C} are presented in Table 5-4 and compared with their nominal values (D). Typically, B values are fairly smaller than D. $B_{L_{PP}}$ is 0.07% of L_{PP}. B_{T_m} is 0.7% of T_m. B_{x_G} is 31.3% of x_G. B_{y_G} = 2 mm. B_m is 0.1% of m for both of the free- and fixed-model cases. B_{I_z} is about 4% of I_z for both the free- and fixed-model cases. B_ρ is negligibly small 0.004% of ρ at T = 20°C. B_{U_C} is 1.4%, 0.7%, and 0.5% of U_C for Fr = 0.138, 0.280, and 0.410, respectively.

Motion parameters: $B_{v_{PMM}}$, $B_{\dot{v}_{PMM}}$, B_ψ, $B_{r_{PMM}}$, and $B_{\dot{r}_{PMM}}$ are presented in Table 5-5 for pure sway, pure yaw, and yaw and drift tests at Fr = 0.280, where at the top part of the table $B_{S_{mm}}$, B_N, B_t, B_β, and $B_{\psi_{max}}$ are also summarized. In general, $\langle B_{v_{PMM}} \rangle$, $\langle B_{\dot{v}_{PMM}} \rangle$, $\langle B_\psi \rangle$, $\langle B_{r_{PMM}} \rangle$, and $\langle B_{\dot{r}_{PMM}} \rangle$ values are all less than 1% of their own D values except for a few cases where D values are negligibly small. $B_{v_{PMM}}$ and $B_{\dot{v}_{PMM}}$ are mostly

from $B_{S_{mm}}$, about 93%. B_{ψ} is from both B_{β} and $B_{\psi_{\max}}$, about 67% and 33%, respectively. $B_{r_{PM\,M}}$ and $B_{\dot{r}_{PMM}}$ are from $B_{\psi_{\max}}$, almost 100%.

B_u, B_v, B_r, $B_{\dot{u}}$, $B_{\dot{v}}$, and $B_{\dot{r}}$ are presented at the lower part of Table 5-5. $\langle B_u \rangle$ is 0.7% for all test types, and mostly (99%) contributed from B_{U_C}. $\langle B_v \rangle$ is about 2% except for PY where D value is negligibly small, and mostly (96%) contributed from B_{ψ} that is from B_{β} and $B_{\psi_{\max}}$. $\langle B_r \rangle$ is 0.7% except for PS where D value is negligibly small, and is the same as $\langle B_{r_{PMM}} \rangle$ that is from $B_{\psi_{\max}}$. $\langle B_{\dot{u}} \rangle$ is about 1% except for pure sway where again D is negligible, and mainly contributed from B_{U_C}, B_{ψ}, and $B_{r_{PMM}}$ for pure sway, pure yaw, and yaw and drift, respectively, 63%, 84%, and 87%, respectively, which are again from B_{β} and $B_{\psi_{max}}$. $\langle B_{\dot{v}} \rangle$ is about 4% and mainly contributed from B_{U_C} and $B_{\dot{v}_{PMM}}$ where the latter is from $B_{S_{mm}}$. $\langle B_{\dot{r}} \rangle$ is 0.7% except for PS for which D is negligible, and is the same as $\langle B_{\dot{r}_{PMM}} \rangle$ that is from $B_{\psi_{max}}$.

Forces and moment: B_F's are presented in Table 5-6 including contributions of the element biases. For static drift, B_F is about 1%, 3%, and 3%, in averages for three Fr cases for F_x, F_y, and M_z, respectively, and mainly contributed from $B_{F,\beta}$, 76%, 97%, and 96%, respectively. For dynamic test, $\langle B_F \rangle$ values are about 1% in general and the main contributors are different by the test type and by the variable. For pure sway, $B_{F,v}$ is the primary bias contributing about 95%. For pure yaw, $B_{F,r}$ is the common primary bias for F_x, F_y, and M_z, contributing 17%, 96%, and 67%, respectively, and $B_{F,\text{fit}}$ and $B_{F,\dot{v}}$ are also main biases for F_x, contributing 32% and 34%, and $B_{F,\dot{r}}$ for M_z, contributing 34%, in averages for three Fr cases. For yaw and drift, $B_{F,u}$ is the primary bias for F_x and $B_{F,v}$ is for F_y and M_z, contributing about 57%, and $B_{F,r}$ is the common primary bias contributing about 31%.

Total Bias Limits B_r's are summarized in Table 5-7 including the contributions of individual element biases. In general, the primary biases vary by the variable and by the test type. For static drift, B_{U_C} and B_F are the common primary biases for X, Y, and N data, where B_T is also large for X. For pure sway, the primary bias is B_u for X and B_F for Y

and N, respectively. For pure yaw, B_u is the primary bias for X, B_F is the primary and B_r is the secondary bias and for Y, and B_F is the primary and B_u is the secondary bias and B_{I_z} is also large for N. For yaw and drift, B_u is the primary and B_F is the secondary bias for X, and B_F is the primary and B_u is the secondary bias for both Y and N, and B_{I_z} is also large for N. The primary biases for static drift and pure yaw data exhibit Fr trends. For static drift, the contribution of B_{U_C} decreases with Fr, whereas B_T and B_F show the opposite trend. For pure yaw, in general, the trend varies by the variable: the contribution of B_u decreases with Fr for X; the contribution of B_r is almost constant with Fr, whereas that of B_F increases with Fr for Y; the contribution of B_u is decreasing and that of B_F is increasing with Fr for N, respectively.

The sources of the primary biases and their propagations were traced back through Tables 5-7, 5-6, and 5-5 and then 5-4, summarized in Table 5-8. For static drift, B_{U_C} and B_F are the common primary biases for B_X, B_Y, and B_N, where the former is directly from U_C and the latter is from β propagated through $B_{F,\beta}$. For dynamic tests, B_u is the primary bias of B_X, commonly for pure sway, pure yaw, and yaw and drift tests, and is propagated from U_C through B_{U_C}. On the other hand, B_F is the primary bias for both B_Y and B_N, but from different sources propagated through different paths; from β and ψ_{max} for pure sway through B_ψ, B_v, and then $B_{F,v}$, from ψ_{max} for pure yaw through $B_{r_{PMM}}$, B_r, and then $B_{F,r}$, and from β and ψ_{max} for yaw and drift test through $B_\psi/B_{r_{PMM}}$, B_v/B_r, and then $B_{F,v}/B_{F,r}$, respectively. Consequently, U_C is the primary bias source for X and β and ψ_{max} are for Y and N, suggesting that improvement of carriage speed (U_C) control is important for X and precise angle-setting for β and $\psi_{\max}$ is important for Y and N to reduce the bias errors.

The overall UA results are summarized in Table 5-9 including the total bias B_{r} and precision P_{r} limits and their contributions to the total uncertainty U_{r}. Herein, $\langle B_{\mathrm{r}} \rangle$, $\langle P_{\mathrm{r}} \rangle$, and $\langle U_{\mathrm{r}} \rangle$ values (B_{r}, P_{r}, and U_{r} values for static drift) are presented in % D, in the order of X, Y, and N, and in averages for three Fr cases for static drift and pure yaw. In

general, uncertainties are larger for dynamic test data than static drift data, and larger for X data than Y and N. For static drift, B_r is predominant, contributing to U_r about 87%, 93%, 91%, respectively, and P_r is relatively small, contributing to U_r about 13%, 8%, 9%, respectively, indicating most DRE variable results are highly repeatable. U_r is about 2%, 4%, 3%, respectively, reasonably small but comparatively larger than resistance test uncertainty U_{CT} = 1% of C_T (Longo et al. 2005). Additional error sources for static drift, such as B_β, may explain the higher uncertainty level than the resistance test result. For dynamic tests, in general $\langle B_r \rangle$ is dominant for Y and N, contributing to $\langle U_r \rangle$ about: 63% and 94% for pure sway; 67% and 89% for pure yaw; and 80% and 92% for yaw and drift, whereas $\langle P_r \rangle$ is dominant for X, contributing to $\langle U_r \rangle$ about 75% for pure sway, 70% for pure yaw, and 71% for yaw and drift. $\langle U_r \rangle$ is about: 5%, 2%, 2%, respectively, for pure sway, similar with static drift; 8%, 5%, 1%, respectively, for pure yaw, usually larger than static drift and pure sway, and tends to decrease with Fr in general; and 7%, 4%, 2%, respectively, larger than static drift and pure sway but similar with pure yaw.

The UA results for motion data z and θ are also presented in Table 5-9. For z, $\langle U_r \rangle$ is about 6%, 5%, 8%, and 3% for static drift, pure sway, pure yaw, and yaw and drift, where usually $\langle P_r \rangle$ is predominant over 80% for all tests. For θ, $\langle U_r \rangle$ is about 81%, 28%, 29%, and 15%, respectively, where $\langle B_r \rangle$ is predominant over 80% in general.

5.1.5 Asymmetry Bias

Static drift test X, Y, N, z and θ are presented in Fig. 5-2 for both positive and negative β ranges. Contrary to expectations, test results show large asymmetry of data between positive and negative β. The asymmetry of X is more apparent and seemingly larger than the U_r limits estimated with (5.29) shown at β = -10°. Similar asymmetry is observed from the motion data, although seemingly better symmetry. With the drift angle bias $B_{F,\beta}$ and the model ship alignment bias $B_{F,align}$ accounted previously in the UA procedures in Section 3.1, further errors such as model fabrication error and/or initial

heeling of the model, probably from imperfect weight ballasting, maybe possible reasons for the asymmetry.

In order to quantify the asymmetry of data r = X, Y,N, z, and θ, data asymmetry Δr_{asym} is defined as

$$\Delta_{asym} = |r^{+} - r^{-}|/r_m \tag{5.33}$$

where r^{+} is the value at positive β, r^{-} is at negative β with proper sign changes for anti-symmetric variables such as Y and N, and r_m is the average of r^{+} and r^{-}. At Fr = 0.280, Δ_{asym} is about 20% for X at β = 10°, which is significantly larger than the total uncertainty width $2U_r$ = 4.3% of r_m, and Δ_{asym} increases up to 40 % at β = 20°. Whereas Δ_{asym} for Y and N exhibit an opposite trend; decreasing with β, and within the $2U_r$ at β = 10°. Due to the lack of solid explanations for those data asymmetry, the mean value r_m is taken as the representing data, and the amount of data asymmetry is added to the total uncertainty U_r defined as a conceptual bias B_{asym} as

$$B_{asym}^2 = D_{asym}^2 - U_r^2 \tag{5.34}$$

if $D_{asym} > U_r$, whereas B_{asym} equals zero if $D_{asym} \leq U_r$. Here, D_{asym} is the difference between r and r_m such that

$$D_{asym} = |r - r_m| \tag{5.35}$$

Subsequently, the total uncertainty U_{T_1} is defined as per equation (30).

Defining asymmetry of dynamic test data, however, may not be as straightforward as for static drift test data. Nonetheless, the use of symmetry and anti-symmetry characteristics of the dynamic test variables can be a possible approach. The time-histories of the dynamic test data are shown in Figure 5-3 for pure sway, pure yaw, and yaw and drift tests, respectively. For pure sway data, as an example, the odd-order harmonics of the symmetric variables such as X, z, and θ and the even-order harmonics of the anti-

symmetric variables such as Y and N are not expected from their Fourier-Series (FS) expansions since the pure sway motions are symmetric with respect to the model towing direction. These symmetry considerations are also true for pure yaw test, but are not appropriate for yaw and drift test due to its asymmetric motion (Fig. 4d). Hence, D_{asym} in equation (5.35) can be redefined for pure sway and pure yaw data as

$$D_{asym} = |\mathrm{r} - \mathrm{r}_{\mathrm{FS}}| \tag{5.36}$$

where r_{FS} is the corrected data by dropping the odd- or even-order FS harmonics according to their symmetry- or anti-symmetry characteristics of the variable, respectively. Then, B_{asym} for pure sway and pure yaw data are defined as per the equations (5.34).

Evaluation results are summarized in Table 5-10, including $\langle D_{asym} \rangle$, $\langle U_{\mathrm{r}} \rangle$, $\langle B_{asym} \rangle$, and $\langle U_{T_1} \rangle$ values, defined similarly as (5.32), presented in % of D_{rm} value. D_{rm} is the absolute value of r_{m} for static drift, whereas for pure sway and pure yaw, D_{rm} is the absolute period-mean value of X, z, and θ and the dynamic range of r_{FS} for Y and N. Herein, the results are presented in the order of X, Y, N, z, and θ data and in averages of the three Fr cases for static drift and pure yaw. In general, B_{asym} is large for X compared to those for Y and N, and also large for z and θ. For static drift data, B_{asym} is 8%, 0%, 0%, 4%, 114%, respectively, where the value for X is considerably larger than the U_{r} estimation, 2%. By including the B_{asym}, the total uncertainty U_{T_1} values are evaluated as 9%, 4%, 3%, 8%, and 126%, respectively. For pure sway, $\langle B_{asym} \rangle$ is 6%, 5%, 0%, 12%, and 0%, respectively, with $\langle U_{T_1} \rangle$ 10%, 5%, 2%, 14%, and 28%, respectively. For pure yaw, $\langle B_{asym} \rangle$ is 5%, 2%, 1%, 30%, and 24%, respectively, with $\langle U_{T_1} \rangle$ 10%, 7%, 2%, 32%, 57%, respectively.

5.1.6 UA Comparisons between Facilities

UA results for three facilities data, IIHR, FORCE, and INSEAN, are compared. The facilities have different dimensions (L×B×D), 100m×3.048m×3.048m,

240m×12m×4.4m, and 500m×12.5m×6.5m, respectively, and different model size, 3.048m, 4.002m, and 5.720m, respectively. Results are summarized in Table 5-11, including the contributions of bias B_r^2 and precision P_r^2 limits presented in % U_r^2 and the total uncertainty U_r presented in % |r| values. The |r| is defined as the X, Y, or N value at $\beta = 10°$ for static drift, the value at $v = v_{max}$ for pure sway, and $r = r_{max}$ for both pure yaw and yaw and drift, respectively. Herein the results are presented in the order of IIHR, FORCE, and INSEAN, and in averages for all variables and Fr cases where applicable, otherwise mentioned. In general, B_r is predominant, 90%, 69%, and 97% for static drift, respectively, and 67%, 95%, and 66% for dynamic tests, respectively, whereas P_r is dominant or both B_r and P_r are large for several cases such as the dynamic tests X for IIHR, static drift N for FORCE, and pure yaw N for INSEAN. Static drift U_r is small, 3% for all facilities data, whereas dynamic test U_r is relatively larger than static drift, 5%, 2%, and 2% for pure sway, respectively, 10%, 6%, and 4% for pure yaw, respectively, and 5%, 4%, and 3% for yaw and drift, respectively.

The U_r (% |r|) values are compared between facilities data observing the data trends with the model length and with Fr. First, U_r values are plotted in Fig. 5-4 against the model length, scaled with the smallest value, i.e., L = 1.0, 1.3, and 1.9, for IIHR, FORCE, and INSEAN, respectively. Although data exhibit scatters, mean values show trends with model length. Static drift mean values in Fig. 5-4 (a) are almost independent of model length, 3.1%, 3.3%, and 28%, respectively, whereas mean values of dynamic tests in Fig. 5-4 (b) decrease with model length, 8.3%, 4.8%, and 3.2%, respectively. Next, static drift and pure yaw U_r values are plotted in Fig. 5-5 (a) and (b), respectively, against Fr numbers, 0.138, 0.280, and 0.410. Again, the U_r values show scatters, while the mean values exhibit a rather clear Fr trend; decreasing with Fr, 4.3%, 2.6%, and 2.3% for static drift, and 11.3%, 4.6%, and 4.2% for pure yaw.

The asymmetry bias B_{asym} is evaluated for FORCE and INSEAN data, and the $\langle U_r \rangle$, $\langle B_{asym} \rangle$, and $\langle U_{T_1} \rangle$ values are presented in % D_{r_m} similarly as defined in Section

5.1.5, summarized in Table 5-12. Results are presented herein in the order of X, Y, and N, and for static drift and pure yaw data in averages of all Fr cases. The $\langle B_{asym} \rangle$ values are evaluated as, for static drift 1%, 0%, and 1% for FORCE, respectively, and 8%, 0%, and 0% for INSEAN, respectively; for pure sway 0%, 0%, and 0% for FORCE, respectively, and 11%, 0%, and 0% for INSEAN, respectively; and for pure yaw 0%, 0%, and 1% for FORCE, and 6%, 2%, and 0% for INSEAN, respectively. The overall mean $\langle B_{asym} \rangle$ values are small for FORCE facility data, 0%, 0%, and 1%, respectively, but relatively large for INSEAN, 8%, 1%, and 0%, respectively, where the INSEAN exhibit similar $\langle B_{asym} \rangle$ values as IIHR, 7%, 2%, and 0%, respectively, as previously shown in Table 5-10. For IIHR and INSEAN, the $\langle B_{asym} \rangle$ values for X data are evaluated as larger than the total uncertainty limits $\langle U_{\mathrm{r}} \rangle$ values, 5% and 2%, respectively, and are combined into $\langle U_{T_1} \rangle$ as per (30), 10% and 9%, respectively.

5.1.7 Facility Bias

UA results show reasonable uncertainty levels in general, nevertheless for several cases, deviations of data from the facility-mean value, $\bar{\mathrm{r}}$, exceed the total uncertainty estimations for each facility data, particularly for many cases for X. Those deviations of the data are considered to be from using different model size, different model manufactures, different towing tank dimensions, different water properties such as density, different towing carriage driving mechanisms, different PMM generators, different measurement systems, and so on, which cannot be accounted for each individual facility UA procedures. The facility biases or certification intervals of facilities are estimated using the M×N-order testing method as per Stern et al. (2005). The method is a statistical approach for assessing probabilistic confidence intervals with the mean facility data as reference values for M facilities with N repeat tests (N-order level testing) under the assumptions of normal distribution for the sample population X_i, 95% confidence level, M ≥ 10, and N

≥ 10. Herein, M = 3 and N = 12 are used. Although the number of facilities, M = 3, is minimal, the results show usefulness of the approach as discussed by Stern.

For the mean facility data $\bar{X}$, where X is either X, Y, or N of individual facility N-order test, the uncertainty $U_{\bar{X}}$ in $\bar{X}$ is the RSS of the bias limit $B_{\bar{X}}$ and the precision limit $P_{\bar{X}}$, which are the average RSS's of the M bias limits B_{X_i} and M precision limits P_{X_i}, respectively. The subscript i represents each facility data. Comparing the difference $D_i = X_i - \bar{X}$ with its uncertainty $U_{D_i}^2 = U_{X_i}^2 + U_{\bar{X}}^2$, if the absolute value of D_i is less than U_{D_i} i.e., $|D_i| \leq U_{D_i}$, then the individual facility is certified at interval U_{D_i}, whereas if $|D_i| > U_{D_i}$ then the facility bias B_{FB_i} which is defined as

$$B_{FB_i}^2 = D_i^2 - U_{D_i}^2 \tag{5.37}$$

with total uncertainty U_{T_2} as per equation (5.31). Interval certification provides additional confidence in measurements accuracy for certified facilities since it validates X_i and accounts for $U_{\bar{X}}$ in assessing the level of certification, and an improved estimate U_{T_2} for noncertified facilities accounting for facility biases.

B_{FB} is evaluated at β = 10° for static drift test, whereas for dynamic tests B_{FB} is evaluated at $v = v_{max}$ for pure sway and $r = r_{max}$ for pure yaw and yaw and drift, respectively. Evaluation results of B_{FB} is summarized in Table 5-13 for IIHR data including $U_{\bar{X}}$, $|D_i|$, U_{D_i}, and U_{T_2}, and in Table 5-14 for FORCE and INSEAN data including $|D_i|$, U_{D_i}, and U_{T_2}, respectively, with all data presented in % $|\bar{X}|$ values. Herein, results are presented in the order of X, Y, and N and in averages for Fr cases where applicable. For static drift, B_{FB} is about 0%, 0%, and 1% for IIHR, respectively, about 0%, 1%, and 1% for FORCE, respectively, and about 3%, 4%, and 3% for INSEAN, respectively. Accordingly, IIHR and FORCE data are certified within certificate interval U_{D_i} about 11%, 4%, and 4% for IIHR, respectively, and about 8%, 3%, and 3% for FORCE, respectively, whereas U_{T_2} for INSEAN data is estimated at about 11%, 5%, and 5%, respectively, in-

creased from the U_{X} estimates about 9%, 3%, and 3%, respectively, by including the B_{FB}. For dynamic test data, in general, most of IIHR data are certified but with relatively large certificate intervals U_D about 3% ~ 30%, whereas FORCE and INSEAN data for several cases are uncertified with facility biases B_{FB} about 2% ~ 7%.

Table 5-1 Sensitivity coefficients of the bias limits for dynamic tests.

θ	B_X	B_Y	B_N
θ_L	$\frac{-2\left(F_x+m(\dot{u}-rv-x_G r^2-y_G\dot{r})\right)}{\rho(u^2+v^2)L^2T}$	$\frac{-2\left(F_y+m(\dot{v}+ru-y_G r^2+x_G\dot{r})\right)}{\rho(u^2+v^2)L^2T}$	$\frac{-4\left(M_z+I_z\dot{r}+m\left(x_G(\dot{v}+ru)-y_G(\dot{u}-rv)\right)\right)}{\rho(u^2+v^2)L^3T}$
θ_T	$\frac{-2\left(F_x+m(\dot{u}-rv-x_G r^2-y_G\dot{r})\right)}{\rho(u^2+v^2)LT^2}$	$\frac{-2\left(F_y+m(\dot{v}+ru-y_G r^2+x_G\dot{r})\right)}{\rho(u^2+v^2)LT^2}$	$\frac{-2\left(M_z+I_z\dot{r}+m\left(x_G(\dot{v}+ru)-y_G(\dot{u}-rv)\right)\right)}{\rho(u^2+v^2)L^2T^2}$
θ_{x_G}	$\frac{-2mr^2}{\rho(u^2+v^2)LT}$	$\frac{2m\dot{r}}{\rho(u^2+v^2)LT}$	$\frac{2m(\dot{v}+ru)}{\rho(u^2+v^2)L^2T}$
θ_{y_G}	$\frac{-2m\dot{r}}{\rho(u^2+v^2)LT}$	$\frac{-2mr^2}{\rho(u^2+v^2)LT}$	$\frac{-2m(\dot{u}-rv)}{\rho(u^2+v^2)L^2T}$
θ_m	$\frac{2(\dot{u}-rv-x_G r^2-y_G\dot{r})}{\rho(u^2+v^2)LT}$	$\frac{2(\dot{v}+ru-y_G r^2+x_G\dot{r})}{\rho(u^2+v^2)LT}$	$\frac{2\left(x_G(\dot{v}+ru)-y_G(\dot{u}-rv)\right)}{\rho(u^2+v^2)L^2T}$
θ_{I_z}	-	-	$\frac{2\dot{r}}{\rho(u^2+v^2)L_{PP}^2T_m}$
θ_ρ	$\frac{-2\left(F_x+m(\dot{u}-rv-x_G r^2-y_G\dot{r})\right)}{\rho^2(u^2+v^2)LT}$	$\frac{-2\left(F_y+m(\dot{v}+ru-y_G r^2+x_G\dot{r})\right)}{\rho^2(u^2+v^2)LT}$	$\frac{-2\left(M_z+I_z\dot{r}+m\left(x_G(\dot{v}+ru)-y_G(\dot{u}-rv)\right)\right)}{\rho^2(u^2+v^2)L^2T}$
θ_u	$\frac{-4u\left(F_x+m(\dot{u}-rv-x_G r^2-y_G\dot{r})\right)}{\rho(u^2+v^2)LT}$	$\frac{2}{\rho(u^2+v^2)LT}\left[mr-\frac{2u\left(F_y+m(\dot{v}+ru-y_G r^2+x_G\dot{r})\right)}{(u^2+r^2)}\right]$	$\frac{2}{\rho(u^2+v^2)L^2T}\left[mx_G r-\frac{2u\left(M_z+I_z\dot{r}+m\left(x_G(\dot{v}+ru)-y_G(\dot{u}-rv)\right)\right)}{(u^2+r^2)}\right]$
θ_v	$\frac{2}{\rho(u^2+v^2)LT}\left[-mr-\frac{2v\left(F_x+m(\dot{u}-rv-x_G r^2-y_G\dot{r})\right)}{(u^2+v^2)}\right]$	$\frac{4v\left(F_y+m(\dot{v}+ru-y_G r^2+x_G\dot{r})\right)}{\rho(u^2+v^2)LT}$	$\frac{2}{\rho(u^2+v^2)L^2T}\left[my_G r-\frac{2v\left(M_z+I_z\dot{r}+m\left(x_G(\dot{v}+ru)-y_G(\dot{u}-rv)\right)\right)}{(u^2+r^2)}\right]$
θ_r	$\frac{-2m(v+2x_G r)}{\rho(u^2+v^2)LT}$	$\frac{2m(u-2y_G r)}{\rho(u^2+v^2)LT}$	$\frac{2(x_G u+y_G v)}{\rho(u^2+v^2)L^2T}$
$\theta_{\dot{u}}$	$\frac{2m}{\rho(u^2+v^2)LT}$	-	$\frac{-2my_G}{\rho(u^2+v^2)L^2T}$
$\theta_{\dot{v}}$	-	$\frac{2m}{\rho(u^2+v^2)LT}$	$\frac{2mx_G}{\rho(u^2+v^2)L^2T}$
$\theta_{\dot{r}}$	$\frac{-2my_G}{\rho(u^2+v^2)LT}$	$\frac{2mx_G}{\rho(u^2+v^2)LT}$	$\frac{2I_z}{\rho(u^2+v^2)L^2T}$
θ_F	$\frac{2}{\rho(u^2+v^2)LT}$	$\frac{2}{\rho(u^2+v^2)LT}$	$\frac{2}{\rho(u^2+v^2)L^2T}$

Table 5-2. Sensitivity coefficients of the bias limits for static drift test.

θ	B_X	B_Y	B_N
$\theta_{L_{PP}}$	$\frac{-2F_x}{\rho U_C^2 L^2 T}$	$\frac{-2F_y}{\rho U_C^2 L^2 T}$	$\frac{-2M_z}{\rho U_C^2 L^3 T}$
θ_{T_m}	$\frac{-2F_x}{\rho U_C^2 L T^2}$	$\frac{-2F_y}{\rho U_C^2 L T^2}$	$\frac{-2M_z}{\rho U_C^2 L^2 T^2}$
θ_ρ	$\frac{-2F_x}{\rho^2 U_C^2 L T}$	$\frac{-2F_y}{\rho^2 U_C^2 L T}$	$\frac{-2M_z}{\rho U_C^2 L^2 T}$
θ_{U_C}	$\frac{-4F_x}{\rho U_C^3 L T}$	$\frac{-4F_y}{\rho U_C^3 L T}$	$\frac{-4M_z}{\rho U_C^3 L^2 T}$
θ_F	$\frac{2}{\rho U_C^2 L T}$	$\frac{2}{\rho U_C^2 L T}$	$\frac{2}{\rho U_C^2 L^2 T}$

Table 5-3. Polynomial models for measured force/moment, $\tilde{F}$.

Pure sway:

$$\tilde{F}_x = A_0 + A_u u + A_v v + A_r r + A_{vv} v^2 + A_{\dot{u}} \dot{u} + A_{\dot{v}} \dot{v} + A_{\dot{r}} \dot{r}$$

$$\tilde{F}_y = B_0 + B_u u + B_v v + B_r r + B_{v|v|} v|v| + B_{\dot{u}} \dot{u} + B_{\dot{v}} \dot{v} + B_{\dot{r}} \dot{r}$$

$$\tilde{M}_z = C_0 + C_u u + C_v v + C_r r + C_{v|v|} v|v| + C_{\dot{u}} \dot{u} + C_{\dot{v}} \dot{v} + C_{\dot{r}} \dot{r}$$

Pure yaw:

$$\tilde{F}_x = A_0 + A_u u + A_v v + A_r r + A_{rr} r^2 + A_{\dot{u}} \dot{u} + A_{\dot{v}} \dot{v} + A_{\dot{r}} \dot{r}$$

$$\tilde{F}_y = B_0 + B_u u + B_v v + B_r r + B_{rrr} r^3 + B_{\dot{u}} \dot{u} + B_{\dot{v}} \dot{v} + B_{\dot{r}} \dot{r}$$

$$\tilde{M}_z = C_0 + C_u u + C_v v + C_r r + C_{rrr} r^3 + C_{\dot{u}} \dot{u} + C_{\dot{v}} \dot{v} + C_{\dot{r}} \dot{r}$$

Yaw and drift:

$$\tilde{F}_x = A_0 + A_u u + A_v v + A_r r + A_{uu} u^2 + A_{vv} v^2 + A_{rr} r^2 + A_{uv} uv + A_{\dot{u}} \dot{u} + A_{\dot{v}} \dot{v} + A_{\dot{r}} \dot{r}$$

$$\tilde{F}_y = B_0 + B_u u + B_v v + B_r r + B_{v|v|} v|v| + B_{uv} uv + B_{v|r|} v|r| + B_{r|v|} r|v| + B_{rrr} r^3 + B_{vrr} vr^2 + B_{rvv} rv^2 + B_{\dot{u}} \dot{u} + B_{\dot{v}} \dot{v} + B_{\dot{r}} \dot{r}$$

$$\tilde{M}_z = C_0 + C_u u + C_v v + C_r r + C_{v|v|} v|v| + C_{uv} uv + C_{v|r|} v|r| + C_{r|v|} r|v| + C_{rrr} r^3 + C_{vrr} vr^2 + C_{rvv} rv^2 + C_{\dot{u}} \dot{u} + C_{\dot{v}} \dot{v} + C_{\dot{r}} \dot{r}$$

Table 5-4 Bias limits of global variables.

Var. (x)	L (m)	T (m)	x_G (m)	y_G (m)	m (Kg)	I_z (Kg·m^2)	ρ (Kg/m^3)	U_C (m/s)
D_x	3.048	0.132	0.016	0.0	82.55 (83.35)	49.79 (44.48)	998.1	2.241
B_x	0.002	0.001	0.005	0.002	0.11 (0.08)	1.84 (1.89)	0.041	0.010
$\%D_x$	0.07	0.7	31.3	-	0.1 (0.1)	3.7 (4.2)	0.004	0.5

( ): values for fixed conditions.

Table 5-5 Bias limits of PMM motion parameters for dynamic tests (Fr = 0.280).

Var. (χ)	Unit	Test type	D_χ	$\langle B_\chi \rangle$ ($\%D_\chi$)	x	S_{mm} (mm)	N (rpm)	t (sec)	β (°)	$\psi_{\max}$ (°)
					D_x	250	15	0.01	30	30
					B_x	0.5	0.0006	0.001	0.22	0.22
					$\%D_x$	0.2	0.0	10.0	0.7	0.7
					Elemental bias B_x contributions $\frac{\langle \theta_x^2 B_x^2 \rangle}{\langle B_\chi^2 \rangle}$ (%)					
v_{PMM}	(m/s)	Pure sway	0.5359	0.1		**92.7**	0.8	6.6	-	-
		Pure yaw	0.5529	0.1		**92.2**	0.8	7.0	-	-
		Yaw & drift	0.5558	0.1		**92.2**	0.8	7.0	-	-
$\dot{v}_{PMM}$	(m/s^2)	Pure sway	0.4512	0.1		**92.6**	0.8	6.6	-	-
		Pure yaw	0.4646	0.1		**92.1**	0.9	7.0	-	-
		Yaw & drift	0.4671	0.1		**92.1**	0.9	7.0	-	-
ψ	(°)	Pure sway	0.1	222.1		-	0.0	0.0	**67.0**	**33.0**
		Pure yaw	20.4	1.3		-	0.0	0.1	**67.0**	**32.9**
		Yaw & drift	20.4	1.3		-	0.0	0.2	**66.9**	**32.9**
r_{PMM}	(rad/s)	Pure sway	0.0032	63.3		-	0.0	0.0	-	**100.0**
		Pure yaw	0.3005	0.7		-	0.0	0.2	-	**99.8**
		Yaw & drift	0.3007	0.7		-	0.1	0.6	-	**99.3**
$\dot{r}_{PMM}$	(rad/s^2)	Pure sway	0.0056	30.9		-	0.0	0.0	-	**100.0**
		Pure yaw	0.2545	0.7		-	0.0	0.2	-	**99.8**
		Yaw & drift	0.2526	0.7		-	0.1	0.6	-	**99.3**

Var. (X)	Unit	Test type	D_X	$\langle B_X \rangle$ ($\%D_X$)	Elemental bias B_x contributions $\frac{\langle \theta_I^2 B_X^2 \rangle}{\langle B_X^2 \rangle}$ (%)					
					U_C	v_{PMM}	$\dot{v}_{PMM}$	ψ	r_{PMM}	$\dot{r}_{PMM}$
u	(m/s)	Pure sway	1.5177†	0.7	**99.1**	0.0	-	0.9	-	-
		Pure yaw	1.5397†	0.7	**100.0**	0.0	-	0.0	-	-
		Yaw & drift	1.5151†	0.7	**98.4**	0.0	-	1.6	-	-
v	(m/s)	Pure sway	0.5382	1.3	0.0	0.7	-	**99.3**	-	-
		Pure yaw	0.0090	81.6	3.0	0.7	-	**96.4**	-	-
		Yaw & drift	0.2672†	2.8	8.2	0.6	-	**91.1**	-	-
r	(rad/s)	Pure sway	0.0032	63.3	-	-	-	-	**100.0**	-
		Pure yaw	0.3005	0.7	-	-	-	-	**100.0**	-
		Yaw & drift	0.3007	0.7	-	-	-	-	**100.0**	-
$\dot{u}$	(m/s^2)	Pure sway	0.0006	115.0	0.0	0.0	0.0	**83.5**	**16.5**	-
		Pure yaw	0.0423	0.3	**63.2**	**16.9**	**17.1**	2.6	0.2	-
		Yaw & drift	0.0418	1.4	**10.1**	0.6	2.5	0.1	**86.6**	-
$\dot{v}$	(m/s^2)	Pure sway	0.4539	0.1	0.0	0.0	**100.0**	0.0	0.0	-
		Pure yaw	0.0161	6.8	**80.8**	0.0	**18.9**	0.3	0.0	-
		Yaw & drift	0.0196	5.6	**77.4**	0.0	**18.1**	4.5	0.0	-
$\dot{r}$	(rad/s^2)	Pure sway	0.0056	30.9	-	-	-	-	-	**100.0**
		Pure yaw	0.2545	0.7	-	-	-	-	-	**100.0**
		Yaw & drift	0.2526	0.7	-	-	-	-	-	**100.0**

† period mean values; - not applicable.

Table 5-6 Bias limits of measured forces and moment (B_F).

Test	F	Unit	Fr	D_F	$\langle B_F \rangle$ ($\%D_F$)	Elemental bias $B_{F,x}$ contribution $\frac{\langle B_{F,x}^2 \rangle}{\langle B_F^2 \rangle}$ (%)										
						β	align	ref	fit	u	v	r	$\dot{u}$	$\dot{v}$	$\dot{r}$	t
Static drift	F_x	(N)	0.138	2.4	0.5	**47.4**	0.9	0.7	**51.0**	-	-	-	-	-	-	-
			0.280	10.9	1.1	**91.8**	1.7	0.0	6.5	-	-	-	-	-	-	-
			0.410	32.5	0.8	**88.0**	1.6	0.0	**10.4**	-	-	-	-	-	-	-
	F_y	(N)	0.138	6.1	2.8	**97.9**	1.8	0.0	0.3	-	-	-	-	-	-	-
			0.280	28.5	2.9	**97.0**	1.8	0.0	1.2	-	-	-	-	-	-	-
			0.410	69.3	3.5	**97.2**	1.8	0.0	1.0	-	-	-	-	-	-	-
	M_z	(Nm)	0.138	8.7	2.6	**95.2**	1.7	1.5	1.5	-	-	-	-	-	-	-
			0.280	44.1	2.5	**96.8**	1.8	0.1	1.4	-	-	-	-	-	-	-
			0.410	108.5	3.1	**97.3**	1.8	0.0	0.9	-	-	-	-	-	-	-
Pure sway	F_x	(N)	0.280	11.50	0.7	-	-	0.0	**12.9**	0.5	**86.4**	0.0	0.0	0.1	0.0	0.0
	F_y	(N)		86.08	1.0	-	-	0.0	1.3	0.0	**97.8**	0.0	0.0	0.8	0.0	0.1
	M_z	(Nm)		94.46	1.4	-	-	0.0	0.5	0.0	**99.4**	0.0	0.0	0.0	0.0	0.0
Pure yaw	F_x	(N)	0.138	2.13	0.8	-	-	0.3	**23.0**	0.0	**32.5**	12.8	5.9	**25.3**	0.2	0.0
			0.280	9.00	0.6	-	-	0.0	**19.1**	0.0	0.0	**11.8**	1.8	**67.0**	0.1	0.1
			0.410	27.49	0.4	-	-	0.0	**53.7**	0.0	3.7	**27.0**	5.0	9.8	0.0	0.7
	F_y	(N)	0.138	11.19	0.8	-	-	0.0	0.4	0.0	0.0	**96.2**	0.0	0.1	3.2	0.0
			0.280	54.36	0.7	-	-	0.0	2.0	0.0	0.1	**96.4**	0.0	1.1	0.3	0.1
			0.410	118.49	0.8	-	-	0.0	1.7	0.0	0.1	**95.9**	0.0	0.6	1.4	0.3
	M_z	(Nm)	0.138	10.25	0.9	-	-	8.7	1.8	0.0	0.0	**53.2**	0.0	0.0	**36.2**	0.0
			0.280	47.67	0.8	-	-	0.6	2.0	0.0	0.0	**72.7**	0.0	0.7	**24.0**	0.1
			0.410	131.07	0.9	-	-	0.1	1.3	0.0	0.1	**74.7**	0.0	0.1	**23.4**	0.3
Yaw & drift	F_x	(N)	0.280	10.23	1.5	-	-	0.0	4.0	**55.5**	1.3	**29.2**	8.5	1.2	0.2	0.1
	F_y	(N)		67.48	1.2	-	-	0.0	3.0	0.0	**54.8**	**38.6**	0.0	3.2	0.3	0.1
	M_z	(Nm)		66.37	1.4	-	-	0.1	2.8	3.1	**62.1**	**24.7**	0.0	3.5	3.8	0.0

- not applicable.

Table 5-7 Total bias limits of non-dimensional forces and moment (B_r).

Test	r	Fr	Elemental bias B_x contributions $\frac{\langle\theta_x^2 B_x^2\rangle}{\langle B_r^2\rangle}$ (%)													
			L	T	x_G	y_G	m	I_z	ρ	$u^\dagger$	v	r	$\dot{u}$	$\dot{v}$	$\dot{r}$	F
Static drift	X	0.138	0.1	7.0	-	-	-	-	0.0	**89.7**	-	-	-	-	-	3.3
		0.280	0.1	**15.8**	-	-	-	-	0.0	**49.4**	-	-	-	-	-	**34.7**
		0.410	0.2	**26.9**	-	-	-	-	0.0	**39.7**	-	-	-	-	-	**33.2**
	Y	0.138	0.0	3.7	-	-	-	-	0.0	**46.7**	-	-	-	-	-	**49.6**
		0.280	0.0	5.3	-	-	-	-	0.0	**16.6**	-	-	-	-	-	**78.0**
		0.410	0.0	4.2	-	-	-	-	0.0	6.2	-	-	-	-	-	**89.5**
	N	0.138	0.1	2.7	-	-	-	-	0.0	**34.0**	-	-	-	-	-	**63.3**
		0.280	0.1	3.2	-	-	-	-	0.0	**10.1**	-	-	-	-	-	**86.6**
		0.410	0.1	2.4	-	-	-	-	0.0	3.5	-	-	-	-	-	**94.1**
Pure sway	X	0.280	0.0	5.1	0.0	0.0	0.0	-	0.0	**86.1**	0.1	0.4	2.6	-	0.0	5.6
	Y		0.0	2.9	0.0	0.0	0.0	-	0.0	8.8	0.6	8.4	-	0.2	0.0	**79.0**
	N		0.1	2.7	0.2	0.0	0.0	0.0	0.0	8.4	0.1	0.0	0.0	0.0	0.4	**88.0**
Pure yaw	X	0.138	0.1	**14.0**	0.1	1.1	0.0	-	0.0	**57.3**	**11.2**	0.0	0.7	-	0.0	**15.5**
		0.280	0.0	5.1	0.0	0.3	0.0	-	0.0	**86.6**	3.8	0.0	0.1	-	0.0	4.1
		0.410	0.0	2.7	0.0	0.1	0.0	-	0.0	**95.5**	1.0	0.0	0.0	-	0.0	0.6
	Y	0.138	0.0	0.2	0.5	0.0	0.1	-	0.0	**18.1**	0.0	**28.8**	-	9.2	0.0	**43.0**
		0.280	0.0	0.6	0.5	0.0	0.1	-	0.0	8.7	0.0	**28.5**	-	3.3	0.0	**58.2**
		0.410	0.0	0.5	0.6	0.0	0.1	-	0.0	3.3	0.0	**29.9**	-	1.9	0.0	**63.7**
	N	0.138	0.1	2.7	1.6	0.0	0.0	**10.6**	0.0	**33.7**	0.0	0.0	0.0	0.0	4.8	**46.4**
		0.280	0.2	5.9	2.3	0.0	0.0	**11.2**	0.0	**17.7**	0.0	0.0	0.0	0.0	3.8	**58.8**
		0.410	0.2	5.1	1.2	0.0	0.0	9.1	0.0	7.3	0.0	0.0	0.0	0.0	4.5	**72.7**
Yaw & drift	X	0.280	0.0	4.4	0.0	0.2	0.0	-	0.0	**70.9**	2.6	1.8	2.1	-	0.0	**17.8**
	Y		0.0	6.6	0.1	0.0	0.0	-	0.0	**21.7**	1.8	7.6	-	0.9	0.0	**61.2**
	N		0.3	**10.3**	0.3	0.0	0.0	1.7	0.0	**29.4**	0.5	0.0	0.0	0.0	0.6	**56.9**

† U_C for static drift test; - not applicable.

Table 5-8 Identifications of primary bias sources and propagations.

Test	Bias	Test type[1)]	Primary biases and propagations	Bias source
Static	B_X, B_Y, B_N	SD	B_{U_C} $B_F \leftarrow B_{F,\beta} \leftarrow B_\beta$	U_C, β
Dyanmic	B_X	PS,PY,YD	$B_u \leftarrow B_{U_C}$	U_C
	B_Y, B_N	PS	$B_F \leftarrow B_{F,v} \leftarrow B_v \leftarrow B_\psi \leftarrow B_\beta$, $B_{\psi_{max}}$	β, ψ_{max}
		PY	$B_F \leftarrow B_{F,r} \leftarrow B_r \leftarrow B_{r_{PMM}} \leftarrow B_{\psi_{max}}$	
		YD	$B_F \leftarrow B_{F,v}/B_{F,r} \leftarrow B_v/B_r \leftarrow B_\psi/B_{r_{PMM}} \leftarrow B_\beta$,$B_{\psi_{max}}$	

1) SD = static drift; PS = pure sway; PY = pure yaw; YD = yaw and drift.

Table 5-9 Summary of UA results.

Test	R	Fr	D_r	$\langle B_r \rangle$	$\frac{\langle B_r^2 \rangle}{\langle U_r^2 \rangle}$	$\langle P_r \rangle$	$\frac{\langle P_r^2 \rangle}{\langle U_r^2 \rangle}$	$\langle U_r \rangle$
		[-]	[-]	($\%D_r$)	(%)	($\%D_r$)	(%)	($\%D_r$)
Static drift	X	0.138	0.021	2.9	**95.9**	0.6	4.1	2.9
		0.280	0.023	2.0	**96.6**	0.3	3.4	1.9
		0.410	0.033	1.5	**69.3**	1.0	30.7	1.8
	Y	0.138	0.054	3.9	**82.7**	1.8	17.3	4.4
		0.280	0.061	3.3	**95.1**	0.8	4.9	3.4
		0.410	0.070	3.7	**99.6**	0.2	0.4	3.7
	N	0.138	0.025	3.3	**80.2**	1.6	19.8	3.6
		0.280	0.031	2.7	**94.5**	0.6	5.5	2.8
		0.410	0.036	3.2	**99.6**	0.2	0.4	3.2
	z (10^{-2})	0.138	0.054	6.1	**76.9**	3.3	23.1	6.9
		0.280	0.296	1.1	**66.6**	0.8	33.4	1.4
		0.410	0.726	0.5	15.8	1.1	**84.2**	1.1
	θ (°)	0.138	0.020	197.6	**99.9**	7.3	0.1	197.7
		0.280	-0.152	26.4	**99.9**	0.9	0.1	26.4
		0.410	0.217	18.4	**88.9**	6.5	11.1	19.6
Pure sway	X	0.280	0.024	3.4	24.8	5.8	**75.2**	4.7
	Y		0.133	1.6	**63.0**	1.2	37.0	2.0
	N		0.065	1.5	**93.6**	0.4	6.4	1.6
	z (10^{-3})		1.928	1.7	11.3	4.7	**88.7**	5.0
	θ (°)		0.163	24.5	**77.0**	13.3	23.0	27.9
Pure yaw	X	0.138	0.018	2.0	3.7	10.3	**96.3**	10.5
		0.280	0.019	3.4	19.0	6.8	**81.0**	7.6
		0.410	0.027	4.6	**66.5**	3.2	33.5	5.7
	Y	0.138	0.026	4.7	36.2	6.7	**63.8**	8.3
		0.280	0.034	3.0	**74.4**	1.9	25.6	3.7
		0.410	0.039	3.3	**89.2**	1.2	10.8	3.6
	Y	0.138	0.025	1.6	**91.3**	0.5	8.7	1.7
		0.280	0.031	1.1	**81.1**	0.5	18.9	1.2
		0.410	0.040	1.2	**93.3**	0.3	6.7	1.2
	z (10^{-3})	0.138	0.294	11.2	**51.0**	10.8	49.0	15.6
		0.280	1.540	2.1	11.5	5.9	**88.5**	6.2
		0.410	4.944	0.7	15.6	1.5	**84.4**	1.7
	θ (°)	0.138	0.094	74.8	**99.3**	4.1	0.7	42.9
		0.280	0.127	31.5	**77.8**	16.8	22.2	35.7
		0.410	0.444	9.0	**86.8**	3.5	13.2	9.7
Yaw & drift	X	0.280	0.022	3.6	28.8	5.6	**71.2**	6.7
	Y		0.065	3.3	**80.1**	1.7	19.9	3.7
	N		0.045	1.9	**91.8**	0.6	8.2	2.0
	z (10^{-3})		3.224	1.0	11.7	2.8	**88.3**	3.0
	θ (°)		0.302	13.2	**75.8**	7.4	24.2	15.2

Table 5-10 Evaluation of asymmetry bias B_{asym} .

Test	r	Fr	D_{rm}	$\langle D_{asym} \rangle$ (%)	$\langle U_{\mathrm{r}} \rangle$ (%)	$\langle B_{asym} \rangle$ (%)	$\langle U_{T_1} \rangle$ (%)
Static drift	X	0.138	0.0196	7.7	3.1	7.0	7.7
		0.280	0.0214	10.5	2.1	10.3	10.5
		0.410	0.0302	7.5	1.9	7.2	7.5
	Y	0.138	0.0524	2.0	4.5	0.0	4.5
		0.280	0.0619	0.4	3.3	0.0	3.3
		0.410	0.0715	1.8	3.6	0.0	3.6
	N	0.138	0.0250	0.0	3.7	0.0	3.7
		0.280	0.0313	0.6	2.8	0.0	2.8
		0.410	0.0365	0.8	3.1	0.0	3.1
	z (10^{-2})	0.138	0.046	18.3	8.1	16.4	18.3
		0.280	0.288	2.9	1.4	2.5	2.9
		0.410	0.714	1.7	1.2	1.2	1.7
	θ (°)	0.138	-0.050	140.2	79.5	115.5	140.2
		0.280	-0.212	28.5	18.9	21.4	28.5
		0.410	0.131	65.7	32.4	57.2	65.7
Pure sway	X	0.280	0.0245	9.0	6.7	6.1	10.0
	Y		0.1327	5.4	2.0	5.0	5.4
	N		0.0653	1.3	1.6	0.1	1.6
	z (10^{-3})		1.9284	13.2	5.0	11.9	13.5
	θ (°)		0.1631	4.1	27.9	0.0	27.9
Pure yaw	X	0.138	0.0185	10.3	10.5	5.7	12.9
		0.280	0.0189	9.5	7.6	5.9	10.4
		0.410	0.0274	6.6	5.7	4.2	7.7
	Y	0.138	0.0241	7.2	9.0	3.1	10.3
		0.280	0.0344	3.2	3.7	1.7	4.7
		0.410	0.0385	4.2	3.6	2.1	4.7
	N	0.138	0.0250	1.2	1.7	0.0	1.7
		0.280	0.0308	1.6	1.2	1.0	1.6
		0.410	0.0397	1.4	1.2	0.5	1.4
	z (10^{-3})	0.138	0.2820	74.0	16.3	71.1	74.8
		0.280	1.5398	18.2	6.2	16.7	18.5
		0.410	4.9434	3.4	1.7	2.9	3.6
	θ (°)	0.138	0.0433	95.1	92.5	52.0	115.5
		0.280	0.1270	33.4	35.7	17.1	42.9
		0.410	0.4442	9.0	9.7	3.7	11.1

Table 5-11 Comparisons of UA between facilities.

Test	r	Fr	IIHR $\lvert r\rvert$	IIHR B_r (%)	IIHR P_r (%)	IIHR U_r (%)	FORCE $\lvert r\rvert$	FORCE B_r (%)	FORCE P_r (%)	FORCE U_r (%)	INSEAN $\lvert r\rvert$	INSEAN B_r (%)	INSEAN P_r (%)	INSEAN U_r (%)
Static drift[1)]	X	0.138	0.0210	**95.9**	4.1	2.9	0.0174	**97.2**	2.8	11.3	0.0169	**92.8**	7.2	3.9
		0.280	0.0234	**96.6**	3.4	1.9	0.0195	**77.8**	22.2	3.4	0.0189	**94.1**	5.9	1.4
		0.410	0.0330	**69.3**	30.7	1.8	0.0278	**89.6**	10.4	1.6	0.0285	**91.2**	8.8	0.7
	Y	0.138	0.0538	**82.7**	17.3	4.4	0.0542	**79.0**	21.0	3.5	0.0552	**99.1**	0.9	3.1
		0.280	0.0611	**95.1**	4.9	3.4	0.0617	**74.2**	25.8	2.1	0.0626	**99.1**	0.9	3.3
		0.410	0.0703	**99.6**	0.4	3.7	0.0729	**69.6**	30.4	1.8	0.0717	**99.5**	0.5	3.9
	N	0.138	0.0251	**80.2**	19.8	3.6	0.0260	**69.2**	30.8	2.2	0.0261	**99.7**	0.3	3.4
		0.280	0.0310	**94.5**	5.5	2.8	0.0306	21.0	**79.0**	2.4	0.0309	**98.9**	1.1	3.1
		0.410	0.0361	**99.6**	0.4	3.2	0.0367	43.4	**56.6**	1.4	0.0363	**99.4**	0.6	2.8
Pure sway[2)]	X	0.280	0.0292	35.2	**64.8**	5.8	0.0207	**98.1**	1.9	3.1	0.0197	46.6	**53.4**	1.3
	Y		0.0548	**73.3**	26.7	5.5	0.0565	**98.3**	1.7	1.8	0.0637	**66.0**	34.0	2.1
	N		0.0316	**98.0**	2.0	4.2	0.0306	**92.6**	7.4	1.5	0.0334	**73.0**	27.0	1.8
Pure yaw[3)]	X	0.138	0.0224	4.0	**96.0**	9.9	0.0177	**97.6**	2.4	11.3	0.0156	**77.0**	23.0	4.2
		0.280	0.0215	20.8	**79.2**	7.4	0.0187	**98.8**	1.2	3.4	0.0168	**52.7**	47.3	1.7
		0.410	0.0303	**68.1**	31.9	5.6	0.0264	**98.0**	2.0	2.9	0.0249	**70.5**	29.5	0.9
	Y	0.138	0.0072	48.9	**51.1**	36.5	0.0114	**90.3**	9.7	15.8	0.0090	**70.1**	29.9	10.3
		0.280	0.0161	**88.0**	12.0	10.8	0.0178	**93.4**	6.6	5.5	0.0178	**85.5**	14.5	4.6
		0.410	0.0168	**90.1**	9.9	12.2	0.0176	**90.6**	9.4	3.5	0.0178	**86.2**	13.8	6.2
	N	0.138	0.0114	**94.7**	5.3	4.0	0.0114	**98.8**	1.2	7.3	0.0119	34.1	**65.9**	2.6
		0.280	0.0146	**90.0**	10.0	2.9	0.0140	**93.9**	6.1	3.3	0.0160	**59.6**	40.4	1.4
		0.410	0.0188	**94.1**	5.9	3.0	0.0186	**87.7**	12.3	1.4	0.0210	**61.4**	38.6	1.8
Yaw & drift[3)]	X	0.280	0.0265	29.8	**70.2**	6.7	0.0234	**99.2**	0.8	5.8	0.0255	**67.6**	32.4	1.3
	Y		0.0470	**79.6**	20.4	4.7	0.0458	**89.0**	11.0	2.1	0.0469	**74.0**	26.0	3.5
	N		0.0135	**92.8**	7.2	4.9	0.0135	**98.0**	2.0	2.7	0.0134	**64.0**	36.0	4.4

[1)] at β = -10° for IIHR and 10° for FORCE and INSEAN; [2)] at $v'(t) = v_0'$; [3)] at $r'(t) = r_0'$.

Table 5-12 Evaluation of asymmetry bias B_{asym} (FORCE and INSEAN data).

	r	Fr	FORCE D_{r_m}	FORCE $\langle U_r \rangle$ (%)	FORCE $\langle B_{asym} \rangle$ (%)	FORCE $\langle U_{T_1} \rangle$ (%)	INSEAN D_{r_m}	INSEAN $\langle U_r \rangle$ (%)	INSEAN $\langle B_{asym} \rangle$ (%)	INSEAN $\langle U_{T_1} \rangle$ (%)
Static drift	X	0.138	0.0185	10.6	0.0	10.6	0.0159	4.2	4.7	6.3
		0.280	0.0199	3.3	0.0	3.3	0.0174	1.5	11.4	11.5
		0.410	0.0285	1.5	1.9	2.5	0.0253	0.8	11.8	11.9
	Y	0.138	0.0539	3.5	0.0	3.5	0.0580	2.9	0.0	2.9
		0.280	0.0607	2.1	0.0	2.1	0.0620	3.3	0.0	3.3
		0.410	0.0718	1.9	0.0	1.9	0.0800	3.5	0.0	3.5
	N	0.138	0.0256	2.3	0.0	2.3	0.0228	2.9	0.0	2.9
		0.280	0.0297	2.5	1.7	3.0	0.0290	3.3	0.0	3.3
		0.410	0.0358	1.5	2.0	2.5	0.0390	2.6	0.0	2.6
Pure sway	X	0.280	0.0201	3.2	0.0	3.2	0.0184	1.2	11.1	11.3
	Y		0.1283	0.8	0.1	0.8	0.1392	0.9	0.0	0.9
	N		0.0615	0.8	0.4	0.9	0.0670	0.8	0.0	0.8
Pure yaw	X	0.138	0.0176	11.2	0.0	11.2	0.0153	3.9	6.0	7.8
		0.280	0.0188	3.4	0.1	3.4	0.0169	1.2	5.4	5.7
		0.410	0.0259	2.9	0.0	2.9	0.0246	0.8	6.4	6.5
	Y	0.138	0.0310	6.0	0.0	6.0	0.0226	4.3	3.8	6.2
		0.280	0.0368	2.7	0.0	2.7	0.0356	1.9	0.7	2.2
		0.410	0.0420	1.4	0.4	1.6	0.0434	2.0	0.4	2.1
	N	0.138	0.0242	3.1	1.5	3.8	0.0251	1.2	0.0	1.2
		0.280	0.0296	1.5	0.5	1.5	0.0329	0.7	0.0	0.7
		0.410	0.0394	0.5	1.4	1.5	0.0434	0.8	0.0	0.8

Table 5-13 Evaluation of facility bias B_{FB}.

Test	X	Fr	$\overline{X}$	$U_{\overline{X}}$ (%)	U_X (%)	$\lvert D \rvert$ (%)	U_D (%)	B_{FB} (%)	U_{T_2} (%)
Static drift	X	0.138	0.0180	4.9	8.4	8.9	9.7	0.0	8.4
		0.280	0.0196	5.2	11.5	9.4	12.6	0.0	10.9
		0.410	0.2800	4.5	8.0	7.9	9.2	0.0	8.0
	Y	0.138	0.0548	2.1	4.3	4.3	4.8	0.0	4.3
		0.280	0.0615	1.7	3.3	0.6	3.7	0.0	3.3
		0.410	0.0744	1.8	3.5	3.9	3.9	0.5	3.5
	N	0.138	0.0245	1.7	3.7	2.2	4.2	0.0	3.8
		0.280	0.0300	1.7	2.8	4.3	3.4	2.7	4.0
		0.410	0.0374	1.6	3.1	2.4	3.4	0.0	3.0
Pure sway	X	0.280	0.0225	5.4	7.6	20.6	9.3	18.3	19.8
	Y		0.0604	3.5	10.2	1.0	10.8	0.0	10.2
	N		0.0322	1.6	4.2	1.3	4.5	0.0	4.2
Pure yaw	X	0.138	0.0175	7.5	17.8	10.0	19.3	0.0	17.8
		0.280	0.0181	5.7	15.4	3.3	16.4	0.0	15.4
		0.410	0.0263	4.3	10.3	4.9	11.2	0.0	10.3
	Y	0.138	0.0096	13.0	27.2	13.0	30.2	0.0	27.3
		0.280	0.0175	4.2	9.9	3.0	10.7	0.0	9.9
		0.410	0.0180	4.5	11.3	2.8	12.2	0.0	3.2
	N	0.138	0.0117	3.5	3.9	0.9	5.3	0.0	3.9
		0.280	0.0150	1.7	3.3	0.4	3.7	0.0	3.3
		0.410	0.0196	1.3	2.8	2.0	3.1	0.0	2.8
Yaw & drift	X	0.280	0.0251	3.0	7.1	5.4	7.7	0.0	7.1
	Y		0.0465	2.1	4.7	0.7	5.2	0.0	4.7
	N		0.0135	2.4	4.9	0.0	5.5	0.0	5.0

Table 5-14 Evaluation of facility bias B_{FB} (FORCE and INSEAN data).

			FORCE					INSEAN				
Test	r	Fr	U_X (%)	$\|D\|$ (%)	U_D (%)	B_{FB} (%)	U_{T_2} (%)	U_X (%)	$\|D\|$ (%)	U_D (%)	B_{FB} (%)	U_{T_2} (%)
Static drift	X	0.138	10.9	2.8	12.0	0.0	10.9	5.6	11.7	7.4	9.0	10.6
		0.280	3.4	1.7	6.2	0.0	3.4	10.2	11.1	11.5	0.0	10.2
		0.410	2.5	1.8	5.2	0.0	2.5	10.8	9.6	11.7	0.0	10.8
	Y	0.138	3.4	1.6	4.0	0.0	3.4	3.1	5.9	3.7	4.6	5.5
		0.280	2.1	1.4	2.7	0.0	2.1	3.4	0.8	3.8	0.0	3.4
		0.410	1.8	3.5	2.6	2.4	3.0	3.8	7.5	4.2	6.2	7.3
	N	0.138	2.4	4.6	3.0	3.6	4.3	2.7	6.8	3.2	6.0	6.6
		0.280	3.0	1.0	3.4	0.0	3.0	3.2	3.3	3.6	0.0	3.2
		0.410	2.4	1.9	2.8	0.0	2.4	2.7	4.3	3.1	2.9	4.0
Pure sway	X	0.280	2.9	8.0	6.1	5.2	5.9	14.1	12.5	15.1	0.0	14.1
	Y		1.7	6.4	3.9	5.1	5.4	2.2	5.5	4.2	3.5	4.2
	N		1.5	5.1	2.2	4.6	4.8	1.9	3.8	2.5	2.9	3.4
Pure yaw	X	0.138	11.4	1.0	13.6	0.0	11.4	7.5	10.9	10.6	2.8	8.0
		0.280	3.5	3.4	6.7	0.0	3.5	6.4	6.7	8.6	0.0	6.4
		0.410	2.9	0.5	5.2	0.0	2.9	7.4	5.4	8.6	0.0	7.4
	Y	0.138	19.1	18.8	23.1	0.0	19.1	20.0	5.9	23.9	0.0	20.0
		0.280	5.6	1.4	7.0	0.0	5.6	5.4	1.6	6.8	0.0	5.4
		0.410	3.2	1.9	5.5	0.0	3.2	6.6	0.9	8.0	0.0	6.6
	N	0.138	9.5	2.6	10.1	0.0	9.5	2.6	1.7	4.4	0.0	2.6
		0.280	3.5	6.7	3.9	5.5	6.5	1.5	6.3	2.3	5.9	6.1
		0.410	1.9	5.3	2.3	4.7	5.1	1.9	7.3	2.3	6.9	7.2
Yaw & drift	X	0.280	5.3	6.8	6.1	3.1	6.2	1.2	1.4	3.2	0.0	1.2
	Y		2.1	1.6	2.9	0.0	2.1	3.5	0.8	4.1	0.0	3.5
	N		2.6	0.4	3.5	0.0	2.6	4.5	0.4	5.1	0.0	4.5

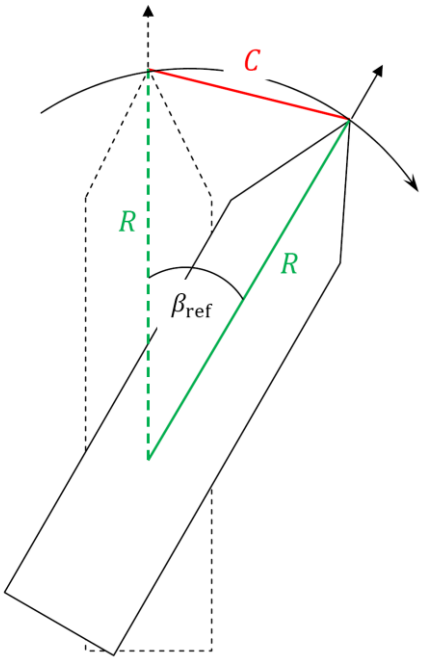

Figure 5-1 Definition of β_{ref} for drift angle calibration.

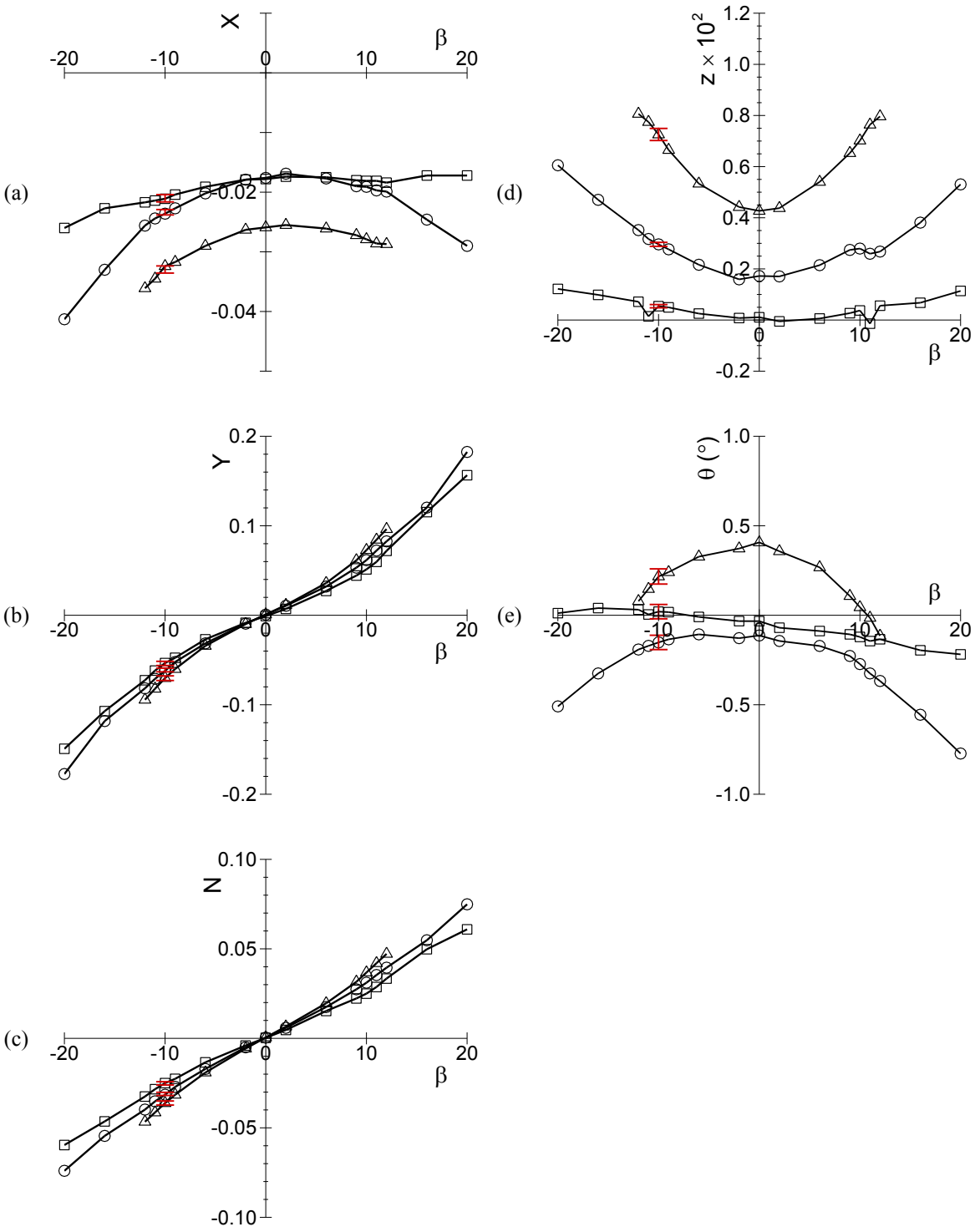

Figure 5-2 Static drift test results: (a) X; (b) Y; (c) N, (d) z, (e) θ, respectively. Symbols: □ Fr = 0.138 o Fr = 0.280, Δ Fr = 0.410.

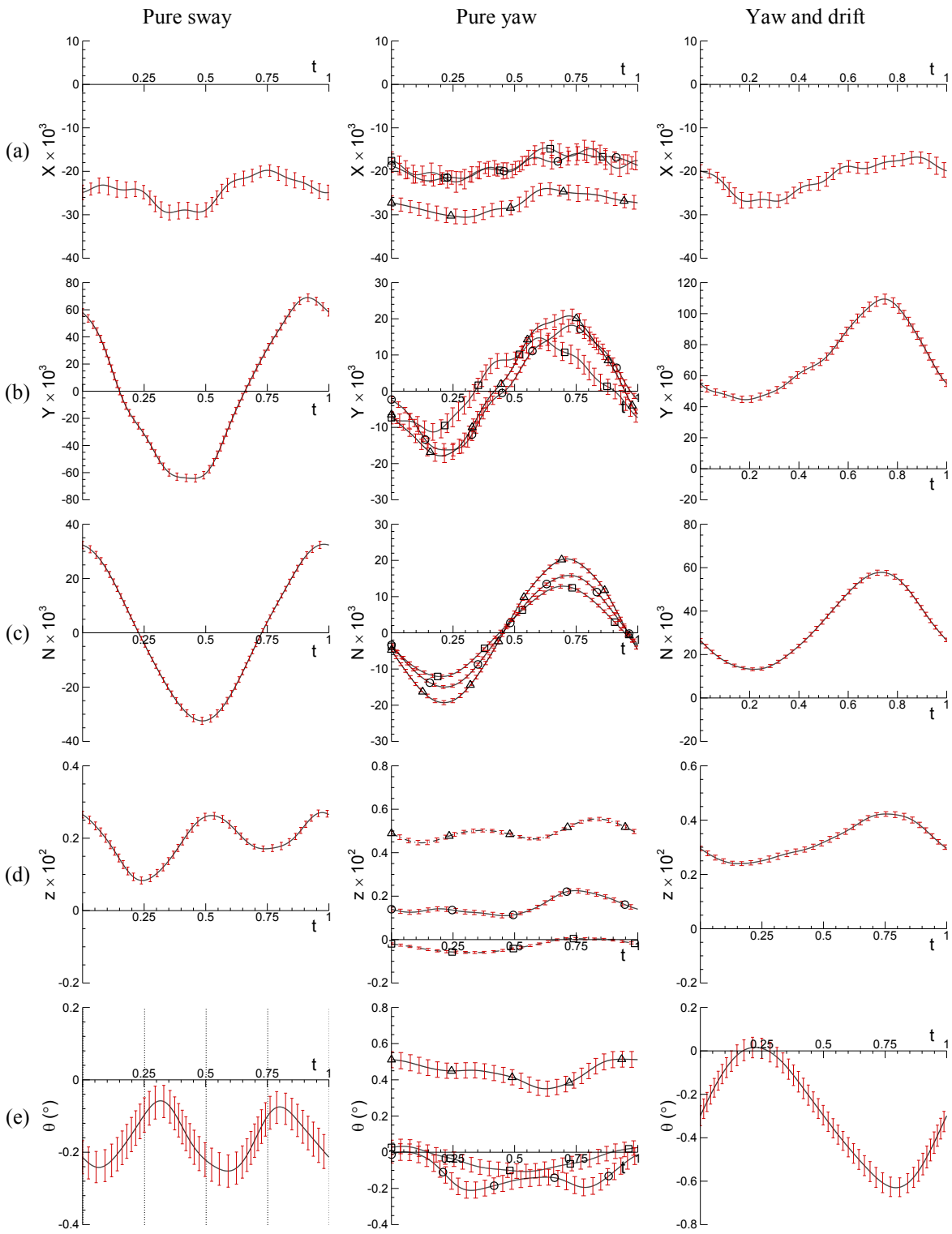

Figure 5-3 Dynamic test results: (a) X, (b) Y, (c) N, (d) z, and (e) θ for pure sway (left, β_{max} = 10°), pure yaw (center, r_{max} = 0.30), and yaw and drift (right, β = 10°) tests, respectively. Symbols for pure yaw data: □ Fr = 0.138 o Fr = 0.280, Δ Fr = 0.410.

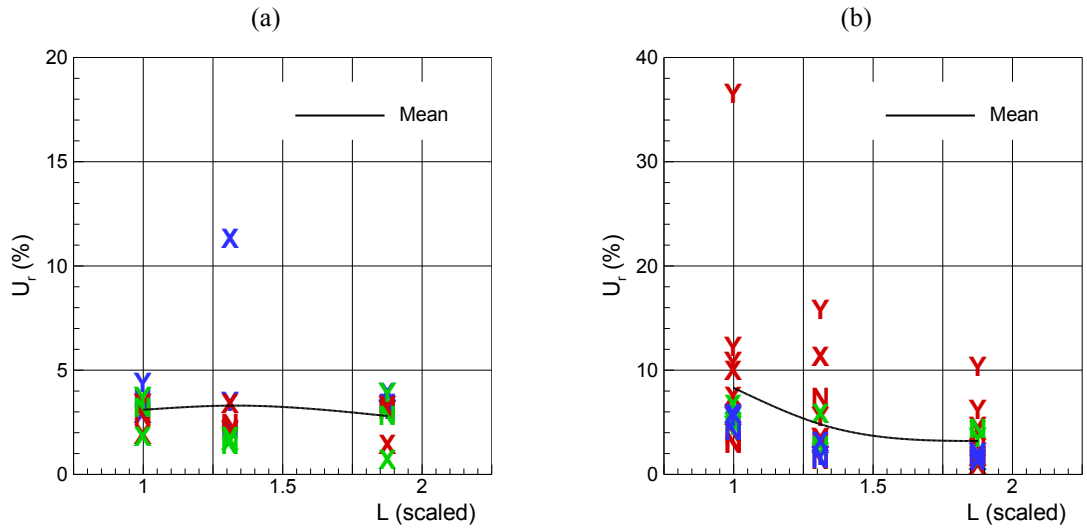

Figure 5-4 Comparisons of UA between facilities (Scale effect): (a) Static drift data (X,Y,N: Fr = 0.138; X,Y,N: Fr = 0.280; X,Y,N: Fr = 0.410) and (b) Dynamic tests data (X,Y,N: Pure sway; X,Y,N: Pure yaw; X,Y,N: Yaw and drift).

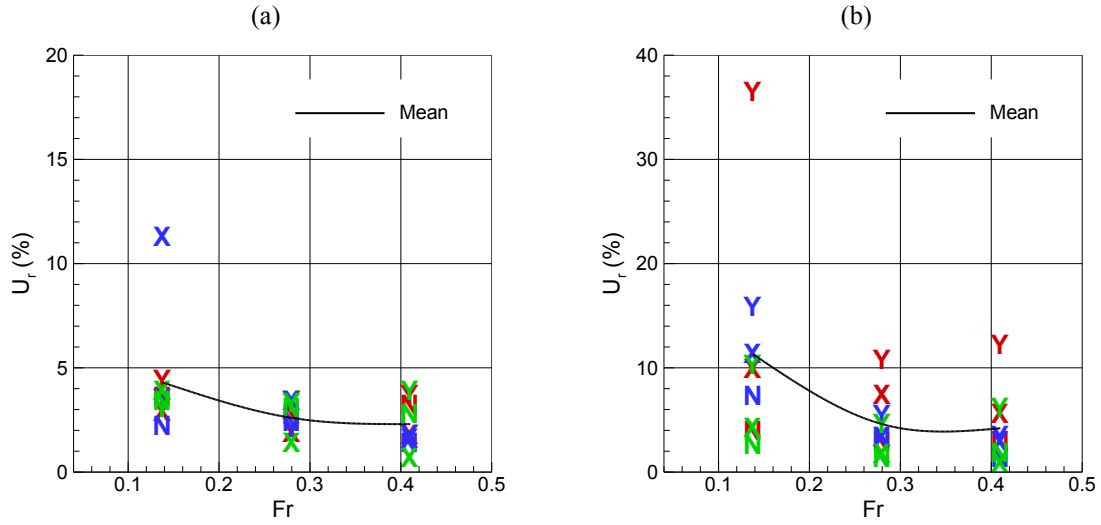

Figure 5-5 Comparisons of UA between facilities (Fr effect): (a) Static drift data and (b) Dynamic tests data. Symbols: X,Y,N, IIHR; X,Y,N, FORCE; X,Y,N, IN-SEAN.

5.2 UA for Phase-Averaged Flow Field

The uncertainty analysis (UA) of phase-averaged Stereo PIV measurement results follows the ASME PTC 19.1-2005 Standard (ASME 2005). The ASME (2005) is a revision of the ASME PTC 19.1-1998 Standard (ASME 1998) that is equivalent to the AIAA (1999) standard. The approach of ASME (1998)/AIAA (1999) is error/uncertainty definitions, systematic/random categorizations, and large sample size/normal distribution 95% level confidence interval assumptions. The details of the ASME (1998)/AIAA (1999) are derived and explained in Coleman and Steele (1995).

The main revision of the ASME (2005) from its previous version, ASME 1998, is focused on the harmonization with the ISO Guide (1995) that utilizes conceptually different error/uncertainty classifications (Type A and Type B) from the ASME (1998)/AIAA (1999). For this, the ASME 2005 adapts nomenclatures more consistent with the ISO Guide (1995): 1) the terms 'bias' and 'precision' are not used therein, however, uncertainties remain conceptualized as 'systematic' and 'random', respectively, and 2) the term 'standard' uncertainty is introduced and the terms such as 'combined standard' uncertainty and 'expanded' uncertainty are used instead of the term 'total' uncertainty.

5.2.1 UA Methodology (ASME 2005)

Measurement error, the difference between the measured value X and the true value, consists of two components: *random error* (ϵ) that varies randomly in repeated measurements and *systematic error* (β) that remains constant throughout the test. Measurement uncertainty is the combination of *random uncertainty* (s) due to the random error and *systematic uncertainty* (b) due to the systematic error.

Random error causes scatters in successive measurements of X from which sample mean $\bar{X}$ and sample standard deviation s_X are calculated. The random standard uncertainty of the sample mean, $s_{\bar{X}}$, then, can be used to define the probable interval containing

the population (true) mean of the measurement with a defined level of confidence, which is given as

$$s_{\bar{X}} = s_X/\sqrt{N} \tag{5.38}$$

where N is the number of repeat measurements. For a normal distribution and a large sample size ($N > 30$), for example, the interval $\bar{X} \pm 2s_{\bar{X}}$ is expected to contain the true mean with 95% confidence.

The measurement is influenced by several different elemental systematic error sources, each of which may be postulated to come from a population of possible error values. Systematic standard uncertainty of the measurement is a combination of the elemental systematic errors from all the error sources such that

$$b_{\bar{X}} = \left[\sum_{k=1}^{K}\left(b_{\bar{X}_k}\right)^2\right]^{\frac{1}{2}} \tag{5.39}$$

where the elemental systematic standard uncertainty $b_{\bar{X}_k}$ represents the dispersion of possible elemental systematic error values $\beta_{\bar{X}_k}$ at the standard deviation level.

The elemental systematic standard uncertainties are usually evaluated from a) engineering judgment, b) published information, or c) special data. *Engineering judgment* is to use engineering analysis and experience to estimate an interval for elemental systematic error within which 95% of possible $\beta_{\bar{X}_k}$ values are expected. Typically $\beta_{\bar{X}_k}$ is assumed as normal distribution and spread symmetric (equally in both the positive and negative directions) with a large degree of freedom ($\nu \geq 30$). Subsequently the elemental systematic standard uncertainty is estimated as

$$b_{\bar{X}_k} = B_{\bar{X}_k}/2 \tag{5.40}$$

where $B_{\bar{X}_k}$ represents the 95% confidence level estimate of the symmetric limits of error associated with the k^{th} elemental error source. Next, the *published information* includes calibration reports, instrument specifications, and other technical references that may provide quantitative information regarding the elemental systematic errors, such as a confidence interval, an ISO expanded uncertainty statement, or a multiple of a standard deviation. In these cases, $b_{\bar{X}_k}$ is estimated by dividing those information values by the statistic value such as the Student's *t*, by the coverage factor (or the "k factor"), or by the multiplier, respectively. Lastly, the *special data* include inter-laboratory or inter-facility tests and comparisons of independent measurements that depend on different principles or that have been made by independently calibrated instruments (See Section 4-3.2.2.3 of ASME 2005).

For a calculated result R that is expressed as a function of measured (averaged) or assigned values of independent parameters (X_i) as

$$R = f(\bar{X}_1, \bar{X}_2, \ldots, \bar{X}_I) \tag{5.41}$$

the uncertainties of those parameters may propagate to the result through the functional relationship. The error propagations can be approximated by a Taylor series method (See Nonmandatory Appendix C of ASME 2005), typically up to the first order, and the sensitivity (or sensitivity coefficient) θ_i of the parameter $\bar{X}_i$ is defined as

$$\theta_i = \frac{\partial R}{\partial \bar{X}_i} \tag{5.42}$$

of which partial differentiation can be evaluated either analytically or numerically. Then, the systematic standard uncertainty of R is determined from the propagation equation as

$$b_R = \left[\sum_{i=1}^{I} \left(\theta_i b_{\bar{X}_i}\right)^2\right]^{\frac{1}{2}} \tag{5.43}$$

When more than one test is conducted with the same instrument package (i.e., repeated tests), the estimate of the standard deviation of the distribution of the results is

$$s_R = \left(\frac{\sum_{m=1}^{M}(R_m - \bar{R})^2}{M-1}\right)^{\frac{1}{2}} \tag{5.44}$$

where M is the number of tests, and the random standard uncertainty of the mean result $\bar{R}$ is

$$s_{\bar{R}} = s_R/\sqrt{M} \tag{5.45}$$

The root-sum-square of the systematic and random standard uncertainties is calculated to determine the 'combined' standard uncertainty of R as

$$u_R = [(b_R)^2 + (s_R)^2]^{\frac{1}{2}} \tag{5.46}$$

Finally, the combined standard uncertainty is expanded to the 95% level of confidence, termed as the 'expanded' uncertainty, by multiplying appropriate expansion factor t_{95} as

$$U_{R,95} = t_{95} \cdot u_R \tag{5.47}$$

where the expansion factor (or 'coverage factor') t_{95} value, with the degree of freedom ν_R known, is obtained from the Student *t* statistic at the 95% confidence level, and $t_{95} = 2$ for large degrees of freedom ($\nu_R \geq 30$). When the degree of freedom for one of the systematic and random standard uncertainties or for both is not large ($\nu_R < 30$), an effective degree of freedom may be obtained by using the Welch-Satterthwaite formula (Nonmandatory Appendix B of ASME 2005).

$$\nu_R = \frac{\left\{\sum_{i=1}^{I}\left[(\theta_i b_i)^2 + (\theta_i s_i)^2\right]\right\}^2}{\sum_{i=1}^{I}\left[\frac{(\theta_i s_i)^4}{\nu_{s_i}} + \sum_{k=1}^{K_i}\frac{\left(\theta_i b_{i_k}\right)^4}{\nu_{b_{i_k}}}\right]} \tag{5.48}$$

where $\nu_{s_i} = N_i - 1$ is the degree of freedom of the random standard uncertainty s_i and $\nu_{b_{i_k}}$ is the degree of freedom of the kth elemental uncertainty of the systematic standard uncertainty b_i which can be approximated as

$$\nu_{b_{i_k}} = \frac{1}{2}\left(\frac{\Delta b_{i_k}}{b_{i_k}}\right)^{-2} \tag{5.49}$$

where the quantity in parentheses is an estimate of the relative variability of the estimate of b_{i_k} (See the ISO Guide 1995)

5.2.2 UA Procedures

The basic underlying idea of present UA procedures for the Stereo PIV (SPIV) measurement is to calibrate the SPIV measured data to the known reference values. An example can be a UA for a measurement of flow velocity V behind a model using a Pitot probe at a towing tank facility. The uncertainty in V may be estimated by using a data reduction equation such as $V = \sqrt{2\Delta p/\rho}$ from the Bernoulli's equation, along with considerations of the elemental uncertainties in the pressure difference Δp and water density ρ measurements. Alternatively, the Pitot measurement can be calibrated to a reference measurement data such as the towing carriage speed U_C data, with known uncertainty. If a calm and open (i.e. no model installed) water is measured with the Pitot probe towed at a certain carriage speed U_C, then, the difference between the V and U_C can be considered as the systematic (bias) uncertainty of the Pitot measurement, relative to the U_C measurement and uncertainty.

Similar UA approach is used herein for SPIV measurement. For this, undisturbed open water is measured with the SPIV that is undergoing a forced PMM motion. As no model is installed, SPIV measured data are the free stream flow data of which values can be determined as well from the PMM measured sway and yaw motion data by using the coordinate transformation relationship between the PMM- and PIV-fixed coordinate sys-

tems as shown in Section 3.1.2. Then, the PMM measured free stream data are used as the reference to be compared with the SPIV measurements estimating the systematic uncertainties.

The open water measurement includes two test cases: *Case 1) Uniform flow measurement* and *Case 2) Open water pure yaw test*. The former case is the simplest case where the calm and open water is measured as the PIV system is towed straight at a constant speed U_C with no PMM motions. For the latter case, the undisturbed open water is measured as the PIV system is undergoing a forced pure yaw PMM motions. Test conditions are summarized in Table 5-15 for both cases.

An overall schematic (flow chart) of the present UA procedure is shown in Fig. 5-6, where the procedures are grouped into three stages; designated as A, B, and C in the figure. A) The systematic standard uncertainties of the measurements are estimated and the sources of the possible elemental errors are identified. B) The PMM measured reference values are calculated and the phase-averaged PIV data from the open water tests are compared. The elemental measurement uncertainties from the previous stage are propagated through the data reduction process. C) The uncertainties in the test results such as the phase-averaged mean velocity, Reynolds stresses, turbulent kinetic energy, and the axial vorticity are estimated by combining the systematic and random standard uncertainties and then expanded to the 95% confidence level by multiplying a proper expansion factor.

5.2.2.1 Systematic standard uncertainty

The elemental systematic uncertainties of measurements include b_{U_C}, b_Y, b_ψ, b_{dx}, and b_{dy} in the measurements of carriage speed U_C, PMM sway displacement Y and yaw angle ψ, and field point location dx and dy, respectively. $b_{U_C} = B_{U_C}/2 = 0.005$ m/s, where the bias limit of carriage speed $B_{U_C} = 0.010$ m/s is from the carriage speed calibration as per Section 5.1.1. $b_Y = 0.05$ mm is from the sway potentiometer calibration. $b_\psi =$

$B_\beta/2 = 0.11°$, where the bias limit $B_\beta = 0.22°$ is from the drift angle calibration as per Section 5.1.1. $b_{dx} = b_{dy} = 0.5$ mm is from the tape measure accuracy for dx and dy measurements. These elemental systematic uncertainties propagate through the data reduction equations (DRE's) shown in Section 3.5.2, and are used to estimate the SPIV measurement results, i.e. the turbulent flow field data around the model in PMM motion, as follows.

Let result $R = U_i$, $u_i u_j$, k, and ω_x from the SPIV measurement. U_i is velocity components and $i = 1, 2, 3$ for U, V, W, respectively, and $u_i u_j$ is Reynolds stress where i, $j = 1, 2, 3$ for uu, vv, ww, uv, uw, vw in combinations, and k is the turbulent kinetic energy, and ω_x is the axial vorticity. The systematic uncertainty is determined herein by comparing (or calibrating) the R with the corresponding reference data, R_{Ref}.

The overall procedure evaluating the systematic standard uncertainty of the results, b_R, is conceptually similar as typical measurement device calibration; the reference data R_{Ref} is used as the calibration standard and the difference that is defined as

$$\delta = R - R_{Ref} \tag{5.50}$$

is considered as the systematic or bias error of R with respect to R_{Ref}. If the standard limit of the systematic error, b_δ, and the systematic standard uncertainty of the reference data, $b_{R_{Ref}}$, are known, then, b_R is the root-sum-square of those elemental uncertainties, b_δ and $b_{R_{Ref}}$, as per the equation (5.39) such that

$$b_R = \left(b_\delta^2 + b_{R_{Ref}}^2\right)^{\frac{1}{2}} \tag{5.51}$$

where

$$b_\delta = \left[\bar{\delta}^2 + \left(2 \cdot \frac{s_\delta}{\sqrt{M}}\right)^2\right]^{\frac{1}{2}}/2 \tag{5.52}$$

$b_\delta = B_\delta/2$ as per (5.40), where B_δ, i.e. the numerator at the right hand side of (5.52), is the systematic limit of δ at the 95% confidence level by assuming a normal distribution of δ with a large degree of freedom ($M > 30$). $\bar{\delta}$ and s_δ in (5.52) are the mean and standard deviation of the δ values collected from a number M of repeat measurements, respectively. The other elemental systematic uncertainty of b_R in (5.51), $b_{R_{Ref}}$, is defined and evaluated in two different ways according to the result variable R as follows.

The R_{Ref} is from the free stream data, introduced at the later part of Section 3.1.2, measured from the aforementioned open water tests. Knowing that the free stream flow is only in the horizontal plane of the ship-fixed x-y coordinate system (Fig. 3-4), expected from the free stream flow are no velocity in the vertical direction, no turbulence in the flow, and no velocity gradient in the cross-flow plane. Accordingly, R_{Ref} data are not measured for $R = W$, $u_i u_j$, k, and ω_x from the open water tests, but the expected value is used as the reference, i.e. $R_{Ref} = 0$, thus $b_{R_{Ref}} = 0$.

For $R = U$ and V, on the other hand, R_{Ref} is using the longitudinal u_P and the lateral v_P velocities of the free stream in the ship-fixed coordinate system (Fig. 3-4), respectively. Let $R_{PMM} = u_P$ and v_P, then R_{Ref} is the normalized R_{PMM} with the carriage speed U_C such as

$$R_{Ref} = R_{PMM}/U_C \tag{5.53}$$

or $R_{Ref} = f(R_{PMM}, U_C)$ in a functional form. Then, the systematic standard uncertainty the reference data, $b_{R_{Ref}}$, is from the elemental systematic standard uncertainties, $b_{R_{PMM}}$ and b_{U_C}, propagated through the data reduction equation (DRE) (5.53) as

$$b_{R_{Ref}} = \left(\theta_{R_{PMM}}^2 b_{R_{PMM}}^2 + \theta_{U_C}^2 b_{U_C}^2\right)^{\frac{1}{2}} \tag{5.54}$$

as per the error propagation equation (5.43), where the sensitivity coefficients $\theta_{R_{PMM}} = \partial R_{Ref}/\partial R_{PMM}$ and $\theta_{U_C} = \partial R_{Ref}/\partial U_C$ are respectively as per (5.42).

The elemental systematic uncertainty $b_{R_{PMM}}$ of $R_{PMM} = f(U_C, V_P, r, \psi, dx, dy)$ as per the DRE's (3.5a) and (3.5b) in Section 3.1.3 (or in Section 3.5.2) for u_P and v_P, respectively, is from the further elemental systematic uncertainties, b_{U_C}, b_{V_P}, b_r, b_ψ, b_{dx}, and b_{dy}. The error propagation equation for $b_{R_{PMM}}$ can be written using (5.43) as

$$b_{R_{PMM}} = \left(\theta_{U_C}^2 b_{U_C}^2 + \theta_{V_P}^2 b_{V_P}^2 + \theta_r^2 b_r^2 + \theta_\psi^2 b_\psi^2 + \theta_{dx}^2 b_{dx}^2 + \theta_{dy}^2 b_{dy}^2\right)^{\frac{1}{2}} \tag{5.55}$$

Where the sensitivity coefficient $\theta_{X_i} = \partial R_{PMM}/\partial X_i$ for $X_i = U_C$, V_P, r, ψ, dx, and dy is respectively as per (5.42).

Of the six elemental standard systematic uncertainties in (5.55), b_{V_P} is for $V_P = f(Y_0, \omega, \gamma)$ as per the DRE (3.23) and b_r is for $r = f(\psi_0, \omega, \gamma)$ as per the DRE (3.24), hence those uncertainties are even further elemental systematic standard uncertainties b_{Y_0}, b_{ψ_0}, b_ω, and b_γ, propagated through the DRE's. Y_0 and ψ_0 are the Fourier Series 1st-order harmonic amplitudes of the Y and ψ measurement data, respectively, thus any possible constant shift in Y and ψ, i.e. the systematic error, does not affect the Y_0 and ψ_0 values. Accordingly, b_Y and b_ψ do not propagate to Y_0 and ψ_0 through data reduction, and $b_{Y_0} = b_{\psi_0} = 0$. Next, b_ω is for $\omega = 2\pi(\mathrm{N}/60)$, where N is the PMM frequency f_{PMM} in RPM. Then, $b_\omega = \left(\frac{2\pi \cdot B_\mathrm{N}}{60}\right)/2 = 0.00003$ Hz, where $B_N = 0.0006$ rpm is the bias limit of N from Table 9 for PMM UA in Section 5.1.2. For IIHR PMM, b_ω is negligibly small such that $b_\omega/\omega = 0.0002$ for $\omega = 0.842$ (corresponding to $f_{PMM} = 0.134$ Hz), it can be assumed that $b_\omega = 0$. Consequently, b_{V_P} and b_r are from b_γ only, and their error propagation equations are written as

$$b_{V_P} = \left(\theta_\gamma^2 b_\gamma^2\right)^{\frac{1}{2}} \tag{5.56}$$

$$b_r = \left(\theta_\gamma^2 b_\gamma^2\right)^{\frac{1}{2}} \tag{5.57}$$

where the sensitivity coefficient $\theta_\gamma = \partial V_P/\partial\gamma$ in (5.56) and $\theta_\gamma = \partial r/\partial\gamma$ in (5.57), respectively. b_γ in (5.56) and (5.57) is for $\gamma = f(Y, \psi, Y_0, \psi_0)$ as per DRE (3.27) in Section 3.5.2, and from the elemental systematic uncertainties b_Y, b_ψ, b_{Y_0}, and b_{ψ_0}, where $b_{Y_0} = b_{\psi_0} = 0$ as previously discussed. Then, the error propagation equation for b_γ can be written as

$$b_\gamma = \left(\theta_Y^2 b_Y^2 + \theta_\psi^2 b_\psi^2\right)^{\frac{1}{2}} \tag{5.58}$$

where the sensitivity coefficients $\theta_Y = \partial\gamma/\partial Y$ and $\theta_\psi = \partial\gamma/\partial\psi$, respectively as per (5.42).

5.2.2.2 Random standard uncertainty

The random standard uncertainty s_R of the previously defined result R is estimated by performing 'end-to-end' multiple tests at the same test conditions. Herein the term 'end-to-end' implies that the whole data acquisition/reduction procedures described in Sections 3.7.2/3.8.2 are repeated to see the overall scatters in the results as a consequence of all possible elemental random errors. For the multiple tests, the location of the PIV system relative to the ship model was perturbed each time of the multiple tests by repositioning the PIV system in the (x, y, z) directions. Note, however, that the same towing tank facilities, the same PMM, the same model, the same PIV system including its calibration are used for the multiple tests due to limited experimental resources.

Total three sets (M = 3) of test are performed; each test consists of more than 100 carriages runs for the phase averaging purposes. Each carriage run is made with about 12-minute interval between the runs to minimize flow disturbances from previous runs. Each test set takes typically one day for test setup and 3 ~ 4 days for data acquisition, thus spanning total 4 ~ 5 days. The mean result $\bar{R}$ is calculated from the results of mul-

tiple tests, used to calculate the random standard uncertainty s_R using the equation (5.38) with $M = 3$.

5.2.2.3 Combined standard and expanded uncertainty

Combined standard uncertainty u_R of the result is the root-sum-square of the systematic standard uncertainty b_R and the random standard uncertainty s_R as per the equation (5.46) in Section 5.2.1. The systematic uncertainty b_R is from (5.51) and the random standard uncertainty s_R is using the equation the equation (5.38) from the multiple tests.

Expanded uncertainty $U_{R,95}$ of the result is as per the equation (5.47) in Section 5.2.1. The expansion factor t_{95} in (5.47) is estimated using the Welch-Satterthwaite formula shown in (5.48) as the degree of freedom of the random standard uncertainty estimation, $\nu_{s_R} = M - 1 = 2$, is smaller than 30 for the large sample assumption. The Welch-Satterthwaite formula (5.48) can be rewritten for the present UA as

$$\nu_R = \frac{\{(b_R)^2+(s_R)^2\}^2}{(b_R)^4/\nu_{b_R}+(s_R)^4/\nu_{s_R}} \tag{5.59}$$

5.2.3 UA Results and Discussions

5.2.3.1 Open water Tests

Case 1) Uniform flow measurement:

The SPIV measurement area is located at 51 mm off from the towing tank centerline and at 93 mm below the calm water free surface line. A total 12 repeat tests are made, where the average towing carriage speed $\overline{U_C}$ = 1.5232 m/s with a standard deviation of 0.0028 m/s (0.2% of $\overline{U_C}$). Each test is a single carriage run with 94 data samples acquired at a rate of 5 Hz (Δt = 200 ms) and reduced as per Section 3.5.2. Note that the data reduction in this case is not a phase-average but a time-average of the 94 data as no phase information.

In Fig. 5-7, test result R (shown as colored contours) and the systematic standard uncertainty b_R (labeled line contours) are shown for (a) U, (b) V, (c) W, (d) uu, (e) vv, (f) ww, (g) uv, (h) uw, (i) vw, (j) k, and (l) ω_x, respectively. R is the mean value of each variable data from the 12 repeat test, non-dimensional with U_C for U, V, W, with U_C^2 for uu, vv, ww, uv, uw, vw, and k, and with U_C/L for ω_x, respectively, where L = 3.048 m is the model length. b_R is evaluated as per Section 5.2.2.1 and presented as non-dimensional similarly as for R. The evaluation of b_R is summarized in Table 5-17 including the elemental uncertainties used in Section 5.2.2.1. All the data in the table are the spatially averaged values of those over the SPIV measurement area.

From Fig. 5-7 (a) – (c), velocities in general U = 0.98 ~ 1.0, V = 0.01 ~ 0.02, W = -0.01 ~ 0.01, respectively, of which mean difference (from the 12 repeat tests) from the reference value (R_{Ref} = 1.0, 0.0, 0.0, respectively) $\bar{\delta}$ = -0.0062, 0.0150, -0.0004 in average, respectively. b_U = 0.004 ~ 0.007, b_V = 0.004 ~ 0.012, b_W = 0 ~ 0.003, corresponding respectively to about 0.6%, 0.8%, and 0.1% of U_C in average. b_U is the root-sum-square (RSS) of b_δ and $b_{R_{Ref}}$ as per (51), where $b_{R_{ref}} = \left(2 \cdot b_{U_C}^2/U_C^2\right)^{\frac{1}{2}}$ = 0.0046 from (54) by using $R_{PMM} = U_C$, and b_{U_C} = 0.005 m/s from Table 5-16. Whereas, b_V and b_W are the same as b_δ of V and W, respectively, as $b_{R_{Ref}}$ = 0 for both. The evaluations of b_δ for U, V, W are as per (52), summarized in Table 5-17.

From Fig. 5-7 (d) – (f), the normal Reynolds stresses in general uu = 0.0001 ~ 0.0004, vv = 0.0001 ~ 0.0003, and ww = 0 ~ 0.0001, corresponding to $\sqrt{uu}$ = 1.6%, $\sqrt{vv}$ = 1.4%, $\sqrt{ww}$ = 0.8% of U_C, respectively, in average. Shear stresses, from Fig. 5-7 (g) – (i), are in general uv = 0.0001 ~ 0.0003, uw = -0.00003 ~ 0.00004, and vw = -0.00004 ~ 0.00004, corresponding to $\sqrt{uv}$ = 1.3% of U_C and $\sqrt{uw} \approx \sqrt{vw} \approx 0$ in average. Turbulent kinetic energy k shown in Fig. 5-7 (j) is similar with uu. The systematic standard uncertainty is as per (51) using (52) and $b_{R_{Ref}}$ = 0 for those variables; b_{uu} = 0.00013, b_{vv} = 0.00010, b_{ww} = 0.00003 for the normal stresses, b_{uv} = 0.00009, b_{uw} = 0.00001, b_{vw} =

0.00001 for shear stresses, and b_k = 0.00013 for turbulent kinetic energy, respectively, summarized in Table 5-17.

From Fig. 5-7 (k), the axial vorticity is in general ω_x = -3 ~ 3 except for the region at the right side where locally strong ω_x = -8 ~ 7 exhibiting a particular cascade-shaped pattern. This pattern will be discussed below. b_{ω_x} = 1.2 in average, evaluated as per (51) using (52) and $b_{R_{Ref}}$ = 0, summarized in Table 5-17.

Possible sources of the systematic uncertainty of SPIV measurement may include the intrusive disturbance effect of the SPIV system. The displacement effect of the SPIV system is measured with a one-hole Pitot probe and the result is shown in Fig. 5-8. The axial velocity U of the free stream is measured along the longitudinal axis x through the center point of the SPIV measurement area, at several locations between x/D = -5 ~ 10, where D = 100 mm is the diameter of the SPIV camera housings (See Fig. 3-10) and x = 0 is located at the measurement area center point. Measurement result reveals the retarded flow around the camera housings, at maximum U/U_C = 0.9585 near at x/D = -4, due to the displacement effect. At x/D = 0, the measurement area location, the retarded velocity U/U_C = 0.9937 or the amount of retardation 1 - U/U_C = 0.0063, which are comparable with $\bar{\delta}$ = 0.9938 and b_U = 0.0058 of the uniform flow U measurement shown at Table 5-17. The error bars shown at x/D = 0 in Fig. 5-8 depict the ±2·s range, where s = 0.0011 is the standard deviation of U/U_C values from five repeated measurements.

Another possible source of the systematic uncertainty may be the SPIV evaluation error such as the registration error (Scarano et al. 2005, Coudert & Schon 2001, Prasad 2000, Willert 1997, Prasad & Adrian 1993). The registration error is due to the mismatched SPIV image pairs in the interrogation process, which produces a particular pattern so called Moiré pattern in the dewarped PIV images. The Moiré pattern can be seen from Fig. 5-7 (a) – (c) and (k) for U, V, W, and ω_x, the cascade-shaped pattern at the right side of the measurement area. The Moiré pattern is more distinct for V which results in the rather strong Moiré pattern of ω_x through the data reduction process.

Case 2) Open water pure yaw test:

A total three tests are conducted with designated as Test 1, 2, and 3 respectively. SPIV measurements are at two different longitudinal positions x/L = 0.935 for Tests 1 and 2 and x/L = 0.002 for Test 3, respectively, where L = 3.048 m is the model length. The vertical location is at z/T = 1.1 for Test 1 and Test 3 and z/T = 0.5 for Test 2, respectively, where T = 0.136 m is the model draft. The lateral position y = 0 for all tests. Where, the locations correspond to the center-point position of the SPIV measurement area in the Ship-fixed coordinate system (Fig. 3-4).

Test conditions are same for all tests, summarized in Table 5-15. A total 100 carriage runs are made for each test. The mean and standard deviation values of carriage speed U_C and PMM sway Y_0 and yaw ψ_0 amplitudes are summarized in Table 5-18 for Test 1. Sway Y and yaw ψ data are phase-sorted into 32 phase groups where the typical number of data is about 270 ~ 280. Phase averaged Y and ψ values are summarized in Table5-19 for Test 1 and for selective phase groups (every 45° nominal phase angle), where the subsequent phase γ values calculated from the Y, ψ, Y_0, and ψ_0 data by using (3.27) in Section 3.5.2. are as well presented.

Test results are shown in Fig. 5-9. Presented in the figure are the difference $\delta = R - R_{Ref}$ defined at (5.50). The results $R = (U, V, W)$ is the SPIV measured flow velocity and the reference data $R_{Ref} = (u_P, v_P, 0)$, where u_P and v_P are respectively as per (3.5a) and (3.5b) in Section 3.5.2 using the PMM measured data. Each symbol in the figure represents the spatially averaged δ value over the SPIV measurement area, measured at each phase angle γ of each test. In general δ is function γ; δ is relatively larger between γ = 180° ~ 360° for U and between γ = 90° ~ 270° for V, whereas almost flat for W, respectively. δ may be a function of SPIV locations as well. For V (green colored), δ for Test 3 (symbol O; at x/L = 0.002) is rather different from those for Tests 1 and 2 (respectively symbols □ and Δ; at x/L = 0.935). For W (blue colored), δ for Test 1 (symbol □

and Δ; at z/T = 1.1) is larger than those for Test 2 (symbol Δ; at z/T = 0.5). Whereas for U (red colored), δ is almost same between the tests.

The evaluation of b_R is summarized in Table 5-20 for all variables. All the data values in the table are first averaged spatially over the SPIV measurement area and then for all phase positions. For velocity data, b_U = 0.0078, b_V = 0.0068, and b_W = 0.0055, corresponding to about 0.8%, 0.7% and 0.6% of U_C, respectively, and about 130%, 90%, and 390% of those from the uniform flow test, respectively. For Reynolds normal stresses, b_{uu} = 0.00020, b_{vv} = 0.00011, and b_{ww} = 0.00004, of which square-root values are corresponding to about 1.4%, 1.0%, and 0.6% of U_C, respectively. For shear Reynolds stresses, b_{uv}= 0.00011, b_{uw} = 0.00001, and b_{vw} = 0.00001, of which square-root values are corresponding to about 1.0%, 0.3%, and 0.3% of U_C, respectively. For turbulent kinetic energy, b_k = 0.00017 and $\sqrt{2/3 \cdot b_k}$ = 1.1% of U_C. b_{uu} and b_k are 154% and 131% of those from the uniform flow test, whereas similar for other stress components. For axial vorticity b_{ω_x} = 1.2 is same as the uniform flow result.

5.2.3.2 Pure yaw test

Test is with model and as per the test conditions shown in Table 5-15, which are the same as those for open water pure yaw tests. The longitudinal location of the SPIV measurement is at x/L = 0.135. Test is more than 100 carriage runs allowing about 270 ~ 280 data per each of 32 PMM phase positions for phase averaging. The whole test procedures are repeated for three times.

UA is estimating the systematic b_R and random s_R standard uncertainties to ascertain the combined standard uncertainty u_R as per (5.46). b_R is from the open water pure yaw test and s_R is from the three repeat tests as per (5.45) using M = 3. u_R is used to estimate the expanded uncertainty $U_{R,95}$ as per (5.47) where the expansion factor t_{95} = 2.365 corresponding to the Student t statistic for a degree of freedom ν_R = 7 and for a 95% confidence level. ν_R is estimated by using (5.59) as per the Welch-Satterthwaite

formula (5.48), where for (5.59), ν_{b_R} = 8 is used as per (5.49) for $b_{i_k} = b_R$ by assuming the relative variability of the estimate $\Delta b_R / b_R$ = 0.25 as per the example case (B-1.10) in Appendix B of ASME (2005).

Pure yaw test result R and the relative expanded uncertainty $U_{R,95}$ (% R) is shown in Fig. 5-10 for (a) U, (b) V, (c) W, (d) uu, (e) vv, (f) ww, (g) uv, (h) uw, (i) vw, (j) k, and (k) ω_x at the PMM phase γ = 236.25° position, respectively. The results shown in the figure are the mean values of the three repeat tests data. The center point position of the SPIV measurement area is located at y/L = -0.0125 laterally and at z/L = 0.0525 (z/T = 1.1765) vertically, respectively. The measurement area is split into two sub regions as shown in Fig. 5-10 (l) using K = 0.45 as a criteria, where $K = \frac{1}{2}(U^2 + V^2 + W^2)$ is the kinematic energy of the fluid. The Inner Region is where $K \leq 0.45$ representing the boundary layer region and the Outer Region is where $K > 0.45$ representing the free stream region of the flow, respectively. All the result values and the UA data value are averaged within the two regions respectively, and summarized in Tables 5-21 and 5-22 for the Inner and Outer region, respectively.

In the Inner Region, the random uncertainty is predominant, 60% ~ 99%, over the systematic uncertainty, 1% ~ 40%, for all variables except for V and W. For V and W, systematic uncertainty is dominant, 69% and 63%, respectively. The expanded uncertainty $U_{R,95}$ = 0.0321, 0.0213, 0.0188 for U, V, W, respectively, corresponding to about 3.2%, 2.1%, and 1.9% of U_C, respectively, and to 3.9%, 29.1%, and 32.1% of the mean U, V, W values, respectively. For the normal Reynolds stresses, $U_{R,95}$ = 0.0014, 0.0007, 0.0003 for uu, vv, ww, respectively, of which squqre-root value corresponds to about 4%, 3%, and 2% of U_C, respectively. For the shear Reynolds stresses, U_{R95} = 0.0008, 0.0003, 0.0002 for uv, uw, vw, respectively, of which square-root value corresponds to about 3%, 2%, and 1% of U_C, respectively. The relative uncertainties of the Reynolds stresses are 24% ~ 33% and 45% ~ 78% of the mean result values for the normal and shear stresses, respectively. For turbulent kinetic energy k, $U_{R,95}$ = 0.0011 and

$\sqrt{2/3 \cdot U_{R,95}}$ = 2.7% U_C, and its relative uncertainty is 25% of the mean k value. For axial vorticity ω_x, $U_{R,95}$ = 15.2 and the relative uncertainty is 36% of the mean ω_x value.

In the Outer Region, the systematic uncertainty is predominant, in general 70% ~ 96%, over the random uncertainty, in general 4% ~ 30%, for all variables except for ω_x. For ω_x, both systematic and random uncertainties are equally large, 52% and 48%, respectively. The expanded uncertainty $U_{R,95}$'s of U, V, W are relatively smaller than those for the Inner Region; about 2.4%, 1.5%, and 1.4% of U_C, respectively, or 2.5%, 12.1%, and 26.1% of the mean values, respectively. $U_{R,95}$ for the Reynolds stresses and the turbulent kinetic energy are also smaller than those for the Inner Region, about 0 ~ 0.0005, of which square-values are about 0 ~ 2% of U_C. However, the relative $U_{R,95}$ values are large, about 100% ~ 200%, due to very small mean values of those variables in the Outer Region. For axial vorticity ω_x, $U_{R,95}$ = 4.0 and the relative uncertainty is large about 140% as well due to smaller mean value of ω_x in the Outer Region.

Consequently, the absolute uncertainty of the SPIV measurement is about 2 ~ 3% of U_C for the out of plane velocity component, U, and about 1 ~ 2% of U_C for the in-plane velocity components, V and W, respectively. The relative uncertainty is about 3 ~ 4%, 12 ~ 29%, and 26 ~ 32% for U, V, W, respectively. The relative uncertainties of U are comparable with the 2.4% of Gui et al. (2001a) and the 1.6% and 1.0 ~ 3.5% of Longo et al. (2007) for steady- and unsteady-flow, respectively. Whereas, the relative uncertainties of V and W are larger than the 4 ~ 8% of Gui et al. (2001a) and the 3 ~ 4% of Longo el al. (2007). Gui et al. (2001a) and Longo et al. (2007) are 2D-PIV measurements using the same IIHR towing tank facility and the same DTMB 5512 model as the present study, respectively. Note that the uncertainties of Gui et al. (2001a) and Longo et al. (2007) are relative to the dynamic ranges of measurements. The relative uncertainties of the Reynolds stresses, about 25% ~ 50% in general at the Inner Region, are larger than the 4 ~ 6% of Gui et al. (2001a) and the 3 ~ 6% of Longo et al. (2007) for steady flow, whereas those are comparable with the 10 ~ 45% of Longo et al. (2007) for unsteady flow. For

the SPIV measurement, the large random uncertainty in the Inner Region may be reduced by increasing the number of PIV images for the phase averaging. On the other hand, the large systematic uncertainty in the Outer Region can be improved by using more sophisticated SPIV algorithm to reduce the SPIV evaluation errors such as the registration error and by using more careful reference data to reduce the calibration errors.

Table 5-15 Open water tests conditions for Stereo PIV UA.

Test Case	Test description	U_C (m/s)	Y_0 (mm)	ψ_0 (°)	f (Hz)	Δt (ms)	$\Delta\gamma$ (°)	Number of data per run L	Number of runs per test K	Number of repeat tests M
Case 1)	Uniform flow	1.531	0.0	0.0	0.0	200.0	-	94	1	12
Case 2)	Open water pure yaw	1.531	326.1	10.2	0.134	233.2	11.25	88	100	3

- : Not applicable

Table 5-16 Elemental systematic standard uncertainties of the SPIV measurements.

Measurement variable X	Description	Unit	Symbol	Systematic standard uncertainty $b_{\bar{X}}$
U_C	Carriage speed	m/s	b_{U_C}	0.005
Y	Sway displacement	mm	b_Y	0.05
ψ	Yaw angle	deg	b_ψ	0.11
dx, dy	Field point location from the midship point	mm	b_{dx}, b_{dy}	0.5

Table 5-17 Systematic uncertainties of SPIV uniform flow measurement†.

Result variable R	Average SPIV data $\bar{R}$	Reference data R_{Ref}	Average difference $\bar{\delta}$	Standard deviation of difference s_δ	Systematic standard uncertainty of difference b_δ	Systematic standard uncertainty of reference $b_{R_{Ref}}$	Systematic standard uncertainty of Result b_R
U	0.9938	1.0	-0.0062	0.0047	0.0034	0.0046	0.0058
V	0.0150	0.0	0.0150	0.0017	0.0075	0.0	0.0075
W	-0.0004	0.0	-0.0004	0.0008	0.0014	0.0	0.0014
uu	0.00025	0.0	0.00025	0.00006	0.00013	0.0	0.00013
vv	0.00019	0.0	0.00019	0.00004	0.00010	0.0	0.00010
ww	0.00006	0.0	0.00006	0.00002	0.00003	0.0	0.00003
uv	0.00017	0.0	0.00017	0.00004	0.00009	0.0	0.00009
uw	0.00000	0.0	0.00000	0.00002	0.00001	0.0	0.00001
vw	0.00000	0.0	0.00000	0.00002	0.00001	0.0	0.00001
k	0.00025	0.0	0.00025	0.00005	0.00013	0.0	0.00013
ω_x	-0.17	0.0	-0.17	2.2	1.2	0.0	1.2

† Presented varles are non-dimensional and averaged over the measurement area.

Table 5-18 Measurement data of U_C, Y_0, and ψ_0†.

Measurement variable X	Unit	Nominal value	Mean value $\bar{X}$	Standard deviation s_X
U_C	m/s	1.531	1.5307	0.0059
Y_0	mm	326.1	328.42	0.0241
ψ_0	deg.	10.2	10.40	0.0566

† From open water pure yaw test with N = 100 carriage runs

Table 5-19 Measurement data of Y, ψ, and γ†.

		Y (mm)			ψ (°)			γ (°)	
Phase Group n	Number of data N	Nominal value	Mean value $\bar{X}$	Standard deviation s_X	Nominal value	Mean value $\bar{X}$	Standard deviation s_X	Nominal value	Measured value
1	276	0.0	0.7	1.6	-10.20	-10.33	0.05	0.0	-0.1
5	274	-230.6	-232.5	1.3	-7.21	-7.40	0.04	45.0	44.9
9	274	-326.1	-329.2	0.6	0.00	-0.06	0.04	90.0	89.7
13	278	-230.6	-234.4	0.4	7.21	7.35	0.05	135.0	134.7
17	273	0.0	-2.1	0.6	10.20	10.39	0.06	180.0	179.6
21	267	230.6	230.1	0.4	7.21	7.49	0.05	225.0	224.2
25	276	326.1	327.4	0.7	0.00	0.17	0.04	270.0	269.1
29	282	230.6	232.0	1.3	-7.21	-7.30	0.05	315.0	314.8

† From open water pure yaw test with N = 100 carriage runs.

Table 5-20 Summary of UA for open water pure yaw test (M = 3 repeat tests)†.

Result variable R	Average difference $\bar{\delta}$	Standard deviation of difference s_δ	Systematic standard uncertainty of difference b_δ	Systematic standard uncertainty of reference $b_{R_{Ref}}$	Systematic standard uncertainty of Result b_R
U	-0.0111	0.0031	0.0060	0.0046	0.0078
V	0.0085	0.0064	0.0064	0.0024	0.0068
W	-0.0090	0.0055	0.0055	0.0	0.0055
uu	0.00038	0.00009	0.00020	0.0	0.00020
vv	0.00021	0.00005	0.00011	0.0	0.00011
ww	0.00007	0.00002	0.00004	0.0	0.00004
uv	0.00022	0.00005	0.00011	0.0	0.00011
uw	0.00000	0.00002	0.00001	0.0	0.00001
vw	0.00000	0.00001	0.00001	0.0	0.00001
k	0.00033	0.00006	0.00017	0.0	0.00017
ω_x	-0.1	1.7	1.2	0.0	1.2

Table 5-21 Summary of UA for pure yaw test with model (Inner Region).

Result variable	Result R	Systematic standard uncertainty b_R	Random standard uncertainty s_R	Combined standard uncertainty u_R	Relative systematic uncertainty contribution b_R^2/u_R^2 (%)	Relative random uncertainty contribution s_R^2/u_R^2 (%)	Expanded uncertainty U_{95R}	Relative expanded uncertainty U_{95R}/R (%)
U	0.8326	0.0081	0.0101	0.0136	39.4	60.6	0.0321	3.9
V	0.0733	0.0071	0.0048	0.0090	68.6	31.4	0.0213	29.1
W	0.0586	0.0059	0.0045	0.0079	63.2	36.8	0.0188	32.1
uu	0.0044	0.0002	0.0005	0.0006	12.0	88.0	0.0014	32.9
vv	0.0026	0.0001	0.0003	0.0003	13.6	86.4	0.0007	26.2
ww	0.0014	0.0000	0.0001	0.0001	7.4	92.6	0.0003	24.0
uv	0.0017	0.0001	0.0003	0.0003	13.1	86.9	0.0008	45.3
uw	0.0004	0.0000	0.0001	0.0001	0.8	99.2	0.0003	74.0
vw	0.0003	0.0000	0.0001	0.0001	0.9	99.1	0.0002	77.8
k	0.0042	0.0002	0.0004	0.0004	16.3	83.7	0.0011	24.9
ω_x	41.8	1.7	6.0	6.4	7.2	92.8	15.2	36.3

Table 5-22 Summary of UA for pure yaw test with model (Outer Region).

Result variable	Result R	Systematic standard uncertainty b_R	Random standard uncertainty s_R	Combined standard uncertainty u_R	Relative systematic uncertainty contribution b_R^2/u_R^2 (%)	Relative random uncertainty contribution s_R^2/u_R^2 (%)	Expanded uncertainty U_{95R}	Relative expanded uncertainty U_{95R}/R (%)
U	0.9772	0.0098	0.0020	0.0102	95.9	4.1	0.0240	2.5
V	0.1236	0.0060	0.0015	0.0063	93.9	6.1	0.0149	12.1
W	0.0536	0.0057	0.0012	0.0059	95.9	4.1	0.0140	26.1
uu	0.0004	0.0002	0.0000	0.0002	94.7	5.3	0.0005	128.3
vv	0.0002	0.0001	0.0000	0.0001	95.1	4.9	0.0003	116.2
ww	0.0001	0.0000	0.0000	0.0000	92.6	7.4	0.0001	105.9
uv	0.0002	0.0001	0.0000	0.0001	95.7	4.3	0.0003	141.3
uw	0.0000	0.0000	0.0000	0.0000	72.5	27.5	0.0000	178.0
vw	0.0000	0.0000	0.0000	0.0000	77.1	22.9	0.0000	212.8
k	0.0004	0.0002	0.0000	0.0002	95.8	4.2	0.0004	118.7
ω_x	2.9	1.1	1.1	1.7	51.7	48.3	4.0	141.4

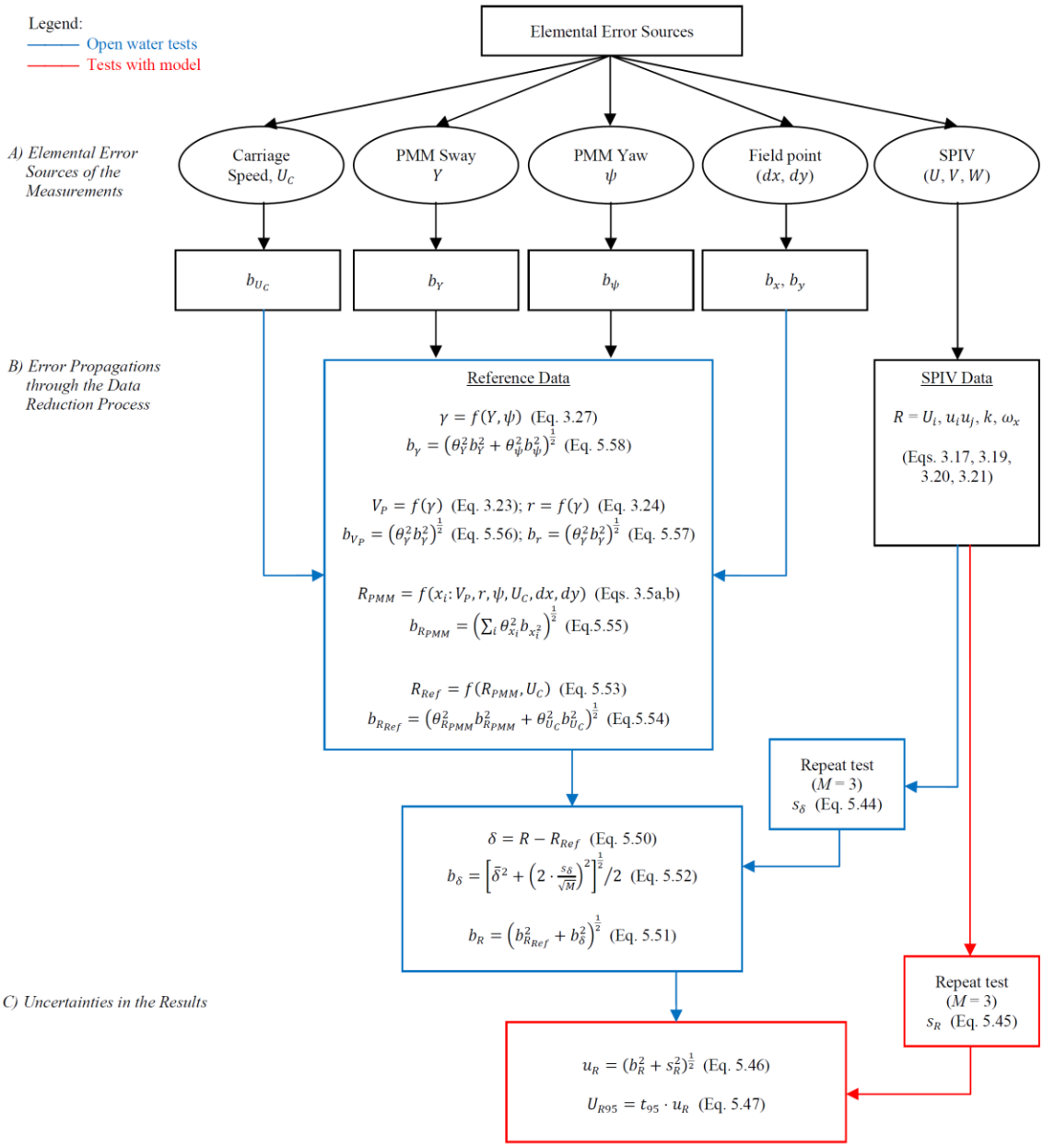

Figure 5-6 Error propagation chart for SPIV measured flow field data.

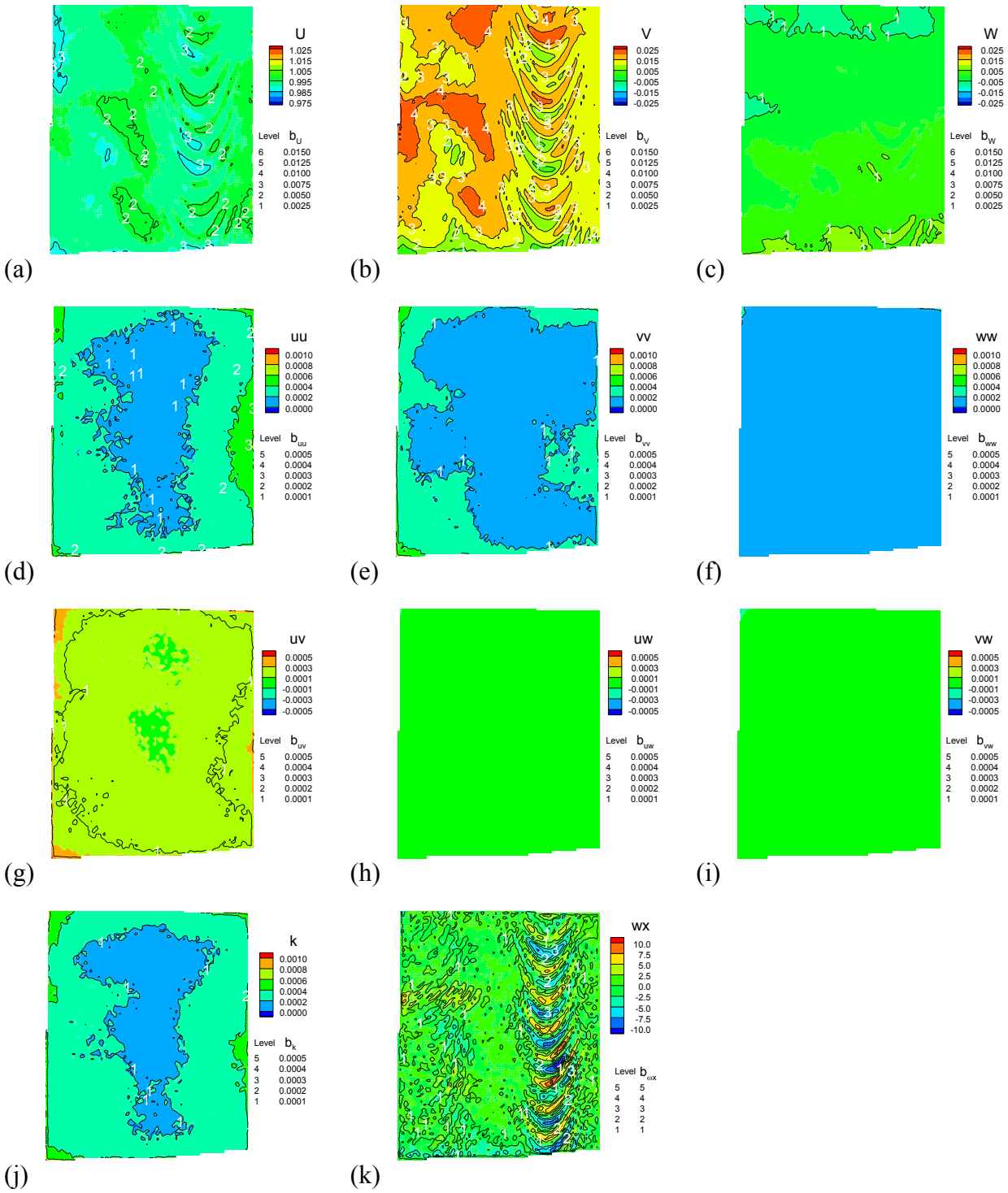

Figure 5-7 SPIV measured uniform flow field and systematic standard uncertainty for (a) U, (b) V, (c) W, (d) uu, (e) vv, (f) ww, (g) uv, (h) uw, (i) vw, (j) k, and (k) ω_x, respectively.

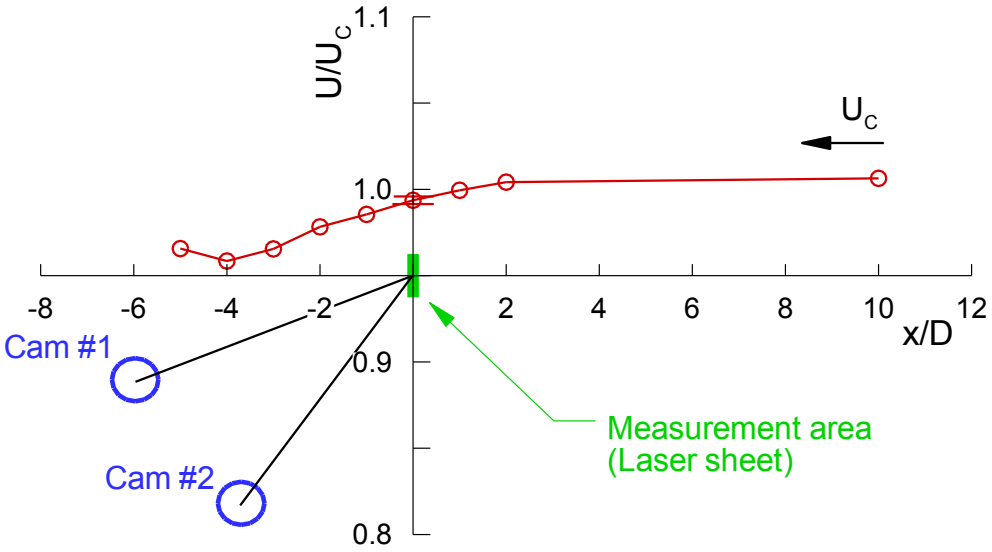

Figure 5-8 Pitot probe open water velocity U with normalized with the carriage speed U_C at various longitudinal locations, x. relative to the PIV measurement area (laser sheet plane) position $x/D = 0$, where $D = 100$ mm is the cylinder diameter of the underwater PIV camera housing.

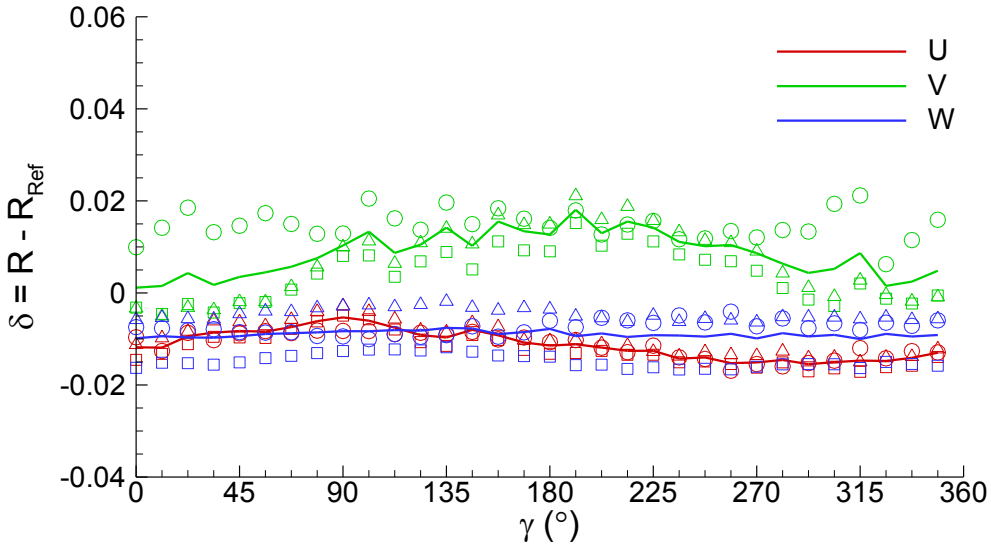

Figure 5-9 Open water pure yaw test result for SPIV UA. Symbols: □, Test 1; Δ, Test 2; ○, Test 3; and solid line is the mean δ of Test 1, 2, and 3. Each symbol shows the spatially averaged δ value over the SPIV measurement area.

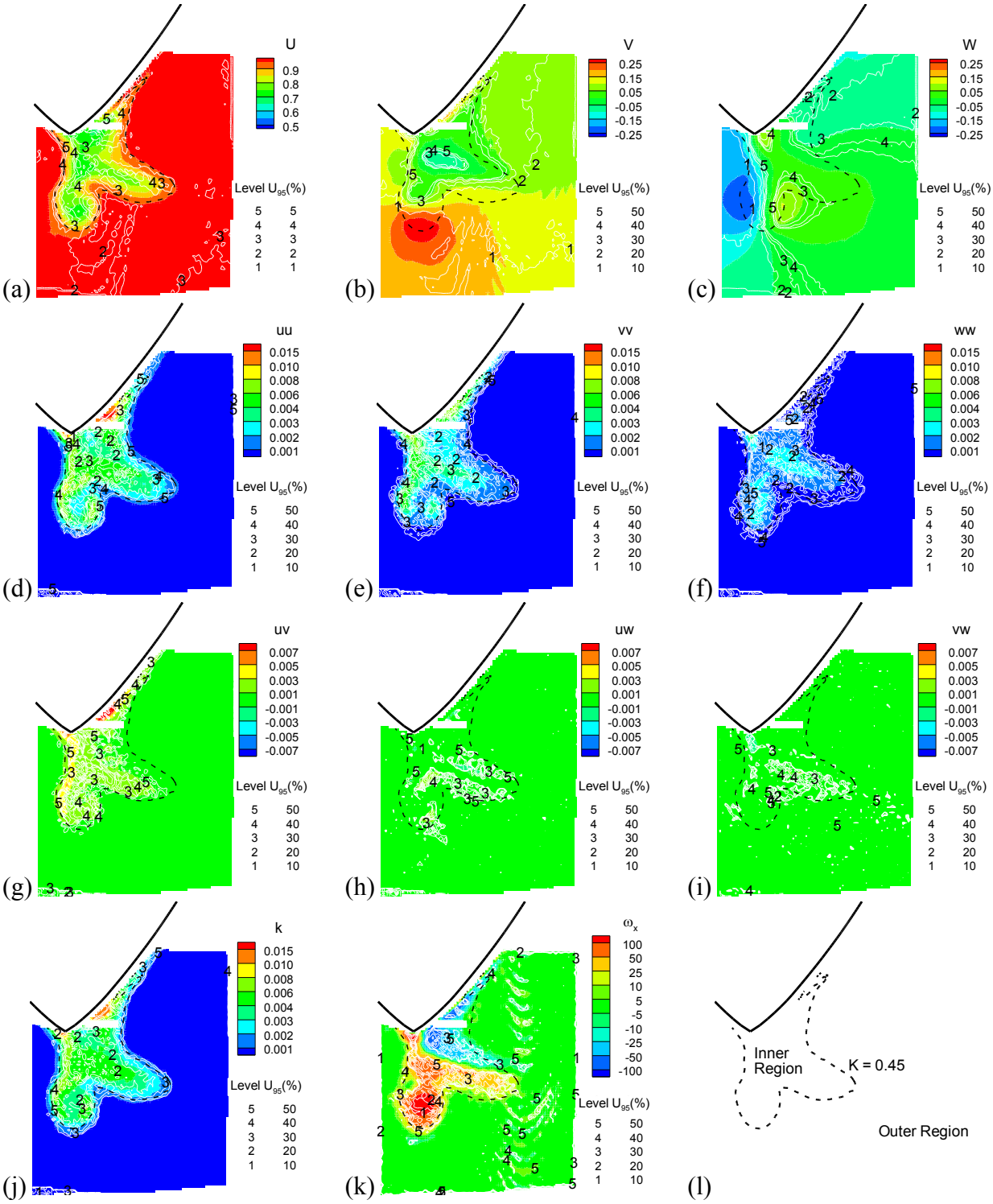

Figure 5-10 SPIV measured pure yaw flow field and relative expanded uncertainty U_{95} (%) for: (a) U, (b) V, (c) W, (d) uu, (e) vv, (f) ww, (g) uv, (h) uw, (i), vw, (j) k, and (k) ω_x, respectively. (l) Inner region, K ≤ 0.45 and Outer region, K > 0.45, where $K = ½(U^2 + V^2 + W^2)$.

CHAPTER 6 RESULTS AND DISCUSSION

6.1 Forces and Moment and Motions

Results are presented and discussed first for the data from the $FR_{z\theta}$ condition. Time-mean and -histories of the forces and moment data from static and dynamic PMM tests are presented in Section 6.1.1. In Section 6.1.2, hydrodynamic derivatives from forces and moment data are determined with the '*Multiple-Run*' and the '*Single-Run*' methods as introduced in Section 2.3.5, and results are compared between the methods by defining and evaluating the data-reconstruction error, E_R. Forces and moment, and the resulting hydrodynamic derivatives from the three different facilities data using ship-models with different size are compared in Section 6.1.3, where the trends of the hydrodynamic derivatives with the model-size are discussed. Heave, pitch, and roll motions of the model during the static and dynamic PMM tests for the $FR_{z\theta}$ and $FR_{z\theta\phi}$ conditions are presented in Section 6.1.4. Lastly, the effects of different mount-conditions including FX_0, $FX_{\sigma\tau}$, and $FR_{z\theta\phi}$ are discussed in Section 6.1.5. Note that all data presented herein are corrected for asymmetry as per discussed in Section 5.1.5.

6.1.1 Time-mean and -histories of Data

Time-mean values of static drift X, Y, and N are shown in Fig. 6-1 (a), (b), and (c), respectively, for Fr = 0.138, 0.280, and 0.410 cases. Data are fitted to quadratic, $X = A + B\beta^2$, and cubic, $Y, N = A\beta + B\beta^3$, functions, respectively, which can be re-written as $X = A \cdot (1 + \lambda)$ and $Y, N = A\beta \cdot (1 + \lambda)$, respectively, where λ is defined as

$$\lambda \equiv \frac{B}{A}\beta^2 \tag{6.1}$$

which is the ratio of the non-linear terms to the linear terms, representing the degree of non-linearity of data[9]. For $\beta << 10°$, $\lambda \approx 0$ (at $\beta = 5°$, $\lambda = 0.06$, 0.04, and 0.02 for X, Y, and N, respectively, at $Fr = 0.280$) and X in (a) is close to a constant value, i.e. $X = A$, and Y and N in (b) and (c) are nearly linear, i.e. $Y, N = A\beta$, with slope A seemingly independent of Fr. This is consistent with Longo et al. (2002) where the authors measured the resistance C_T, side force C_S, and drift moment C_M (corresponding to X, Y, and N, respectively) of the Series 60 $C_B = 0.6$ model in oblique towing for a range of $\beta = 0° - 10°$ and $Fr = 0.1 - 0.35$. The authors curve-fitted data as $C_T = a\beta + b$ and $C_{S,M} = a\beta^2 + b\beta + c$, respectively, and reported that for the former a is independent of Fr and for the latter b is nearly independent of Fr. For $\beta > 10°$, however, data become non-linear as $\lambda > 0$ (at $\beta = 10°$, $\lambda = 0.26$, 0.18, and 0.07 for X, Y, and N, respectively, at $Fr = 0.280$) and B exhibits rather strong dependency on Fr for all variables (See Fig. 6-9, where X_*, Y_v, and N_v correspond to A; X_{vv}, Y_{vvv}, and N_{vvv} correspond to B; and Δu corresponds to Fr).

Time-histories of the forced PMM motions, and those of the responses in forces and moment are shown in Fig. 6-2 for pure sway (left column), pure yaw (center column), and yaw and drift tests (right column), respectively. Forced motions are defined in equations (2.14a) – (2.14c) and (2.15) for pure sway, (2.16a) – (2.16c) for pure yaw, and (2.17a) – (2.17b) for yaw and drift tests, respectively (typical examples of the motions are illustrated in Fig. 2-4 (b), (c), and (d), respectively). Shown in Fig. 6-2 (a) are drift angle β for pure sway test (for β_{max} = 2°, 4°, and 10° cases), heading ψ for pure yaw (for r_{max} = 0.05, 0.15, 0.30, 0.45, 0.60, and 0.75 cases) and yaw and drift tests (for β = 9°, 10°, and

---

[9] λ can be rewritten by using the mathematic models (2.19a), (2.19b), and (2.19c) for X, Y, and N as:

$$\lambda = \frac{X_{vv}}{X_*}v^2;\ \frac{Y_{vvv}}{Y_v}v^2;\ \frac{N_{vvv}}{N_v}v^2$$

respectively.

11° cases with r_{max} fixed at 0.30), respectively. Specific test conditions are summarized in Table 3-3.

The responses in X, Y, and N shown in Fig. 6-2 are typically the 2nd-order dominant oscillations for X with super posed on the period-mean values, whereas the 1st-order dominant oscillations for Y and N with phase shifted with respect to the forced motions, except for the yaw and drift. For yaw and drift, the 1st-order oscillations are dominant with superposed on the period mean value for all variable. The forces and moment time-histories are expressed in Fourier series (FS) forms such as

$$\chi(t) = \chi_0 + \sum_n \chi_n \cos\left(n\omega t + \varphi_{\chi n}\right) \tag{6.2}$$

for $\chi = X$, Y, and N, where χ_0 is the period-mean of χ, and χ_n and $\varphi_{\chi n}$ are the nth-order amplitude and phase terms, respectively. In Table 6-1, the harmonic amplitudes χ_n for n = 1, … , 6 are presented in percentages of the data oscillation amplitudes and in averages of all β_{max} , r_{max} , and β cases, respectively. For pure sway, the 2nd-order amplitude X_2 is the largest, 72.8%, while the 4th- and 6th-order amplitudes X_4 and X_6 are also fairly large, 12.7% and 33.1%, respectively, for X; the 1st-order amplitudes Y_1 and N_1 are predominant 99.3% and 98%, respectively, whereas the higher-order amplitudes Y_3, Y_5 and N_3, N_5 are all small, less than about 3%, for Y and N. For pure yaw, the overall trends are similar as for pure sway whereas the 3rd-order amplitudes Y_3 and N_3 are relatively larger, 11.6% and 5.8%, respectively. For yaw and drift, the 1st-order amplitude X_1 is dominant, 69.4%, but the higher-order amplitudes $X_{2,3,4,5,6}$ are also large, about 10% - 30%, for X, and the 1st-order amplitudes Y_1 and N_1 are the largest, 93.5% and 98.0%, respectively, the 2nd-order amplitudes Y_2 and N_2 are the 2nd largest, 22.2% and 11.1%, respectively, and the higher-order amplitudes $Y_{3,4,5,6}$ and $N_{3,4,5,6}$ are all small, less than about 5%, for Y and N.

The 1st-order phase angles φ_{Y1} and φ_{N1} are seemingly constant from Fig. 6-2 where $\varphi_{Y1}/2\pi$ and $\varphi_{N1}/2\pi$ values about 0.09 (32°) and 0.02 (9°) for pure sway, about

0.28 (102°) and 0.29 (105°) for pure yaw, and about 0.29 and 0.28 for yaw and drift, respectively. However, those phase values are functions of the motion parameters such as y_{max}, ψ_{max}, ω, and/or β (or v_{max}, r_{max}, ω, and/or v) as will be discussed later.

Table 6-1 Harmonics of Dynamic Tests Time-histories (% Amplitude, Fr = 0.280).

Test	Var (χ)	χ_1	χ_2	χ_3	χ_4	χ_5	χ_6
Pure sway	X	-	72.8	-	12.7	-	33.1
	Y	99.3	-	3.1	-	2.1	-
	N	98.0	-	2.5	-	0.4	-
Pure yaw	X	-	66.8	-	23.9	-	31.8
	Y	89.2	-	11.6	-	2.9	-
	N	95.7	-	5.8	-	1.1	-
Yaw and drift	X	69.4	30.4	14.6	9.5	10.8	21.7
	Y	93.5	22.2	5.8	2.1	1.6	1.9
	N	98.0	11.1	3.0	0.7	0.9	0.8

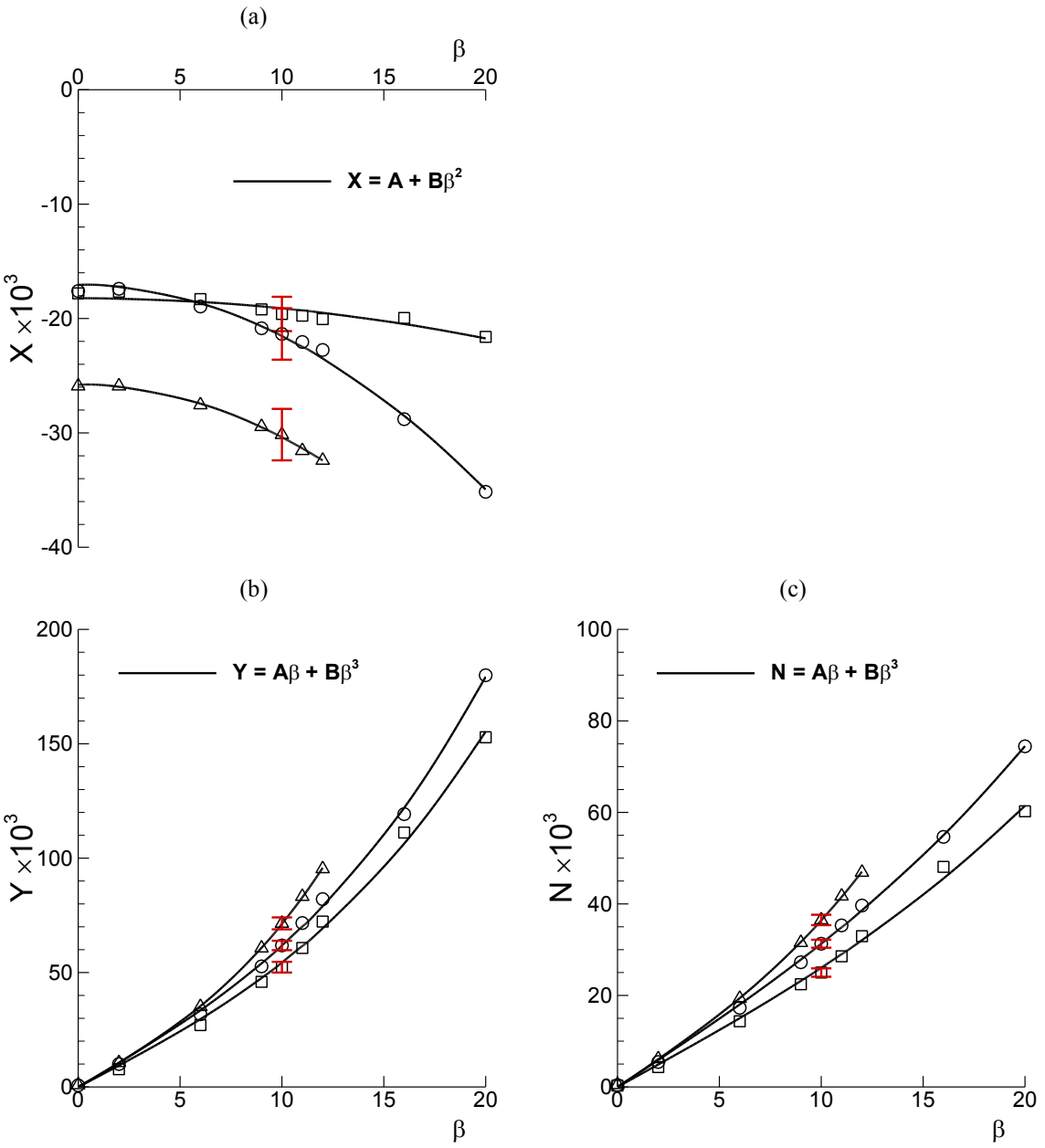

Figure 6-1 Static drift test data (Corrected for symmetry): (a) X, (b) Y, and (c) N. Symbols: □ Fr = 0.138, o Fr = 0.280, Δ Fr = 0.410.

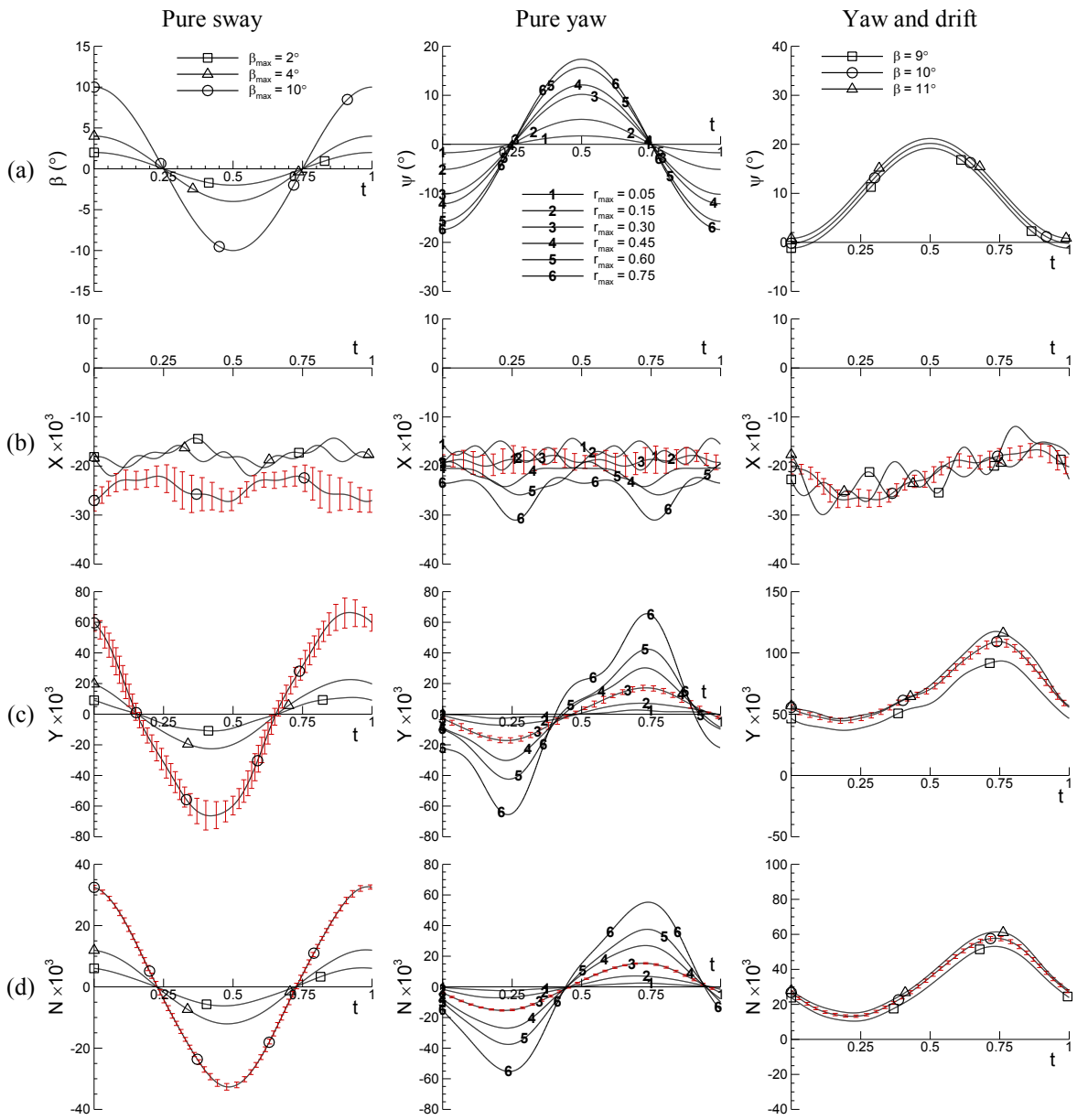

Figure 6-2 Time-histories for pure sway (left), pure yaw (center), and yaw and drift (right) tests at Fr = 0.280 (Corrected for symmetry): Forced-motions (a) β and ψ; and responses in (b) X, (c) Y, and (d) N.

6.1.2 Hydrodynamic Derivatives

6.1.2.1 Static drift test

Hydrodynamic derivatives X_*, X_{vv}, Y_v, Y_{vvv}, N_v, and N_{vvv} in the mathematic models (2.19) in Section 2.3.3 are presented in Table 6-2. Those derivatives were determined by fitting the time-mean values of static drift X, Y, and N data shown in Fig. 6-1 to the polynomial equations (2.27) by using the relation $v = -\sin\beta$ derived in (2.13). The polynomial coefficients A's and B's in (2.27) were evaluated by using a Least-Squared-error (LS) method and then used in (2.28) to determined the derivatives.

6.1.2.2 Dynamic tests

Hydrodynamic derivatives in the mathematic models (2.20), (2.22), and (2.24) in Section 2.3.3 are determined from the pure sway, pure yaw, and yaw and drift tests data, respectively, through the harmonics forms of the mathematic models, (2.21), (2.23), and (2.25), respectively. The harmonics X_0, X_{Sn}, X_{Cn}, Y_0, Y_{Sn}, Y_{Cn}, N_0, N_{Sn}, and N_{Cn} for n = 1, 2, or 3, in the mathematic models were evaluated as per (2.30) in Section 2.3.5 for the dynamic PMM tests X, Y, and N time-histories (e.g. Fig. 6-2), plotted in Figs. 6-3, 6-4, and 6-5 for pure sway, pure yaw, and yaw and drift tests data, respectively. In the figures, the harmonics data are plotted against v_{max} , $\dot{v}_{max}$, r_{max} , $\dot{r}_{max}$, or v as necessary per the mathematic models summarized in Table 2-3. Determinations of hydrodynamic derivatives are as per introduced in Section 2.3.5, either by using the '*Multiple-Run*' method (including MR_L and MR_H) or by using the '*Single-Run*' method (including SR_L and SR_H), as summarized in Tables 2-4 and 2-5, respectively.

'Multiple-Run' method:

Hydrodynamic derivatives using the MR_L and MR_H methods are presented in Tables 21 and 22, respectively. Herein, the results for MR_L are discussed first in the or-

der of sway, yaw, and cross-coupled derivatives, and then the derivatives from MR_H are compared with the MR_L.

Sway derivatives X_{vv} (including X_*), and Y_v, Y_{vvv} and N_v, N_{vvv}, and $Y_{\dot{v}}$ and $N_{\dot{v}}$ are determined from the pure sway data FS harmonics, shown in Fig. 6-3 (a) X_0, (c) Y_{C1} and N_{C1}, and (d) Y_{S1} and N_{S1}, respectively, for β_{max} = 2°, 4°, and 10° (correspond to v_{max} = 0.035, 0.070, and 0.174, respectively) cases. From Fig. 6-3 (a) and (c), harmonics data exhibit quadratic for X_0 and cubic for Y_{C1} and N_{C1} trends with v_{max} (i.e. with β_{max}), respectively, similarly as static drift data discussed previously in Section 6.1.1. However, the magnitudes of data are in general larger, smaller, and similar with (than) the static drift X, Y, and N data (shown as dashed lines), respectively. When λ is defined[10] similarly as for static drift data in (6-1), with β replaced with β_{max}, then λ = 0.43, 0.25, and 0.07 for X_0, Y_{C1}, and N_{C1} at β_{max} = 10°, respectively, indicating that the non-linearity of those harmonics data are more stronger than the static drift X, Y, and N data (λ = 0.26, 0.18, and 0.07, respectively, at β = 10° and at Fr = 0.280). This will be discussed again later at the MR_H method part. Y_{S1} and N_{S1} data shown in Fig. 6-3 (d) exhibit linear trend with $\dot{v}_{max}$ as expected from their mathematic models presented Table 2-3. In that Y_{S1} and N_{S1} stem from the acceleration terms ('added-mass') in the mathematic models (2.20b) and (2.20c) and Y_{C1} and N_{C1} from the velocity terms ('damping'), the ratios between the harmonics may of interest. For Y as an example, Y_{S1}/Y_{C1} represents the ratio

---

[10] λ can be rewritten by using the mathematic models for X_0, Y_{C1}, and N_{C1} shown in Table 2-3 as:

$$\lambda = \frac{1}{2}\frac{X_{vv}}{X_*}v_{max}^2 \; ; \; \frac{3}{4}\frac{Y_{vvv}}{Y_v}v_{max}^2 \; ; \; \frac{3}{4}\frac{N_{vvv}}{N_v}v_{max}^2$$

respectively.

between the 'added-mass' and 'damping' forces, which corresponds to the tangent value of the 1st-order phase of the Y time-history as[11]

$$\tan\varphi_{Y1} = \frac{Y_{\dot{v}}\omega}{Y_v(1+\lambda)} \tag{6.3}$$

Similarly, $\tan\varphi_{N1}$ can be written by replacing $Y_{\dot{v}}$ and Y_v in (6-3) with $N_{\dot{v}}$ and N_v, respectively. For λ = 0, then, the ratio (or the 1st-order phase) is a constant value, for present case, 0.730 and 0.135 (or, φ_{Y1} = 36.1° and φ_{N1} = 7.7°) for Y and N, respectively, for a given ω = 1.672, indicating that the 'damping' force is larger than the 'added-mass' force for Y and the former is predominant for N, respectively.

X_*, X_{vv}, Y_v, Y_{vvv}, N_v, and N_{vvv} are compared in Table 6-3 with those from the static drift data at Fr = 0.280 presented in Table 6-2. In general, the linear derivatives X_*, Y_v, and N_v are close to static drift values with ratios 1.02, 0.88, and 1.01, respectively, whereas the non-linear derivatives X_{vv}, Y_{vvv}, and N_{vvv} are larger with ratios 3.12, 1.53, and 1.30, respectively, possibly due to the stronger non-linearity in the pure sway FS harmonics data discussed previously.

Yaw derivatives X_{rr} (including X_*), and Y_r and Y_{rrr}, and $Y_{\dot{r}}$, and N_r and N_{rrr}, and $N_{\dot{r}}$ are determined from the pure yaw data FS harmonics, shown in Fig. 6-4 (a) X_0, (c) Y_{S1}, (d) Y_{C1}, (f) N_{S1}, and (g) N_{C1}, respectively, for r_{max} = 0.05 – 0.75 cases at Fr = 0.138, 0.280, and 0.410. In general, X_0, Y_{S1}, and N_{S1} in Fig. 6-4 (a), (c), and (f) exhibit curve shapes similar as the static drift X, Y, and N curves shown in Fig. 6-1. However, pure

---

[11] A combination of sine and cosine functions, $A\sin\omega t + B\cos\omega t$, can be rewritten as $\sqrt{A^2+B^2}\cdot\cos(\omega t+\varphi)$ where,

$$-\tan\varphi = A/B$$

In this case, $A = Y_{S1}$ and $B = Y_{C1}$, where $Y_{S1} = Y_{\dot{v}}\dot{v}_{max}$ and $Y_{C1} = -\left(Y_v v_{max} + \frac{3}{4}Y_{vvv}v_{max}^3\right)$, which can be rewritten as $Y_{S1} = Y_{\dot{v}}\omega\cdot v_{max}$ and $Y_{C1} = -Y_v\lambda\cdot v_{max}$, respectively.

yaw harmonics data are less non-linear with r_{max} with λ = 0.08, 0.06, and 0.07, respectively, at r_{max} = 0.30 (ψ_{max} = 10.2°) at Fr = 0.280, defined[12] similarly as (6-1) with β replaced with r_{max}, than static drift X, Y, and N data (λ = 0.26, 0.18, and 0.07, respectively, at β = 10° and at Fr = 0.280). Y_{C1} and N_{C1} shown in Fig. 6-4 (d) and (g) exhibit linear trend with $\dot{r}_{max}$ as expected from their mathematic models shown in Table 2-3, whereas more scatters in data curve-fits are observed (particularly for Y_{C1} at Fr = 0.280) than the pure sway Y_{S1} and N_{S1} data shown in Fig. 6-3 (d). The ratio Y_{S1}/Y_{C1} or N_{S1}/N_{C1} can be similarly defined as (3) for pure sway as (See footnote 11)

$$-\tan\varphi_{Y1} = \frac{Y_r(1+\lambda)}{Y_{\dot{r}}\omega} \tag{6.4}$$

and $\tan\varphi_{N1}$ as well, which are the ratios of the 'damping' force to the 'added-mass' force as discussed previously. For λ = 0 (and for a fixed ω = 1.672), the ratios are 3.223 and 4.144 (or, φ_{Y1} = 107.2° and φ_{N1} = 103.6°) for Y and N, respectively, at Fr = 0.280, indicating that the 'damping' forces are about three and four times, respectively, larger than the 'added-mass' forces.

Cross-coupled derivatives X_{vr}, Y_{rvv} and N_{rvv}, and Y_{vrr} and N_{vrr} are from the yaw and drift data FS harmonics, shown in Fig. 6-5 (b) X_{S1}, (d) Y_0 and N_0, and (e) Y_{S1} and N_{S1}, respectively, for β = 9°, 10°, and 11° (correspond to v = -0.156, -0.174, and -0.191, respectively) cases. X_{S1} in Fig. 6-5 (b) is solely due to the cross-couple effect between the sinusoidal yaw motion and the drift angle β, which is not measured from pure yaw tests. Data exhibit roughly linear trend with v, however, with rather large scatters in the

---

[12] λ can be rewritten by using the mathematic models for X_0, Y_{S1}, and N_{S1} shown in Table 2-3 as:

$$\lambda = \frac{1}{2}\frac{X_{rr}}{X_*}r_{max}^2 \;;\; \frac{3}{4}\frac{Y_{rrr}}{Y_r}r_{max}^2 \;;\; \frac{3}{4}\frac{N_{rrr}}{N_r}r_{max}^2$$

respectively.

curve-fit. Y_0 and N_0 shown in Fig. 6-5 (d) are from both of the drift angle β and the cross-couple effect, and those harmonics values are about 11% and 5% larger at β = 10° than the static drift Y and N at the same drift angle (shown as dashed and dash-dot lines, respectively). Y_{S1} and N_{S1} in Fig. 6-5 (e) are from both of the sinusoidal yaw motion and the cross-couple effect. Cross-couple effect is rather stronger for Y_{S1} and N_{S1} than for Y_0 and N_0 cases, and their values at β = 10° are about 89% and 44% larger than the pure yaw Y_{S1} and N_{S1} data (shown as dashed and dash-dot lines, respectively) at the same r_{max} = 0.3 condition.

Non-linear derivatives X_{vv}, X_{rr}, Y_{vvv}, Y_{rrr}, Y_{vrr}, N_{vvv}, N_{rrr}, and N_{vrr} determined using the MR_H method are presented in Table 6-4. For MR_H, X_{vv} is determined from the 2nd-order cosine harmonic X_{C2} of pure sway data, shown in Fig. 6-3 (b), where the data exhibit quadratic trend with v_{max} as expected from its mathematic model shown in Table 2-3. The MR_H, however, gives rather smaller X_{vv} value than the MR_L, with a ratio 0.27, nevertheless, the value is closer to static drift X_{vv} value with a ratio 0.85 than the MR_L value (the ratio was 3.12 in Table 6-3). The MR_H gives smaller X_{rr} values than the MR_L similarly for X_{vv}, showing ratio values between 0.2 – 0.5 presented in Table 6-4. This may indicate that the X force in dynamic PMM is more non-linear than the 2nd-order, i.e., functions of v^2 or r^2 as assumed in the mathematic models (2.20a) and (2.22a), respectively, and suggests to include higher order terms such as v^4, v^6 and r^4, r^6 to the mathematic models, which result in additional terms $\frac{3}{8}X_{vvvv}v_{max}^4$, $\frac{5}{16}X_{vvvvvv}v_{max}^6$ and $\frac{3}{8}X_{rrrr}r_{max}^4$, $\frac{5}{16}X_{rrrrrr}r_{max}^6$ to the 0th-order harmonic X_0, respectively. Those higher order terms as well result in the 4th- and the 6th-order harmonics $X_{C4}\cos 4\omega t$ and $X_{C6}\cos 6\omega t$ to the X mathematic models (2.21a) and (2.23a), which may explain the relatively larger X_4 and X_6 in the pure sway and pure yaw X time-histories discussed previously in Section 6.1.1. On the other hand, the Y derivatives such as Y_{vvv}, Y_{rrr}, and Y_{vrr} and the N derivatives such as N_{vvv}, N_{rrr}, and N_{vrr} values from MR_H are usually larger than those from MR_L with the ratios about 1.0 – 3.0 except for a few cases as shown in Table 6-4.

'Single-Run' Method:

Sway derivatives using the 'Single-Run' (SR) method are shown in Fig. 6-6 for (a) linear derivatives Y_v, N_v, $Y_{\dot{v}}$, and $N_{\dot{v}}$ including X_* and (b) non-linear derivatives X_{vv}, Y_{vvv}, and N_{vvv}, for β_{max} = 2°, 4°, and 10° cases. In the figures, the derivatives are shown as scaled values to the MR_L for comparisons. Typically, the linear derivatives shown in Fig. 6-6 (a) are close to MR_L with ratios between 0.9 – 1.1 except for a few cases. In contrast, the non-linear derivatives in Fig. 6-6 (b) are in general larger than MR_L values with ratios 1.0 – 3.0 except for a few cases, showing a tendency to approach to the MR_L values as β_{max} increases.

Yaw derivatives using the SR method are shown in Fig. 6-7 for (a) Y_r, N_r, $Y_{\dot{r}}$, and $N_{\dot{r}}$ including X_* and (b) X_{rr}, Y_{rrr}, and N_{rrr}, respectively, for r_{max} = 0.05 – 0.75 at Fr = 0.138, 0.280, and 0.410 conditions, with scaled to the MR_L values. The overall trends are similar as the sway derivatives; values are close to MR_L for the linear derivatives and larger than MR_L for the non-linear derivatives. The linear derivatives shown in Fig. 6-7 (a) at small r_{max} are in general smaller or larger than the MR_L with ratios 0.1 – 1.7 and approach to the MR_L values as r_{max} increases, except for Y_r at Fr = 0.138 and 0.280, continuously decreasing with r_{max}. The non-linear derivatives shown in Fig. 6-7 (b) exhibit huge ratio values ranging between -210 and 60 (used in the figure are the absolute values for the log scale), decreasing with r_{max} but still larger ratio values 0.5 – 3.5 at r_{max} = 0.75.

Cross-coupled derivatives X_{vr}, Y_{vrr}, N_{vrr}, Y_{rvv}, and N_{rvv} are shown in Fig. 6-8 (a) with scaled to the MR_L values, where the Y_{vrr} and N_{vrr} are from the SR_L method and those from the SR_H are shown in Fig. 6-8 (b), respectively, for β = 9°, 10°, and 11° cases. X_{vr}, Y_{rvv}, and N_{rvv} shown in Fig. 6-8 (a) are fairly close to the MR_L values with ratios 0.8 – 1.2. The ratios for Y_{vrr} and N_{vrr} using the SR_L method shown in Fig. 6-8 (a) are relatively large, 0.5 – 1.4, whereas the ratios for those derivatives using the SR_H method

shown in Fig. 6-8 (b) are very close to 1.0 for Y_{vrr} and relatively large, 1.4 – 1.7, for N_{vrr}, respectively.

In summary, the '*Single-Run*' method gives the linear sway and yaw, and the cross-coupled derivatives similar values as the '*Multiple-Run*' method as the dynamic PMM motion becomes larger (i.e, larger β_{max} and r_{max} values), whereas it gives typically larger or smaller non-linear sway and yaw derivatives values particularly at smaller PMM motion conditions.

Reconstruction Errors:

The validities of the hydrodynamic derivatives determined using the '*Multiple-Run*' and '*Single-Run*' methods are evaluated by examining the errors in reconstruction of forces and moment time-histories data. Reconstructions are by using the mathematic models (2.21), (2.23), and (2.25) where first the harmonic amplitude terms such as X_0, X_{C2}, …, N_{S3} are calculated using the derivatives values and then the time-histories of X, Y, and N are reconstructed (also see Table 2-3). Subsequently, the reconstruction error E_R is defined as

$$E_R(\%) = \frac{\sum_i^M |D_i - R_i|}{\sum_i^M |D_i|} \times 100 \tag{6.5}$$

where, D_i is the measured data from the PMM tests, R_i is the reconstructed data by using the mathematic models, subscript i represents the time t_i, and M is the total number of data points.

The E_R's in reconstructing the time-histories of pure sway, pure yaw, and yaw and drift data shown in Fig. 6-2 are calculated using the sway, yaw, and cross-coupled derivatives, respectively, using the '*Multiple-Run*' (MR_L and MR_H) and the '*Single-Run*' (SR) methods, and the average errors $\overline{E_R}$ for all β_{max}, r_{max}, and β cases, respectively, are presented in Tables 6-5, 6-6, and 6-7, respectively. For sway and yaw derivatives in

Tables 6-5 and 6-6, the $\overline{E_R}$'s are the smallest for the derivatives using the MR_L method, and the $\overline{E_R}$'s for the derivatives using the MR_H method are relatively larger in general. The $\overline{E_R}$'s for derivatives using the SL method are typically large, particularly for the derivatives from the smallest motion cases such as the sway derivatives from the pure sway data for β_{max} = 2° case ($SR_{2°}$) and the yaw derivatives from the pure yaw data for r_{max} = 0.30 case ($SR_{0.30}$), and tend to decrease as the PMM motions become large, showing similar values as the MR_H in general. In Table 6-5, the $\overline{E_R}$'s for the sway derivatives from the static drift test are compared with those from the pure sway test, of which values are relatively larger than those for MR_L method but close to those for MR_H method case. For cross-coupled derivatives in Table 6-7, the $\overline{E_R}$'s are similarly small for all method cases as the yaw and drift motions are sufficiently large (β = 9°, 10°, and 11° and r_{max} = 0.30) from which the derivatives are determined. Consequently, the '*Multiple-Run*' (MR_L) method is more rigorous than the '*Single-Run*' method determining the hydrodynamic derivatives and the latter method is suggested only when the PMM motions are large enough.

6.1.2.3 Speed variation test

Surge derivatives were evaluated as per Section 2.3.5 using the sway and yaw derivatives determined previously for three *Fr*'s, 0.138, 0.280, and 0.410, cases. For this, the sway derivatives from the static drift tests (Table 6-2) and the yaw derivatives using the MR_L method (Table 6-3) were used, which are shown in Fig. 6-9 as functions surge velocity, u. In the figure, surge velocity is non-dimensionalized such that $\Delta u = (u - U)/U$, where u is the surge velocity at each *Fr* and U is that at *Fr* where the surge derivatives are determined (herein, *Fr* = 0.280). In the figure, all derivatives were normalized with the values at *Fr* = 0.280. From Fig. 6-9 (a), for sway derivatives, X_* and X_{vv} show strong dependency on Δu, i.e. *Fr*, with their normalized values changing between 1.1 to 1.5 and 0.2 to 1.0, respectively. Whereas Y_v and N_v are almost independent on Δu showing the normalized values ranging between 0.9 and 1.0 and 0.8 and 1.0, respectively.

The yaw derivatives in Fig. 6-9 (b) show similar trends. The normalized X_{rr} values increase rather monotonically from 0.3 to 1.4 within the speed range, and the normalized Y_r and N_r values vary moderately between 0.6 ~ 1.1 and 0.8 ~ 1.0. In summary, typically the linear derivative such Y_v, N_v, Y_r, and N_r are nearly in dependent with the speed (Fr) changes, whereas the non-linear derivatives X_{vv}, Y_{vvv}, N_{vvv}, X_{rr}, Y_{rrr}, and N_{rrr} exhibit rather strong dependency on the speed (Fr) changes.

Subsequently, those derivatives were curve fitted to the 2nd-order polynomial functions of Δu as per equation (2.35), from which surge derivatives such as X_u, X_{uu} and X_{vvu}, Y_{vu}, Y_{vuu}, N_{vu}, N_{vuu} are evaluated using (2.36) and (2.37), respectively, and presented in Table 26. Note that the derivatives X_{uuu} and X_{vru} are not evaluated herein due to the limited number of Fr cases in the present PMM test matrix (shown in Table 3-3) for static drift and yaw and drift tests, respectively.

Table 6-2 Hydrodynamic Derivatives (Static Drift).

Derivative	Fr = 0.138	Fr = 0.280	Fr = 0.410
X_*	-0.0182	-0.0170	-0.0258
X_{vv}	-0.0301	-0.1528	-0.1544
Y_v	-0.2637	-0.2961	-0.2963
Y_{vvv}	-1.6256	-1.9456	-3.7914
N_v	-0.1396	-0.1667	-0.1717
N_{vvv}	-0.3426	-0.4355	-1.2591

Table 6-3 Hydrodynamic Derivatives (MR_L Method).

Derivative	Fr = 0.280	Derivative	Fr = 0.138	Fr = 0.280	Fr = 0.410	Derivative	Fr = 0.280
X_*	-0.0173 (1.02)	X_*	-0.0181 (0.99)	-0.0177 (1.04)	-0.0260 (1.01)		
X_{vv}	-0.4765 (3.12)	X_{rr}	-0.0078	-0.0282	-0.0385	X_{vr}	0.0819
Y_v	-0.2601 (0.88)	Y_r	-0.0276	-0.0485	-0.0548	Y_{vrr}	-0.8682
Y_{vvv}	-2.9686 (1.53)	Y_{rrr}	-0.0370	-0.0452	-0.0710	Y_{rvv}	-1.5172
N_v	-0.1681 (1.01)	N_r	-0.0382	-0.0485	-0.0548	N_{vrr}	-0.1989
N_{vvv}	-0.5677 (1.30)	N_{rrr}	-0.0211	-0.0505	-0.0821	N_{rvv}	-0.7220
$Y_{\dot{v}}$	-0.1135	$Y_{\dot{r}}$	-0.0146	-0.0090	-0.0127		
$N_{\dot{v}}$	-0.0136	$N_{\dot{r}}$	-0.0065	-0.0070	-0.0077		

( ): ratio to static drift

Table 6-4 Hydrodynamic Derivatives (MR_H Method).

Derivative	Fr = 0.280	Derivative	Fr = 0.138	Fr = 0.280	Fr = 0.410	Derivative	Fr = 0.280
X_{vv}	-0.1296 (0.27)	X_{rr}	-0.0016 (0.21)	-0.0132 (0.47)	-0.0163 (0.42)		
Y_{vvv}	-2.2962 (0.77)	Y_{rrr}	-0.0927 (2.51)	-0.1305 (2.89)	-0.1210 (1.70)	Y_{vrr}	-0.9066 (1.04)
N_{vvv}	-0.8533 (1.50)	N_{rrr}	-0.0312 (1.48)	-0.0473 (0.94)	-0.0387 (0.47)	N_{vrr}	-0.3161 (1.59)

( ): ratio to MR_L

Table 6-5 Reconstruction Errors (Sway derivatives).

Errors	Var.	MR_L	[1)]MR_H	$SR_{2°}$	$SR_{4°}$	$SR_{10°}$	[2)]Static drift
$\overline{E_R}$ (%)	X	9.4	12.0	22.8	9.4	19.5	12.2
	Y	5.5	6.2	5.1	10.1	7.3	10.5
	N	2.9	4.0	30.2	6.1	3.9	3.6

[1)] $Y_{\dot{v}}$, $N_{\dot{v}}$, Y_v, and N_v from the MR_L were used for reconstructions
[2)] $Y_{\dot{v}}$ and $N_{\dot{v}}$ from the MRL were used for reconstructions

Table 6-6 Reconstruction Errors (Yaw derivatives).

Errors	Var.	MR_L	[1)]MR_H	$SR_{0.05}$	$SR_{0.15}$	$SR_{0.30}$	$SR_{0.45}$	$SR_{0.60}$	$SR_{0.75}$
$\overline{E_R}$ (%)	X	7.6	9.5	549.4	52.2	12.1	8.5	9.2	13.8
	Y	17.2	29.5	106.2	56.3	25.2	27.2	31.2	45.7
	N	5.2	5.2	616.2	22.4	5.3	6.6	5.5	6.7

[1)] $Y_{\dot{r}}$, Y_r, $N_{\dot{r}}$, N_r values from the MR_L method were used for reconstructions.

Table 6-7 Reconstruction[1)] Errors (Cross-coupled derivatives).

Errors	Var.	MR_L	[2)]MR_H	$SR_{L9°}$	$SR_{L10°}$	$SR_{L11°}$	[3)]$SR_{H9°}$	[3)]$SR_{H10°}$	[3)]$SR_{H11°}$
$\overline{E_R}$ (%)	X	11.0	-	11.1	11.0	11.0	-	-	-
	Y	3.5	3.5	3.6	5.2	5.5	3.6	3.5	3.7
	N	2.7	3.0	2.4	2.4	4.6	2.9	2.5	3.6

[1)] For reconstructions, X_*, X_{vv}, Y_v, Y_{vvv}, N_v, and N_{vvv} from static drift, and $Y_{\dot{r}}$, Y_r, Y_{rrr}, $N_{\dot{v}}$, N_r, and N_{rrr} using the MR_L method were used.
[3)] X_{vr}, Y_{rvv}, N_{rvv} using MR_L were used for reconstructions
[4)] X_{vr}, Y_{rvv}, N_{rvv} using SR_L were used for reconstructions.

Table 6-8 Surge-derivatives (Fr = 0.280).

Derivative	Value	Derivative	Value
X_u	-0.0088		
X_{uu}	-0.0220		
X_{vvu}	-0.1172	X_{rru}	-0.0308
Y_{vu}	-0.0307	Y_{ru}	-0.0268
Y_{vuu}	0.0653	Y_{ruu}	0.0284
N_{vu}	-0.0311	N_{ru}	-0.0183
N_{vuu}	0.0439	N_{ruu}	-0.0066

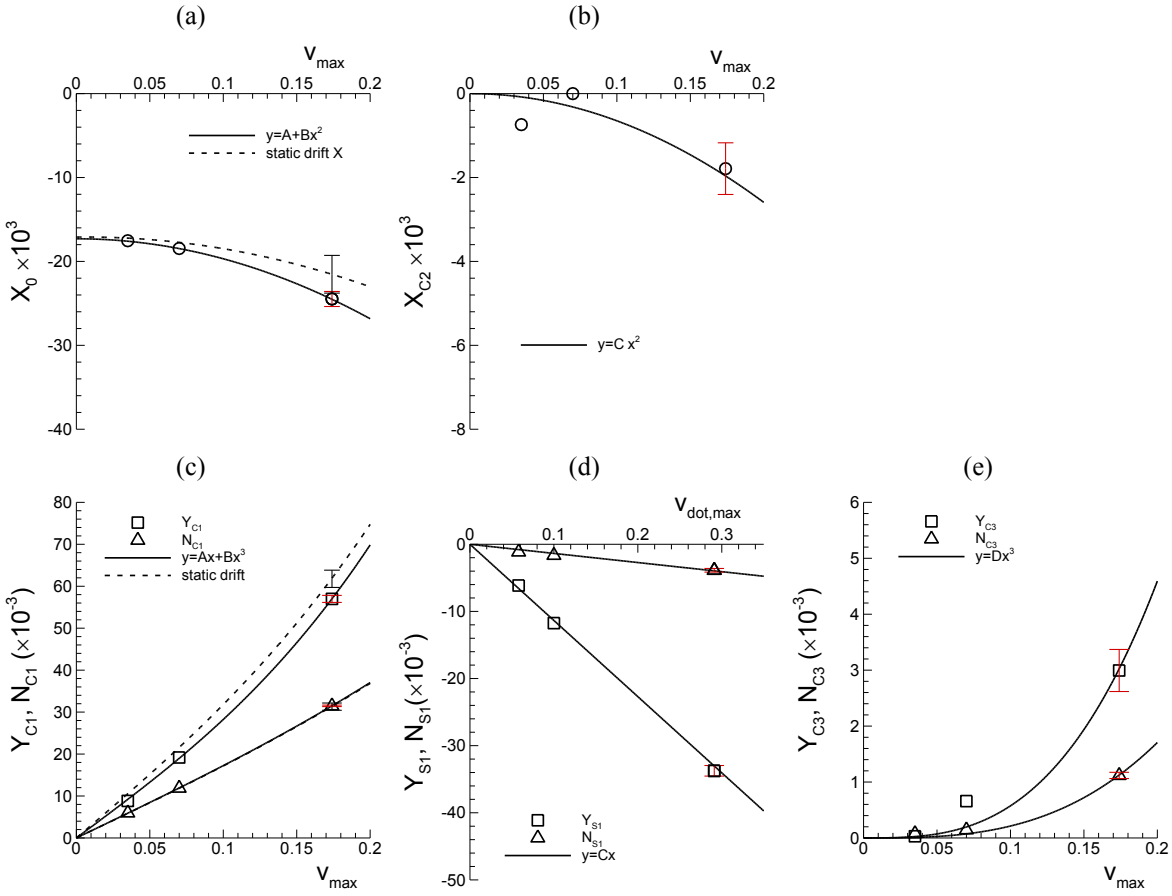

Figure 6-3 Pure sway X, Y, and N data FS harmonics: (a) X_0, (b) X_{C2}, (c) $Y_{C1}$and N_{C1}, (d) Y_{S1} and N_{S1}, and (e) Y_{C3} and N_{C3}.

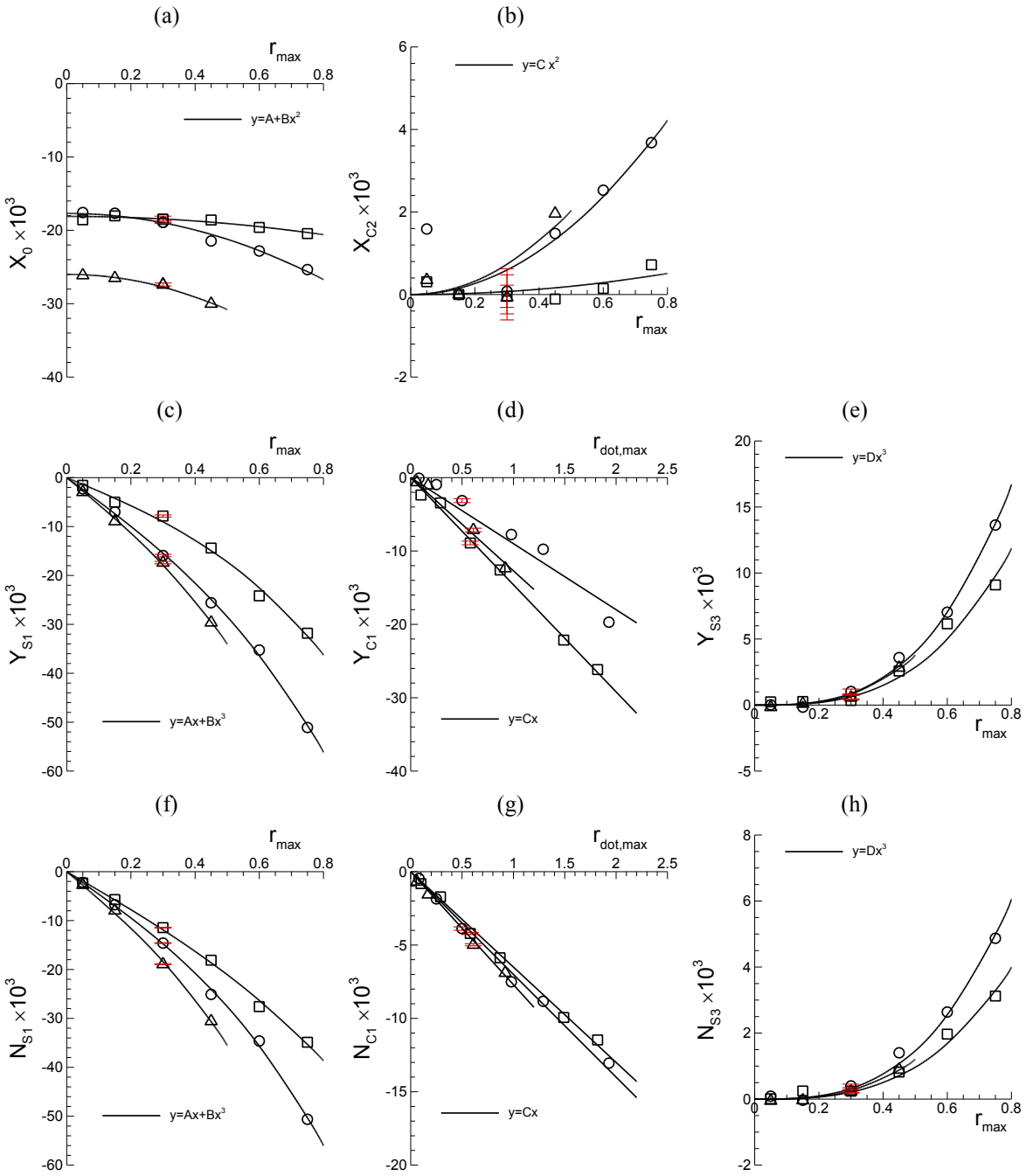

Figure 6-4 Pure yaw X, Y, and N data FS harmonics: (a) X_0, (b) X_{C2}, (c) Y_{S1}, (d) Y_{C1}, (e) Y_{S3}, (f) N_{S1}, (g) N_{C1}, and (h) N_{S3}. Simbols: □, Fr = 0.138; o, Fr = 0.280; Δ, Fr = 0.410.

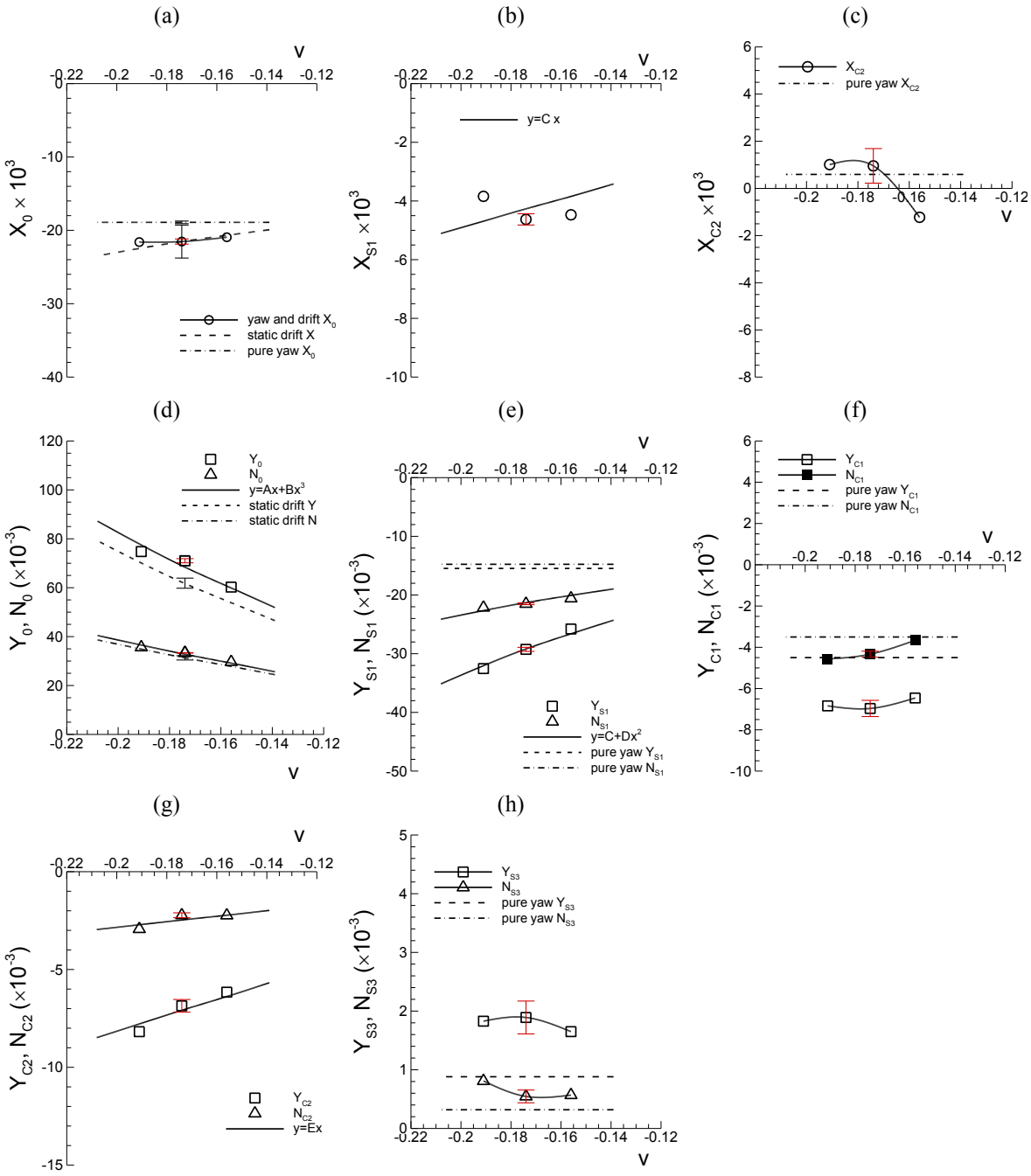

Figure 6-5 Yaw and drift X, Y, and N data FS harmonics: (a) X_0, (b) X_{S1}, (c) X_{C2}, (d) Y_0 and N_0, (e) Y_{S1} and N_{S1}, (f) Y_{C1} and N_{C1}, (g) Y_{C2} and N_{C2}, and (h) Y_{S3} and N_{S3}.

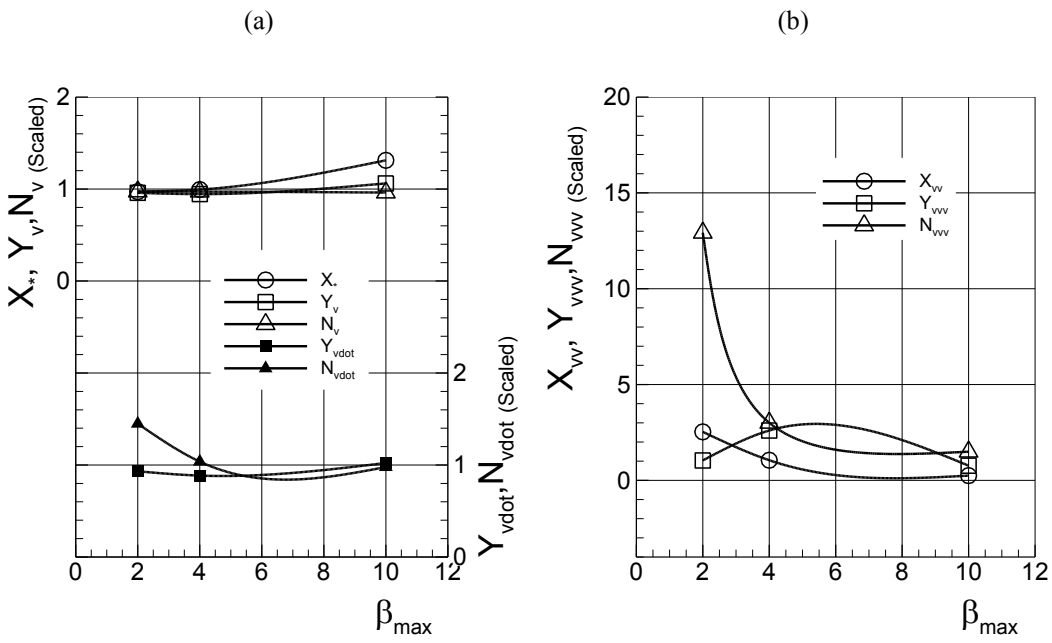

Figure 6-6 Single-run method (sway derivatives): (a) linear and (b) non-linear derivatives. Hydrodynamic derivatives shown are scaled with MR_L.

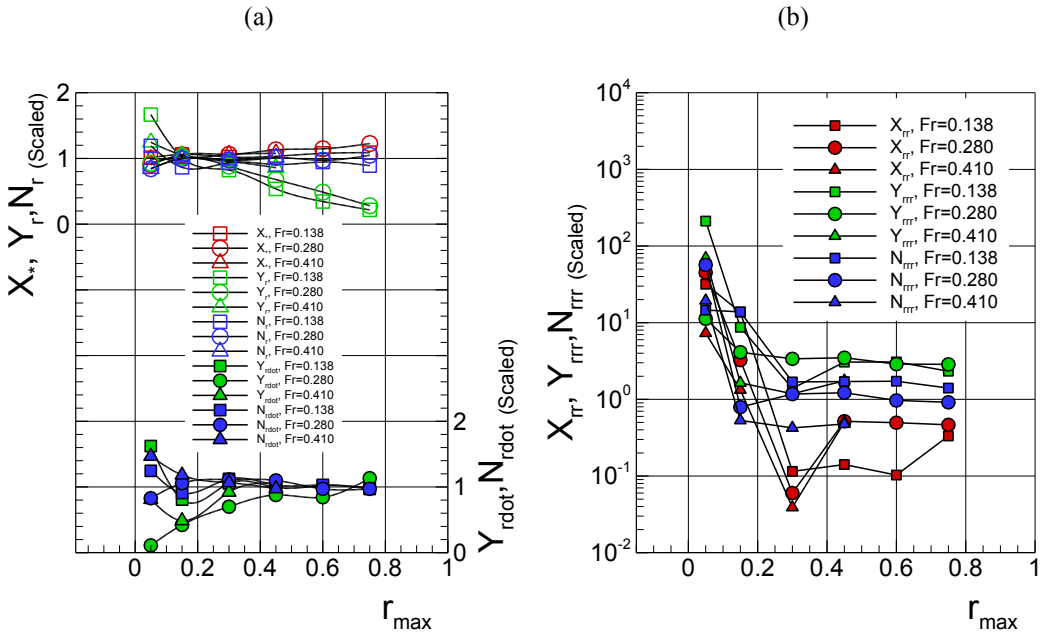

Figure 6-7 Single-run method (yaw derivatives): (a) linear and (b) non-linear derivatives. Hydrodynamic derivatives shown are scaled with MR_L.

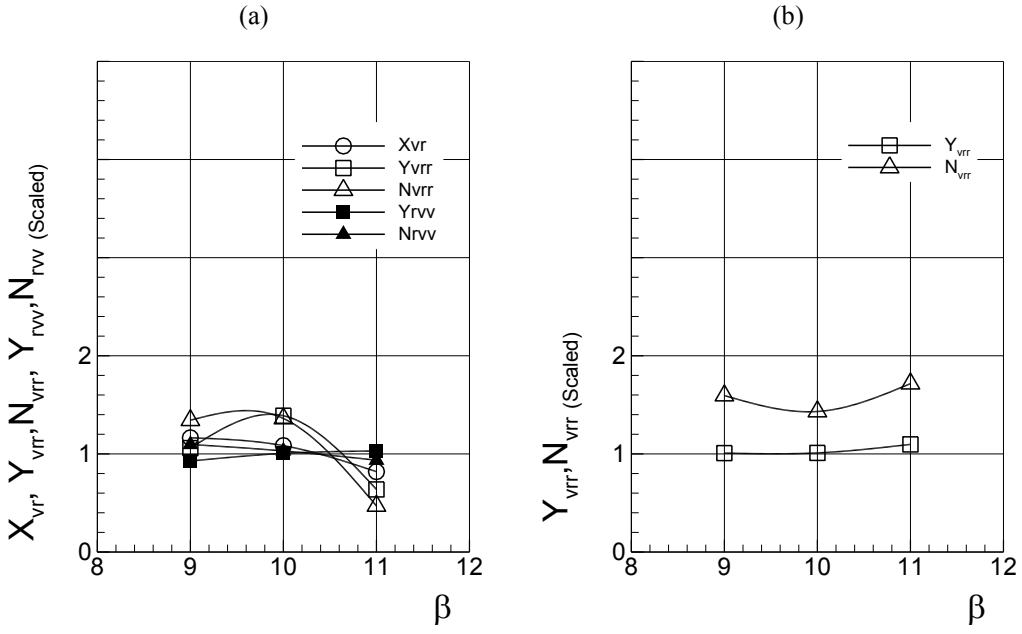

Figure 6-8 Single-Run method (cross-coupled derivatives): (a) SR_L (b) SR_H. Hydrodynamic derivatives shown are scaled with MR_L.

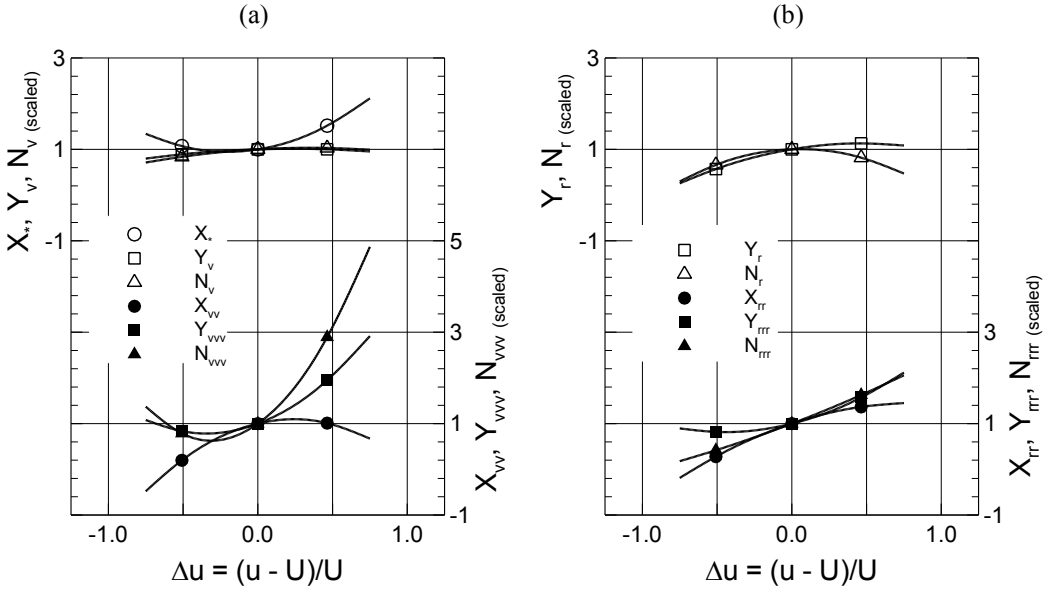

Figure 6-9 Speed variation test: Hydrodynamic derivatives with surge velocity change Δu: (a) Sway and (b) yaw derivatives. Hydrodynamic derivatives shown are scaled with the values at $\Delta u = 0$ (Fr = 0.280).

6.1.3 Comparisons between Facilities

Forces and moment and subsequent hydrodynamic derivatives from three facilities (IIHR, FORCE, and INSEAN) are compared. All the facilities shared the same geometry (DTMB 5415) and the same PMM test matrix (Table 3-3, for the $FR_{z\theta}$ condition only). The model length L used for each facility is 3.048 m, 4.002 m, and 5.720 m, respectively, and the specific model particulars are summarized in Table 3-1. The comparisons include evaluations of the standard deviation[13] from the facility mean values (the mean values of the three facilities data) of the time-mean values of X, Y, and N data for static drift test and those of the harmonic amplitude and phase of the time-histories data as per (2) for dynamic tests. Herein, the standard deviation values are presented in percent of the facility mean values. Subsequently, hydrodynamic derivatives are compared between the facilities data and possible effects of model size are discussed.

Static drift X, Y, and N are shown in Fig. 6-10 (a), (b), and (c), respectively, for Fr = 0.138 (left), 0.280 (middle), and 0.410 (right) cases, respectively. The facility mean and standard deviation values of X, Y, and N data at β = 10° for the three Fr cases are presented in Table 6-9. From Fig. 6-10 (a), X data exhibit relatively large deviations from facility to facility with standard deviations about 9% - 11% at β = 10°. Y and N data in Fig. 6-10 (b) and (c) in general show good agreements between facilities, where the standard deviations at β = 10° are about 1% - 4% except for a few cases. In the figure, data are curve fitted (solid lines for FORCE and INSEAN, and dashed lines for IIHR) to quadratic, $X = A + B\beta^2$, and cubic, $Y, N = A\beta + B\beta^3$, functions similarly as discussed in Section 6.1.1. For X in Fig. 6-10 (a), the intercept A is different from facility to facility, more or less, whereas the 2nd-order coefficient B is seemingly similar between

[13] Although the number of facilities, three, is minimal for a normal distribution, nevertheless the standard deviation shows a value close to the average deviation of data from the facility mean values.

facilities except for the Fr = 0.138 case. For Y and N in Fig. 6-10 (b) and (c), the 1st-order (linear) coefficient A is similar between facilities, whereas the 3rd-order (non-linear) coefficient B is different from facility to facility in general. The quantitative comparisons of those coefficients will be discussed later with related to the comparisons of the sway derivatives.

Dynamic test time-histories of X, Y, and N are shown in Fig. 6-11 (a), (b), and (c), respectively, for pure sway (left, β_{max} = 10° case), pure yaw (middle, r_{max} = 0.30 case), and yaw and drift (right, β = 10° case) tests for Fr = 0.280 case, respectively. While the data exhibit in general good agreements between facilities, the mean and standard deviation values of the dominant harmonic amplitude and phase are presented in Table 6-10. In Fig. 6-11 (a), X time-histories show relatively large deviations between facilities data. Nonetheless, the standard deviations of the 0th-order amplitude X_0 are fairly small, 14.9%, 6.2%, and 7.5% for pure sway, pure yaw, and yaw and drift tests, respectively, whereas those of the 2nd-order amplitude X_2 and phase φ_{X2} (for yaw and drift X_1 and φ_1) are in general large, 42.9%, 8.3%, and 69.2%, respectively, for the former, and 5.8%, 307.3%, and 76.8%, respectively, for the latter. For Y and N, the time-histories shown in Fig. 6-11 (b) and (c) exhibit good agreements between facilities, where the standard deviations of the 1st-order amplitude Y_1 and phase φ_{Y1} are small, about 4% - 6% and about 2% - 10%, respectively, for all test types. For yaw and drift Y and N, the standard deviations of the 0th-order amplitude Y_0 and N_0 are also small about 2%.

Hydrodynamic derivatives from the facilities data are compared in Tables 6-11 through 6-14 for the sway, yaw, cross-coupled, and surge derivatives, respectively. Presented in the tables are the facility mean and standard deviation values and the ratio values of each facility data to the facility mean values. The sway velocity derivatives X_{vv}, Y_v, Y_{vvv}, N_v, and N_{vvv}, including X_*, are determined from the static drift data and the sway acceleration derivatives $Y_{\dot{v}}$ and $Y_{\dot{v}}$ are from the pure sway data using the MR_L method. The yaw derivatives X_{rr}, Y_r, Y_{rrr}, $Y_{\dot{r}}$, N_r, N_{rrr}, and $N_{\dot{r}}$ and the cross-coupled de-

rivatives X_{vr}, Y_{vrr}, Y_{rvv}, N_{vrr}, and N_{rvv} are as well using the MR_L method. The surge derivatives X_u, X_{uu}, X_{vvu}, Y_{vu}, Y_{vuu}, N_{vu}, N_{vuu}, X_{rru}, Y_{ru}, Y_{ruu}, N_{ru}, and N_{ruu} are derived from the aforementioned sway and yaw derivatives as per (2.36) and (2.37) in Section 2.3.5.

Sway and yaw derivatives are compared in Tables 6-11 and 6-12 where the facility mean and standard deviation values are presented. For sway derivatives, X_* and X_{vv} correspond to the intercept A and the 2nd-order coefficient B of the static drift X data curve fits, and Y_v, N_v and Y_{vv}, N_{vvv} correspond to the 1st- and 3rd-order coefficients A and B of the static drift Y and N data curve fits, respectively, discussed previously. Recalling Fig. 6-10 (a), the standard deviation of the intercept values of X data (X_*) is relatively large, about 10% - 14%, whereas the standard deviation of the 2nd-order coefficient (X_{vv}) is relatively small, about 7% - 10% except for the Fr = 0.138 case. For Y and N in Fig. 6-10 (b) and (c), the standard deviations of the 1st-order coefficients (Y_v and N_v) are small, about 2% - 7%, whereas the 3rd-order coefficients (Y_{vvv} and N_{vvv}) are large, about 10% - 30%. On the other hand, from Table 6-11, the standard deviations of the sway acceleration derivatives $Y_{\dot{v}}$ and $N_{\dot{v}}$ are small, 4.4% and 8.8%, respectively. Similar overall trends in comparisons are observed from the yaw derivatives in Table 6-12; relatively small deviations of linear derivatives and large deviations of non-linear derivative, whereas the standard deviation values are rather larger than the sway derivatives cases. The standard deviations of the linear derivatives Y_r and N_r are about 5% - 27%, while those of the non-linear derivatives X_{rr}, Y_{rrr}, and N_{rrr} are fairly large, 37% - 91%, 15% - 72%, and 20% - 55%, respectively. The standard deviations of $Y_{\dot{r}}$ and $N_{\dot{r}}$ are 21% - 34% and 15% - 25%, respectively, which are larger than the sway acceleration derivatives cases.

Ratios of the derivative values to the facility means presented in Tables 6-11 and 6-12 are plotted against the model length in Figs. 6-12 and 6-13 for sway and yaw derivatives, denoted with a '*' symbol, respectively, revealing the possible effect of model size. In the figures, the model lengths of each facility, IIHR, FORCE, and INSEAN, are scaled with the smallest model size corresponding to $L^* = L/L_{3.048\ m} = 1.0$, 1.31, and 1.88, respectively. Subsequently, the ratio values are linear-curve fitted to $y = AL^* + B$, where the coefficient $A = \Delta y/\Delta L^*$ indicates the amount of change of derivative value, Δy, (in fraction of the facility mean value) as the model size is doubled, i.e $\Delta L^* = 1$. From Fig. 6-12 (a), the ratios of the linear derivatives, Y_v^* and N_v^*, are close to 1.0 whereas the ratios of the non-linear derivatives, X_{vv}^*, Y_{vvv}^*, and N_{vvv}^*, are distributed over a rather wide range in general between 0.6 and 1.04. The curve-fit coefficient A's for the linear and non-linear derivatives are near to zero, 0.01 and -0.03, respectively, indicating that the derivatives are nearly independent of model size. The ratios $Y_{\dot{v}}^*$ and $N_{\dot{v}}^*$ shown in Fig. 6-12 (b) are also near to 1.0, similarly as Y_v^* and N_v^*, whereas the values tend to decrease with model size, however, the number of data (6 points) is very limited for a general remark. From Fig. 6-13 (a), the ratios of the linear derivatives, Y_r^* and N_r^*, are close to 1.0 distributed between 0.8 and 1.2, whereas the ratios of the non-linear derivatives, X_{rr}^*, Y_{rrr}^*, and N_{rrr}^* are distributed over a quite wide range between 0.2 and 1.8. The curve-fit coefficient A's are 0.14 and -0.16 for the linear and non-linear derivatives, respectively, indicating that those derivatives values can increase 14% and decrease 16%, respectively, as the model length is doubled. The ratios of yaw acceleration derivatives, $Y_{\dot{r}}^*$ and $N_{\dot{r}}^*$, exhibit rather strong dependency on the model size as shown in Fig. 6-13 (b). The curve-fit coefficient A is large, $A = 0.52$, meaning that $Y_{\dot{r}}$ and $N_{\dot{r}}$ values can increase as much as 52% as the model size is doubled. In summary, generally, sway derivatives are nearly independent of model size whereas yaw derivatives (particularly yaw acceleration derivatives) exhibit considerable dependency on the model size. However, general conclusions

are precluded for the non-linear derivatives due to large scatters in the ratio values distributions.

Cross-coupled derivatives and Surge derivatives are compared in Tables 6-13 and 6-14, respectively. The standard deviations from and the ratios to the facility mean values of those derivatives values are typically larger than those for the sway and yaw derivatives, and clear trends with the model size are not observed for those derivatives.

Table 6-9 Comparisons between Facilities: Static drift test (β = 10°).

Var.	Fr = 0.138		Fr = 0.280		Fr = 0.410	
	Mean	StDev(%)	Mean	StDev(%)	Mean	StDev(%)
X	-0.0176	9.2	-0.0197	10.7	-0.0281	9.2
Y	0.0559	3.4	0.0616	1.0	0.0746	6.3
N	0.0250	7.5	0.0300	3.9	0.0372	4.1

Table 6-10 Comparisons between Facilities: Dynamic tests (Fr = 0.280).

Var.	Harmonics	Pure sway		Pure yaw		Yaw and drift	
		Mean	StDev(%)	Mean	StDev(%)	Mean	StDev(%)
X	X_0	-0.0210	14.9	-0.0182	6.2	-0.0225	7.5
	X_2	0.0017	42.9	0.0007	8.3	[1)]0.0026	69.2
	φ_{X2}	-0.75 π	5.8	-0.18 π	307.3	[2)]0.25 π	76.8
Y	Y_0	-	-	-	-	0.0698	2.0
	Y_1	0.0665	3.8	0.0175	6.4	0.0318	6.1
	φ_{Y1}	0.17 π	7.0	0.58 π	2.1	0.59 π	3.2
N	N_0	-	-	-	-	0.0333	1.6
	N_1	0.0315	3.7	0.0153	5.8	0.0221	5.8
	φ_{N1}	0.04 π	10.1	0.59 π	2.2	0.57 π	1.8

[1)] X_1 and [2)] φ_{X1} for yaw and drift test.

Table 6-11 Comparisons between Facilities (Sway derivatives).

Derivative	Fr	Mean	StDev (%)	Facility data (ratio to Mean)		
				IIHR	FORCE	INSEAN
X_*	0.138	-0.0164	13.7	1.11	1.04	0.85
	0.280	-0.0155	12.4	1.10	1.05	0.86
	0.410	-0.0239	9.8	1.08	1.03	0.89
Y_v	0.138	-0.2673	5.4	0.99	0.95	1.06
	0.280	-0.3000	1.8	0.99	0.99	1.02
	0.410	-0.2941	2.9	1.01	1.02	0.97
N_v	0.138	-0.1351	5.9	1.03	1.04	0.93
	0.280	-0.1628	2.2	1.02	1.00	0.98
	0.410	-0.1749	7.0	0.98	0.94	1.08
X_{vv}	0.138	-0.0427	51.6	0.70	0.70	1.60
	0.280	-0.1421	6.5	1.08	0.96	0.96
	0.410	-0.1392	9.5	1.11	0.94	0.96
Y_{vvv}	0.138	-1.7940	13.9	0.91	1.16	0.93
	0.280	-1.7875	7.8	1.09	0.97	0.94
	0.410	-4.5105	25.7	0.84	0.86	1.30
N_{vvv}	0.138	-0.2866	31.2	1.20	1.16	0.64
	0.280	-0.3284	31.0	1.33	0.96	0.71
	0.410	-1.3113	11.0	0.96	1.12	0.92
Y_p	0.280	-0.1111	4.4	1.02	1.03	0.95
N_p	0.280	-0.0131	8.8	1.04	1.07	0.90

Table 6-12 Comparisons between Facilities (Yaw derivatives).

Derivative	Fr	Mean	StDev (%)	Facility (ratio to Mean)		
				IIHR	FORCE	INSEAN
Y_r	0.138	-0.0313	15.3	0.88	1.17	0.95
	0.280	-0.0457	27.2	1.06	0.70	1.24
	0.410	-0.0572	5.6	0.96	0.98	1.06
N_r	0.138	-0.0372	5.8	1.03	0.93	1.04
	0.280	-0.0487	5.4	0.94	1.05	1.01
	0.410	-0.0543	14.5	0.84	1.03	1.13
X_{rr}	0.138	-0.0090	36.9	0.87	0.71	1.42
	0.280	-0.0191	41.5	1.48	0.71	0.81
	0.410	-0.0190	91.4	2.03	0.68	0.29
Y_{rrr}	0.138	-0.0454	31.5	0.82	0.82	1.36
	0.280	-0.0570	71.8	0.79	1.80	0.41
	0.410	-0.0608	14.6	1.17	0.93	0.90
N_{rrr}	0.138	-0.0255	31.8	0.83	0.81	1.37
	0.280	-0.0342	55.3	1.48	0.39	1.13
	0.410	-0.0773	20.1	1.06	0.78	1.16
$Y_{\dot{r}}$	0.138	-0.0162	21.0	0.90	0.86	1.24
	0.280	-0.0136	33.3	0.66	1.01	1.33
	0.410	-0.0184	33.5	0.69	0.95	1.36
$N_{\dot{r}}$	0.138	-0.0073	17.8	0.89	0.91	1.21
	0.280	-0.0096	24.6	0.73	1.07	1.21
	0.410	-0.0092	14.6	0.83	1.06	1.10

Table 6-13 Comparisons between Facilities (Cross-coupled derivatives).

Derivative	Mean	StDev (%)	Facility (ratio to Mean)		
			IIHR	FORCE	INSEAN
X_{vr}	0.0300	152.1	2.73	0.39	-0.12
Y_{vrr}	-1.3683	42.7	1.48	0.65	0.87
N_{vrr}	-0.4011	64.3	1.72	0.48	0.81
Y_{rvv}	-1.7067	12.1	1.10	1.03	0.87
N_{rvv}	-0.5512	20.8	0.79	1.00	1.21

Table 6-14 Comparisons between Facilities (Surge derivatives).

Derivative	Mean	StDev (%)	Facility (ratio to Mean)		
			IIHR	FORCE	INSEAN
X_u	-0.0087	2.3	1.01	1.01	0.97
X_{uu}	-0.0205	7.9	1.07	1.00	0.92
X_{vvu}	-0.0903	31.6	1.30	1.03	0.67
X_{rru}	-0.0094	212.5	3.28	0.65	-0.93
Y_{vu}	-0.0242	98.7	1.27	1.83	-0.09
N_{vu}	-0.0397	54.3	0.78	0.60	1.62
Y_{vuu}	0.0794	18.2	0.82	0.99	1.19
N_{vuu}	0.0294	71.3	1.49	1.33	0.18
Y_{ru}	-0.0265	14.3	1.01	0.85	1.14
N_{ru}	-0.0208	12.5	0.88	1.00	1.13
Y_{ruu}	0.0033	1728.6	8.61	-19.03	13.45
N_{ruu}	0.0034	486.6	-1.94	6.56	-1.65

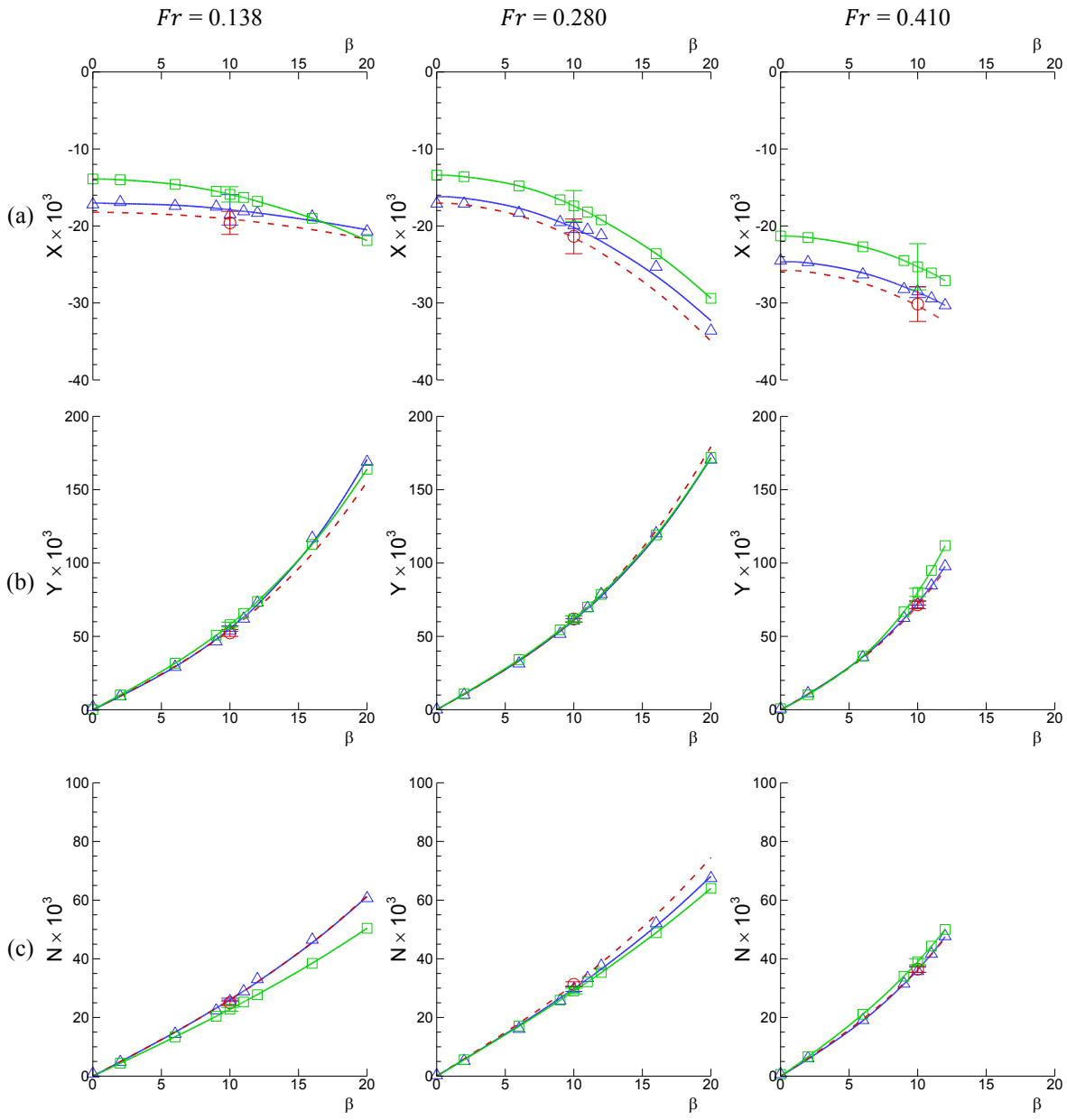

Figure 6-10 Comparisons between facilities – Static drift data (Corrected for symmetry): (a) X, (b) Y, and (c) N at Fr =0.138 (left), 0.280 (center), 0.410 (right), respecitively. Symbols: O, IIHR; Δ, FORCE; □, INSEAN.

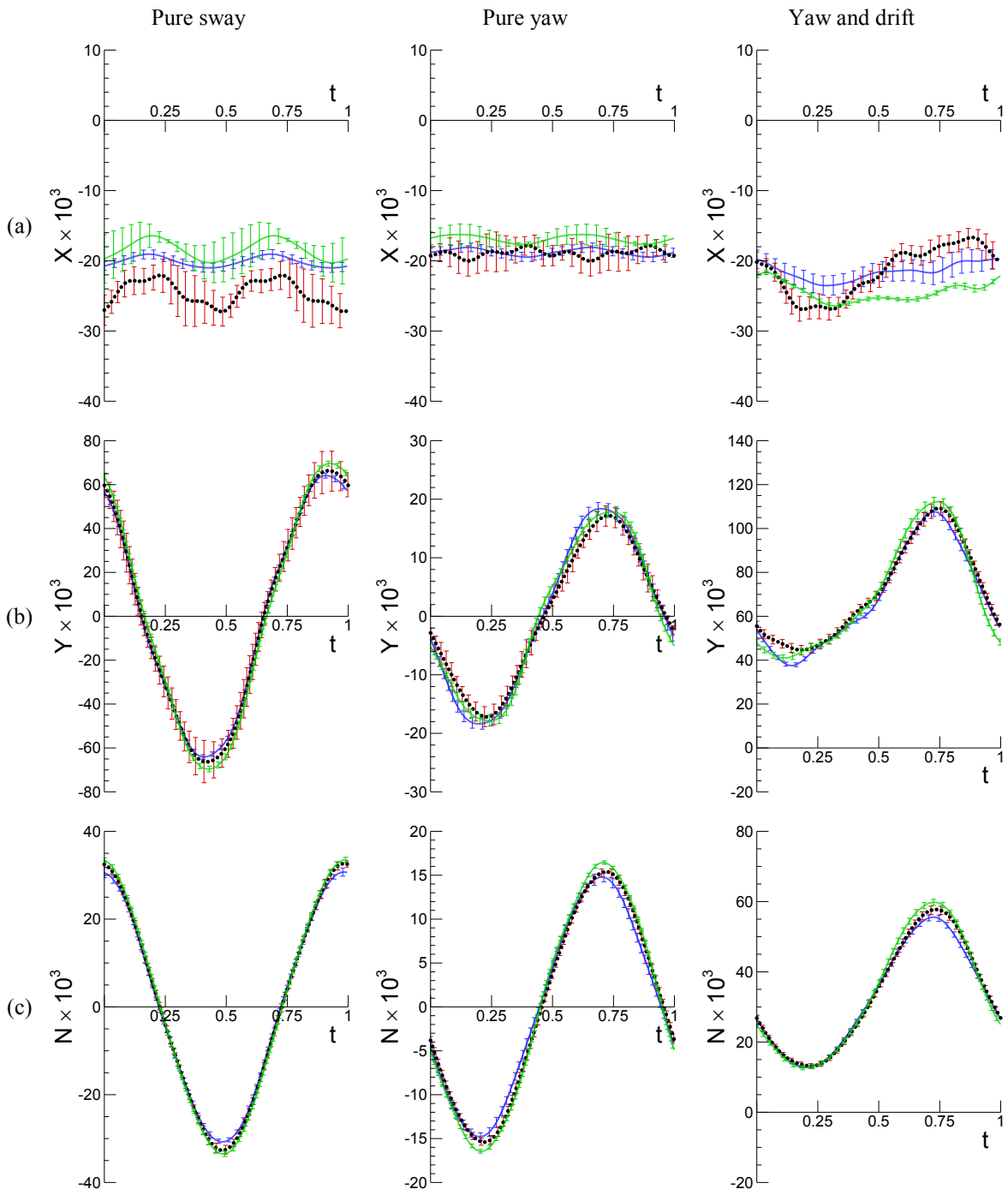

Figure 6-11 Comparisons between facilities – Dynamic tests data (Corrected for symmetry): (a) X, (b) Y, and (c) N for pure sway (left, β_{max} = 10°), pure yaw (center, r_{max} = 0.30), and yaw and drift (right, β = 10°) tests at Fr = 0.280, respectively. Symbols (colors): •, IIHR; —, FORCE; and —, INSEAN.

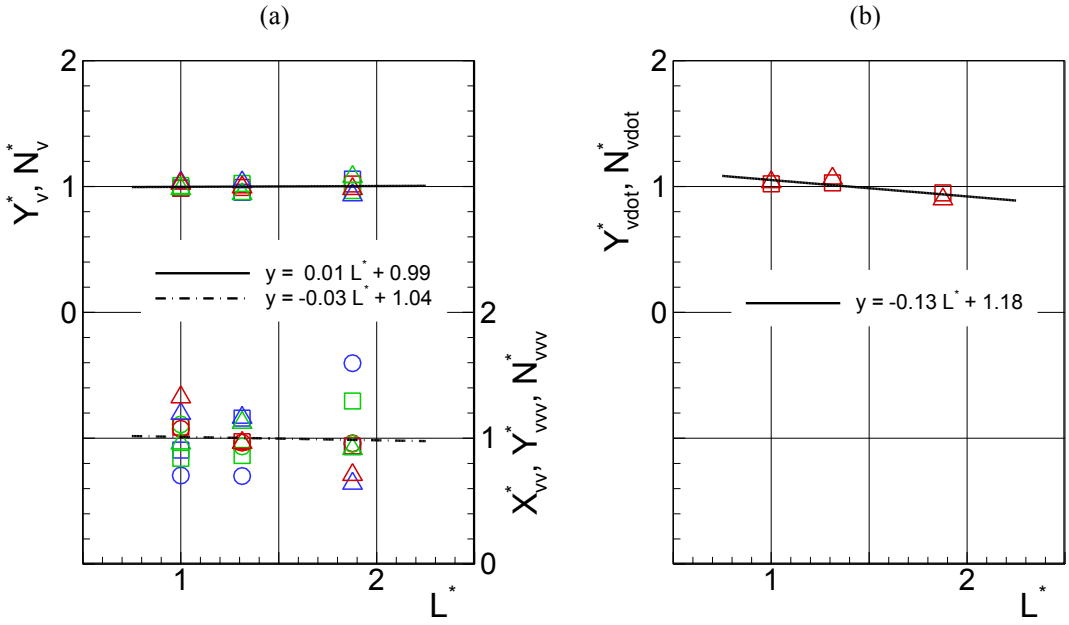

Figure 6-12 Comparisons between facilities: (a) sway-velocity and (b) -acceleration derivatives. Derivatives and model lengths are scaled values. Symbols: O, X_{vv}; □, Y_v^*, Y_{vvv}^*, or $Y_{\dot{v}}^*$; and Δ, N_v^*, N_{vvv}^*, or $N_{\dot{v}}^*$, respectively. Color codes: Fr = 0.138 (blue), 0.280 (red), and 0.410 (green), respectively.

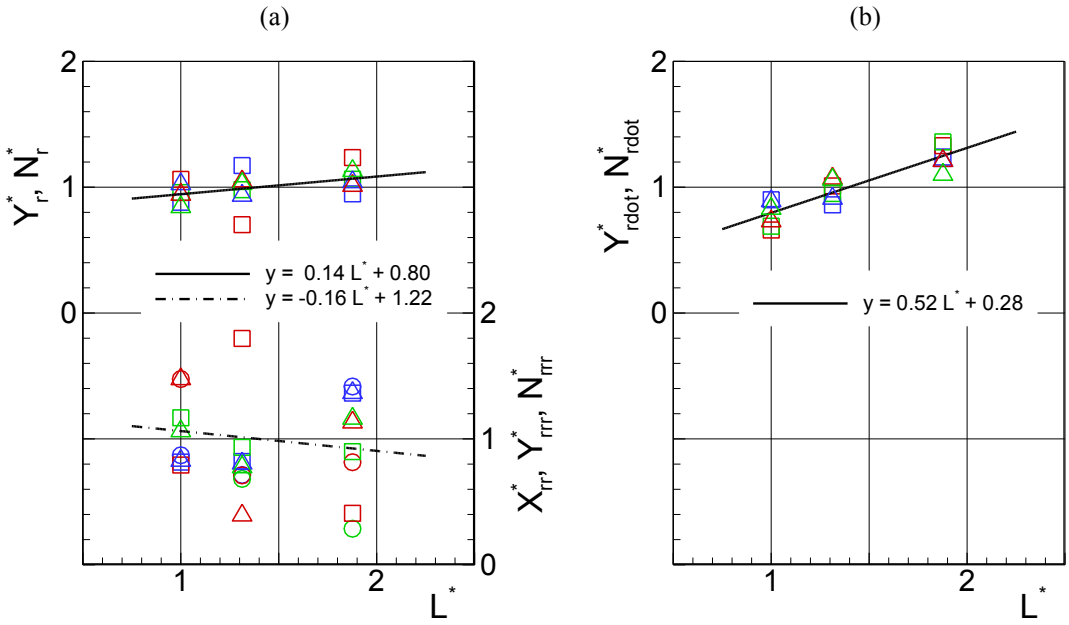

Figure 6-13 Comparisons between facilities: (a) yaw-rate and (b) -acceleration derivatives. Derivatives and model lengths are scaled values. Symbols: O, X_{rr}^*; □, Y_r^*, Y_{rrr}^*, or $Y_{\dot{r}}^*$; and Δ, N_r^*, N_{rrr}^*, or $N_{\dot{r}}^*$, respectively. Color codes: Fr = 0.138 (blue), 0.280 (red), and 0.410 (green), respectively.

6.1.4 Heave, Pitch, and Roll Motions

Time-mean values of static drift z, θ, and ϕ data are shown in Fig. 6-14 (a), (b), and (c), respectively. From (a) and (b), z and θ increase with β from the values at 0° to positive for the former (downward sinkage) and to negative for the latter (bow-down trim), respectively. From (c), ϕ is zero at β = 0° and increases to positive (heel to star-board) with β. Data are curve fitted to quadratic or cubic functions of β such that $z, \theta = A + B\beta^2$ and $\phi = A\beta + B\beta^3$, respectively, where the coefficients A's and B's are presented in Table 6-15. In general, both of the polynomial coefficients A and B are functions of *Fr*. From Fig. 6-14 (a) and (b), while the A (corresponding to the values at β = 0°) is increasing monotonically with *Fr* for z and oscillating for θ, respectively, more complete trends will be discussed later at the next Section with related to surge force X. The 2nd-order coefficient B for z and θ are shown in Fig. 6-14 (d) and (e), respectively, plotted against *Fr* numbers. In the figures, *Fr* is scaled with the lowest number, *Fr* = 0.138, and B is scaled with its value at the *Fr*, which are designated as Fr^* and B^*, re-spectively. Note that B for θ shown in Fig. 6-14 (e) is scaled with the value at Fr = 0.280 to avoid using a near-to-zero B value at Fr = 0.138 for the $FR_{z\theta}$ condition case. From the figures, B^* for z is quadratic whereas that for θ is nearly linear with Fr^*, respectively, indicating that

$$\Delta z \sim Fr^2 \cdot \beta^2 \quad \text{and} \quad \Delta\theta \sim Fr \cdot \beta^2 \tag{6.6}$$

where $\Delta z = z - A$ and $\Delta\theta = \theta - A$, respectively. Similarly, A^* and B^* for ϕ are shown in Fig. 6-14 (f) where the A^* increases nearly linearly for $Fr^* < 2$ and then more steeply with Fr^*, whereas the B^* is almost independent of Fr^*, thus, approximately for small *Fr* and β,

$$\phi \sim Fr \cdot \beta \tag{6.7}$$

For z and θ, also presented in Table 6-15 are the ratio ζ_ϕ values, defined in (6-13), for the polynomial coefficients for $FR_{z\theta}$ condition to those for $FR_{z\theta\phi}$ condition revealing the effect of roll motion to heave and pitch motions. As $\phi = 0$ at $\beta = 0°$, the ζ_ϕ for A's reveal no more than the errors in measurement of z and θ at the drift angle. For z, the ζ_ϕ values for B are close to unity, indicating that the effect of roll motions on heave is small or that the heave motion is independent with the roll motion. For θ, in contrast, ζ_ϕ values for B are considerably larger than unity, about 4 ~ 12, revealing that the pitch and roll motions are rather strongly coupled each other.

Time-histories of z, θ, and ϕ are shown in Fig. 6-15 (b), (c), and (d), respectively, for pure sway (left column), pure yaw (center column), and yaw and drift (right column) tests at $Fr = 0.280$, respectively. Shown in Fig. 6-15 (a) are the forced PMM motions; drift angle β for pure sway and heading angle ψ for pure yaw and yaw and drift tests, which are identical with those shown in Fig. 6-2 (a) for forces and moment. The FS harmonic amplitudes of the time-histories are evaluated as per (2) and summarized in Table 6-16 for $\beta_{max} = 10°$ case of pure sway test, $r_{max} = 0.30$ case of pure yaw test, and $\beta = 10°$ case of yaw and drift test, respectively. In the table, A is the oscillation amplitude of z, θ, and ϕ time-histories, respectively, and $z_{10°}$, $\theta_{10°}$, and $\phi_{10°}$ represent the static drift z, θ, and ϕ values at $\beta = 10°$, respectively.

For the heave z shown in Fig. 6-16 (b), the 2nd-order amplitude z_2 is most dominant for pure sway and pure yaw, about 100% of A. The oscillation amplitude A is small compared to the static drift, about 20% and 10% of $z_{10°}$ for pure sway and pure yaw, respectively. The 0th-order amplitude z_0, i.e. the period-mean value, is comparable with static drift, about 70% and 60% of $z_{10°}$ for pure sway and pure yaw, respectively. For yaw and drift, both A and z_0 are larger than those for pure sway and pure yaw, about 30% and 110% of $z_{10°}$, respectively. The 1st-order amplitude z_1 is dominant for yaw and drift, about 95% of A, and the 2nd-order amplitude z_2 is the second dominant, about 20% of A. For all test types harmonic amplitudes higher than 3rd-order $z_{3,4,5,6}$ are small, usually less

than 5% of A. Comparing the results between $FR_{z\theta\phi}$ and $FR_{z\theta}$ conditions, the ratio ζ_ϕ values for the dominant harmonic amplitudes including A's are close to unity, between about 0.8 – 1.4, indicating that the effects of the roll motions shown in Fig. 6-16 (d) on the heave motions are small.

For the pitch θ shown in Fig. 6-15 (c), the 2nd-order amplitude θ_2 is most dominant for pure sway and pure yaw, similarly as for heave, about 100% of A. Despite the fact for static drift test that θ for $FR_{z\theta\phi}$ condition is considerably larger than that for $FR_{z\theta}$ as shown in Fig. 6-14 (b) (where $\zeta_\phi = 2.67$ for θ at $\beta = 10°$), for pure sway test, however, similar values of the 0th-order amplitude θ_0 ($\zeta_\phi = 0.81$) and oscillation amplitude A ($\zeta_\phi = 0.86$) are observed from both of the conditions. The magnitudes of those θ_0 and A are about 80% and 40% of $\theta_{10°}$ for $FR_{z\theta}$ condition, respectively, and about 20% and 10% for $FR_{z\theta\phi}$ condition, respectively. In contrast, for pure yaw test, A for $FR_{z\theta\phi}$ is considerably large than that for $FR_{z\theta}$ ($\zeta_\phi = 2.14$) whereas θ_0 is similar for both conditions ($\zeta_\phi = 0.78$), indicating that the effect of roll motion on pitch is mainly for the oscillation amplitude A for pure yaw test. The magnitudes of those θ_0 and A are about 60% and 30% of $\theta_{10°}$ for $FR_{z\theta}$ condition, respectively, and about 15% and 20% for $FR_{z\theta\phi}$ condition, respectively. For yaw and drift test, both θ_0 and A for $FR_{z\theta\phi}$ is larger than those for $FR_{z\theta}$ ($\zeta_\phi = 2.62$ and 2.38, respectively), which are 142% and 152% of $\theta_{10°}$ for the former condition, respectively, and 123% and 120% for the latter condition, respectively. The harmonic amplitudes of higher than 3rd-order $\theta_{3,4,5,6}$ are small for all the test types, usually less than 5% of A, except for θ_4 for pure sway and pure yaw tests, about 10%.

For the roll ϕ shown in Fig. 6-15 (d), the 1st-order amplitude ϕ_1 is the most dominant, about 100% of A, for all test types. The oscillation amplitude A for pure sway test is larger than static drift ϕ, 124% of $\phi_{10°}$, whereas smaller for pure yaw and yaw and drift tests, about 70%, respectively. For yaw and drift test the 0th-order amplitude ϕ_0 is slightly larger than static drift ϕ, 106% of $\phi_{10°}$. Higher-order harmonic amplitudes $\phi_{2,3,4,5,6}$ are all small, usually less than 5% of A, for all test types, except for a few cases.

The 0th- and 2nd-order harmonic amplitudes of the heave motions z_0 and z_2 for all pure yaw test cases at Fr = 0.138, 0.280, and 0.410 are shown in Fig. 6-16 (a) and (b), respectively, with plotted against r_{max} values. In general, the overall appearances of z_0 data resemble the static drift z data shown in Fig. 6-14 (a), accordingly data are curve-fitted as $z_0 = A + Cr_{max}^2$ where the same A values for static drift z curve-fit corresponding to each Fr case is used for the curve-fits. z_2 shown in Fig. 6-16 (b) also exhibits quadratic trends with r_{max} and data are curve-fitted as $z_2 = D + Er_{max}^2$. Subsequently, the curve-fit coefficients C and E are scaled with those values for Fr = 0.138 case, designated as C^* and E^*, respectively, and shown in Fig. 6-16 (c) and (d), respectively, plotted against the Fr^* similarly as B^* shown in Fig. 6-14 (d) for static drift z data. From Fig. 6-16 (c), C^* increases with Fr^* roughly following a cubic line, which is much faster than the quadratic increase of B^*. Whereas from Fig. 6-16 (d), the E^* follows a $Fr^{*2.5}$ line, slower than C^* yet relatively faster than B^*. Accordingly, for those harmonic amplitudes,

$$\Delta z_0 \sim Fr^3 \cdot r_{max}^2 \qquad \text{and} \qquad \Delta z_2 \sim Fr^{2.5} \cdot r_{max}^2 \tag{6.8}$$

respectively, where $\Delta z_0 = z_0 - A$ and $\Delta z_2 = z_2 - D$, respectively. The coefficient D will be discussed later at next paragraph for pitch motion. Consequently, for dynamic pure yaw test, the magnitudes of z_0 and z_2 are smaller than static drift z, respectively about 80% and 10% from discussions above, however increases with Fr faster than static drift z.

Similarly, the 0th- and 2nd-order harmonic amplitudes of the pitch motions θ_0 and θ_2 for all pure yaw test cases are shown in Fig. 6-17 (a) and (b), respectively. Data are curve-fitted as $\theta_0 = A + Cr_{max}^2$ and $\theta_2 = D + Er_{max}^2$, respectively, and the scaled coefficients C^* and E^* are shown in Fig. 6-17 (c) and (d), respectively, for the former coefficient similarly as B^* for static drift θ shown in Fig. 6-14 (e) and for the latter coefficient similarly as E^* for z_2 discussed previously. From Fig. 6-17 (a), the overall appearances

of θ_0 are similar to those of the static drift θ data shown in Fig. 6-14 (b), whereas the θ_0 at $Fr = 0.410$ increases with r_{max} in contrast to the static drift θ at the same Fr, decreasing with β. Accordingly, the C^* shown in Fig. 6-17 (c) exhibits more complicated curve pattern than the simple linear pattern of static drift B^{**} shown in Fig. 6-14 (e), rather the E^* shown in Fig. 6-17 (e) exhibits linear trend with Fr^*. Thus, for those harmonic amplitudes,

$$\Delta\theta_0 \sim C(Fr)\cdot r_{max}^2 \qquad \text{and} \qquad \Delta\theta_2 \sim Fr\cdot r_{max}^2 \tag{6.9}$$

respectively, where $\Delta\theta_0 = \theta_0 - A$ and $\Delta\theta_2 = \theta_2 - D$, respectively, and more data may be necessary to determine a functional form for $C(Fr)$. For $FR_{z\theta\phi}$ condition, however, the θ_2 values are much larger than those for $FR_{z\theta}$ condition, as shown in Fig. 6-17 (b), due to the cross coupling between pitch and roll motions. When ϕ_1^* and θ_2^* are defined similarly as for the scaled coefficients for the data curve-fits, both exhibit quadratic trends with Fr^* as shown in Fig. 6-17 (e), thus it can be written as $\Delta\theta_2 \sim Fr^2\cdot r_{max}^2$ for $FR_{z\theta\phi}$ condition.

The 2nd-order harmonic amplitudes z_2 and θ_2 of heave and pitch motions are supposed to become zero as the forced PMM motions are getting smaller, e.g. $r_{max} \rightarrow 0$ for pure yaw test. Thus, the non-zero z_2 and θ_2 values at $r_{max} = 0.05$ shown in Fig. 6-16 (b) and Fig. 6-17 (b), respectively, (accordingly non-zero D's for the curve-fits) are out of expectation.

Table 6-15 Polynomial Fit Coefficients for Static Drift Motions Data.

Coeff.	Fr	$z \times 10^2$			θ (°)			ϕ (°)
		$FR_{z\theta}$	$FR_{z\theta\phi}$	ζ_ϕ	$FR_{z\theta}$	$FR_{z\theta\phi}$	ζ_ϕ	$FR_{z\theta\phi}$
A	0.138	0.006	-0.017	-2.83	-0.039	-0.004	0.10	0.056
	0.280	0.176	0.217	1.23	-0.097	-0.026	0.27	0.119
	0.410	0.434	0.516	1.19	0.396	0.453	1.14	0.239
$B \times 10^3$	0.138	0.284	0.291	1.02	-0.153	-1.759	11.50	0.096
	0.280	0.983	0.810	0.82	-1.326	-6.875	5.18	0.139
	0.410	2.692	2.428	0.90	-2.769	-10.609	3.83	0.115

Table 6-16 Harmonic Amplitudes[1)] of Motions for Dynamic Tests (Fr = 0.280).

Var.	Harmonic amplitude	Pure Sway (β_{max} = 10°)			Pure Yaw (r_{max} = 0.30)			Yaw and Drift (β = 10°)		
		$FR_{z\theta}$	$FR_{z\theta\phi}$	ζ_ϕ	$FR_{z\theta}$	$FR_{z\theta\phi}$	ζ_ϕ	$FR_{z\theta}$	$FR_{z\theta\phi}$	ζ_ϕ
z	z_0	0.67	0.81	1.16	0.54	0.76	1.37	1.12	1.12	0.96
	A	0.24	0.19	0.76	0.09	0.08	0.80	0.32	0.27	0.83
	z_1	-	-	-	-	-	-	0.95	0.94	0.82
	z_2	1.01	0.99	0.75	0.98	1.00	0.82	0.21	0.21	0.82
	z_3	-	-	-	-	-	-	0.01	0.02	1.40
	z_4	0.05	0.04	0.74	0.12	0.12	0.79	0.00	0.03	6.00
	z_5	-	-	-	-	-	-	0.00	0.02	7.00
	z_6	0.03	0.03	0.65	0.06	0.07	1.00	0.02	0.01	0.50
θ	θ_0	0.77	0.21	0.81	0.60	0.15	0.78	1.42	1.23	2.62
	A	-0.42	-0.12	0.86	-0.30	-0.22	2.14	-1.52	-1.20	2.38
	θ_1	-	-	-	-	-	-	0.97	0.99	2.44
	θ_2	0.99	1.03	0.89	0.99	1.01	2.19	0.12	0.14	2.90
	θ_3	-	-	-	-	-	-	0.02	0.01	1.62
	θ_4	0.09	0.10	1.02	0.13	0.05	0.78	0.00	0.01	4.30
	θ_5	-	-	-	-	-	-	0.00	0.01	6.06
	θ_6	0.01	0.02	2.48	0.04	0.02	1.14	0.00	0.01	6.87
ϕ	ϕ_0	-	-	-	-	-	-	-	1.06	-
	A	-	1.24	-	-	0.71	-	-	0.67	-
	ϕ_1	-	1.00	-	-	1.01	-	-	1.03	-
	ϕ_2	-	-	-	-	-	-	-	0.02	-
	ϕ_3	-	0.09	-	-	0.01	-	-	0.04	-
	ϕ_4	-	-	-	-	-	-	-	0.01	-
	ϕ_5	-	0.06	-	-	0.01	-	-	0.01	-
	ϕ_6	-	-	-	-	-	-	-	0.01	-

[1)] Those values presented herein are χ_0 ($\chi = z, \theta, \phi$) and A in % of $\chi_{10°}$ and χ_n (n = 1, 2, …, 6) in % of A, respectively, where $\chi_{10°}$ represents the static drift χ value at β = 10°.

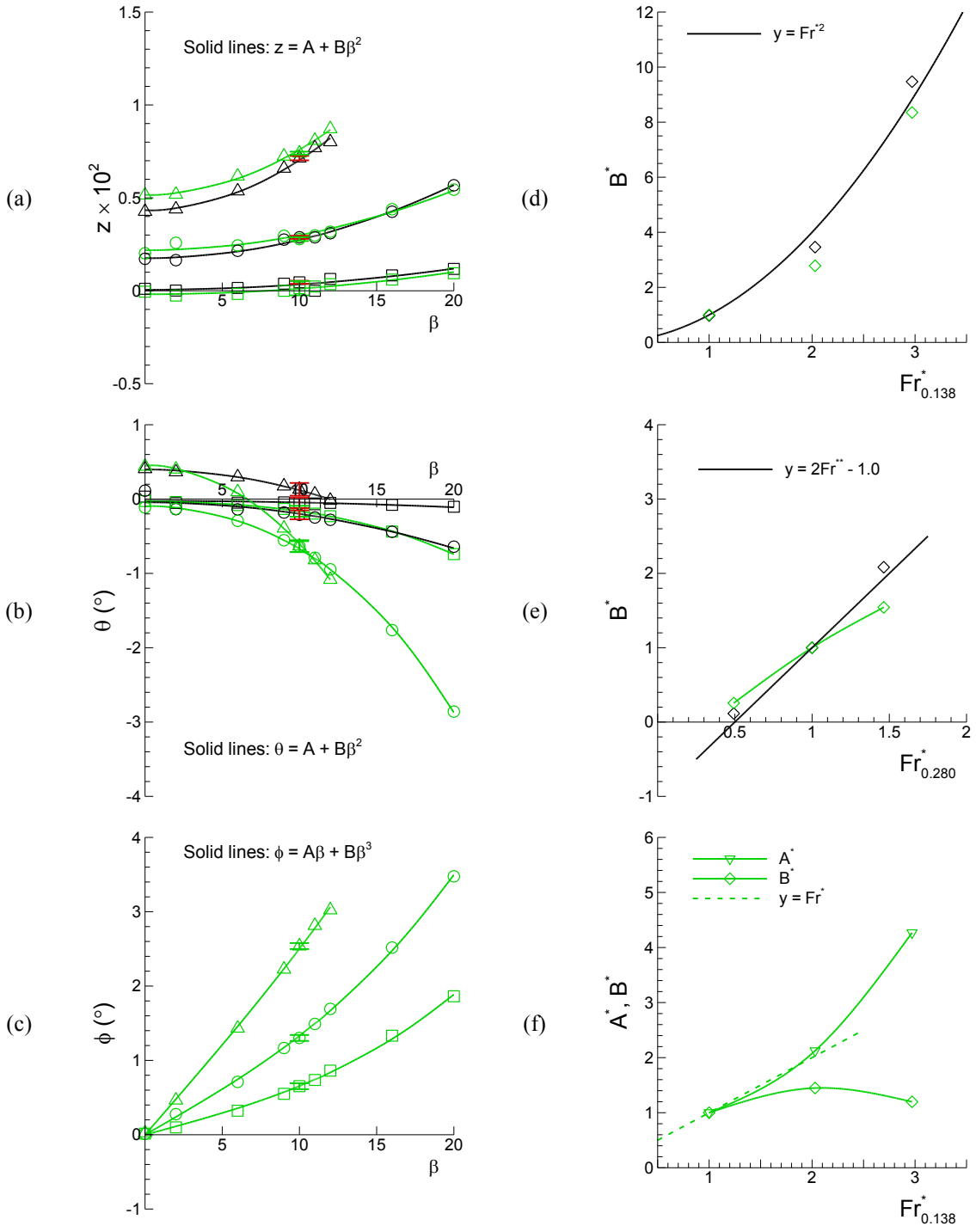

Figure 6-14 Motions data for static drift tests (Corrected for symmetry): (a) z, (b) θ, and (c) ϕ, and the polynomial-fit coefficients (scaled): (d) B^* for z, (e) B^* for θ, and (f) A^* and B^* for ϕ, respectively. Symbols for (a), (b), and (c): □, Fr = 0.138; o, Fr = 0.280; Δ, Fr = 0.410; ∇, A^*; ◊, B^*. Color codes: —, $FR_{z\theta}$ and —, $FR_{z\theta\phi}$.

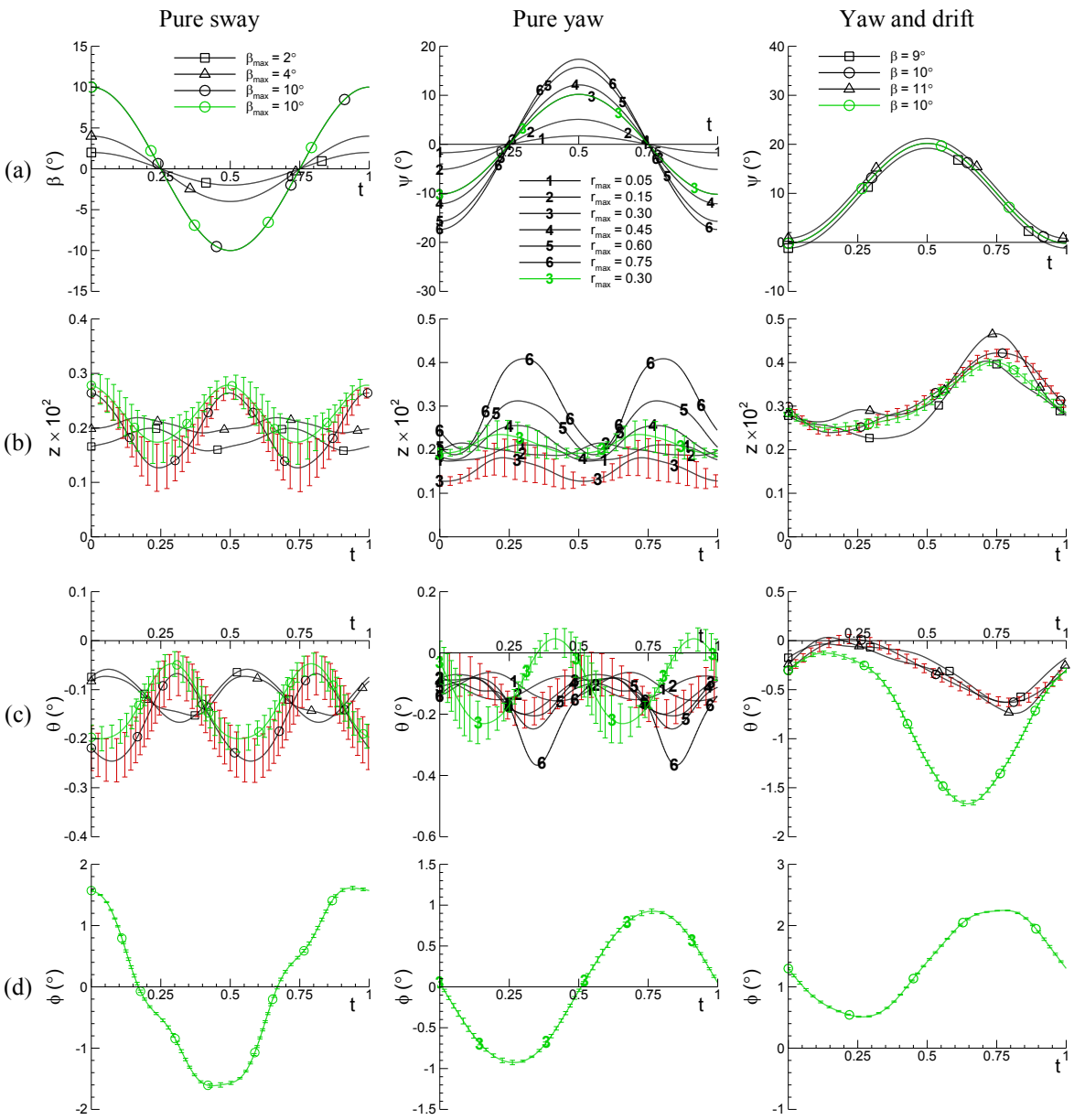

Figure 6-15 Time-histories of motions data (Corrected for symmetry) for pure sway test (left column), pure yaw test (center column), and yaw and drift test (right column) at $Fr = 0.280$, resepctively: (a) input motions β or ψ, and responses in (b) z, (b) θ, and (c) ϕ. Color codes: —, $FR_{z\theta}$ and —, $FR_{z\theta\phi}$.

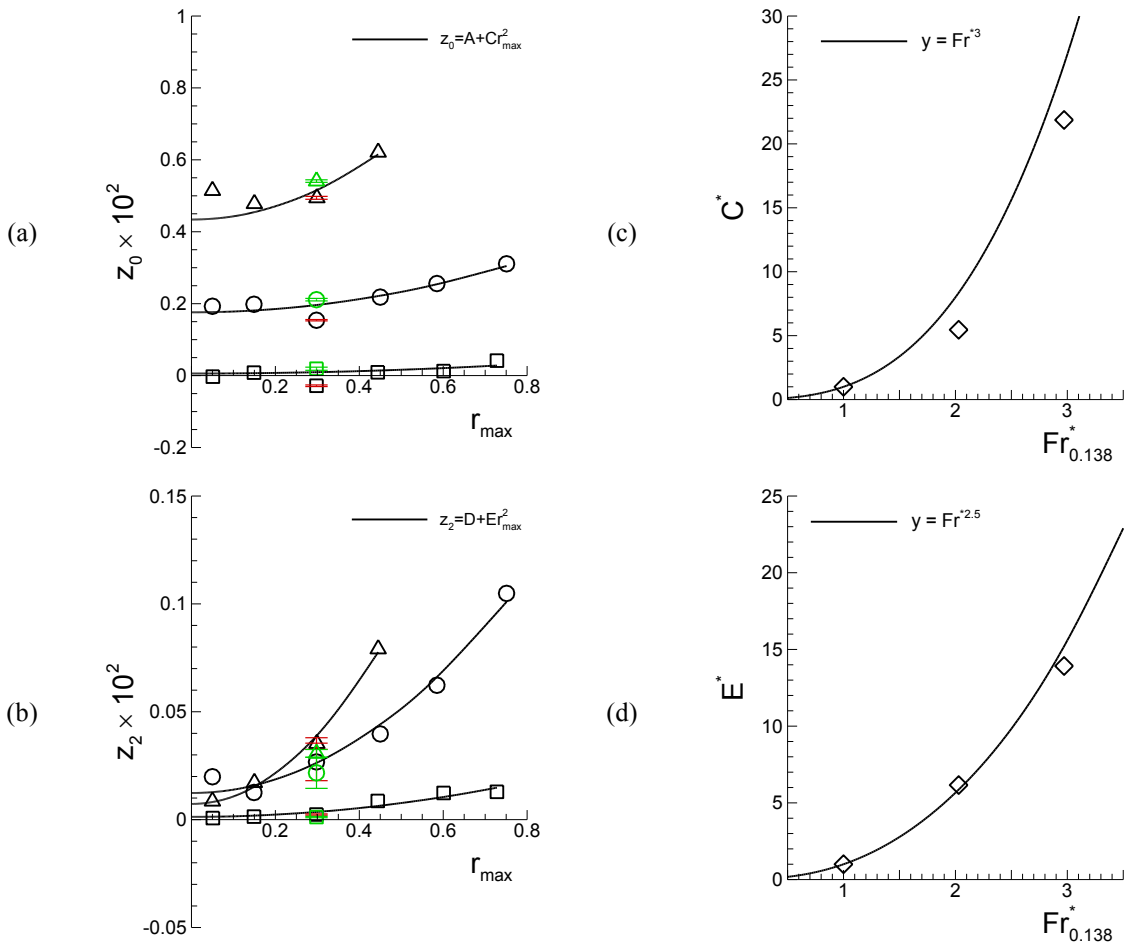

Figure 6-16 Pure yaw heave 0th- and 2nd-order harmonic amplitudes: (a) z_0 and (b) z_2, and scaled curve-fit coefficients: (c) C^* and (d) E^*. Simbols for (a) and (b): □ $Fr = 0.138$, o $Fr = 0.280$, Δ $Fr = 0.410$. Color code: —, $FR_{z\theta}$ and —, $FR_{z\theta\phi}$.

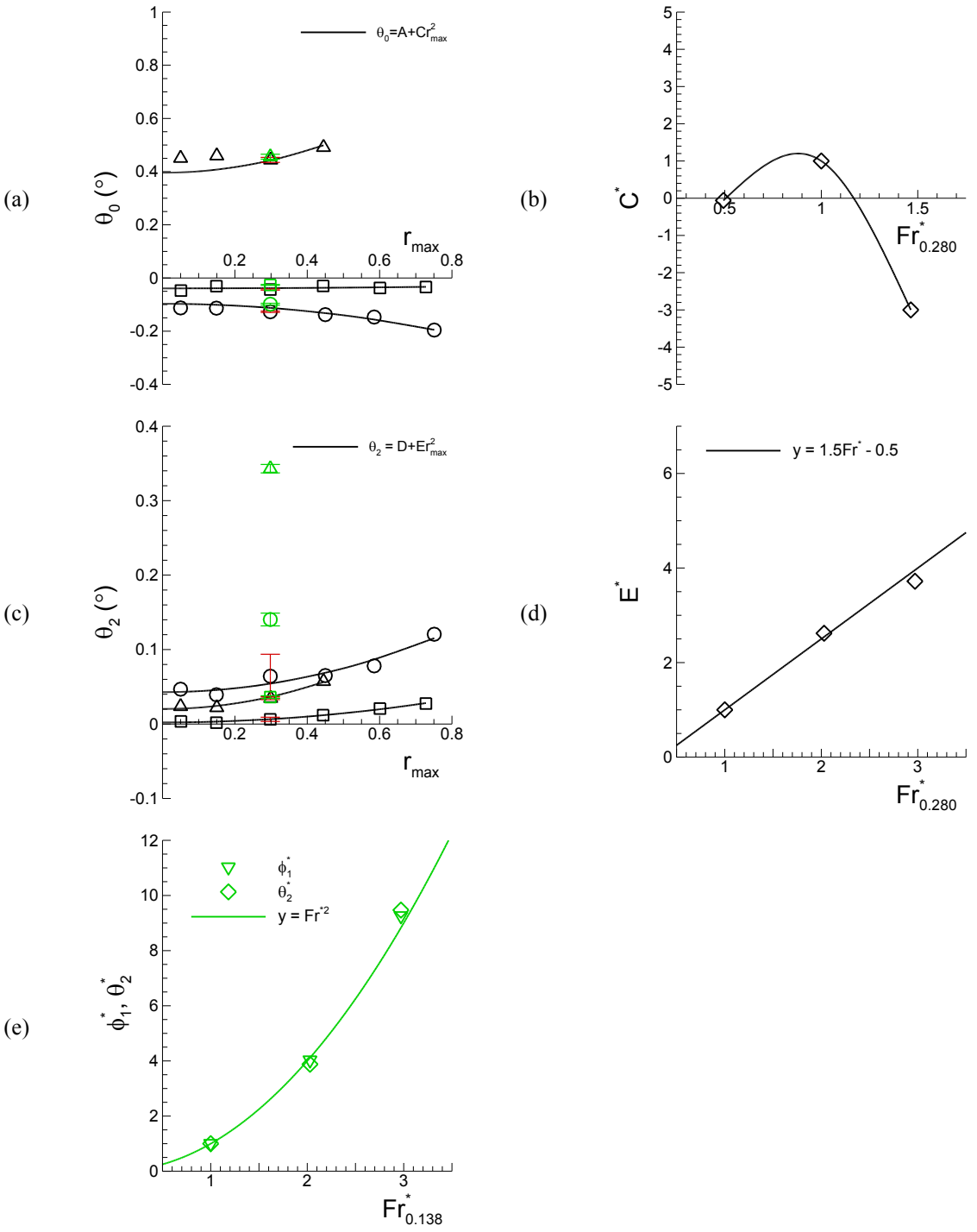

Figure 6-17 Pure yaw pitch 0th- and 2nd-order harmonic amplitudes: (a) θ_0 and (b) θ_2, and scaled curve-fit coefficients: (c) C^* and (d) E^*, and (e) scaled 1st-order roll and 2nd-order pitch harmonic amplitudes, ϕ_1^* and θ_2^*. Simbols for (a) and (b): □ Fr = 0.138, o Fr = 0.280, Δ Fr = 0.410. Color codes: —, $FR_{z\theta}$ and —, $FR_{z\theta\phi}$.

6.1.5 The Effects of Motions and Mount Conditions

Forces and moment and subsequent hydrodynamic derivatives are compared between four mount-conditions, FX_0, $FX_{\sigma\tau}$, $FR_{z\theta}$, and $FR_{z\theta\phi}$ (Sections 3.3 and 3.4), and the effect of heave, pitch, and roll motions on those variables are discussed. For the comparisons the ratios of data $\xi_{\sigma\tau}$, $\xi_{z\theta}$, and $\xi_{z\theta\phi}$ are defined as

$$\xi_{\sigma\tau,z\theta,z\theta\phi} \equiv \frac{x_{\sigma\tau,z\theta,z\theta\phi}}{x_0} \tag{6.10}$$

where $x_{\sigma\tau}$, $x_{z\theta}$, $x_{z\theta\phi}$, and x_0 can be any quantity from the $FX_{\sigma\tau}$, $FR_{z\theta}$, $FR_{z\theta\phi}$, and FX_0 conditions, respectively. As all motions are restrained for FX_0 condition (except for the forced PMM motions), the ratios $\xi_{\sigma\tau}$, $\xi_{z\theta}$, and $\xi_{z\theta\phi}$ signify the effect of sinkage and trim, heave and pitch motions, and heave, pitch, and roll motions, respectively, on the variable x of interest. Note that ζ_ϕ defined in (6-13) is equivalent to $\xi_{z\theta\phi}/\xi_{z\theta}$ such that $\zeta_\phi = \xi_{z\theta\phi}/\xi_{z\theta}$, which emphasizes the effect of roll motion. The ratios values for some select cases are presented for static drift X, Y, and N in Table 35 and for the dominant harmonic amplitude and phase of dynamic tests in Table 36, respectively.

Static drift X, Y, and N data for all mount conditions are shown in Fig. 6-18. In general, data are close between the $FX_{\sigma\tau}$ and FX_0 conditions and as well between the $FR_{z\theta}$ and $FRz_{\theta\phi}$ conditions, whereas considerably different between the $FR_{z\theta}$ and FX_0 conditions. Between $FX_{\sigma\tau}$ and FX_0, at $Fr = 0.280$ (middle column) in Fig. 6-18, $\xi_{\sigma\tau} = 1.05$ in average for X, Y, and N at $\beta = 10°$ indicating that the forces and moment increased about 5% due to sinkage and trim ($\sigma = 0.192\times10^{-2}\ L$ and $\tau = -0.136°$; fixed) from those for FX_0 condition ($\sigma = \tau = 0$; fixed). When the model is released free in heave and pitch for $FR_{z\theta}$ condition ($z = 0.288\times10^{-2}\ L$ and $\theta = -0.212°$ at $\beta = 10°$; $z/\sigma = 1.5$ and $\theta/\tau = 1.6$), then the increase in forces and moment from FX_0 becomes considerably larger, where $\xi_{z\theta} = 1.14$ in average at $\beta = 10°$. As β increased to 20°, the increase in forces and moment as well grows with β for $FR_{z\theta}$ condition ($\xi_{z\theta} = 1.28$ in average), whereas remains

almost constant with β for $FX_{\sigma\tau}$ condition ($\xi_{\sigma\tau}$ = 1.05 in average), respectively. The forces and moment increase even larger at Fr = 0.410 for $FR_{z\theta}$ condition, shown at the right column of Fig. 6-18, where $\xi_{z\theta}$ = 1.28 in average at β = 10°. On the other hand, for $FR_{z\theta\phi}$ condition, forces and moment data are not different from those for $FR_{z\theta}$ with $\xi_{z\theta\phi}$ values close to $\xi_{z\theta}$ for all cases, i.e. $\zeta_\phi \approx 1.0$, indicating that the effect of roll motion (ϕ = 0.7°, 1.3°, and 2.5° at β = 10° for Fr = 0.138, 0.280, and 0.410, respectively) on the forces and moment is almost negligible.

For the $FR_{z\theta}$ condition, the increase of forces and moment from FX_0, say Δx for x = X, Y, or N, can be written as

$$\Delta x = x_{z\theta} - x_0 = x_0\left(\xi_{z\theta} - 1\right) \tag{6.11}$$

where $x_{z\theta}$ and x_0 are the x of $FR_{z\theta}$ and FX_0 conditions, respectively. Shown in Fig. 6-19 are (a) the Δx for X, Y, and N of Fr = 0.280 case over $0 < \beta < 20°$ range and (b) those at β = 10° of Fr = 0.138, 0.28, and 0.410 cases, respectively. In the figures, the β values and Fr numbers at the abscissa are scaled with 10° and 0.138, respectively, denoted as β^* and Fr^*, respectively, and the Δx values at the ordinate are scaled with its value at β =10° and at Fr = 0.138, respectively, denoted as Δx^*. Consequently, the results indicate that Δx is proportional to β^{*2} and $Fr^{*1.5}$ such as

$$\Delta x \sim Fr^{1.5} \cdot \beta^2 + f(Fr) \tag{6.12}$$

where $f(Fr)$ is for β = 0° and f = 0 for Y and N. Recalling (6.6) in Section 6.1.4 that $\Delta z \sim Fr^2 \cdot \beta^2$ and $\Delta\theta \sim Fr \cdot \beta^2$ for static drift heave and pitch at $\beta > 0$, the rate of increase in forces and moment Δx is similar as heave and pitch with β whereas relatively slow with Fr, respectively. In that, however, pitch motion is strongly coupled with roll motion as discussed in Section 6.1.4 (with $\zeta_\phi > 4$ for θ) whereas Δx is almost independent of roll

with $\zeta_\phi \approx 1.0$ as discussed above, it is considered that Δx for $\beta > 0$ is mainly attributed to the heave motion.

On the other hand, from (6.12), $\Delta x \sim f(Fr)$ at $\beta = 0°$ for X. As $\beta = 0°$ corresponds to the steady, straight towing condition, the X, z, and θ values at $\beta = 0°$ shown in Fig. 6-1 (a), Fig. 6-14 (a), and Fig. 6-14 (b), respectively, are converted into the total resistance C_T, sinkage σ, and trim τ of the model, respectively[14]. The $C_{T_{15C}}$, σ, and τ data are presented in Fig. 6-20 showing good agreements with Longo et al. (2005)[15] where the authors used the same DTMB 5512 model as the present study and measured $C_{T_{15C}}$, σ, and τ over a range of Fr = 0.05 - 0.45. The Results of Longo et al. reveals more clearly the Fr trends of $C_{T_{15C}}$, σ, and τ, i.e. X, z, and θ at $\beta = 0°$; C_{T15C} first decreases for $Fr < 0.25$, oscillates small at $0.25 < Fr < 0.35$, and sharply increases for $Fr > 0.35$; σ increases rather monotonically; τ increases first to negative (bow-down), then oscillates, and sharply increases to positive (bow-up), respectively. Noticing similar Fr trends between the data, C_{T15C} data were curve-fitted with σ and τ data using a regression equation[16] $y(\sigma, \tau) =$

---

[14] Those are defined as:

$$C_T = -F_x/0.5\rho U_C^2 S;\ \sigma = (\Delta FP + \Delta AP)/2L;\ \tau = (\Delta AP - \Delta FP)/L$$

respectively, where S is the wetted-surface area of the model and ΔFP and ΔAP are the model displacements at the forward- (FP) and aft-perpendiculars (AP), respectively, related to z and θ as:

$$\Delta FP = z - \tfrac{1}{2}L\sin\theta \text{ and } \Delta AP = z + \tfrac{1}{2}L\sin\theta$$

respectively. Typically, C_T is converted into $C_{T_{15C}}$ with all data calibrated to a standard water temperate 15°C, which allows direct comparisons of the C_T values between tests at different Reynolds number (Re) conditions.

[15] Those data presented in Longo et al. (2005) were found to be erroneous as confirmed with the authors by personal communications. The C_{T15C} in Fig. 3 and σ and τ data in Fig. 4 of Longo et al. (2005) were found to be C_T, 4σ, and 2τ, respectively, accordingly those data were corrected for Fig. 21 of the present study.

[16] Also tested were three other regression equations: $y = a + b\sigma$; $y = a + c\tau$; $y = a + b\sigma + c\tau$. The resulting correlation coefficients were r = 0.80, 0.93, and 0.96, respectively.

$a + b\sigma + c\tau + d\sigma\tau$. The result shown in Fig. 6-20 (a) demonstrates a good agreement between C_{T15} and $y(\sigma, \tau)$ with a correlation coefficient r = 0.99, indicating that C_{T15C}, i.e. X for static drift, is strongly correlated with σ and τ, i.e. heave and pitch, such that $X \sim f(\sigma, \tau; Fr)$ at $\beta = 0°$.

Dynamic test results are shown Fig. 6-21 for pure sway at β_{max} = 10° (left column), pure yaw at r_{max} = 0.3 (middle column), and yaw and drift at β = 10° (right column) cases, respectively. Overall trends are similar as for static drift; for dominant harmonic amplitudes such as the 0th-order amplitude X_0 and the 1st-order amplitudes Y_1 and N_1, data are close between the $FX_{\sigma\tau}$ and FX_0 conditions and between the $FR_{z\theta}$ and $FR_{z\theta\phi}$ conditions, but different between the $FR_{z\theta}$ and FX_0 conditions. Between the $FX_{\sigma\tau}$ and FX_0 conditions, for pure sway and pure yaw tests, data are fairly close each other with $\xi_{\sigma\tau}$ = 0.9 ~ 1.0 for X_0 and $\xi_{\sigma\tau}$ = 1.0 ~ 1.1 for Y_1 and N_1. For $FR_{z\theta}$ condition, compared to FX_0 condtion, the dominant harmonic amplitudes are fairly larger for pure sway data with $\xi_{z\theta}$ = 1.1 ~ 1.3, and moderately larger for pure yaw data with $\xi_{z\theta}$ = 1.0 ~ 1.1 and for yaw and drift data with $\xi_{z\theta}$ = 1.1 ~ 1.2, respectively. For yaw and drift data, however, the 1st-order amplitude X_1 of $FR_{z\theta}$ is significantly larger than FX_0 with $\xi_{z\theta}$ = 3.7. Those data for $FR_{z\theta\phi}$ condition are close to $FR_{z\theta}$ in general with similar values of $\xi_{z\theta}$ for the dominant harmonic amplitudes and thus $\zeta_\phi \approx 1.0$ indicating the effect of roll motions on those dominant harmonics data is small or nearly negligible. In contrast, the 1st-order phases φ_{Y1} and φ_{N1} are close between all mount conditions for all test types, with $\xi_{\sigma\tau}$, $\xi_{z\theta}$, $\xi_{z\theta} \approx 1.0$, implying that the ratios between the added-mass and the damping forces, as shown in (3) and (4), remains almost constant despite the changes in the harmonic amplitudes Y_1 and N_1 between mount conditions. Nonetheless, no clear trend of those data such as (12) for static drift data, is observed from the dominant harmonics data with the PMM motion parameters such as β_{max}, r_{max}, or β, or with Fr.

Hydrodynamic derivatives are compared between the mount conditions in Table 6-19 for sway, yaw, and cross-coupled derivatives. For the sway derivatives, sway velocity derivatives Y_v, N_v, X_{vv}, Y_{vvv} and N_{vvv} are by using the static drift data and the sway acceleration derivatives $Y_{\dot{v}}$ and $N_{\dot{v}}$ are using the MR_L method (Section 2.3.5) for the pure sway test data, respectively. The yaw derivatives Y_r, N_r, X_{rr}, Y_{rrr}, N_{rrr}, $Y_{\dot{r}}$, $N_{\dot{r}}$ and the cross-coupled derivatives X_{vr}, Y_{vrr}, Y_{rvv}, N_{vrr}, N_{rvv} are as well using the MR_L method for the pure yaw and yaw and drift tests data, respectively. Note that those derivatives for $FR_{z\theta\phi}$ condition are using the SR_L method (Section 2.3.5) due to the limited number of test case, except for the sway velocity derivatives. As $FR_{z\theta}$ is the most common mount condition for PMM tests, of interest herein are the ratios ζ_0, $\zeta_{\sigma\tau}$, and ζ_ϕ of those derivatives for FX_0, $FX_{\sigma\tau}$, and $FR_{z\theta\phi}$ condition, respectively, to for $FR_{z\theta}$ condition defined as

$$\zeta_{0,\sigma\tau,\phi} \equiv \frac{x_{0,\sigma\tau,z\theta\phi}}{x_{z\theta}} \tag{6.13}$$

where x_0, $x_{\sigma\tau}$, $x_{z\theta\phi}$, and $x_{z\theta}$ can be any quantity from the FX_0, $FX_{\sigma\tau}$, $FR_{z\theta\phi}$, and $FR_{z\theta}$ conditions, respectively. For sway derivatives, linear derivatives Y_v and N_v values of FX_0 condition are slight smaller than $FR_{z\theta}$ about 10% with $\zeta_0 = 0.9$ in average, while those of $FX_{\sigma\tau}$ condition are close to $FR_{z\theta}$ with $\zeta_{\sigma\tau} \approx 1.0$, respectively. The non-linear derivatives X_{vv}, Y_{vvv}, and N_{vvv} of both FX_0 and $FX_{\sigma\tau}$ conditions, however, are considerably smaller than $FR_{z\theta}$ with ζ_0, $\zeta_{\sigma\tau} \approx 0.6$, and the sway acceleration derivatives $Y_{\dot{v}}$ and $N_{\dot{v}}$ are as well smaller, with ζ_0, $\zeta_{\sigma\tau} \approx 0.8$ for the former derivative and ζ_0, $\zeta_{\sigma\tau} \approx 0.6$ for the latter, respectively. On the other hand, for $FR_{z\theta\phi}$ condition, all the sway derivative values are close to $FR_{z\theta}$ with $\zeta_\phi \approx 1.0$ except for a few cases. For yaw derivatives, linear derivatives Y_r and N_r of all mount conditions are close to $FR_{z\theta\phi}$ typically with ζ_0, $\zeta_{\sigma\tau}$, $\zeta_\phi = 0.9 \sim 1.2$, whereas the non-linear derivatives X_{rr}, Y_{rrr}, N_{rrr} are usually smaller than $FR_{z\theta\phi}$ for FX_0 and $FX_{\sigma\tau}$ conditions with ζ_0, $\zeta_{\sigma\tau} = 0.5 \sim 0.7$ in general. Those non-linear derivatives of $FR_{z\theta\phi}$ condition, however, are rather scattering both magnitude and sign of the derivatives

as those are determined using the 'Single-Run' method usually unreliable determining non-linear derivatives as discussed previously in Section 6.1.2. The yaw acceleration derivative $Y_{\dot{r}}$ values also scatter between the mount conditions with ζ_0, $\zeta_{\sigma\tau}$, ζ_ϕ = 0.5 ~ 1.3 but without consistency between cases, while $N_{\dot{r}}$ values for FX_0 and $FX_{\sigma\tau}$ conditions are smaller than $FR_{z\theta}$ with ζ_0, $\zeta_{\sigma\tau} \approx 0.8$ and for $FR_{z\theta\phi}$ condition larger with ζ_ϕ = 1.1 ~ 1.2, respectively. The comparisons results for the cross-coupled derivatives X_{vr}, Y_{vrr}, Y_{rvv}, N_{vrr}, and N_{rvv} are similar with for $N_{\dot{r}}$ but with larger ratio values; $\zeta_0 \approx 0.3$ for FX_0 condition (except for Y_{vrr} and Y_{rvv} for which ζ_0 = 1.0 and 0.8, respectively) and ζ_ϕ = 1.1 ~ 1.3 for $FR_{z\theta\phi}$ condition, respectively.

Consequently, by imposing a fixed amount of singkage and trim or by allowing the model to move freely in heave, pitch, or roll, the forces and moment increased up to about 10% and up to about 30% within the range of test conditions, respectively, from a condition where the model is completely restrained in all motions. For static drift test, the increase in forces and moment was mainly attributed to the heave motion for $\beta > 0°$, whereas at $\beta = 0°$, X force was correlated with both heave (sinkage) and pitch (trim) motions. Typically, the effect of roll motion was small or negligible for both static and dynamic forces and moment, possibly due to the small magnitudes of the roll motions. Despite the differences in forces and moment due to the heave and pitch motions, usually the linear hydrodynamic derivatives were close between the mount conditions, within a range of 90% ~ 110% range, whereas the non-linear derivative values were smaller for the fixed-model conditions typically more or less than 40% ~ 70% compared to the free-model conditions. The effect of roll motions was as well small or negligible for the hydrodynamic derivatives.

Table 6-17 Comparisons between mount-conditions (Static drift).

β	Var.	Fr = 0.138			Fr = 0.280				Fr = 0.410		
		$\xi_{z\theta}$	$\xi_{z\theta\phi}$	ζ_ϕ	$\xi_{\sigma\tau}$	$\xi_{z\theta}$	$\xi_{z\theta\phi}$	ζ_ϕ	$\xi_{z\theta}$	$\xi_{z\theta\phi}$	ζ_ϕ
0°	X	1.05	1.04	0.98	1.03	1.07	1.10	1.03	1.26	1.30	1.03
10°	X	1.08	1.07	0.99	1.03	1.14	1.14	1.00	1.32	1.37	1.03
	Y	1.08	1.06	0.99	1.05	1.11	1.12	1.00	1.25	1.29	1.03
	N	1.10	1.09	0.99	1.07	1.17	1.18	1.00	1.29	1.29	1.00
20°	X	1.16	1.15	0.99	1.03	1.26	1.21	0.96	-	-	-
	Y	1.06	1.07	1.01	1.06	1.24	1.21	0.98	-	-	-
	N	1.09	1.11	1.01	1.07	1.33	1.26	0.95	-	-	-

Table 6-18 Comparisons between mount-conditions (Dynamic tests at Fr = 0.280).

Var.	Har.	Pure Sway (β_{max} = 10°)				Pure Yaw (r_{max} = 0.30)				Yaw and Drift (β = 10°)		
		$\xi_{\sigma\tau}$	$\xi_{z\theta}$	$\xi_{z\theta\phi}$	ζ_ϕ	$\xi_{\sigma\tau}$	$\xi_{z\theta}$	$\xi_{z\theta\phi}$	ζ_ϕ	$\xi_{z\theta}$	$\xi_{z\theta\phi}$	ζ_ϕ
X	X_0	0.98	1.34	1.17	0.87	0.94	1.10	1.09	0.99	1.14	1.12	0.99
	X_1	-	-	-	-	-	-	-	-	3.74	4.05	1.08
Y	Y_0	-	-		-	-	-		-	1.13	1.12	0.99
	Y_1	1.08	1.12	1.13	1.01	1.00	1.00	0.99	0.99	1.13	1.09	0.97
	φ_{Y1}	1.00	1.03	1.03	1.00	1.03	0.98	0.98	1.00	0.98	1.00	1.02
N	N_0	-	-		-	-	-		-	1.22	1.22	1.00
	N_1	1.09	1.21	1.21	1.00	1.10	1.13	1.13	1.00	1.25	1.21	0.97
	φ_{N1}	1.00	1.03	1.02	1.00	1.01	1.00	1.00	1.00	1.00	1.00	1.00

Table 6-19 Comparisons between mount-conditions (Hydrodynamic derivatives).

Derivative	Fr	ζ_0	$\zeta_{\sigma\tau}$	ζ_ϕ
Y_v	0.138	0.92	-	0.97
	0.280	0.96	1.00	1.02
	0.410	0.89	-	1.07
N_v	0.138	0.90	-	0.97
	0.280	0.90	0.97	1.03
	0.410	0.86	-	1.05
X_{vv}	0.138	0.40	-	1.02
	0.280	0.65	0.67	0.89
	0.410	0.54	-	1.03
Y_{vvv}	0.138	0.98	-	1.07
	0.280	0.62	0.67	0.92
	0.410	0.56	-	0.91
N_{vvv}	0.138	0.95	-	1.14
	0.280	0.27	0.27	0.69
	0.410	0.41	-	0.78
$Y_{\dot{v}}$	0.280	0.81	0.87	1.02
$N_{\dot{v}}$		0.55	0.57	0.95
Y_r	0.138	1.05	-	0.65
	0.280	0.98	1.08	0.86
	0.410	1.18	-	1.19
N_r	0.138	0.98	-	0.95
	0.280	1.12	0.99	0.98
	0.410	0.91	-	1.17
X_{rr}	0.138	-0.55	-	-0.14
	0.280	0.71	1.02	-0.31
	0.410	0.57	-	0.02
Y_{rrr}	0.138	1.43	-	2.54
	0.280	0.47	0.47	3.56
	0.410	0.68	-	-0.36
N_{rrr}	0.138	1.00	-	1.53
	0.280	0.44	0.72	1.06
	0.410	0.55	-	0.06
$Y_{\dot{r}}$	0.138	0.73	-	1.12
	0.280	1.29	0.46	0.71
	0.410	0.98	-	0.95
$N_{\dot{r}}$	0.138	0.89	-	1.18
	0.280	-0.59	0.80	1.16
	0.410	0.81	-	1.06
X_{vr}	0.280	0.28	-	1.17
Y_{vrr}		1.03	-	1.26
Y_{rvv}		0.84	-	0.93
N_{vrr}		0.30	-	1.27
N_{rvv}		0.21	-	0.98

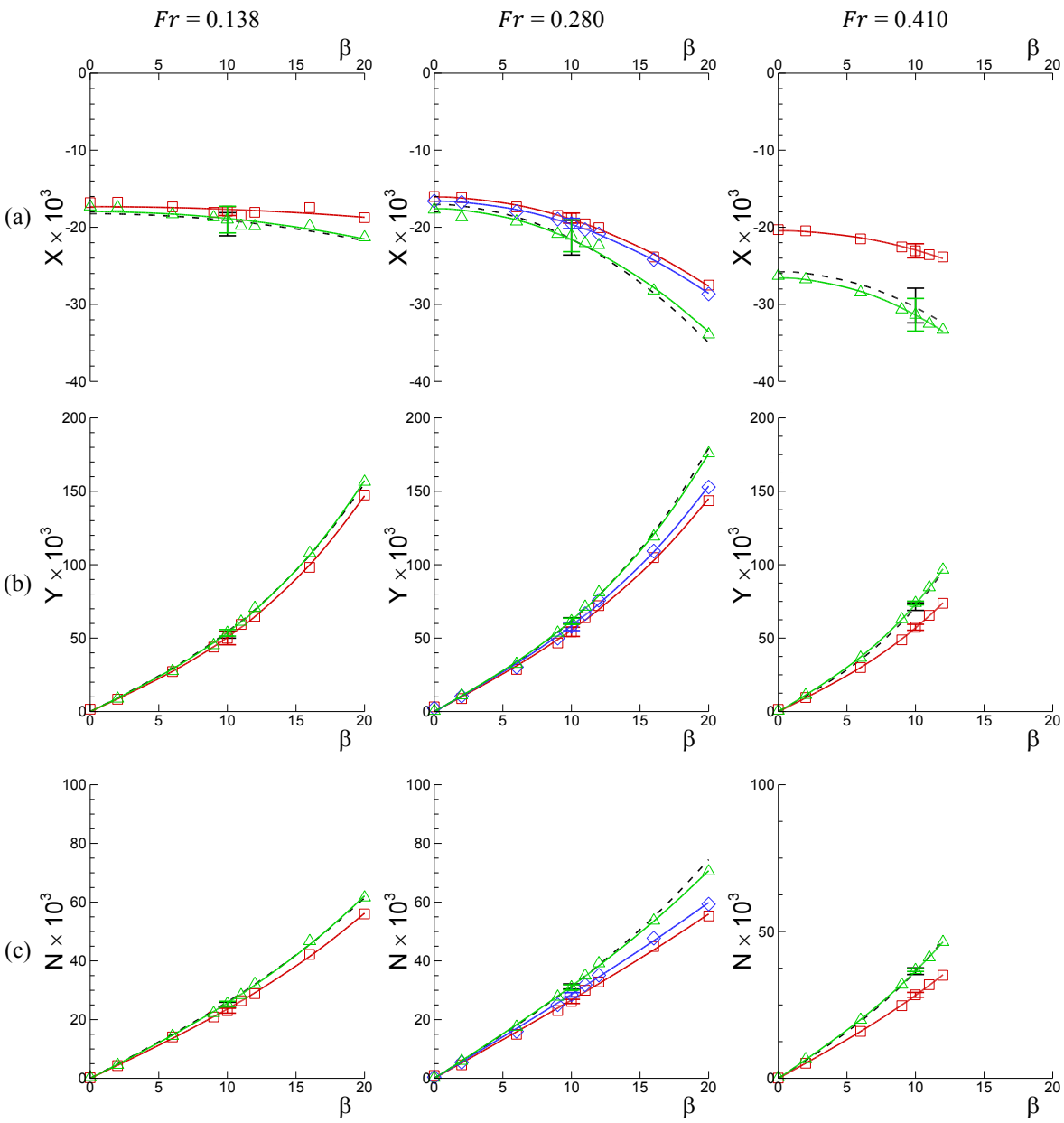

Figure 6-18 Comparisons between mount-conditions – Static drift data (Corrected for symmetry) at Fr=0.138 (left), 0.280 (center), and 0.410 (right): (a) X, (b) Y, and (c) N. Symbols (colors): □, FX_0; ◊, $FX_{z\theta}$; dash-line, $FR_{z\theta}$; and Δ, $FR_{z\theta\phi}$.

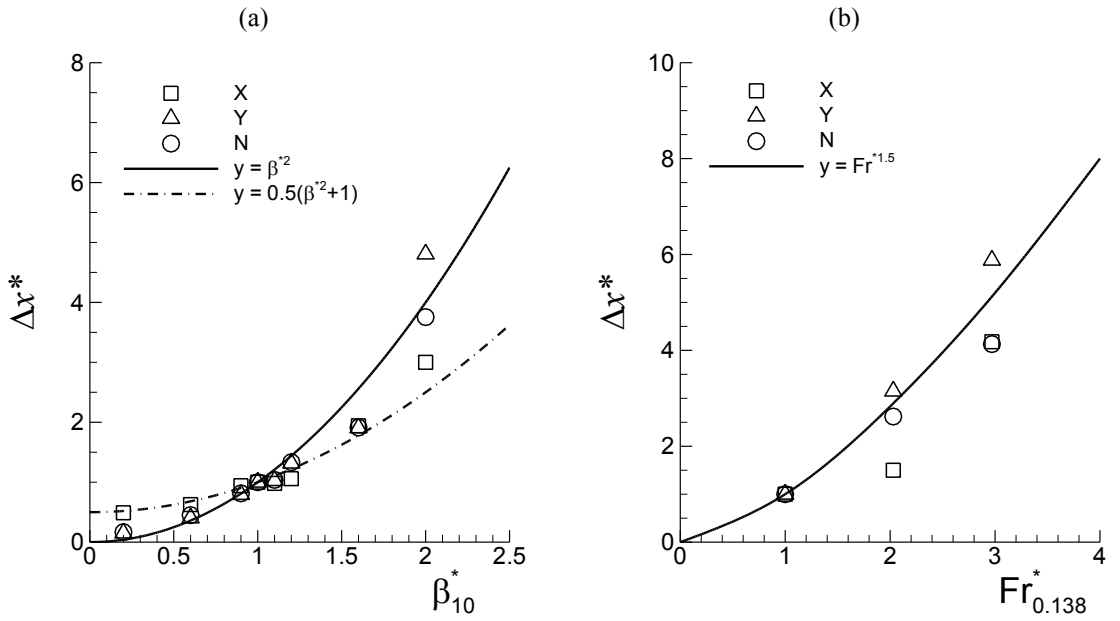

Figure 6-19 Comparisons of static drift X, Y, and N data between the $FR_{z\theta}$ and FX_0 mount conditions: (a) Δx vs. β at $Fr = 0.280$ and (b) Δx vs. Fr at $\beta = 10°$, where the Δx values are scaled with those at $\beta = 10°$ and with those at $Fr = 0.138$, respectively.

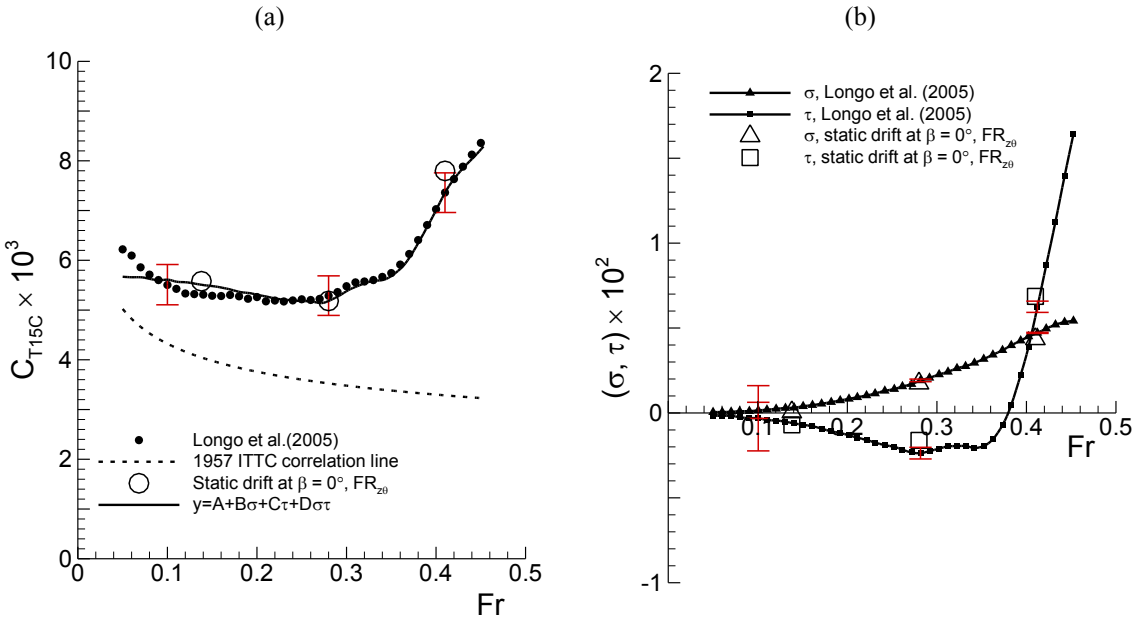

Figure 6-20 Comparisons of the static drift X, z, and θ data at $\beta = 0°$ with the resistance test (Longo et al. 2005): (a) C_{T15C} and (b) σ and τ.

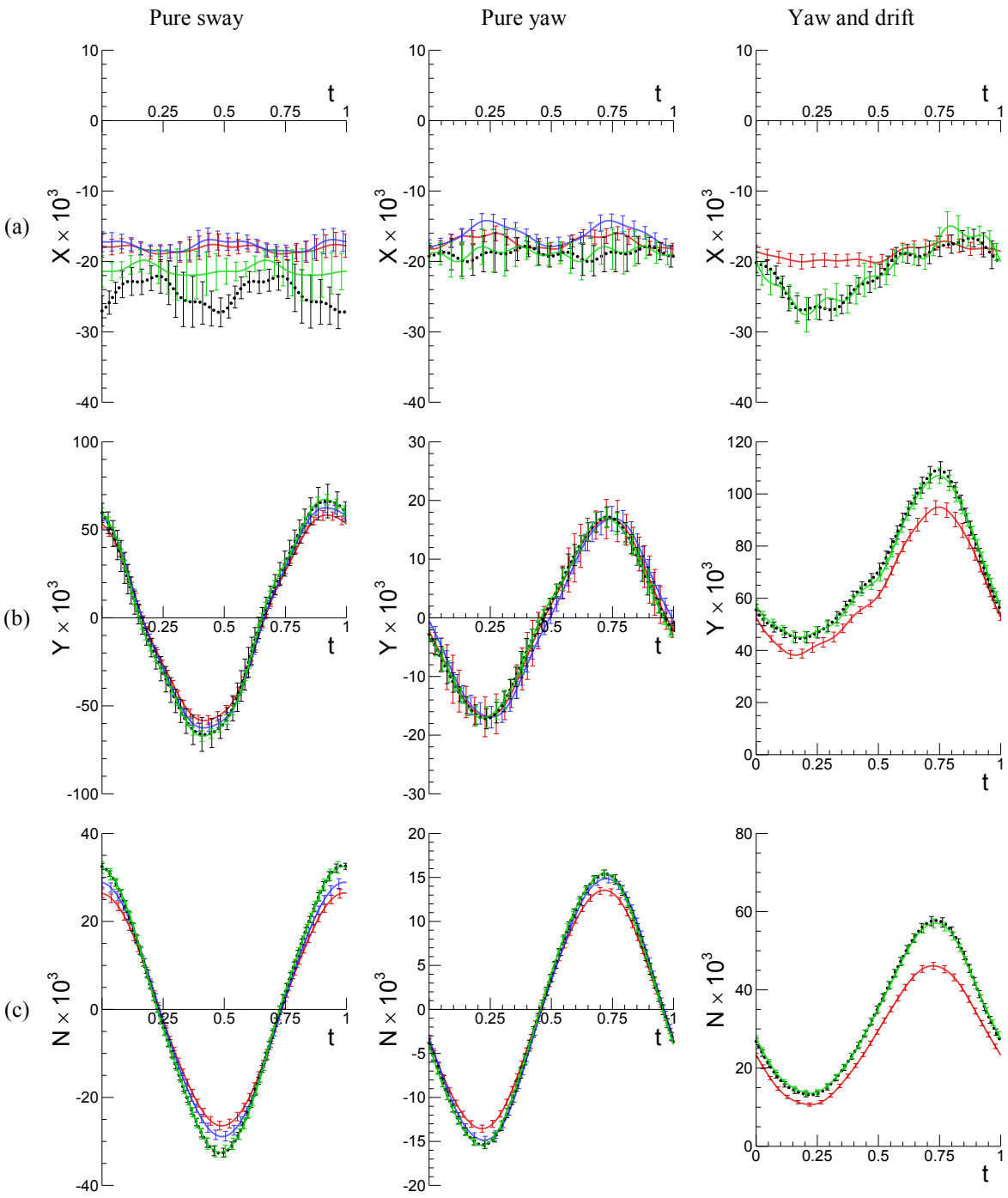

Figure 6-21 Comparisons between mount-conditions – Pure sway (left, β_{max} = 10° case), pure yaw (center, r_{max} = 0.30 case), and yaw and drift (right, β = 10° case) tests at Fr = 0.280 (Corrected for symmetry): (a) X, (b) Y, (c) N, (d) z, (e) θ, and (f) ϕ. Symbols (colors): —, FX_0; —, $FX_{z\theta}$; •, $FR_{z\theta}$; and —, $FR_{z\theta\phi}$.

6.2 Stereo-PIV measured flow fields

6.2.1 Pure sway flow field

The trajectory of model and overviews of flow around the model in pure sway motion are shown in Fig. 6-22. At the top of the figure model trajectory, i.e. the path line of model mid-ship point, is shown with a dashed line. The trajectory or the path line for pure sway motion is a combination of a constant towing carriage speed U_C and a cyclic sway motion $y = -y_0 \cdot \sin\omega t$, where the amplitude $y_0 = 0.104\ L$ and the frequency $\omega = 1.672\ U_C/L$ (period $T = 2\pi/\omega = 3.748\ L/U_C$) and $L = 3.048$ m is the model length and $U_C = 1.531$ m/s. In physical units, the sway frequency $f = 0.134$ Hz and the sway period $T = f^{-1} = 7.463$ sec. In the figure, the outlines of the model water-plane are shown at every 45° phases of the pure sway motion, $\gamma = \omega t = 0°$, 45°, 90°, 135°, 180°, 225°, 270°, 315°, and 360°, with numbered 1 through 9, respectively. For the first half of the cycle, model moves with its maximum negative (toward portside) sway velocity $v = -y_0\omega = -0.174$ at (1) $\gamma = 0°$ and decelerates through (2) $\gamma = 45°$ to (3) $\gamma = 90°$ where $v = 0$, and then changes its sway direction (toward starboard) and accelerates through (4) $\gamma = 135°$ to (5) $\gamma = 180°$. For the second half of the cycle, 5, 6, 7, and 8 are anti-symmetric with the 1, 2, 3, and 4, respectively, and 9 is identical with 1.

Below the model trajectory in Fig. 6-22, shown are the overviews of the SPIV measured flow field around the model at each of those phase positions. As well shown is the model path line (the curved lines with colored in light blue through the model) to emphasize the movement of model. As the model moving along the path line, accordingly the direction of incoming flow changes with the phase angle continuously, e.g. 10°, 7°, 0°, and -7° at $\gamma = 0°$, 45°, 90°, and 135°, respectively, (shown as blue arrows below at the model sonar dome in Fig. 6-1) with respect to the model center line, and in the opposite directions at the second half of the sway cycle. The flow field data presented in the figures are the contours of axial velocity U (≤ 0.95) and the cross flow streamlines, respec-

tively at four longitudinal locations, x = 0.135, 0.235, 0.735, and 0.935. Note that the streamlines are relative to model movements, i.e., seen from onboard. The overall flow pattern is with growing boundary layers in the longitudinal direction (thin at the fore body and thick at the aft body), and is mainly lateral flow in the cross planes where several apparent vortices are seen clearly, in general at the leeward side of the cross flow.

6.2.1.1 Vortical structure of the flow

More complete vortical structure of the flow can be seen from CFD simulations such as Sakamoto (2009) where the flows around DTMB 5512 geometry in steady and dynamic PMM motions are simulated. Simulation results for steady PMM motions are shown in Fig. 6-23, presenting the vortical flow structures for (a) straight-ahead and (b) static drift with drift angle $\beta = 10°$ cases. Sakamoto (2009) visualized the vortical flow structures by using the Q-criterion (Hunt et al., 1988) along with the relative helicity values; positive values for counterclockwise rotation (red colored) when viewed from behind a body and negative values for clockwise rotation (blue colored). For the straight-ahead case, i.e. $\beta = 0°$, the vortical structure is symmetry about hull center plane and with vortices in pairs of counter-rotating vortices. At the fore body sonar dome vortex (SD) and fore body keel vortex (FK) are generated behind the sonar dome and along the keel line, respectively. At the aft body, bilge keel vortex (BK), aft body keel vortex (AK), and transom vortex (T) are seen behind the bilge keels, neat at the aft body keel, and after the transom, respectively, however those vortices persist locally and are small in size in general. Note that the subscripts of the labels in the figure such as P, S, and C represent the portside, starboard, and center keel of the hull, respectively, where the vortices are generated. For $\beta = 10°$, the vortical structure is asymmetric about the hull center plane and vortices becomes considerably larger and global compared to the straight-ahead case.

The vortical flow structures for pure sway are shown in Fig. 6-24 (a) and (b), with vortices visualized from the CFD simulations by Sakamoto (2009) and from the vorticity

field measured by SPIV, respectively. In the figures vortical structures are shown at four sequential sway phase positions, $\gamma = 0°$, 45°, 90°, and 135°, in a column, so that the trajectory of the hull and the dynamic features of the vortical structures are envisioned. For CFD in (a), the vortical structures are in general similar with those for static drift with $\beta =$ 10° case shown in Fig. 6-23 (b), whereas the size, location, and the sign (direction of vortex rotation) of the vortices may change along the sway motion. For SPIV in (b), vortices are visualized with the vorticity ω_x contours with colored in red for $\omega_x \geq 20$ and in blue for $\omega_x \leq -20$ representing the counter-clockwise and clockwise rotations seen from behind the model in accordance with the helicity color coding for CFD. The ω_x contours are compared with the helicity iso-surfaces of CFD and corresponding vortices are identified with labeled in the figure. From CFD, SD_S vortex is first short and away from the hull at $\gamma = 0°$ and stretching in length and approaching toward the hull at $\gamma = 45°$ and thinning and straightened and close to the center plane at $\gamma = 90°$ and then detaches from the sonar dome and begins a counter rotating SD_P vortex at $\gamma = 135°$. Sakamoto (2009) reported that the angle between the SD_S and the hull center plane α_{SDs1} ~15° at non-dimensional time $t/T \sim 0.14$ or at $\gamma \sim 50°$. BK_P vortex at the portside, the second largest one, exhibits similar trend as SD; stretching and straightening, thinning, and then begins a counter rotating vortex. From SPIV, SD is not captured well at the stern side for $\gamma = 0°$ and 45°, maybe its location is out of the SPIV measurement area. At the fore body and for $\gamma = 90°$ and 135°, however, SD vortices can be seen clearly from the SPIV and seemingly in good agreement with CFD in terms of their size, location, and sign. FK vortices are not detected from SPIV or hard to be seen due to the lack of spatial resolution of SPIV measurement in the longitudinal direction, only two locations, $x = 0.135$ and 0.235, at the fore body where the FK vortices are from CFD. Whereas both BK_P and BK_S clearly seen from SPIV and in general exhibit qualitatively good agreements with CFD for their size, location, and direction of rotation, from a visual inspection. For other vortices, AK_C vortex near at the center of x = 0.935 plane in general matches well between CFD and SPIV,

whereas FS vortices are not clear from SPIV due to its limited amount of data and relatively larger uncertainty in measurements near at the free surface. The transom vortex T of CFD is out of SPIV measurement scope.

6.2.1.2 Phase-averaged velocity field

Phase-averaged mean axial velocity U is shown in Fig. 6-25 for the four longitudinal locations, x = 0.135, 0.235, 0.735, and 0.935 (from top to bottom), and for the four pure sway phase positions, γ = 0°, 45°, 90°, and 135° (from left to right), where the SPIV measurements were made. The flows at the later phase positions, γ = 180°, 225°, 270°, and 315°, are the horizontally mirrored images of those, respectively. In the figures, contours (with flooded) are presented for $U \leq 0.95$ and those for $U > 0.95$ are blanked out and not shown, to emphasize the parts where the flow is retarded from the incoming free stream (or the boundary layers) only. As well shown are the cross-sections of the model (the light gray part) cut at the four longitudinal x locations and the front part of the model from the cut positions with projected into the paper (the darker gray part) to highlight the details of the model hull form such as the locations of the sonar dome and the bilge keels. The flow is seen from behind the model, looking upstream, thus, the longitudinal direction of the incoming flow is out of paper from the figures. The transverse direction of the incoming flow is from the portside to starboard (left to right in the figure) with respect to the model for the first two phases, γ = 0° and 45°, and with no transversal flow at 90° and in reverse (right to left in the figure) for 135°. The incoming flow directions at the several sway phase positions are depicted in Fig. 6-1, together with the path lines of the model in the pure sway motion.

From Fig. 6-25, the mean axial velocity contours at x = 0.135 reveal very thin boundary layers near around the hull, and under the keel a retarded flow region that is in the SD vortex and in the wake of the sonar dome. At x = 0.235, the retarded flow region becomes smaller in size and is confined at near beneath the keel, may be the flow is out

of the sonar dome wake and recovers its momentum. At $x = 0.735$, the boundary layer thickens at the girth-wise middle of the bilges at portside and starboard, $(y, z) = (-0.04, -0.03)$ and $(0.04, -0.03)$, respectively, thicker at leeward side, and apparently interacting with the BK vortices. At $x = 0.935$, the boundary layer thickens considerably, and a large size dead-flow zone where $U < 0.5$ appears at $\gamma = 90°$, underneath the aft body keel, near around $(y, z) = (0, -0.1)$.

The shape and size of the boundary layers typically changes along with the model sway motion, possibly interacting with nearby vortices; mainly with the SD vortex at $x = 0.135$ and 0.235, with the BK and SD vortices at $x = 0.735$, and with the BK, AK, and SD vortices at $x = 0.935$. The shape of boundary layers at $\gamma = 0°$, 45°, and 135°, as expected, is asymmetry with respect to the hull center plane (i.e., $y = 0$) due to the transverse flow caused by the model sway motion, whereas it is notable that the boundary layer is as well asymmetry, particularly at the aft body, even at $\gamma = 90°$ where the incoming free stream flow is zero in transverse direction such that the incoming free stream flow is tangential to the model path line, i.e. straight ahead condition. This is due to the dynamic motions of the model such that while the vortices around the model are changing their size, spatial location relative to the model, and the direction of rotation, dynamically, as shown in Fig. 6-24, those changes may not in-phase with the model sway motions. The phase difference between the vortices and the model motion will be discussed later together with the vorticity field.

In Figs. 6-26 and 6-27, the average $U_{\leq 0.9}$ and minimum $U_{\min}$ values of the phase-average axial velocity U within the boundary layers at each phase (top) and the Fourier Series (FS) 0^{th}- and 2^{nd}-order harmonics, H_0 and H_2, of those values respectively (bottom) are presented. The $U_{\leq 0.9}$ and $U_{\min}$ are the average value for $U \leq 0.9$ and the minimum value, respectively, out of the SPIV measured U data within the boundary layer at each phase positions and x locations shown in Fig. 6-25. Note that the $U_{\leq 0.9}$ and $U_{\min}$ for $180° \leq \gamma < 360°$ shown in Figs. 6-26 (top) and 6-27 (top) are the mirrored values from those for

$0° \le \gamma < 180°$ anti-symmetrically. From Fig. 6-26 (top), in spite of the considerable dynamic changes of the boundary layers in shape and size, the $U_{\le 0.9}$ values are almost constant about 0.8 through the sway phase and along the hull longitude. From Fig. 6-26 (bottom), H_0 of $U_{\le 0.9}$, the period mean value, first slightly increases from 0.81 at x = 0.135 to 0.84 at x = 0.235, and then decreases at the aft body to 0.81 and 0.79 at x = 0.735 and 0.939, respectively. From Fig. 6-26 (bottom), H_2, i.e. the oscillation amplitude of $U_{\le 0.9}$ values along with the sway motion, is 0.014 in average, corresponding to about 2% of H_0, which has the largest value of 0.022 at x = 0.735, about 3% of H_0. In contrast, from Fig. 6-27, the changes of $U_{\min}$ with γ and x are larger than $U_{\le 0.9}$. The H_0 of $U_{\min}$ is 0.65 at x = 0.135 and then decreases to 0.43 at x = 0.935 rather monotonically. The average H_2 value along x is 0.056, about 10% of average H_0 = 0.55, and the maximum H_2 is 0.092 at x = 0.735, about 18% of the H_0 value at the location.

Cross flow velocity (V, W) vector field is shown in Fig. 6-28. In the figure, shown are the every 6th vectors from the SPIV measurement grid points in both y and z directions. While the vector field exhibits directions of the flow and the presence of vortices around the model, as an alternative way presenting the cross flow, in Fig. 6-29, the cross flow vector magnitude $S = (V^2 + W^2)^{1/2}$ and the cross flow streamlines are shown together. The spots where flow is accelerating or stagnant are obvious from the S contours and directions of the flow is clear from the streamlines and the location and size of the vortices exposed as well from the streamlines. At the fore body, x = 0.135 and 0.235, the cross flow at γ = 0° and 45° is directed downward and accelerating along the hull at the portside and overturns the keel and the SD vortex (that is not generated by the cross flow, rather it is being pushed and displaced by the cross flow stream to the leeward side) and then merges with the flow at the starboard. The SD vortex at x = 0.135 is small in size, $\phi \sim 0.01\ L$, and grows at x = 0.235, $\phi \sim 0.02\ L$. ϕ is the diameter of concentric streamline spirals. At γ = 90° where the incoming flow is tangent to the model path line, flow is nearly symmetry about the model center plane and mainly down- and outward

with displaced by the volume of fore body. At $\gamma = 135°$, the whole flow reverses as the model changes its direction in sway motion. At the aft body, $x = 0.735$ and 0.935, the flow at $\gamma = 0°$ and 45° is nearly lateral at the portside and turns to upward past the center plane becoming reversal in part where it meets the BK vortex at starboard. At $\gamma = 90°$, flow is mainly up- and inward, however, the flow is not symmetry about the center plane due to the presence of the SD vortex at the starboard. The flow reverses at $\gamma = 135°$, similarly as at the fore body.

6.2.1.3 Turbulent kinetic energy and Reynolds stresses

Turbulent kinetic energy k field is shown in Fig. 6-30. In the figure, the k field is shown only for $k \geq 0.001$ and blanked out for $k < 0.001$. Reynolds number of the flow is $\mathrm{Re} = U_C L/\nu = 4.6\times10^6$ where U_C and L are the towing carriage speed and model length, respectively, and ν is the kinematic viscosity of fresh water. It is noted that for pure sway test only a limited number of data (N) is used for phase-averaging, typically $N \sim 60$ for $x = 0.135$, 0.235, 0.735 and $N \sim 200$ for $x = 0.935$. Thus, phase-averaged turbulent variable values such as Reynolds stresses including the turbulent kinetic energy may not be fully converged statistically, and may include the statistical convergence error E_U up to 50% for data at the former and to 25% at the later x locations, respectively (See Chapter 4 and Fig. 4-7b for $s^2/s_{\mathrm{ref}}^2 = 1.0$). From Fig. 6-30, the shapes of k contours in general coincide with those of the mean axial velocity contours shown in Fig. 6-25, and typically k exhibits larger value inside the boundary layer of the model and at the core region of the vortices.

In Figs. 6-31 and 6-32, presented are the time histories (top) and the FS harmonics (H_0 and H_2 respectively for 0^{th}- and 2^{nd}-order) of the time history (bottom) for k_{mean} and k_{max}, respectively. Herein k_{mean} and k_{max} are defined as the average k value for $k \geq 0.001$ and for $k \geq 0.01$, respectively, which represents approximately the mean and the maximum k values within the flow region of interest, respectively. The $k = 0.001$ contour line

corresponds to the boundary line (flow side) of each contour plot, and the $k = 0.01$ contour line is shown at each contour plots in Fig. 6-30 (white colored contour lines), respectively. From Fig. 6-31 (top), k_{mean} is oscillating between 0.004 ~ 0.008 ($I = 0.052$ ~ 0.073, or about 5 ~ 7% of U_C) at $x = 0.135$ and 0.235, whereas almost flat with $k_{mean} \approx$ 0.004 ($I = 0.052$ or about 5% of U_C) at $x = 0.735$ and 0.935. From Fig. 6-31 (bottom), H_0 = 0.006 and $H_2 = 0.002$ at $x = 0.135$ are respectively the largest, and then both decreases gradually to $H_0 = 0.004$ and $H_2 \sim 0$ at $x = 0.935$. On the other hand, from Fig. 6-32 (top), k_{max} is between 0.011 ~ 0.015 and oscillates with the sway phase γ. The turbulent intensity within the flow region is $I = (2/3 \cdot k)^{1/2} = 0.086 \sim 0.1$, corresponding to about 9 ~ 10% of U_C. From Fig. 6-32 (bottom), the period mean value of k_{max} is the largest at $x = 0.135$ with $H_0 = 0.014$ and the oscillation amplitude is the largest at $x = 0.235$ with $H_2 = 0.002$ that is about 14% of the largest H_0 value. In a mean sense, consequently, the flow may have $k \sim 0.013$ ($I \sim 9\%$ of U_C) locally at the high turbulent region and $k \sim 0.005$ ($I \sim 6\%$ of U_C) in overall average, typically larger at the bow but tend to be local while decreasing along the ship length gradually.

Reynolds normal (*uu*, *vv*, *ww*) and shear (*uv*, *uw*, *vv*) stress fields are shown in Fig. 6-33 through Fig. 6-38. Of the normal stresses, *uu* and *vv* fields shown in Figs. 6-33 and 6-34, respectively, exhibit almost and nearly similar appearances as the *k* field shown in Fig. 6-30, respectively, indicating that those components are dominant, whereas *ww* field shown in Fig. 6-35 is seemingly weaker than the other components. On the other hand, the shear stress *uv*, *uw*, and *vw* fields shown in Figs. 6-36 ~ 6-38, respectively, reveal smaller order of magnitude than the normal stresses, where the *uv* is apparently the dominant component. The Reynolds stresses are averaged over the regions where $k \geq$ 0.001 and $k \geq 0.01$, similarly as for k_{mean} and k_{max}, respectively, and the period mean values of those (corresponding to H_0) are shown in Figs. 6-39 and 6-40, respectively, with the normal stresses shown at top and the shear stresses at the bottom, respectively. For the region where $k \geq 0.001$ (i.e. the overall field average), from Fig. 6-39, the mean nor-

mal stress *uu*, *vv*, *ww* values are 0.005, 0.003, 0.002, respectively, and the mean shear stress *uv*, *uw*, *vw* values are 0.002, 0.001, and 0.001, respectively. For the region where $k \geq 0.01$, from Fig. 6-40, the mean values of normal stresses *uu*, *vv*, *ww* are 0.013, 0.009, 0.004 along the ship length, respectively, and those of the shear stresses *uv*, *uw*, *vw* are 0.006, 0.002, 0.002, respectively. The Reynolds stresses are anisotropic, if normalized with the isotropic stress value, $(2/3)\cdot k$, the normal stresses *uu*, *vv*, *ww* are 1.5, 1.0, 0.5, respectively, and the shear stresses *uv*, *uw*, *vw* are 0.7, 0.2, and 0.2, respectively, which are almost common for both of the $k \geq 0.01$ and $k \geq 0.001$ regions.

6.2.1.4 Axial vorticity field

Axial vorticity ω_x field is shown in Fig. 6-41, where presented are vorticity fields with values $\omega_x \geq 10$ and $\omega_x \leq -10$, otherwise blanked and not shown. The vorticity field is seen from behind the model and the axis is out of the paper from the figures, thus the positive axial vorticity ($\omega_x > 0$, colored in red) is rotating counter-clockwise and the negative axial vorticity ($\omega_x < 0$, colored in blue) is rotating clock-wise in the figure, respectively. Several vortices are observed from the ω_x field, such as the sonar dome (SD) vortex at the fore body, at $x = 0.135$ and 0.235, below and underneath the keel, respectively, and bilge keel (BK) vortices at the aft body, at $x = 0.735$ and 0.935, at the mid-bilge positions and below around the bottom profile, respectively, and the aft body keel (AK) vortex beneath the center keel position. A couple of minor vortices can be observed at the fore body, such as the fore body keel (FK) vortex beneath the keel and the free surface (FS) vortex typically at the windward side free surface, however, those vortices are in general not clear from the figures, and for the latter vortex its locations maybe out of the view of present SPIV measurement and measured partially. The overall structure of the vortical flow is presented in Fig. 6-24, and therein the CFD simulation result (Sakamoto 2009) discloses more complete pictures of the vortical flow.

In Fig. 6-42, the time histories of the maximum/minimum ω_x value of the SD vortex along the model sway motion phase position γ, respectively for x = 0.135 and 0.235 locations. The maximum ωx value is when the SD vortex has positive ω_x values, e.g. at γ = 0° and 45° from Fig. 6-41, and the minimum value is when negative ω_x value, e.g. at γ = 135° from Fig. 6-41. When the maximum/minimum values are FS reconstructed such that $H\cdot\cos(\omega t - \phi)$, the harmonic amplitude H = 293 and 213 and ϕ = 11° and 27° at x = 0.135 and 0.235, respectively, indicating about 3% decrease of its magnitude and a phase difference $\Delta\phi$ = 16° between the two locations, respectively. The trend of SDV vortex at the later x locations, however, is precluded, due to the lack of the measurement data at the after body locations.

Similarly, in Fig. 6-43, the maximum/minimum ωx value time histories of the BK vortex are shown for x = 0.735 and 0.935 locations. Note that the time history of BK vortex, however, is defined in a different way form the SD case. As can be seen from Fig. 6-41 for x = 0.735 location, the BK vortices at the portside and starboard are asymmetry respectively with respect to the model sway motion; one is at the wind side and the other is at the leeward side and after one half cycle respectively at the reverse side. Thus, the time histories at the portside/starboard may not be continuous along the model sway motion, i.e. along γ, but at the wind/leeward side of the flow. In other words, from Fig. 6-43, the data at the first half of the cycle are from the BK vortices at the portside and those at the second half are from the BK vortices at the starboard side, which are at the wind side through the cycle. When data are FS reconstructed similarly as for the SD vortex, H = 424 and 274 and ϕ = 19.4 and 35.9° at x = 0.735 and 0.935, respectively. The H's of the BK vortices at x = 0.735 and 0.935 are 145% and 85% of the SD vortex H value at x = 0.135, indicating that BK vortex may be stronger than SD vortex locally and decay fast. Whereas the phase difference of the BK vortices between the two x locations, $\Delta\phi$ = 16.5°, is similar with that for the SD vortex.

Lastly, the time history of AK vortex maximum/minimum ωx is shown in Fig. 6-44. The AK vortex is located nearly at the aft body keel center position and its behavior is symmetry with respect to the model sway motion, and the time history is defined as the same way as for SD vortex. AK vortex is observed only at $x = 0.935$, where H = 189 (about 65% of SD vortex H at $x = 0.135$) and $\phi = -11.3°$ from the FS reconstruction.

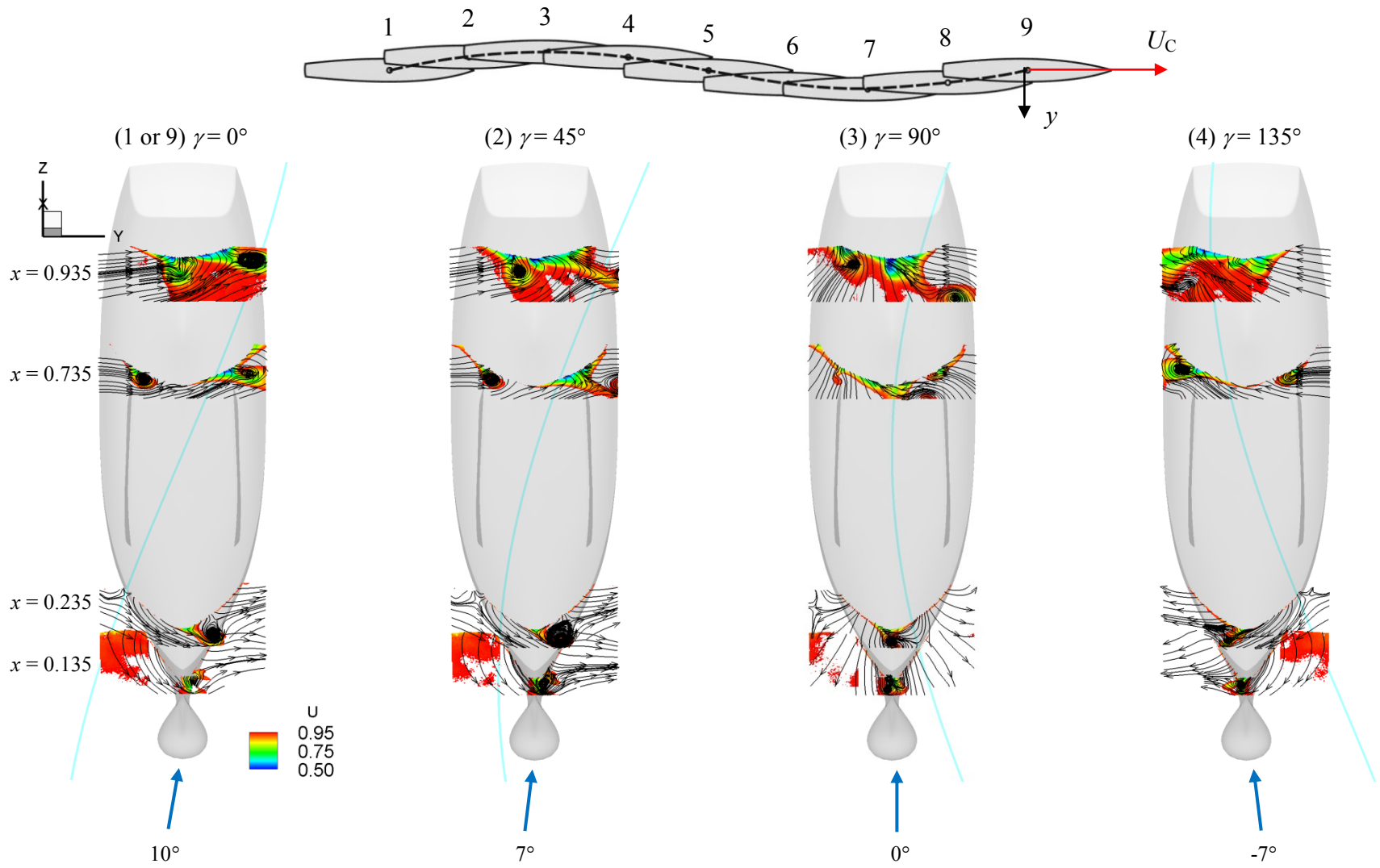

Figure 6-22 Trajectory of model in pure sway motion (top) and overviews of the flow around the model (below).

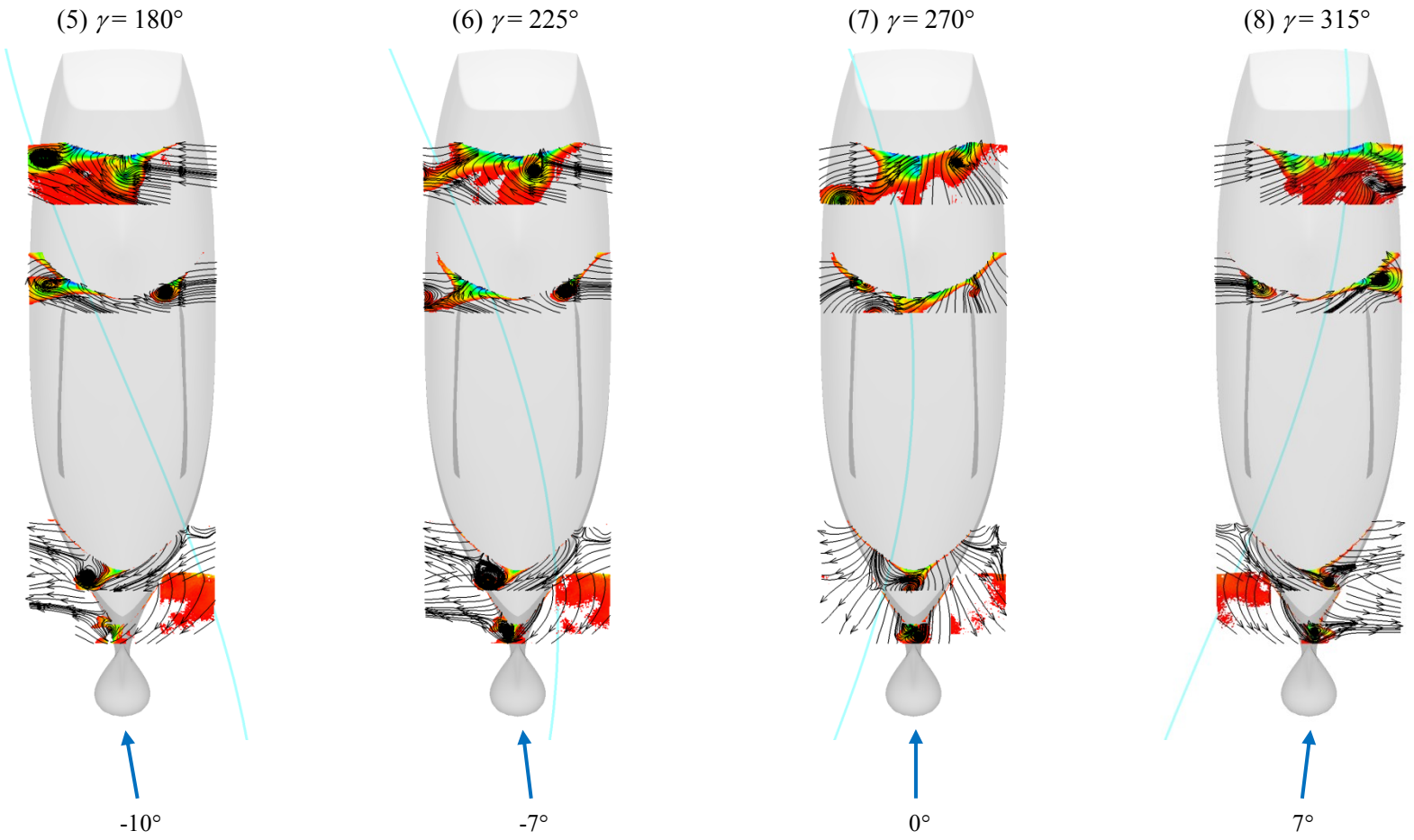

Figure 6-22–Continued

(a) (b)

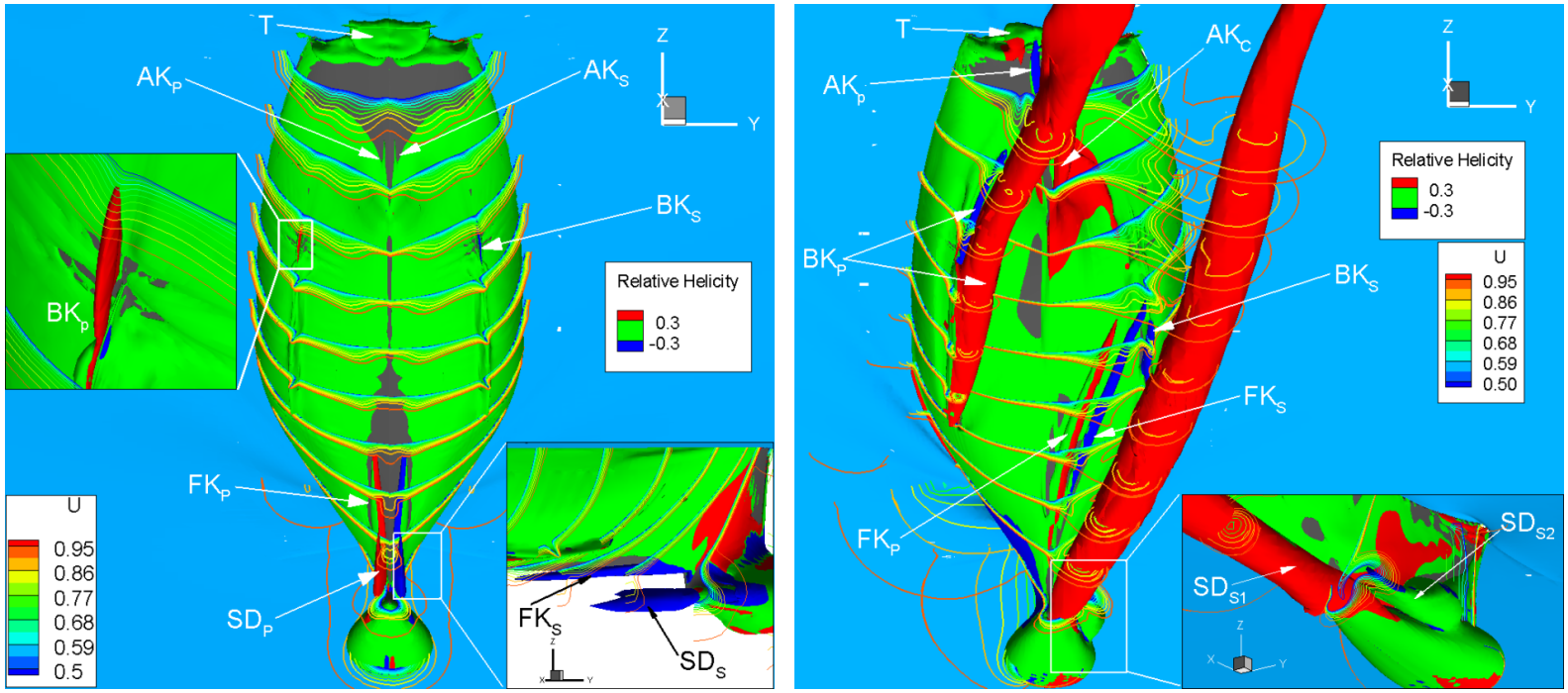

Figure 6-23 Vortical flow structures around the DTMB 5512 geometry in steady maneuvers for: (a) straight-ahead and (b) static drift at $\beta = 10°$ cases. (CFD simulations by Sakamoto 2009).

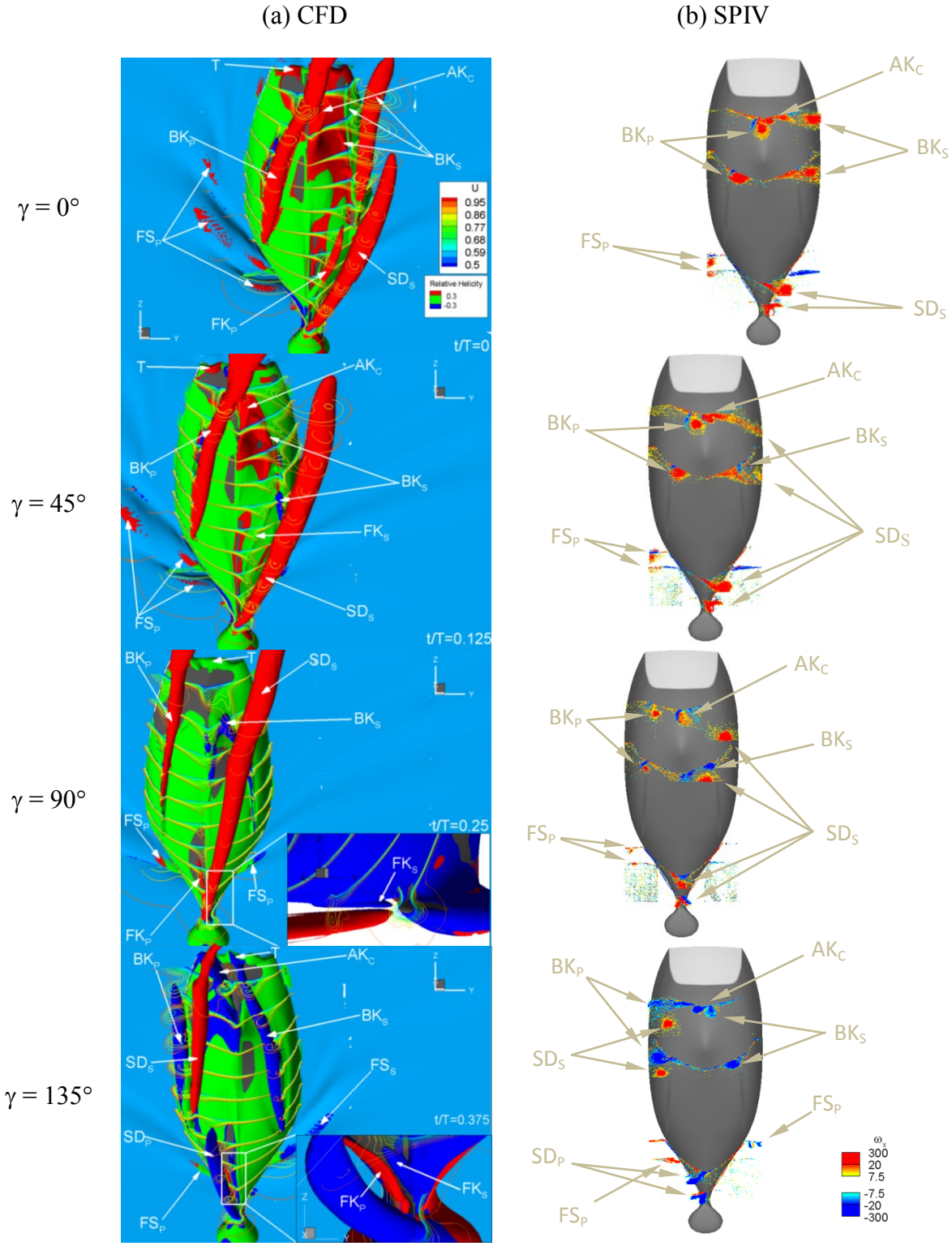

Figure 6-24 Vortical flow structures around the DTMB 5512 geometry in pure sway maneuvering with β_{max} = 10°: (a) Iso-surfaces of relative helicity (CFD simulations by Sakamoto 2009) and (b) contours of axial vorticity (SPIV).

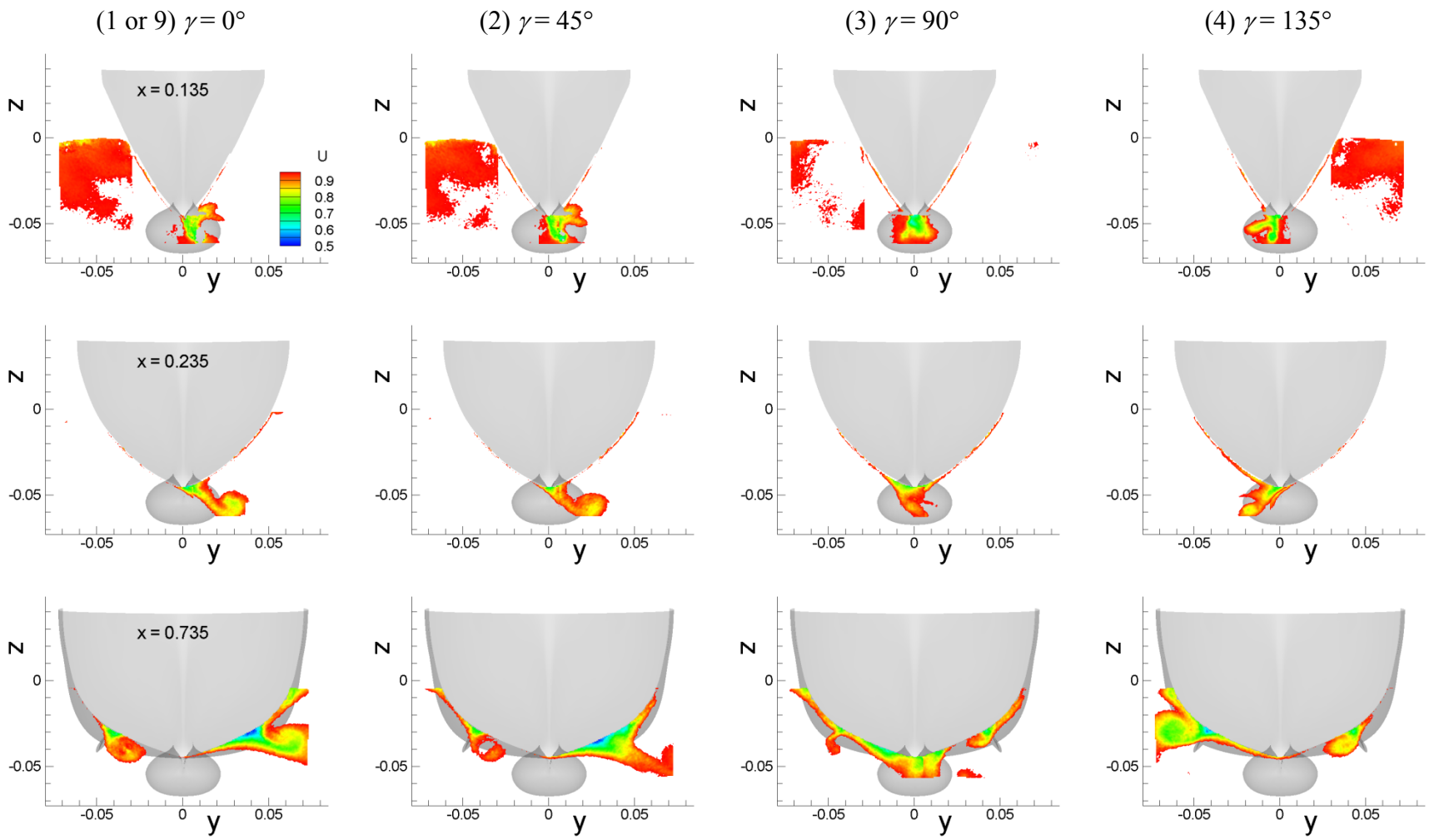

Figure 6-25 Phase-averaged axial velocity *U* field for pure sway test.

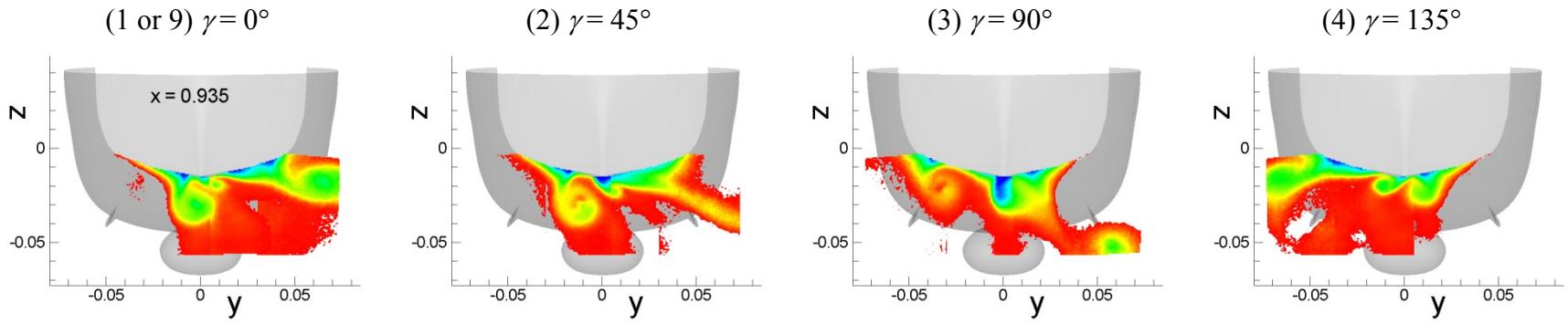

Figure 6-25–Continued

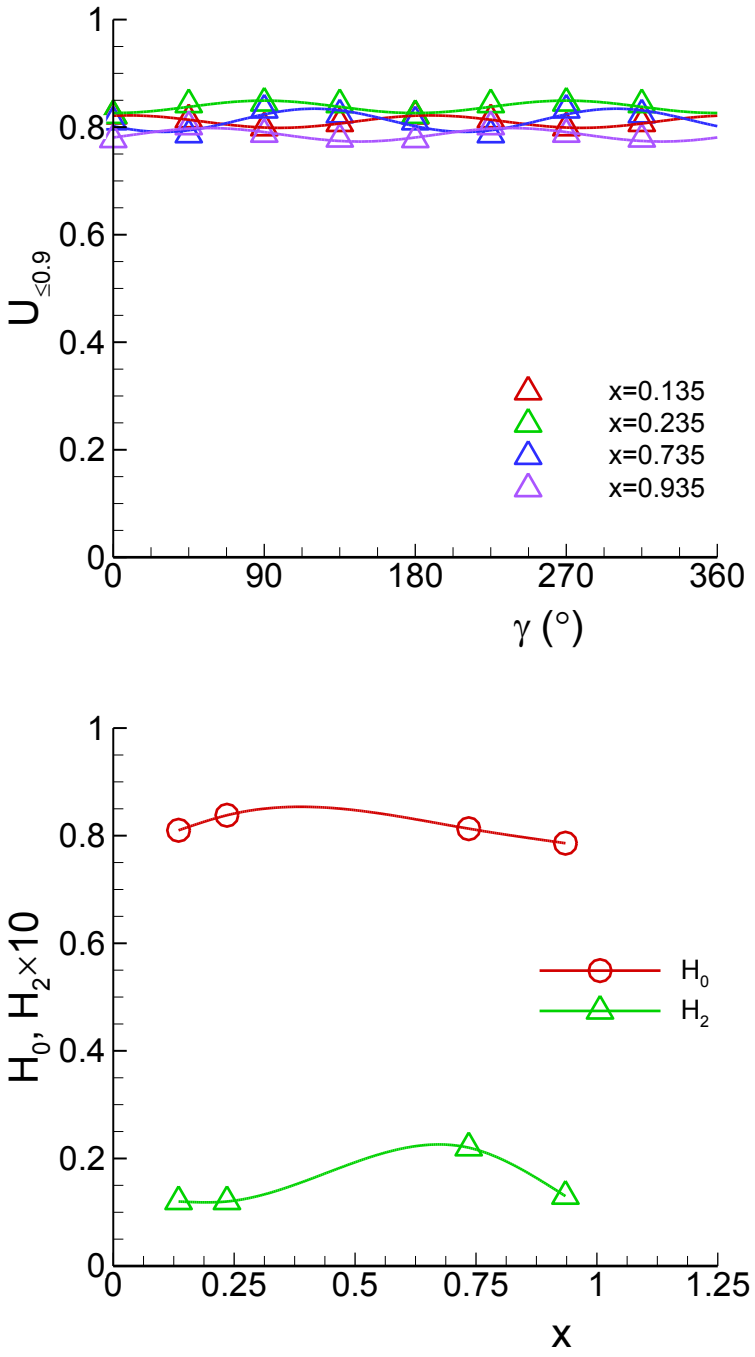

Figure 6-26 Time histories of the average axial velocity $U_{\leq 0.9}$ (top) and FS harmonics (bottom) for pure sway test.

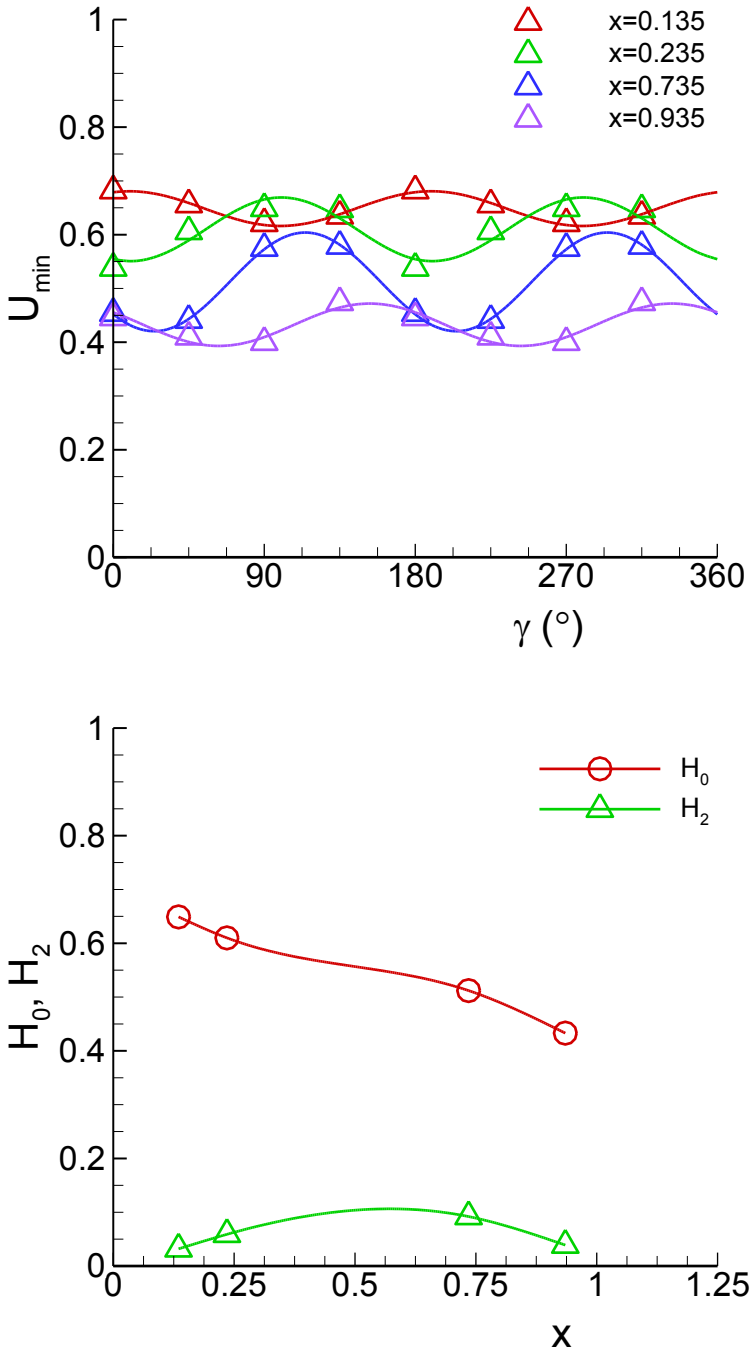

Figure 6-27 Time histories of the minimum axial velocity U_{min} (top) and FS harmonics (bottom) for pure sway test.

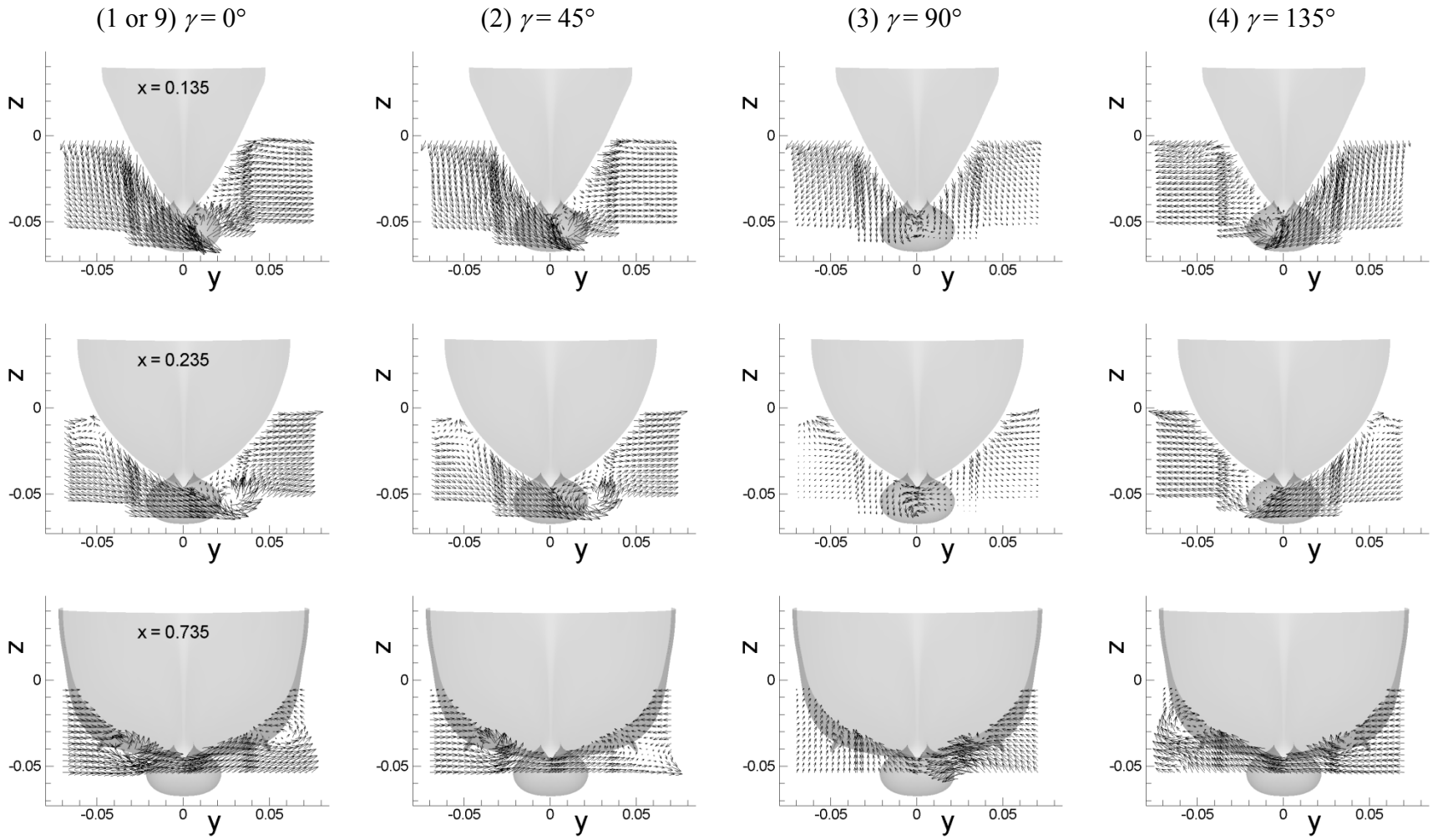

Figure 6-28 Phase-averaged cross-flow (V,W) vector field for pure sway test.

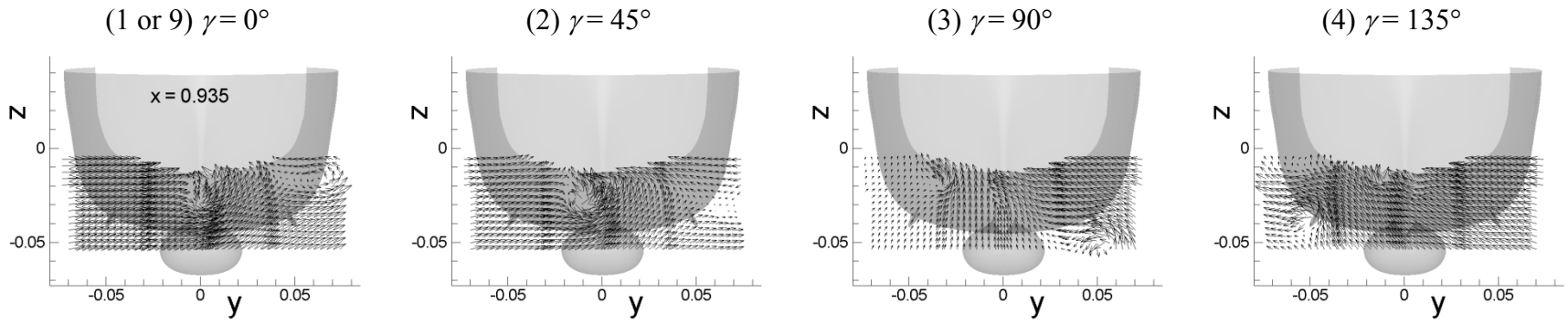

Figure 6-28–Continued

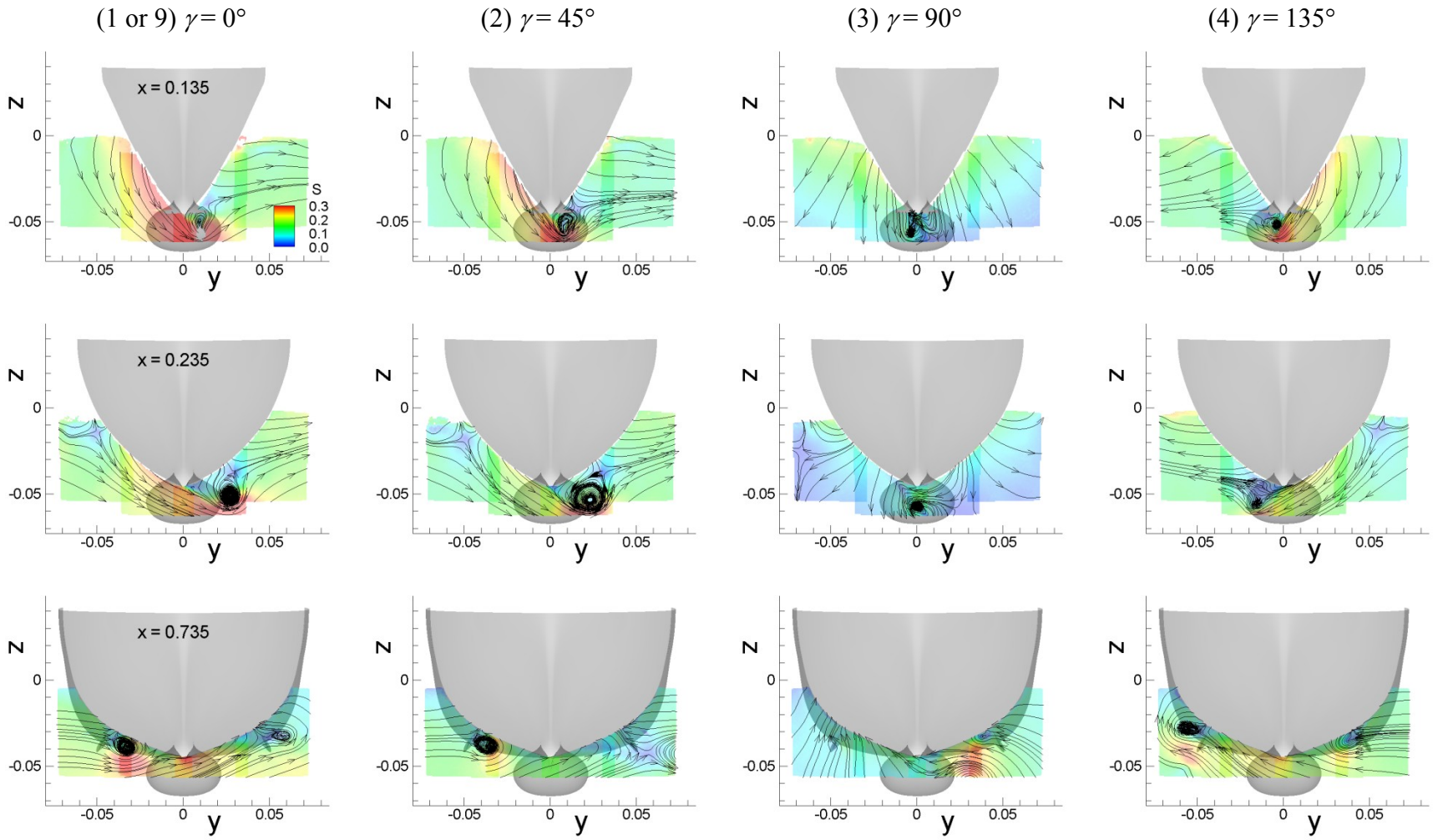

Figure 6-29 Cross flow velocity vector magnitude $S = (V^2 + W^2)^{1/2}$ and streamlines for pure sway test.

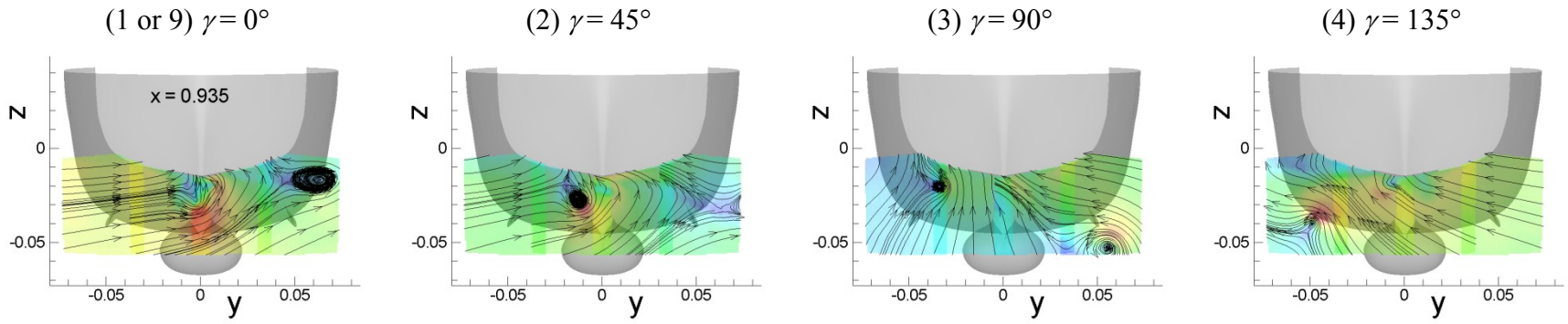

Figure 6-29–Continued

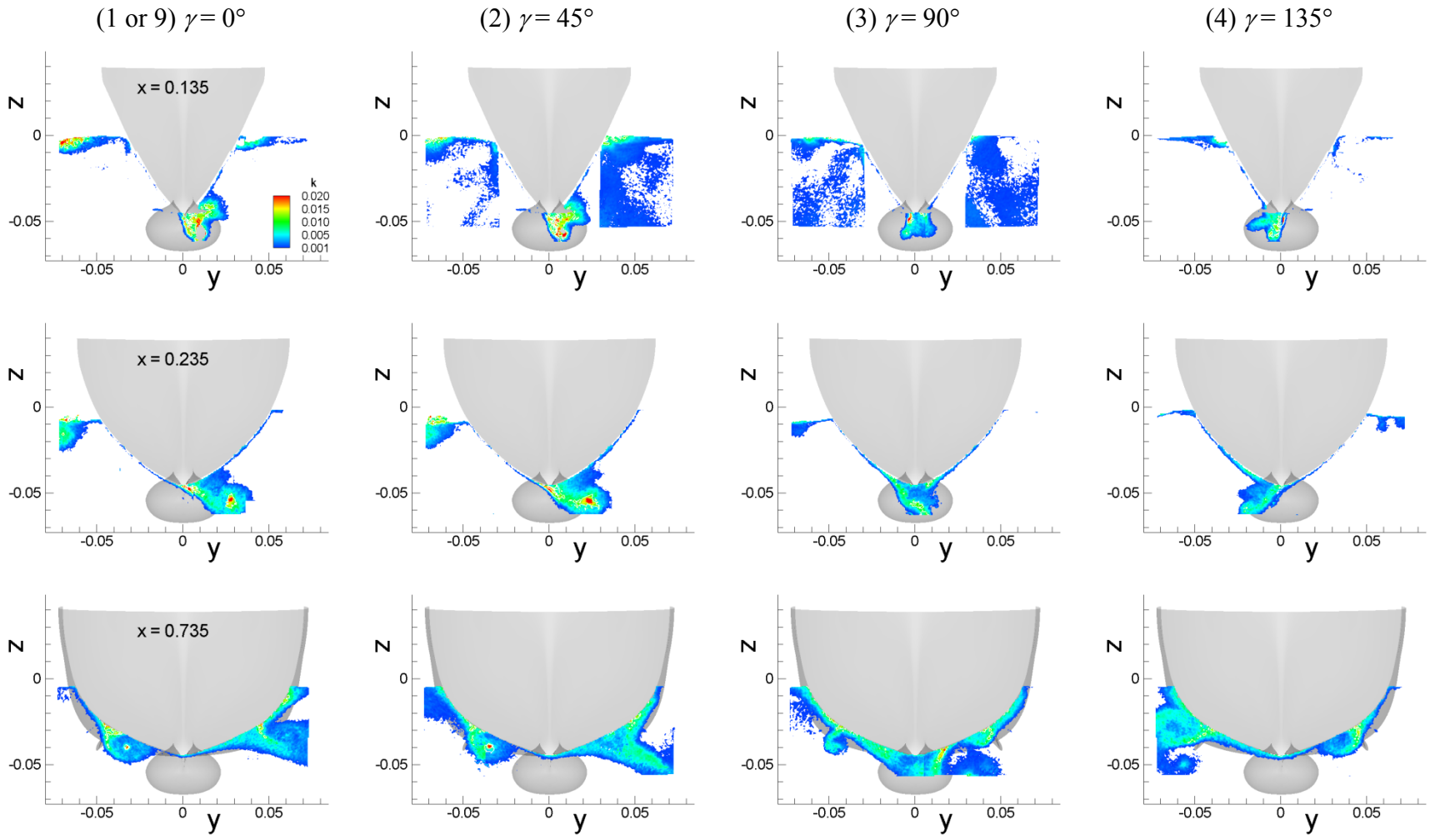

Figure 6-30 Phase-averaged turbulent kinetic energy *k* field for pure sway test.

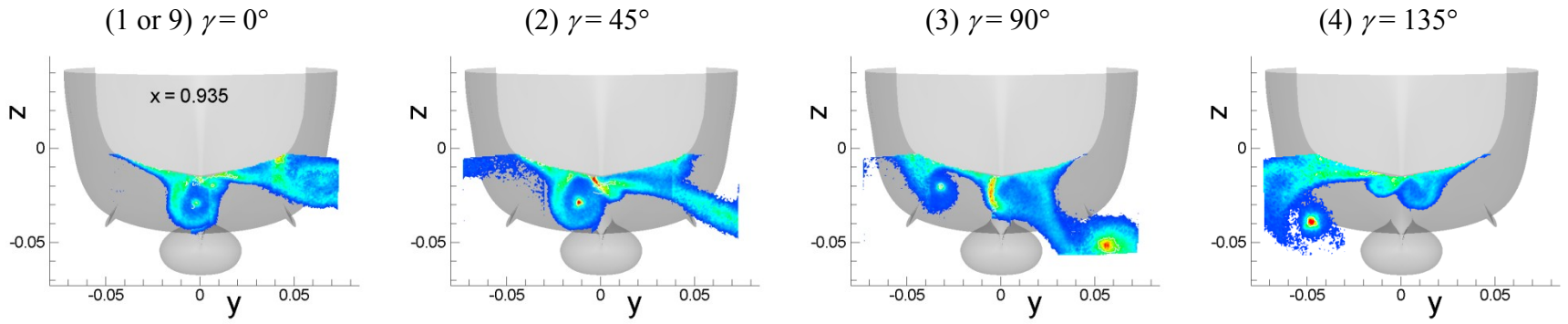

Figure 6-30–Continued

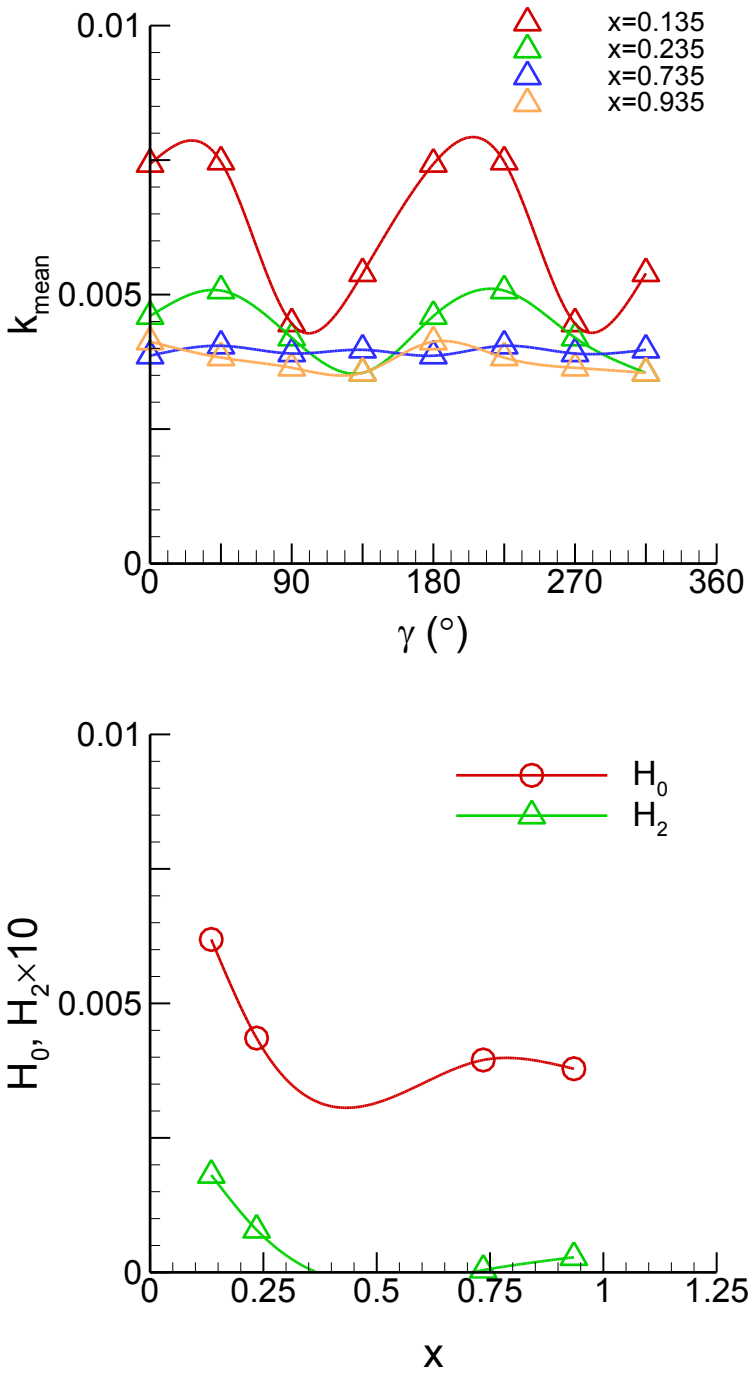

Figure 6-31 Time histories of k_{mean} (top) and FS harmonics (bottom) for pure sway test.

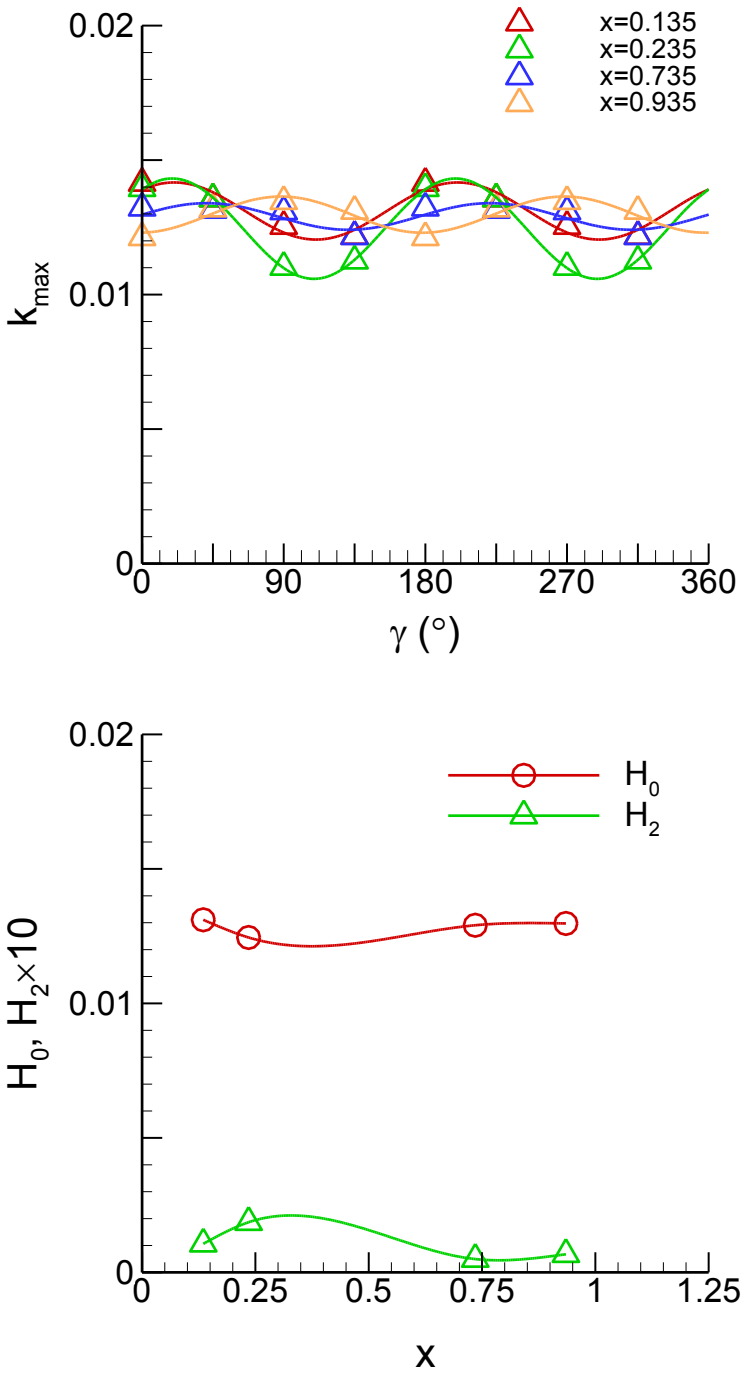

Figure 6-32 Time histories of k_{max} (top) and FS harmonics (bottom) for pure sway test.

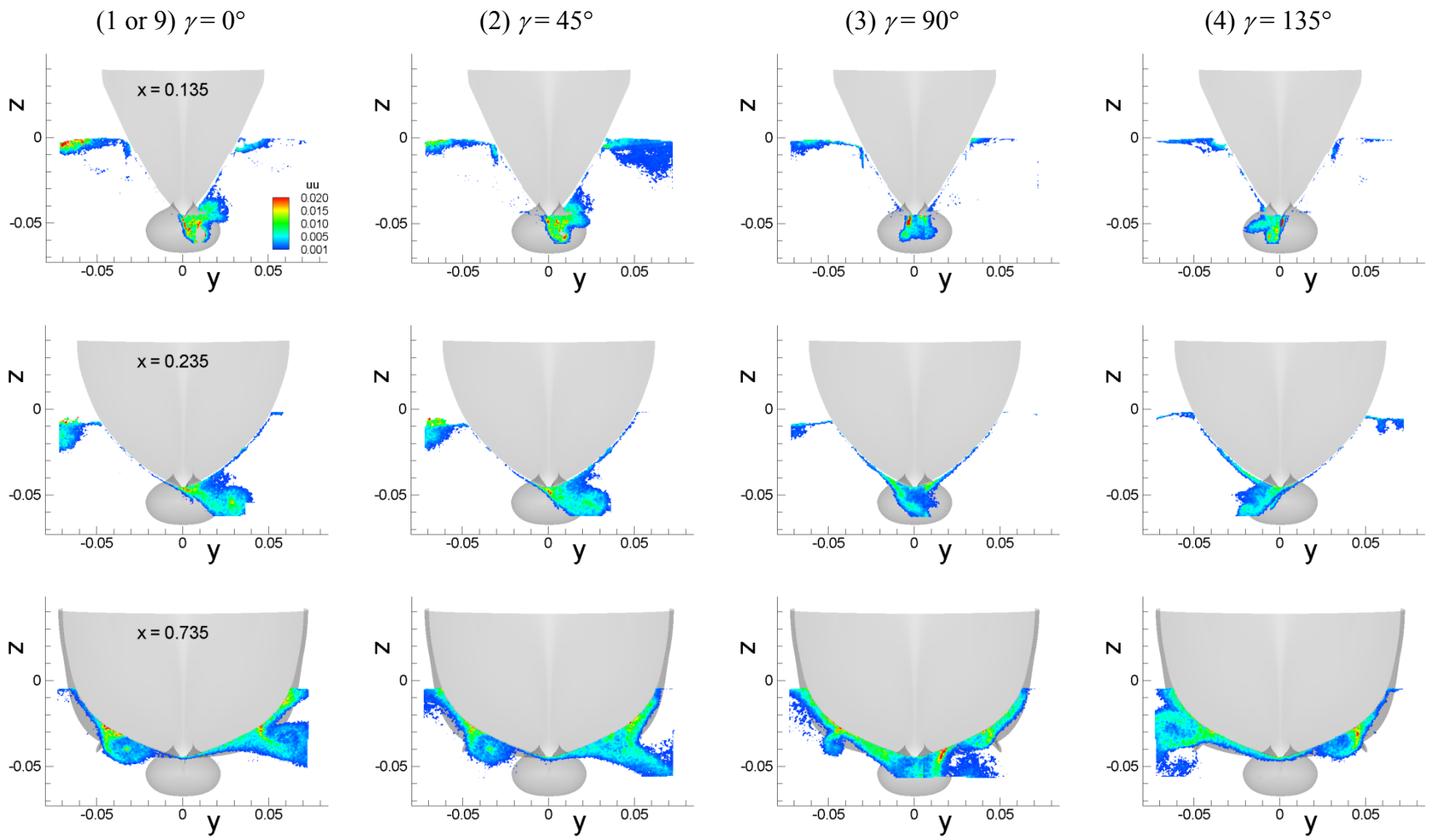

Figure 6-33 Phase-averaged Reynolds stress *uu* field for pure sway test.

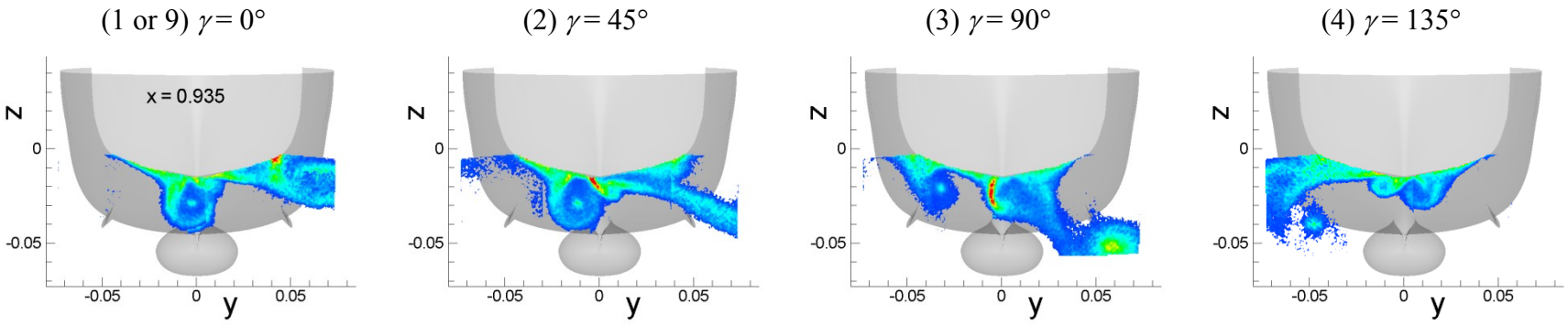

Figure 6-33–Continued

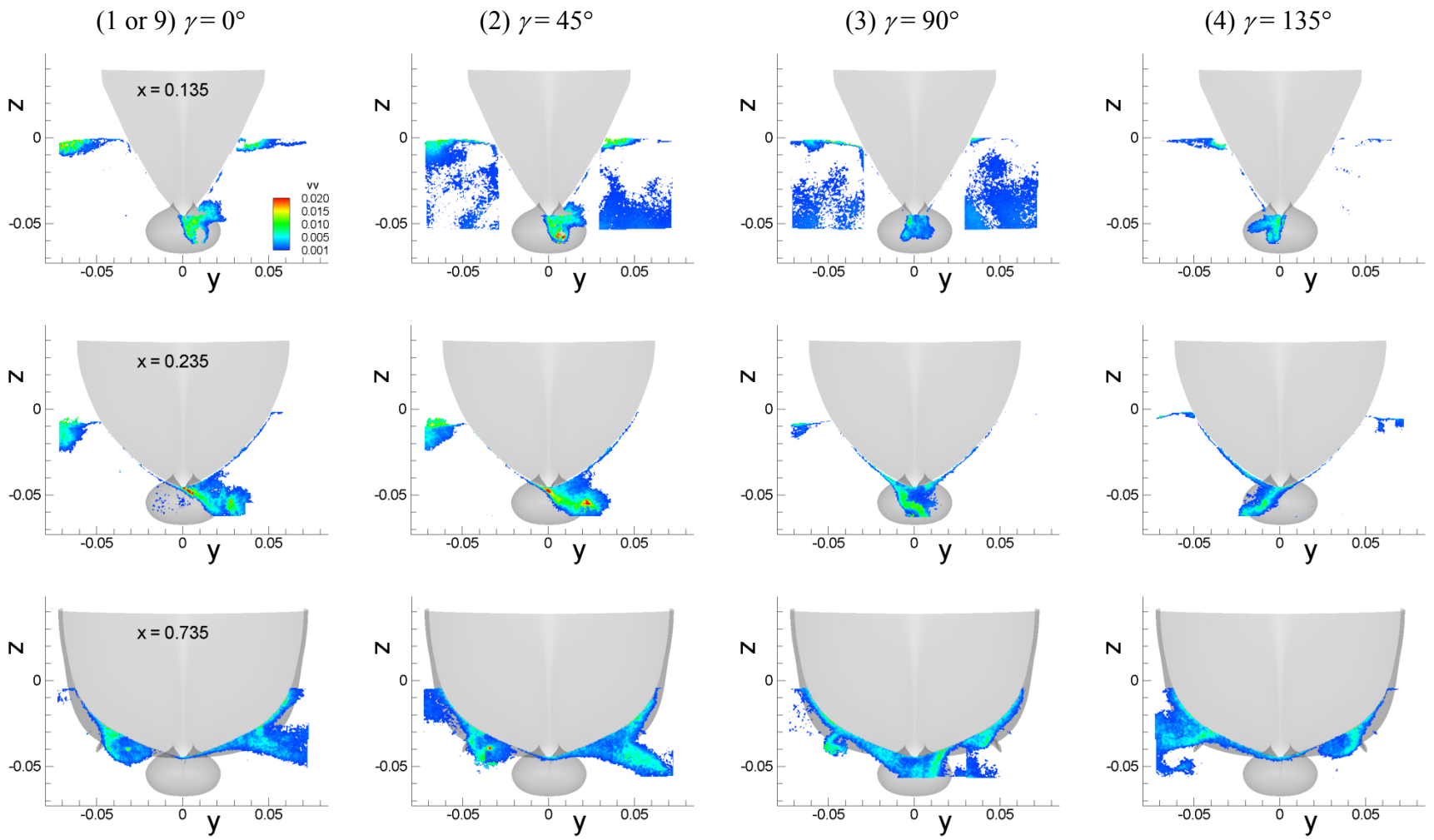

Figure 6-34 Phase-averaged Reynolds stress *vv* field for pure sway test.

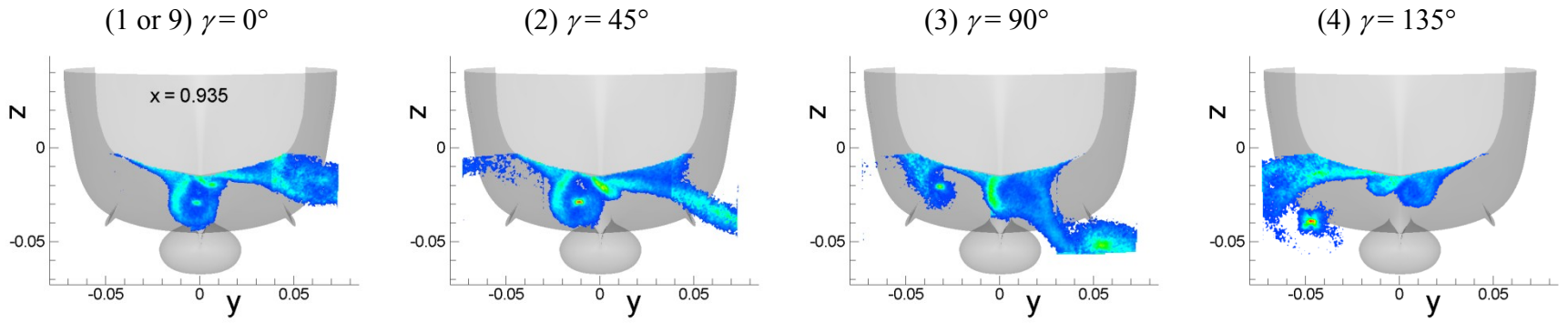

Figure 6-34–Continued

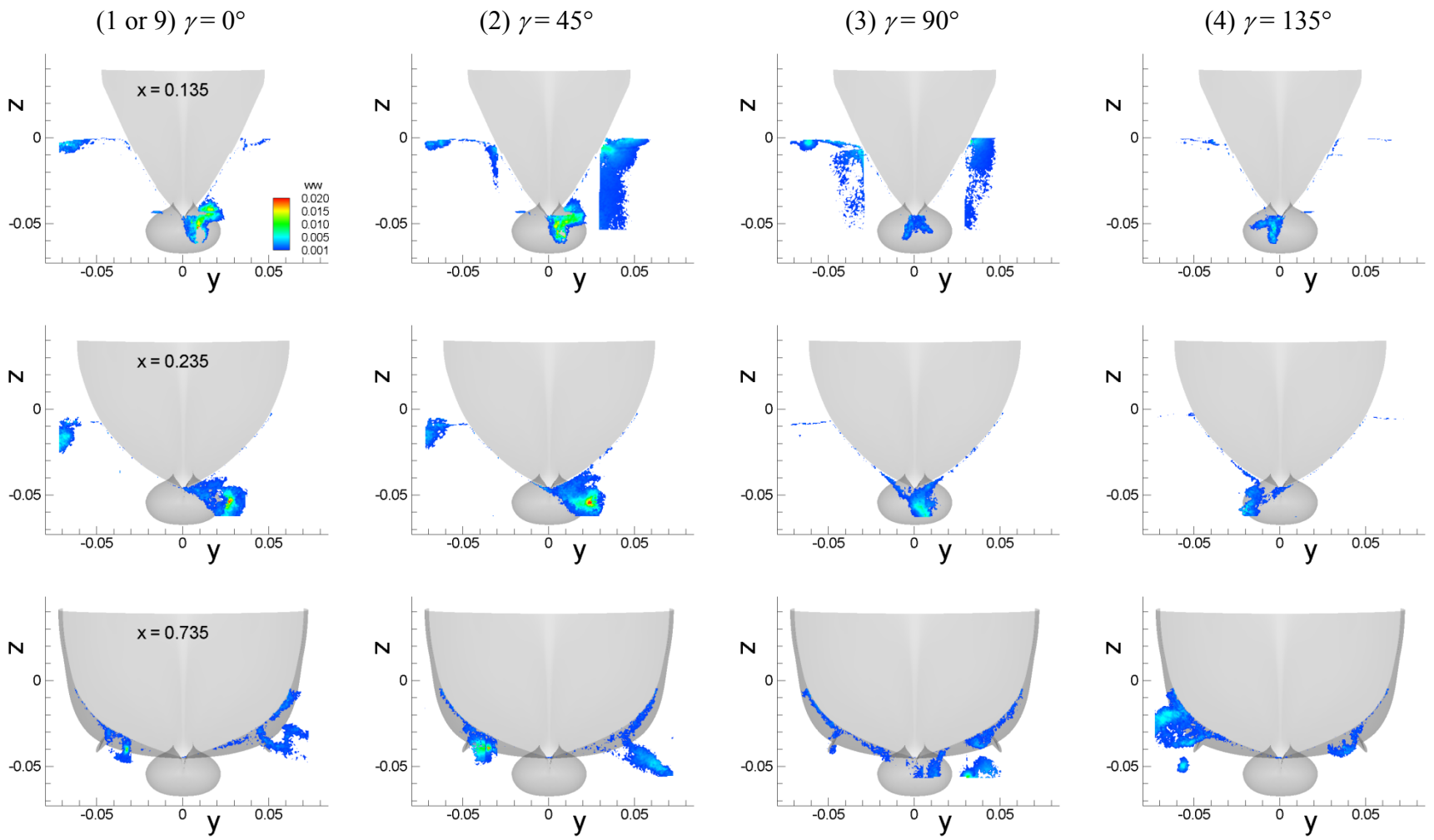

Figure 6-35 Phase-averaged Reynolds stress *ww* field for pure sway test.

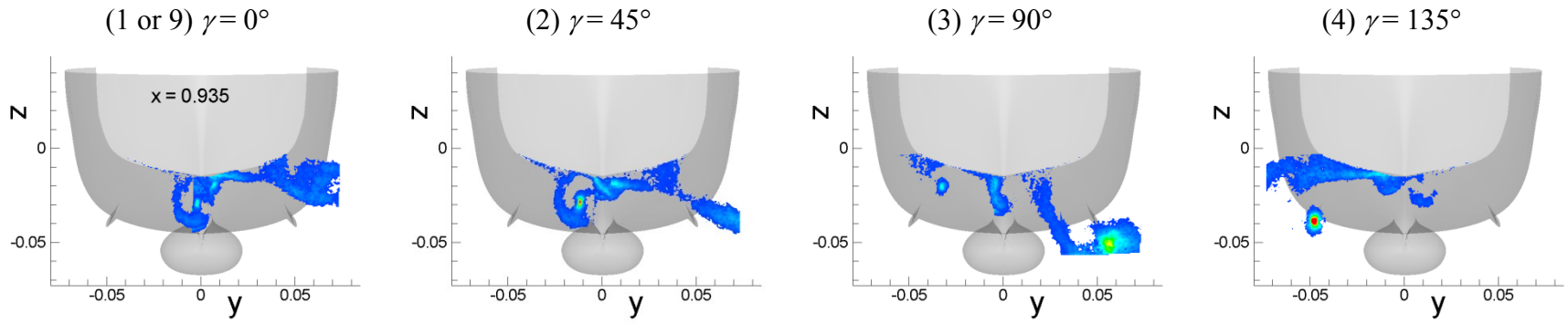

Figure 6-35–Continued

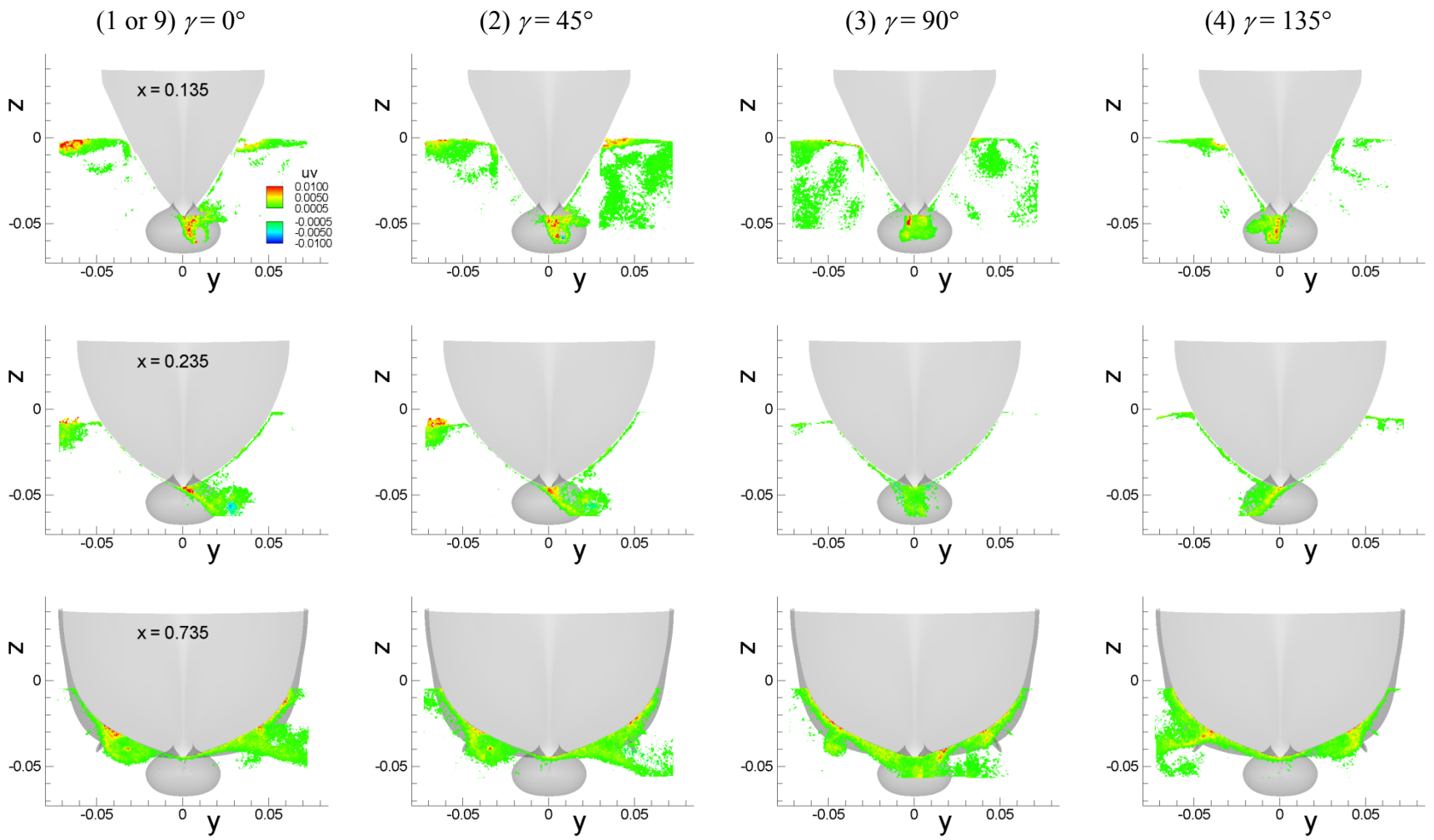

Figure 6-36 Phase-averaged Reynolds stress *uv* field for pure sway test.

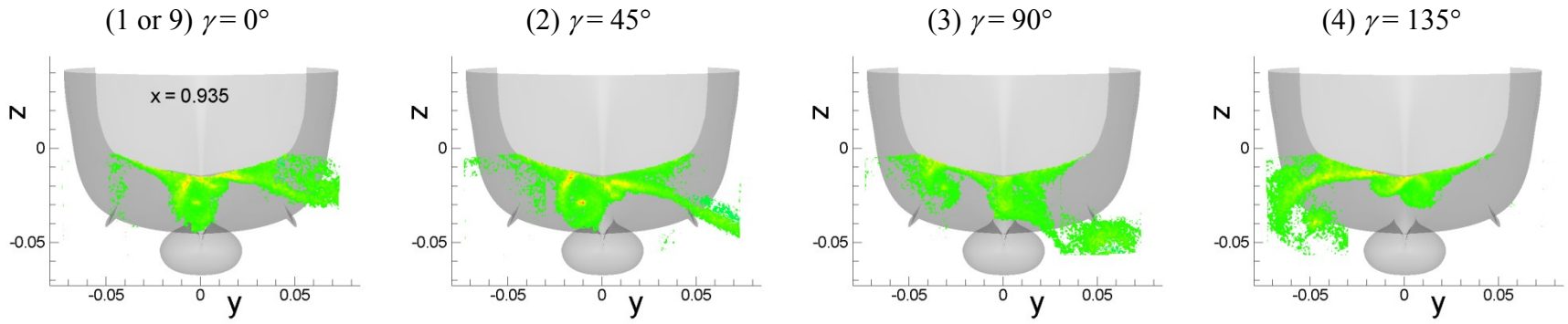

Figure 6-36–Continued

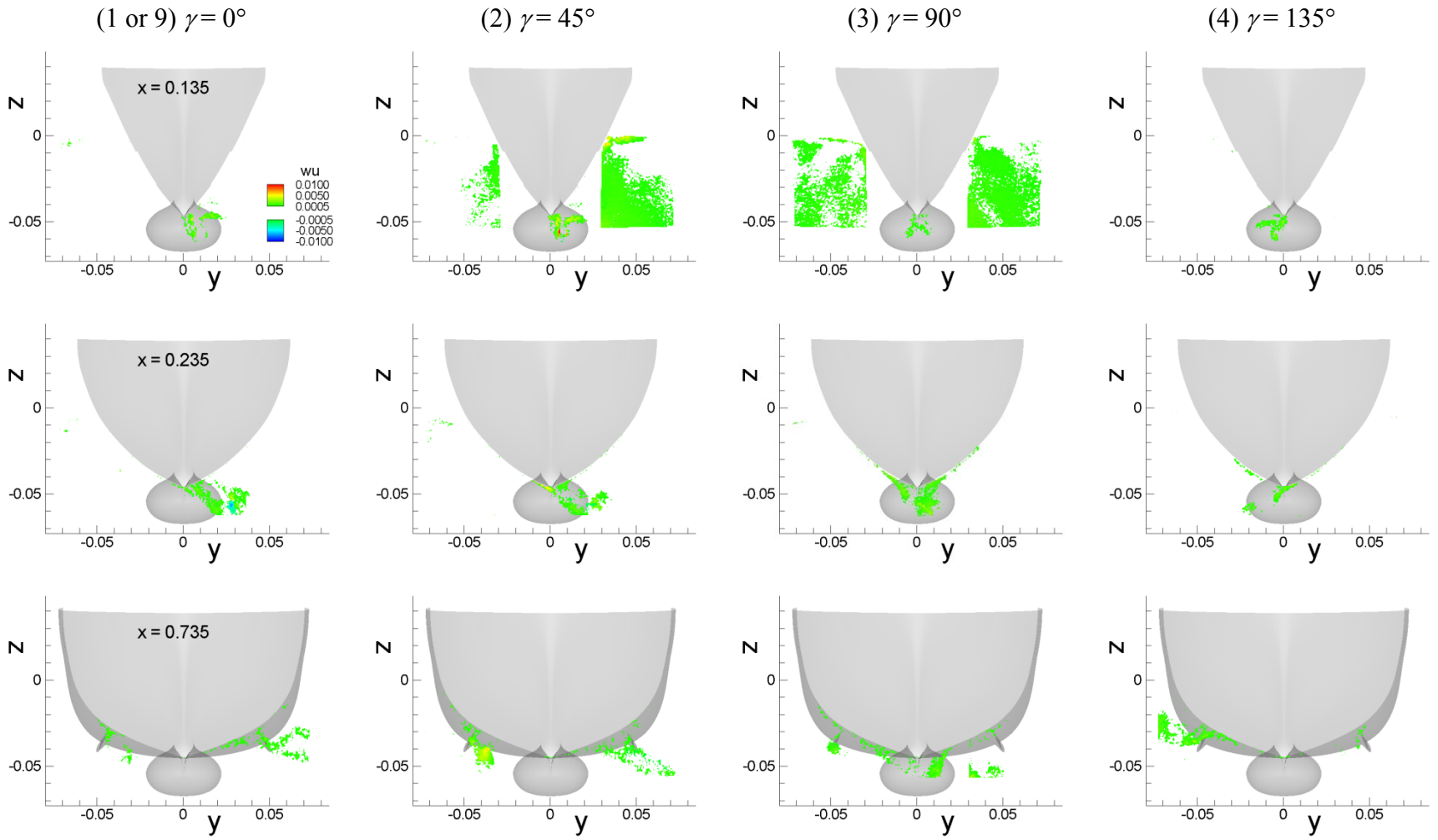

Figure 6-37 Phase-averaged Reynolds stress *uw* field for pure sway test.

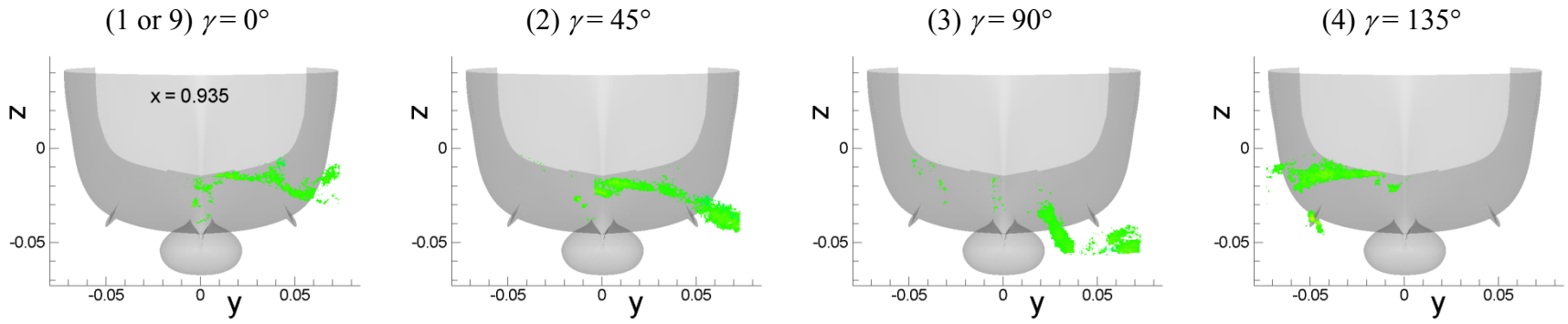

Figure 6-37–Continued

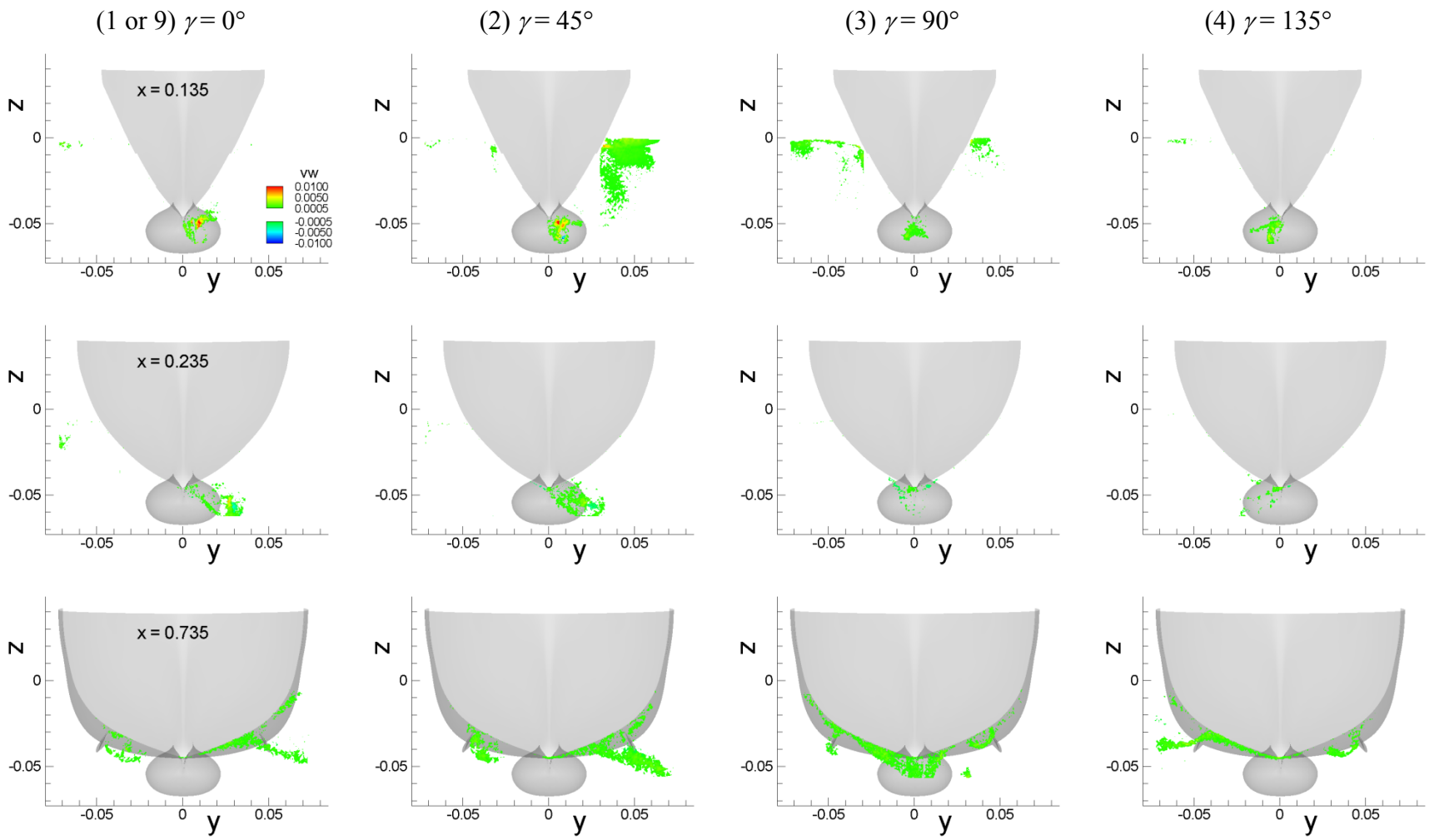

Figure 6-38 Phase-averaged Reynolds stress *vw* field for pure sway test.

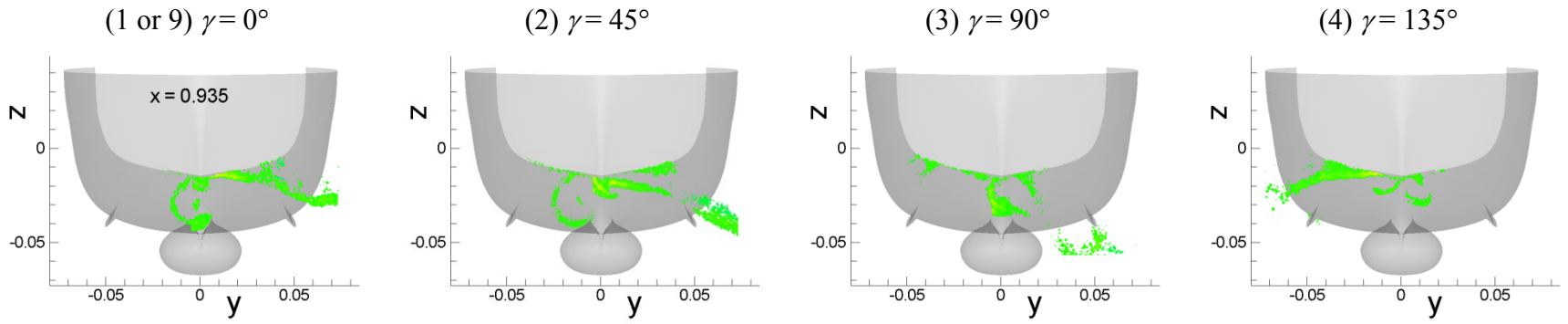

Figure 6-38–Continued

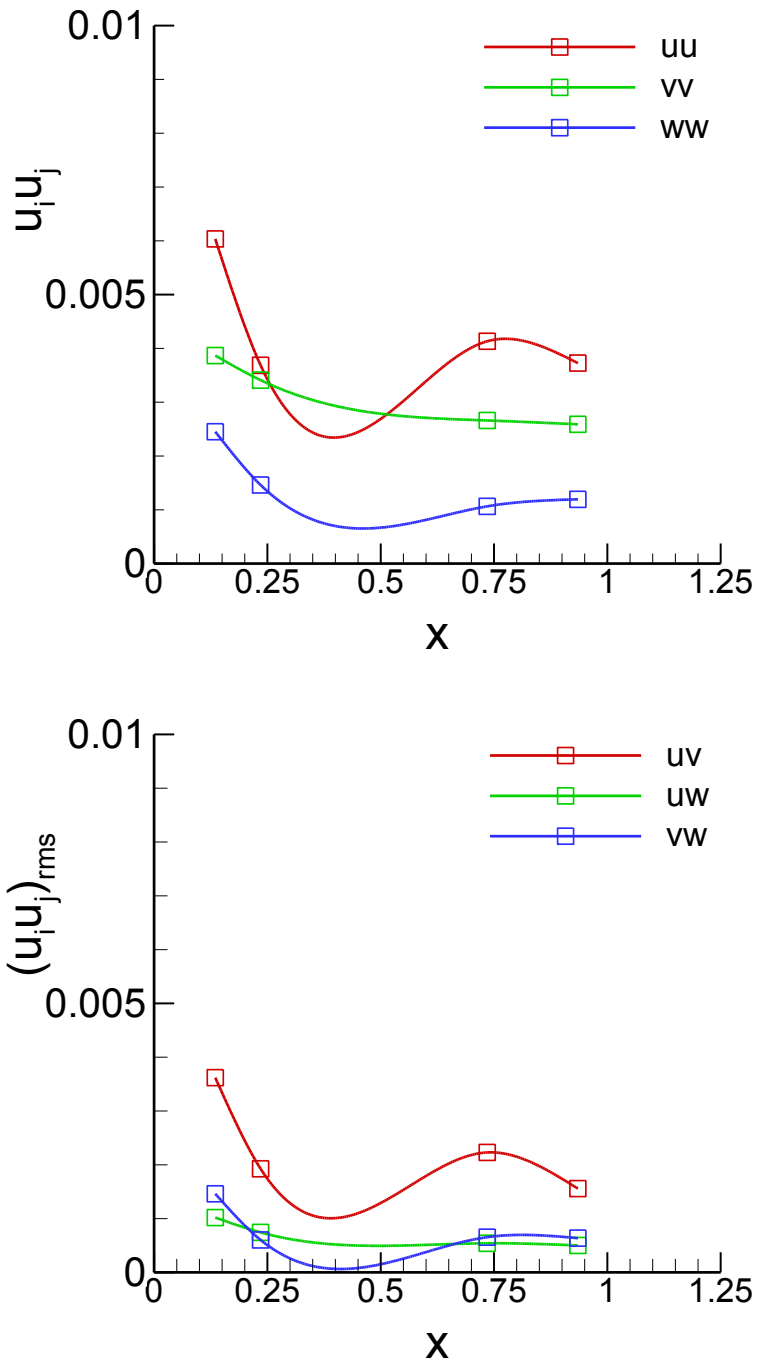

Figure 6-39 Average normal (top) and shear (bottom) Reynolds stresses for k_{mean} (Pure sway test).

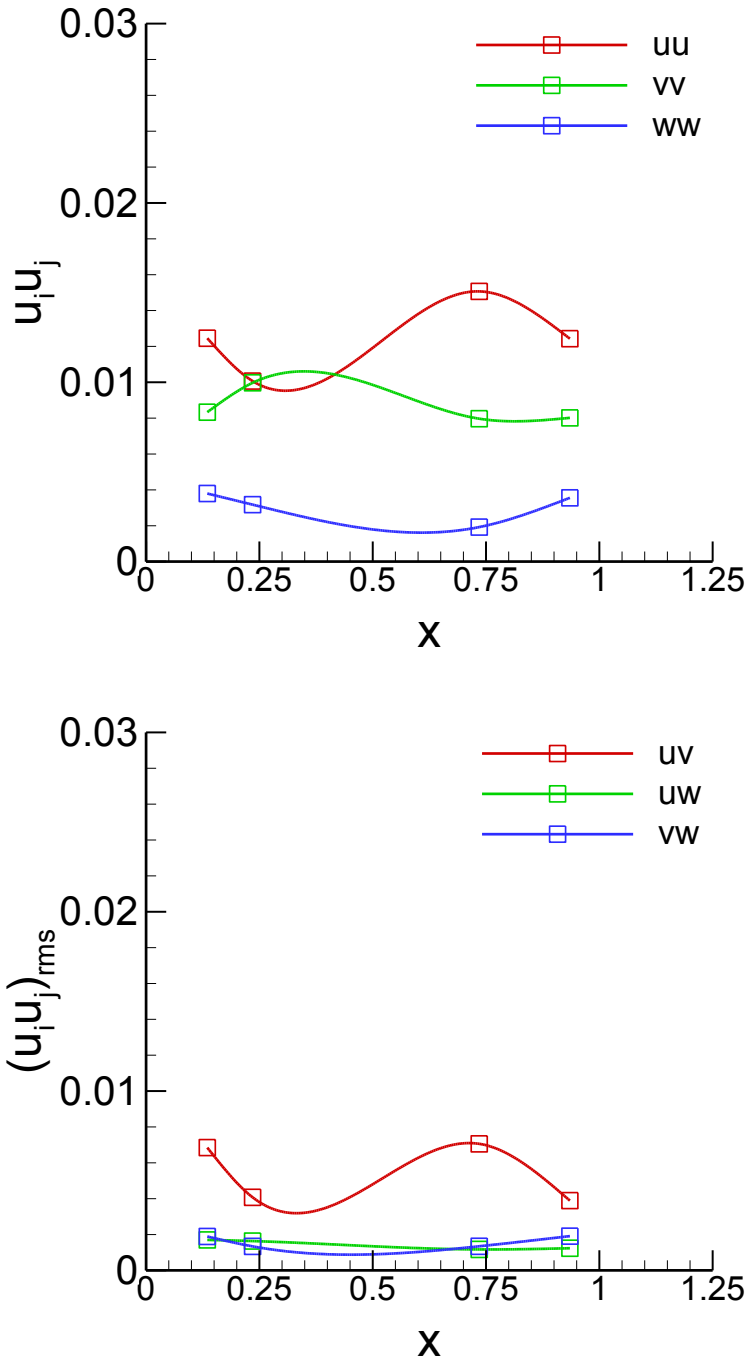

Figure 6-40 Average normal (top) and shear (bottom) Reynolds stresses for k_{max} (Pure sway test).

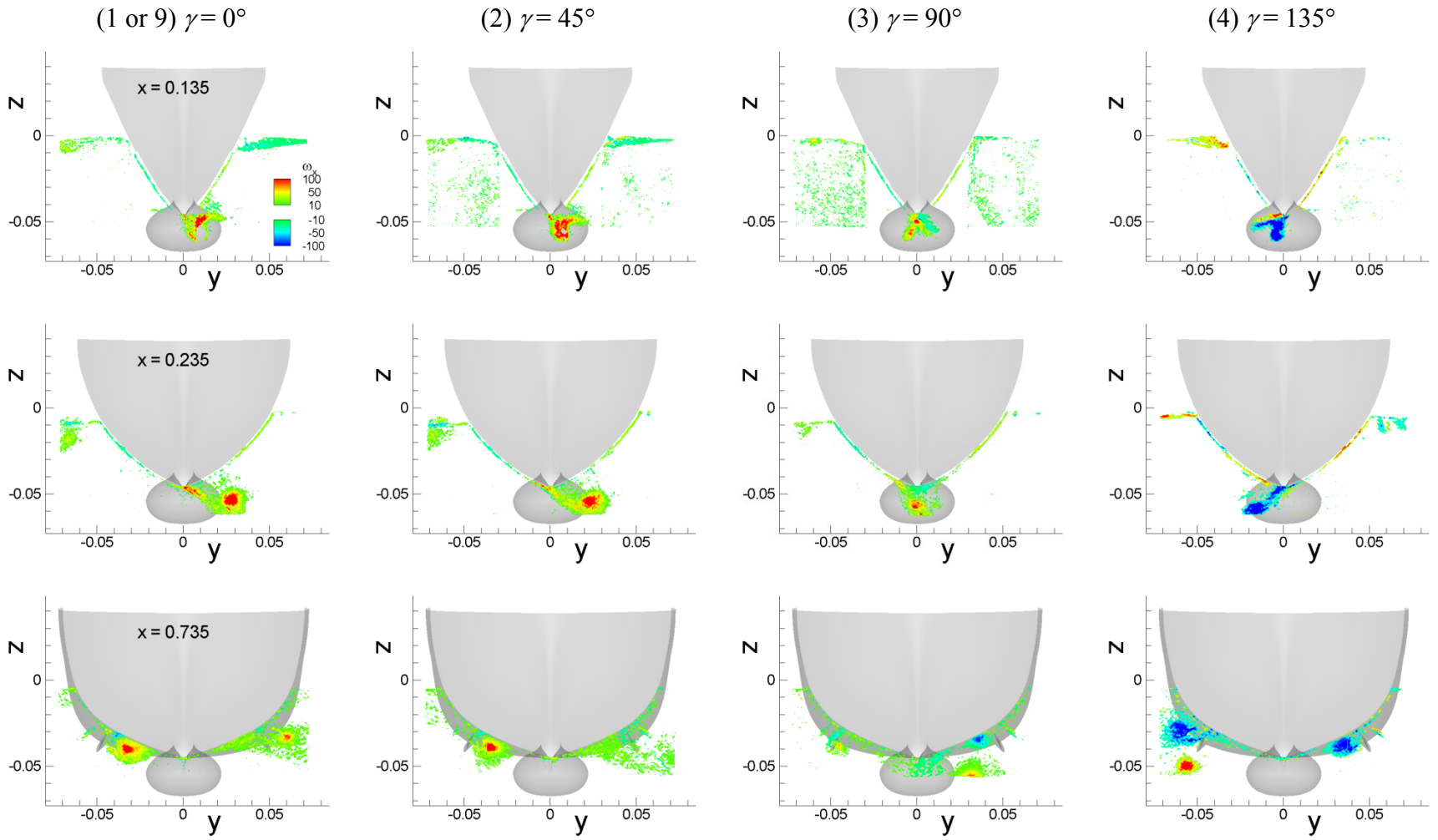

Figure 6-41 Axial vorticity ω_x field for pure sway test.

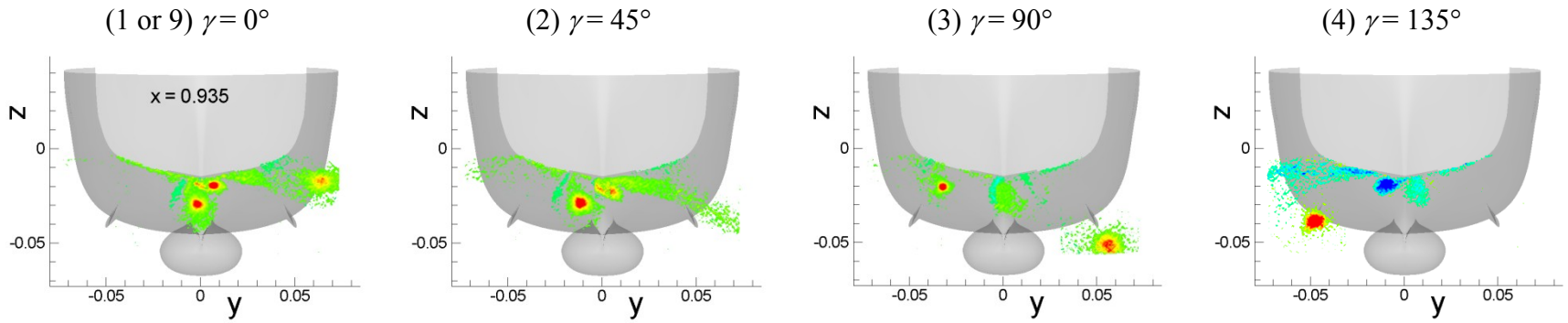

Figure 6-41–Continued

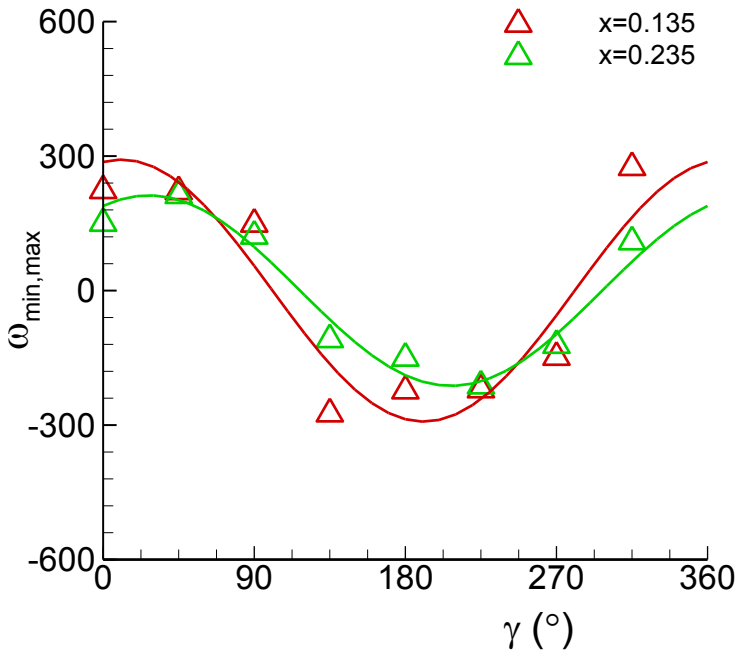

Figure 6-42 Time histories of maximum/minimum axial vorticity value of the sonar dorm vortex (SD) for pure sway.

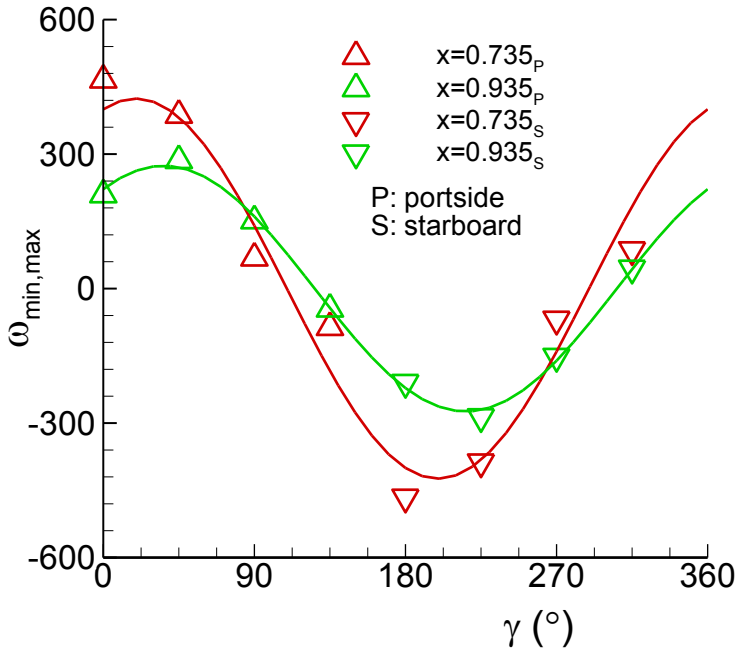

Figure 6-43 Time histories of maximum/minimum axial vorticity value of the bilge keel vortex (BK) for pure sway.

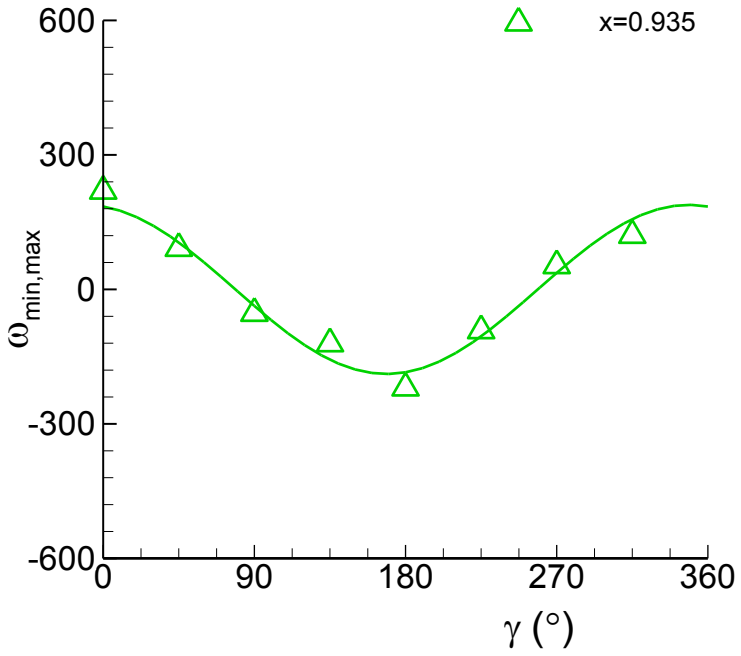

Figure 6-44 Time histories of maximum/minimum axial vorticity value of the aft-body keel vortex (AK) for pure sway test.

6.2.2 Pure yaw flow field

Presentations of the pure yaw flow field data herein are using the same format and methodology as for the discussions for pure sway at the previous section. The details of the presentation methodology and formats, thus, are not repeated in the discussions herein, such as: blanking out flow data and not showing in the contour plots for the data in a certain range, e.g. $U > 0.95$, $k < 0.001$, $-10 < \omega_x < 10$; defining $U_{\leq 0.9}$ as the mean U value over a flow region where $U \leq 0.9$ and $U_{\min}$ as the minimum U value (see Section 6.2.1.2); presenting the cross-flow field by showing the contours of the velocity (V, W) vector magnitude, $S = (V^2+W^2)^{1/2}$, with overlaid the cross-flow streamlines over the contours, to represent respectively the magnitude and direction of the flow (also see Section 6.2.1.1); defining $k_{\geq 0.005}$ (corresponding to $k_{\geq 0.01}$ for pure sway) and $k_{\geq 0.001}$ as the mean k values over the flow regions where $k \geq 0.005$ and $k \geq 0.001$, respectively, to represent the maximum and average k value, respectively, within the flow (see Section 6.2.1.3); and defining the maximum and minimum ω_x values as those values when $\omega_x > 0$ and $\omega_x < 0$, respectively, within a flow region of interest (see Section 6.2.1.4).

At the top of Fig. 6-45, the trajectory of model (shown as a dashed-line; the path-line of the model mid-ship point) in a pure yaw motion is shown. The model is in a rotary yaw (or its heading) $\psi = -\psi_0 \cdot \cos \omega t$ motion, turning about its mid-ship point, such that the model is always tangent to the path-line while towed at a constant speed U_C (depicted with a red colored arrow in the figure). Where, the maximum heading angle $\psi_0 = 10.2°$, the yaw motion angular frequency $\omega = 1.672\ U_C/L$ (or a cyclic frequency $f = \omega/2\pi = 0.134$ Hz), and the towing speed $U_C = 1.531$ m/s, and the model length $L = 3.048$ m, respectively. Angular velocity of the model rotation, yaw rate $r = \mathrm{d}\psi/\mathrm{d}t$, is positive when it turns to starboard (depicted with a blue colored circular arc arrow in the figure). At every $\gamma = \omega t = 45°$ phase angle positions of the path-line, the outline of the model is shown with numbered 1 to 9, respectively. Below the model trajectory, overviews of the flow around the model at each of those phase angles are shown, along with the model

path-line (the light-blue colored line) similarly as in Fig. 6-22 for pure sway. Flow data shown are the axial velocity U contours and the cross-flow (V,W) streamlines at five model-longitudinal locations, x = 0.135, 0.335, 0.535, 0.735, and 0.935, respectively. Under below the sonar dorm of the model drawing shown at each phase position, the turning direction, heading angle ψ and yaw rate r values of the model at the instant are presented. At (1) γ = 0°, model heading is the maximum to the negative direction, ψ = -10.2°, yet, the incoming flow is parallel to the model longitudinal as the model is tangent to its path-line. Whereas the model yaw rate r = 0 at the instant, thus the flow pattern exhibits a typical one for the case when the model is in a 'straight-ahead' condition; down- and outward at the bow and up- and inward at the stern as per Longo et al. (2007), Gui et al. (2001a), and Olivieri et al. (2001). However, the apparent size of the vortical flow from the figure is considerably bigger than those from the straight-ahead case (e.g. Fig. 6-23a), obviously formed at the previous cycle of the yaw motion and lasting. The model, then, begins turning to starboard with increasing yaw rate, at (2) γ = 45°, ψ = -7.2° with r = 0.21, until (3) γ = 90° where ψ = 0° and yaw rate is the maximum r = 0.3 (U_C/L), and continues turning but with decreasing yaw rate, at (4) γ = 135°, ψ = 7.2° with r = 0.21, and then finishes the turning at (5) γ = 180° where the heading ψ = 10.2° is the maximum to the positive direction with r = 0; which completes the first half cycle of the pure yaw motion. Through the yaw motion, due to the rotary motion of the model, the cross-flow at the bow typically becomes down- and inward at the wind side and transversal and outward at the leeward side; and at the stern, vice versa. The vortical flow, on the other hand, changes its size and the direction of its rotation. The model motion and the flow at the second half of the cycle are anti-symmetric mirrors of those at the first half cycle, such that γ = (5) 180°, (6) 225°, (7) 270°, and (8) 315° to γ = (1) 0°, (2) 45°, (3) 90°, and (4) 135°, respectively, and γ = 360° is identical with γ = 0°.

6.2.2.1 Vortical flow structure

The vortical flow around the DTMB 5512 geometry, the same geometry of the model, in two steady maneuvers, static drift and steady turn, are shown in Fig. 6-46 (a) and (b), respectively. In the figures, vortices in the flow were visualized from the CFD simulations by Sakamoto (2009), by using the Q = 30 iso-surfaces (Hunt et al., 1988) with colored by the normalized relative helicity density level. Simulation was with drift angle $\beta = 10°$ for the static drift maneuver (transversal incoming flow left to right from Fig. 6-46a) and with a constant yaw rate $r = 0.3$ for the steady turn maneuver (turning to the starboard side; transversal incoming flow right to left at the bow whereas in reverse at the stern from Fig. 6-46b), respectively. Note that Fig. 6-46 (a) for static drift is the same as Fig. 6-23 (b), repeated herein for comparisons with the steady turn flow. Compared to static drift, the same kind of vortices are observed from the steady turn maneuver, such as SD, BK, and AK vortices (major ones) from the sonar dome, bilge keels, and aft body keel, respectively and FK, FS, and T vortices (minor ones) from the fore body keel, free surface, and transom, respectively. Of the vortices, SD vortex exhibits opposite signs (red vs. blue in the figure; direction of rotation) between two maneuvers due to the different directions of transversal in coming flow, which is generated from the sonar dome at the fore body and then convected downstream, whereas the other vortices that formed at the aft body show the same signs for both maneuvers as the flow direction is same. The size of vortices for steady turn in general is relatively small compared to static drift (considerably small for BK) as the overall incoming flow direction is more aligned to the hull longitude (tangent to the circular path-line) for the former case. The shape of the vortices is rather straight for the static drift case, aligned with the incoming flow direction, whereas rather curvy for the steady turn case, following the circular path-line of the hull form.

Fig. 6-47 (a) and (b) shows the vortical structure of flow around the hull form in a pure yaw maneuvering, with visualized from the CFD simulations by Sakamoto (2009)

and from the SPIV measurements, respectively, at the four phases of pure yaw cycle, γ = 0°, 45°, 90°, and 135°, in a sequence. From the CFD simulation result shown at Fig. 6-47 (a), the overall vortical flow structure for pure yaw maneuver is similar as that of the steady turn shown previously in Fig. 6-46 (b) with the same kinds of vortices, whereas the sign (direction of vortex rotation), shape, size, and location of those vortices are changing dynamically in time along with the yaw motion. At γ = 0°, the SD vortex is the major one, with stretched along the ship length from the bow to the stern. FK and AK vortices are the second largest, whereas BK vortex is very small in size at both the port and starboard sides. At γ = 45°, the SD vortex generated from earlier phase (SD_S in the figure) is detached from the sonar dorm and a new one with opposite sign (SD_P in the figure) is formed. At γ = 90°, the newly generated SDP vortex is growing (i.e., convecting to the downstream), and the BK vortex at the portside (BKP in the figure) is as well growing, and then those vortices become the major ones at γ = 135°. Note that the steady turning maneuver shown in Fig. 6-46 (b) corresponds to the γ = 90° case where the yaw rate is the same as the steady turn case with $r = 0.3$ but with a non-zero yaw acceleration, $dr/dt = 0.5\ (U_C^2/L)$. On the other hand, from Fig. 6-47 (b), the SPIV measurement results shows a very similar vortical structure at each phase, with visualized with the axial vorticity ω_x contours. Each of the vortices are identified by comparing the sign and the positions of ω_x contours with those of the helicity iso-surfaces from the CFD simulations, and labeled in the figures.

6.2.2.2 Phase-averaged velocity field

In Fig. 6-48, shown are the phase-averaged axial velocity U field at four phase positions, γ = 0°, 45°, 90°, and 135°, and at six longitudinal locations, x = 0.135, 0.335, 0.535, 0.735, 0.935, and 1.035. The flow field is seen from behind the model, i.e. looking upstream, and the incoming flow is coming out of the paper from the figure, and the model is turning its head to the starboard side (from left to right in the figure) about the

mid-ship point. The overall trend of U field for pure yaw is similar as for pure sway; at the bow appears thin boundary layer that is growing with the model longitudinal length, and becomes very thick at the stern. Dead flow zone (e.g., where $U \leq 0.5$, the dark-blue colored contour level in the figures) appears at $x = 0.735$ and 0.935, locally inside the boundary layer, and at the wake region, $x = 1.035$, becomes considerably large near the free surface. The flow is also retarded at the regions where the vortices present, e.g. under below the model where the SD vortices are, near around aft body bilges where the BK vortices are, and at the aft body keel where the AK vortices are. The shape and size of the boundary layers are typically asymmetric about the model center plane, and change continuously with time, i.e. with γ, in accordance with the yaw motion, may possibly be interacting with the flows induced by the nearby vortices.

In Figs. 6-49 and 6-50, time histories (top) and FS harmonics (bottom) of $U_{\leq 0.9}$ and those of $U_{\min}$ are shown, respectively. $U_{\leq 0.9}$ is the average U value over the region where $U \leq 0.9$ and $U_{\min}$ is the minimum U value within the region, respectively, at a given γ and x. Time histories are shown for all the 32 phase positions available from the SPIV measurements, from 0° to 348.75° with a phase step $\Delta\gamma = 11.25°$, and FS harmonics are shown for the 0^{th}- and 2^{nd}-order with designated as H_0 and H_2, respectively, in the figures. From Fig. 49 (top), the $U_{\leq 0.9}$ values oscillate with γ for all x locations. The period mean values of $U_{\leq 0.9}$ time-history is almost flat along the model length, i.e. $H_0 \approx 0.8$ for $x = 0.135 \sim 0.935$ from Fig. 6-49 (bottom), except for $x = 1.035$ where $H_0 = 0.75$. The oscillation amplitude of $U_{\leq 0.9}$ time-history is as well nearly constant with $H_2 \approx 0.009$, about 1.2% of H_0, again except for $x = 1.035$ where $H_2 = 0.023$ that is about 3% of the H_0 at the same x location. Next for $U_{\min}$, from Fig. 50 (top), time-histories as well exhibit oscillations along with the γ position. Contrary to $U_{\leq 0.9}$, the period mean H_0 and the oscillation amplitude H_2 of $U_{\min}$ time histories are not flat, but change along the model length. From Fig. 6-50 (bottom), $H_0 = 0.67$ at $x = 0.135$ and decreases nearly linearly along x, $H_0 = 0.39$ at $x = 1.035$, whereas $H_2 = 0.015$ (2% of H_0) at $x = 0.135$ and increases

gradually with x, $H_2 = 0.038$ (9% of H_0) at $x = 0.935$, then sharply at $x = 1.035$ where $H_2 = 0.071$ (18% of H_0).

Cross-flow vector (V,W) field is shown in Fig. 6-51, and the contours of $S = (V^2+W^2)^{1/2}$ with overlaid the cross-flow streamlines, showing the magnitude and the direction of the cross-flow, respectively, are shown in Fig. 6-52. From Fig. 6-51, the cross-flow vectors are in general pointed to the portside at the bow and to the starboard at the stern, as the model is turning its head to the starboard and its tail to the portside, respectively. Whereas the vectors point outward at $x = 0.335$ and inward at $x = 0.535$, respectively, but the velocity magnitude is usually small compared with those at the bow or stern. On the other hand, cross-flow vectors visualize clearly the rotational motions of the fluid at the vortical flow regions, such as near around the sonar dome (from the figures as shown with the model projected into the paper), around the bilge keels at the port- and starboard-side, and below the aft body center keel, where the SD, BK, and AK vortices exist, respectively.

The directions of cross-flow are even more obvious with vortices exposed clearly from the cross-flow streamlines as shown in Fig. 6-52. At $x = 0.135$, cross-flow in general directs toward portside as the model is turning to the starboard side, with accelerated locally at the starboard side, i.e., the wind side, where the cross flow velocity magnitude $S = 0.2 \sim 0.3$. Compared to model tangential speed $V_t = r \cdot dx = 0.11$ at $\gamma = 90°$, where the model yaw rate $r = 0.3$ and the radial distance $dx = 0.365$ from the mid-ship, the cross-flow speed at the region is about $2 \sim 3$ times faster than the V_t in general. The cross-flow speed weakens at $x = 0.336$ and 0.535 typically with $S < 0.1$, where in general flow is diverging from and converging to the hull, respectively. At the aft body, $x = 0.735$, 0.935, and 1.035, cross-flow is usually toward the starboard side as the model in turning its tail to the portside. Typically cross-flow speed $S = 0.05 \sim 0.15$, usually slower than the model tangential velocity $V_t = 0.13$ at $x = 0.935$ at $\gamma = 90°$, except for the regions near the vortices. The SD vortex is clearly seen from the streamlines. Particularly at $\gamma = 0°$ where

the model yaw rate $r = 0$, the concentric or spiral flow discovers the size and position of the SD vortex along the entire model length. The approximate sizes of SD vortex $\phi \sim 0.01\ L$ at $x = 0.135$, and then grows along the model length, $\phi = 0.02 \sim 0.025\ L$ between $x = 0.335$ and 0.535, and $\phi = 0.03 \sim 0.04\ L$ between $x = 0.735 \sim 1.035$, where ϕ is an approximate outer diameter of the concentric streamlines at $\gamma = 0°$, respectively. The approximate center point of SD vortex at $\gamma = 0°$ is just below the model keel position, $(y,z) \approx (0,-0.05)$ at $x = 0.135$, and then shifted in both lateral and vertical directions. In lateral direction, the center point first remains near the center plane at the fore body and then gradually moves to portside at the aft body, and located at $y \approx -0.028$ at $x = 1.035$. In vertical direction, the center point first shifts down at the fore body, to $z \approx -0.065$ at $x = 0.535$, and then up at the aft body, to $z \approx -0.04$ at $x = 1.035$, following the model bottom profile. At the other γ positions, the size and location (including the direction of rotation) of the SD vortex is changing in time, i.e. with γ, and is often superposed with the parallel transverse flow at the aft body, the vortex streamlines open up or not clearly seen. The strength of the SD vortex including the difference kinds of the vortices will be discussed later together with the axial vorticity field.

6.2.2.3 Turbulent kinetic energy and Reynolds stresses

Turbulent kinetic energy k field (for $k \geq 0.001$) is shown in Fig. 6-53 for $\gamma = 0°$, 45°, 90°, and 135° cases. Reynolds number of the flow $\mathrm{Re} = U_C L/\nu = 4.6\times10^6$, same as for pure sway test. The overall structure of the field exhibit coherence with the phase-averaged axial velocity U field shown in Fig. 6-48; at the bow with thin layer that is growing along the model length and becomes very thick at the stern, i.e. within the boundary layers and inside the vortical flow regions. The core regions with high k values (e.g. $k \geq 0.01$) exist typically near at the model hull surfaces, at the center of the vortical flow regions, and near the free surface behind the model transom. The apparent shapes of the k field and the locations of the core region vary in time, i.e. along with the phase of pure

yaw motion. In Figs. 6-54 and 6-55, time histories (top) and FS harmonics (bottom) of k_{mean} and those of k_{max} are shown, respectively. Similarly for pure sway case, herein the k_{mean} and k_{max} are defined as the average k values respectively within the core regions where $k \geq 0.001$ and within the overall k field where $k \geq 0.01$, which respectively represents the approximate maximum and average k value within the turbulent flow. In the figures, time histories are from the all 32 phase positions of the SPIV measurement, and the FS harmonics are for the 0^{th}- and 2^{nd}-order harmonics (with designated respectively as H_0 and H_2) corresponding to the period mean value and to the dominant amplitude of the time-history oscillations. From Fig. 6-54 (top), $k_{mean} = 0.0025 \sim 0.0045$ oscillating with γ particularly at $x = 0.135$. From Fig. 6-54 (bottom), the period-mean value of the oscillating k_{mean} is nearly constant along the model length with $H_0 \approx 0.003$ whereas slightly larger H_0 values at $x = 0.135$ and 1.035. This indicates that in a mean sense the overall turbulence intensity $I = (2/3 \cdot k)^{1/2} \sim 0.045$ in the flow, or a turbulent velocity fluctuation ~ 4.5% of U_C. The k_{mean} oscillation amplitude is the maximum at $x = 0.135$ with $H_2 = 0.0007$ (19% of H_0), and then undulates with x with a mean $H_2 = 0.0002$ that is about 7% of H_0. On the other hand, at the core region, $k_{max} = 0.011 \sim 0.016$ from Fig. 6-55 (top) as well oscillating with γ. From Fig. 6-55 (bottom), the period mean k_{max} value decreases gradually along the model length from $H_0 = 0.014$ at $x = 0.135$ to $H_0 = 0.011$ at $x = 0.935$, and then just behind the model it increases sharply with $H_0 = 0.014$ at $x = 1.035$. Turbulence intensity $I = 0.086 \sim 0.097$ in the core region, or about 9 ~ 10% U_C of turbulent velocity fluctuations. The oscillation amplitude of k_{max} is the maximum at the bow with $H_2 = 0.0015$ (11% of H_0) at $x = 0.135$, and drops fast along the model length with $H_2 \approx 0.0005$ (3 ~ 4% of H_0) between $x = 0.335$ and 0.535 and with $H_2 \approx 0.00025$ (~ 2% of H_0) at the aft body.

Reynolds normal (uu, vv, ww) and shear (uv, uw, vw) stress fields are shown in Fig. 6-56 through Fig. 6-61, respectively. Despite the quite dissimilar flow structures between the phase-average axial U and cross-flow (V,W) velocity fields shown in Fig. 6-48

and Fig. 6-51 (or Fig. 6-52), respectively, the apparent structures of the Reynolds stress fields from the figures exhibit a coherence between the stress components, rather similar to the U field. In general, the order of magnitude of the normal stresses is larger than the shear stresses, and typically the uu and uv stresses respectively are the largest of the normal and shear stresses. In Figs. 6-62 and 6-63, the average normal (top) and shear (bottom) stress values over the regions for k_{mean} ($k \geq 0.001$) and k_{max} ($k \geq 0.01$) are shown, which are as well averaged values over the pure yaw motion period, i.e. corresponding to H_0's of the FS for those variables. Note that shear stresses shown in the figures are root-mean-squared (rms) values. From Fig. 6-62, both the normal and shear stresses are nearly constant along the model length with average values (uu, vv, ww) = (0.0029, 0.0019, 0.0009) and (uv, uw, vw) = (0.0012, 0.0005, 0.0003), respectively. The normal stress values, however, tend to increase at the bow (x = 0.135) and in the wake (x = 1.035). Of the normal stresses, uu is the largest, followed by vv, and ww is the smallest, whereas for the shear stresses, uv is the largest and uw and vw are both small. On the other hand, at the core region where $k \geq 0.01$, from Fig. 6-63 the normal (top) and shear (bottom) stresses are nearly constant with x, (uu, vv, ww) ≈ (0.0167, 0.0072, 0.0011) and (uv, uw, vw) ≈ (0.0077, 0.0013, 0.0008), up to x = 0.735, where the uu and uv are respectively the largest normal and shear stresses. After x = 0.735 at the stern part, nevertheless the sharp increase in k_{max} value as shown in Fig. 6-55 (bottom), those uu and uv stress values decrease fast whereas the other stresses values increase with x, respectively, thus the Reynolds stress field becomes more of isotropic than at the front part of the model. The Reynolds stress anisotropic tensor $b_{ij} = u_i u_j/2k - \delta_{ij}/3$ values shown in Fig. 6-64 for the normal (top) and the shear (bottom) stresses reveals this more clearly. The Reynolds stress anisotropic tensor b_{ij} is the deviatoric part of the Reynolds stress tensor, $a_{ij} = u_i u_j - (2/3)k\delta_{ij}$ with normalized with $2k$. The b_{ij} values show how far the elemental stress is deviated from the mean value, thus b_{ij} values close to zero indicate more isotropic stress tensor.

Consequently, the flow has a turbulent kinetic energy $k^{1/2} \approx 5.4\%$, the normal Reynolds stresses ($uu^{1/2}$, $vv^{1/2}$, $ww^{1/2}$) ≈ (5.4%, 4.4%, 3%), and the rms of the shear Reynolds stresses ($uv^{1/2}$, $uw^{1/2}$, $vw^{1/2}$) ≈ (3.5%, 2.2%, 1.7%) of U_C, respectively, in average over the turbulent flow field. Locally, the flow may have turbulent kinetic energy $k^{1/2} \geq$ 11.3%, and normal stresses ($uu^{1/2}$, $vv^{1/2}$, $ww^{1/2}$) ≥ (12.9%, 8.5%, 3.3%) of UC, and the rms values of the shear Reynolds stresses ($uv^{1/2}$, $uw^{1/2}$, $vw^{1/2}$) ≥ (8.8%, 3.6%, 2.8%) of U_C, respectively. The Reynolds stresses are anisotropic; however, locally those may become less anisotropic at the stern part and in the wake region. Those average k and Reynolds stress values are similar or smaller than the maximum values of ($k^{1/2}$, $uu^{1/2}$, $vv^{1/2}$, $ww^{1/2}$, $uv^{1/2}$, $uw^{1/2}$) = (5.4%, 5.3%, 4.1%, 3.7%, 2.4%, 2.8%) of U_C from the steady test by Longo et al. (2007). The steady test was using the same model with a straight-ahead condition and the flow was measured at the nominal wake region (i.e., $x = 0.935$).

6.2.2.4 Axial vorticity

Axial vorticity ω_x field (for $\omega_x \leq -10$ and $\omega_x \geq 10$) is shown in Fig. 6-65 for $\gamma = 0°$, 45°, 90°, and 135°. From the figures vortices such as the sonar dome (SD), bilge keel (BK), and aft body center keel (AK_C) vortices are more clearly seen than from the cross-flow vector or streamline field shown in Figs. 6-51 and 6-52, respectively, from which the vortices at certain phases are not obvious with superposed with the nearby parallel transverse flow and streamlines open up. SD vortex is the most dominant one, which can be seen most clearly from the Fig. 6-65 at $\gamma = 0°$ (the first column from the left), where the SD vortex is located at the portside of the model within a range of $y = -0.04 \sim 0.01$ and $z = -0.03 \sim -0.07$ in general. At $\gamma = 45°$, a new counter rotating SD vortex is formed at the fore body, $x = 0.135 \sim 0.535$, and the old one from $\gamma = 0°$ is detached from the sonar dome and weakens at the aft body, $x = 0.735 \sim 1.035$. At $\gamma = 90°$ and 135°, the new SD vortex strengthens and propagates to the aft body and moves to the starboard side. BK vortex is the second dominant one, which can be seen most clearly from the Fig. 6-65

at x = 0.735 (the third row from the bottom), where two BK vortices are respectively located near around the portside and starboard bilge keel positions (as appears in the figures with the model projected). The BK vortices are first generated at x = 0.535 near around the port- and starboard side bilge keels but very locally, and grows in size at x = 0.735, and then both BK vortices converge toward the model center plane at x = 0.935 and 1.035, but usually diffused and not clearly seen from the figures. AK_C vortex is the third dominant one, which can be seen most clearly from the Fig. 6-65 at x = 0.935 (the second row from the bottom), where the AD vortex is located near below the aft body center keel position at (y,z) = (0.0, -0.015). The AK_C vortex remains in the wake at x = 1.035, nearly at the similar (y,z) position, but typically defused and mixed with other vortices such as BK and not clearly seen from the figures. Other than those three vortices a couple of vortices as well can be seen from the figures. This includes the vortices near below the fore body keel (FK) at x = 0.335 and 0.535, near below the aft body keel (AK) at x = 0.735 and 0.935, and near the free surface (FS). Typically, however, these vortices are weak in strength compared to those dominant three vortices, and data were not sufficient for analysis due to limited longitudinal resolution of the measurement (six x locations along the model length), and data may contaminated for the FS vortex from the errors of SPIV measurement near the free surface, which precludes further discussions for those vortices.

In Fig. 6-66, shown are the SD vortex (top) time histories of the maximum/minimum ω_x values, $\omega_{x,\max/\min}$, for x = 0.135 ~ 1.035 and (bottom) the FS 1st-order amplitude H and phase angle ϕ values of the $\omega_{x,\max/\min}$ time histories such that $f(t) = H\cdot\sin(\omega t+\phi)$ at give x locations. The $\omega_{x,\max/\min}$ is defined herein such that the maximum ω_x value when $\omega_x > 0$ and the minimum ω_x value when $\omega_x < 0$ at a given phase position γ. From Fig. 6-66 (bottom), H = 292 is the largest at x = 0.135 and drops fast to H = 159 at x = 0.335 and increases gradually with x to H = 189 at x = 0.735 and then decreases to H =129 at x = 1.035. Whereas, phase angle ϕ decreases nearly linearly along the model length with a slop $d\phi/dx = -118.9°/L \approx -2\pi/3L$ where L is the model length and an inter-

cept $\phi_0 = 191.3° \approx \pi$. This suggests that the phase term ϕ in f(t) is a function of x such that $\phi(x) = -(m/L)x + \phi_0$ where $m = 2\pi/3$ and $\phi_0 = \pi$, and thus the $\omega_{x,max/min}$ propagates in space and time in a wave-like form such that $f(x,t) = H(x)\cdot\sin(kx - \omega t)$. The wave number $k = m/L$ (wave length $\lambda = 2\pi/k = 2\pi L/m$) and the circular frequency $\omega = 2\pi f$ where $f = T^{-1}$ and T is the period of pure yaw motion (note that the f is as well the shedding frequency for SD vortex). Then, the phase velocity $v_p = \omega/k = \lambda/T = 2\pi fL/m$, or in a non-dimensional form $v_p/U_C = (2\pi/m)\cdot St$, where m is the phase change over a ship length L and $St = fL/U_C$ is the Strouhal number of the SV vortex shedding. For $f = 0.134$ Hz, $L = 3.048$ m, and $U_C = 1.531$ m/s, which gives $St = 0.2668$, and with $m = 2\pi/3$, then the phase velocity $v_p = 0.8\ U_C$. This indicates that $\omega_{x,max/min}$ propagates along the model length with a speed about 80% of the model towing speed U_C. At a given x location, f(x,t) becomes pure sine waves with a amplitude H(x) and with a phase shift $\phi = \pi - kx$ as shown in Fig. 6-66 (top) for six x location. On the other hand, at a given time t (or at a phase angle γ), f(x,t) becomes a sine-like wave of which amplitude H(x) is not a constant value but changes with x and with a phase shift $\phi = -\omega t$ (or $\phi = -\gamma$). Examples of the wave form at four phase positions, $\gamma = 0°$, 45°, 90°, and 135° are shown in Fig. 6-67 with compared with the $\omega_{x,max/min}$ values measured from the SPIV. From the figure, the wave model (shown as lines) agrees well with the measured $\omega_{x,max/min}$ values (shown as symbols) except for $\gamma = 45°$ case, may possibly due to the effect of higher order of harmonics in the $\omega_{x,max/min}$ time histories shown in Fig. 6-66.

BK vortices are generated in pairs; one is the portside and another at the starboard side, which can be best seen from figures in Fig. 6-65 for $x = 0.735$ (the third row from the bottom), near around the bilge keels positions. These two vortices typically have the same direction of rotation whereas different strength according to direction and magnitude of the nearby incoming cross-flow velocity around the bilge keels. From the vector field figures in Fig. 6-51 (or Fig. 6-52 for streamlines) for $x = 0.535$ (the third row from the top), at first when $\gamma = 0°$ the cross-flow near the bilge keels is stronger at starboard

than at portside, next at $\gamma = 45°$ the flow weakens at both sides, and then at $\gamma = 90°$ and 135° the stronger cross-flow comes from the other side, i.e. from the portside. Accordingly the BK vortex and the axial vorticity is stronger first at the starboard side and then switches its position to the portside and continues to develop (with changed its sign), and vice versa for the weaker BK vortex at the other side. Herein the side where the incoming flow is stronger is referred as the 'wind' side and the other side as the 'leeward' side, respectively. In Fig. 6-68 the time histories of the $\omega_{x,max/min}$ values of the BK vortices at the wind and leeward sides for $x = 0.535$ (left) and $x = 0.735$ (right), respectively. In the figures two different symbols ('delta' and 'gradient') are use to indicate from which side came the vortices. At x = 0.535, although the BK vortices are very local and small in size, the ωx,max/min value is large with H = 115 at the wind side and H = 71 at the leeward side, respectively, from the FS, where the phase angle $\phi = -48.4°$ and -51.3°, respectively. At $x = 0.735$, the BK vortices grow in size but decayed in strength with H = 80 at the wind side and H = 25 at the leeward side, respectively, where the phase angle $\phi = -27.5°$ and -30.3°, respectively. Compared to H = 292 of the SD vortex at x = 0.135 (the strongest), the H's at $x = 0.535$ and 0.735 are about 39% and 27% for wind side, respectively, and about 24% and 9% for leeward side, respectively.

Time histories of the $\omega_{x,max/min}$ values of AK_C vortex is shown in Fig. 69 for $x = 0.935$ and 1.035. When FS reconstructed, at $x = 0.935$ and 1.035, H = 95 and 63, respectively, and ϕ -36.9° and -52.1°. The H's are about 33% and 22% of the SD vortex H value at $x = 0.135$.

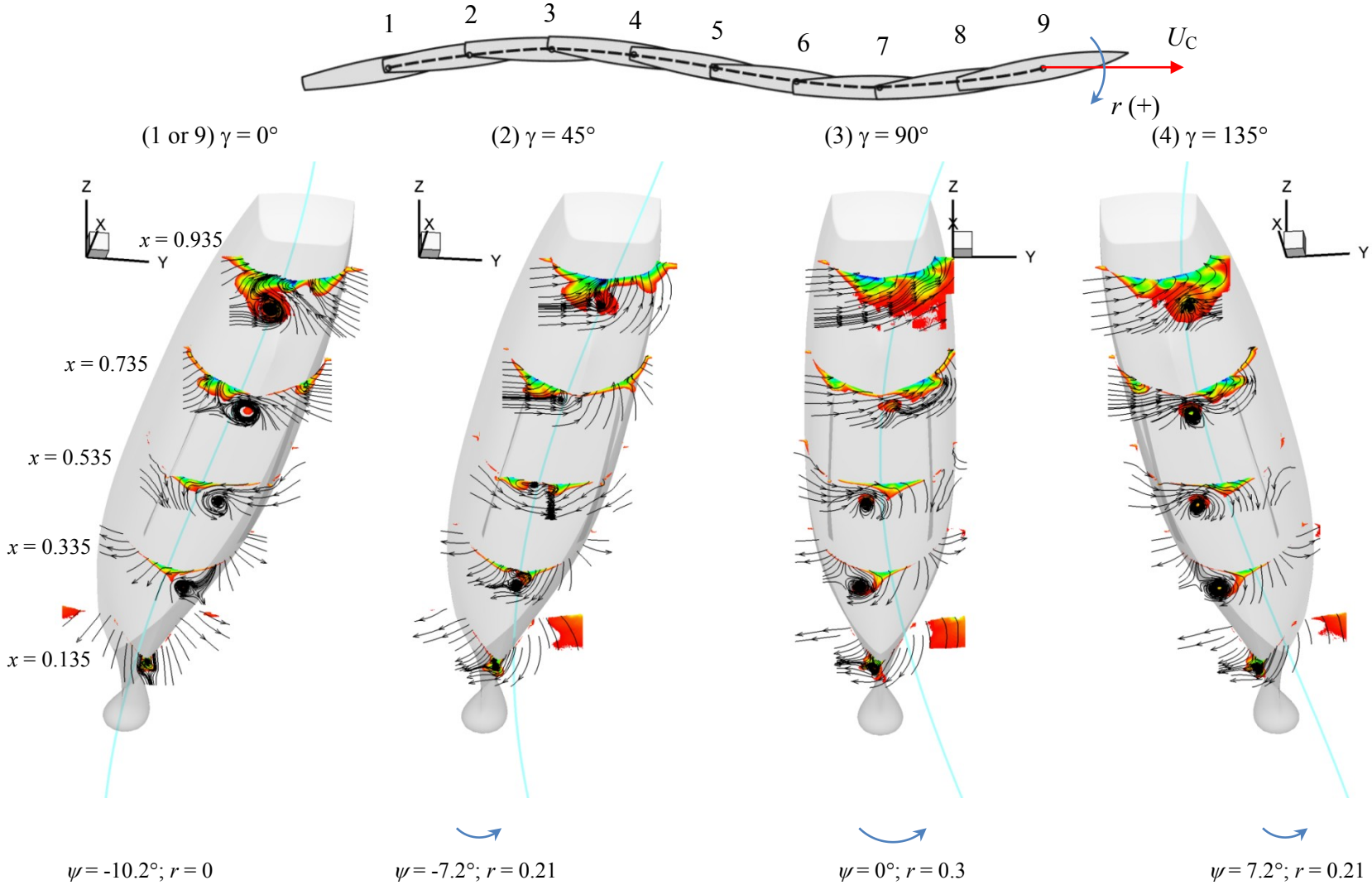

Figure 6-45 Trajectory of model (top) in pure yaw motion and overviews of the flow around the model (below).

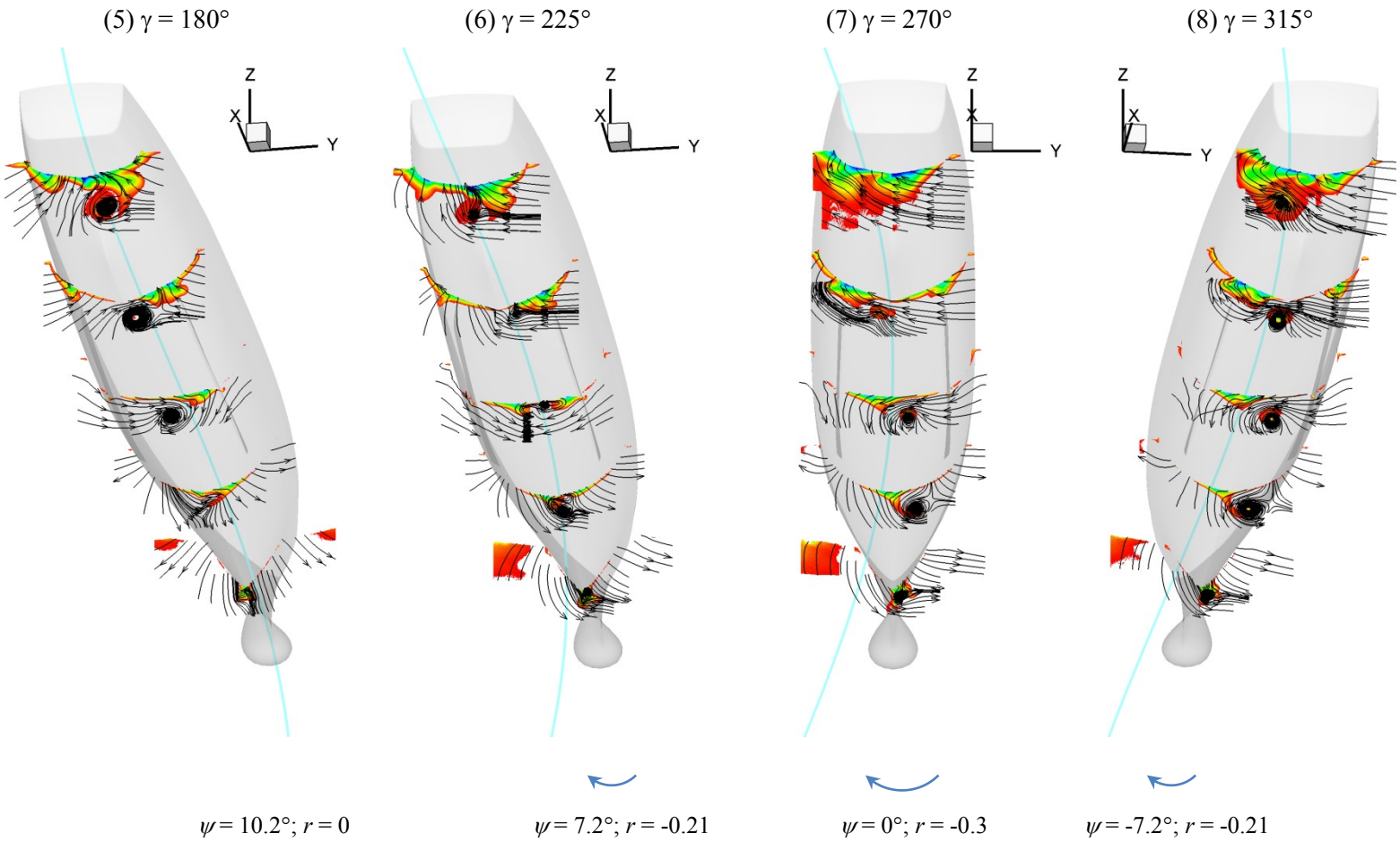

Figure 6-45–Continued

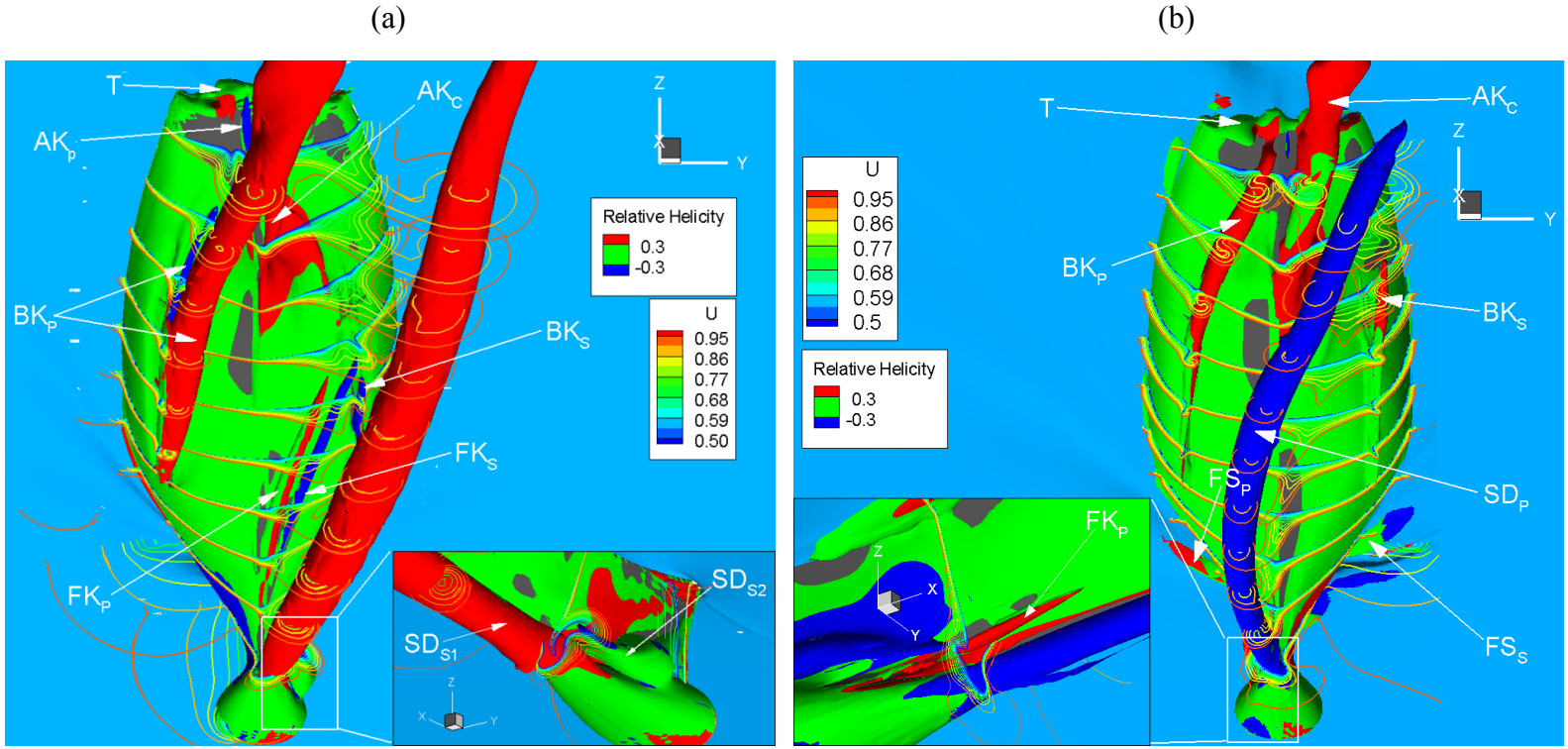

Figure 6-46 Vortical flow structures around the DTMB 5512 geometry in steady maneuver for: (a) static drift at $\beta = 10°$ and (b) steady turn at $r = 0.3$ cases. (CFD simulations by Sakamoto 2009).

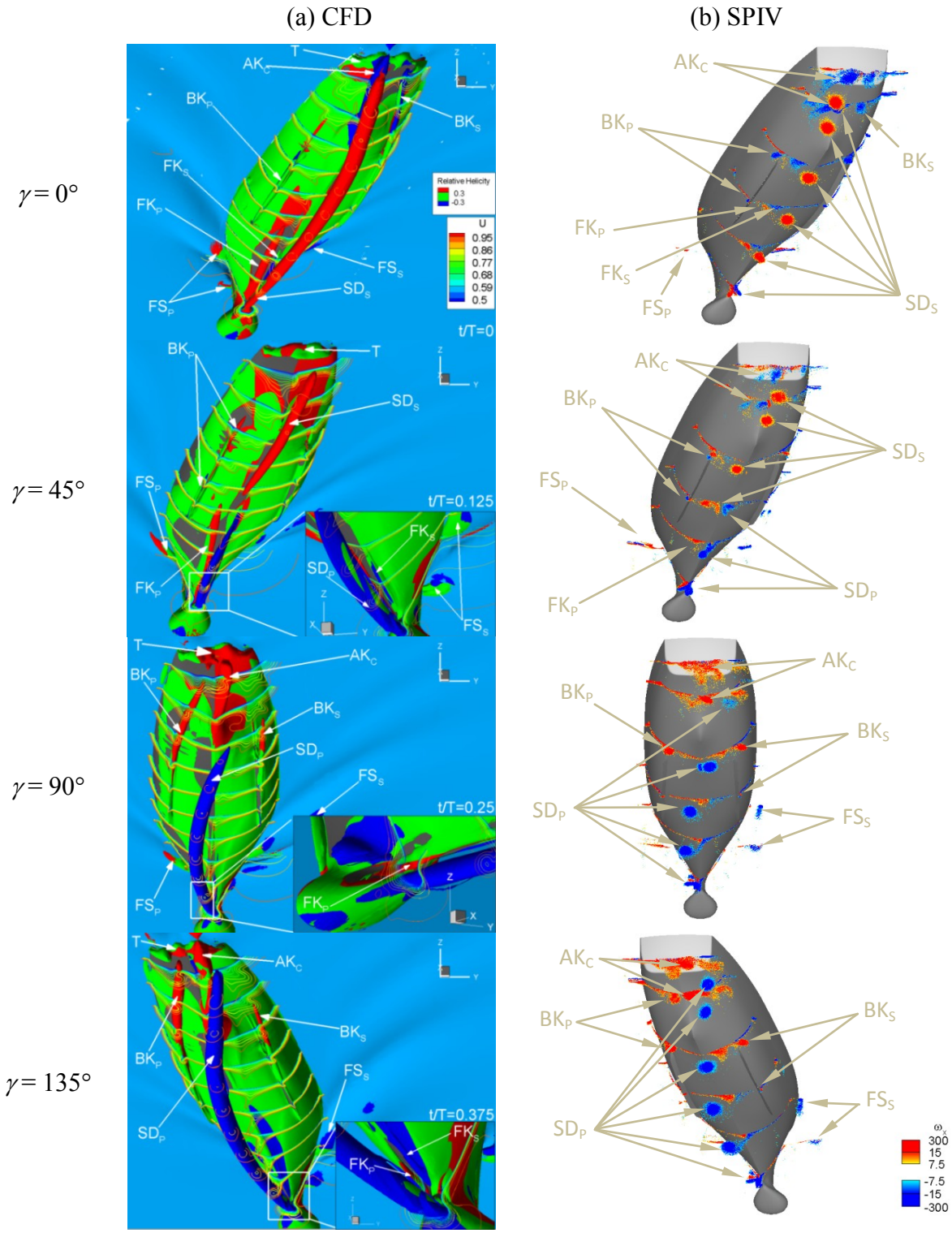

Figure 6-47 Vortical flow structures around the DTMB 5512 geometry in pure yaw maneuvering with r_{max} = 0.3: (a) Iso-surfaces of relative helicity (CFD simulations by Sakamoto 2009) and (b) contours of axial vorticity (SPIV).

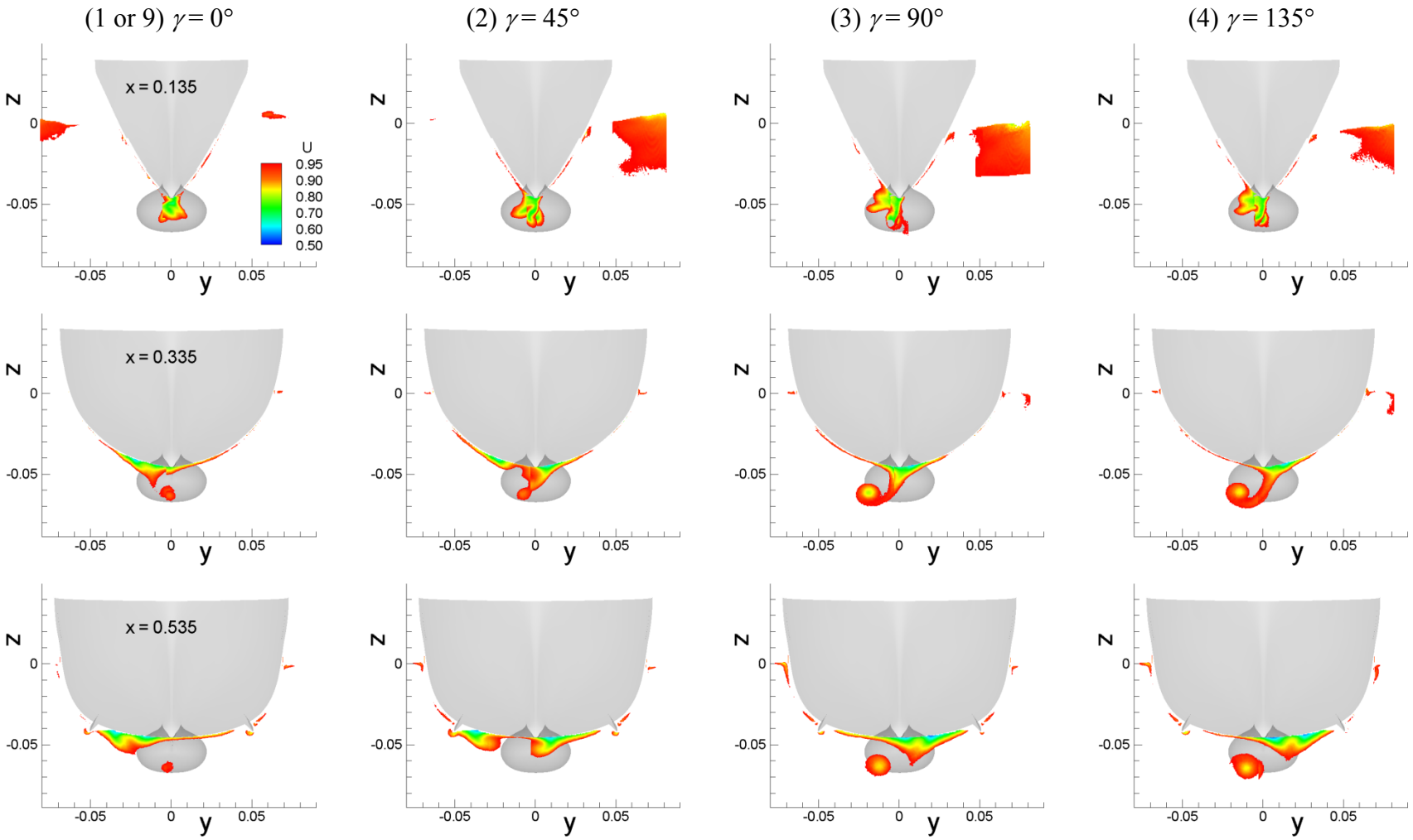

Figure 6-48 Phase-averaged axial velocity *U* field for pure yaw test.

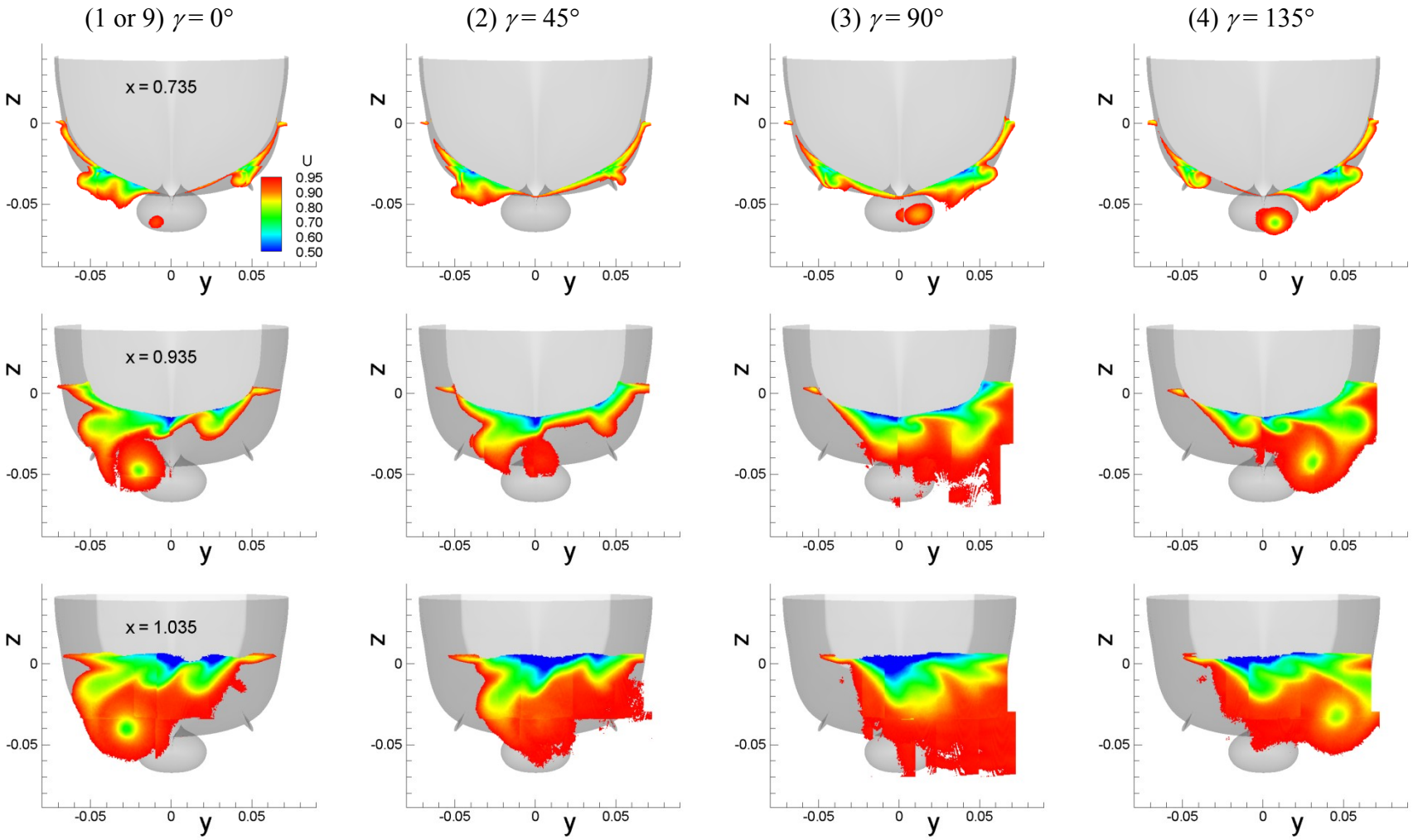

Figure 6-48–Continued

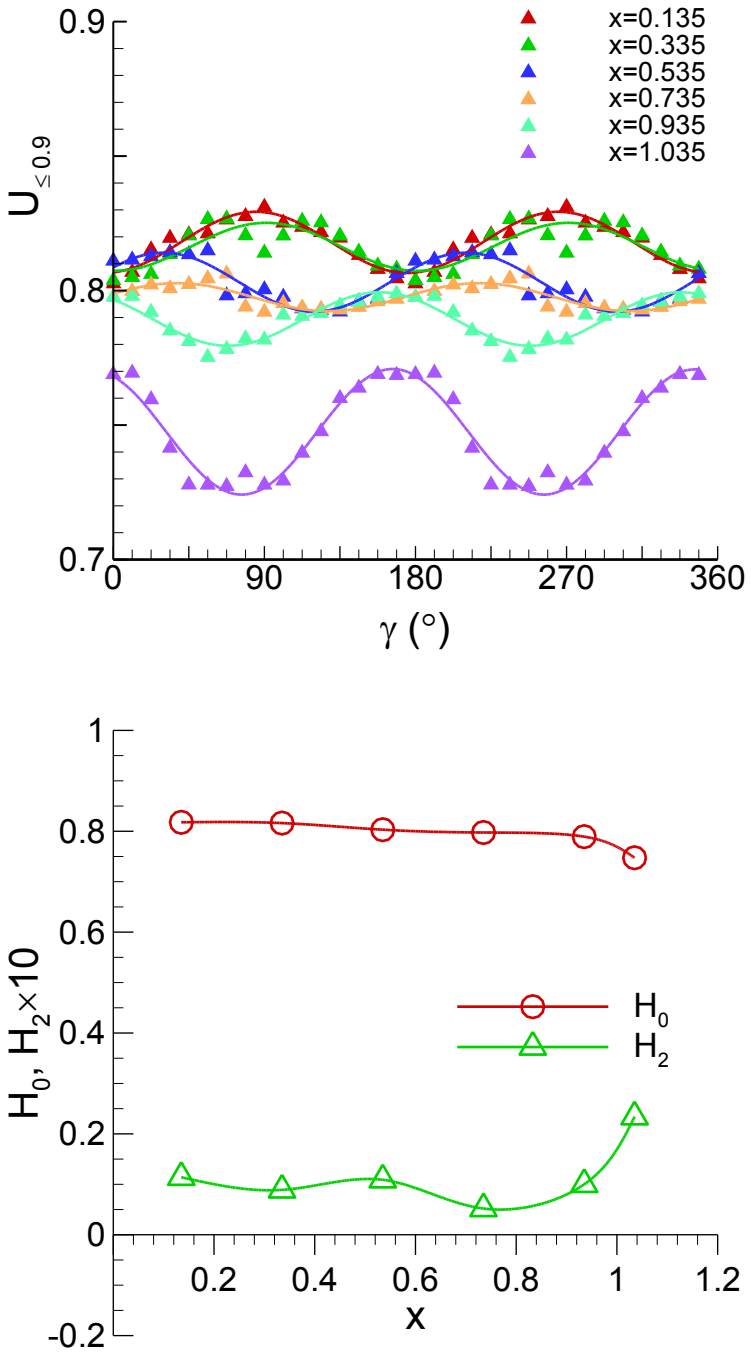

Figure 6-49 Average axial velocity for $U \leq 0.9$ (top) and FS harmonics (bottom).

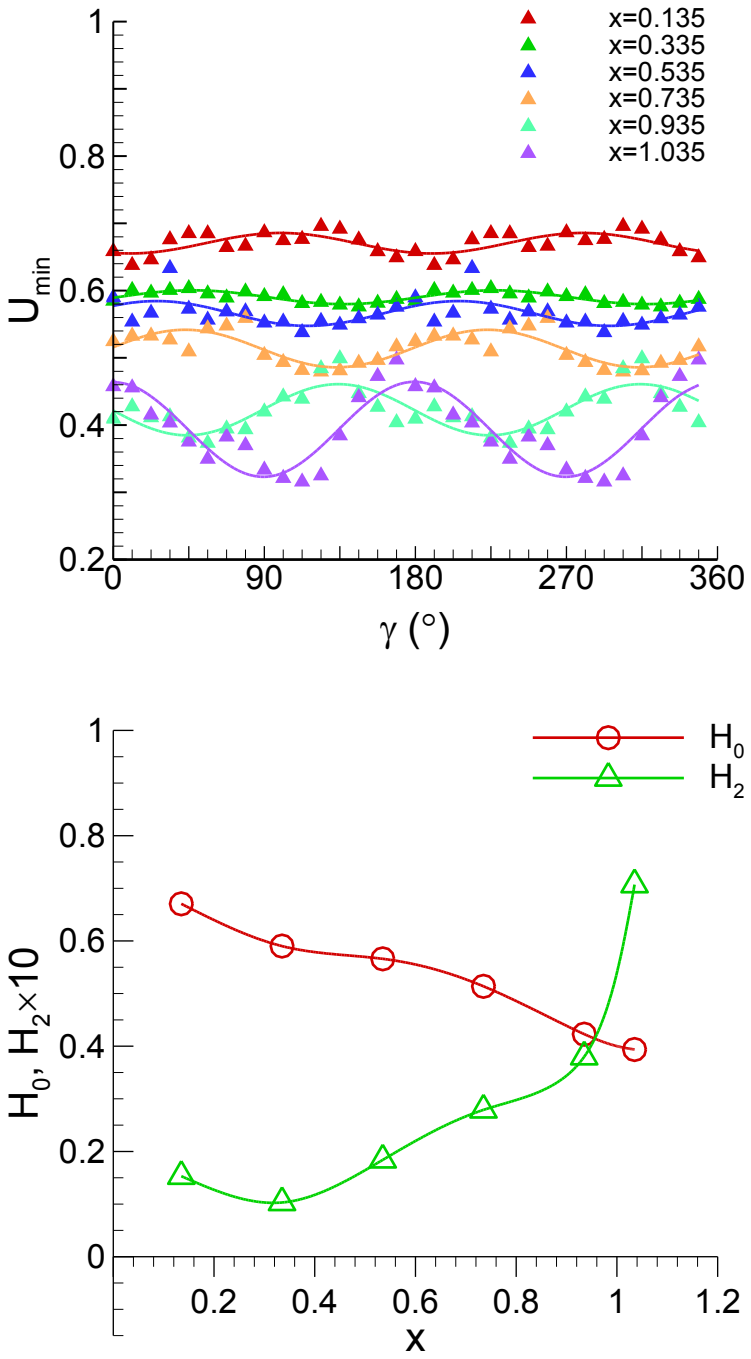

Figure 6-50 Minimum axial velocity (top) and FS harmonics (bottom).

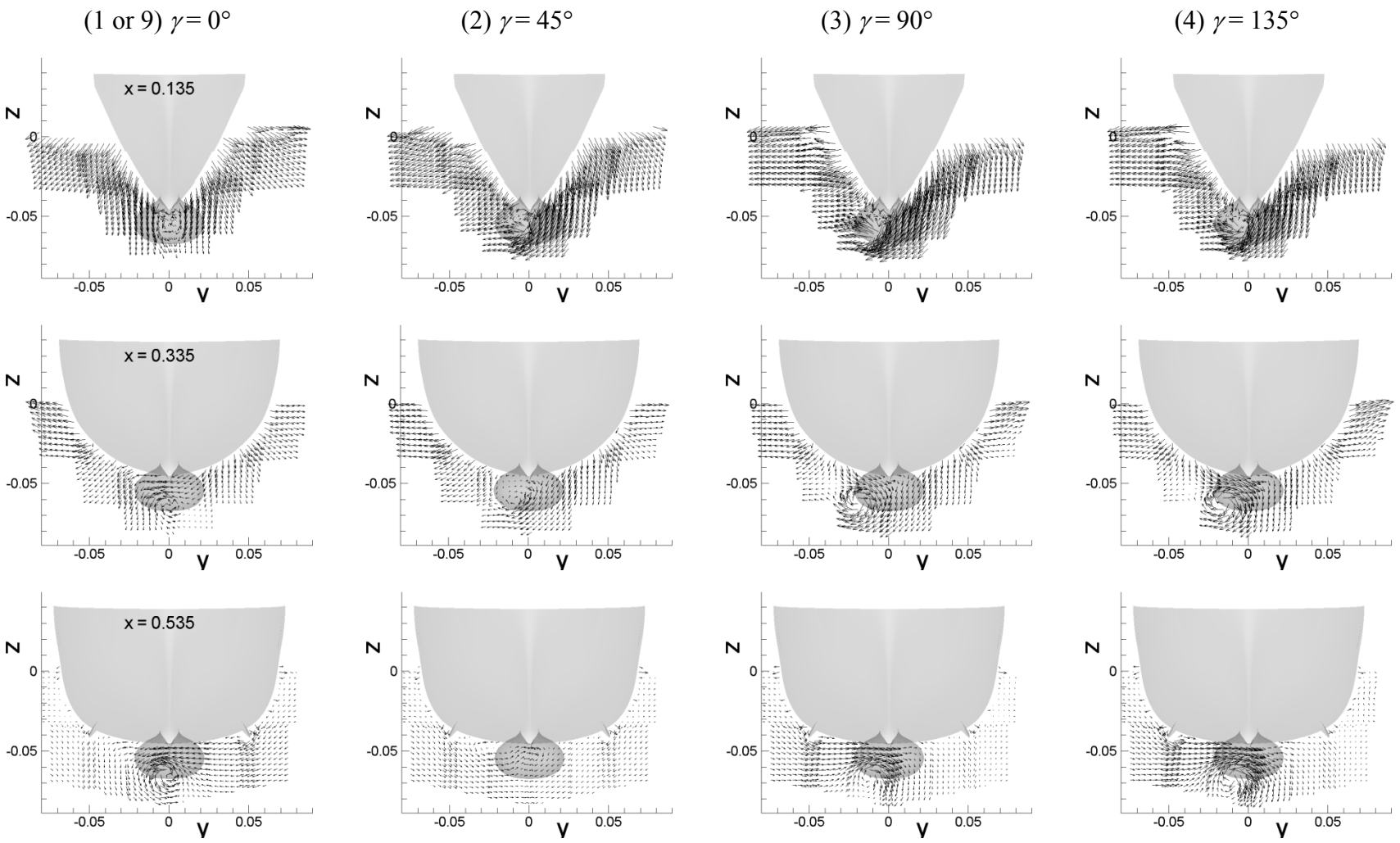

Figure 6-51 Phase-averaged cross-flow (V,W) vector field for pure yaw test.

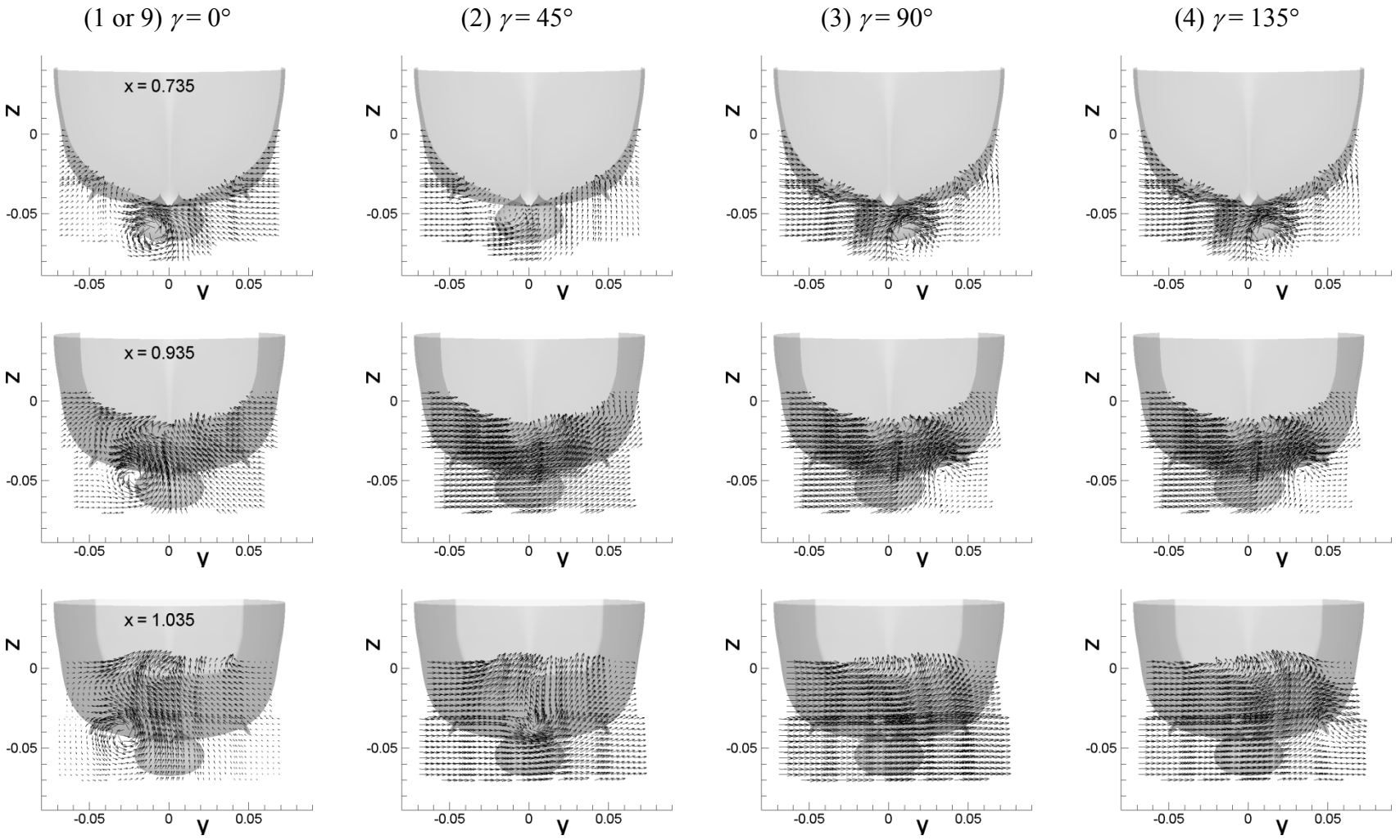

Figure 6-51–Continued

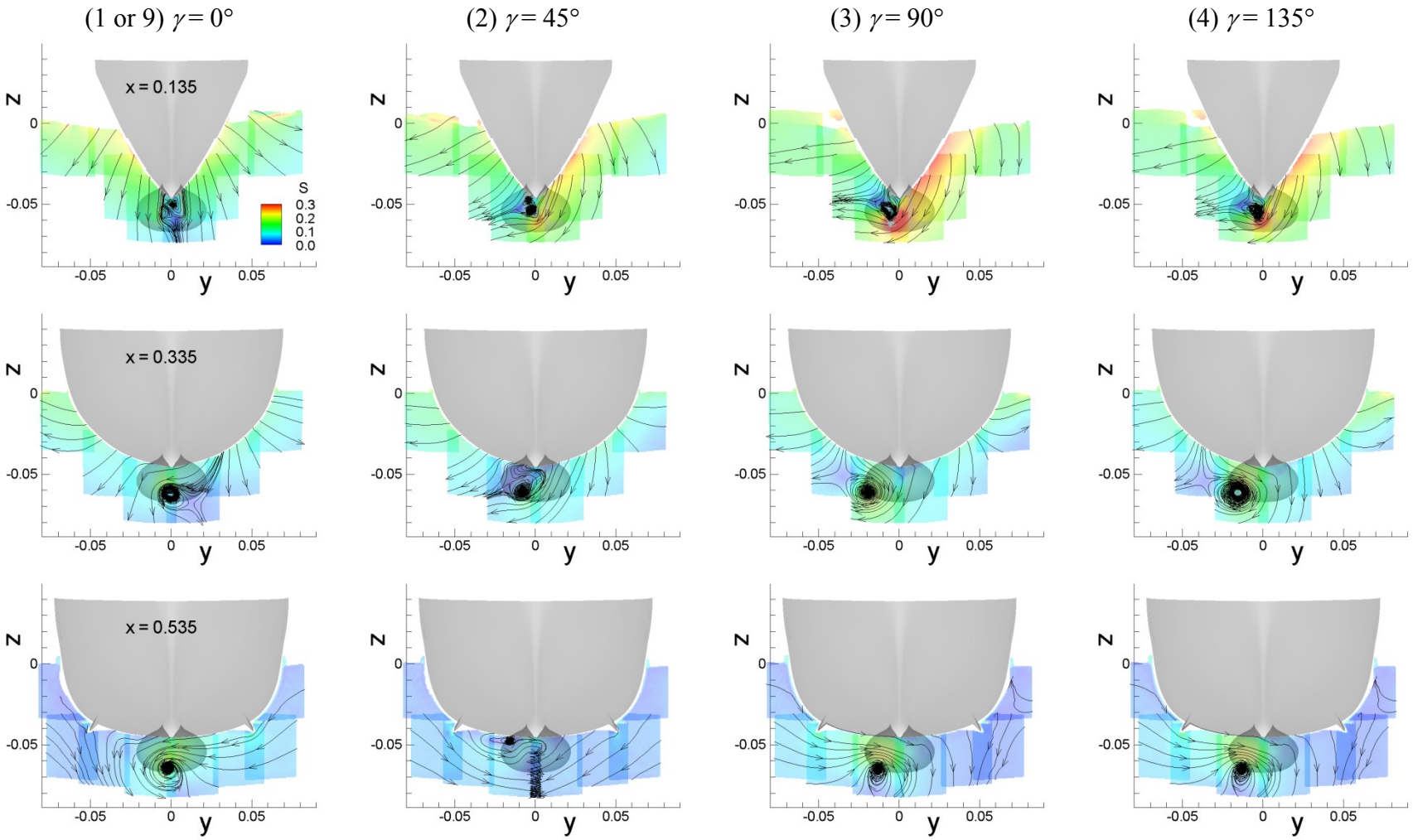

Figure 6-52 Cross flow velocity vector magnitude $S = (V^2 + W^2)^{1/2}$ and streamlines for pure yaw test.

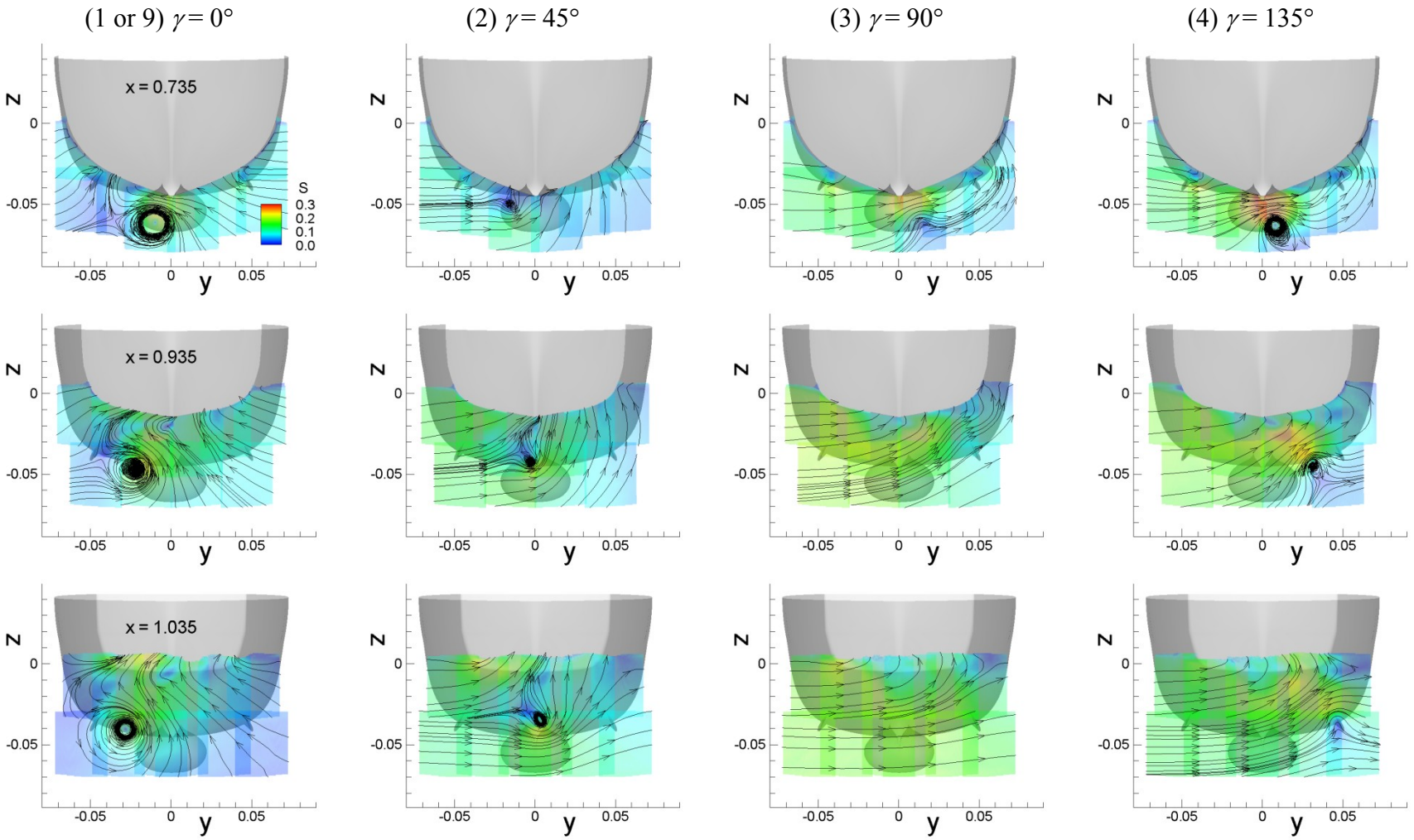

Figure 6-52–Continued

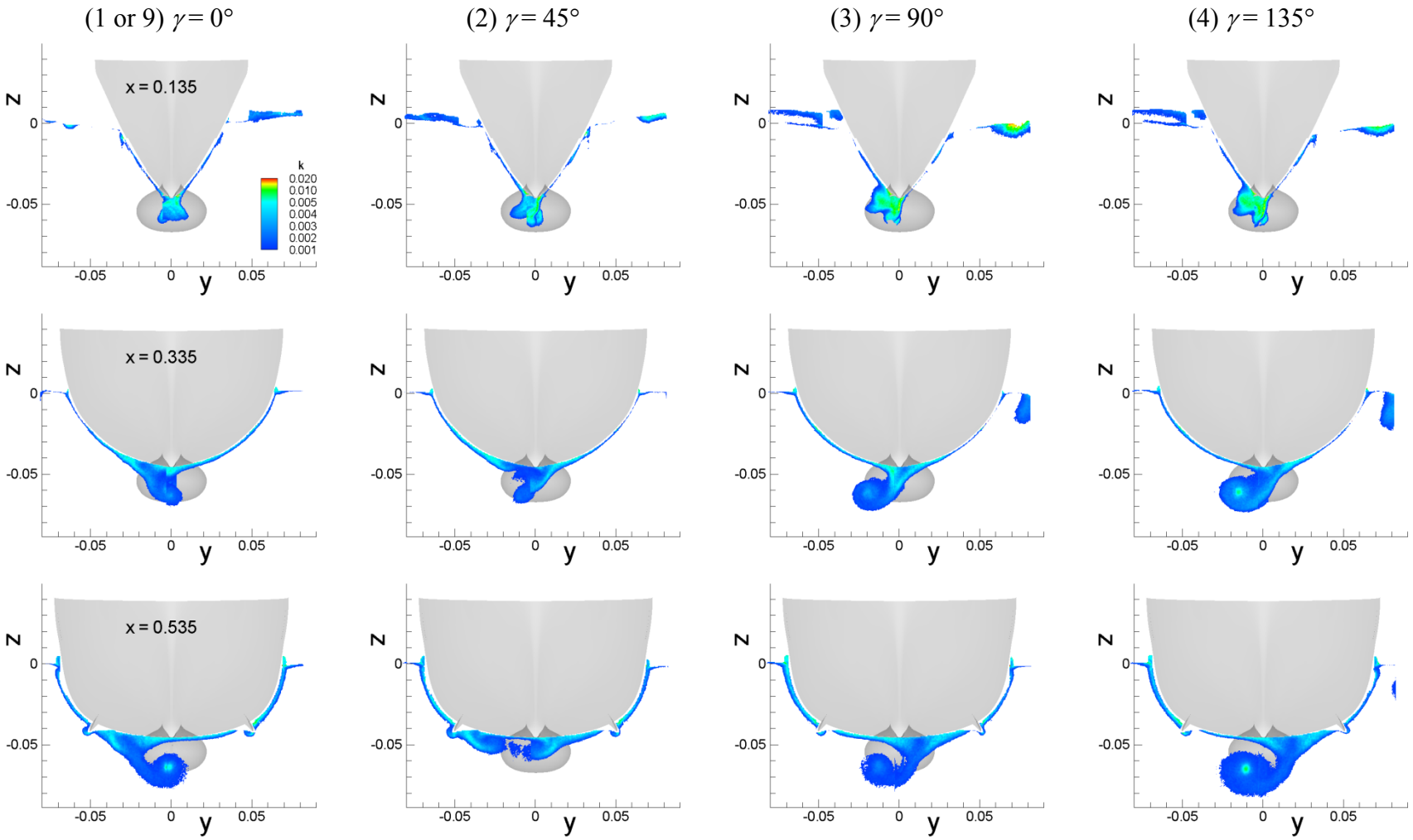

Figure 6-53 Phase-averaged turbulent kinetic energy *k* field for pure yaw test.

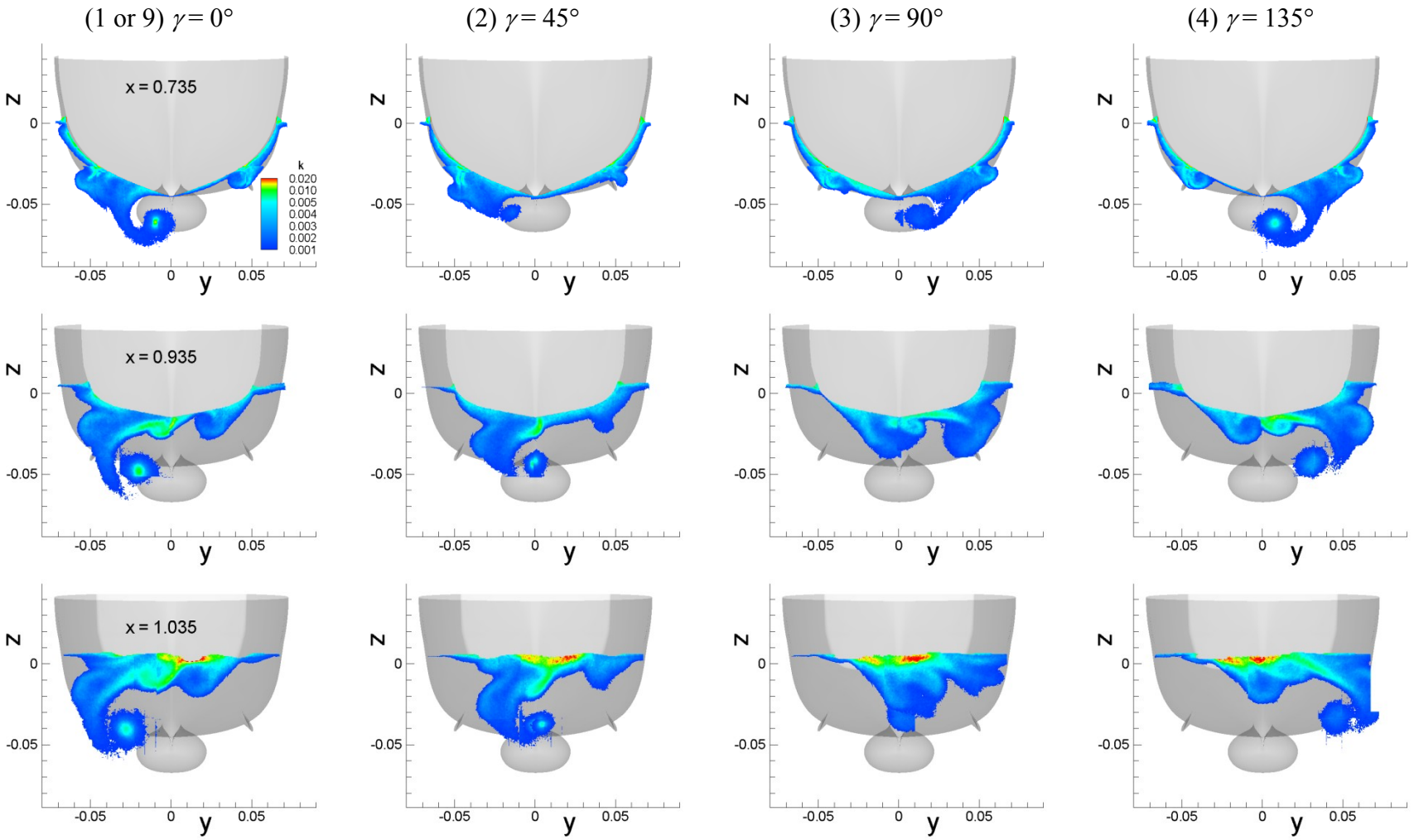

Figure 6-53–Continued

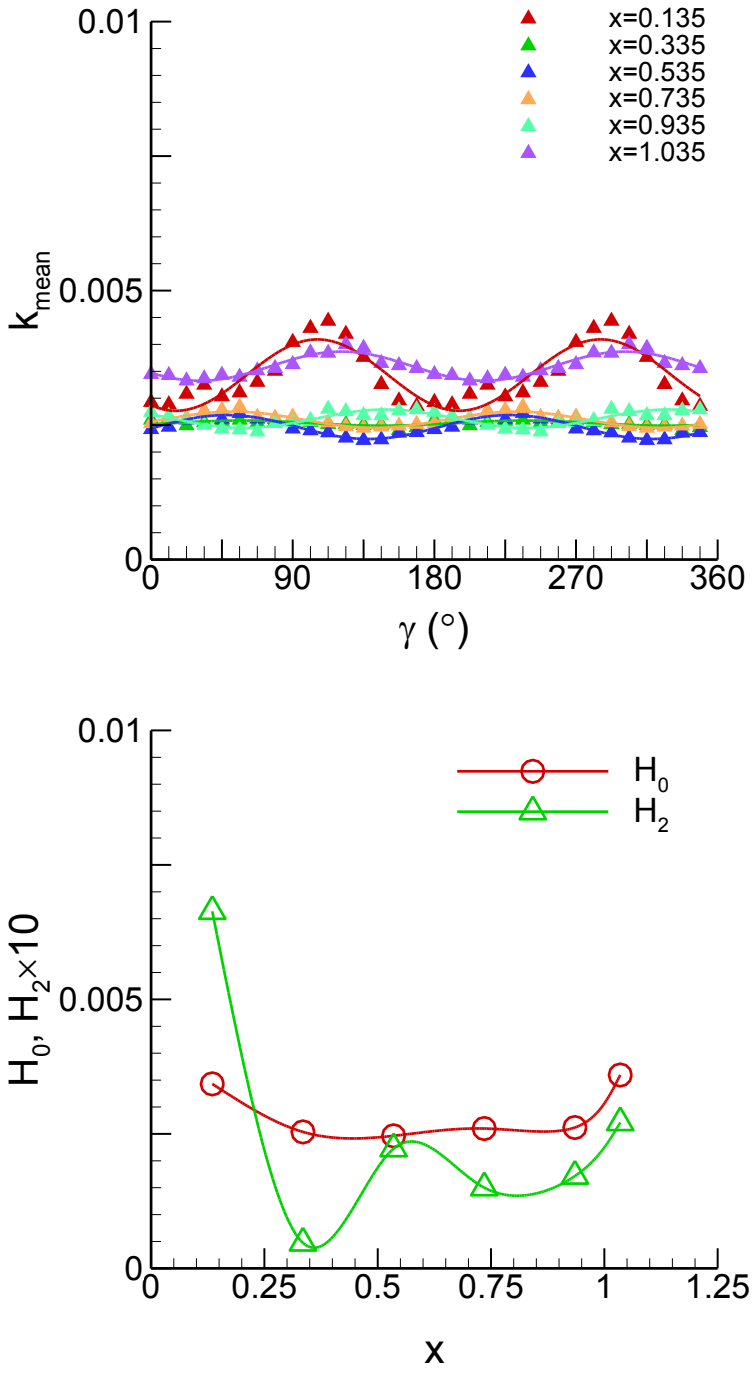

Figure 6-54 Average turbulent kinetic energy k_{mean} (top) and FS harmonics (bottom).

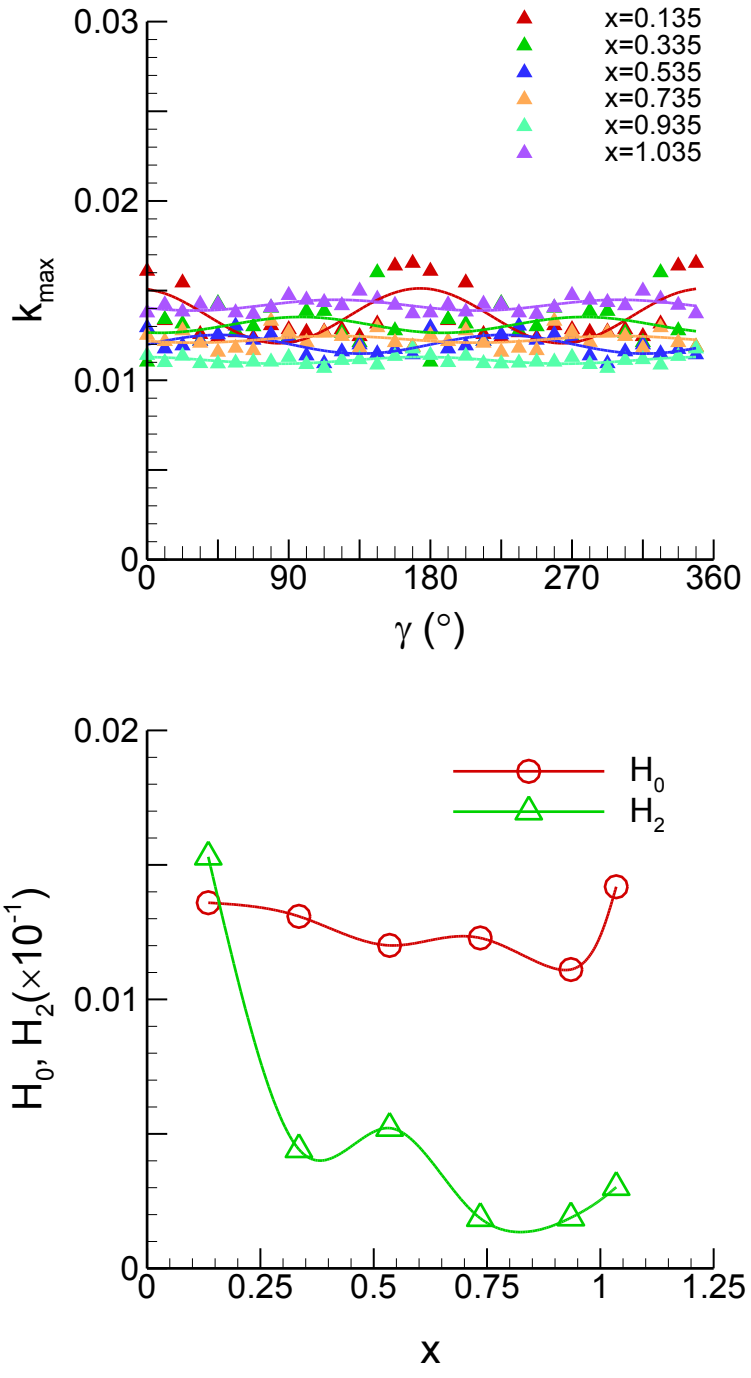

Figure 6-55 Maximum turbulent kinetic energy k_{max} (top) and FS harmonics (bottom).

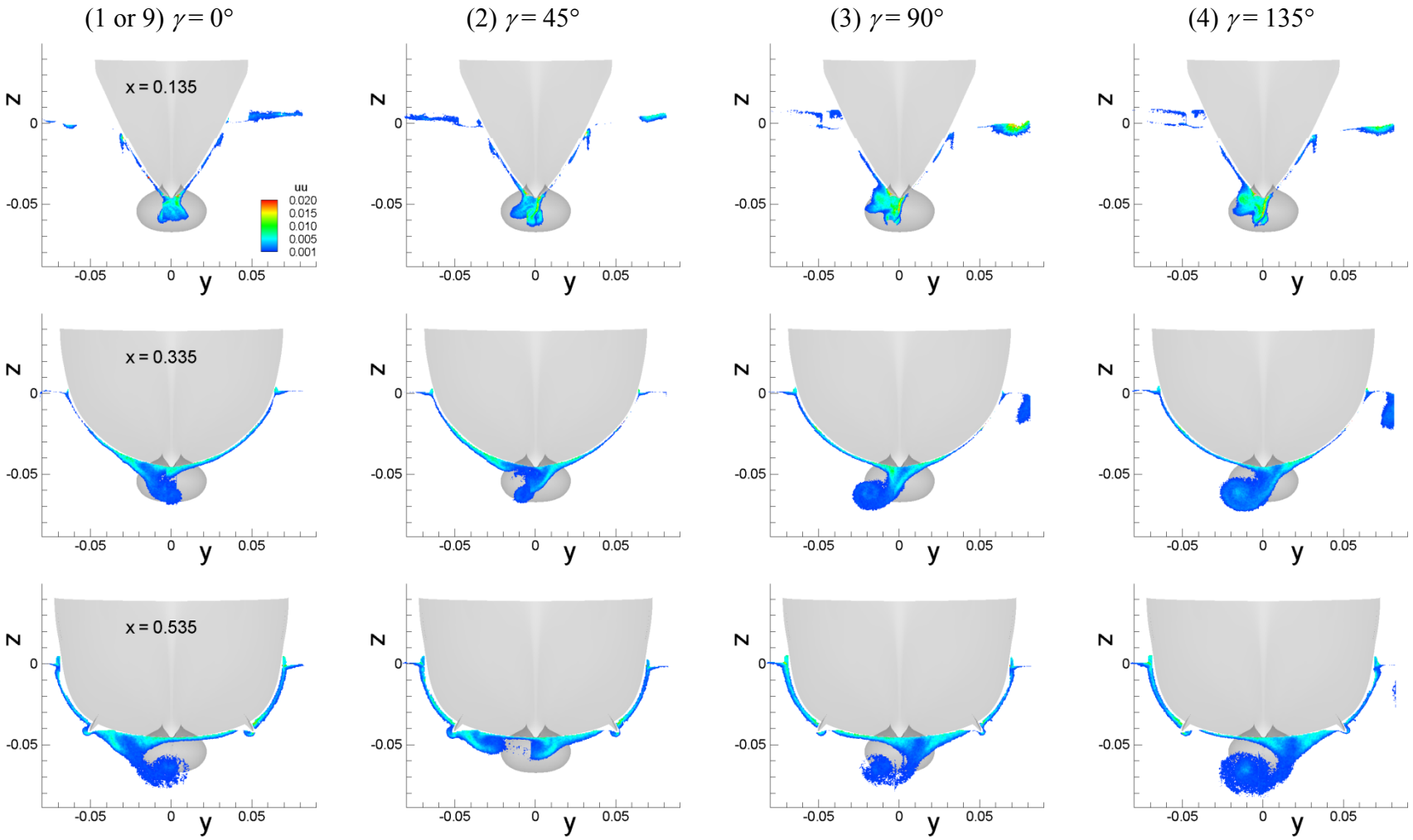

Figure 6-56 Phase-averaged Reynolds stress *uu* field for pure yaw test.

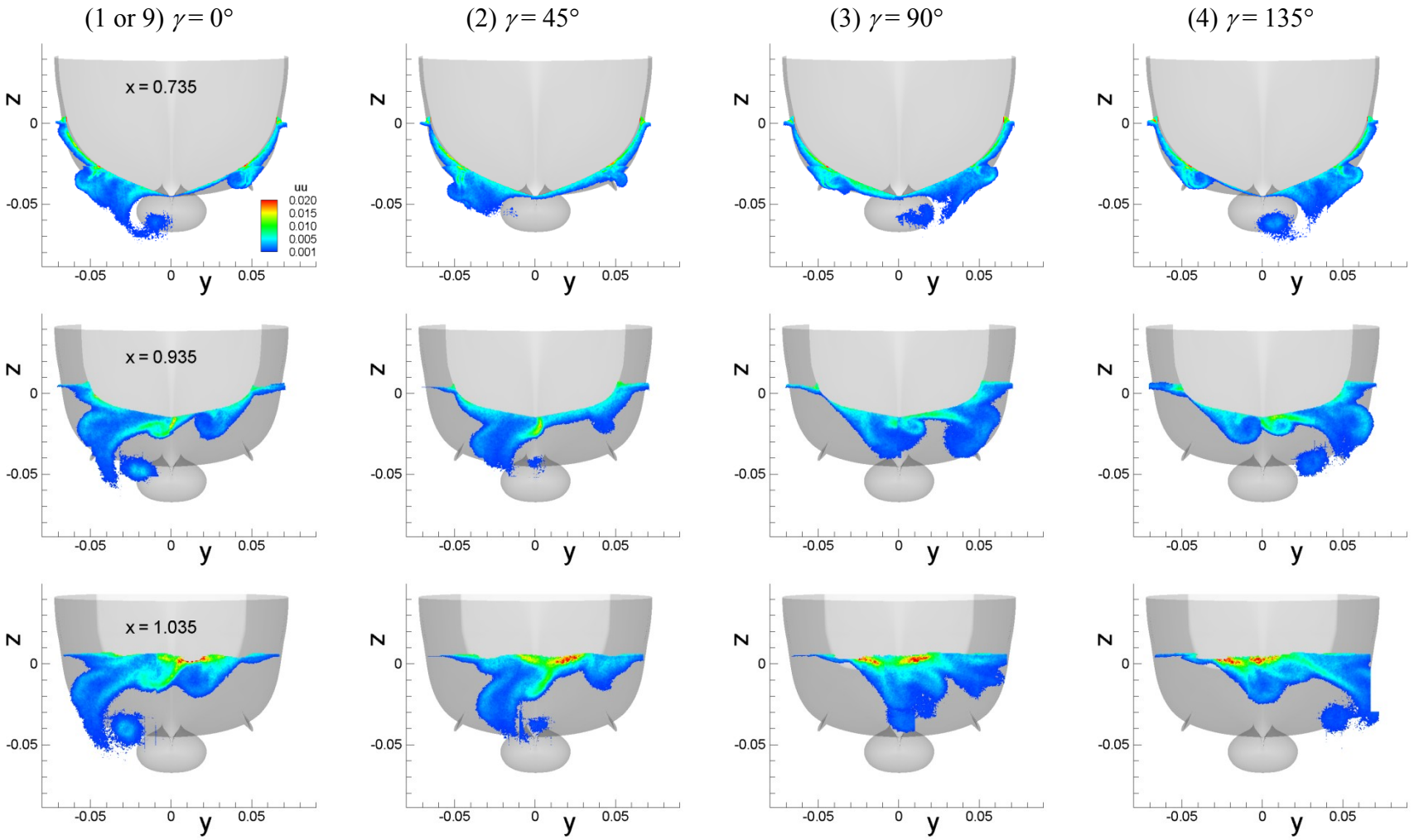

Figure 6-56–Continued

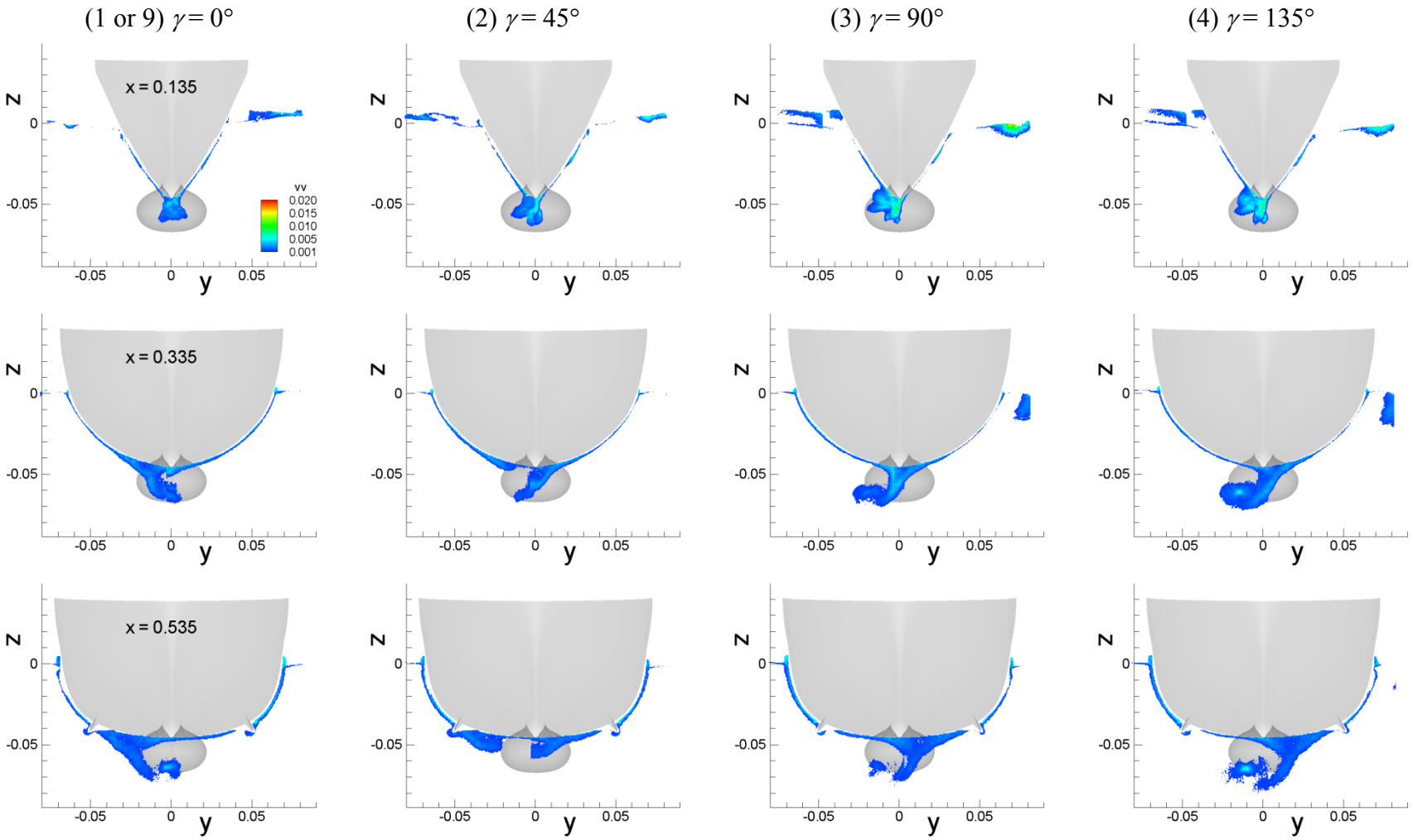

Figure 6-57 Phase-averaged Reynolds stress *vv* field for pure yaw test.

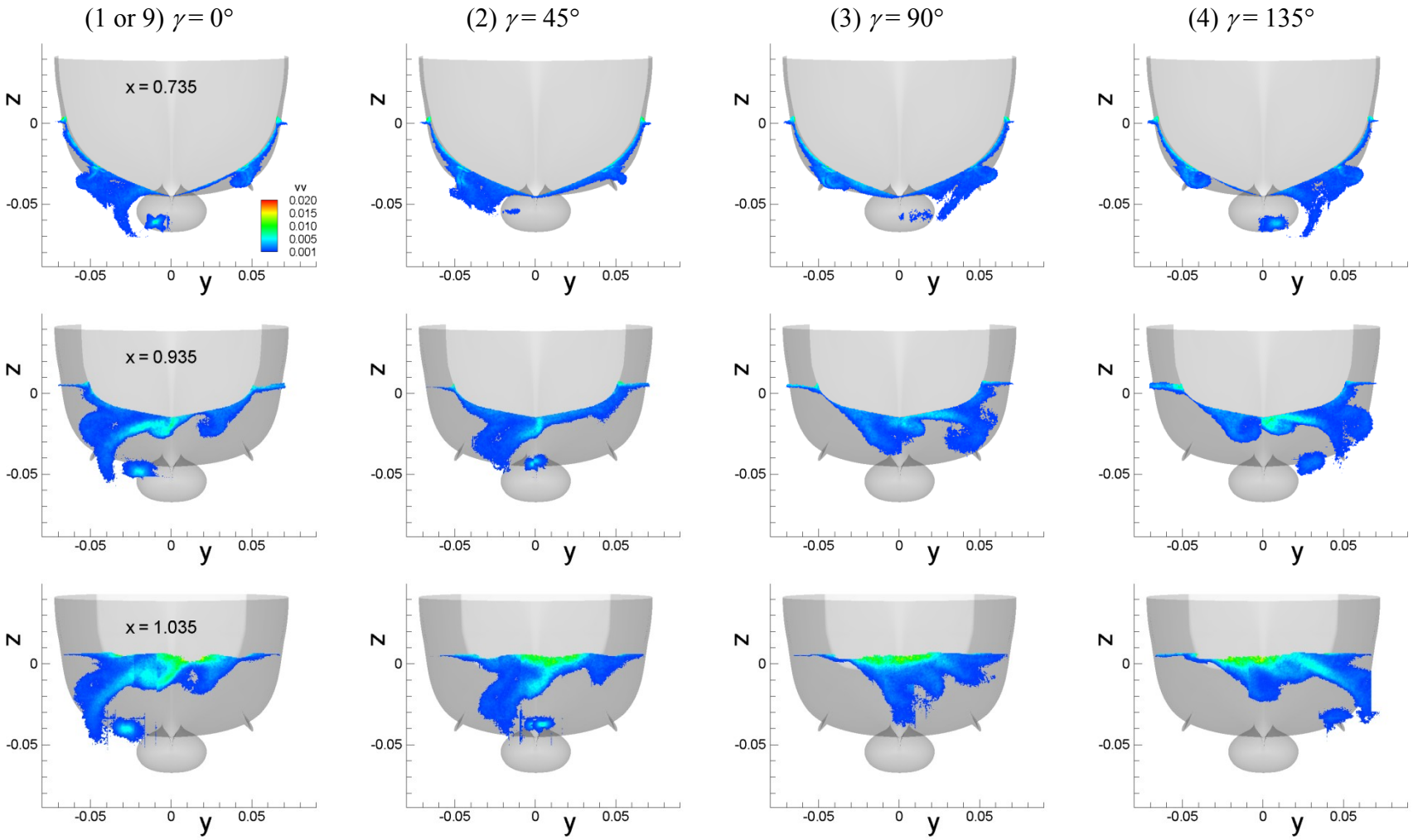

Figure 6-57–Continued

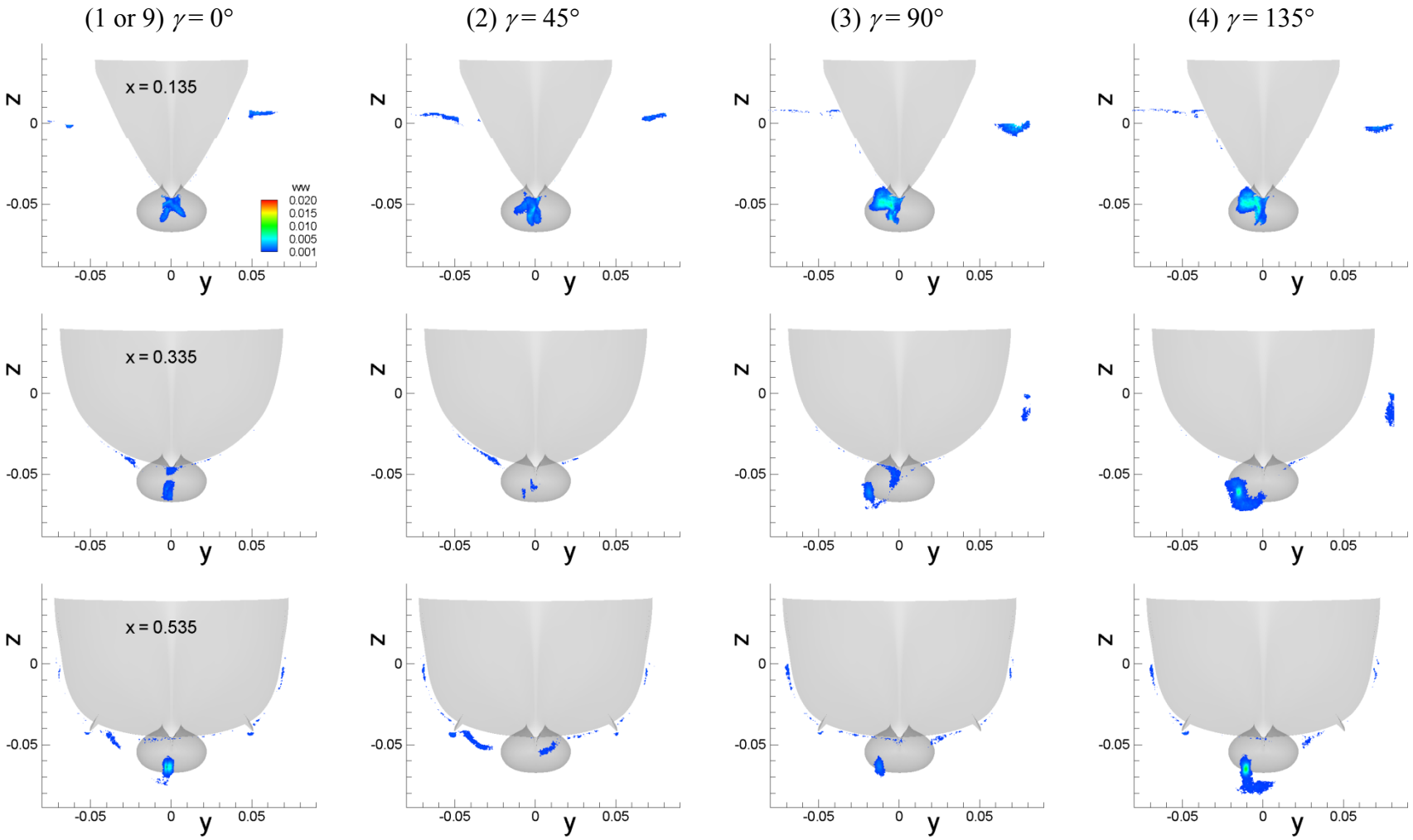

Figure 6-58 Phase-averaged Reynolds stress *ww* field for pure yaw test.

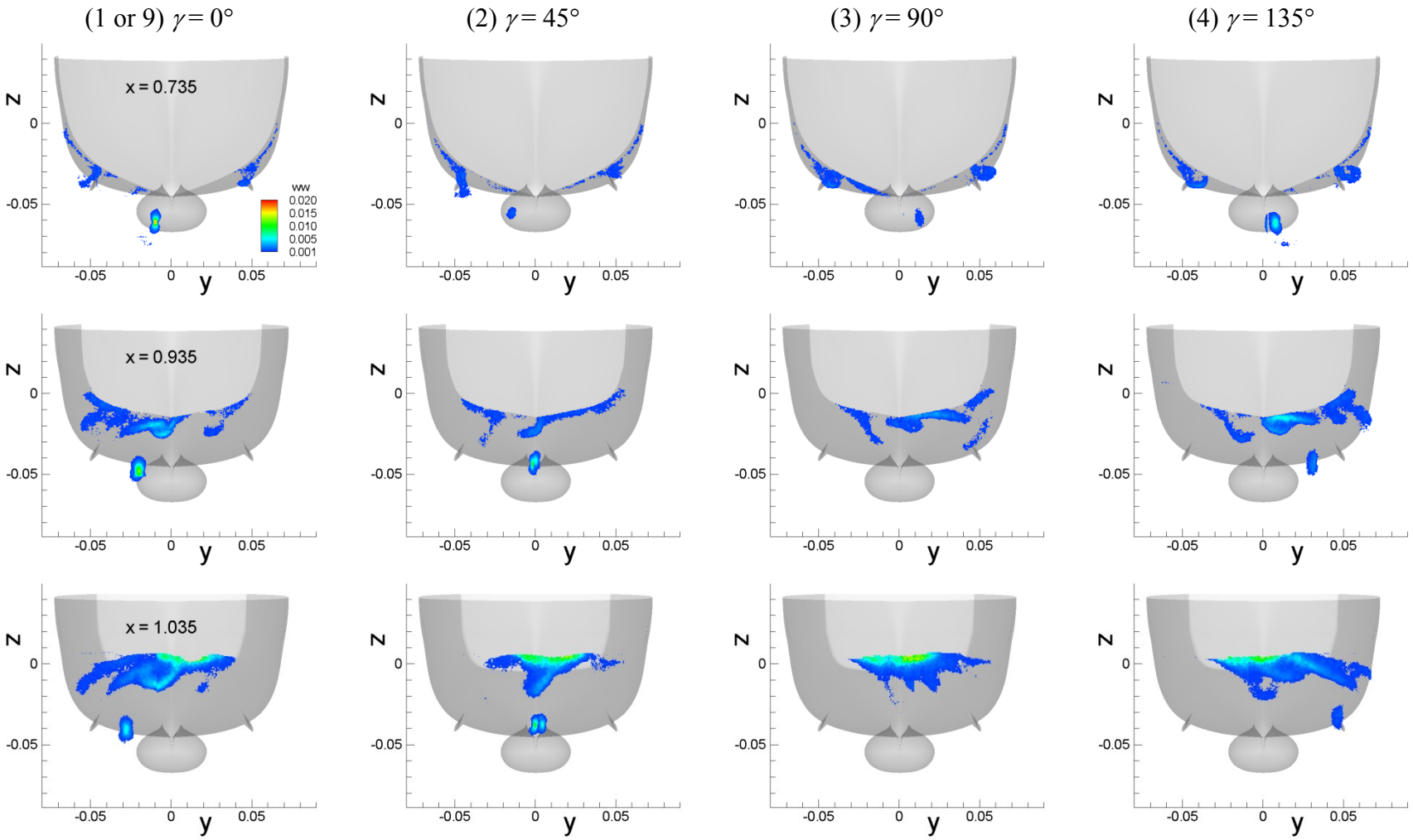

Figure 6-58–Continued

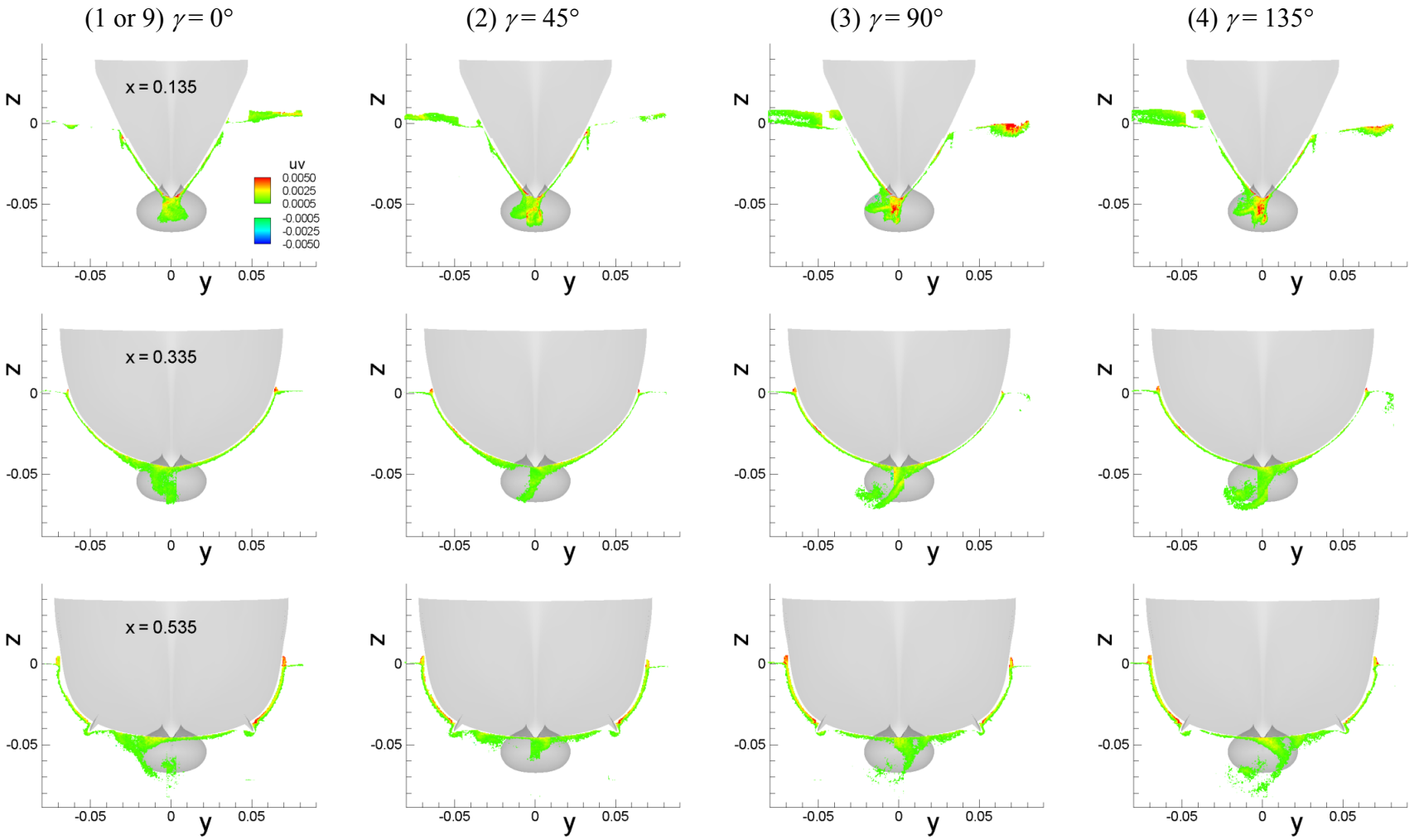

Figure 6-59 Phase-averaged Reynolds stress *uv* field for pure yaw test.

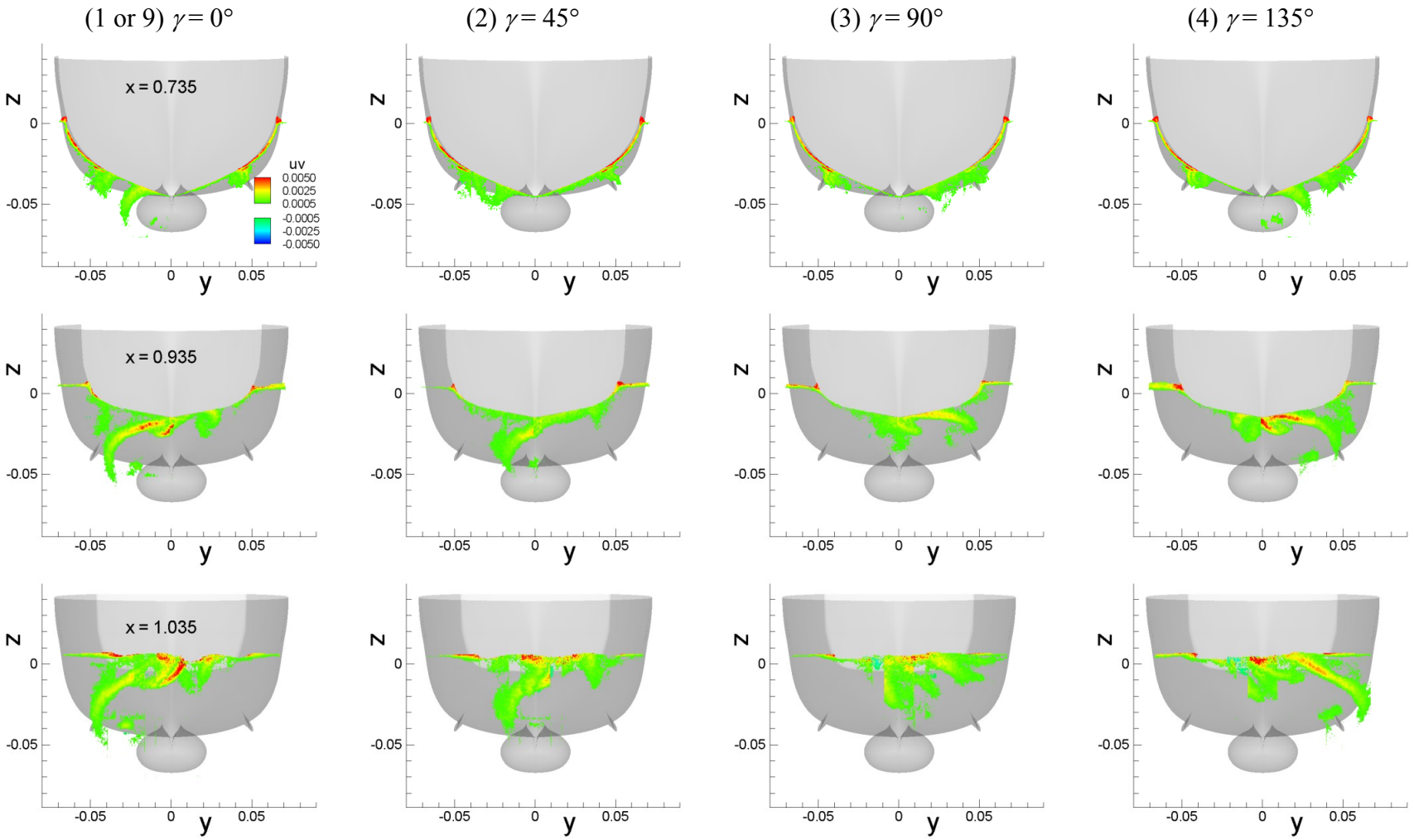

Figure 6-59–Continued

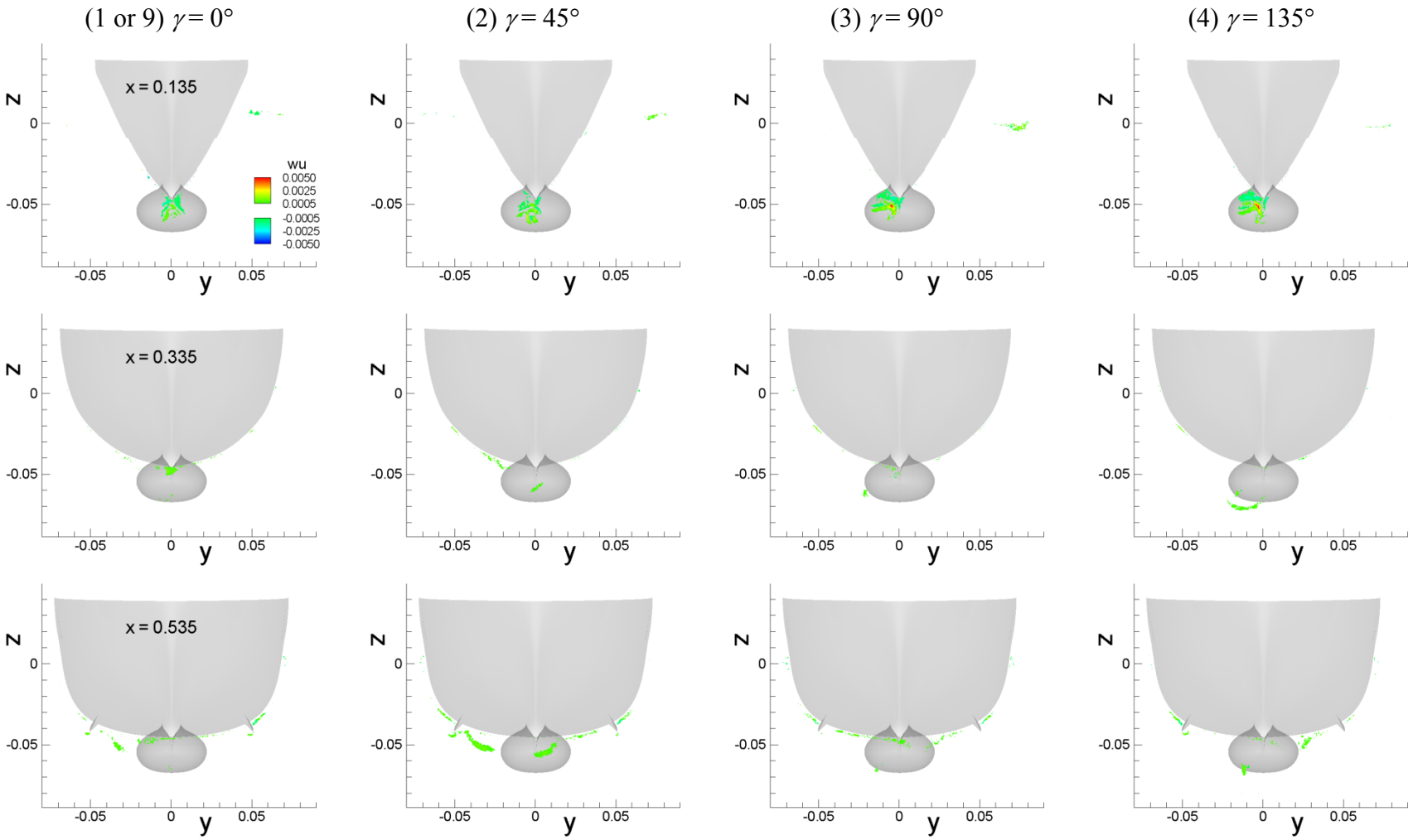

Figure 6-60 Phase-averaged Reynolds stress *uw* field for pure yaw test.

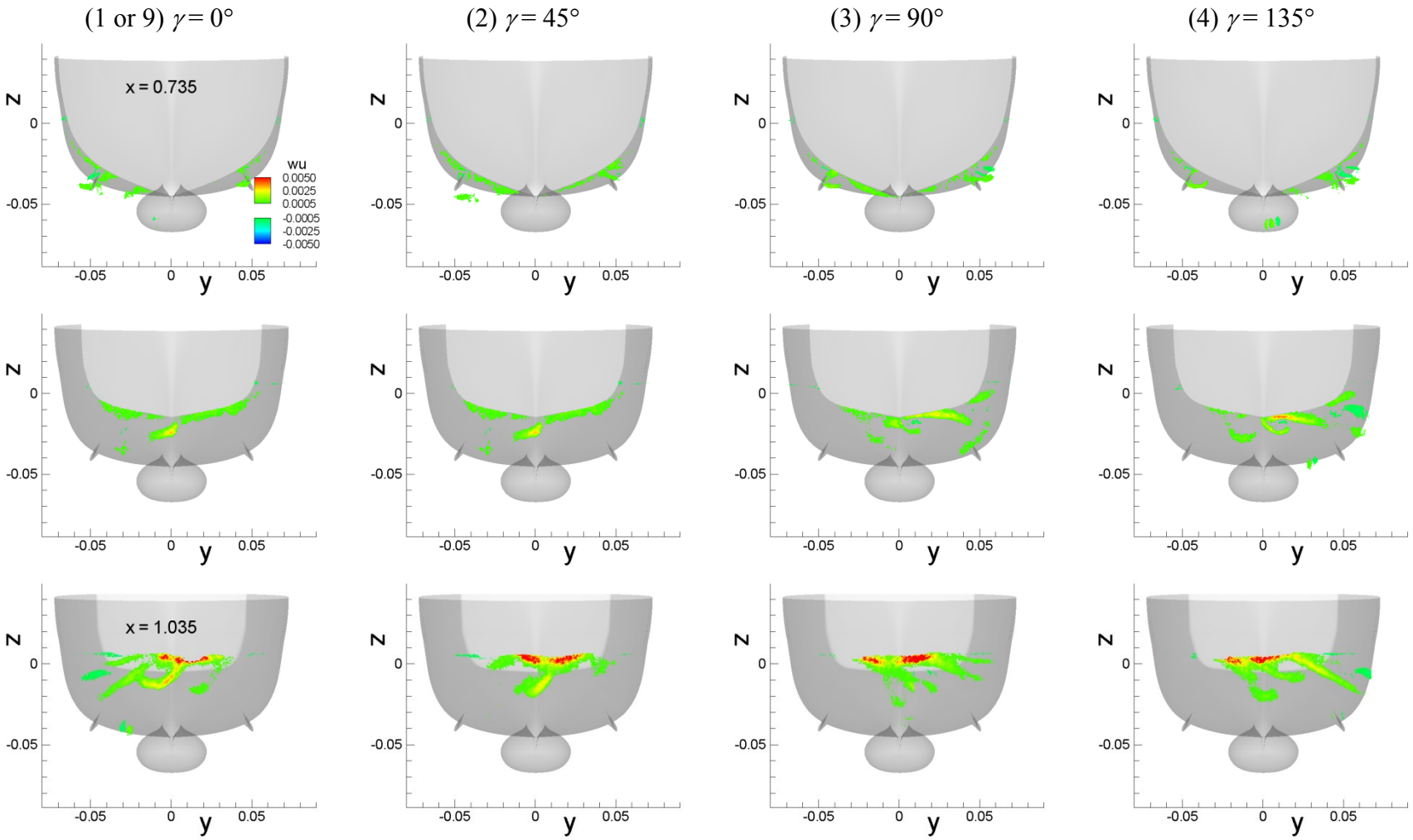

Figure 6-60–Continued

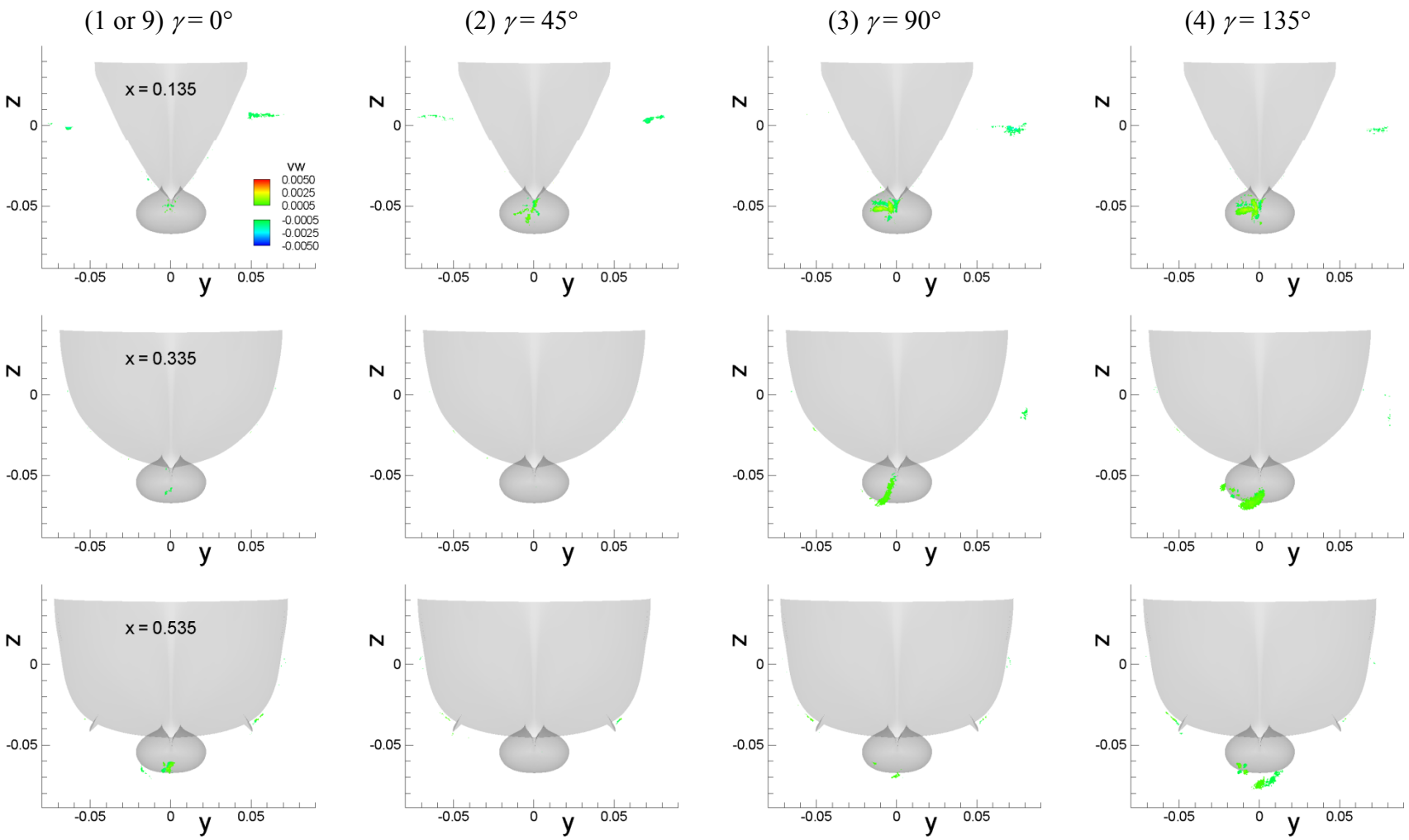

Figure 6-61 Phase-averaged Reynolds stress *vw* field for pure yaw test.

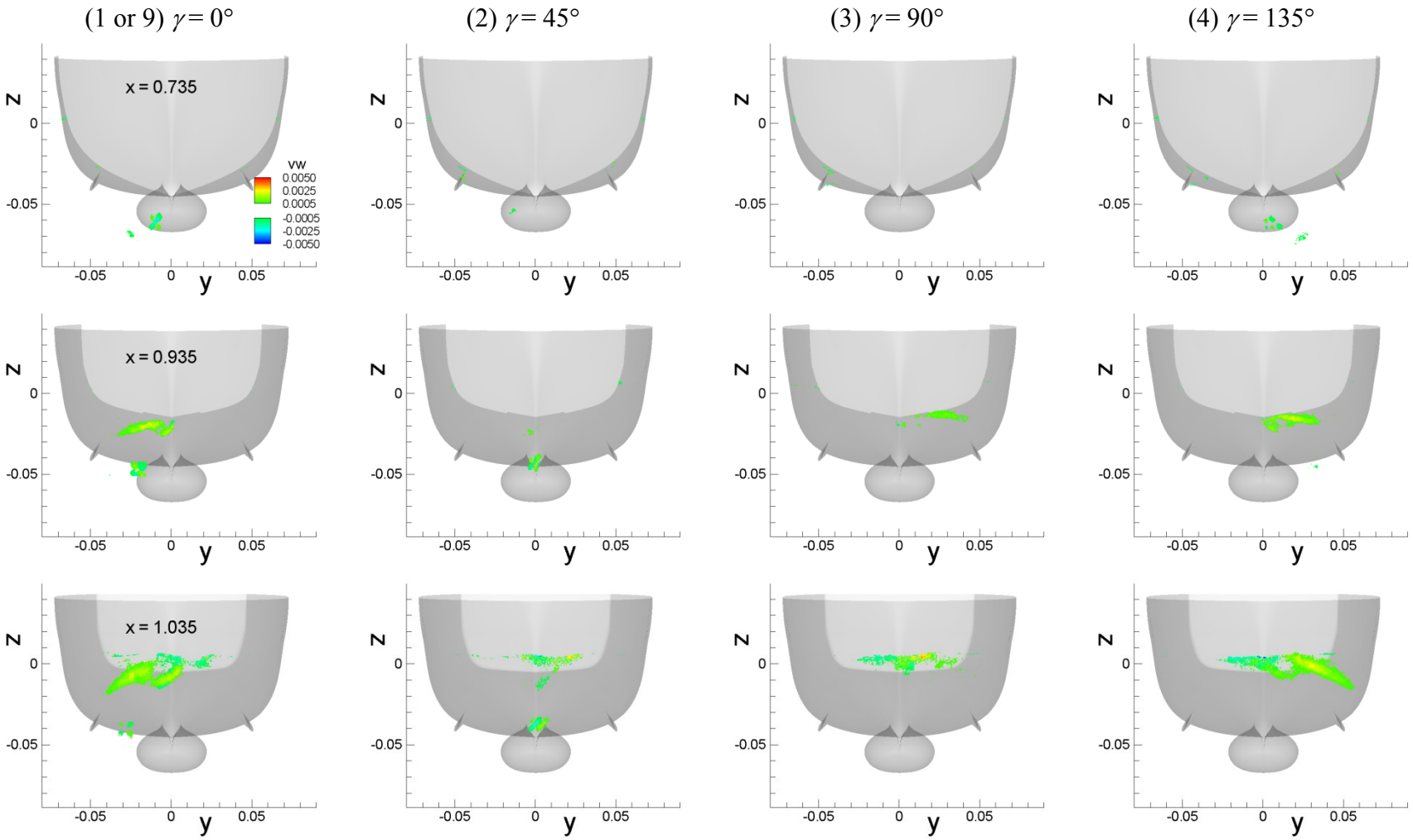

Figure 6-61–Continued

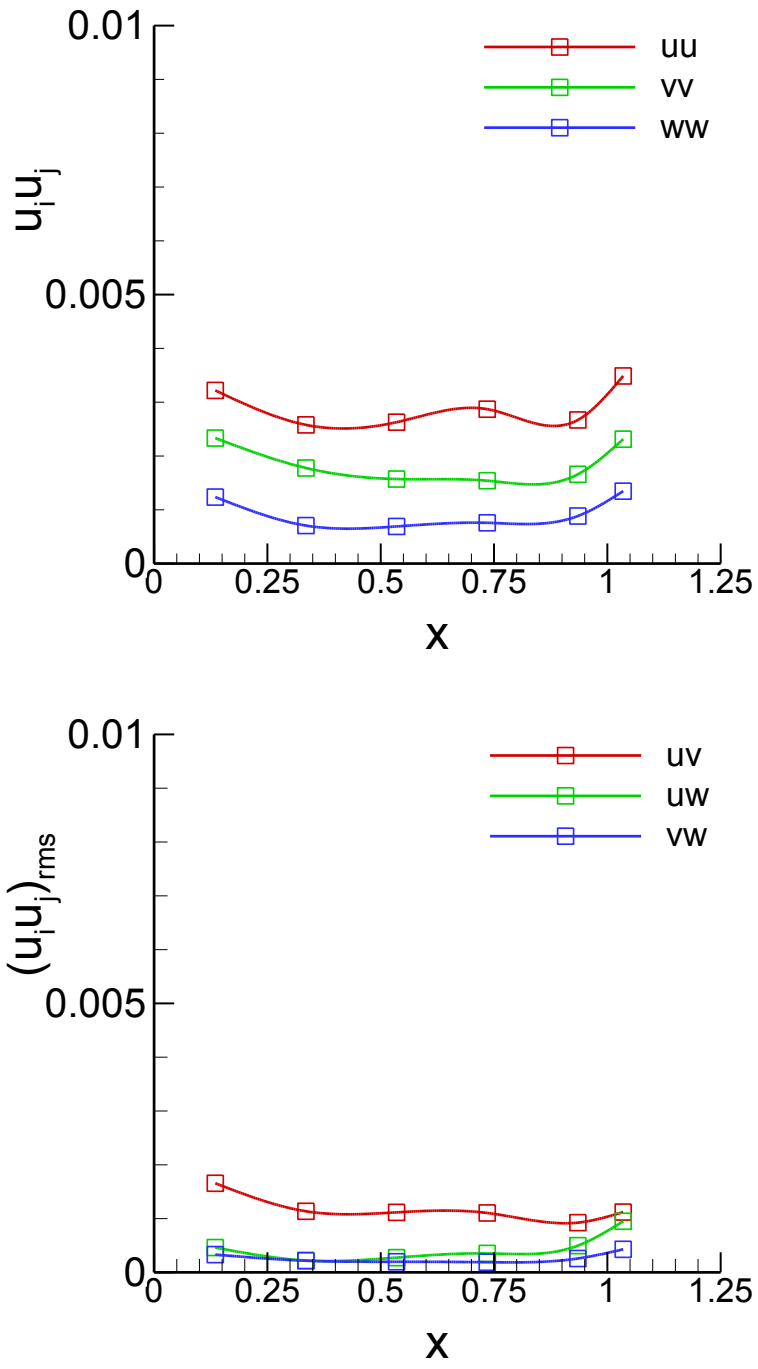

Figure 6-62 Average Reynolds normal (top) and shear (bottom) stresses for k_{mean}.

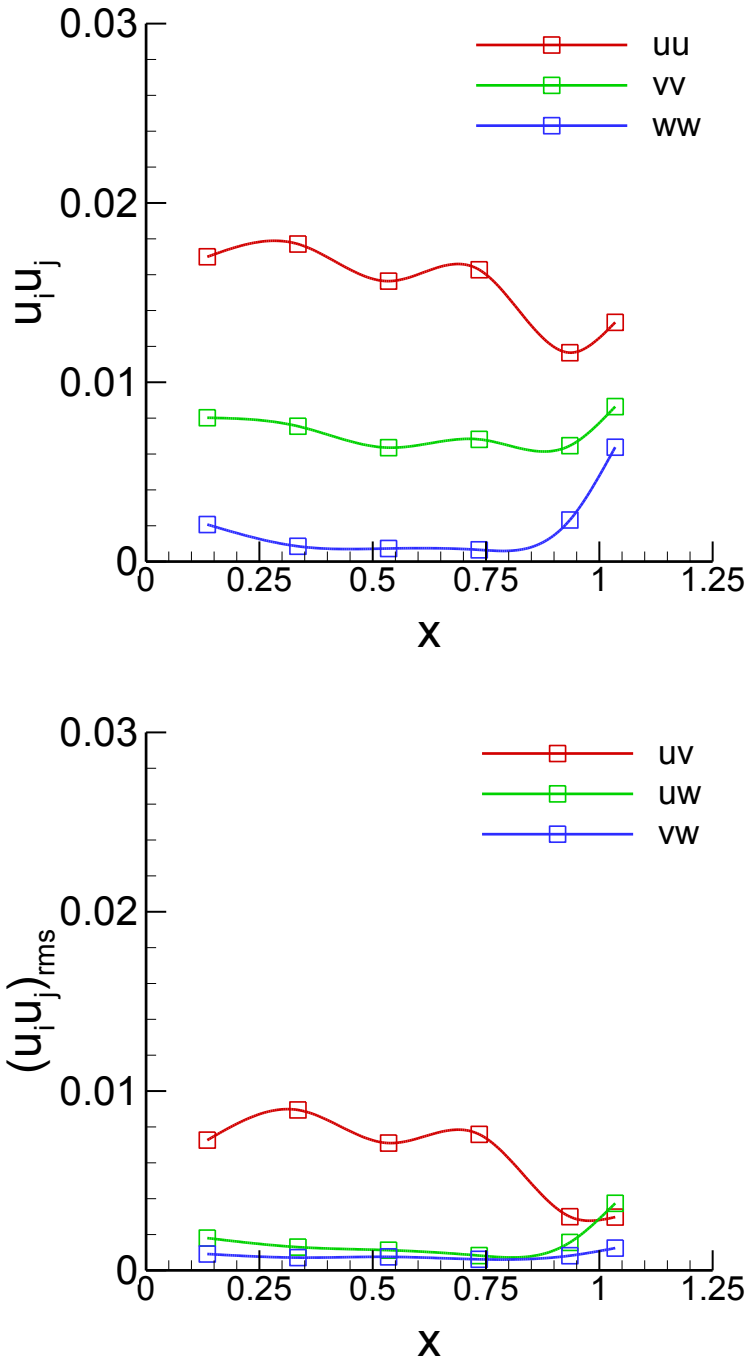

Figure 6-63 Average Reynolds normal (top) and shear (bottom) stresses for k_{max}.

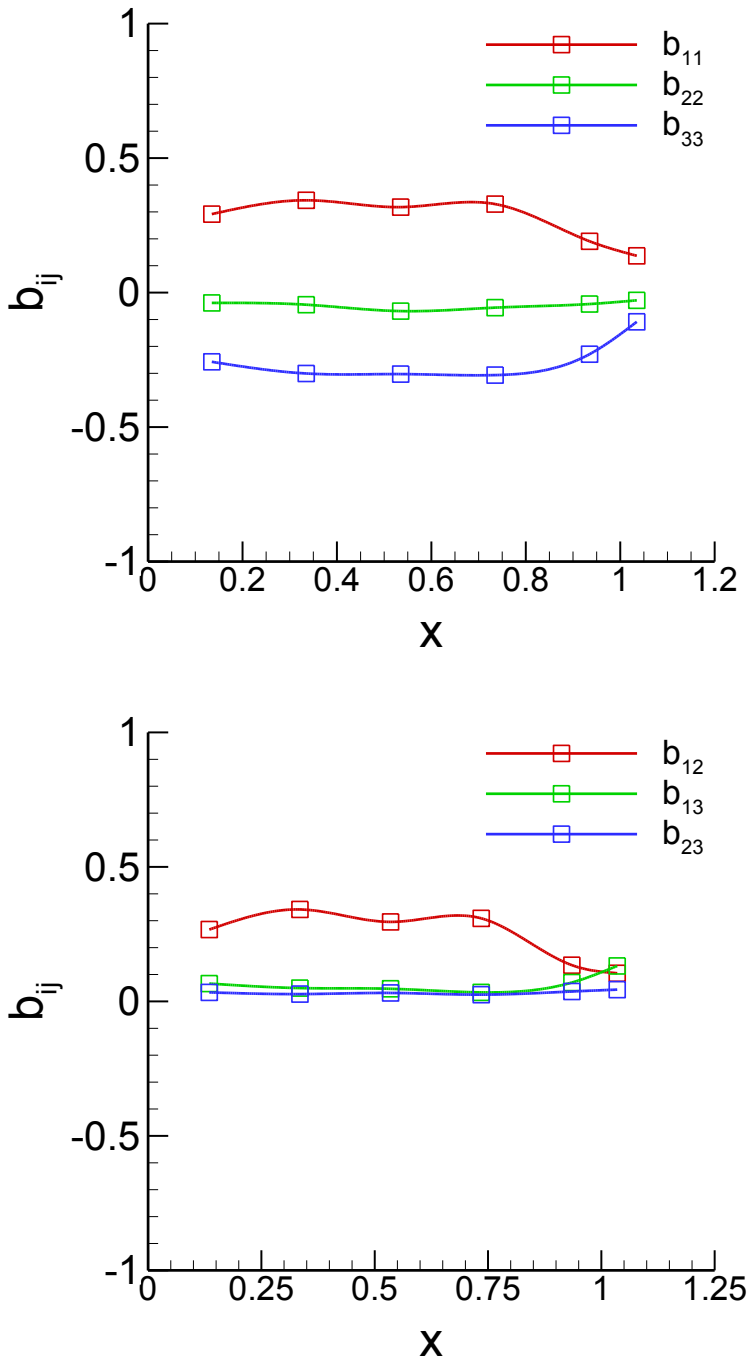

Figure 6-64 Average anisotropy b_{ij} of normal (top) and shear (bottom) Reynolds stresses for k_{max}.

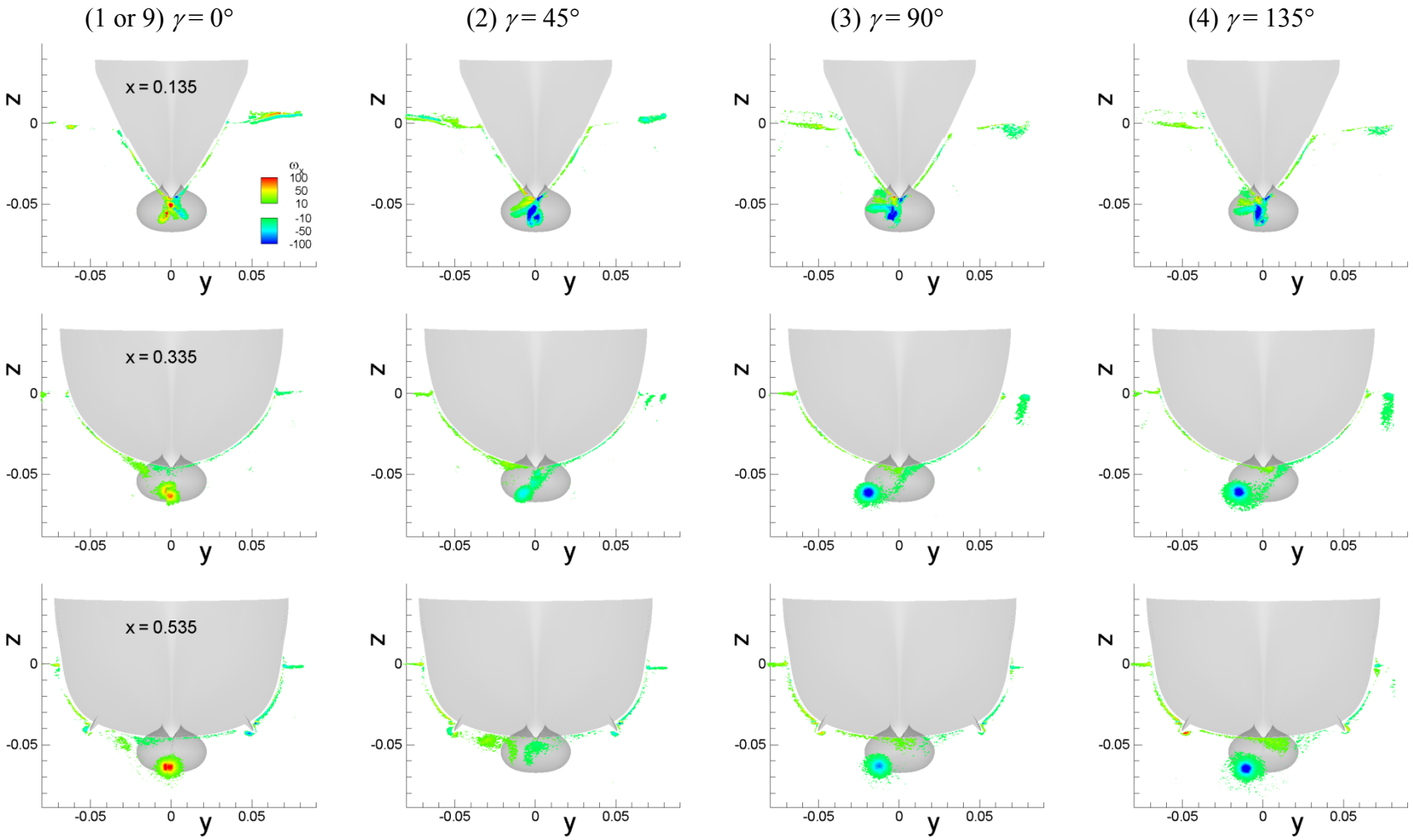

Figure 6-65 Axial vorticity ω_x field for pure yaw test.

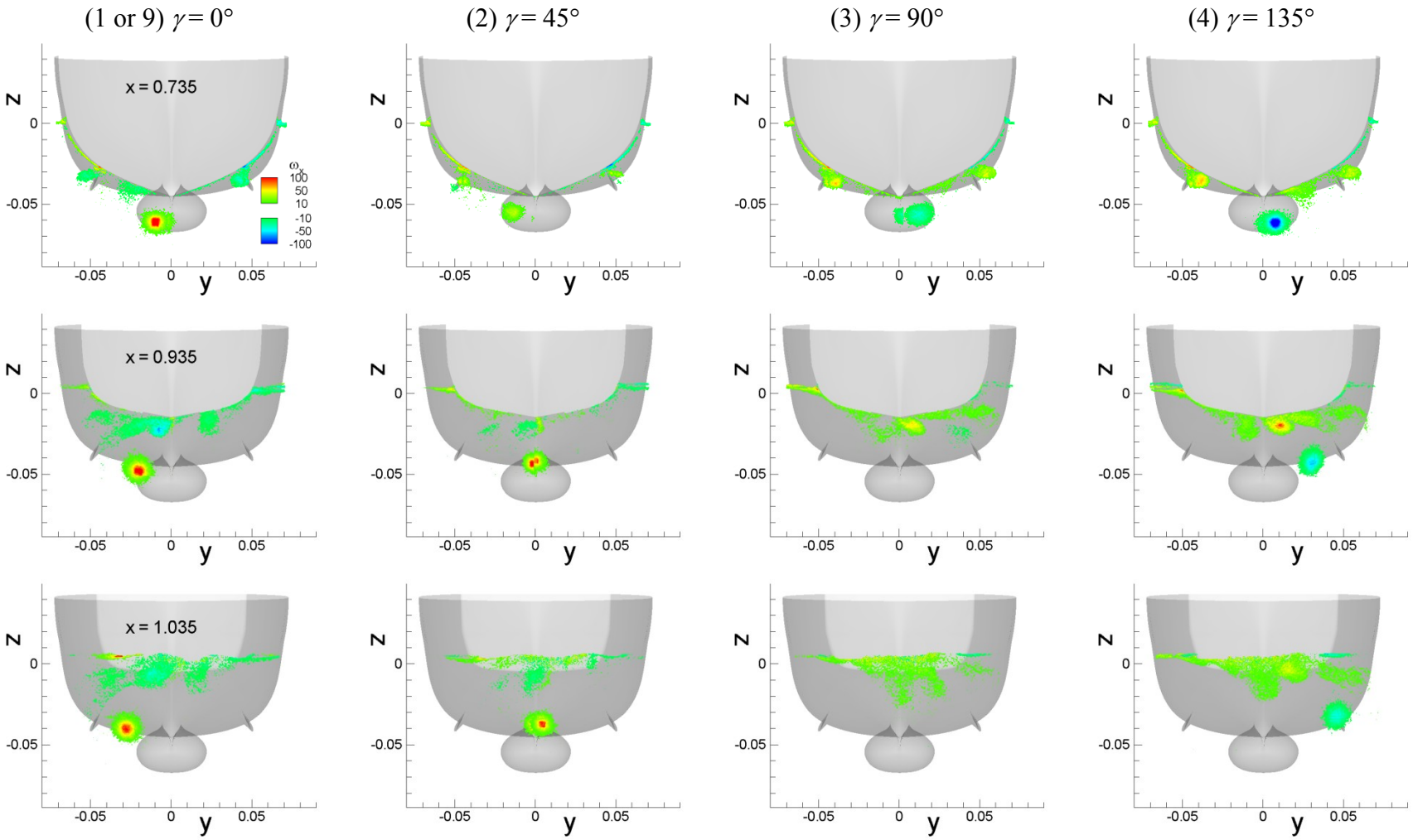

Figure 6-65–Continued

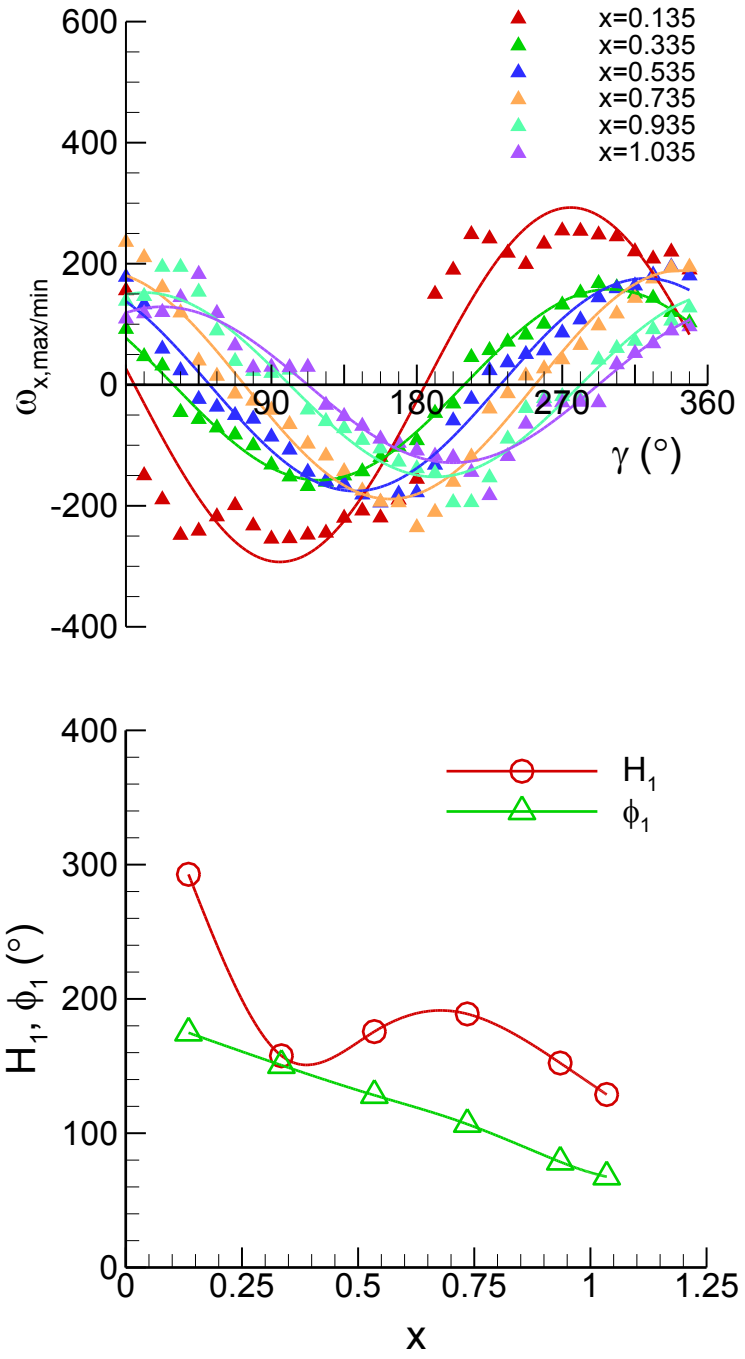

Figure 6-66 Time histories of the maximum/minimum axial vorticity ω_x values of sonar dome (SD) vortex (top) and FS harmonics (bottom) for pure yaw.

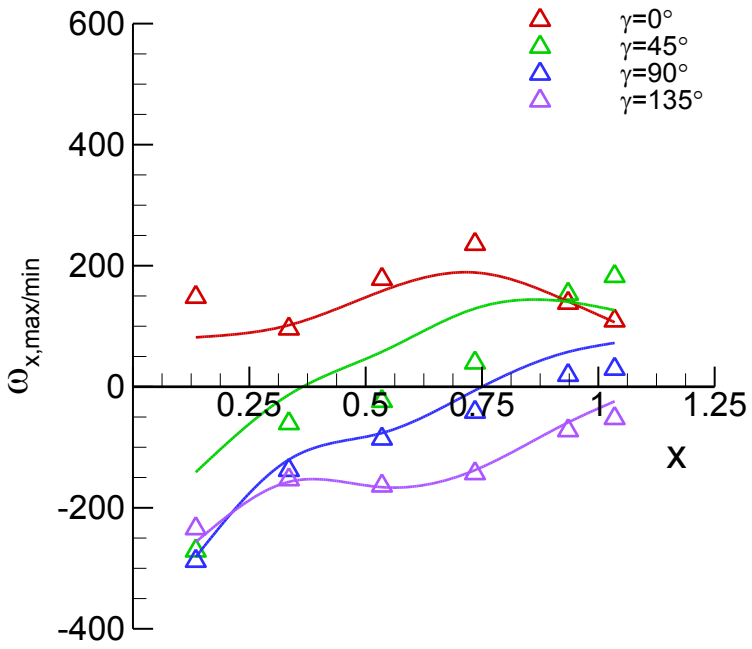

Figure 6-67 Measured (symbols) and reconstructed (lines) $\omega_{x,max/min}$ values of the sonar dome (SD) vortex for pure yaw.

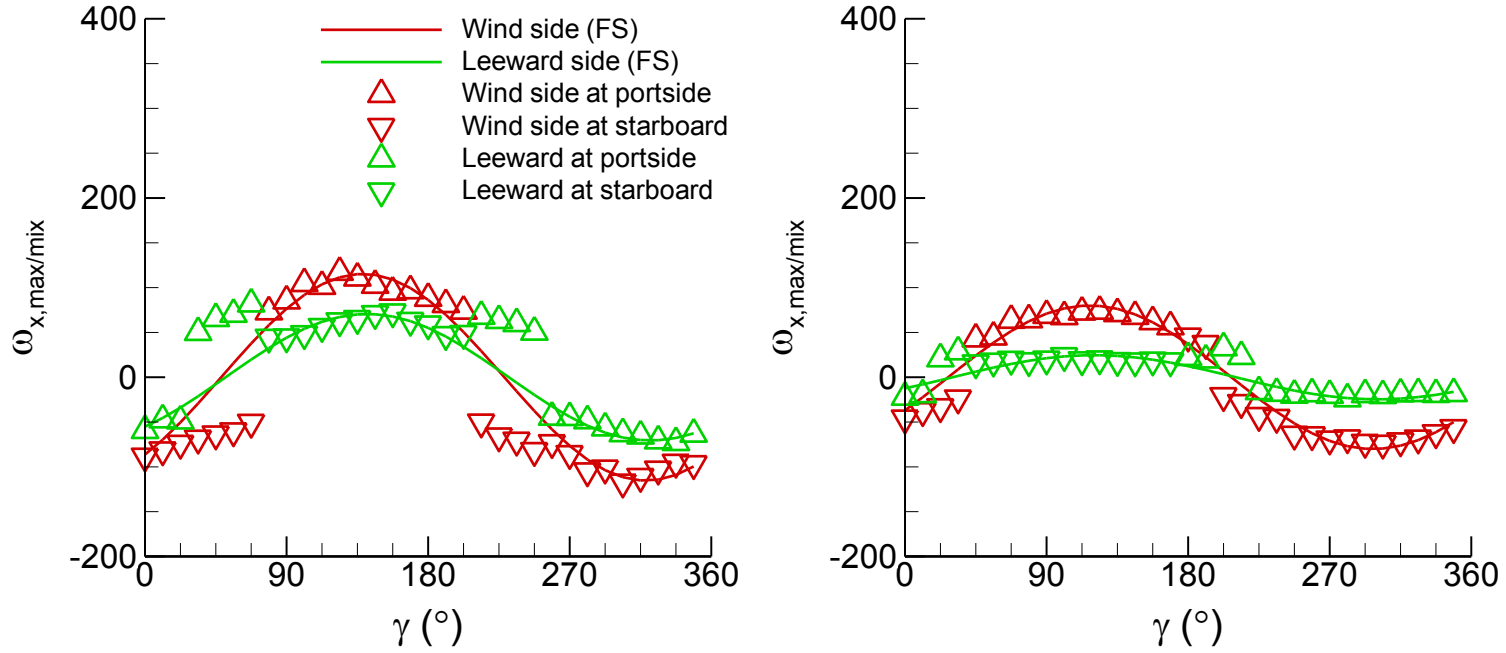

Figure 6-68 Time histories of the maximum/minimum axial vorticity ω_x values of the bilge keel (BK) vortices at x = 0.535 (left) and x = 0.735 (right), respectively, for pure yaw.

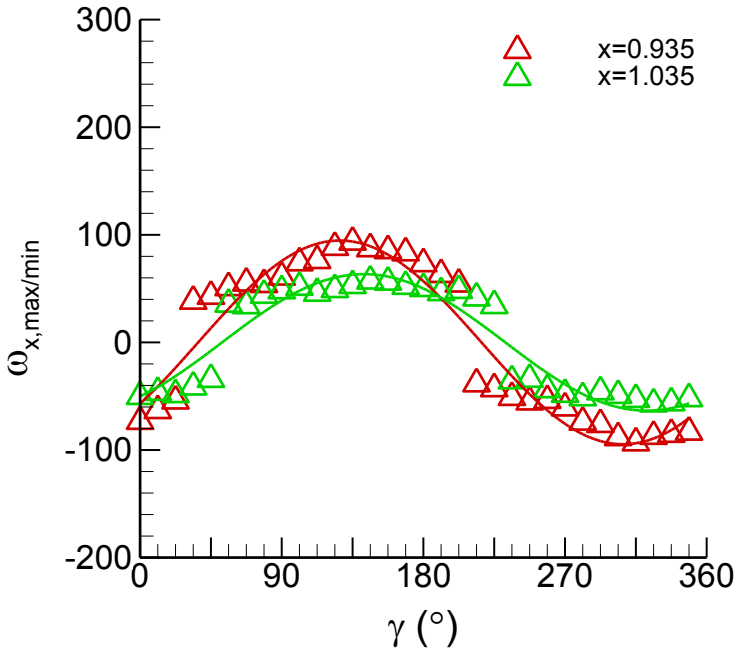

Figure 6-69 Time histories of the maximum/minimum axial vorticity ω_x values of the aft-body keel (AK) vortex for pure yaw test.

CHAPTER 7 SUMMARY AND CONCLUSIONS AND FUTURE WORK

Towing-tank experiments are performed for a surface combatant advancing in calm water as it undergoes static and dynamic planar motion mechanism (PMM) maneuvers. The geometry is DTMB model 5512, which is a 1/46.6 scale geosym of DTMB model 5415 (DDG-51), with L = 3.048 m. The experiments are performed in a 3.048 × 3.048 × 100 m towing tank. The measurement system is a custom-designed towing-tank maneuvering test flow-map measurement system, which features a PMM for captive model testing with an integrated stereoscopic particle image velocimetry (SPIV), a Krypton contactless motion tracker, and a 6-component load cell. The data includes static drift and dynamic maneuvering forces and moments, motions, and phase-averaged local flowfields for dynamic maneuvers. Quality of the data is assessed by evaluating the statistical convergence and by estimating the measurement uncertainty. The forces/moment measurements and UA are conducted in collaboration with Force Technology (FORCE)/Danish Maritime Institute (DMI), Istituto Nazionale per Studi ed Esperienze di Architettura Navale (INSEAN), and the 24th-25th ITTC Maneuvering Committee. The collaboration includes overlapping tests using the same model geometry with different scales, for validation of procedures and identification of facility biases and scale effects.

Statistical convergence of data is evaluated by monitoring the convergence of confidence interval of mean value while increasing the number of data, N. Data are first tested for randomness, stationarity, and normality. For the tests, deterministic components of the data are removed from the data time histories, which are the time-mean values for static drift data and the harmonic oscillations with the PMM frequency as the fundamental harmonic for the dynamic tests. Test for randomness is by inspecting the frequency spectrum of the data via Fast Fourier Transform (FFT). Forces and moment data are random fluctuations, but narrow-banded with peak frequencies near at 3, 4, 5, 7, and 10 Hz, for both static drift and dynamic tests. The peak frequencies are from the natural

frequencies and the mechanical vibrations of the loadcell and the PMM and the deriving carriages, or in combination. Motions (heave and pitch) data are superposition of random fluctuations on a transient oscillation. The transient oscillation is of typical frequency f_{tr} ≈ 0.255 Hz due to start-up transient, which decays with time. Test for stationarity is by using two non-parametric (i.e., distribution-free) statistical procedures, 'Run test' and 'Trend test'. Forces and moment and motions data for the most of cases of static drift and dynamic tests are stationary from the tests at a 5% level of significance (i.e., with a 95% probability). Normality of data is examined by using the Chi-square (X^2) goodness-of-fit test. Test results indicate that all data variables are not normal as those fail the test with typical X^2 values, 61, 72, 120, 122, 146 for F_x, F_y, M_z, z, θ, respectively, at a 5% significance level (the acceptance region is $X^2 \leq 51$ for a degree of freedom $n = 36$). Monitoring the statistical convergence of data is by defining a statistical convergence error, $E_{sc} = c \cdot s/N^{1/2}$, where c is a constant, s is the standard deviation of data, and N is the number of data. For a 95% confidence level, the constant $c = 2.0$ by using the Student-t statistic when data is normal, whereas $c = 4.5$ by using the Tchebycheff inequality when data is not normal with an unknown distribution. For static drift data, $E_{sc} \leq 3\%$ for all the forces and moment and motions data with $N = 2{,}000$, a typical data number, and with $c = 4.5$ by using the Tchebycheff inequality as those data variables are not normal from the normality test. Nonetheless, for forces and moment, the apparent shapes of the probability density function (pdf) are close to a normal pdf, suggesting that those variables data may be close to normal in a practical sense. If normality is assumed for those data, then $E_{sc} \leq 1\%$ with $c = 2.0$ from the Student-t statistic. Evaluations of statistical convergence for dynamic tests data are still on going. On the other hand, for the SPIV flow field data, phase-averaged velocity data are normal (as well in a practical sense). Then, the phase-averaged normal Reynolds stresses (corresponding to the variance of velocity in terms of statistics) follow the χ^2-distribution. Accordingly, the statistical convergence error E is defined for phase-average velocity by using the Student-t statistic and E_U for Reynolds

stress by using the χ^2-statistic, respectively, similarly as E_{sc} for forces and moment and motions data. Even with a relatively smaller number of data for phase-averaging, $N \sim 200$, the statistical convergence error values are fairly small, usually $E \leq 1\%$ of U_C for velocity data and $E_U \leq 10\%$ of the range value of turbulent kinetic energy, $[k]$, for Reynolds stress data.

UA for forces and moment and motions data follows the ASME (1998) and AIAA (1999) Standard and guidelines; errors/uncertainties definitions, systematic/random categorization, and large sample size/normal distribution 95% level of confidence assumptions. The procedures are based on estimates of systematic bias and random precision limits, and their root-sum-square combination to ascertain total uncertainty, U_r. For static drift test, U_r is typically about 2 ~ 4% for forces and moment and about 1 ~ 2% for heave and 20 ~ 30% for pitch motions, respectively. For both forces/moment and motions data, bias limit is predominant over the precision limit, contributing more than 90% to U_r for the most of cases. For dynamic tests, U_r is about 1 ~ 10% for forces and moment, usually larger for X force, and about 2 ~ 6% for heave and 10 ~ 40% for pitch motions. Precision limit is dominant for X force and heave motion, while bias limit is dominant for Y and N and pitch motion, respectively contributing more than 70% to U_r in most of cases. For forces and moment data, compared with two different facilities (FORCE and INSEAN) using different scales (model length L = 4 m and 5.7 m, respectively), the overall U_r values are almost independent of L for static drift test, whereas decreasing with L for dynamic tests. The U_r values as well show a trend with Fr, usually decreasing with Fr. In addition to the aforementioned UA procedures, two conceptual biases, data asymmetry bias B_{asym} and facility bias B_{FB}, are defined and evaluated. B_{asym} is to account for data asymmetry that exceeds U_r estimations. B_{asym} is typically large for X force and heave and pitch motions, in general about 7%, 20%, 40%, respectively. B_{asym} for X is negligible for FORCE data and about 8% for INSEAN data. However, B_{asym} for Y and N are typically small or negligible for all the facilities data. B_{FB} is to account for the use of different test

facilities and different measurement equipments between the facilities. For static drift, IIHR and INSEAN data are certified within a certificate interval U_D about 3 ~ 11%, whereas INSEAN data include B_{FB} about 3 ~ 4%. For dynamic test data, most of IIHR data are certified but with relatively large U_D about 3 ~ 30%, whereas FORCE and INSEAN data for several cases are uncertified with B_{FB} about 2 ~ 7%.

On the other hand, the UA for phase-average SPIV flow field data follows the ASME PTC 19.1-2005 Standard (ASME 2005) that is a revision of the ASME (1998) Standard. The procedures are estimations of the systematic and random standard uncertainties at the standard deviation level, and their root-mean-square combination to ascertain the combined standard uncertainty and subsequently the expanded uncertainty $U_{R,95}$. The systematic standard uncertainty is estimated by calibrating the SPIV to the 'open-water' test results. The open-water test is to measure the free-stream flow field without the model installed, while the SPIV is towed straight (for uniform flow test) or in pure yaw motion (for open water pure yaw test). The random standard uncertainty is estimated end-to-end by repeating the test (the actual test with model installed). From the UA, the absolute uncertainty ($U_{R,95}$) of the SPIV measurement is about 2 ~ 3% of U_C for U (out of plane component), and about 1 ~ 2% of U_C for V and W (in-plane components), respectively. Whereas the relative uncertainty ($U_{R,95}/R$) is about 3 ~ 4%, 12 ~ 29%, and 26 ~ 32% for U, V, and W, respectively. For Reynolds stresses, the square root of absolute uncertainties, $U_{R95}^{1/2}$, are about 2 ~ 3% of U_C for the normal (uu, vv, ww) stresses and about 1 ~ 2% of U_C for the shear (uv, uw, vw) stresses, respectively. The relative uncertainties are about 25 ~ 50% inside the boundary layer region, whereas typically large > 100% at the outer region due to the small magnitude of the R. The present UA results are generally similar with Gui et al. (2001a) for steady test and relatively larger than Longo et al. (2007) for unsteady tests.

Forces and moment data trends with the drift angle β for static drift test are as per predicted by the Abkowitz (1966) mathematic model; quadratic for X and cubic for Y and

N. Time histories of forces and moment data for dynamic pure sway and pure yaw tests are typically the 2nd-order dominant (about 70% of amplitude) oscillations for *X* with superposed on mean values, whereas the 1st-order dominant (90 ~ 99% of amplitude) oscillations for *Y* and *N* with phase shifted with respect to the forced motions. For yaw and drift tests, all of the *X*, *Y* and *N* time histories are the 1st-order dominant oscillations with superposed on non-zero mean values. Hydrodynamic derivatives are evaluated from the forces and moment data by using two different methods; '*Multiple-Run* (MR)' method and '*Single-Run* (SR)' method. The MR method is by curve fitting the forces and moment data obtained from a series of tests over a range of PMM parameter of interest. In contrast, the SR method is using the data from a single realization of dynamic test. Linear derivative values by using the MR and the SR methods are similar each other, with a ratio value, SR/MR = 0.5 ~ 1.5 in general. The ratio value approaches closer to a unity as the PMM motion becomes larger. In contrast, non-linear hydrodynamic derivatives values using the SR method are considerably different from those using the MR method, with the ratio SR/MR = 10^{-1} ~ 10^{2}. The ratio value is particularly larger/smaller when the PMM motion is small. Validities of the hydrodynamic derivatives are examined by evaluating the error, E_R (%), in reconstructing the forces and moment time history by substituting the derivative values back into the Abkowitz (1964) mathematic model. For MR method, the error value is in general E_R (%) < 20 over the whole range of the tested PMM parameters. However, for SR method, the error value is typically huge, E_R (%) < 600, when the PMM motion is small and relatively large, E_R (%) < 50, as the PMM motion becomes larger. Consequently, the MR method is more rigorous than the SR method, and the SR method is only suggested when the PMM motion is large enough. From the speed variation test, the hydrodynamic derivative values exhibit trends with *Fr*. Typically the linear derivatives are nearly independent of *Fr*, whereas the non-linear derivatives exhibit rather strong dependency on *Fr*. Hydrodynamic derivative values as well exhibit a trend with the model size (scale). When compared with the two different facilities

(FORCE and INSEAN) data, generally the sway derivatives are nearly independent of model size whereas the yaw derivatives (particularly yaw acceleration derivatives) exhibit considerable dependency on the model size. However, for the non-linear derivatives, general conclusions are precluded as the data exhibit large scatters in the comparisons.

Motions data trends with drift angle β for static drift test and the trends of the time histories for dynamic tests resemble those of the forces and moment data; the overall trends of heave and pitch motions are similar to X (quadratic with β and the 2nd-order dominant oscillations) and those of roll motion is similar to Y and N (cubic with β and the 1st-order dominant oscillations). Between the motions, heave and roll motions are nearly independent, whereas pitch and roll motions are rather strongly coupled each other. Motions data as well exhibit correlations with forces and moment. Four different mount conditions are compared to see the effect of motions on the forces and moment; FX_0 (fixed at evenkeel), $FX_{\sigma\tau}$ (fixed sunk and trim), $FR_{z\theta}$ (free to heave and pitch), and $FR_{z\theta\phi}$ (free to heave, pitch, and roll). Between FX_0 and $FX_{\sigma\tau}$, forces and moment usually increase up to about 10% ($\xi_{\sigma\tau} = 1 \sim 1.1$) due to the effect of sinkage and trim. Between FX_0 and the $FR_{z\theta}$, the increase in forces and moment is typically 10% ~ 30% ($\xi_{z\theta} = 1.1 \sim 1.3$) due to the effect of heave and pitch motions. Between $FR_{z\theta}$ and $FR_{z\theta\phi}$, forces and moment are similar each other ($\zeta_\phi \approx 1$) indicating the effect of roll motion on the forces and moment is small or negligible. Despite the differences in forces and moment, the linear hydrodynamic derivatives from the FX_0 and $FX_{\sigma\tau}$ conditions are usually similar with those of the $FR_{z\theta}$ condition ($\zeta_{0,\sigma\tau} = 0.9 \sim 1.1$), whereas the non-linear derivatives for the former conditions are smaller than for the later condition ($\zeta_{0,\sigma\tau} = 0.2 \sim 1.0$). Between the $FR_{z\theta}$ and $FR_{z\theta\phi}$ conditions, in general linear derivatives are similar ($\zeta_\phi = 0.9 \sim 1.1$) between the mount conditions, whereas the non-linear derivatives values show rather large differences ($\zeta_\phi = -0.4 \sim 3.6$). Consequently, the effects of the motions on hydrodynamic derivatives are small for linear derivatives, however may large for non-linear derivatives.

Phase-averaged flow field measurement results indicate maneuvering-induced vortices and their interactions with the turbulent boundary layers. The data comprises axial velocity contours, cross-flow velocity vectors and streamlines, turbulent kinetic energy and Reynolds stresses contours, and axial vorticity contours, respectively for pure sway and pure yaw tests. The vortical flow structure includes sonar dome vortex, bilge keel vortices, fore and aft body keel vortices, and free surface vortices, which can be more clearly identified from the complementary CFD simulation results. The average axial velocity within the boundary layers and inside vortices is about 0.8 U_C, nearly constant along the model length. Local minimum value is 0.65 ~ 0.4 U_C, larger at the bow and decreases monotonically along the model length. Turbulent kinetic energy $k^{1/2}$ is about 5% of U_C for pure sway and about 7% of U_C for pure yaw, respectively, in average. The local maximum $k^{1/2}$ value is about 11% of U_C for both tests. Reynolds stress is anisotropic, where uu and uv are the largest normal and shear stresses, respectively. Sonar dome vortex is the strongest one, and bilge keel and aft body keel vortices are the second and third ones. The maximum axial vorticity value of the sonar dome vortex is similar for both pure sway and pure yaw tests, whereas the bilge keel and the aft body keel vortices are about 2 ~ 3 times stronger for pure sway.

Limitations of the present work include: 1) the model is un-appended except for portside and starboard bilge keels, and not equipped with shafts, struts, propellers, or rudders. Accordingly the hydrodynamic derivatives values evaluated from the forces and moment data and the vortical flow field data (particularly at the stern where the rudders and propellers are working) may differ from those from a fully appended condition, 2) the model is constrained in heave, pitch, and roll motions for the SPIV measurements, thus the flow field data may differ from the free motions condition, 3) the number of longitudinal locations for SPIV measurements is limited (six x-locations) and the flow field data in the direction are sparse and not sufficient to be connected to show the fully three dimensional flow structures. The near future works planed, in conjunction with and to

resolve those limitations, include a PMM test in headwind and/or wave for a fully appended (except for propellers) model (ONR Tumblehome), a fully three-dimensional PIV (e.g., a tomographic PIV) flow field measurement for the DTMB 5512 model in a static drift maneuver with a large drift angle $\beta = 20°$, and a fully 3-D (or Stereoscopic) PIV flow field measurement for a free running model.

REFERENCES

Abkowitz, M.A., 1964, "Lectures on ship hydrodynamics – Steering and maneuvering", Hydro- and Aerodynamics Laboratory Report Hy-5, Lyngby, Denmark.

AGARD AR-304, 1994, "Quality Assessment for Wind Tunnel Testing", Advisory Group for Aerospace Research and Development, North Atlantic Treaty Organization, Neuilly-sur-Seine, France.

AIAA S-071A-1999, "Assessment of Experimental Uncertainty with Application to Wind Tunnel Testing," American Institute of Aeronautics and Astronautics, Reston, Virginia, USA.

Artyszuk, J., 2003, "A look into motion equations of the ESSO OSAKA manoeuvring," International Shipbuilding Progress, Vol. 50, No. 4, pp. 297-315.

ASME PTC 19.1-1998, "Test Uncertainty," American Society of Mechanical Engineers, New York.

ASME PTC 19.1-2005, "Test Uncertainty," American Society of Mechanical Engineers, New York.

Atsavapranee P., Forlini T., Furey D., Hamilton, J., Percival, S., and Sung, C.-H., 2004, "Experimental Measurements for CFD Validation of the Flow about a Submarine Model (ONR Body-1)," 25th ONR Symposium on Naval Hydrodynamics, St John's, Canada.

Bendat, J. S., and Piersol, A. G., 1966, *Measurement and Analysis of Random Data*, John Wiley and Sons, Inc., New York, USA.

Benedetti, L., Bouscasse, B., Broglia, R., Fabbri, L., La Gala, F., and Lugni, C. 2006 "PMM Model Test with DDG51 Including Uncertainty Assessment," INSEAN Report No. 14, 174 pp.

Bhushan, S., Xing, T., Carrica, P., and Stern, F., 2007, "Model- and Full-scale URANS/DES Simulations for Athena R/V Resistance, Powering, and Motionos," 9th Numerical Ship Hydrodynamics Conference, Vol. II, pp. 122-142.

Bishop, R., Atsavapranee, P., Percival, S., Shan, J., and Engle, A., "An Investigation of Viscous Roll Damping Through the Application of Particle-Image Velocimetry," Proceedings 25th ONR Symposium on Naval Hydrodynamics, St. John' s, Newfoundland, Canada, 2004.

Bishop, R. E. D. & Parkinson, A. G., 1970, "On the planar motion mechanism used in ship model testing." Philosophical Transactions for Royal Society of London, Series A, Mathematical and Physical Sciences, Vol. 266, 35-61.

Bishop, R. E. D., Burcher, R. K. & Price, W. G., 1972, "The uses of functional analysis in ship dynamics," Proceedings of the Royal Society of London, Series A, Mathematical and Physical Sciences, Vol. 332, 23-35.

Bishop, R. E. D., Burcher, R. K., & Price, W. G., 1973, "Application of Functional Analysis to Oscillatory Ship Model Testing," Proceedings of the Royal Society of London, Series A, Mathematical and Physical Sciences, Vol. 332, 37-49.

Brard, R., 1948, "Introduction à l`etude théorique du tangate en marche", Bulletin de l`ATMA, No. 47, p. 455-479

Broglia, R., Muscari, R., and Di Mascio, A., 2006, "Numerical analysis of blockage effects in PMM tests," 26th ONR Symposium on Naval Hydrodynamics, Rome.

Burcher, R. K., 1975, "Studies into the Validity of Quasi Steady Prediction Techniques," Proceedings, Vol. 2, International Towing Tank Conference, pp. 404-407.

Burg, C.O.E. and Marcum, D.L., 2003, "Moving towards high fidelity RANS calculations of maneuvering surface vessels using unstructured grids", 8th International Conference on Numerical Ship Hydrodynamics, Busan, Korea.

Calcagno, G., Di Felice, F. D., and Pereira, F., 2002, "Propeller Wake Analysis Behind a Ship by Stereo PIV," in Proceedings of the 24th ONR Symposium on Naval Hydrodynamics, Fukuoka, Japan, pp. 112-127.

Carrica, P. M., Wilson, R. V., Noack, R., Xing, T., Kandasamy, M., Shao, J., Sakamoto, N., Stern, F., 2006, "A dynamic overset, single phase level set approach for viscous ship flows and large amplitude motions and maneuvering," 26th ONR Symposium on Naval Hydrodynamics, Rome, Vol. 1, pp. 97 – 116.

Carrica, P. M., and Stern, F., 2008, "DES simulations of KVLCC1 in turn and zigzag manoeuvring with moving propeller and rudder," SIMMAN 2008, Copenhagen.

Clarke, D., Gedling, P. and Hine, G.., 1983, "The Application of Manoeuvring Criteria in Hull Design Using Linear Theory", Transactions of RINA, pp 45-68.

Coleman, H. W., and Steel, G. W., 1999, *Experimentation and Uncertainty Analysis for Engineeers*, 2nd ed., Wiley, 275 pp.

Controni, A., Di Felice, F., F., Romano, G. P., and Elefante, M., 2000, "Investigation of the Near Wake of a Propeller Using Particle Image Velocimetry," Exp. Fluids, 29, pp. S227-S236.

Coudert, S., and Schon, J. P., 2001, "Back-projection algorithm with misalignment corrections for 2D3C stereoscopic PIV," Meas. Sci. Techno. 12:1371-1381.

Cura Hochbaum, A., and Vogt, M., 2003, "On the Prediction of Hydrodynamic Forces on a Manoeuvring Ship", International Conference on Marine Simulation and Ship Maneuverability (MARSIM 2003), Kanazawa, Japan.

Cura Hochbaum, A., 2006, "Virtual PMM Tests for Manoeuvring Prediction," 26th ONR Symposium on Naval Hydrodynamics, Rome, Italy.

Depascale, R., Elefante, M. Sebastiani, L., Soave, M. and Viviani, M., 2002, "Identification of hydrodynamic coefficient from standard manoeuvres," Proc. of HIPER '02, pp. 14-17.

Di Felice, F., and De Gregorio, F., 2000, "Ship Model Wake Analysis by Means of PIV in Large Circulating Water Channel," in Proceeding of the 10th International Offshore and Polar Engineering Conference, Seattle, WA, pp. 392-397.

Di Felice, F., Romano, G., and Elefante, M., 2000, "Propeller Wake Analysis by Means of PIV," in Proceedings of the 23rd ONR Symposium on Naval Hydrodynamics, Val de Reuil, France, pp. 493-510.

Di Mascio, A. and Broglia, R., 2003, "Unsteady RANS calculations of the flow around a moving ship hull", 8th International Conference on Numerical Ship Hydrodynamics, Busan, Korea.

Di Mascio, A., Broglia, R., Muscari, R., and Dattola, R., 2004, "Unsteady RANS simulations of a manoeuvering ship hull", 25th ONR Symposium on Naval Hydrodynamics, St. John's, Canada.

Di Mascio, A., Broglia, R., and Muscari, R., 2007, "Numerical Simulations of Viscous Flow Around a Fully Appended Hull with Enforced Motion," 9th Numerical Ship Hydrodynamics Conference, Vol. I, pp. 191-207.

Dong, R. R., Katz, J., and Huang, T. T., 1997, "On the Structure of Bow Waves on a Ship Model," J. Phy. (Paris), Colloq., 346, pp. 77-115.

El Moctar, O.M., 2001, "Numerical computations of flow forces in ship manoeuvring", Ship Technology Research, Vol. 48, N. 3, pp. 98-123.

Feller, W., 1968, "The Strong Law of Large Numbers," §10.7 in *An Introduction to Probability Theory and Its Apllications*, Vol. 1, 3rd ed., New York: Wiley, pp. 243-245, 1968.

Felli, M., Di Felice, F., and Lugni, C., "Experimental Study of the Flow Field Around a Rolling Ship Model," Proceedings 25th ONR Symposium on Naval Hydrodynamics, St. John's, Newfoundland, Canada, 2004.

Fossen, T. I., 1994, *Guidance and Control of Ocean Vehicles*, John Wiley & Sons Ltd., England, pp. 30.

Fu, T. C., Atsavapranee, P., and Hess, D. E., 2002, "PIV Measurements of the Cross-Flow Wake of a Turning Submarine Model (ONR Body-1)," in Proceeding of the 25th ONR Symposium on Naval Hydrodynamics, Fukuoka, Japan, pp. 154-166.

Gertler, M., 1966, "Cooperative Rotating-arm and Straight line Experiments with ITTC Standard model (Mariner type Ship)", David Taylor Model Basin, Report 2221, June.

Gui., L., Longo, J., and Stern, F., 2001a, "Towing Tank PIV Measurement System, Data and Uncertainty Assessment for DTMB Model 5512," Exp. Fluids, 31, pp. 336-346.

Gui, L., Longo, J., Metcalf, B., Shao, J., and Stern, F., 2001, "Forces, Moment, and Wave Pattern for Surface Combatant in Regular Head Waves-Part 1: Measurement Systems and Uncertainty Assessment," Exp. Fluids, 31, pp. 674-680

Gui., L., Longo, J., Metcalf, B., Shao, J., and Stern, F., 2002, "Forces, Moment, and Wave Pattern for Naval Combatant in Regular Head waves-Part 2: Measurement Results and Discussions," Experiments in Fluids, Vol. 32, pp. 27-36.

Hess, D., and Faller, W., 2000, "Simulation of ship manoeuvres using recursive neural networks," Proc. of 23rd Symposium on Naval Hydrodynamics, pp. 17-22.

Hess, D., Faller, W., and Lee, J., 2008, "Realtime nonlinear simulation of manoeuvres for US Navy Combatant DTMB 5415," SIMMAN 2008, Copenhagen.

Hino, T., Editor, 2005, "CFD Workshop TOKYO 2005 Workshop on Numerical Ship Hydrodynamics," National Maritime Research Institute, Tokyo, Japan.

Hooft, J.P., 1994, "The cross-flow drag on a manoeuvring ship', Ocean Eng. 21, pp. 329 - 342.

Hunt J., A. Wray, and P. Moin, 1988: Eddies, stream, and convergence zones in turbulent flows. *Proc. CTR Summer Program*, Stanford, CA, Center for Turbulence Research, 193–208.

Inoue, S, Hirano, M. and Kijima, K., 1981, "Hydrodynamic Derivatives on Ship Manoeu-vring", International Shipbuilding Progress, Vol. 28, No.321, pp 112-125.

Irvine, M., Longo, J., and Stern, F., "Towing-Tank Tests for Surface Combatant for Free Roll Decay and Coupled Pitch and Heave Motions," Proceedings 25th ONR Symposium on Naval Hydrodynamics, St. John's, Newfoundland, Canada, 2004.

Irvine, M., Longo, J., and Stern, F., 2008, "Pitch and Heave Tests and Uncertainty Assessment for a Surface Combatant in Regular Head Waves," Journal of Ship Research, Vol. 52, No. 2, pp. 146-163.

ISO, 1995, "Guide to the Expression of Uncertainty in Measurement," International Organization for Standardization, Genève, Switzerland.

ITTC. 1999, *Proceedings*, 22nd International Towing Tank Conference, Seoul, Korea/Beijing, China.

ITTC. 2002, *Proceedings*, 23rd International Towing Tank Conference, Venice, Italy.

ITTC, 2005, *Proceedings*, 24th International Towing Tank Conference, Edinburgh, Scotland.

ITTC, 2008, *Proceedings*, 25th International Towing Tank Conference, Fukuoka, Janpan.

ITTC, 2008, "Captive Model Test Procedure," ITTC Recommended Procedures and Guidelines 7.5-02-06-02.

Jensen, G., Klemt, M. and Xing-Kaeding, Y., 2004, "On the way to the numerical basin for seakeeping and manoeuvring", 9th Symposium on practical design of ship and other floating structures, Luebeck Travemuende, Germany.

Judge, C. Q., Oweis, G. F., Ceccio, S. L., Jessup, S. D., Chesnakas, C. J., and Fry, D. J., 2001, "PIV Measurements of a Tip Leakage Vortex," Proceedings of the 26th American Towing Tank Conference, Glen Cove, New York.

Kijima, K. and Nakiri, Y., 2003, "On the Practical Predic-tion Method for Ship Manoeuvring Characteristics", Proceedings of MARSIM'03, pp RC-6, or Trans West Japan Soc Naval Arch, 105, pp 21-31.

Kijima, K., Nakiri,Y., Tsusui, Y., and Matsunaga, M., 1990, “Prediction Method of Ship Manoeuvrability in Deep and Shallow Waters”, MARSIM & ICSM_, Tokyo, Japan.

Kijima, K., Tanaka, S. Furukawa, Y. and Hori, T., 1993, “On a Prediction Method of Ship Manoeuvring Characteristics”, Proceedings of MARSIM-93, Vol. 1, pp 285-294.

Kim, S.E. and Rhee, S.H., 2002, “High-Incidence and Dynamic Pitch-Up Maneuvering Characteristics of a Prolate Spheroid - CFD Validation”, 24th ONR Symposium on Naval Hydrodynamics, Fukuoka, Japan.

Kim, W. J., Van, S. H., and Kim, D.-H., 2001, “Measurement of Flows Around Commercial Ship Models,” Exp. Fluids, 31(5), pp. 567-578.

Kim, S.Y. et al., 2003, “Manoeuvring characteristics of a large container ship”, Proceedings of MARSIM’03, pp RC-8.

Larsson, L., Stern, F., and Bertram, V., 2003, “Benchmarking of Computational Fluid Dynamics for Ship Flows: The Gothenburg 2000 Workshop,” J. Ship Res., 47(1), pp. 63-81.

Lee, S.-J., Kim, H.-R., Kim, W.-J., and Van, S.-H., 2003, “Wind Tunnel Tests on Flow Characteristics of the KRISO 3,600 TEU Container Ship and 300K VLCC Double-Deck Ship Models,” J. Ship Res., 47(1), pp. 24-38.

Lee, S. j., Paik, B. G., Yoon, J. H., and Lee, C. M., 2004, “Three-Component Velocity Field Measurements of Propeller Wake Using a Stereoscopic PIV Technique,” Exp. Fluids, 27, pp. 575-585.

Lee, T. et al., 2003, “On an Empirical Prediction of Hydrodynamic coefficients for modern ship hulls”, Proceedings of MARSIM’03, pp RC-1.

Leeuwen, G. van, 1964, “The lateral damping and added mass of an oscillating ship-model,” Shipbuilding Laboratory, Technological University Delft, Publication No. 23.

Leeuwen, G. van, 1969, “Some problems concerning the design of a horizontal oscillator,” (in Dutch), Shipbuilding Laboratory, Technological University Delft, Report No. 225.

Longo, J. and Stern, F., 2002, “Effects of Drift Angle on Model-Scale Ship Flow,” Experiments in Fluids, Vol. 32, pp. 558-569.

Longo, J., Gui, L., and Stern, F., 2004, “Ship Velocity Fields,” *PIV and Water Waves, Advances in Coastal and Ocean Engineering*, World Scientific, Singapore.

Longo, J. and Stern, F., 2005, “Uncertainty Assessment for Towing Tank Tests With Example for Surface Combatant DTMB Model 5415,” J. of Ship Research, Vol. 49, No. 01, pp. 55-68.

Longo, J., Shao, J., Irvine, M., and Stern, F., 2007, “Phase-averaged PIV for the Nominal Wake of a Surface Ship in Regular Head Waves,” ASME J. Fluids Eng. Vol. 129, pp. 524-540.

Martinussen, K., and Linnerud, I., 1987, "Techniques for Predicting Maneuvering Characteristics of Ships at the Design Statge," Ship Maneuverability Prediction and Archievement, RINA, London.

Martinussen, K., and Ringen, E., 2008, "Simulation of KVLCC1 and KVLCC2 manoeuvring motion," SIMMAN 2008, Copenhagen.

Milanov, E., 1984, "On the use of quasisteady PMM-test results," International Symposium on Ship Techniques, Rostock, Germany.

Moffat, R. J., 1982, "Contributions to the Theory of Single-Sample Uncertainty Analysis," ASME Journal of Fluids Engineering, Vol. 104, No. 2, pp. 250-260.

Moffat, R. J., 1985, "Using Uncertainty Analysis in Planning an Experiment," Journal of Fluids Engineering, Vol. 107, No. 2, pp. 173-178.

Moffat, R. J., 1988, "Describing the Uncertainties in Experimental Results," Experimental Thermal and Fluids Science, Vol. 1, No. 1, pp. 3-17.

Moreira, L., and Soares, C. G., 2003, "Dynamic model of manoeuvrability using recursive neural networks," Ocean Engineering, Vol. 30, Issue 13, pp. 1669-1697.

"Nomenclature for Treating the Motion of a Submerged Body through a Fluid," SNAME Technical and Research Bulletin 1-5, 1952.

Nomoto, K., 1975, "Ship response in directional control taking account of frequency dependent hydrodynamic derivatives," Proceedings of the 14th ITTC, Ottawa, Canada, Vol. 2, p.408-413.

Norrbin, N.H., 1971, "Theory and Observations on the Use of a Mathematical Model for Ship Manoeuvring in Deep and Confined Waters", SSPA, Gothenburg, Sweden, Publication No. 68.

Olivieri, A., Pistani, F., Avanzini, A., Stern, F., and Penna, R., 2001, "Towing Tank Experiments of Resistance, Sinkage and Trim, Boundary Layer, Wake, and Free surface Flow Around a Naval Combatant INSEAN 2340 Model," IIHR Report No. 421, Iowa Institute of Hydraulic Research, University of Iowa, 56 pp.

Olivieri, A., Pistani, F., Wilson, R., Benedetti, L., La Gala, F., Campana, E. F., and Stern, F., 2004, "Froude Number and Scale Effects and Froude Number 0.35 Wave Elevations and Mean-Velocity Measurements for Bow and Shoulder Wave Breaking of Surface Combatant DTMB 5415," IIHR Report No. 441, IIHR-Hydroscience and Engineering, University of Iowa, p 62.

Oltmann, P., 1992, "Coefficient Estimation," Hamburg Ship Model Basin, Internal Report, Unpublished.

Oltmann, P., 2000, "25 years Computerized Planar Motion Carriage at HSVA – A resume," International Workshop on Ship Manoeuvrability at the Hamburg Ship Model Basin, Hamburg, 2000.

Oltmann, P., 2003, "Identification of Hydrodynamic Damping Derivatives – a Pragmatic Approach," MARSIN'03, pp. RC-3.

Paik, B. G., Lee, C. M., and Lee, S. J., 2004, "PIV Analysis of Flow Around a Container Ship Model With a Rotating Propeller," Exp. Fluids, 36, pp. 833-846.

Pankajakshan, R., Remotigue, S.H., Taylor, L.K., Jiang, M., Briley, W.R. and Whitfield, W.R., 2002, "Validation of Control-Surface Induced Submarine Maneuvering Simulations using UNCLE", 24th ONR Symposium on Naval Hydrodynamics, Fukuoka, Japan.

Prasad, A., 2000, "Stereoscopic particle image velocimetry," Experiments in Fluids 29:103-116.

Prasad, A.K., & Adrian, R. J., 1993, "Stereoscopic particle image velocimetry applied to liquid flows," Experiments in Fluids 15:49-60.

Ratcliffe, T. J., Mutnick, I., and Rice, J., 2001, "Stern Wave Topography and Longitudinal Wave Cuts Obtained on Model 5415, With and Without Propulsion," NSWCCD-50-TR-2000/028, Bethesda, Maryland.

Roth, G. I., Mascenik, D. T., and Katz, J., 1999, "Measurements of the Flow Structure and Turbulence Within a Ship Bow Wave," Phys. Fluids, 11, pp. 3512-3523.

Sakamoto, N., 2009, "URANS and DES Simulations of Static and Dynamic Maneuvering for Surface Combatant," Ph.D. thesis, The University of Iowa, Iowa City, Iowa, USA.

Scarano, F., David, L., Bsibsi, M., and Calluaud, D., 2005, "S-PIV comparative assessment: image dewarping+misalignment correction and pinhole+geometric back projection," Experiments in Fluids 39:257-266.

Simonsen, C. D., and Stern, F., 2003a, "Verification and validation of RANS manoeuvring simulation of Esso Osaka: effects of drift and rudder angle on forces and moments," Computers & Fluids, Vol. 32, No. 10, pp. 1325 – 1356.

Simonsen, C. D., and Stern, F., 2003b, "Flow pattern around an appended tanker hull form in simple maneuvering conditions," 8th International Conference on Numerical Ship Hydrodynamics, Busan, Korea.

Simonsen, C. D., and Stern, F., 2003c, "RANS maneuvering simulation of ESSO Osaka with rudder and body-force propeller," 15th International Conference on Hydrodynamics in Ship Design, Safety and Operation, Gdansk, Poland.

Simonsen, C., 2004, "PMM Model Test with DDG51 Including Uncertainty Assessment," Force Technology Report No. ONRII187 01, 145 pp.

Simonsen, C. D., Stern, F., and Agdrup, K., 2006, "CFD with PMM test validation for manoeuvring VLCC2 tanker in deep and shallow water," MARSIM 2006, Terschelling, Netherlands, M-4-1.

Simonsen, C. D., and Stern, F., 2006, "Flow structure around maneuvering tanker in deep and shallow water," 26th ONR Symposium on Naval Hydrodynamics, Rome, Italy.

Stern, F., Longo, J., Penna, R., Olivieri, A., Ratcliffe, T., and Coleman, H., 2000, "International Collaboration on Benchmark CFD Validation Data for Naval Surface Combatant," Invited Paper, Proceedings 23rd ONR Symposium on Naval Hydrodynamics, Val de Reuil, France.

Stern, F., Wilson, R. V., Coleman, H., and Paterson, E., 2001, "Comprehensive Approach to Verification and Validation of CFD Simulations-Part 1: Methodology and procedures," ASME J. Fluids Eng., Vol. 123, Issue 4, pp. 793-802.

Stern, F., Olivieri, A., Shao, J., Longo, J., and Ratcliffe, T., 2005, "Statistical Approach for Estimating Intervals of Certification or Biases of Facilities or Measurement System Including Uncertainties," ASME J. Fluids Eng., Vol. 127, No 2, pp. 604-610.

Stern, F., and Agdrup, K., Editor, 2008, SIMMAN 2008 Workshop on verification and validation of ship maneuvering simulation methods: Volume 1 and Volume 2, Lyngby, Denmark.

Strøm-Tejsen, J. and Chislett, M.S., 1966, "A Model Testing Technique and Method of Analysis for the Prediction of Steering and Manoeuvering Qualities of Surface Vessels", Hydro & Aerodynamic Laboratory Report No. Hy-7, Lyngby, Denmark.

Tahara, Y., Longo, J., and Stern, F., 2002, "Comparison of CFD and EFD for the Series 60 CB=0.6 in steady drift motion", Journal of Marine Science and Technology, Vol. 7, N. 1, pp. 17-30.

Tanaka, S., and Kimura, K., 2003, "A Numerical Study on Hydrodynamic Interaction among Oblique Ship Hull, Propeller and Rudder", International Conference on Marine Simulation and Ship Maneuverability (MARSIM 2003), Kanazawa, Japan, pp RC-21.

Toxopeus, S., 2006, "Calculation of hydrodynamic manoeuvring coefficients using viscous-flow calculations," ICHD 2006, Ischia, Italy.

Toxopeus, S. L., and Lee, S. W., 2008, "Comparison of manoeuvring simulation programs for SIMMAN test cases," SIMMAN 2008, Copenhagen.

US Guide to the Expressions of Uncertainty in Measurement (American National Standards Institute) 2000 ANSI/NCSL Z540-2-1997

Viviani, M., Depascale, R., Sebastiani, L., Bonvino, C. P., Dattola, R., and Soave, M., 2003, "Alternative Method for the Identification of Hydrodynamic Coefficients from Standard Manoeuvres," MARSIM '03, p. RC-5.

Wagner-Smitt, L., 1971, "Steering and Manoeuvring of Ships – Full Scale and Model Tests", European Shipbuilding, Vol. 19, No. 6, 1970, and Vol. 20, No.1.

Wagner Smitt, L., and Chislett, M. S., 1974, "Large amplitude PMM tests and manoeuvring predictions for a Mariner class vessel," 10th Symposium on Naval Hydrodynamics, Boston, USA, p.131-157.

Wehausen, J. V. and Laitone, E. V., 1960, "Surface waves," Encyclopaedia of Physics, Vol. 9, p.446-778, Springer Verlag, Berlin, Germany.

Willert, C., 1997, "Stereoscopic digital particle image velocimetry for application in wind tunnel flows," Meas. Sci. Technol. 8:1465-1479.

Williams, C. A., Jr., 1950, "One the Choice of the Number and Width of Classes for Chi-Square Test of Goodness of Fit," J. Am. Statistical Assoc., 45, pp. 77-86.

Wilson, R. V., Nicholas, D. S., Mitchell, B., Karman Jr., S. L., Betro, V. C., Hyams, D. G., Sreenivas, K., Taylor, L. K., Briley W. R., and Whitfield, D. L., 2007, "Simulation of a Surface Combatant with Dynamic Ship Maneuvers," 9th Numerical Ship Hydrodynamics Conference, Vol. I, pp. 208-223.

Xing, T., Shao, J., and Stern, F., 2007, "BKW-RS-DES of Unsteady Vortical Flow for KVLCC2 at Large Drift Angles," 9th Numerical Ship Hydrodynamics Conference, Vol. I, pp. 172-190.

Yoon, H. K. and Rhee, K. P., 2003, "Identification of hydrodynamic coefficients in ship maneuvering equations of motion by Estimation-Before-Modeling technique," Ocean Engineering, Vol. 30, Issue 18, pp. 2379-2404.

Yoshimura, Y., and Ma, N., 2003, "Manoeuvring prediction of fishing vessels", Proc. of MARSIM'03, pp RC-29.